Dissertation

Novel Approach for Organic Devices Based on Doped Crystalline Layers

"How to make everything from rubrene"

Franz Michael Sawatzki

Born on: 11.06.1990 in Räckelwitz

to achieve the academic degree

Doctor rerum naturalium (Dr. rer. nat)

Contents

Abstract

Abstract

The main motivation of this thesis was originally the realization of the Organic Bipolar Junction Transistor (OBJT), an electronic device that has not been shown in literature yet. Its functionality is intimately tied to minority charge carrier diffusion. However, diffusion lengths are usually low in amorphous organic semiconductors. Thus, methods regarding the growth and doping of thin-films of crystalline rubrene crystals are investigated. The higher degree of order provided by crystals makes longer diffusion lengths possible.

The first part of this thesis studies the growth of different crystal polymorphs of rubrene on various substrates and changing conditions, including the influence of doping on the growth process. Three crystal phases are optimized for reproducible processing and investigated via structural measurements. The analysis of the crystal properties is followed up by a study of vertical conduction properties of pristine, p-doped, and n-doped crystals. All three types of crystals are successfully doped. The analysis reveals record-high vertical charge carrier mobilities for the triclinic polymorph of the thin-film form of rubrene.

The second part of this thesis presents electronic devices based on these layers. At first, organic Schottky, pn, and pin diodes are discussed, including the influence of the individual layers on the electric properties. As an exemplary application, half-wave rectifiers operating in the GHz-regime are studied, representing the fastest organic electronic device to date. Furthermore, Organic Field-Effect Transistors (OFETs) and Vertical Organic Field-Effect Transistors (VOFETs) based on these crystalline thin-films are made, showing promising properties in the field of vertical transistor designs. The last chapter presents investigations of several designs, stacks, and geometries regarding OBJTs. The worlds first functioning OBJT is developed, showing amplification of the input-current. It is the first step towards an entire new class of organic devices, offering not only new technological opportunities, but new aspects of physics in regard to minority carrier diffusion as well.

Kurzdarstellung

Das Hauptziel dieser Arbeit war ursprünglich die Umsetzung des Konzeptes des Bipolartransistors mit organischen Halbleitern. Obwohl dieses elektronische Bauteil eine Grundfeste klassischer Elektronik darstellt, war es bislang nicht möglich Stromverstärkung mit organischen Halbleitern nachzuweisen. Das Prinzip des Bipolartransistors ist eng verknüpft mit der Diffusionslänge der Minoritätsladungsträger. Aufgrund der amorphen Struktur typischer organischer Materialien, sind Diffuionsprozesse in der Regel stark unterdrückt. Eine mögliche Lösung sind organische Halbleiterkristalle, welche aufgrund ihrer Ordnung signifikant längere Diffusionslängen gewährleisten sollten.

Der erste Teil dieser Arbeit untersucht Wachstumsmethoden unterschiedlicher Kristallkonfiguration des Halbleiters Rubrene in Dünnschichtform. Ein besonderer Fokus liegt hierbei auf dem Einfluss von Dotierung auf den Kristallisationsprozess. Drei der Kristallphasen werden auf optimale Reproduzierbarkeit optimiert und umfangreich mit strukturellen Methoden untersucht. Die Strukturanalyse wird erweitert durch Untersuchungen des vertikalen Leitungsverhaltens der unterschiedlichen Kristallphasen in reiner, lochdotierter und elektronendotierter Form. Dünne Schichten aus Rubrene in der triklinen Kristallform zeigen hierbei Rekordwerte für die vertikale Beweglichkeit.

Der zweite Teil dieser Arbeit untersucht elektronische Bauelemente basierend auf diesen Kristallen. Zunächst werden organische Schottky, pn und pin Dioden analysiert sowie der Einfluss der einzelnen Schichten auf die elektrischen Eigenschaften der Bauelemente. Als eine mögliche Anwendung dieser Dioden werden Halbwellengleichrichter untersucht, welche im Bereich über 1 GHz operieren können. Diese stellen somit die zur Zeit schnellsten organischen Halbleiterbauelemente dar. Des Weiteren werden organische Feldeffekttransistoren in lateraler und vertikaler Ausführung untersucht, um den Nutzen dieser Kristallschichten für moderne Transistorkonzepte zu verdeutlichen. Schlussendlich werden Konzepte zur Realisierung eines organischen Bipolartransistors untersucht. Darauf basierend wird das erste Bauelement dieser Art vorgestellt, welche funktionierende Stromverstärkung zeigt. Dies stellt den ersten Schritt in der Untersuchung einer neuen Klasse an organischen Bauelementen dar. Des Weiteren bietet es neue Möglichkeiten der Untersuchung fundamentaler Eigenschaften, im Speziellen im Bezug auf Minoritätsladungsträgerdiffusion.

Abstrakt

Hłowny zaměr tutoho doktorskeho dzěła je realizacija prěnjeho bipolarneho transistora na zakładźe organiskich połwodźakow. Byrnjež je tuta komponenta jedna z najwažnišich a najstaršich w polu klasiskeje elektroniki, njeběše hač dotal móžno priběranje sylnosće na zakładźe milinoweho pruda pokazać. Princip bipolarneho transistora je wusko zwjazany z konceptom diffuzije minoritnych nabitkow. Organiske materialije su zwjetša amorfne, štož na difuziju bazowace procesy potłóči. Problem hodźi so rozrisać hdyž so wužija organiske połwodźace kristale kotřiž jich wjetšeho porjada dla, dlěšu difuziju zmóžnja.

Prěni dźěl dźěła wopisa wšelakore konfiguracije kristalow organiskeho połwodźaka rubren w formje ćenkich worštow. Wosebity fokus leži při tym na dotěrowanju kristalow a wliw dotanta na kristalizaciju. Tři wuzwolene polymorfy so optiměruja a wobšěrnje strukturelnje přepytuja. Dale so elektriske kajkosće wšěch třoch kristalnych fazow přepytuja na zakładźe intrinsiskich, p-dotěrowanych a n-dotěrowanych kristalow. Trikliniske kristale pokazuja rekordne hódnoty za wertikalnu pohibliwosć.

Druhi dźěl wobjednawa elektroniske komponenty na bazy tutych kristalow. Schottky, pn a pin diody na zakładźe rubrena so prezentuja, kaž tež wliw jednotliwych worštow na elektriske kajkosće. Jako prikład so jednore wusměrjaki pokazaja, kotřiž hodźa we wobłuku ultra-wysokich frekwencow nałožować. Potajkim jedna so wo najspěšniše organiske komponenty po nětcišim stawje wedomosće. Dale so organiske transistory na bazy pólneho efekta přepytuja, kotřiž pokazaja hódnosć tutych worštow za elektroniske komponenty kotřiž wužija lateralny a wertikalny transport zromadnje. Posledni dźěl wobjednawa eksperimenty na polu organiskich bipolarnych transistorow. Wopisa so prěni organiski elektroniski element, kiž pokaza posylnjenje signala na zakładźe miliny. Je to prěni krok přepytowanja noweje klasy organiskeje elektroniki, kiž skiči nowe metody přepytowanja fundamentalnych procesow w tutych materialijach.

Publications

- M. Sawatzki, B. Boroujeni, F. Ellinger, H. Kleemann, K. Leo "Organic GHz Electronics based on Doping of Highly Crystalline Rubrene Thin-Films". submitted an in review at Nature Materials (2020)

- Y. Zheng, A. Fischer, M. Sawatzki, D. H. Doan, M. Liero, A. Glitzky, S. Reineke, and S. C. B. Mannsfeld. "Introducing pinMOS Memory: A Novel, Nonvolatile Organic Memory Device". In: Advanced Functional Materials 30.4 (2020), p. 1907119. doi: 10.1002/adfm.201907119

- F. M. Sawatzki, D. H. Doan, H. Kleemann, M. Liero, A. Glitzky, T. Koprucki, and K. Leo. "Balance of Horizontal and Vertical Charge Transport in Organic Field-Effect Transistors". In: Phys. Rev. Applied 10 (2018), p. 034069. doi:10.1103/PhysRevApplied.10.034069, (Editor's Suggestion)

- F. M. Sawatzki, A. A. Hauke, D. H. Doan, P. Formanek, D. Kasemann, T. Koprucki, and K. Leo. "On Razors Edge: Influence of the Source Insulator Edge on the Charge Transport of Vertical Organic Field Effect Transistors". In: MRS Advances 2.23 (2017), pp. 1249-1257. doi: 10.1557/adv.2017.29

- A. A. Günther, M. Sawatzki, P. Formanek, D. Kasemann, and K. Leo. "Contact Doping for Vertical Organic Field-Effect Transistors". In: Advanced Functional Materials 26.5 (2016), pp. 768-775. doi: 10.1002/adfm.201504377

- A. A. Günther, C. Hossbach, M. Sawatzki, D. Kasemann, J. W. Bartha, and K. Leo. "Controlling threshold voltage and leakage currents in vertical organic field-effect transistors by inversion mode operation". In: Applied Physics Letters 107.23 (2015), p. 233302. doi: 10.1063/1.4937439

Conferences

- F. M. Sawatzki, H. Kleemann, and K. Leo, "Rubrene based diodes for rectification applications". SPIE Optics + Photonics, San Diego (2018), Talk

- F. M. Sawatzki, and K. Leo, "Epitactically grown Rubrene single crystal arrays for use in organic transistors", ECME, Dresden (2017), Poster

- F. M. Sawatzki, A. Günther, D. H. Doan, C. Hoßbach, P. Formanek, D. Kasemann, J. Widmer, T. Koprucki, and K. Leo. "Vertical Organic Light Emitting Transistors - Investigation of Charge Transport in VOFETs". 8th School on Organic Electronics : Nano-Organics and Devices, Paris (2016), Poster

- Marco Höppner, A. Günther, M. Sawatzki, J. Widmer, and K. Leo. "Optimizing Vertical Organic Field Effect Transistors". 8th School on Organic Electronics : Nano-Organics and Devices, Paris (2016), Poster

- F. M. Sawatzki, A. Günther, D. H. Doan, C. Hoßbach, P. Formanek, D. Kasemann, J. Widmer, T. Koprucki, and K. Leo. "Vertical Organic Light Emitting Transistors for Investigation of Charge Transport in Vertical Organic Field Effect Transistors". Material research Society Fall Meeting, Boston (2016), Talk

- F. M. Sawatzki, A. A. Günther, D. H. Doan, C. Hoßbach, P. Formanek, D. Kasemann, J. Widmer, T. Koprucki, and K. Leo. "Vertical Organic Light Emitting Transistors for Investigation of Charge Transport in Vertical Organic Field Effect Transistors". Frühjahrstagung der deutschen physikalischen Gesellschaft, Regensburg (2016), Talk

- A. A. Günther, M. Sawatzki, C. Hoßbach, P. Formanek, D. Kasemann, J. Widmer, J. W. Bartha, and K. Leo, "Vertical Organic Field-Effect Transistors - Functional Principles and Applications". Frühjahrstagung der deutschen physikalischen Gesellschaft, Regensburg (2016), Talk

Patents

- M. Sawatzki, and H. Kleemann, "Verfahren zum Überwachen der strukturellen Integrität eines Bauteils und flexible Sensorstruktur zum Überwachen der strukturellen Integrität eines Bauteils".
application number: 2020021810502300DE (2020)

1 Introduction

When thinking about science itself, two general approaches are conceivable. One might assume that every type of research is valuable just for the accumulation of knowledge alone. Thus, as long as the scientific method of empiricism is followed and experiments are comprehensible and reproducible, every result is satisfying. Even when the original theory must be dismissed, the findings do not have any immediate real-world application, or the new material system or device shows no significant improvement compared to the state of the art, each gain in knowledge is valuable for knowledge sake. Experiments like the Large Hadron Collider or the James Webb Space telescope are conceptualized in this "pure" idea, as – in their core – gigantic philosophy machines.

A contrary approach to this is to focus only on "useful" research [1]. Only topics with an actual application or the improvement of existing concepts are worth investigating. The benefits are evident since resources are focused, however, it is usually only possible to judge in hindsight which research and approach were worth pursuing in this sense. For example, the laser was initially regarded as an invention looking for a problem [2]. It later became one of the most important tools in science and technology in general. Other inventions, like the microwave, artificial sweeteners, or penicillin were created on accident. Prior to the rise of solid-state semiconductor transistors, vacuum tubes were king in the field of computation. The resulting computers filled cabinets or even rooms and individual components of the circuits had to be replaced frequently due to the fragile nature of the tubes themselves. In hindsight, the benefits of semiconductor devices are obvious, however, contemporary researchers might have judged differently in this regard, based on the steady progress of vacuum-ray technology and the initially inferior performance of the first transistors. They could have been easily disregarded as novelty toys, lacking any type of real-world application.

Instead, the presentation of the first Bipolar Junction Transistor (BJT) by W. Shockley, J. Bardeen, and W. Brattain [3] on the 23rd of December 1947 kick-started the micro-electronic revolution that – presumably – would not have been possible to realize with the "old" technology. Once again, the discovery was more of an accident, since the original intent was to built the Field-Effect Transistor (FET), whose principle was predicted by Julius Edgar Lilienfeld in 1925 [4]. Further significant improvement of the concept was introduced on the 12th of April 1950 by G. Teal, M. Sparks, and W. Shockley with the first bipolar junction transistor [5]. Further research and steady progress made these devices far superior to all prior technologies, especially since the invention of the Metal-Oxide-Semiconductor Field-Effect Transistor (MOSFET) in 1959 by M. Atalla and S. Kahng [6], made the mass production of electronics possible.

The field of organic semiconductor-based electronics tells a similar story. Research on materials started in the 60s, however, even to this day, the performance defining parameter – the charge carrier mobility – always lags behind inorganic semiconductors. Only when in 1987, C. Tang and S. Van Slyke presented the

first efficient two-layer Organic Light Emitting Diode (OLED) [7], the specific properties of organic materials could be utilized. Flexibility, transparency, thin-film processing, low material consumption, naturally wide optical spectra are a few of the many advantages of organic molecular semiconductors.

Today, OLEDs are standard technology for display technology, illuminating smartphones and screens alike. They are part of a multi-billion dollar market that was not conceivable 30 years ago. Although not all of these applications were quite so commercially successful, over time, many more electronic devices were realized using organic semiconductors. Some are direct copies of inorganic counterparts, like the organic solar cell (Tang et al. in 1986 [8]), the Organic Field-Effect Transistor (OFET) (Koezuka et al. in 1987), or the optically excited organic laser (N. Tessler in 1995). Other ideas take the specific properties and possibilities offered by organic materials into account, such as the light-emitting transistors [9], electrochemical transistors [10], or infrared-detectors [11]. However, some device types common in inorganic electronics are noticeably absent, namely the Organic Bipolar Junction Transistor (OBJT) and the electrically driven lasers. That is by no means an accident but the result of the distinct short-comings of organic semiconductors in regard to charge carrier mobility, diffusion length, purity of materials, and ease of doping. The main goal of this thesis is to realize a functioning OBJT. Arguing along the lines discussed earlier, the value of researching these not yet realized concepts in organic semiconductors is twofold. First, the analysis and discussions that lead towards this goal enrich the scientific discourse in itself, while each small discovery along the way might have its own purpose or later use. On the other hand, inorganic BJTs have certain advantages compared to FETs that make their use favorable in certain applications, mainly in regard to linearity, noise, and maximum frequency of operation. Having the choice of transistor type can certainly not be a disadvantage for circuits based on organic electronics. Thus, this discovery might be the missing impetus needed to push organic transistor technology towards a commercial application.

The BJT is a device-dependent on charge carrier diffusion, a process that is heavily suppressed in organic semiconductors due to their amorphous nature. The route chosen in this thesis is to overcome this problem by using a highly-ordered system, in the form of crystalline films. The crystallinity – order – of these films allows for processes to take place efficiently that are not possible in amorphous materials. The material chosen here is rubrene which is a well-known and well-investigated organic semiconductor. A special method is employed to grow rubrene poly- and single-crystals on substrates, combining the advantages of thin-film processing with high crystallinity.

The following thesis is split into several parts. First, a brief introduction into the structure of organic molecular solids is given, with a special focus on crystalline systems. This introduction includes an analysis of growth methods for these organic crystals. The chapter continues with a description of charge transport

in organic semiconductors in general and the working principles of a selection of electronic devices. A special focus is on organic Schottky, pn, and pin diodes and, based on these, on BJTs. The second chapter describes the techniques, tools, and concepts used for this work to manufacture and analyze crystals, thin-films, and entire electronic devices. The third chapter gives a technical summary of the materials and used electrode designs, including some of the relevant material properties. Finally, the next four chapters present the results of studying the previously described rubrene crystals and devices made from these layers. First, an extensive description of the crystallization process is given, investigating the properties of crystal phases grown under different conditions. This summary provides sets of optimal parameters for the three crystal polymorphs used in devices. The second half of the fourth chapter is describing the electrical properties of these films, with a focus on p- and n-type doping, including an analysis of vertical charge carrier mobility using Space Charge Limited Currents (SCLCs). Chapter five gives the first devices based on these films in the form of Schottky, pn, and pin diodes. The influences of each of the individual layers on the properties of the diode are thoroughly discussed. In the end, two applications for the diodes are investigated: high-power OLEDs and half-wave rectifiers operating in the Ultra High Frequency (UHF) regime. The next chapter presents a preliminary analysis of these films for use in OFETs and Vertical Organic Field-Effect Transistors (VOFETs). Finally, in the last chapter, experiments regarding the implementation of an OBJT are presented.

2 Theoretical Background

To fully understand the functionality of semiconductor devices, which parameter influences what, which part is important for which process, and which material should be chosen or changed to realize or optimize a certain aspect, it is of great importance to follow the underlying physics of the problem at hand. The following chapter gives an introduction to the fundamentals necessary to understand the experiments and basic concepts. However, only short summaries are given. References – books and scientific review articles – are provided at the beginning of each topic.

This chapter is divided into three parts. Since growth and analysis of molecular crystals are important aspects, the first chapter discusses the fundamentals of the structure of organic solids. The second section is dedicated to electronic processes in these materials. This includes charge transport, diffusion, and doping. The last part is based upon the first two and features the basics of specific electronic devices and discusses: diodes, Field-Effect Transistor (FET), and Bipolar Junction Transistor (BJT). Each of the sections contains a subsections discussing the topic of each part on the material system rubrene. This organic semiconductor is used to fabricate all of the electronic devices shown in this thesis due to unique properties. Accordingly, the structural features of this material are highlighted in the first section, while the electrical properties are discussed in the second.

2.1 Structure of Organic Solids

The internal structure has an enormous impact on many aspects of a solid. From mechanical stability over chemical inertness to optical and electrical properties, almost every parameter is determined not directly by the building blocks alone, but heavily by their arrangement. The material system used in this thesis is in a gray area between amorphous structures – often found in organic solids – and well-organized crystals that can be found in many inorganic semiconductors and metals. Therefore, this chapter takes a closer look into the different types of bonds that occur in solids (2.1.1) and the resulting crystal structures (2.1.2). Additionally, a discussion of crystal growth follows, to elucidate the specifics of growing these kinds of crystals (2.1.3). The specific properties of charge transport that result from the different forces and structure in these organic materials that distinguish them from common inorganic materials id then discussed in the next section 2.2.

2.1.1 Atomic Bonds

The structural properties of solids are heavily dependent on the bonds between their individual parts. The dominant type of bond determines the binding energy and cohesion of the system, as well as its electronic and vibrational properties. It is typically differentiated into ionic bonds, metallic bonds, valence bonds, Van der Waals bonds, and hydrogen bonding. A description can be found in any book covering solid-state physics (e.g. [12] or [13]). The following chapter gives a short overview focusing on the specific properties relevant for molecular crystals.

Ionic bonds are dominant between different atoms with a large difference in electronegativity. The binding force is based on the Coulomb attraction of permanent dipoles originating from shifted electrons. Metallic bonds are present in most metals. The delocalization of free electrons over the full crystal allows for a decreased energy of the system and, therefore, an effective binding. Hydrogen bonding occurs in some molecular systems containing hydrogen atoms. It is a weaker form of ionic bonding. Although these types of bonds are prominent in many materials (e.g. metals and salts), they are only of minor importance for the semiconductors investigated here.

Covalent Bonding   Covalent bonds occur in most inorganic semiconductors (e.g. silicon) and organic molecules as the intramolecular force. Electrons are localized between atoms to fill up atomic electronic orbitals and minimize the energy of the system. The resulting molecular orbitals can be approximated using the method of Linear Combination of Atomic Orbitals (LCAO). The atomic wave functions of the individual atoms are superposed to find the setup with the lowest total energy.

Many classic inorganic semiconductors are formed with covalent bonds. The bonding strength is high compared to Van der Waals bonding, but weaker than typical ionic or metallic bonds.

material	phase	binding energy per atom in eV
C	diamond	7.36 [12]
C	C-C single bond	3.6 [14]
C	C-C double bond	6.2 [14]
Si	diamond	4.64 [12]
Ge	diamond	3.87 [12]

Table 2.1: Typical binding energies of covalent bonds.

Van der Waals Bonding   Van der Waals bonding is the weakest of the common bond types, with the shortest interaction distance, mostly acting only between nearest neighbors. This force is only relevant if none of the other binding mechanisms apply. This is, for example, the case for noble gases, because of their saturated electronic configurations that cannot interact via covalent bonding. Noble gases usually form solids only at low temperatures, when the thermal energy is lower than the binding energy.

The force is based upon fluctuating dipole-dipole interaction. Atoms will induce an oscillating dipole moment p_i when in vicinity of each other. These two dynamic dipoles lead to lowering of the energy of the system and hence bonding between

the atoms. The dipole creates a field of $E = \frac{p_1}{r^3}$ and a binding potential of

$$\phi = -\frac{1}{2\pi\epsilon_0}\frac{p_1 p_2}{r^6} = -\frac{B}{r^6}, \tag{2.1}$$

while B describes the polarizability of the partners. For simple, isotropic systems (e.g. noble gases), B is a scalar – this changes for molecular solids.

The attractive force is heavily dependent on the distance between the partners of the bond, which is of significant importance for molecular solids. For close distances, the Pauli principle excludes overlap of electronic orbitals, thus a repellent force of sufficient strength must be added. A possible description is the well established Lennard-Jones potential:

$$\phi = \frac{A}{r^{12}} - \frac{B}{r^6} = 4\epsilon\left[\left(\frac{\sigma}{r}\right)^{12} - \left(\frac{\sigma}{r}\right)^6\right], \tag{2.2}$$

with ϵ being the depth of the potential and σ the zero-crossing or A and B as modeling parameters.

To obtain the binding energy within a solid, the corresponding energies in equilibrium between all pairs of atoms must be summed up. Usually, summing over nearest neighbors is sufficient. The resulting binding energies for noble gas crystals are in the range of dozens to hundreds of meV (see table 2.2) and are thus significantly weaker than ionic, metallic, and covalent bonding.

material	binding energy per atom in meV
Ne	20 [12]
Ar	81 [12]
Kr	116 [12]

Table 2.2: Typical binding energies of noble gas crystals.

Van der Waals Bonding in Organic Solids   In molecular solids, two different forces are present: the intramolecular forces binding the individual atoms to form a molecule and the extramolecular forces to form the solid. In the case of organic semiconductors, the inner bonds are usually covalent and sometimes ionic, while the outer bonds are commonly of Van der Waals type. The strength of the internal covalent bonds is significantly stronger than the external forces, such that the individual properties of the molecules stay intact much more compared to fully covalently bound systems. One can, therefore, describe molecular solids as a type of oriented gas, with molecules as particles.

In contrast to condensed noble gases, organic molecules can show an effective outer dipole or multipole moment. Thus, additionally to the induced dipole-dipole interaction, permanent dipoles can add to the bond. For many aromatic (and thus symmetric) organic compounds – like rubrene – there is no permanent resulting dipole moment.

Since these molecules usually do not have spherical symmetry, the polarizability will be anisotropic – e.g. the different polarizability of σ- and π-bonds. For static and non-static dipoles, the potential of two dipoles that are not aligned but rotated by an angle β can be written as:

$$\phi = -\frac{1}{2\pi\epsilon_0} \frac{p_1 p_2}{r^6} \left(3\cos^2(\beta) - 1\right). \tag{2.3}$$

Additionally to the strong dependence on the distance ($\frac{1}{r^6}$), a strong dependence on the orientation of the molecules is introduced ($3\cos^2(\beta)$).

There is much more variation in the properties of organic molecules compared to the small set of nobles gas atoms. Some typical values of binding energies are summarized in table 2.3.

material	binding energy meV	-
alkane molecules	73 [15]	per CH_2-group
neighboring π-systems in crystals	10-100 [16]	-

Table 2.3: Typical binding energies of molecular Van der Waals crystals.

2.1.2 Crystal Structure

The driving force during the formation of a solid is the minimization of the total energy of the system. As discussed in the previous section, different binding mechanisms can occur, resulting in different strength and energy scales. The general concepts, however, are the same for most types of solids. In this section, only the driving factors for a specific crystal structure and its description are discussed, the importance and influence of the crystal structure will be highlighted in chapter 2.2.2, focused on charge transport and diffusion.

The difference between an amorphous and a crystalline solid is in the periodicity (position and orientation) of its building blocks. However, even amorphous materials can show a certain degree of ordering on short scales, to minimize the interaction energy between direct neighbors. The influence of building blocks further away is usually negligible. The energy of the total solid is thus not as minimized as it would be in a perfectly ordered system. Figure 2.1 depicts the difference between single-crystals, poly-crystals and, amorphous materials. Amorphous structures feature no significant large scale ordering, while single-crystals have perfect translational order throughout the entire solid (with
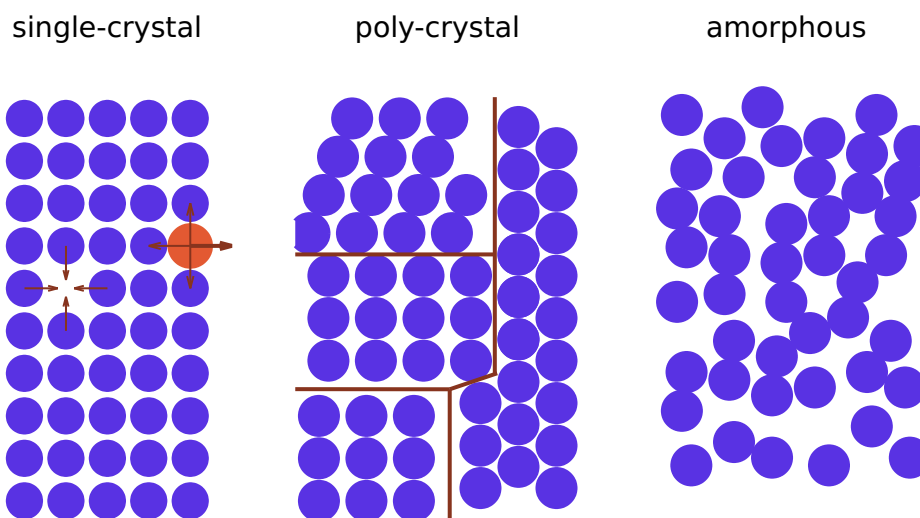
single-crystal   poly-crystal   amorphous

Figure 2.1: Schematic depiction of ordering in single-crystalline, poly-crystalline, and amorphous solids: Electronic states are delocalized over an entire grain in a crystal. Grain boundaries in poly-crystals are scattering spots for charge transport, traps for charge carriers, and recombination centers. Charge carriers are localized on individual points in amorphous solids. Charge-transfer is dominated by hopping from site to site.
red: Resulting effective forces in a single-crystal as a result of missing lattice point, foreign atom, or the surface. Fault lines are marked in the poly-crystalline solid.

exception of certain defects). Poly-crystals lie in between, showing high order on a medium scale, but randomness over a large volume.

For many inorganic solids and especially inorganic metals or semiconductors (like silicon), the building blocks are more or less "spherical" atoms. As a result, the energy of the system is the smallest when the individual parts are packed the closest. However, the force between two atoms must not necessarily be isotropic. For example, because of its sp^3-hybridization, silicon favors a tetragonal orientation to its neighbors and is thus crystallizing in a zinc-blende or diamond structure, instead of a denser packing.

When describing the crystal structure, several different approaches can be chosen, beginning from attributing lattice points to the individual repeating building blocks. The lattice points are called "the basis" of the lattice and can consist of single atoms, groups of atoms, molecules, or groups of molecules. The primitive unit cell describes the smallest possible volume around one lattice point, which – when repeated infinitely – describes the entire solid without overlap or gaps. Although this is technically all that is needed for a complete description, the choice of shape of this unit cell is arbitrary and can hide symmetries that are present in the structure if a larger volume is taken into account (i.e. more than one lattice point).

There are 14 so-called Bravais lattices that are not equivalent to each other. A selection relevant for later discussion is depicted in figure 2.2. Symmetric shapes of the base (i.e. spheres) and isotropic binding forces, favor lattices of higher
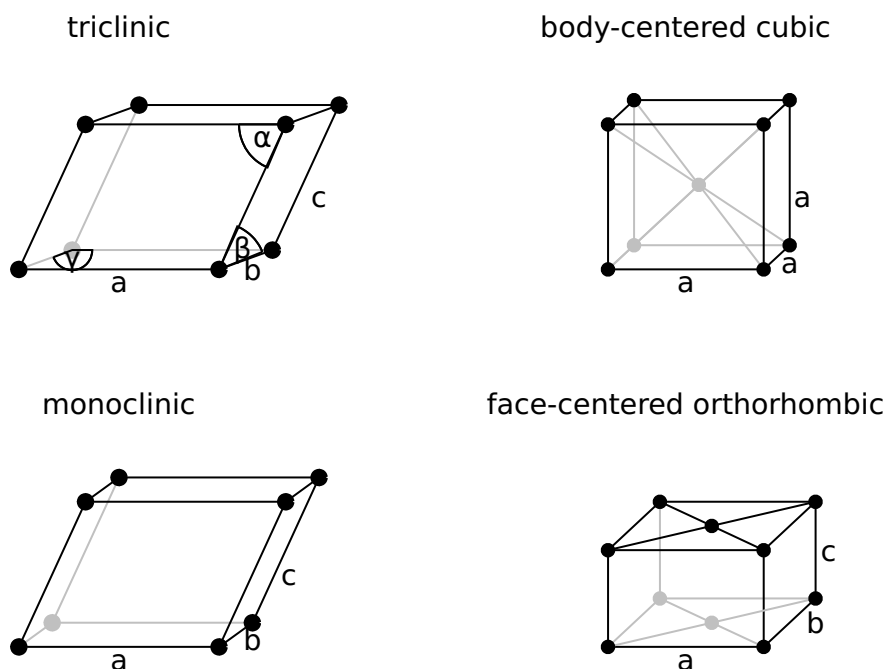
triclinic

body-centered cubic

monoclinic

face-centered orthorhombic

Figure 2.2: 3D-depiction of selected Bravais lattices:
triclinic: $a \neq b \neq c$, no angle 90° and $\alpha \neq \beta \neq \gamma$: lowest possible symmetry
monoclinic: $a \neq b \neq c$, $\alpha = 90°$, but $\alpha \neq \beta \neq \gamma$
body-centered cubic: $a = b = c$, $\alpha = \beta = \gamma = 90°$ (Highest possible packing density.) –
bcc features an additional lattice point in the middle of the simple cubic lattice. [Not
shown: face-centered cubic, simple cubic.]
base centered orthorhombic: $a \neq b \neq c$, but $\alpha = \beta = \gamma = 90°$ – bco features an additional
lattice point in the middle of the top and bottom faces, defined by the two longer axis.
[Not shown: simple orthorhombic, face-centered orthorhombic, and body-centered
orthorhombic.].

symmetries. As a result, inorganic solids are often of cubic- or hexagonal-type.
On the other hand, the building blocks for organic semiconductors are comparably
large molecules, often irregularly shaped, as discs or strings. Additionally, the
forces involved are highly anisotropic. As a result, many organic solids crystallize
– if at all – in a triclinic structure with only a low degree of symmetry. Typical
packing arrangements for organic molecular solids are herringbone or brick wall
formations, with varying degrees of offset. A selection is shown in figure 2.3.
In contrast, the main material used in this thesis – rubrene – can, among others,
crystallize in an orthorhombic base centered crystal structure. The results are
sheets of rubrene, bound to each other via π-electrons at a distance c, while the
molecules within each sheet are bound by Van der Waals forces. The orientation
of molecules in this crystal structure is depicted in figure 2.10. Since the rubrene
molecule is not circularly symmetric, the distance between molecules along the
long axis and along the short axis is not the same. The lattice constants are labeled
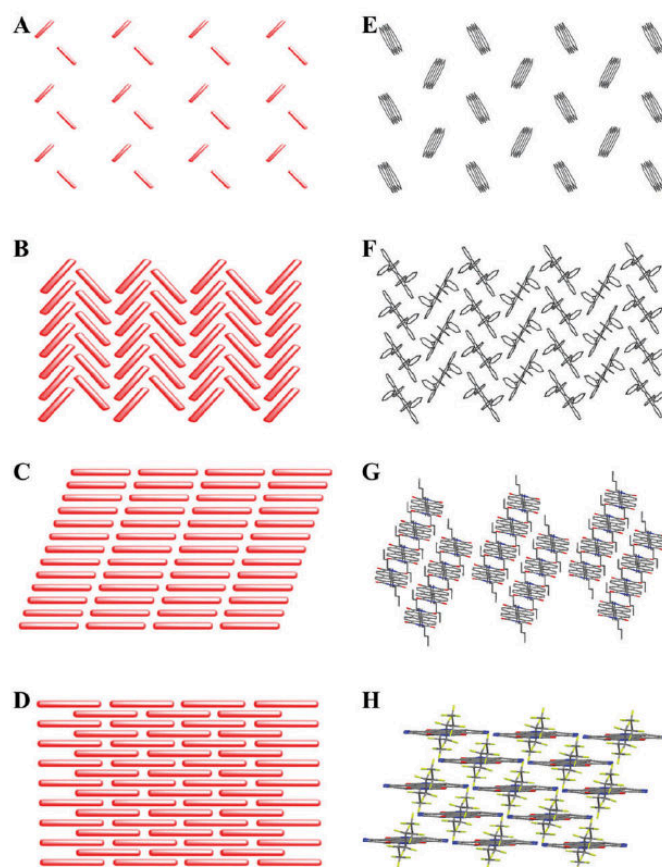
Figure 2.3: Molecular crystal packing of common organic semiconductors (left: schematic representation, right: molecular orientation). A: Herringbone structure without $\pi - \pi$ stacking (e.g. pentacene), B: Herringbone structure with $\pi - \pi$ stacking (e.g. rubrene), C: Brick-wall structure with in-line (1D) $\pi - \pi$ stacking (e.g. C_8–PTCDI), D: Brick-wall structure with lamellar (2D) $\pi - \pi$ stacking (e.g. TIPS–PEN). Figure taken from [17].

with a, b, and c, respectively[1]. This illustrates the different influences of shape and size of the molecule and the binding forces.

Especially organic solids do not necessarily crystallize in one single-crystal structure at all times. Rubrene, for example, can crystallize into orthorhombic single-crystals, orthorhombic poly-crystals and mixed phases consisting of orthorhombic and triclinic parts, from the methods shown in this thesis alone (see chapter 4.1). Other crystal phases, such as monoclinic states and other mixed configurations have been described in literature (e.g. Fielitz et al. [19]). Table 3.6 in chapter 3.3 presents a summary of lattice constants measured for rubrene fabricated with different methods. This phenomenon is called polymorphism. Thus, depending on the external parameters, several different minima in the energy of the system can be reached. The relevant parameter is the Gibbs free energy G, describing the maximum amount of heat and mechanical work that can be exchanged with its surroundings under constant temperature, pressure, and number of particles. A certain crystal phase can be a local minimum (in G)

---

[1]Note that because of the base centered nature of the crystals structure, the distance between nearest neighbors of molecules is smaller than b or c.

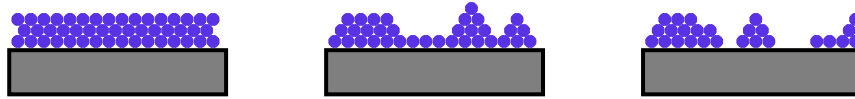Frank-van-der-Merwe   Stranski-Krastanov   Volmer-Weber

Figure 2.4: Growth modes of organic thin-films:
Frank-van-der-Merwe: Surface adhesive forces are stronger than the cohesive forces between the molecules, results in layer by layer growth.
Stranski-Krastanov: Surface adhesive forces are stronger than cohesive forces for the initial layers. Strain inside the layer causes a change in the energetic landscape resulting in a reversal of sign in $\frac{d\mu}{dn}$. The result is layer by layer growth in the beginning and island growth beginning at a certain critical thickness.
Volmer-Weber: Surface adhesive forces are weaker than cohesive forces, results in island growth.

and thus reasonably stable, even though a more favorable crystal structure would exist. This happens when the energy barrier to reach that other state is larger than the thermal energy. Which minimum in Gibbs energy is realized can be described by the Curtin-Hammett principle depicted in figure 2.5: Decisive is not only the absolute energy of the final system but also how fast a state or configuration can be established. A high energetic barrier towards the energetically favorable state (at $G_{\text{thermodyn.}}$ below the starting energy) can slow down the transformation process significantly. The crystal can be transformed into a competing, energetically higher, state (at G_{kinetic} below the starting energy) that can be established faster before any significant part of the crystal is at $G_{\text{thermodyn.}}$. An even higher energetic barrier is then suppressing the transformation into the deeper state. As a result, not necessarily the energetically favored state is reached, but the state that can be established the fastest.
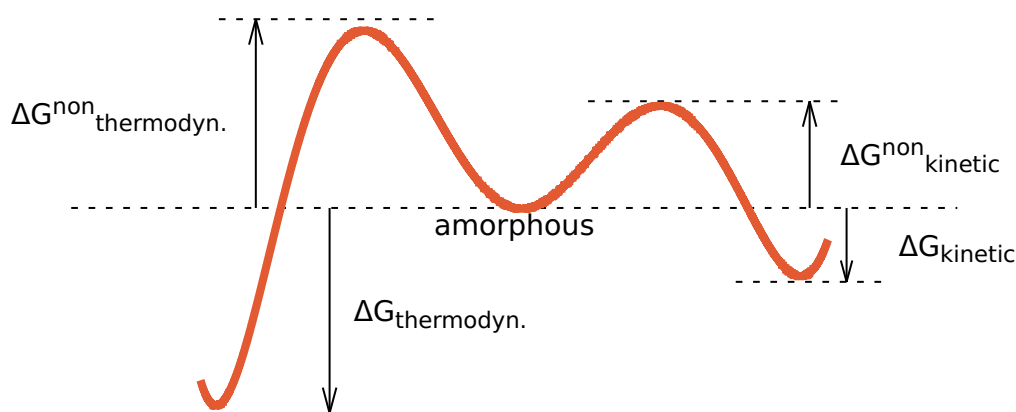
Figure 2.5: Model system for the Curtin-Hammett principle: From an amorphous starting state (e.g. from solution), two energetically more favorable configurations can be reached: A thermodynamically more stable state – with a free enthalpy $\Delta G_{\text{thermodyn.}}$ lower than the starting energy and an activation barrier of $G^{non}_{\text{thermodyn.}}$ – and an energetically less favorable state – at $\Delta G_{\text{kinetic}}$, with an activation enthalpy of $\Delta G^{non}_{\text{kinetic}}$. Although the thermodynamic state has lower final system energy, the route to the kinetic state is significantly faster due to the lower activation barrier. Not necessarily the energetic lowest state is reached, but the fastest (for similar activation energy, the energetically lowest state is reached). Figure according to [18].

2.1.3 Growth of Organic Crystals

Since one focus of this thesis is the growth and investigation of thin, highly crystalline layers of rubrene, some basics of organic crystals are discussed. Similar to the vast amount of different organic molecules, there are many different types of organic molecular solids. The focus will be on non-polar crystals, for which Van der Waals forces are defining. An overview of organic molecular solids can be found in [20] by Schwoerer et al., while a particular focus on the simulation of molecular arrangement in growing films of crystals is given by Gilmer et al. [21]. Recent developments in the formation of highly ordered films, mostly for use in organic thin-film transistors, have been presented by Liu et al. [22]. The following chapter gives a short overview of the most common methods for growing high-quality organic crystals in general; their benefits and weak points, with the special focus on use in organic thin-film devices. Additionally, spherulitic and dendritic growth are highlighted. The last part is presenting the state of the art in rubrene crystals found in literature.

2.1.3.1 Growth Methods of Organic Crystals

Many organic materials form amorphous solids because of their weak intermolecular interaction. Special precautions have to be made to enable the organization

into ordered structures, i.e. poly-crystals and single-crystals. Several methods are used, depending on the material, desired quality of the crystal, and time constraints. A general categorization is into crystals grown from gas -phase, melt, or solution.

Solution-based approaches are usually based upon the evaporation of the solvent from a prepared thin-film (by spin, spray, or dip-coating). A review of recent techniques for generating high-quality, well-oriented crystalline layers can be found in [23], by Li et al. The quality of the film depends delicately on the vapor pressure and temperature of the evaporation process, as well as the exact concentration of the solution. To obtain large, high-quality crystals, an additional concern is the reduction of condensation centers. Large, highly ordered films can be pulled from solution as Langmuir-Blodget films. However, their use is limited due to the specific requirements for the molecules in use.

Other techniques to generate films from solution are shear- and blade coating. Here, a knife or cantilever edge is moved through the liquid during the evaporation process, creating a defined density gradient at the growth front and streamlining the crystallization process [24].

Crystals from melt can be made for example via the Bridgman process. A zone of temperature above the melting point is moved through the solid. This process additionally serves as a purification step, since imperfections are gathered at the start and end of the heating zone. This procedure allows for large crystals, although their quality is lower than with other methods [20].

Growing crystals from the gas-phase is by far the most common and universal method. Additionally, it creates the highest purity solids. The two most common procedures are vacuum evaporation and molecular-beam-epitaxy. The material is evaporated or sublimed and condenses on a cooler substrate. The temperature and surface properties of the surface are of paramount importance. If a molecule hits the substrate at temperatures close to $0\,\mathrm{K}$, the molecule is stuck in the position and orientation it arrived. The result is an amorphous and low-density film. At higher temperatures, the thermal movement and vibration of the molecules allow for transport on the surface and reorganization to energetically more favorable configurations. However, if the temperature is too large, entropy will render the formation of any crystalline order unlikely. For these methods, only slow growth rates are applicable to give arriving molecules enough time to arrange into the existing crystal structure.

An additional aspect important for crystalline thin-films and amorphous layers, is the interaction with the substrate. One of the key aspects is the surface energy between two materials ϵ [25], quantified by the change of chemical potential at the surface $\frac{d\mu}{dn}$ when adding more molecules. An overview of the importance of surface energies on nm-sized system can be found in [26]. If the interaction between the molecules is stronger than between molecules and substrate ($\frac{d\mu}{dn} > 0$), layers grow islands first (e.g. Au or pentacene on SiO_2 [27]). This growth mode

is called Volmer-Weber growth. If the substrate interaction is favored ($\frac{d\mu}{dn} < 0$), the material covers the whole area before increasing in thickness. The result is a layer by layer growth mode called Frank-van-der-Merwe, or Stranski-Krastanov if the growth starts with closed layers and island growth occurs only after a certain thickness. The different growth modes are depicted in figure 2.4. One way of describing the strength and type of interaction of surfaces is by its interaction with water. A hydrophobic surface repels water, while a hydrophilic attracts it. The effect is quantified via the contact angle of droplets of defined liquids (commonly water) at the surface [28]. This categorization can have a significant effect on growth mechanisms, as presented by Wang et al. [29].

Solids of organic molecules show some specific properties with regard to their growth that are not common in atomic crystals or small simple molecules. The size and geometry of the building blocks allow for additional inner degrees of vibration and rotation. Orientation of the molecules within the crystal (twist) can change, as well as the orientation of the molecules towards the substrate (laying or standing). The interaction energies are on a completely different scale compared to inorganic solids, thus, temperature levels at which a reorganization of the crystal lattice can take place are usually in a more manageable magnitude (50 °C to 400 °C compared to 1400 °C for zone melting process in Si ([28], [30]). However, because of this low internal interaction energy and the comparably stronger interaction with the substrate, formation of well-ordered films might be suppressed within the first few monolayers.

2.1.3.2 Condensation Centers in Thin-Films

The start of growth of a specific crystal grain requires a nucleation seed. This is of especially critical to thin crystalline layers grown on substrates made from other materials, since most of the crystal is in close proximity to this interface. The smoothness and cleanness of the surface can have a significant impact on the final density of individual crystal grains, thus, usually a low density of surface defects is desired to obtain large grains. Yu et al. [31], describe a method to utilize this effect by intentionally introducing condensation centers in a certain pattern to generate grain formation accordingly. Another method is to increase the thickness of the crystal in certain areas, to increase the probability of bulk condensation centers. The latter method is only possible if the crystallization is not heavily dominated by surface effects. The goal is to pre-arrange the shape and orientation of certain crystal grains. In the simplest possible application, the crystal grains can be aligned with pre-manufactured electrodes for FETs. However, it could also be utilized to tweak properties of individual devices according to their purpose in an integrated circuit. For example, a lower or higher transconductance of specific transistors can limit the need for additional external components, such as resistors.

2.1.3.3 Dendritic Growth of Organic Crystals

For many crystals (e.g. inorganic salts) the macroscopic properties of the crystalline solid are a representation of the unit cell of their building blocks. Thus, cubic unit cells create cubic crystals or at least plane surfaces [13]. This effect can also be observed in organic crystals, although to a less pronounced extent. The rhombic surface structure of the rubrene single-crystals shown in chapter 4.1.3 is a direct cause of the orthorhombic nature of its unit cell. However, for this perfect ordering to occur, the molecules have to be sufficiently mobile to fill every position perfectly (equilibrium during the growth). One effect that occurs when the supply of molecules towards the growth front is limited by diffusion, is the growth of dendrites. Kobayashi et al. [33] simulate which minimal set of parameters – or external influences – are required to create a certain type of dendrite. Although effects like gravity or density change caused by solidification can have an impact, the main driving factor is diffusion. Every protuberance at the surface of the growth front causes an increase in the diffusion gradient at this point. The result is an increase in growth rate towards the protuberance. Opposite to that process, the surface tension increases the required energy for growth which limits the extent of swirling.

Additionally to twisting and branching perpendicular to the growth axis, the growth front can twist along the growth direction, as investigated by Fang et al. [34]. The reasons for this twisting are not yet fully understood. A possible explanation is bending moments resulting from molecular mismatch. These additional forces result in constantly changing crystal orientations throughout the solid. The final shape of the crystal depends on the exact properties of the surroundings and the material itself and can range from heavily curved spherulites to long
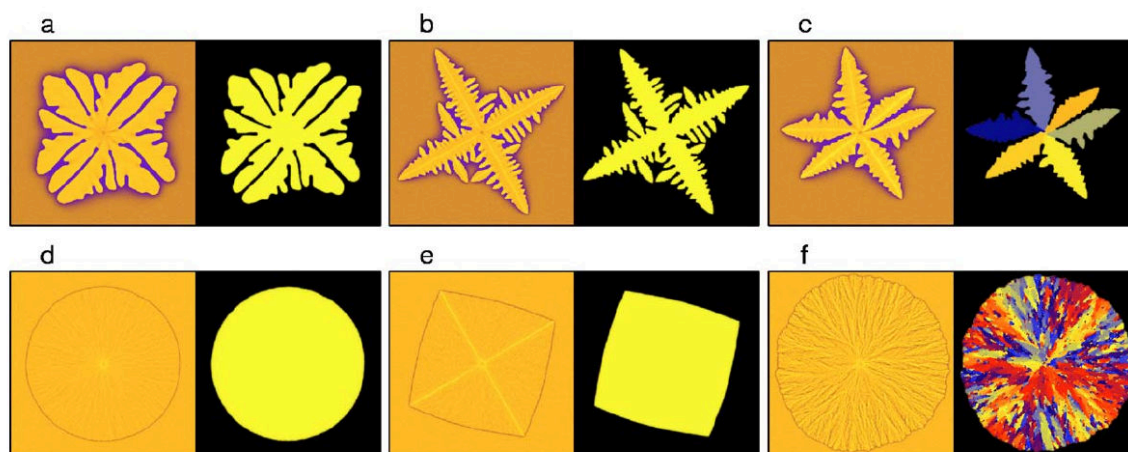
Figure 2.6: Simulation of dendritic growth under different conditions (left: crystal, right: colormap of uniform phase orientation): Isotropic interfacial free energy growth with high orientational mobility leads to single-phase single-crystals: solid (a) and dendritically twisted (d). Allowing for anisotropic growth causes a shift of phase depending on the direction of growth (b) and (e). Reduction of orientational mobility creates poly-crystals (c) and (f). Figure from [32].

intertwined needles over networks of – in principle single-crystal-like – dendrites. Considering 2D-layers, the growth can be simulated without knowledge of the underlying cause. Fang et al. [34] utilize phase-field modeling applying an external driving force to recreate different shapes of dendritic growth, including the twisting along the growth axis. By changing the applied force and energetic landscape of the film, turning- and branching rates can be adjusted to realize optimal area coverage. How different growth conditions influence the outcome is shown in figure 2.6. This approach could be utilized to optimize the growth of real layers.

Since the orientation and order of neighboring branches are almost completely random, a crystal grown from dendrites has a high density of grain boundaries perpendicular to the branch. The branches are usually mismatched in order and orientation. However, in thin crystalline films, where the width of a branch is significantly larger than the thickness of the layer, this only applies to the lateral orientation. The direction perpendicular to the layer can be considered as highly ordered. Thus, these kinds of layers offer themselves to epitaxy, when well-ordered crystals are only needed along one direction.

2.1.3.4 Growth of Spherulites

As the name suggests, a spherulite is a spherical – so circle- or ellipse-shaped – structure, in contrast to a classic single-crystal that has geometrically defined angles specified by its unit cell. They can manifest in a variety of crystal structures, ranging from dendrites to poly-crystals with large single-crystal cells. Gránásy et al. [32] describe and simulate possible mechanisms for the formation of spherulites in different systems. Thus, spherulites originate from static inhomogeneities – like defects – or dynamic inhomogeneities – intrinsic to super-cooled liquids. The purity of the used material is of paramount importance. However, even when pure raw materials are used, the temperature- and energy-landscapes of
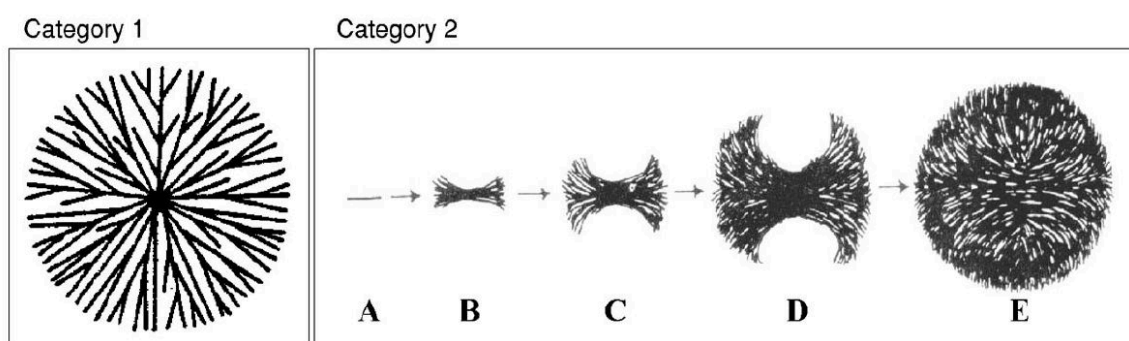

Figure 2.7: Concept of growth mode of spherulites: Category 1 spherulites originate from central multidirectional growth, typical for dendritic crystals with strong branching. Category 2 spherulites originate from a folded chain single-crystals, due to strongly inhomogeneous or unidirectional growth under low branching. Figure from [32].

the growth-area (mostly governed by the substrate) are key to enforce or inhibit spherulite growth.

According to Gránásy, spherulites can be categorized into two systems (see figure 2.7). Category I spherulites are created from central, multidirectional growth. There is little to no anisotropy in crystal growth, but strong branching, resulting in twisting and curling. The resulting grains are perfect circles with high macroscopic homogeneity.

Category II spherulites are caused by strong anisotropic growth. Starting from an initial single-crystalline seed, growth is significantly faster in one direction. The internal pressure perpendicular to the main growth direction causes the crystal to fan out. A sufficiently large grain can meet up with its center again, creating a circular shape. Under certain circumstances, two eyes adjacent to the initial seed can occur that remain amorphous.

The large scale growth kinetics are similar for most systems. The theoretical case of low driving forces and purely diffusion-driven growth causes an increase in grain radius R with time of

$$R \propto \sqrt{t}. \tag{2.4}$$

At higher driving forces, the resulting growth pattern is of dendritic (seaweed) type. The competition between diffusion and surface energy results in a decrease of the mean length an individual molecule has to travel until it is integrated into the crystal. The grains grow with

$$R \propto t. \tag{2.5}$$

Another interesting aspect is the occurrence of twisting and orientational variation within a poly-crystalline spherulite. According to simulations, the defining factor is the ratio between lateral diffusion – the speed at which the molecules reach the growth front – and rotational diffusion – how fast they are able to rotate into the needed orientation. Both parameters are temperature-dependent. However, twisting behavior can change with temperature, since the diffusion does not necessarily have the same dependence for rotation and movement.

One other effect is that the morphology and speed of growth only depend on the external parameters at a certain time and not on the history of crystal growth. Thus, arises the possibility of complex crystal arrangements by cycling of process parameters. Conditioning or patterning of a crystal array and thus a transistor array might be a possible application.

2.1.3.5 Growth of Rubrene Crystals

Rubrene is the main model material used in this thesis. It crystallizes in many different phases, can be fabricated into amorphous layers, thin-film crystals, micro-crystallites, or cm-sized crystal platelets. The following section demon-
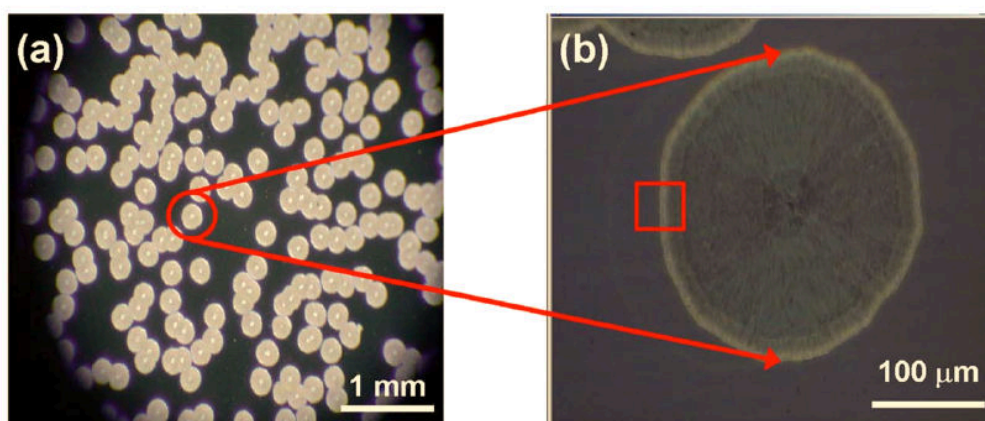
Figure 2.8: First published rubrene crystals grown from amorphous thin-film by Park et al. [35]. Crystal growth is triggered by a high rate of thermal evaporation in vacuum. It can be assumed that the energy needed for re-crystallization of the initially amorphous film – usually provided by heating or photons – is transferred as molecular vibrations during the evaporation. The total amount of energy is low, thus, only triclinic/dendritic crystals appear with limited size and area coverage. Image is taken from [35].

strates several methods of crystal growth with a specific focus on the method used in this thesis. The benefits and problems of each method as well as general properties of rubrene crystals are discussed.

Rubrene Crystals from Vacuum Furnace As described earlier, the methods to fabricate crystals of the highest quality are usually based on physical vapor transport, resulting in free-standing, macroscopic crystals. However, depending on the external parameters and the setup itself, different results can be achieved. Monoclinic, triclinic, and different types of orthorhombic crystals have been grown using rubrene [37]. Record values for field-effect mobility have been shown using vacuum gaps as gate dielectric) ([38], [39], [40], and [41]. This approach for the gate solves one key problem of thin-film transistors – defects at the interface – which become dominant once the order of the material itself is sufficiently high. However, even with polymer dielectrics directly at the surface of the crystal, high mobilities can be reached ([39], [42], and [43]). One noteworthy effect in these types of rubrene crystals is a phase transition at around 150 K when the crystal is cooled [37], resulting in a drop in mobility.

Although interesting as a benchmark, the main drawback of these kinds of large scale organic single-crystals remains the difficulty in using them in applications. Growing them on surfaces of usable substrates remains challenging. Vacuum gap based transistors have to be built up by hand [41], while deposition of insulators onto existing crystals is limited to certain depositions techniques (e.g. spin coating is difficult to realize). Depending on the desired quality, the growth time can reach into dozens of hours. Additionally, the size (needle- or platelet-shaped and thickness in the range of µm) limits the use of these materials to lateral devices.
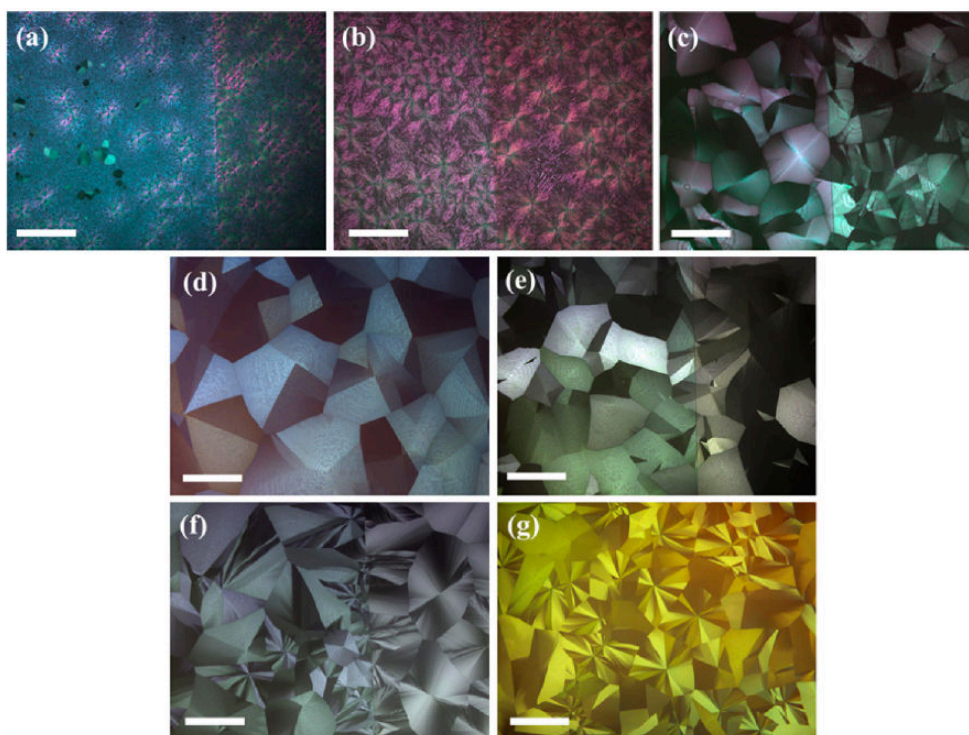
Figure 2.9: Thin-film crystals of rubrene grown via heating at $140\,°C$ on different under-layers with varying T_g. Definition of naming of different crystal phases based on this and other publications:
(a): amorphous and randomly crystallized layers
(b): dendritically grown layers (Category I spherulite) with triclinic unit cell
(c): spherulites (Category II spherulite) with orthorhombic unit cell
(d)-(e): platelet-shaped single-crystals with orthorhombic unit cell
(f)-(g): ray-like broken platelets with orthorhombic unit cell (poly-orthorhombic)
Figure by Fusella et al. [36].

Rubrene Crystals from Solution   Matsukawa et al. [44] present a study investigating growth of rubrene single-crystals from solution. They show that solubility of rubrene depends little on the polarity of the solvent but more on the presence of benzene rings in the solvent. The resulting crystals were free-standing, similar to crystals obtained by vapor deposition. Size and geometry are comparable, while the field-effect mobility is significantly reduced, which might be a result of the lower crystal quality. Preparation time is only slightly lower compared to the previously discussed methods, however, expensive vacuum machinery is not required. Huang et al. [45] show a series of rubrene micro-crystals, grown from solution. The triclinic and monoclinic phases investigated, are mostly neglected by other publications. They describe the formation of either of the crystallographic phases by a series of local minima of the Gibbs free energy at different degrees of supersaturation. Their results are backed by simulations. These kinds of local energetic minima in dependence of external parameters during the crystallization might be a key aspect for the other crystal phase (i.e. orthorhombic) too. Stingelin-Stutzmann et al. [46] present thin rubrene layers grown from solution on a substrate utilizing a vitrifying agent. The option to modify the crystal-
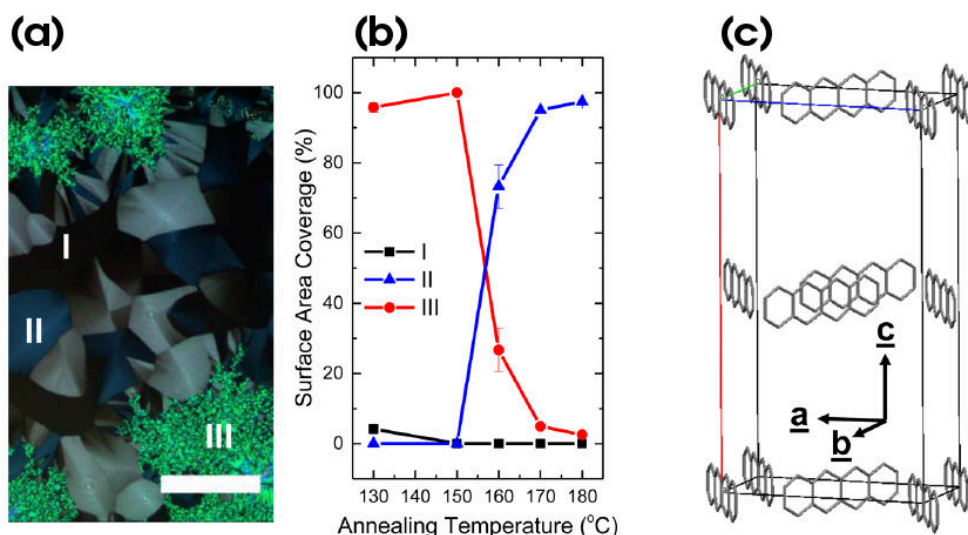
Figure 2.10: Orientation of rubrene molecules within the orthorhombic platelet crystal structure (according to [19]) (c). (Only the tetracene core of the rubrene molecule is depicted.) Phase III in part (a) is identified as triclinic. Prevalence of triclinic vs. orthorhombic phase set via annealing temperature (b). The turnover temperature is 150 °C to 170 °C. Figure from [19].

lization with additives is a unique feature of solution processing. However, the poly-crystalline films made, show comparably small grains and a more needle-like structure. Additionally, the additive might remain trapped within the crystal, further reducing the order of the system. The field-effect mobilities shown are significantly lower compared to vapor deposition-based single-crystals.

Rubrene Crystals from Amorphous Thin-Films   The common methods for growing organic crystals in general – or single-crystals in particular – suffer from specific disadvantages. Although vapor deposition techniques like sublimation-based approaches create large crystals of supreme quality, the time required and unsatisfactory scalability make them unusable for most applications. Additionally, doping of such crystals – aside of surface doping – is extraordinarily difficult, since the sublimation temperature of the matrix and the dopant must be close to identical – that is, if high crystal quality is to be preserved at the same time. Stacking of differently doped layers, as is essential for vertical devices with any functionality, can only be done manually.

Solution processing-based approaches can be more suitable for a reproducible and scalable process. However, procedures for deposition like spin coating are limited by the substrate size. Adding special agents for control of crystallization can make processes more stable and reproducible. However, they also introduce additional impurities. The question of dopability is difficult to answer. Although it is less problematic compared to sublimation-based methods, the dopant has to be solvable in the same solvent as the matrix and should not change the crys-

tallization process in a significant manner. Stacking of layers can be a problem, since the addition of solvent to an already cured layer can lead to dissolution of the bottom layers and consecutive intermixing of doped, undoped or differently doped layers.

The approach used in this thesis is based upon induced crystallization of a previously amorphous thin-films – which is usually created by vacuum evaporation. This process can be induced by fast evaporation, illumination, or rapid heating. An overview of the different crystal structures obtainable with this method is shown in figure 2.9, as a reference. The first utilization of this effect was shown by Park et al. [35]. They present thin-film transistors with completely amorphous layers and transistors with channels partially filled with rubrene crystalline disks. These disks are created randomly by fast evaporation. Although it is not discussed in this publication, the crystals shown seem to be of the dendritic-triclinic type. The field-effect mobility increases with the amount of channel covered with the crystalline disks up to $1.23 \cdot 10^{-4}\,\mathrm{cm^2\,V^{-1}\,s^{-1}}$.

Lee et al. [47] present a method of controlling the crystal growth, by rapidly heating a previously amorphous layer of rubrene. By choosing the right temperature and external parameters, arrays of large platelets of single-crystals could be grown. The orthorhombic phase presented here is more suitable for lateral thin-film transistors. A patterning technique based upon the selective crystallization of these films has been further optimized by Kim et al. [48].

A hybrid technique between solution processing and this rapid heating method is shown by Jo et al. [49]. Rubrene in solution mixed with a binding polymer is spin-coated onto a substrate. Immediately after the deposition, the previously shown heating step is performed. An additional quenching (heating for stress relaxation) at $80\,^\circ\mathrm{C}$ takes place, although the impact of that is not discussed. The focus is on the orthorhombic crystal phase, while the temperatures for the first (triclinic structure) and second (orthorhombic structure) crystallization are presented. Thus, at least $125\,^\circ\mathrm{C}$ are required to trigger the crystallization into the triclinic crystals, while a minimum of $170\,^\circ\mathrm{C}$ is necessary for the orthorhombic type. Field-effect mobilities of these films are lower than in devices with the simple heat treatment of evaporated films. However, it might be a suitable method for utilizing the low-cost fabrication of solution processing.

These thin layers are well ordered – although the quality is not on the level of free-standing single-crystals grown from a furnace. However, their use is mostly limited to lateral thin devices, i.e. thin-film transistors. Utilizing these layers as a seed, additional vacuum evaporation can result in any thickness desired, maintaining the high crystallinity by homoepitaxy and guaranteeing a void-free layer. This combination of heat-treated seed crystal and consecutive homoepitaxy is described by Verreet et al. in [50] and then further by Fusella et al. in [51] and [36]. The experiments by Verreet et al. [50] represent the first usage of these rubrene layers in stacked vertical devices. They utilize the crystalline rubrene as

an absorption layer for solar cells, adding doped C_{60} as the donor-side. While the performance of the cell itself is not impressive, they show that an increase in rubrene layer thickness is not decreasing the short-circuit current. In contrast, it is increasing for all tested layer thicknesses till 400 nm. They conclude a free diffusion length for excitons within this type of rubrene of at least 200 nm and thus much more than the several tens of nm common in amorphous organic semiconductors [52].

Fusella et al. [51] take a closer look into the epitaxy itself, investigating the growth method under structural considerations and growth defects. They describe a Stranski-Krastanov growth mechanism and – in contrast to that – no significant increase in surface roughness with higher layer thickness. The transition into island growth and the prevalence of line and screw defects suggest a strain within the crystal structure that should not occur within a crystal grown via homoepitaxy. Even layers grown on a bulk rubrene single-crystal – eliminating the substrate mismatch – show the same type of strain-relief symptoms.

In [36], the influence of the substrate (in particular the addition of an underlayer) on the formation of the seed crystal is investigated. The impact of the glass transition temperature T_g of the underlayer for reaching the platelet-type of seed crystals is studied in detail. T_g characterizes the temperature at which an amorphous material undergoes a phase transition from a solid structure to a viscous, more fluid system [17]. In contrast to Sinha et al. [29], they argue that the decisive factor for proper crystallization is the spatial orientation – hence rotation – of the rubrene molecules and not the transport across the surface, which would be influenced by the hydrophilic/hydrophobic nature of the substrate. They conclude that if the transition temperature is too high, the rigidity of the substrate hinders proper orientation of the individual molecules. In contrast, a transition temperature that is too low causes too much distortion and already positioned molecules tend to not remain in the properly oriented state. They propose a sweet spot of bulk glass transition temperature of around 70 °C to 90 °C.

A further point regarding all types of polymorphs is the structure of the underlying rubrene molecules themselves. Sutton et al. [53], found two distinct configurations for the tetracene core of the rubrene, based on simulations. The energetically favored configuration features twisting in the central backbone, resulting in less orbital overlap to its neighbors compared to the straight counterpart. They suggest the introduction of phenyl side-chains to stabilize the molecular configuration in the electrically favorable state. In a system of pure rubrene, a mixture of straight and twisted molecules should be expected otherwise.

2.2 Electronic Properties of Organic Semiconductors

To realize a usable electronic device it is not only necessary to understand the structure of the main components and their fabrication, but also the properties

of the materials and phenomena involved. The following chapter describes the basics of organic semiconductors, often in contrast to inorganic materials – or to be more precise, the difference in conduction between unordered and ordered solids. The first section focuses on the formation of energy states and the resulting bandgap – decisive for the semiconducting character. The second part highlights the mechanisms and properties of charge transport that arise from the special structural and energetic characteristics of organic semiconductors. Finally, two short sections discuss diffusion and doping of organic semiconductors.

2.2.1 Fundamentals of Organic Semiconductors

To understand the forces and mechanisms at play in semiconducting devices, the physical fundamentals have to be understood. Fundamentals of inorganic semiconductors are covered in books about solid-state physics or special books about semiconductors (e.g. [13], [54], [55]), while organic semiconductors are usually only covered in specialized literature ([20], [56]). The basis of each semiconducting behavior is the presence of a sufficiently small bandgap between two energetic states of the system: one completely filled at 0 K and one completely empty. The term "sufficiently small" is thereby a matter of discussion. Organic semiconductors, however, show a larger bandgap than common inorganic semiconductors which offers additional possibilities in the area of absorption and emission of certain wavelength but also opens up problems in regard to traps and efficient doping.
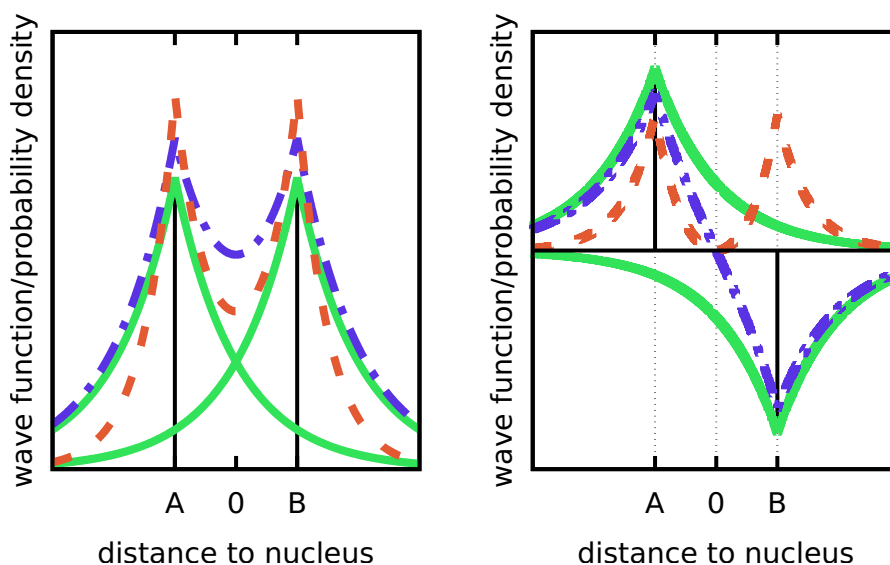

Figure 2.11: Wave function (blue, dot/dash) and probability density (red, dash) of H_2^+ molecule in Born-Oppenheimer approximation. The dashed lines represent the molecular state and the solid lines the individual atomic wave functions. The bonding state with $\Phi_A + \Phi_B$ is shown left. The probability density for the electron between the cores is a finite value. The anti-bonding state with $\Phi_A - \Phi_B$ is shown right. The probability density for the electrons vanishes between the cores.
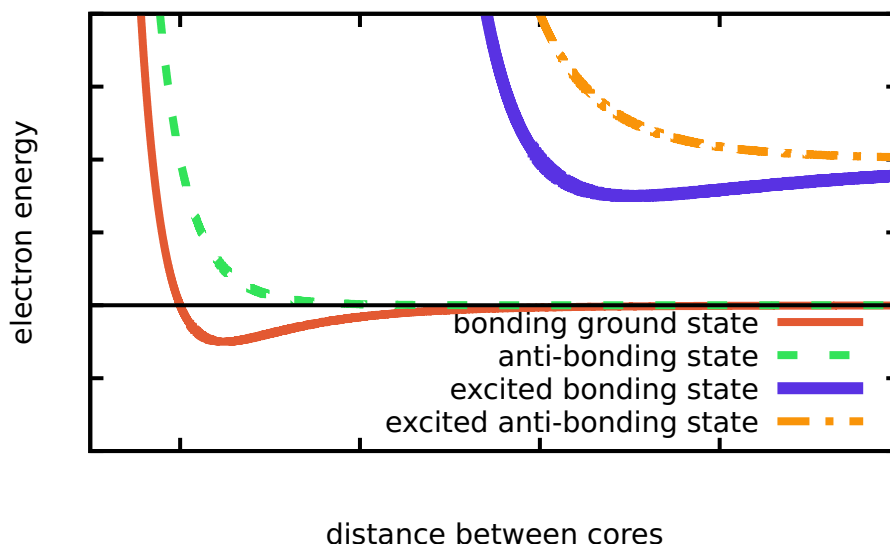
distance between cores

Figure 2.12: Energy of H_2^+ molecule in Born-Oppenheimer approximation in dependence of the core to core distance. Bonding states have solid lines, anti-bonding states have dashed lines. The ground state is indicated in red (deeper energies). The state has a distinct minimum and at finite core distance, stabilizing the molecule. The first excited state (green, higher energies) is anti-bonding without a finite minimum. Excited states (blue and yellow) can be found at higher energies, both with bonding and anti-bonding features. Evident is the energetic gap between the two stable states.

In inorganic semiconductors, the two involved energy levels are called "valence band" – for the bound electrons – and conduction band – for the potentially free electrons. These energy states and the split between them originate from the periodic structure of the crystal structure of the individual materials. In most organic semiconductors, the energetic split between two levels is already present in the individual molecules that constitute the organic solid. The semiconducting properties are thus to a much larger degree a consequence of the energetic properties of these individual components. However, the packing and orientation of the molecules have nevertheless a significant impact.

2.2.1.1 The H_2^+ Molecule

The splitting of energy levels can already be observed on the simplest possible molecule, the H_2^+ molecule. Regardless of its simplicity, the Schrödinger equation for this system cannot be solved analytically. However, it is possible to obtain approximations of the resulting wave functions and energies when certain simplifications are utilized. A more thorough deduction can be found in literature [57]. It follows a shortened calculation: The Schrödinger equation for a single electron (wave function: $\Phi(\vec{R}_i)$) at the position $\vec{r}_{el}$ in the vicinity of two hydrogen cores (i = A, B) at the positions $\vec{R}_i$ can be written as:

$$H\Phi(\vec{R}_i, \vec{r}_{el}) = E\Phi(\vec{R}_i, \vec{r}_{el}), \qquad (2.6)$$

with the corresponding Hamiltonian:

$$H = \frac{\hbar^2}{2M} \left(\Delta_{\vec{R}_A} + \Delta_{\vec{R}_B} \right) + \frac{\hbar^2}{2m} \Delta_{\vec{r}_{el}} + U(\vec{R}_A, \vec{R}_B, \vec{r}_{el}) \tag{2.7}$$

and the simple Coulombic potential describing the interaction between the cores and between the cores and the electron:

$$U = \frac{e^2}{4\pi\epsilon_0} \left(\frac{1}{|\vec{R}_A - \vec{R}_B|} - \frac{1}{|\vec{R}_A - \vec{r}_{el}|} - \frac{1}{|\vec{R}_B - \vec{r}_{el}|} \right). \tag{2.8}$$

Here, M is the mass of one hydrogen core and m the mass of an electron. As already mentioned, these equations are not analytically solvable. Due to the large difference in mass between electron and core (the core is around 1800 times as heavy as the electron), it is possible to simplify these equations with the Born-Oppenheimer approximation, which neglects the movement of the cores. It is thus feasible to separate the wave function into a part for the electron and one for the core movement. The resulting equation for the electron is, therefore:

$$\Delta_{\vec{r}} \Psi_{el}(\vec{R}, \vec{r}) + \frac{2m}{\hbar^2} \left[E_{el}(\vec{R}) + \frac{e^2}{4\pi\epsilon_0} \left(\frac{1}{r_A} + \frac{1}{r_B} \right) \right] \Psi_{el}(\vec{R}, \vec{r}) = 0, \tag{2.9}$$

with $r_i = |\vec{R}_i - \vec{r}|$ as the distance of the electron to the core i.

The solutions for these equations are depicted in figure 2.12 for the four relevant states with the lowest energies. The lowest energetic state is called the ground state, while all other states are called excited states. There are two types of states: one type, for which the energy of the system has a minimum at a certain distance between the hydrogen cores, while the other type of solution is missing such a minimum. We call the first type bonding states Φ^+, since they reduce the total energy of the system and are thus bonding the two hydrogen atoms and the second type anti-bonding states Φ^- which do not promote bonding.

The reason for the bond is apparent from the resulting wave functions (figure 2.11). While the probability density of the bonding states has a finite value between the two cores, this value is zero for the anti-bonding states. As a consequence, the negatively charged electron acts as a glue between the positively charged hydrogen cores.

2.2.1.2 The H$_2$ Molecule

The H$_2$ molecule is similar to its ionic counterpart. An analytic solution is thus also not possible in this system. One possibility to find the energies and wave functions of the system is the so-called Linear Combination of Atomic Orbitals (LCAO), which uses the orbitals of the individual atoms and linearly superposes them to find the configuration with the lowest energy. As an example, one could

use the method on the H_2 molecule and imagine the bonding states as the positive superposition of two hydrogen ground states, while the anti-bonding states are the negative sum:

$$\Phi_{H_2^+}^\pm = N_\pm \left(\Phi_A \pm \Phi_B \right). \tag{2.10}$$

This method can be extended to include the second electron of the H_2 molecule. However, to fulfill Pauli's principle, the spin orientation of the two electrons has to be taken into account.

2.2.1.3 Benzene Molecule

The previous paragraphs illustrate how the electrons in molecules show distinct states with energetic gaps. This is not yet sufficient for the semiconducting behavior, since the electrons are still locally bound to one molecule – or even a local bond. The organic ring-molecule benzene serves as an example of how delocalization enables semiconducting properties in molecules.

The electronic configuration of carbon is $1s^2\, 2s^2\, 2p^2$. The outer p-orbitals can bond in a straightforward – covalent – fashion to two other atoms, however, carbon shows hybridization. One of the $2s$-orbitals and the $2p$-orbitals form hybrid states that are energetically unfavorable at first, but which allow for more numerous and more stable bonds to other atoms. This shift lowers the energy of the total system. The p-orbitals that are not hybridized can participate in common p-bonds. Possible are sp-hybrid orbitals that can be found in triple bonds of some aliphatic compounds, while sp^3 orbitals are prominent in methane, featuring a tetrahedral shape.

Most aromatic molecules feature sp^2 hybridization. The two hybridized electrons are called σ-electrons, binding the individual carbon atoms to a ring at a distinct 120° angle. The leftover p-orbitals cause bonding as well, they are called π-electrons. However, they are not localized to one specific atom like the σ-electrons but smeared out over the length of the ring. The hybridization and
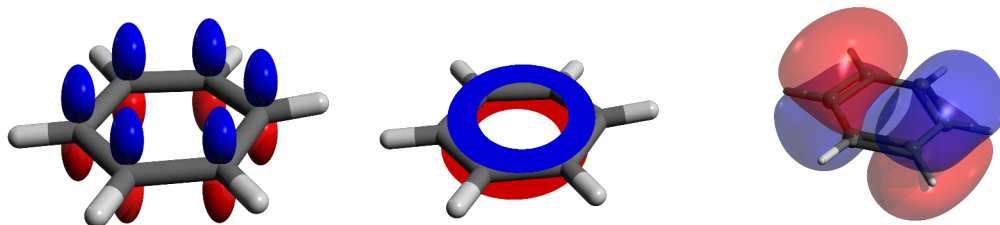

Figure 2.13: Delocalization of π-electron system in organic semiconductors: Outer electrons of carbon in benzene are sp^2-hybridized (left). Bound σ-orbitals form the ring (grey) and connect to hydrogen atoms (white) while the leftover π-orbitals (blue/red) are delocalized over the entire ring (middle). The resulting molecular orbitals can have complex shapes (right: HOMO of benzene). Figures from [58].

smearing out is illustrated in figure 2.13. This delocalization is the key to the semiconducting behavior of organic molecules.

Analogously to the hydrogen molecule, the outer electrons of benzene can be in different energetic states. The highest used state is called HOMO (Highest Occupied Molecular Orbital), while the first excited state is called the LUMO (Lowest Unoccupied Molecular Orbital), featuring an energetic gap in between. The π-electron system can be extended to include additional rings or chains featuring π-bonds too, which increases the delocalization. Utilizing the Heisenberg's uncertainty principle, it is evident that a higher uncertainty of location will decrease the uncertainty in momentum and thus energy. Hence, a larger π-electron system features a smaller bandgap. This can be roughly estimated by utilizing the energy eigenvalues of an infinite quantum well structure [57]:

$$\Delta E = \frac{\hbar^2(2n+1)}{2m_{\mathrm{e}}L^2},$$ (2.11)

where L is the confinement defining length scale. In case of the Benzene molecule, this is the circumference of the ring. Note that this estimation refers to the energy gap of the molecular states only.

Through interaction with neighboring molecules and energetic splitting, the two molecular states (HOMO and LUMO) cause the electronic states of the solid that are equivalent to a valence and conduction band in an inorganic semiconductor. The physics of charge transport will be discussed in the following chapter 2.2.2.

2.2.2 Charge Transport in Organic Semiconductors

Conduction in organic semiconductors (more details can be found in [20], [59], or [60]) shows some specific differences compared to conduction in typical inorganic materials like silicon. First, for organic materials, even seemingly undoped systems feature dominant hole or electron conduction[2]. Most of the high-end mobility materials are of p-type behavior, although progress has been made for n-type materials too [61]. Many organic semiconductors show a distinct anisotropy in charge transport, due to the anisotropy of the molecules themselves [62]. This effect is more pronounced in crystalline systems, however, even the properties of amorphous thin-films are impacted by the molecular stacking on the substrate [63]. Mostly only one direction of charge transport is optimal, which limits devices that require a change in transport direction. The dimensionality of the system can have a significant impact too; in two different ways. The molecules themselves can feature 1D (alkane chains), 2D (pentacene), or 3D (rubrene) dimensionality of the delocalized pathway. The molecules themselves can be arranged in 1D to 3D configurations too, allowing for transport only in

---

[2]Both types of charge carriers are contributing to transport, however, one type of transport is for various reasons noticeably more efficient and thus dominant.

the selected direction, while sometimes enabling quantum well properties. For effective charge transport in bulk layers, higher dimensionality is usually of advantage [16].

Conduction of charges, be it electrons, holes, or excitons, can be the result of two different driving forces. Drift transport, caused by an electric field and diffusion transport, as the result of a concentration gradient. Diffusion in organic semiconductors will be discussed in the following subsection.

Current j caused by an electric field E can be described using Ohm's law:

$$\vec{j} = \overleftrightarrow{\sigma}\vec{E}, \tag{2.12}$$

with σ as the conductivity. The simple form of this equation is treacherous, since the conductivity can change depending on the strength of the field, temperature, external illumination, and many other parameters. It can be calculated as

$$\overleftrightarrow{\sigma} = en\overleftrightarrow{\mu}, \tag{2.13}$$

with e as the electric charge of one electron, n as the density of free charge carriers and μ as the mobility of those carriers. The carrier density and mobility are usually not constant. The tensor character of the mobility is hidden in the anisotropy of mobility. In many systems the anisotropy can be neglected, reducing the parameters to one-dimensional numbers σ and μ.

Carrier mobility is by far the more common quantity to measure and discuss[3], compared to the carrier density. However, the carrier mobilities found with different techniques are rarely identical. Taking rubrene as an example: Pundsack et al. present $0.29\,\mathrm{cm^2\,V^{-1}\,s^{-1}}$ to $0.70\,\mathrm{cm^2\,V^{-1}\,s^{-1}}$ [64] from time of flight measurements, Takeya et al. show $18\,\mathrm{cm^2\,V^{-1}\,s^{-1}}$ to $40\,\mathrm{cm^2\,V^{-1}\,s^{-1}}$ for measurements of single-crystals at a vacuum gap, while Podzorov et al. [42] finds $0.1\,\mathrm{cm^2\,V^{-1}\,s^{-1}}$ to $1\,\mathrm{cm^2\,V^{-1}\,s^{-1}}$ and Park et al. [35] $1.23 \cdot 10^{-4}\,\mathrm{cm^2\,V^{-1}\,s^{-1}}$. Hence, the same material can appear to have orders of magnitude different charge carrier mobilities. Even when taking only systems with the same crystal structure into account, the differences are substantial. Therefore, the mobility values presented in literature are not the intrinsic property of the individual material, but an averaged quantity, based upon the specific measurement technique and circumstances, be it geometry, procedure, or external bias. An overview of mobilities measured with rubrene-based devices and techniques is presented in table 3.5 of chapter 3.3.

It is common practice to assume the carrier density to be constant and to define an effective mobility containing all changes to the system; thus $\mu\,(T, E, n, I)$. For example, in case of deep traps, the mobility can be written as:

$$\mu_{\mathrm{eff}} = \frac{\mu_p + \mu_{\mathrm{T}} p_{\mathrm{T}}}{p + p_{\mathrm{T}}}, \tag{2.14}$$

---

[3]In most techniques the measured quantity is the conductivity σ and the mobility is extracted via a model.

with, p and μ as parameters of the free carriers and p_T and μ_T as parameters of the traps. Considering that trapped carriers cannot move, the mobility can be simplified to:

$$\mu_{\mathrm{eff}} = \frac{p}{p + p_T}\mu, \qquad (2.15)$$

reducing the "visible" mobility to a fraction of the value intrinsic to the material. Measurement and discussion of mobility values are nevertheless valuable. First, it offers an easy way to compare different materials, systems, preparation techniques, and geometries; given sufficient care in the analysis. An overview of high mobility organic semiconductors – polymers and small molecule – is presented by Sirringhaus et al. [59]. Additionally, from an application standpoint, the performance and usability in the final device is the important factor and not necessarily the reason why one material is superior to another. As an example: vacuum gap transistors feature the highest charge carrier mobilities for organic semiconductor transistors. However, their delicate manual construction renders them virtually unusable for any real application.

2.2.2.1 Charge Carrier Transport in Ordered and Disordered Systems

The charge transport mechanisms in ordered systems (most inorganic semiconductors) and disordered systems (low conductivity organic semiconductors) are different. The conduction mechanisms are depicted in figure 2.14. Highly crystalline materials feature energy-band-based transport. Free charge carriers are created through thermal excitation over a sufficiently small bandgap. These free charges can be transported in delocalized states by applied electric fields. In contrast, organic semiconductors are usually described as featuring hopping transport between localized states. This hopping is a significantly slower and less efficient process, causing most organic semiconductors to feature significantly lower charge carrier mobilities than inorganic semiconductors. The differences and common traits of both types of charge transport are especially interesting for well-ordered organic semiconductors, since their mode charge transport is a mixture of both.
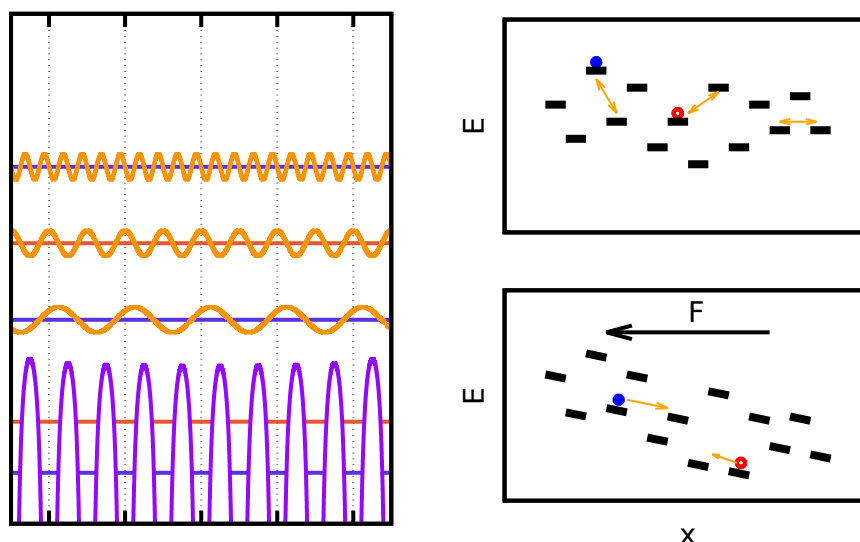
Figure 2.14: Illustration of the difference in charge transport between ordered and disordered semiconductors:
left: Ordered system (e.g. atomic, inorganic semiconductors): Inner electrons are strongly bound by the Coulomb potential of the atomic cores (violet, deep energies) and do not contribute to charge transport. Outer electrons are only loosely bound, they form solid-wide delocalized states (blue and red, above coulomb peaks) with wavefunction spanning from perturbation to perturbation (orange).
right: Disordered system (e.g. low mobility organic semiconductors): Energetic states of charge carriers are localized on individual molecules. Transport is the non-coherent hopping from molecule to molecule. Individual jumps can be energetically favorable or unfavorable. The latter requires thermal activation. Applying high electric fields causes the energy landscape to shift (bottom). This offers more possible hopping targets in the direction of the field and, thus, higher mobilities.

2.2.2.2 Band Transport

Charge transport in highly ordered crystals stems from the periodicity of its parts and the subsequent delocalization of charge carriers. The derivation of the so-called Bloch-states can be found in every book about semiconductors (e.g. [54] or [65]) or semiconductor devices (e.g. [55]).
In short: The Schrödinger equation of an electron within a potential $V(x)$ can be written as:

$$\left[\frac{p^2}{2m} + V(x)\right]\Psi(x) = E\Psi(x). \tag{2.16}$$

For the Bloch model, the electrons are free and the potential represents the periodicity of the solid with $V(x + a) = V(x)$, with a being the distance between two points in the lattice. Blochs Ansatz uses plane waves and modulates them with functions $u_k(x)$ that feature the periodicity of the lattice $u_k(x + a) = u_k(x)$, to:

$$\Psi_k(x) = u_k(x)e^{ikx}. \tag{2.17}$$

It describes the wave function of electrons as packets of plane waves weighted by the periodicity of the lattice. Solving the Schrödinger equation leads to discrete

solutions with $u_{n,k}(x)$ and $E_{n, k}$, with n as a quantum number defining the state and k as the wavenumber of the electron wave function. Bands of allowed and forbidden energetic regions emerge, which are occupied by electrons beginning from the lowest possible energy. If the highest occupied energetic band is not fully filled, these electrons can find energetically close empty states and move freely inside the solid (metals). If the highest energetic band (called valence band) is fully filled, charge transport is not possible. However, if the gap (bandgap E_g) towards the next – empty – band (conduction band) is small enough, electrons can be promoted thermally. This is the case in semiconductors. Bloch functions represent electronic states spread over the whole solid. Transport of electrons is efficient, as long as the periodicity of the lattice is intact.

This simplified picture neglects many specific properties of real solids. The shapes of real band diagrams are usually complicated and can change depending on the crystal orientation, static defects in the crystal, or dynamic effects, like phonons.

2.2.2.3 Hopping Transport

Charge transport in disordered (low mobility) systems can be modeled quite well with hopping behavior. The concepts are described in many review articles, each with a specific focus ([59], [60], or [66]). The idea originates from the chemical approach of describing the molecules of the solid as separate systems and current as a perturbation. Based on this point of view, the HOMO and LUMO levels of the molecule lay the basis for the excited electronic states, while charge transport consists of instantaneous hopping of these states from molecule to molecule. Important parameters for these processes are the transfer integral J and the reorganization energy λ.

The transfer integral describes the energetic overlap of the two involved molecular orbitals. It is highly dependent on the distance and orientation of the molecules involved. Phonons or molecular vibrations in general assist in achieving a good overlap by varying the distance and orientation of neighboring molecules. The reorganization energy accounts for the change in energy, caused by the transfer of charges from one to the other molecule. This includes the internal change of the molecular energy itself and the external, through reorganization of neighboring molecules. High reorganization energy tends to localize charge carriers. The ratio between transfer integral and reorganization energy can be seen as a measure for band- to hopping-like transport.

The resulting conduction behavior can be modeled as being heavily trap-limited. The current can be described using the Poole-Frenkel equation at an average trap energy E_A:

$$J = J_0 V \exp\left(\frac{-E_A + \sqrt{\frac{eF}{\pi\epsilon}}}{k_B T}\right), \tag{2.18}$$

based upon the thermal excitation of trapped states into the so-called valence band, assisted by an electric field F. The multiple trap and release model (MTR), describes the same without the field dependence. Both systems work well in modeling low mobility organic semiconductors. The resulting mobility can be written as:

$$\mu = \mu_0 e^{\sqrt{\frac{F}{F_0}}}, \tag{2.19}$$

with μ_0 and F_0 as temperature-dependent material parameters. They contain the energetic landscape and overlap of molecular orbitals between neighboring molecules.

2.2.2.4 Band Transport vs. Hopping Transport

As a result of the different conduction mechanisms, the charge carrier mobility in organic semiconductors is usually significantly lower than in typical inorganic semiconductors. However, materials used for Organic Field-Effect Transistors (OFETs) show comparably high mobilities, with a conduction mechanism being partly band-like and partly hopping. It is not easy to distinguish which transport mechanism is dominant. Stallinga [67] assumes, every semiconductor above $1 \cdot 10^{-4} \, \mathrm{cm^2 \, V^{-1} \, s^{-1}}$ to feature band-like behavior, while Sirringhaus [59] demands a mobility of more than $1 \, \mathrm{cm^2 \, V^{-1} \, s^{-1}}$ for the possibility of band-like transport alone.

The focus in this thesis is on highly crystalline organic solids which, due to their high order, feature mobilities that put them into this important transition region. To distinguish these two conduction mechanisms, the temperature-dependence could be measured. While the mobility of charge carriers with band-like transport decreases with higher temperature

$$\mu \propto T^{-\alpha}, \text{ with } \alpha > 0, \tag{2.20}$$

the mobility for hopping transport is thermally activated:

$$\mu \propto e^{-\frac{E_a}{k_B T}}, \text{ with } E_a > 0. \tag{2.21}$$

However, measuring these changes of mobilities at different temperatures proves to be difficult, since the influence of changing charge carrier density may mask the behavior of the mobility. Nevertheless, Minari et al. [68] presented a transition from band-like to hopping limited transport based on temperature-dependent mobility measurements of single grain pentacene transistors.

In contrast, Ren et al. [69] describe a phase-shift of rubrene, causing an increase of mobility from low temperatures to around 150 K. At this temperature the side chains are able to move through the back-plane of the molecule, enabling better matching of transfer integrals. The existence of band-like transport depends on more than just order of the lattice alone.

2.2.2.5 Transport in Organic Crystals

A hypothetical perfect single-crystal of an organic semiconductor would have the same degree of order as an inorganic crystal. Hence, one could expect a similar degree of delocalization and charge transport properties and resulting charge carrier mobilities. However, static disorder – caused by misalignment or foreign atoms – is not the only thing that limits the periodicity of the lattice. Dynamic disorder changes the distance and orientation of lattice points over time (electron-phonon coupling). This includes phonons of the lattice – the vibrations of lattice points – and the internal vibration of individual molecules. Since organic solids show Van der Waals bonds, the energies are significantly lower and vibrations have a stronger effect than in inorganic crystals. The displacement measures up to 0.5 Å at room temperature [70]. If the transfer integral is larger than the impact of electron-phonon coupling[4], transport is band-like. Vice versa, if the vibrational impact is dominant, the result is hopping transport. A similar contribution in the Hamiltonian will result in an intermediate conduction mechanism, showing a more complicated behavior.

The research on the effect of molecular structure on its vibrational spectrum and in particular on its charge transport is a rather new subject. First results utilizing diffuse electron scattering by Midgley et al. [72] and – with a focus on understanding the differences between standard materials and high mobility materials – by Illig et al. [70], show a strong correlation between the vibra-

---

[4]These parts can be split into local and non-local parts which have different effects and causes. The discussion of those, however, does not add much in the scope of this introduction.
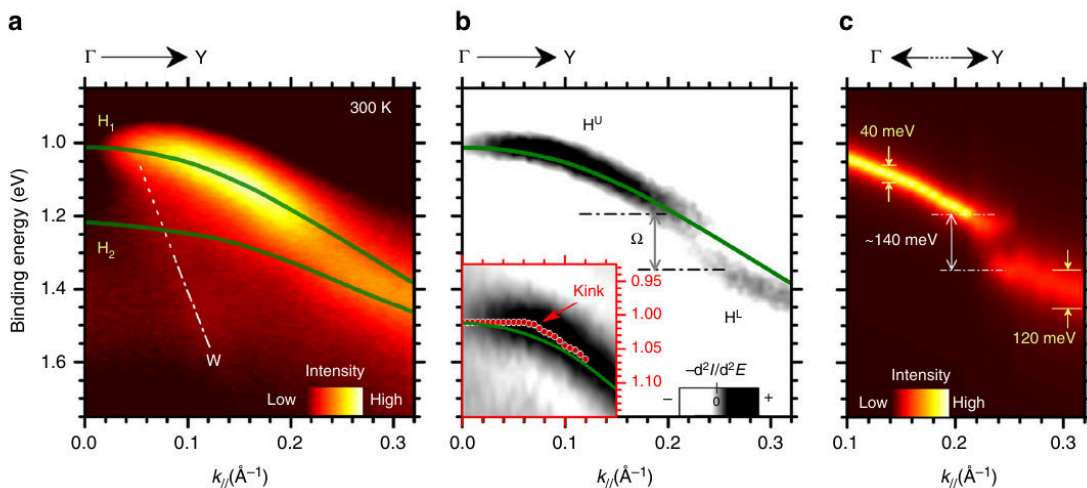

Figure 2.15: Phonon interaction with charge transport in rubrene. **a** ARUPS intensity of rubrene at 300 K along the ΓY-direction. Visible is the split in HOMO bands (Green lines are theoretical calculations.). **b** First derivative of measurement a. **c** Intensity of H peak Lorentzian component, extracted via peak fitting from a.
Figure from [71].

tion along the long axis of the π-electron system and the mobility[5]. A larger amplitude and a lower frequency of phonons are detrimental for band-like charge transport. Additionally, they show that side chains along the long axis can lock the motion of molecules in space and reduce dynamic disorder. As an example, the molecule 2,7 – Dioctyl[1]benzothieno[3,2 – b][1]benzothiophene (C8-BTBT) features lower vibrations and higher mobilities than standard materials like 6,13 – Bis(triisopropylsilylethynyl)pentacene (TIPS-Pentacene) or 5,11- Bis(triethylsilylethynyl)anthradithiophene (TES-ADT). In contrast, the vibration along the long axis of rubrene layers is in the same order of magnitude or higher than these molecules, despite featuring higher carrier mobility. As discussed by da Silva et al. [73], it is not the vibration itself that causes the dynamic disturbance, but the electron-phonon coupling. The transfer integral for rubrene is in a local extremum of the distance to its nearest neighbor. A change in position caused by vibration has thus a significantly smaller impact than in other materials, causing a small electron-phonon coupling. While the introduction of side chains can be a valid path to minimize detrimental vibrations, the special effect of rubrene is difficult to replicate.

Depending on the lattice structure and the energies involved, electron-phonon coupling can also have positive effects on carrier scattering time[6]. Bussolotti et al. [71] present data of Angle Resolved Photo Electron Spectroscopy (ARUPS) to investigate the dispersion of rubrene single-crystals (see figure 2.15). They found gap-like features in the dispersion relation that could be correlated to electron-phonon coupling with intramolecular vibrations of 140 meV. These gaps reduce hole scattering for free carriers on the upper part (upper branch, low momentum) of the dispersion curve, since scattering of charge carriers into the gap is not possible. Charge carriers travel undisturbed under these conditions. However, scattering is mediated by phonon coupling for carriers on the bottom part (upper branch, high momentum) of the dispersion curve, decreasing the mean free path of transport.

The mobility of finished layers can be altered by the introduction of strain. Reyes-Martinez et al. [74] present a method of increasing mobility of rubrene-based field-effect devices via compression of the channel through wrinkling of a pre-tensed substrate. They explain the effect through the change of molecular distance. A different explanation is given by Kubo et al. [75] and Matta et al. [76] who describe a suppression of molecular vibration via strain and a direct change of hole-phonon coupling, even in directions perpendicular to the straining. Strain cannot only be introduced by mechanical stress, but also by lattice mismatch between substrate and semiconductor. Mei et al. [77] report a transition from band-like transport to thermally activated transport in field-effect devices, caused by traps originating from mismatch between semiconductor and gate dielectric.

---

[5]A low electron-phonon coupling is not sufficient for high mobility. High static order and a large transfer integral are similarly essential.

[6]Not to be confused with the recombination-based lifetime.

Highly crystalline or even single-crystalline organic semiconductors offer the possibility to reduce static disorder to a level that allows for delocalization over many molecules. However, the impact of dynamic disorder caused by molecular and lattice vibrations on charge transport is often difficult to understand and manage.

2.2.3 Charge Carrier Diffusion

Diffusion is a transport phenomenon driven by a local gradient in density. It is essential for the working principle of both semiconductor-based diodes and BJTs. The general description is identical in most systems, regardless of size and the investigated property (charges, particles, etc.).
With the example of diffusion of a local distribution of charge carriers, the resulting diffusion current $\vec{J}_n$ can be written as using Fick's first law:

$$\vec{J}_n = -D\nabla n, \tag{2.22}$$

with D as the diffusion constant and n as the density distribution of electrons. Fick's second law can be derived using charge conservation and describes the change of density over time caused by diffusion:

$$\frac{\partial n}{\partial t} = D\Delta n. \tag{2.23}$$

Wannier-Mott exciton Charge-transfer exciton Frenkel exciton
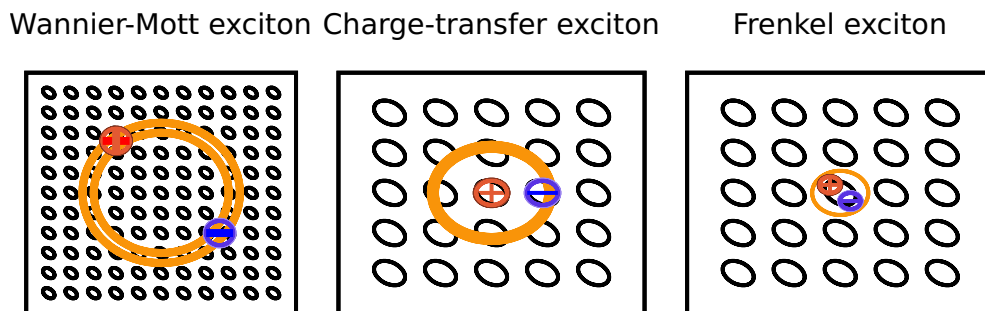
Figure 2.16: Classification of excitons:
Wannier-Mott: Electron-hole pair separated by several lattice constants due to strong dielectric screening.
(typical for inorganic semiconductors)
Charge-transfer: In terms of energy and spatial extension between Wannier-Mott and Frenkel exciton. Hole and Electron separated on different molecules, but binding radius is in the range of few lattice constants.
(important for donor-acceptor interaction)
Frenkel: Electron-hole pair bound on one molecule. Diffusion and field-assisted transport only as a whole. Binding energy low.
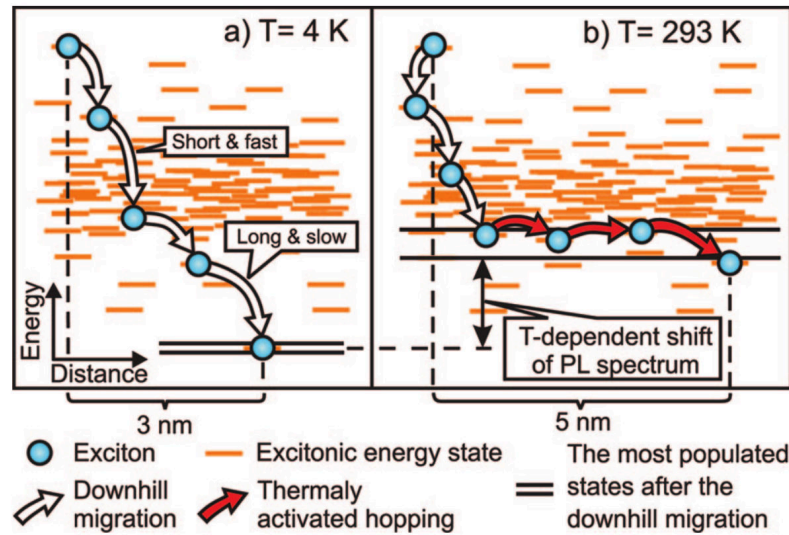(typical for organic semiconductors)
Figure according to [20].

Figure 2.17: Depiction of exciton diffusion processes at different temperatures. The energetic downhill migration is dominant at low temperatures, while the thermally activated hopping assists at higher temperatures, effectively increasing the diffusion length. Figure from [80].

In most systems the diffusion constant is linked to the mobility of the particles moving via the Einstein-Smoluchowski relation [7]. In general form:

$$D = \mu k_{\mathrm{B}} T \tag{2.24}$$

and in the case of electric charges:

$$D = \frac{\mu_{\mathrm{e}} k_{\mathrm{B}} T}{q}, \tag{2.25}$$

with the carrier mobility μ_{e}, the Boltzmann constant k_B and the temperature T. Since charge carrier mobility, especially in organic semiconductors, is not necessarily isotropic, diffusion can also be an anisotropic process. However, since the diffusion constant and mobility are linked directly, the direction of best drift transport is also the direction of most efficient diffusion. Additionally to the linear temperature-dependence visible in the Einstein relation, the mobility is usually temperature-dependent too. The result is a strong temperature-dependence of most diffusion processes.

Diffusion in Organic Semiconductors   In the context of organic semiconductors, diffusion is mostly discussed for excitons. A review of exciton diffusion can be

---

[7]The Einstein-Smoluchowski relation is originally not suited for disordered systems and a generalized relation is supposed to be used [78]. In most cases a simple approach is sufficient [79].

found in [52] by Mikhnenko et al.[8] Excitons are quasi-particles that describe pairs of holes and electrons with the semiconductor. Different types of excitons are possible. Wannier-Mott excitons are delocalized over several lattice constants, the radius is therefore large and the binding energy small. It can be described equivalently to the hydrogen problem in a Coulomb potential:

$$E = \frac{e^4 m_0}{32\pi^2 \epsilon^2 \epsilon_0^2 \hbar^2} \frac{1}{n^2}. \tag{2.26}$$

It is typical in inorganic semiconductors. In organic semiconductors, charge-transfer excitons and Poole-Frenkel excitons dominate. Charge-transfer excitons are electron-hole pairs of neighboring molecules, while Poole-Frenkel excitons represent an excited molecular state, with both hole and electron bound to the same molecule. The different types of excitons are depicted in figure 2.16. The excitonic states play a major role in the function of both organic solar cells and light-emitting diodes. In a solar cell, the exciton is created by the absorption of light of a certain wavelength. Splitting the exciton into a free electron and a free hole via a suitable interface creates an electric field that enables current. In an OLED, separate charge carriers are brought together and form an exciton on one molecule. The relaxation of this state emits light.

Recombination and Scattering Diffusion describes only the driving forces for the movement of electrons caused by a gradient in density. The effectiveness of this transport is governed by how disturbed the resulting movement is. Similar to field-driven transport, charge carriers can scatter on lattice defects, phonons, or other electrons. Analogously to a gas, it is possible to define a mean free path:

$$L_{\text{diff}} = \sqrt{D\tau}, \tag{2.27}$$

called the diffusion length L_{diff}. It depends on the average lifetime τ of a minority charge carrier until recombined. The time-dependent recombination of a non-equilibrium state can be described as:

$$\Delta n = \Delta n_0 e^{-\frac{t}{\tau}}. \tag{2.28}$$

Therefore, to reach long diffusion length it is necessary to have a large diffusion constant (and therefore high mobility), as well as a low rate of recombination. Both parameters can be optimized by increasing the order of the lattice and decreasing impurities. It is possible to reach diffusion lengths of several mm in Si [81]. Exciton diffusion lengths in organic semiconductors are typically in the

---

[8]This does not change the general description of the diffusion process itself. However, parameters measured for exciton diffusion cannot be translated directly to free charge carriers.

range of 5 nm to 10 nm. This is mainly a result of the low degree of order in many amorphous semiconductors. It has been observed that more crystalline systems feature longer diffusion length [52]. Najafov et al. [82] report on exciton diffusion lengths of several µm measured with photoconductivity on the surface of rubrene single-crystals. It is thus essential to find high mobility and well-ordered organic materials with high-purity to enable diffusion-based devices like BJTs and certain types of diodes. Diffusion is highly temperature-dependent, especially in organic materials. Figure 2.17 shows, how an increase in temperature increases the diffusion length by enabling thermally activated hopping, similar to charge transport. However, if the limiting factor is scattering on phonons, an increase in temperature will decrease the diffusion length rather than increase it.

2.2.4 Doping of Organic Semiconductors

Doping is the –usually– intentional introduction of a guest material into a host semiconductor with the goal of creating additional free charge carriers. The basics of doping in inorganic systems are discussed in every solid-state or semiconductor book (e.g. [54] or [55]), while organic doping is only described in books specialized in organic semiconductors [83] or review papers discussing doping of organic semiconductors ([84], [85]). An overview of the application of doping, with a special focus on organic transistors has been published by Xu et al. [86].
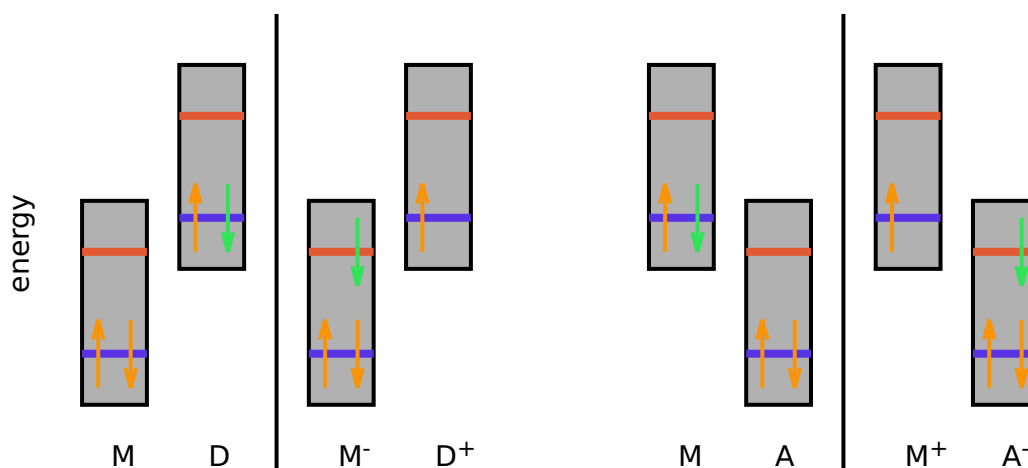
Figure 2.18: Molecular/chemical doping in organic semiconductors (n-doping left, p-doping right): A set of matrix (M) and dopant (D, A) materials with matching energy levels can trigger charge-transfer between the molecules and therefore the formation of free charge carriers within the matrix. If the HOMO (blue, deeper state for each molecule) of the dopant is energetically higher than the LUMO (red, higher state for each molecule) of the matrix, a transfer of electrons from the dopant to the matrix is favorable: n-doping occurs. The same logic applies in reverse orientation for p-doping.

The free hole density in a non-degenerate inorganic semiconductor is given as

$$p = N_V e^{\frac{E_C - E_F}{k_B T}} \tag{2.29}$$

with N_V as the effective density of states and $E_C - E_F$ as the distance between Fermi level and valence band. Doping in inorganic systems is achieved with impurities that create energetic states within the energy gap of the host system. The closer the impurity state to the conduction or valence band, the easier a thermally excited free electron or hole is created. In silicon, boron is an effective p-dopant due to its 3-fold bond leaving a dangling bond in the silicons 4-fold lattice, while phosphorous creates free electrons due to its non-saturated bonds. The hole density can be calculated for non-degenerate systems at high temperatures to be

$$p \approx \sqrt{\frac{N_A N_V}{2}} e^{\frac{E_A - E_V}{2 k_B T}} , \tag{2.30}$$

with N_A being the concentration of acceptor dopants creating an energy level at E_A. In both systems, intrinsic and doped, the carrier density is heavily temperature-dependent.

Because of their intrinsically lower charge carrier mobility, organic semiconductors rely heavily on doping to reach high conductivities for transport layers in OLEDs and solar cells. Additionally, doping is used to reduce injection resistance at metal electrodes. The concept of doping – i.e. the shifting of the Fermi level[9] to create free charge carriers – is the same as for inorganic semiconductors, however, the specific mechanisms can vary because of the special – hopping-based – transport governing organic materials, strong reorganization energies involved inside the molecules, and significantly lower dielectric screening compared to inorganic materials.

For doping to be successful, the energy levels of guest and host have to match. In case of p-doping, the electron affinity of the dopant has to be larger than the ionization potential of the host. As a rule of thumb[10] the LUMO of the guest is lower than the HOMO of the matrix so that an electron is transferred from the dopant to the host, leaving a hole behind. The rule applies vice versa for n-doping. Electron doping of organic semiconductors is therefore significantly more difficult to achieve, since materials with high HOMO levels are chemically less stable, due to oxidation.

Whether doping occurs and how efficient it is, depends on the chosen combination of guest and matrix. The doping mechanism can be quite different from species

---

[9]The Fermi energy is defined as a constant at 0 K and does not change with doping. The Fermi level (or chemical potential) should be used for the discussion of temperature and doping dependence of charge carrier concentrations. It gives the energy at 50 % occupation. However, it is common practice in semiconductor literature to use the designation Fermi energy for both concepts.

[10]The HOMO and LUMO levels and the corresponding ionization potential and electron affinities are not identical.

to species. Even an electron detached from its guest molecule is influenced by the Coulomb interaction of its now ionized original position. This effect is stronger in organic materials because of their comparably low permittivity. The resulting doping efficiency is rather low compared to inorganic materials [83], [87]. To realize high charge carrier densities, organic semiconductors are therefore not doped in the ppm- but the percentage range.

An additional factor is the diffusion of dopants within the matrix. Depending on the size of the dopant and the packing of the host, molecules can travel through the matrix, which results in a different doping profile than intended. Parthasarathy et al. [88] found diffusion of Li-atoms of up to 100 nm. The effect is more common for small symmetric molecules but can occur for larger molecules too [89].

Several routes for doping are possible. For bulk doping, the dopant has to be deposited at the same time as the bulk material. In the case of vacuum processing, this is done by the standard process of co-evaporation. Solution-processed semiconductors can be doped using appropriate solvents and parameters [90], however, stack-wise deposition of differently doped layers is challenging due to intermixing of already deposited and new layers.

Surface doping can be used when the film is thin enough so diffusion of dopants allows for a homogeneous distribution. Another application is injection doping at metal electrodes. In both cases, a sufficiently thin layer of dopant is deposited onto the intrinsic material. The injection barrier between semiconductor and a metal with non-ideal work function can be thinned down so much that effective tunneling is possible. The result is a quasi-ohmic contact.

Doping of Rubrene   Although rubrene has been investigated for a long time and has many promising applications, doping of the material is not commonly done. Kim et al. [91] present a study on furnace-grown rubrene single-crystals, utilizing surface doping with fluoroalkyltrichrolosilane (FTS). A mixture of bulk and surface doping is shown by Ohashi et al. [92]. They co-evaporate rubrene and $FeCl_3$ onto a vapor-grown pristine rubrene single-crystal for Hall-effect measurements.

Although not usually referred to as doping, the addition of dyes into light-emitting or absorbing layers is one application for rubrene too. Zhi-lin et al. [93] show how rubrene can be used not only as a matrix material for transport but also as a dye for Organic Light Emitting Diodes (OLEDs). In contrast to that, Choi et al. [94] show that efficient OLEDs based on rubrene are possible if doped with the emitter material DBP.

2.3 Device Physics

Investigating the intrinsic properties and physical processes of individual materials, structures or phenomena can give interesting insights, however, whether a certain system is suitable for an application cannot always be decided by fundamental investigations alone. For example, rubrene single-crystals show remarkable mobilities and performance in vacuum gap devices. However, these structures are not easily utilized in real applications because each device has to be "built" by hand, individually. Other aspects can be of importance too. For commonly used microelectronics amorphous silicon is used whenever possible, while poly-crystalline silicon or even single-crystals are used only for the highest performance applications, due to the high price.

The following chapters will describe the working principles of different electronic devices, mainly organic diodes, FETs, and BJTs.

2.3.1 Organic Schottky and pin Diodes

Diodes are the simplest possible non-linear device that can be made from doped semiconductors. Their key characteristic is the high (usually exponential) conductivity in one direction and low (blocked) current in the other. There are two basic types of diodes, pn diodes – based on the interface between two differently doped semiconductors – and Schottky diodes – based on a metal-semiconductor interface. The properties of the individual diode can be tweaked to suit certain applications. Devices used for power rectifiers might need a high conductivity to supply large currents to supply circuits. High Frequency (HF) applications require fast switching speeds and low capacitance, while protection diodes feature precise reverse breakdown voltages and peak current stability. The on/off-ratio can be an important parameter too.

2.3.1.1 pn Diodes

The rectifying behavior of diodes originates from a layer depleted of free charge carriers. The formation of this depletion layer can be understood by investigating a model system consisting of two blocks of infinitely large, uniformly doped layers of semiconductor, one is p-doped while the other is n-doped. Alternatively, in case of organic hetero-junctions, a p-type and an n-type material can be used. At room temperature there are more free holes in the p-doped region than electrons – vice versa for the n-doped area. If brought into contact, a transfer of charges occurs, due to diffusion of charge carriers from lower concentration to higher. The charges on both sides neutralize each other creating a space without any free charge carriers, while only the immobile charges of the leftover dopant molecules remain. The shifted charges create an electric field through the interface that in
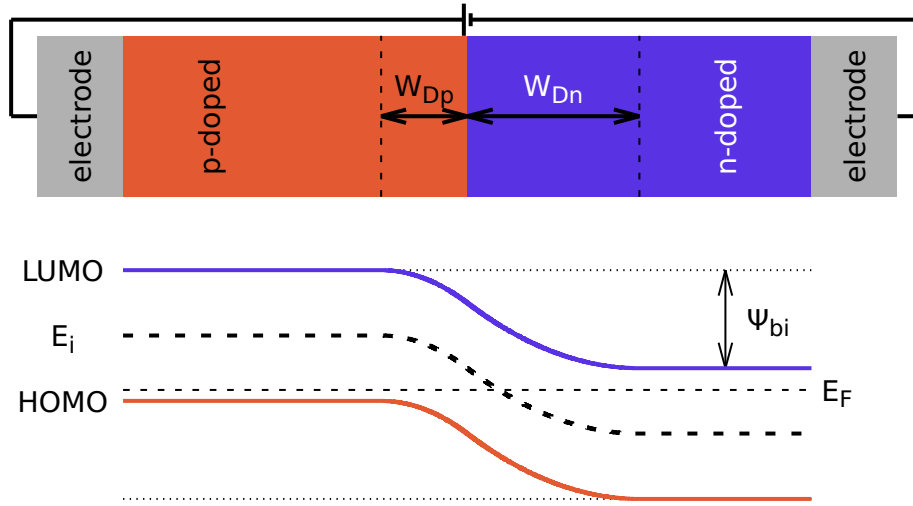
Figure 2.19: Stack and energy levels of an organic pn junction diode: Between two electrodes (grey, most left and right) are a p-doped and an n-doped layer of organic semiconductor (Alternatively a p- or n-type material). The depletion layer thickness W_i is indicated with arrows (not to scale!). The bottom part shows the corresponding energy gradient.

return counteracts the diffusion. The balance between diffusion and drift defines the size of the depletion layer and the built-in potential. For the steady-state, this leads to:

$$\frac{dE_F}{dx} = 0, \tag{2.31}$$

thus, the Fermi level[11] is constant throughout the device. The total built-in potential Ψ_{bi} can be split into the part that drops over the n-region Ψ_n and the p-region Ψ_p separately, with $\Psi_{bi} = \Psi_n + \Psi_p$.

In case of (i) an abrupt change of doping from the donor concentration N_D to the acceptor concentration N_A[12], (ii) a depletion zone without any free charge carriers and recombination, and (iii) an assumed box-profile for the charges, the field and potential can be calculated from the Poisson equation.

$$\Psi_n = \frac{E_{max}}{2} W_{Dp} \tag{2.32}$$

$$\Psi_p = \frac{E_{max}}{2} W_{Dn} \tag{2.33}$$

$$E_{max} = \frac{q N_D}{\epsilon_s} W_{Dn} = \frac{q N_A}{\epsilon_s} W_{Dp}. \tag{2.34}$$

---

[11] The Fermi energy is defined as a constant at 0 K and does not change with doping. The Fermi level (or chemical potential) should be used for the discussion of temperature and doping dependence of charge carrier concentrations. It gives the energy at 50 % occupation. However, it is common practice in semiconductor literature to use the designation Fermi energy for both concepts.

[12] To keep the equations simple, complete ionization is assumed, thus: $N_A = N_A^-$ and $N_D = N_D^+$

With W_{Dp}, W_{Dn} as the depth of the depletion zone on the p- and n- side respectively and E_{max} as the maximum electric field directly at the interface. The charge, field and potential distribution are shown in figure 2.20 for the pin-diode, a similar device discussed later. Thus, the depth of the depletion zone can be written as

$$W_{Dp} = \sqrt{\frac{2\epsilon_s \Psi_{bi}}{q} \frac{N_D}{N_A(N_D + N_A)}} \tag{2.35}$$

for the p-side. For a one-sided abrupt junction (e.g. $N_D \ll N_A$), the total depletion width is governed by the part in the weaker doped material. It can be simplified to

$$W_D = \sqrt{\frac{2\epsilon_s \Psi_{bi}}{qN}}, \tag{2.36}$$

with N being the doping concentration of the weaker doped side.

The influence of an external voltage can be described by a change of the built-in potential. Thus, Ψ_{bi} is replaced by $\Psi_{bi} - V$[13]. The capacitance per area of the depletion zone at different external voltages can then be written as

$$C_D = \frac{\epsilon_s}{W_D} = \sqrt{\frac{q\epsilon_s N}{2(\Psi_{bi} - V)}}. \tag{2.37}$$

Plotting the inverse squared capacitance over the bias voltage (called a Mott-Schottky plot), allows to determine the built-in potential Ψ_{bi} from the inset and the doping profile $N(x)$ from the slope of a linear fit:

$$\frac{1}{C_D^2} = \frac{2}{q\epsilon_s N}(\Psi_{bi} - V). \tag{2.38}$$

2.3.1.2 Schottky Diodes

The second class of basic diode design is the so-called Schottky diode, featuring a Schottky barrier. Instead of two differently doped semiconductors, it consists of a semiconductor-metal interface. A depletion zone forms in the semiconductor due to the difference in the work function between the two materials. To create a strong barrier, n-doped semiconductors should be paired with noble metals like Au or Ag and p-type materials with Al. This injection barrier can have detrimental effects on devices that require effective injection via a metal-semiconductor interface. In that case, an ohmic contact is desireable with the opposite choice of electrode metals [95].

The method of derivation of the size and capacitance of the depletion layer is identical to the one-sided abrupt pn junction. Equations 2.36 and 2.38 apply. By

---

[13]To account for the Boltzmann tails of the ionization of dopants, $\Psi_{bi} - V - \frac{2k_BT}{q}$ has to be used.

measuring the capacitance of a Schottky diode at varying external voltages, it is possible to calculate the effective doping concentration and thus the doping efficiency.

2.3.1.3 pin Diodes

Doping concentrations in devices based on organic semiconductors are much higher than common in inorganic systems. The resulting depletion layers are significantly thinner. Kleemann et al. showed values below 10 nm [96]. These thin-films are usually not suited for blocking because of tunneling. To realize devices with a low reverse current, intrinsic layers without any doping are commonly introduced in between the p- and the n-layers, resulting in the so-called pin-design. However, classic pn junction diodes have been realized with organic materials too [79]. The resulting depletion width can be deduced via the same method as for the pn junction. The corresponding charge, field, and potential distributions are depicted in figure 2.20. Integrating over the undoped
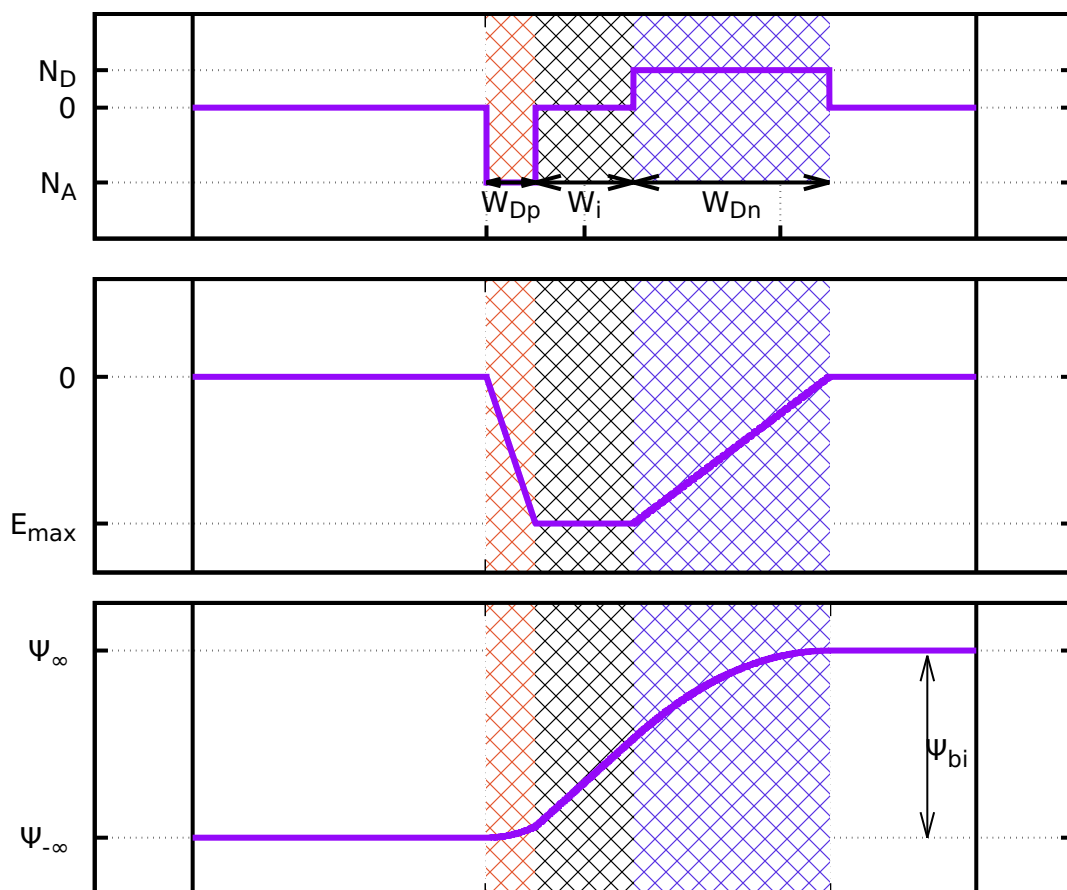
Figure 2.20: Charge density (top), internal electric field (middle), and potential (bottom) distributions within an ideal pin diode. Intrinsic, and depleted areas on the p- and n-side are marked.

intrinsic layer with thickness W_i gives a constant field E_{max}, defined by the doped layers. Additionally to the potential dropping over the depleted n- and p-area in equation 2.34, voltage is dropping over the intrinsic layer given by

$$\Psi_i = E_{max} W_i. \tag{2.39}$$

The internal voltage is, therefore:

$$\Psi_{bi} = \Psi_n + \Psi_i + \Psi_p. \tag{2.40}$$

Typical intrinsic layer thicknesses are similar in size or larger than the depletion layers created by neutralization of the two doped layers. A significant part of the applied voltage is thus dropping over the intrinsic part of the diode. The depletion layers on the p- and n-side are not the same as for the case without the intrinsic layer, because of the change in field distribution. It can then be calculated to be

$$W_{Dp} = \frac{N_D}{N_A + N_D} \left(\sqrt{\frac{2\epsilon_s}{q} \frac{N_D + N_A}{N_A N_D} \Psi_{bi} + W_i^2} - W_i \right) \tag{2.41}$$

for the p-side. The total depletion layer thickness is

$$W_D = \sqrt{\frac{2\epsilon_s}{q} \frac{N_D + N_A}{N_A N_D} \Psi_{bi} + W_i^2}. \tag{2.42}$$

Analog to equation 2.38, the Mott-Schottky equation is changed to:

$$\frac{1}{C_D^2} = \frac{1}{\epsilon_s^2} \left[\frac{2\epsilon_s}{q} \frac{N_D + N_A}{N_A N_D} (\Psi_{bi} - V) + W_i^2 \right]. \tag{2.43}$$

If the doping is one-sided, it can be used to calculate the doping profile, while the built-in potential can only be estimated if the intrinsic layer thickness is known. Kleemann et al. ([96], [97]), demonstrate the influence of the intrinsic layer thickness and doping concentration on the properties of the diodes using this method.

2.3.1.4 Stationary Current-Voltage (IV) Characteristics of the Ideal pn Junction

The Current-Voltage (IV) characteristics of a pn junction can be calculated under certain idealized assumptions:

- The depletion layer is abrupt. The internal field and potential are generated by a dipole. Outside of the depletion layer, the material is considered neutral.

- Low-injection limit applies[14].

- Boltzmann statistics can be used to describe free charge carriers, i.e. neither sides are degenerate.

- No generation or recombination of charge carriers within the depletion layer occurs.

The minority carrier concentration on the contacts is increased or decreased when an external voltage is applied. It is useful to define so-called quasi-Fermi levels for electrons E_{Fn} and holes E_{Fp} that equal the theoretical Fermi level that would generate this minority density with the standard Boltzmann equation. Utilizing charge neutrality and calculating the drift and diffusion currents, gives a boundary condition for the minority carrier density (n_{p} electrons on the p-side, p_{n} holes on the n-side) at the edge of the depletion zone ($-W_{\mathrm{Dp}}$, W_{Dn}):

$$p_{\mathrm{n}}(-W_{\mathrm{Dn}}) \approx p_{\mathrm{n}0} e^{\frac{qV}{k_{\mathrm{B}}T}}, \tag{2.44}$$

with $p_{\mathrm{n}0}$ as the equilibrium density of holes in the n-doped region and V as the externally applied voltage. This unbalance is compensated inside the neutral region within the diffusion length L_{D}, given in equation 2.27:

$$p_{\mathrm{n}}(x) - p_{\mathrm{n}0} = p_{\mathrm{n}0} \left[e^{\frac{qV}{k_{\mathrm{B}}T}} - 1 \right] e^{-\frac{x-W_{\mathrm{Dn}}}{L_{\mathrm{Dp}}}}, \tag{2.45}$$

for holes.
The current necessary to realize this relaxation via diffusion can be calculated to be:

$$j = j_{\mathrm{p}} + j_{\mathrm{n}} = j_0 \left[e^{\frac{qV}{nk_{\mathrm{B}}T}} - 1 \right], \tag{2.46}$$

with

$$j_0 = \frac{qD_{\mathrm{p}}p_{\mathrm{n}0}}{L_{\mathrm{Dp}}} + \frac{qD_{\mathrm{n}}n_{\mathrm{p}0}}{L_{\mathrm{Dn}}}. \tag{2.47}$$

This equation is known as the Shockley equation and describes the ideal behavior of a perfect pn junction, depicted on the left of figure 2.21. Even for inorganic diodes, this equation describes the real behavior only qualitatively. Diodes based on organic semiconductors show significant deviation from this ideal case, especially because of recombination and series resistance. The parameter n is called the ideality factor and equals one for an idealized device. It describes how close the IV characteristic behaves compared to this idealized version of the pn junction. It is heavily influenced by recombination.

---

[14]Low-injection limit refers to the injected minority carrier density being lower than the intrinsic majority carrier limit.

2.3.1.5 Properties of Non-Ideal Organic Diodes

Actual devices differ from the ideal case, sometimes in significant ways. Every real device – organic and inorganic – features series and shunt resistances that can dominate the IV characteristics at high and low voltages. Furthermore, recombination inside the charge depletion zone has been neglected during the derivation of the Shockley equation, which is especially problematic when investigating organic semiconductors with their tendency for traps and short diffusion lengths. Organic diodes show additional complications. As already mentioned earlier, the depletion width of doped organic diodes is usually small due to the high doping concentration [96], leading to tunneling currents. Additionally, injection barriers at the electrodes and the dependence of mobility on the carrier density and strength of the electric field modify the IV characteristics. Investigating and understanding the complex shape of the IV relation can give valuable insight not only into basic material and system properties ([98], [99]), but can also illuminate the pathway to optimization of entire devices ([100], [101]). Complementary to pn-, pin-, and Schottky diodes, so-called metal-insulator-metal devices are regarded as diodes in the field of organic semiconductors. It is assumed that because of the small layer thickness (order of magnitude: 100 nm)
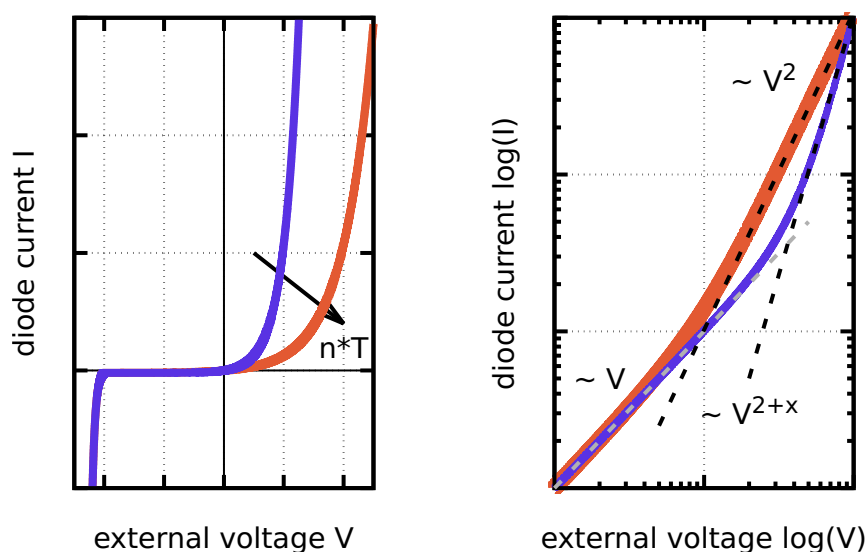
Figure 2.21: IV behavior of ideal and real diodes:
left: Ideal IV-curve of pn junction according to Shockley equation 2.46 including breakdown behavior in reverse direction. Forward current is heavily dependent on temperature and ideality factor. Breakdown in reverse direction features steep slopes (breakdown voltage and behavior can change with temperature depending on the mechanism.).
right: IV characteristics of realistic organic diodes: low voltage regime is dominated by ohmic currents. The red (fat) curve shows the direct transition from ohmic over Shockley to Space Charge Limited Current (SCLC) behavior without trap limitation. The current at high fields is $\propto V^2$. The blue (thin) curve depicts a trap-limited device. Currents are below the trap-free junction at any voltage. The slope is $\propto V^{2+x}$, with x depending on the trap density, layer thickness, field, and density dependence of the mobility.

and the comparably low background doping of pristine organic semiconductors, the depletion zone formed by the metal electrodes stretches over the entirety of the device. The semiconductor can then be treated as an insulator without any intrinsic free charge carriers. Aside from asymmetric electrodes. These devices are not rectifying and therefore do not qualify as a diode. However, they are still suited to investigate fundamental properties of diode behavior, e.g. the balance between injection limitation and bulk limitation of transport.

It is often not possible to describe the IV response of a device over the full range of applied voltages with a single theory, since different mechanisms and processes are dominant. Nevertheless, several groups proposed model systems to give a unified model for a wide spectrum of voltages ([102], [103], [104]). According to Jain et al. [104], the IV-curve can, in general, be split into several distinct regions. The forward direction shows ohmic behavior at low voltages transitioning either into a Shockley-like or power-law dependency. For high voltages, the slope saturates either into a quadratic dependency in case of ideal space charge limitation or another power-law, when other factors such as trap-release or field-dependent mobility play a dominant role. The reverse voltage regime shows the same initial ohmic behavior followed by a breakthrough at higher fields [97].

For the operation of OLEDs, the high voltage regime is significant, since light emission only starts at an onset voltage V_d larger than the built-in potential. While organic solar cell operation takes place below the open-circuit voltage, which roughly corresponds to the built-in voltage [105].

The origin and exact description of the low field ohmic contribution are broadly discussed. One contribution is the existence of leakage paths through the semiconductor causing ohmic behavior [78]. Additionally, assuming an ohmic contact, current can arise from a finite doping concentration n, be it intentional or intrinsic. The resulting current through a layer thickness L with mobility μ is then given by:

$$j = nq\mu\frac{V}{L}.$$

(2.48)

However, Wetzelaer et al. [106] found the current to be of diffusive origin, caused by the level bending at the interface. It is created by an accumulation of charge carriers at the interface diffusing from the metal into the semiconductor. The resulting current shows a stronger dependence on the layer thickness:

$$j = 4\pi^2\frac{k_B T}{q}\epsilon\mu\frac{V}{L^3}.$$

(2.49)

Kim et al. [105] present a model system for the low voltage regime of asymmetric single layer diodes. They attribute a non-ideality factor to the standard Shockley equation to account for trapping. A deeper analysis of the diffusion currents at low voltages has been given by Wetzelaer et al. [78]. Plotting the ideality factor,

defined as

$$n = \left(\frac{k_\mathrm{B}T}{q} \frac{\partial j}{\partial V} \right)^{-1},$$
(2.50)

gives information about the trapping related behavior of the transport. An ideality factor of one corresponds to an ideal diode as described by the Shockley theory. An ideality factor of two is the result of Shockley-Read-Hall assisted recombination, described by Sah et al. [107].

Fischer et al. [98] propose a method to derive the trap density from measurements of IV-curves of pip (doped-intrinsic-doped) devices with varying thickness of the intrinsic layer. The profile of hole density throughout the device changes for different thicknesses of the total stack. The corresponding trap concentration can then be extracted from the exponents of the power-law-dependence of the IV characteristic.

At sufficiently high fields, the charge transport is limited by the space charge of the moving carriers themselves and (SCLC) occurs. The current follows the so-called Mott-Gurney law [108]:

$$j = \frac{9}{8} \epsilon_\mathrm{s} \mu \frac{(V - V_\mathrm{bi})^2}{L^3}.$$
(2.51)

Measurements of the space charge limited current allow for an extraction of the vertical charge carrier mobility. However, this regime is only observable if all other limiting factors are negligible. Classic Shockley theory applies for diffusion-based systems, while space charge limitation is a field-driven phenomenon. Kim et al. [105] report that the SCLC regime is not measurable if the injection barrier at the limiting interface is larger than $0.3\,\mathrm{eV}$. According to Arkhipov et al. [100], this limit is variable. They report a change in the dominant mechanism between injection and space charge limited current depending on the temperature.

Equation 2.51 gives a direct approach to measure charge carrier mobilities in vertical devices. However, the device preparation and analysis is difficult, since space charge limited current only occurs when injection is sufficiently efficient and negligible. Even when SCLC behavior can be observed, care must be taken, since a slope of two in the double-logarithmic plot can mistakenly be the cause of trapped carrier release [98]. The typical thickness variation ($\propto \frac{1}{L^3}$) can differ too, due to density-dependent mobilities, described by Agrawal et al. [109]. In contrast to that, carrier densities occurring in organic diodes are often deemed too small to show any significant impact on the average mobility [105].

Jain et al. [104] discuss the transition from ohmic to SCLC behavior for doped films. The doping allows for initial ohmic conduction due to free charge carriers, which transitions into space charge limitation once the injected carrier concentration is higher than the effective doping concentration. Under the assumption of no injection barrier at the interface, measurement of the transition voltage V_tr allows

for estimation of the real doping concentration via:

$$V_{\text{tr}} = \frac{8 q n_0 L^2}{9 \epsilon_{\text{s}}}.$$

(2.52)

As an alternative to SCLC or numerical methods, Wetzelaer [110] proposes an analytical model to extract mobilities from IV-data using the injection- and drift limited regime. A different approach has been presented by Widmer at al. [111], mapping the mobility and carrier density through the stack using a variation in thickness called Electric Potential Mapping by Thickness Variation (POEM).

2.3.2 Devices and Applications Based on Organic Diodes

2.3.2.1 Organic Light Emitting Diodes (OLEDs) and Organic Solar Cells

The pn junction of inorganic and organic diodes alike can be used to generate photons from electrical current or to generate electrical power by harvesting photons. Solar cells are not in the scope of this thesis and will not be discussed further. Information can be found in recent review articles ([112], [113], and [114]). However, they are one of the first vertical devices fabricated using the crystalline-type of rubrene presented here [50]. From these measurements, it is possible to extract a lower boundary for the exciton diffusion length in this material system of 200 nm.

The viability to utilize crystalline rubrene as a base for homo-junction organic light-emitting diodes is investigated in chapter 5.4.1. Since it is not a major topic, only the basics of OLED function will be discussed. Further explanation can be found in review articles, covering current improvement in OLED efficiency [115], optical design [116], white OLEDs [117], or their application in display technology [118].

Organic light-emitting devices are usually vertically stacked structures of metallic and organic layers, each with their individual function. They can be broadly split into top- and bottom-emitting, depending on which side of the substrate/structure the light out-coupling takes place. Although the spectrum of organic emitters is – compared to inorganic semiconductors – rather wide, white emission is usually obtained by either stacking or partnering of multiple cells with different colors or via conversion layers. Not only the electrical performance but also the geometric out-coupling of photons is a major field of investigations and crucial for an efficient device.

The general structure of an OLED is shown in figure 2.22 and consists of: 1. injection of charge carriers, 2. transport of charge carriers towards the emission layer, 3. trapping of charge carriers within the emission layer, 4. creation of excitons, 5. radiative recombination of excitons. Carrier injection takes place at the bottom and top electrode, for either electrons or holes. Electrodes can be optimized to provide optimal ohmic injection. Special care has to be taken on

the side of light out-coupling, to minimize the amount of quenched photons. The injected carriers are transported in hole transport layers (HTL) and electron transport layers (ETL) on both sides of the device. Via the thickness of these layers, the field distribution, carrier balance, and total thickness can be controlled. For efficient devices, the conductivity has to be high, thus, HTL and ETL are usually heavily doped. Adjacent to the transport layers are the electron and hole blocking layers (EBL and HBL). The HOMO and LUMO values of these materials
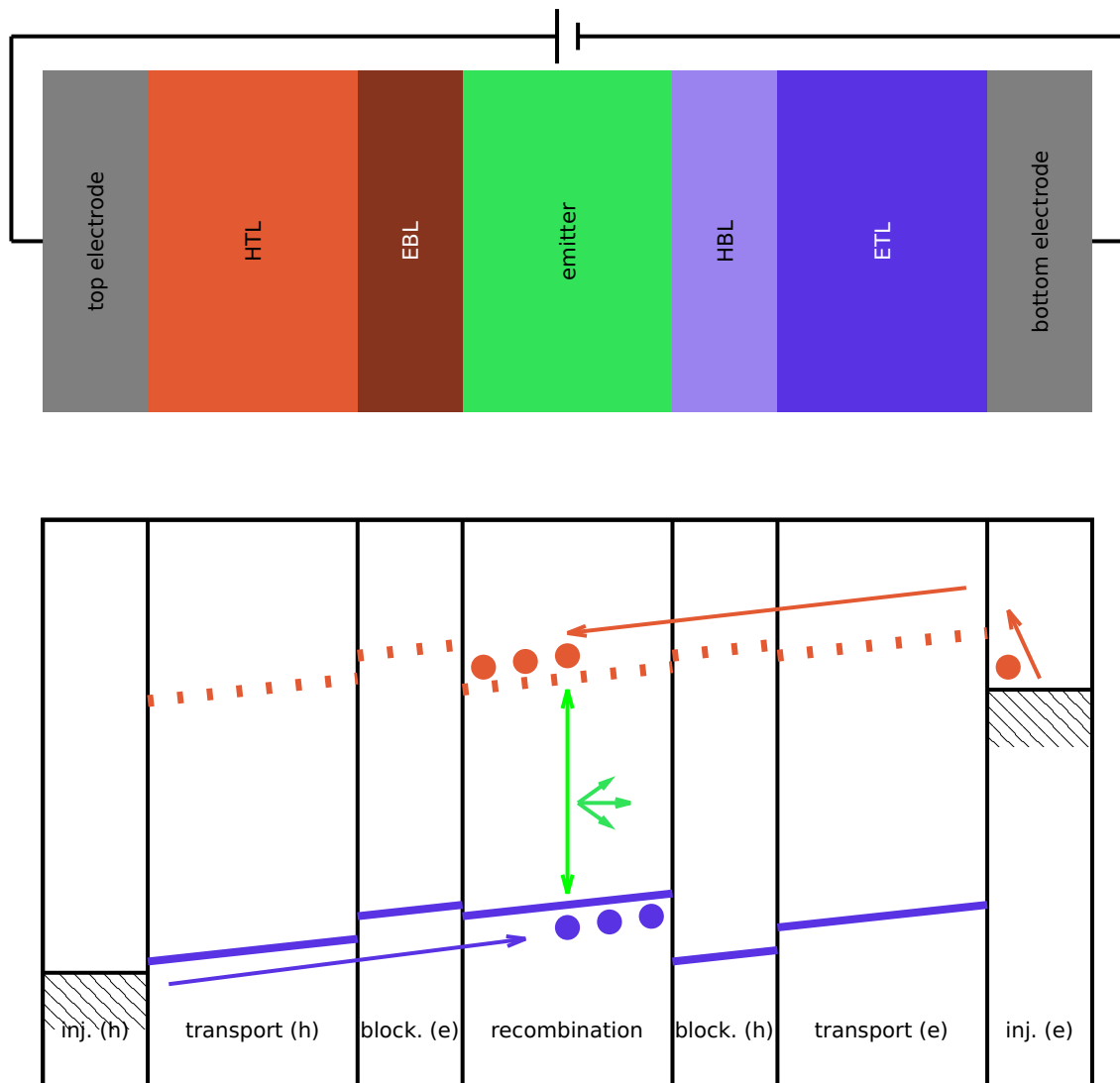
Figure 2.22: Stack and energy levels of standard, single-cell OLED:
-top and bottom electrode optimized for efficient hole and electron injection (fitting energy levels or contact doping)
-Hole Transport Layer (HTL) and Electron Transport Layer (ETL) for optimized carrier transport (high mobilities and strong doping)
-electron and hole blocking layers (EBL and HBL) prevent the escape of carriers from the emission layer (high step in Lowest Unoccupied Molecular Orbital (LUMO) or Highest Occupied Molecular Orbital (HOMO))
-emission layer for exciton formation and radiative recombination (emitter doping if necessary).

are chosen to minimize the injection of electrons into the HTL and holes into the ETL from the wrong direction. Therefore, they actively trap charge carriers in the emitter layer to give more time for exciton formation. The emission layer can consist of only a single material. However, usually a matrix material (efficient in exciton formation and carrier injection) is doped with an emitter material (efficient in radiative relaxation of excitons). An efficient transfer mechanism for excitons from the matrix to the dopant must be available, for example via Foerster resonant energy transfer (FRET). It is essential for an efficient OLED to ensure charge carrier balance, thus, the same amount of holes as electrons reaching the emission layer. An imbalance results in excitons being created outside of the emission layer, resulting in inefficient or no light emission at all.

2.3.2.2 Organic Diodes as Circuit Components - Organic Half-Bridge Rectifiers

Aside from energy conversion from and into light, diodes can serve several different roles in electronic circuits in general. Most of the focus in the field of organic electronics is on organic transistors, utilizing the specific properties of organic semiconductors like flexibility [119] or biological compatibility [120]. Elsobky et al. present a library of organic transistors circuits and possible applications [121]. Even some more complicated circuits, like digital to analog converters, are already realized [122].

Transistors are the standard choice for switching applications. However, some basic digital circuits can be realized with diodes too. Figure 2.23 depicts a

Figure 2.23: Alternative roles for diodes in circuits.
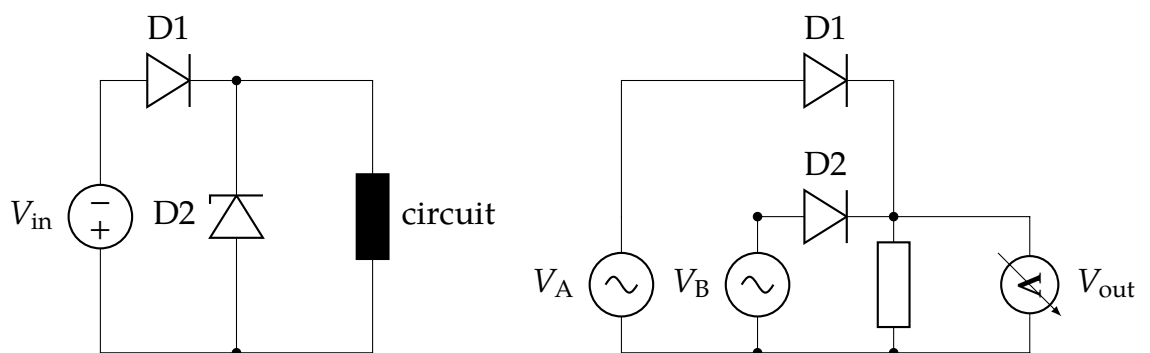
(a) Circuit protection diodes: D1 serves as polarity protection, blocking any current to the circuit if the external polarity is wrong. D2 (Zener diode) blocks current up to a certain breakdown voltage. Any input voltage higher causes a strong current through the diode, limiting the voltage applied to the circuit.

(b) Diodes as logic-OR operator: A HIGH-signal on either input A or B causes current flow through the corresponding diode and therefore through the resistor. The resulting voltage drop can be measured as the output signal.

logic-OR operator realized with diodes. Using diodes instead of transistors is usually significantly less power efficient (especially compared to FET circuits) and the degree of cascading (passing of a signal down a logic chain) is significantly limited. However, switching speeds of the fastest organic transistors are in the range of MHz [123], while organic diodes are already advancing into the GHz region ([124], [125]).

In applications where current flow is supposed to be restricted into one direction only, diodes are the obvious choice. Diodes with low forward voltage drop are suitable for polarity protection and devices with tailored reverse breakdown [97] can be used as over-voltage protection (see figure 2.23). One major application for diodes is rectification. Power rectifiers are used to transform comparably low frequency AC voltage (from transformers or induction coils in wireless devices) into DC voltage. For this purpose, diodes should feature a low forward voltage drop and be capable of driving high currents. Switching speeds are usually low (Hz to kHz). Signal rectifiers transform a HF radio signal into a DC signal. The higher the frequency of the carrier wave, the further signal transmission can take place and the higher data densities are possible. These circuits are a key component of Radio Frequency Identification (RFID) technology that has shown steady progress in performance and field of application [126]. Currently used systems are based on the HF band at 13.56 MHz, featuring medium transmission rates and ranges of dozens of cm to 1.7 m. Ultra High Frequency (UHF) (860 MHz to 960 MHz) transmit up to several m, while frequencies in the GHz-regime transmit up to dozens of meters. An overview of frequency bands and applications is described by Lou et al. [127].

The simplest possible rectifier is the half-wave rectifier, consisting of a single diode and a smoothing capacitor. The circuit diagram is depicted in figure 2.24a. During the positive half of the AC input signal, the diode is conductive and charges the capacitor. During the negative half, the diode blocks and no current flows from input into the circuit. Without the capacitor, the average voltage across

Figure 2.24: Non-bridged rectifier circuits.
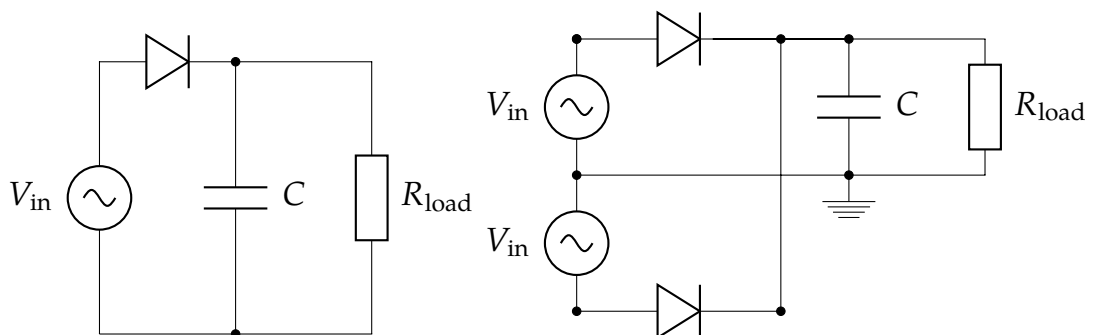
(a) Half-wave rectifier circuit.

(b) Full-wave rectifier circuit with middle ground connection.
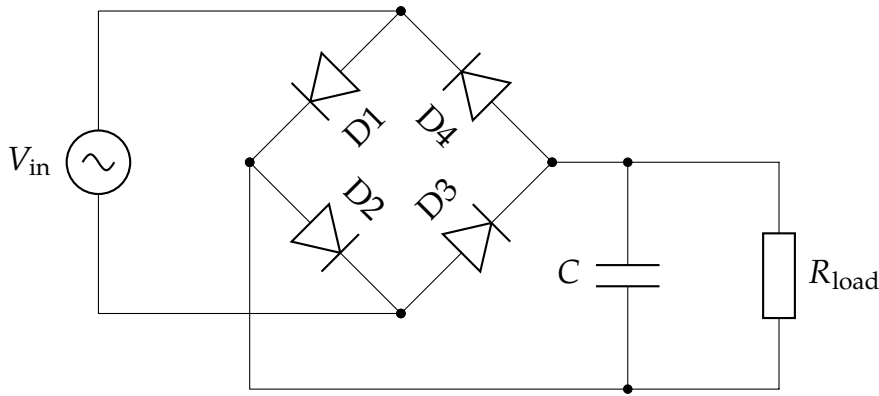
Figure 2.25: Full-bridge rectifier circuit.

the load is given by the integral over half of a cycle. Thus, for a sinusoidal input rectified by an operation f_{rect}:

$$\overline{V_{out}} = \int_0^T f_{rect}\left(V_{max}sin(\omega t)\right) dt = \int_0^{\frac{T}{2}} V_{max}sin(\omega t)dt = \frac{V_{max}}{2\pi}. \qquad (2.53)$$

Using a smoothing capacitor C, a constant DC output voltage V_{out} is generated. The remaining ripple voltage V_{pp} – the leftover AC signal superimposed with the DC-offset – at a given DC driving current I through a load R_{load}, is given by:

$$V_{pp} = \frac{I}{fC} = \frac{V_{out}}{R_{load}Cf}. \qquad (2.54)$$

The resulting smoothed output voltage at no load is given by the maximum input voltage V_{in}^{max} reduced by the voltage drop over the diode V_D to be $V_{out} = V_{in}^{max} - V_D$. For simple half-wave rectifiers, the ripple voltage is large and the possible output power is low, since only 50 % of each phase contributes to usable current. If more power and higher signal quality are needed, full-wave rectifiers should be used. The full-wave rectifier, depicted in figure 2.24b, consists of two diodes, fed from an AC signal featuring a middle ground connection. For the positive half cycle, the upper diode conducts current, while the second diode is active at negative voltages. The resulting medium voltage without a smoothing capacitor is

$$\overline{V_{out}} = \int_0^T V_{max}|sin(\omega t)|dt = \frac{V_{max}}{\pi} \qquad (2.55)$$

while the remaining ripple voltage, while using a capacitor C is

$$V_{pp} = \frac{I}{2fC} = \frac{V_{out}}{2R_{load}Cf}. \qquad (2.56)$$

Note, that the remaining AC-ripple for this setup has double the frequency of the initial signal. Voltage loss is identical to the half-wave rectifier. While this setup features significant performance improvements, realizing a symmetric signal with middle ground connection is only common for transformer-based power supplies. The implementation of this circuit for data-carrying signals is difficult, especially at high frequencies. An alternative circuit is the so-called full bridge rectifier, shown in figure 2.25. It utilizes a set of four diodes and does not need a special signal or power source. The main disadvantage is an increased complexity due to double the number of diodes and double the voltage loss, since current has to pass two diodes in series at every time. Ripple voltage and frequency are identical to the full-wave rectifier.

Power rectification is usually applied with low-frequency signals, e.g. 50 Hz power lines. The limiting factor is the amount of power or current the diodes can provide in forward direction and the voltage they can block in reverse direction without breaking[15]. However, for high-frequency situations – as needed for RFID application – the switching speed of the diode is relevant.

The maximum switching speed – or transition frequency f_T – can be estimated roughly via the transit-time of charge carriers through the thickness of the device dictated by the mobility [128]:

$$
f_{max} = \frac{1}{t_T} = \frac{\mu\,(V_{in} - V_{dc})}{d^2}.
\tag{2.57}
$$

However, this method assumes a constant mobility and a homogeneous field distribution, both not necessarily fulfilled in organic devices. Additionally, many other processes can limit the transition frequency of a diode or reduce the maximum frequency of operation of a circuit. A better approach has been suggested by Steudel et al. [129] integrating the current flow during forward bias and comparing it to the current flow through the load during one full cycle:

$$
\frac{V_{dc}}{R_{load}} \frac{1}{f} = \int_{t}^{t+T} I_{diode\ forward} dt.
\tag{2.58}
$$

However, this approach explicitly assumes no reverse current and leaves the IV-behavior of the diode open. Unless the exact IV response at the frequency in question is known, proper calculations are difficult. The only certain way of measuring the HF capabilities of a rectifier circuit is the measurement of the output signal at increasing input frequencies.

One effect of AC-biasing that is not visible in DC measurements is the transient properties of diodes. When applying a voltage, charge carriers have to move into their equilibrium distribution before steady-state operation is reached. For

---

[15]Note that the peak reverse voltage is approximately twice the amplitude of the input voltage, since the negative input voltage in the negative half cycle is in series to the voltage held by the capacitor.
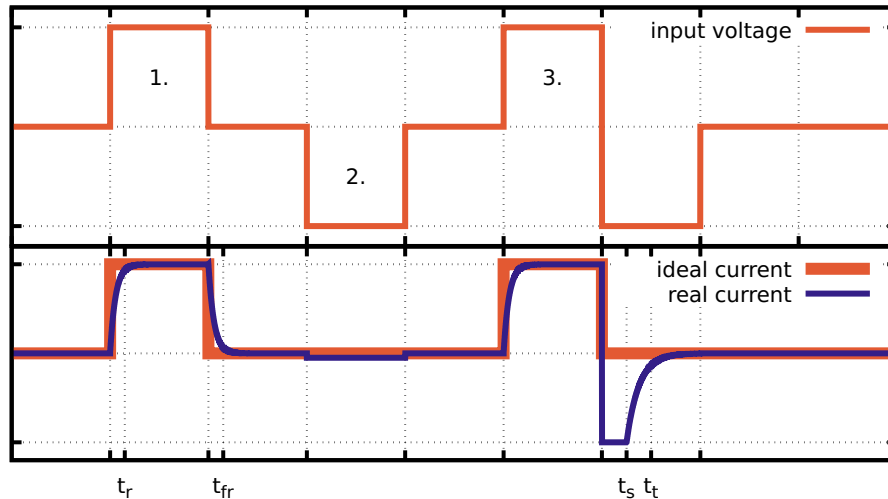
Figure 2.26: Ideal and real current through a model pn junction diode at different pulse conditions:
First pulse: Positive current caused by positive bias requires time to build up and relax.
Second pulse: Negative current through reverse bias pulsed from zero bias causes low reverse leakage current.
Third pulse: Negative current through reverse bias pulsed from positive bias causes high leakage current.

example, the charges stored in the junction capacitance creating the built-in potential have to be extracted if forward bias is applied before a forward current can flow. A detailed description and calculation can be found in Sze et al. [55]. The transient behavior of a classic diode is shown in figure 2.26. The rise time t_r is the time needed to switch a diode from zero bias to 90 % of its steady-state forward current I_F. While t_{fr} – the forward recovery time – gives the time required to drop below 10 % of the forward current after the external voltage has been set to zero. Applying a negative – blocking – voltage to the diode from zero voltage does not change the capacitance of the device significantly. Since there are no free charge carriers, the current is given by the saturation current I_0, which is reached comparably quickly. However, different behavior can be observed when the diode is switched from forward bias into reverse bias, as is usually the case for rectification. Directly after the switching, free charge carriers are still present in the depletion zone and the conductivity of the device is high. While the carrier density is higher than the equilibrium density, the reverse current I_R is practically constant. This so-called storage time can be estimated via:

$$t_s \approx \tau_i ln \left(1 + \frac{I_F}{I_R} \right),$$ \hfill (2.59)

with τ_i as the minority carrier lifetime in the weaker doped side. After t_s, the minority density sinks below the equilibrium value during the transition time t_t. The reverse current is lowered to its final value close to the saturation current

and the voltage drop over the diode reaches its maximum. The total time needed to reach full depletion of the junction is called reverse recovery time t_{rr}.

Since the diode conducts current in reverse direction during the reverse recovery time, rectification is heavily reduced once the frequency of the input signal approaches $\frac{1}{t_{rr}}$. Other properties that influence the switching speed of the diode are its capacitance and its conductivity. A high capacitance, be it the geometric capacitance of the metal electrodes or the junction capacitance, increases recharging times of the entire device. High conductivity is needed to not only speed up the charging speed of the internal capacitances but additionally to supply enough current to the load.

2.3.2.3 State of the Art Organic High Frequency (HF) Diodes

The transition frequency showed steady progress during the last years, peaking into the first GHz-capable components. To compare different devices, a measurable value has to be defined. In literature, two different approaches can be found. The more common value is the so-called 3 dB-cutoff frequency f_{3dB}. At this frequency, the output power is half of its low-frequency value. For a rectifier, this means the output voltage is reduced to $\frac{1}{\sqrt{2}}$th of its original value, since $P = UI = \frac{U^2}{R}$. If a rectifier supplies only a single ohmic load, the frequency-dependence of the output voltage follows the following dependence [131]:

$$V_{\text{out}} = \frac{V_0}{\sqrt{1 + \left(\frac{f}{f_{3dB}}\right)^2}}, \tag{2.60}$$

with V_0 as the maximum output voltage at low frequencies.

An alternative approach for HF signal rectification is to determine f_0 – the frequency at which the DC output voltage is zero. Since at these extreme frequencies efficiency and power of the conversion are of minor interest, the maximum frequency at which a signal can be obtained at all is more significant. However, measurement of f_0 is difficult, which is why it is usually extrapolated. An additional difficulty in measuring at these frequencies is resonances. Because of the small wavelength of the input signal, device dimensions in the cm-regime, closed-loop parasitic inductances, and parasitic capacitances in general, can cause additional oscillations. If these are not taken into account or properly filtered, the resulting output voltage can feature distinct oscillating frequency-dependencies, masking the real diode properties. Many publications do not address these issues at all, which suggests that values for cutoff frequencies presented might be higher than the intrinsic device property. Resonance at the input of the circuit would increase the effective applied voltage and thus compensate for the reduced response of the device. The measured frequency response is hence a convolution of the diodes frequency behavior and the circuits resonance pattern.
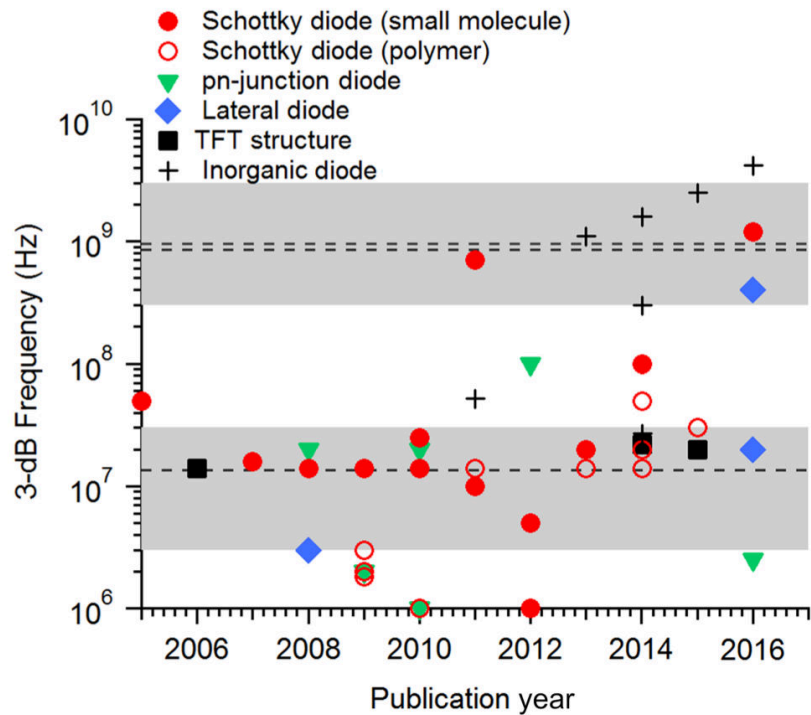
Figure 2.27: Frequency characteristics of organic rectifiers published over time. The gray shades indicate the range of the HF (3 MHz to 30 MHz) and UHF 0.3 GHz to 30 GHz bands and the dashed lines denote the standard frequencies. (Taken from Kang et al. [130].).

Kraft et al. [132] present a review of different technologies and theoretical descriptions for printed and organic HF diodes. Not only rectifiers but also charge pumps and other circuits are discussed. Kang et al. [130] present a summary of the progress in transition frequency from 2005 to 2016, comparing the different technologies. The overview graph is shown in figure 2.27. Mostly half-wave rectifiers are investigated due to their simple design. Inorganic diodes are still occupying the positions for the fastest diodes, even for printed devices. Zhang et al. [133] present IGZO-based diodes with a cutoff frequency of 4.2 GHz. Sani et al. [125] produced fully printed devices based on Si and $NbSi_2$ operating at 1.6 GHz. The fastest reported organic pin-devices – based on doped pentacene$/C_{60}$ – are shown by Kleemann et al. [124], extrapolating their data to $f_0 > 1$ GHz and s corresponding cutoff frequency of ≈ 20 MHz. In case of organic diodes, Schottky diodes show the fastest reported switching. The – up to date – fastest organic diodes are shown by Kang et al. [131], based on modified injection from pentacene into gold electrodes. The interface between the metal and the semiconductor has been altered with the SAM PFBT. They claim a f_{3dB} of 1.24 GHz, however, according to their data – depicted in figure 2.28, the value has been extracted at $\frac{V_{out}}{2}$ and thus at half voltage and not half power. The real cutoff frequency is around 500 MHz. Thus, organic diodes that can rectify signals with f_{3dB} of over 1 GHz have not been shown till now. Organic diode rectifiers are not only a tool to experimentally explore the limits of transient behavior: Sirringhaus et al. [134]
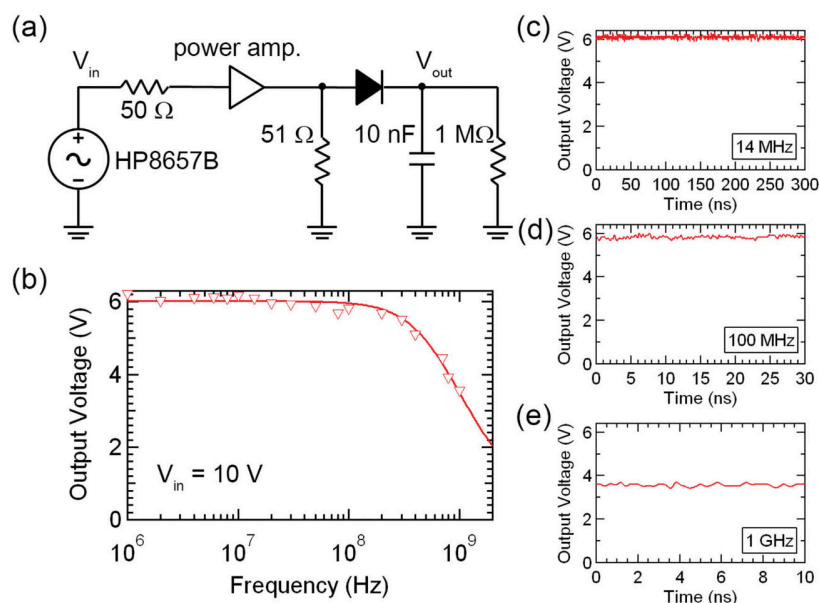
Figure 2.28: Measurement by [131]: Half-wave rectifier(a) based on surface modification on pentacene layers. Direct Current (DC)-output signal at different input frequencies(c-e). f_{3dB} is claimed to be 1.24 GHz (Does not fit the measurement in (b)!).

present circuits utilizing the power and signal rectification in a fully organic RFID tag, although at comparably low frequencies.

2.3.3 Organic Field-Effect Transistors (OFETs)

FETs are the backbone of microelectronics and, therefore, to a certain extent of modern society. The dominant technology is the so-called Metal-Oxide-Semiconductor Field-Effect Transistor (MOSFET). They serve various roles: Ultra-fast switching enables high-speed calculations in processors for super-computers and smartphones alike. High power transistors can switch gigantic currents enabling not only the power modulation of consumer-grade electric appliances, but also the control of large scale DC-power transmission, enabling the transition from traditional, but inefficient Alternate Current (AC)-power distribution to DC-systems. This extreme scalability and the comparably low-cost, given the main ingredient is abundant Si, are the main strength of this technology. However, economically, the manufacturing costs are still one of the strongest driving factors for technological development. In the case of inorganic FETs, there is a clear separation, based on the requirements of the application: low-power and low-frequency transistors are made cheaply with amorphous Si ($\approx 1 \, cm^2 \, V^{-1} \, s^{-1}$ [135]), medium demands are satisfied with poly-crystalline Si ($\approx 1 \, cm^2 \, V^{-1} \, s^{-1}$ to $100 \, cm^2 \, V^{-1} \, s^{-1}$ [136]), while only the highest performing transistors are based on expensive single-crystalline material ($\approx 100 \, cm^2 \, V^{-1} \, s^{-1}$ to $1500 \, cm^2 \, V^{-1} \, s^{-1}$ [136]).

Many high-mobility organic semiconductors are in the range of (or even surpass) amorphous silicon. There is already a niche for organic semiconductors to fill in regard to low-cost electronics since cost of manufacturing and material are
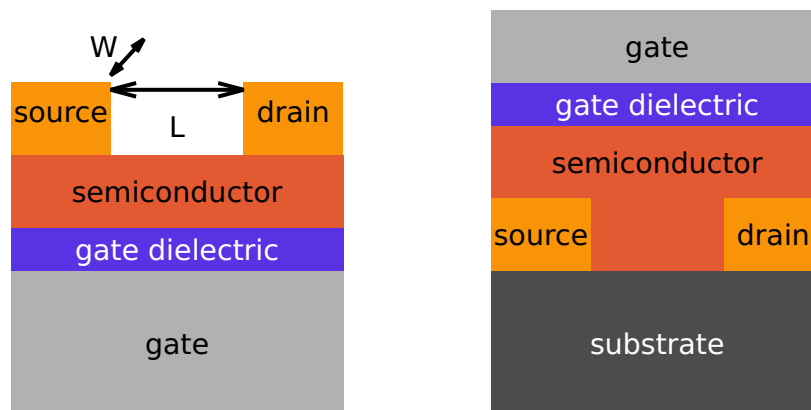
Figure 2.29: Two typical layouts for thin-film transistors: bottom-gate/top-contact (left) and top-gate/bottom-contact (right)
The channel length L is defined as the distance between source and drain for both configurations. The channel width W is defined as the length of electrode perpendicular to the channel but in the plane of transport.

at least potentially lower than for inorganic devices. Additionally to the roles opened up by their other distinct advantages, like flexibility and transparency. However, despite the steady improvement in mobility of organic semiconductors, the speed of poly-crystalline Si or even single-crystals will unlikely be reached, simply due to physical limitations caused by the molecular structure. Regardless, organic transistors showed impressive progress during the last couple of years, increasing currents, on/off-ratios, and transition frequencies. However, there is still a large potential for improvement open to this technology.

This chapter describes the basic working principles and performance defining properties of the FET-technology, as can be found in literature about semiconductor devices (e.g. [55] for inorganic materials). A special focus will be set on the use of high-crystalline/high-mobility organic semiconductors and the transition to vertically stacked organic transistor designs. The discussion of mobility measured with OFETs can be found in chapter 2.2.2.

2.3.3.1 Basics of Field-Effect Transistors (FETs)

The defining element of the FET is the Metal-Insulator-Semiconductor (MIS) structure. The archetype is the Metal-Oxide-Semiconductor stack, used in MOSFET technology. Understanding the MIS-capacitor enables understanding of the FET. In its heart, it represents a geometric/static capacitance in series to a variable capacitance, defined by accumulated charge carriers at the interface between the semiconductor and the insulator. The energetic landscape of the device is shown in figure 2.30 for a p-type semiconductor. Assuming a perfect
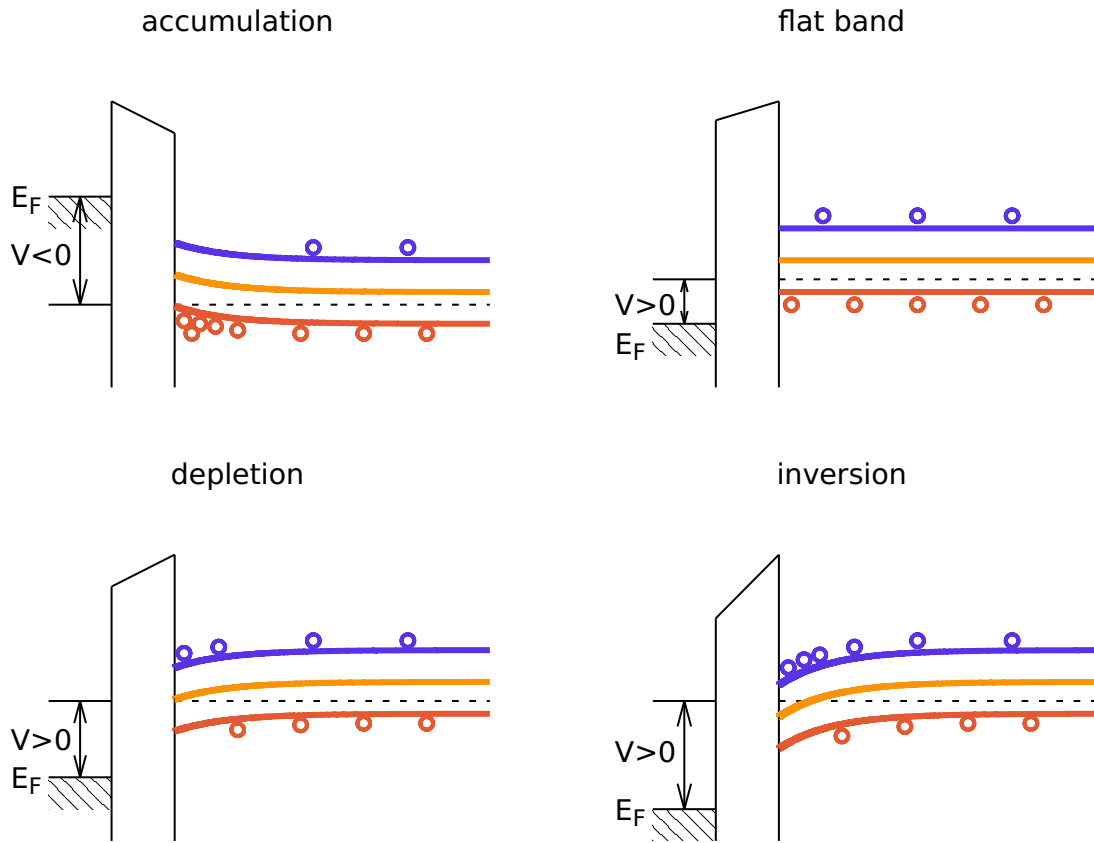
Figure 2.30: Energetic cut through p-type transistor stack perpendicular to the channel: gate, gate insulator, semiconductor (left to right). (HOMO: red, deepest energy; Fermi level: orange, middle energy; LUMO: blue, highest energy)

top left: In the accumulation regime, energy levels of the semiconductor close to the insulator are bent upwards by the gate field. The result is an accumulation of majority charge carriers at the interface.

top right: In the flat band regime, energy levels of the semiconductor are flat. Any level bending present at the interface based on a potential mismatch between the work functions of metal and semiconductor are canceled out by the gate field. Both majority and minority charge carrier density is constant throughout the semiconductor.

bottom left: In the depletion regime, energy levels of the semiconductor close to the insulator are bent downwards by the gate field. The result is a depletion of majority charge carriers at the interface.

bottom right: In the inversion regime, energy levels of the semiconductor close to the insulator are bent strongly downwards by the gate field. The result is an accumulation of minority charge carriers at the interface.

insulator (no current through the insulator layer), the different work functions of the metal and the semiconductor will cause a compensation of charge carriers, similarly to the pn- and Schottky-junction described in section 2.3.1. The energy diagram is bent upwards close to the interface. In the example, this leads to an increased amount of holes in the semiconductor which will be concentrated at the interface due to the electrostatic attraction of the leftover electrons in the metal. The result is a higher majority carrier (hole) concentration close to the insulator. When an external, negative voltage $V < 0$ (the metal is on a lower potential in comparison to the semiconductor) is applied to the stack, even more holes are pushed into the semiconductor and removed from the metal. The charge density at the interface is increasing even more. This state, where the majority carrier density at the interface $p_p(x = 0)$ exceeds the equilibrium concentration p_{p0} is called accumulation. In contrast, if a positive voltage is applied to the stack, the hole concentration is reduced. The voltage needed to get a perfectly flat energy level at the interface, and thus the same carrier density throughout the semiconductor, is called the flat-band voltage $V_{FB} > 0$. If the positive voltage is larger than the flat-band voltage, the bands are bent downwards, reducing the majority carrier density at the interface, compared to the equilibrium state (thus $p_p(x = 0) < p_{p0}$). This arrangement is called depletion, since the interface between semiconductor and insulator is depleted from free charge carriers. For high positive voltages, the bending exceeds the Fermi level of the bulk material. Then, the minority carrier concentration at the interface exceeds the majority concentration $n_p(x = 0) > p_p(x = 0)$. This is the so-called weak inversion regime. For even higher positive bias, the minority concentration exceeds the equilibrium majority concentration, leading to strong inversion: $n_p(x = 0) > p_{p0}$.

Similarly to the method used for the pn- and Schottky junction (see chapter 2.3.1), the charges can be integrated using the Poisson equation. For Accumulation and strong inversion, the space charge density at the interface is given by

$$Q \propto e^{\frac{e(V - V_{FB})}{k_B T}} \tag{2.61}$$

and in the depletion regime and weak inversion by

$$Q \propto \sqrt{(V - V_{FB})}. \tag{2.62}$$

The charge density on the interface is non-linear with the applied voltage, thus, the capacitance of the system changes. It can be written as a series connection of the insulator (plate-) capacitor C_i (defined by the thickness of the insulator d and the depletion capacitance C_D) to:

$$C = \frac{C_i C_D}{C_i + C_D}. \tag{2.63}$$

For strong accumulation, the capacitance is practically independent of the external bias. Since the carrier density is increased at the semiconductor insulator interface, the stack is equivalent to a metal-insulator-metal plate capacitor, defined by the capacitance of the insulator. For depletion and weak inversion, the surface charge density is $\propto \sqrt{(V - V_{FB})}$. The resulting depletion capacitance is thus:

$$C_D = \sqrt{\frac{\epsilon_s q p_{p0}}{2 (V - V_{FB})}} = \frac{\epsilon_s}{W_D}, \qquad (2.64)$$

with

$$W_D = \sqrt{\frac{\epsilon_s^2}{C_i^2} + \frac{2 \epsilon_s (V - V_{FB})}{q N_D}} - \frac{\epsilon_s}{C_i} \qquad (2.65)$$

as the distance from the interface until the carrier density is restored to equilibrium/bulk values. Since the carrier density is low in the depletion layer, it can be seen as an additional insulator layer with the thickness W_D.

The behavior at strong inversion depends on the speed of the measurement process. If the capacitance is measured with low frequencies, minority charge carriers have enough time to accumulate at the interface. The result is similar to the accumulation state: Total capacitance is governed by the geometric insulator capacitance. At high frequencies and sweep speeds, minority carriers are too slow to accumulate. The result is a large depletion layer and thus a thick layer of low total carrier density. The total capacitance is low. Measurement of the CV-behavior of the MIS-structure allows for the analysis of the fundamental properties, like geometric insulator capacitance and depletion/accumulation behavior.

Interface Traps   Till now, all charge carriers added and removed from the interface are assumed to be mobile. However, real devices show trap states at the interface. Trap states can differ significantly in their origin and behavior. They can be a result of the changed morphology of the semiconductor at the interface, either caused by the mismatch between the lattice constant of insulator and semiconductor or because of the surface roughness of both. A different type of traps is caused by unsaturated bonds or other chemical reactions taking place at the interface. Finally, electrostatic traps can occur, due to strong differences between the permittivity of semiconductor and dielectric. These traps can have donor or acceptor character, so trapping of holes or electrons and can be deep or shallow. The type of trap can be investigated by time and frequency-dependent CV-measurements. A summary of the impact of traps on the behavior of MIS- and FET devices has been provided by Konezny et al. [137].

Field-Effect Transistors (FETs)   There are several different types of FET devices. The focus here will be on the MOSFET or similar designs. The basic structure can

be seen in figure 2.29. The device consists of a MIS-capacitor, with two separate electrodes on the semiconductor side, called source and drain. The metal electrode on the insulator side is called the gate. The setup is termed either top-gate or bottom-gate, depending on the position of the gate with regard to the other two electrodes and top or bottom electrode, depending on the position of the source and drain electrodes with regard to the semiconductor. Hence, there are four standard geometries, with different advantages and disadvantages. Inorganic and organic FETs can, in general, be discussed similarly. Most differences are based upon different processing and field and density-dependent mobilities. A detailed review of organic field-effect transistor technology can be found in [138] by Klauk et al., [139] by Sirringhaus et al., or [140] by Yan et al., with a special focus on printed devices.

The basic operation mode of a transistor is the manipulation of the conductivity between source and drain by the gate field. If the intrinsic conductivity is low and is increased via the gate field, the device is called enhancement type. The inverted configuration is called depletion transistor. Inorganic transistors usually operate as inversion transistors. In the most classic setup, the off-current is blocked by a reverse-biased pn junction at the source and drain electrodes (in a p-channel FET, the contacts are p-doped, the bulk is n-doped). Creating inversion at the MIS-interface and thus a channel of holes between the source and drain enables effective charge transport. OFETs are commonly run in accumulation mode. The off-current is low because the intrinsic conductivity of the transistor is low. Causing an accumulation of charge carriers at the interface creates a thin channel of high conductivity, allowing for effective charge transport. The IV characteristics of both types are similar. The equations for the ideal transistor can be derived under the following assumptions:

- the MIS-capacitor of the transistor is ideal, as defined earlier

- gradual channel approximation holds (the drain to source field is small compared to the gate to source field)

- no diffusion current

- reverse leakage current is negligible

- if the channel is doped, the doping profile is uniform

- contact resistance is zero.

The derivation can be found in semiconductor literature (e.g. [55]). The drain current is then given by:

$$I_D(V_{GS}, V_{DS}) = \begin{cases} 0 & \text{if } V_{GS} < V_{Th} \\ k_{p,n}\left[(V_{GS} - V_{Th})V_{DS} - \frac{V_{DS}^2}{2}\right] & \text{if } V_{GS} < V_{Th} \ and \ V_{DS} < V_{DS,\,sat.} \\ k_{p,n}\frac{1}{2}(V_{GS} - V_{Th})^2 & \text{if } V_{GS} > V_{Th} \ and \ V_{DS} > V_{DS,\,sat.} \end{cases}$$

(2.66)

The IV-curves of the ideal FET are shown in figure 2.31. I_D over V_{GS} at static V_{DS} is called the transfer characteristics, since it describes the output at varying input. I_D over V_{DS} at static V_{GS} is called the output characteristics, showing the output conductivity of the transistor. Three distinct regimes can be identified. If the gate-source voltage is below a certain threshold voltage V_{Th}, the current is zero and the transistor is switched off. V_{Th} is a value that describes the onset of the formation of the channel. If many traps are present at the interface, more or less voltage is necessary to create or remove a conductive channel, thus the threshold voltage shifts. In inversion transistors, the threshold voltage can be controlled via the initial doping, as has been shown for organic transistors by Lüssem et al. [141] and Günther et al. [142]. However, the precise influence of traps on the threshold voltage, its shift, and its stability is still a matter of scientific discussion ([143], [144]).

For gate-source voltages higher than the threshold voltage, the transistor is switched on. If the drain-source voltage is smaller than the saturation voltage $V_{DS,\,sat.} = V_{GS} - V_{Th}$, the transistor is in the linear regime. Here the output current depends linearly on the gate-source voltage. Signal amplification is hence done in the linear regime, minimizing non-linear distortions.

If $V_{DS} > V_{DS,\,sat.}$, the device is in the saturation regime. It occurs because of a pinch-off of the channel by the drain field. More charge carriers are extracted by the drain than can be restored via the gate field. As a result, the channel is shortened compared to the distance between source and drain. The depleted part close to the drain electrode is passed with ballistic transport and the resulting current is constant with V_{DS}. This regime lends itself well for logic operations, because a change in supply voltage (V_{DS}) does not affect the output significantly. The factor $k_{p,n}$ is given by the geometry and material setup of the transistor:

$$k_{p,n} = \frac{W}{L}\mu_{n,p}C_{ins.},$$

(2.67)

with

$$C_{ins.} = \frac{\epsilon_0\epsilon_r}{d}$$

(2.68)

as the geometric capacity of the insulator, W as the channel width, L the channel length (as defined by figure 2.29), ϵ_r as the relative permittivity of the insulator, and μ as the mobility of the semiconductor. The output current thus heavily
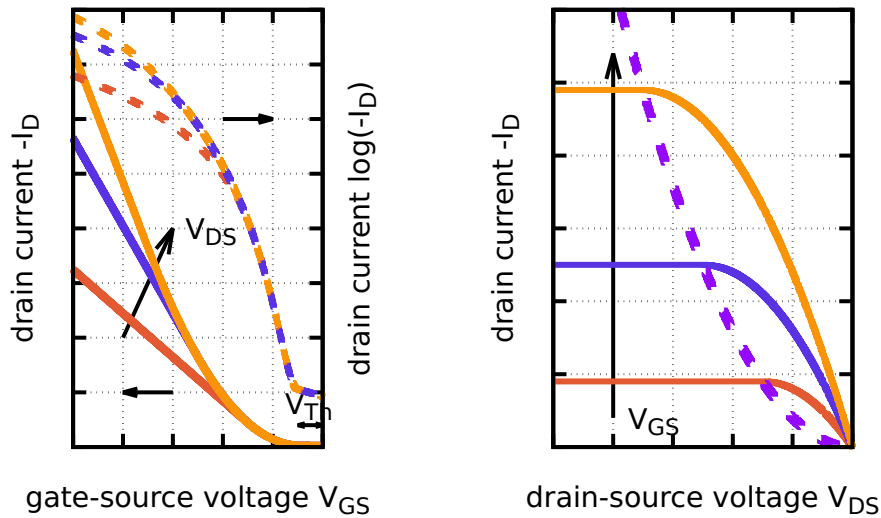
Figure 2.31: IV characteristics of an ideal FET:
left: Transfer characteristic at different drain-source voltages and identical threshold voltage: subthreshold is indicated below V_{Th}.
right: Output characteristic at different gate-source voltages and identical threshold voltage: $V_{\text{DS, sat}}$ is indicated with a dashed line.

depends on the mobility, geometry, and the overall gate capacitance of the MIS-cell. Unsurprisingly, high mobilities are beneficial for the performance of the transistor in many aspects. A higher gate capacitance can be realized either by a thinner gate dielectric or by a higher ϵ_{r}. The thinner the gate dielectric, the higher the danger of destructive gate-breakdowns. However, good results have been presented using nm-thin oxidized metal layers, grown with plasma, covered with organic self-assembled monolayer-buffers ([145], [146]). The total thickness of the gate insulator is only 5.3 nm, reaching a capacitance of $800\,\text{nF}\,\text{cm}^{-2}$. Increasing the permittivity of the dielectric can improve the gate control by enhancing the capacitance of the MIS-element, however, a large mismatch between the ϵ of the semiconductor and insulator can cause additional traps at the surface. The result is a reduced mobility [147], which is equivalent to a reduction of output current. For inorganic devices, the gate insulator is often made from oxides like SiO_2 or Al_2O_3. This is a common choice for organic transistors too, however, fully organic, polymer-based gate dielectric have promising properties too ([148], [149]).

The FET is not only useful as an electronic device but also as a benchmark for measurement and comparison of semiconductor mobilities. Based on the equations 2.66, the mobility can be derived from linear fits of the output and transfer curves. It follows:

$$\mu_{\text{FET, lin}} = \frac{L}{W} \frac{d}{\epsilon_0 \epsilon_{\text{r}}} \frac{1}{V_{\text{DS}}} \frac{\partial I_{\text{D}}}{\partial V_{\text{GS}}} \tag{2.69}$$

for the linear region and

$$\mu_{\text{FET, sat}} = 2\frac{L}{W}\frac{d}{\epsilon_0\epsilon_r}\left(\frac{\partial\sqrt{I_D}}{\partial V_{GS}}\right)^2 \tag{2.70}$$

for the saturation regime, respectively. However, especially for short channel devices or non-ideal transistors, extracting the carrier mobility via these equations can be tricky [150]. The values gained are closer to an empiric value describing the property of the overall device than a material-specific mobility.

As an alternative to the output current, it is sometimes helpful to discuss the output transconductance:

$$g_m = \frac{\partial I_D}{\partial V_{DS}}, \tag{2.71}$$

which represents the small-signal conductivity of the output. To allow for comparisons between transistors of different size or different design, output current and transconductance can be normalized to the channel width

$$\overline{I_D^W} = \frac{I_D}{W}, \tag{2.72}$$

$$\overline{g_m^W} = \frac{1}{W}\frac{\partial I_D}{\partial V_{DS}}, \tag{2.73}$$

or active device area:

$$\overline{I_D^A} = \frac{I_D}{A}, \tag{2.74}$$

$$\overline{g_m^A} = \frac{1}{A}\frac{\partial I_D}{\partial V_{DS}}. \tag{2.75}$$

However, these values have to be compared carefully, since it is often not obvious which area is part of the active device. Practically, a "technological" device area could be used that includes the entire device area including all electrodes, lines, and pads. However, devices made in laboratory-scale are rarely optimized in this regard.

Additionally, the values can be normalized to the MIS-capacitance of the insulator:

$$\overline{I_D^{W,C}} = \frac{I_D}{WC_i}, \tag{2.76}$$

$$\overline{g_m^{W,C}} = \frac{1}{WC_i}\frac{\partial I_D}{\partial V_{DS}}. \tag{2.77}$$

2.3.3.2 Non-Ideal Field-Effect Transistors (FETs)

The current for the switched off ideal transistor is zero, since diffusion currents are neglected. This is not the case for real devices. The regime below the threshold is characterized by a sharp exponential increase, given by the subthreshold swing S

[55]:

$$S = \frac{\partial V_{GS}}{\partial \left(log_{10}I_D \right)} = \frac{k_B T}{q} ln\,(10)\,n_i = \frac{k_B T}{q} ln\,(10) \left(\frac{C_D + C_i}{C_i} \right),$$ (2.78)

with the ideality factor $n_i = \left(\frac{C_D + C_i}{C_i} \right)$, which is associated with deep trap states far away from the transport levels of the semiconductor. Organic transistors reach values between 1000 mV dec^{-1} to 65 mV dec^{-1} ([138], [151], [152]). The theoretical minimum is given by $\frac{k_B T}{q} ln(10)$=58.5 mV dec^{-1} [152]. Assuming a trap-free bulk semiconductor, equation 2.78 can be used to determine the maximum density of trap states per energy at the interface $N_T^{A,E}$ [152]:

$$N_T^{A,E} = \frac{C_i}{q^2} \left(\frac{qS}{k_B T ln(10)} - 1 \right).$$ (2.79)

Analogously, by setting the surface trap density to zero and assuming the depletion width to be equal to the Debye length, it is possible to estimate the maximum bulk trap density to:

$$N_T^{V,E} = \frac{C_i^2}{\epsilon_{sc} q^2} \left(\frac{qS}{k_B T ln(10)} - 1 \right)^2,$$ (2.80)

where ϵ_{sc} is the permittivity of the semiconductor.

Contact Resistance   In the derivation of the transistor curves, the transport of charge carriers towards the channel is considered to be perfect. However, real devices show a distinct contact resistance, consisting of the injection resistance from the metal electrodes into the semiconductor and – depending on the geometry – the vertical transport from electrode to the interface, which are not enhanced by accumulation. For devices with low mobilities or sufficiently long channels, the effects of contact resistance are negligible compared to the channel resistance and thus the standard equations hold. However, for highly crystalline, high-mobility materials, like pentacene, DNTT, or rubrene and short channels, this is no longer the case. Klauk et al. [153] demonstrate the importance of contact resistance. Even moderate mobilities suffice to reach several 100 MHz (maximum frequency of operation) if the contact resistance is sufficiently small, while in contrast, even the highest mobilities fail to allow fast transistors if contact resistance is high.

Usually, bottom-contact devices show a higher contact resistance than top-contact devices [154]. The exact reasons are a matter of discussion, however, evaporation of metal into the organic layers in top-contact devices seems to be an important factor. Injection resistance at metal interfaces can be reduced either with self-assembled monolayers or via plasma-cleaning for bottom-contact devices [155] or injection doping for top-contact transistors [156]. The total resistance of the

channel can be written as a series of the channel resistance and the injection resistance:

$$R_{\text{total}}W = \frac{L}{\mu C_{\text{i}}\left(V_{\text{GS}} - V_{\text{Th}}\right)} + R_{\text{C}}W \tag{2.81}$$

Strong contact resistance in a transistor can usually be seen by a characteristic S-kink in the output characteristic. Instead of showing a linear increase with drain-source voltage, the curve is voltage-activated, usually by the modulation of the injection barrier by the gate field.

There are several methods to extract the contact resistance ([157], [158]). One of the most common is the transmission line method (TLM). Here, the channel length of a set of transistors is varied. Under the assumption that all other parameters stay the same, the contact resistance is the intercept with the y-axis in the resistance over channel length plot. The influence of the contact resistance can also be expressed as an increase in the effective channel length called the transfer length L_{T}. It represents the length underneath or on top of the source from which the current is collected to feed the channel. The concept is called the crowded current model. Equation 2.67 then changes to

$$k_{\text{p,n}} = \frac{W}{L + L_{\text{T}}}\mu_{\text{n,p}}C_{\text{ins.}}. \tag{2.82}$$

Frequency Response of Field-Effect Transistors (FETs) The most important parameter when discussing the switching speed of a transistor is the so-called unity-current gain cutoff or transition frequency f_{T}, defined as

$$f_{\text{T}} = f\left(\frac{|i_{\text{D}}|}{|i_{\text{G}}|} = 1\right) = \frac{g_{\text{m}}}{2\pi C_{\text{G}}}, \tag{2.83}$$

where C_{G} is the total capacitance of the gate (not just the channel overlap regions). f_{T} represents the maximum frequency at which a signal can still be amplified, so the small-signal drain current is larger than the gate current. In the linear regime of an ideal transistor without overlap capacitances, this can be written as:

$$f_{\text{T}} = \frac{\mu_{\text{eff}}V_{\text{DS}}}{2\pi L^2}. \tag{2.84}$$

To reach fast devices, high mobilities and source-drain voltages are beneficial. An even greater impact can be achieved by the reduction of the channel length. Since the transit path and the capacitance are both directly dependent on L, the resulting impact is squared. However, assuming real devices, this estimation should be corrected for the contact resistance and the technologically necessary overlap areas represented by an additional geometric channel length L_{ov} between
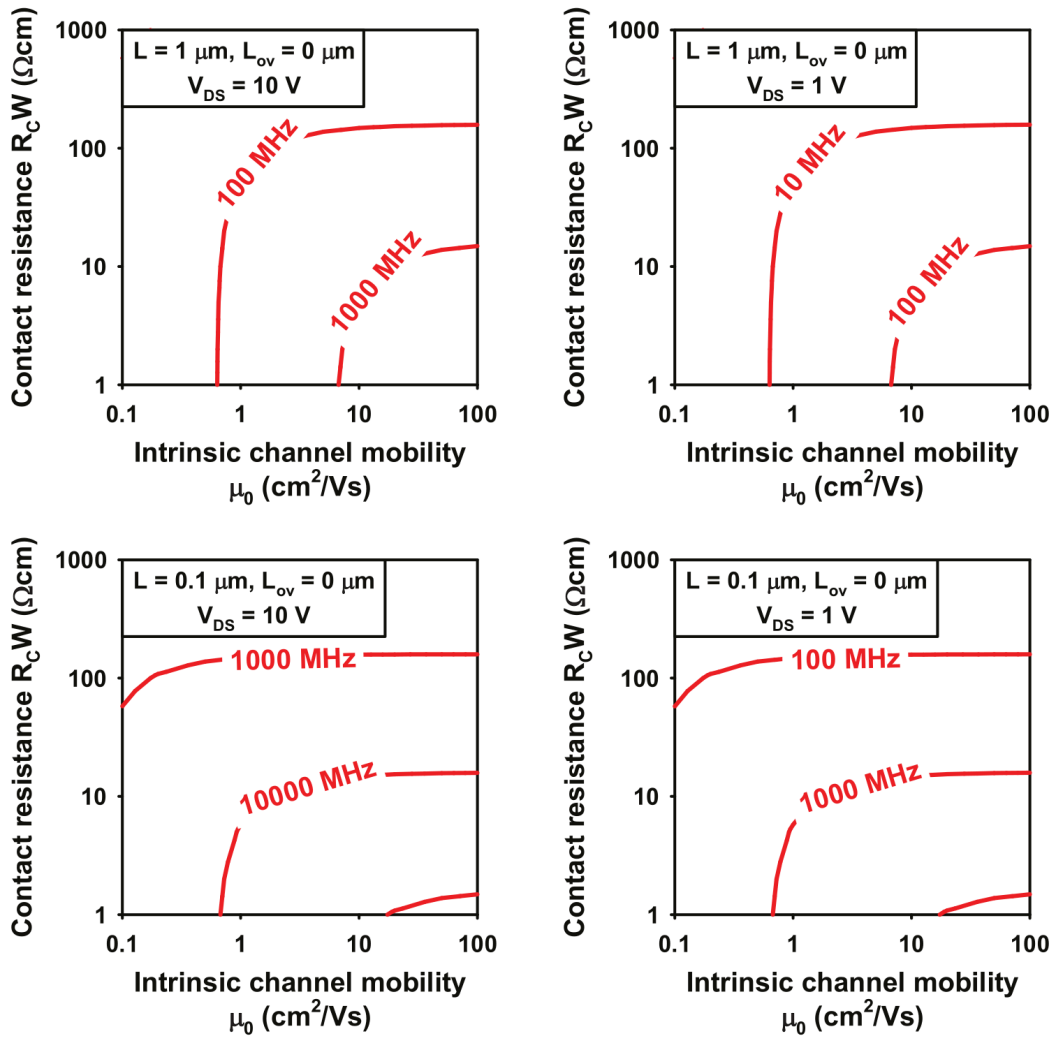
Figure 2.32: Contour-plots of transit frequency:
top: Maximum contact resistance acceptable to reach specific transit frequencies with a given charge carrier mobility at fixed channel length of $L = 1\,\mu m$ and zero overlap area for $V_{DS} = 10\,V$ (left) and $V_{DS} = 1\,V$ (right).
bottom: Maximum contact resistance acceptable to reach specific transit frequencies with a given charge carrier mobility at fixed channel length of $L = 0.1\,\mu m$ and zero overlap area for $V_{DS} = 10\,V$ (left) and $V_{DS} = 1\,V$ (right).
Graphs from [153].

gate and source and gate and drain, respectively.

$$f_T = \frac{\mu_{eff} V_{DS}}{2\pi(L + L_T)(L + 2L_{ov})}. \tag{2.85}$$

Thus, large overlaps and injection resistance have to be avoided. The influence of overlap length and contact resistance on the transition frequency has been investigated by Klauk et al. [153]. The corresponding contour plots are shown in figure 2.32.

Short Channel Effects   Reduction of channel length is a valid strategy to increase general transistor performance, however, in the initial deduction of the transistor characteristics the gradual channel approximation is used. Once the field between source and drain is comparable in strength to the field between gate and source, this assumption does not hold. The resulting changes are summarized under the concept of short channel effects. They are discussed in standard semiconductor literature, e.g. [55]. The most prominent effects are channel length modulation, drain induced barrier lowering (DIBL), threshold voltage roll-off, and space charge limitation. These effects commonly cause loss of proper saturation in the output characteristics, increased off-currents, and a shift in the threshold voltage with drain-source voltage. The standard FET equations do not hold anymore and have to be modified. A detailed analysis of short channel effects in organic thin-film transistors can be found by Locci et al. [159].

2.3.3.3 Vertical Organic Field-Effect Transistors (VOFETs)

As is obvious from equations 2.66 and 2.84, a reduction of the channel length can improve the performance of a transistor significantly. However, the lateral spacing of drain and source – that defines the channel length in common thin-film transistors – is limited by the structuring method. Modern photolithography for inorganic systems can reach far into the sub-μm range. In contrast, photolithography on organic semiconductors is significantly more challenging. Special types of orthogonal lithography can only reach down to single μm [160], while printed systems and shadow mask depositions are limited to several μm [140]. Even if complicated structuring methods are used, one predicted advantage of the OFET – or organic devices in general – is the low material and manufacturing cost. Adding expensive processes like UV-lithography would undermine that. An alternative to these processes is the adoption of a vertical device stacking. Instead of structuring lateral gaps between source and drain, the two electrodes are separated vertically by the semiconductor. The resulting channel length is then – theoretically – defined by the thickness of the semiconductor layer. Several different types of vertical transistors have been presented over the years. Two typical device types are shown in figure 6.1. Additionally, the current transport paths in comparison to the lateral OFET are depicted. Devices that resemble closely the classic lateral OFET structure are the Vertical Organic Field-Effect Transistor (VOFET) and the Schottky Barrier Vertical Organic Field-Effect Transistor (SB-VOFET) ([161], [162]). Here, the source and drain electrodes overlap directly. Leakage currents are suppressed by an insulator in the VOFET and by the Schottky Barrier at the semiconductor-metal interface for the SB-VOFET. First VOFET designs were based on a step-edge structure, where a step is formed into or on top of the substrate, defining an angled vertical separation between source and drain. Stutzmann et al. [163] present a step-edge embossed into the substrate, while Kudo et al. [164], Uno et al. [165], and Parashkov et al. [166] show
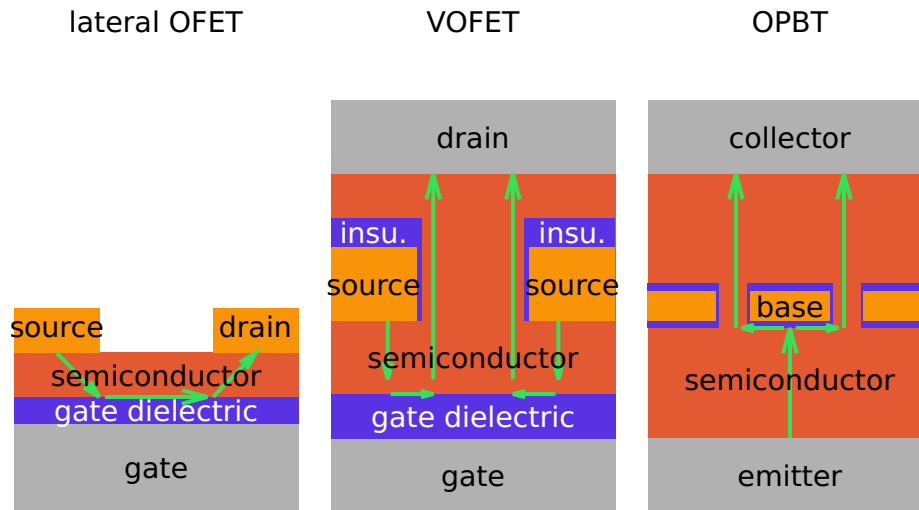
Figure 2.33: Basic geometry of the standard bottom-gate/top-contact lateral organic thin-film transistor and two vertical designs – the VOFET and the Organic Permeable Base Transistor (OPBT): Path of current flow during normal operation in the turned-on device is indicated with green arrows. (lateral and vertical dimensions are not to scale).

devices with steps structured either based on insulators or the gate electrode. A structure closer to the classic OFET, where a distinct step is not necessary, has first been presented by Nakamura et al. [167] and further developed by Kleemann et al. [168]. It is usually referred to as the VOFET. This device type was improved steadily over the years. Major points are the introduction of injection doping [169], control of threshold voltage by inversion [142] by Günther et al., a detailed analysis of the charge transport [170] by Sawatzki et al., and an investigation on light-emitting devices [171] by Lee et al. Although these devices show constant progress in transconductance and transition frequency, they do not come close to the performance one would assume based on equations 2.84 and 2.67 for a transistor with a nm-sized channel. First, the channel is not completely vertical. The source insulator that limits the leakage current [172], always shows a certain amount of overlap into the channel, larger than the source itself. This lateral part has to be overcome the same way as in classic lateral transistors. Secondly, contact resistance limits the devices, thus, equations 2.85 and 2.82 are more appropriate, highlighting the importance of injection doping and gate overlap reduction. Nevertheless, this device type has much room for improvement, especially the adaptation of high-mobility crystalline materials as semiconductors or even single-crystals is promising as is already common for lateral devices.

Another type of vertical transistor is the so-called Organic Permeable Base Transistor (OPBT). The structure is closer to a classic triode design, however, the function is comparable to an OFET with a distinct electrode and channel design. It has first been presented by Fujimoto et al. [173] and then later refined by Fischer et al. [174] and Klinger et al. [175]. Despite the low charge carrier mobility $\mu \approx 0.1\,\mathrm{cm^2\,V^{-1}\,s^{-1}}$ used in these devices, they still represent the fastest

organic transistors at a transition frequency of 40 MHz [123]. An adaptation of these devices to highly crystalline materials with high mobilities could increase the performance significantly.

2.3.4 Bipolar Junction Transistors (BJTs)

The BJT was the first transistor realized in 1947/1948 by Bardeen et al. [3] as a point-contact transistor and 1951 by Shockley et al. [5] as the junction transistor. It showed steady progress in performance, making it the dominant switching device and replacing the previously used vacuum triodes, due to its compact size and (over time) cheaper manufacturing.

In principle, it can be seen as two pn junctions stacked on top of each other with an additional electrode in between, called the base. The top and bottom electrodes are called emitter and collector. The stack can be seen in figure 2.34. A BJT can be made as an npn- or as a pnp-device. The basic operation principle is similar to the FET. The output current – here from emitter to collector – is controlled by the base. However, in stark contrast to the FET, the output is modulated via the base current, not the voltage. This might appear to be a significant disadvantage, since for the BJT a current is needed for switching operation that requires a certain amount of power. However, they offer some advantages too. Since the BJT is a bulk device, it is much less dependent on the manufacturing process. In contrast, the FET as an interface device is dependent on proper surface treatment. This is one of the main reasons why BJT were realized ahead of field-effect devices for inorganic semiconductors.

Other advantages are

- low input impedance: important for impedance matching

- high amplification/gain (with less effort than for FETs)

- less susceptibility for electrostatic damage

- lower overlap capacitances and therefore easier realization of fast transistors

- on average cheaper to make (depending on the technology).

- output stable with no input (FETs float).

However, considering the vast use of FETs in most processors, there are also significant disadvantages:

- low input impedance: energy consumption and circuit load

- lower temperature stability

- larger in size – difficult for high-density integration.

The majority of transistors produced and used today are FETs. Mostly, because the high integration density in chips for consumer and computational electronics rules BJTs out. However, they can serve as a superior alternative in many applications, such as signal and power amplification and cost-sensitive non-integrated circuits.

2.3.4.1 Fundamentals of Bipolar Junction Transistors

For inorganic semiconductors, the BJT was the first solid-state switching device shown, long before the inorganic FET. In contrast, the OFET is realized for many years, while there is no functioning example of an Organic Bipolar Junction Transistor (OBJT), yet. To understand the reason for that it is necessary to examine the principle of amplification of this device type. The general derivation can be found in any book about semiconductor basics, e.g. [55]. The BJT can be connected in different configurations, depending on which of the three electrodes is shared by the input and output side. The standard common-emitter circuit for a pnp-transistor is assumed[16]. Here, the base-emitter junction is in forward and the collector-emitter junction in reverse bias. It is the universal circuit for most amplification[17], since it provides the highest power amplification. The signal is represented by the base current I_B, driven by a voltage applied between base and emitter B_{EB}. A supply voltage V_{SS} is applied between the collector and ground, while the emitter is connected in series to the load[18].

Figure 2.34 shows the doping profile, sketched current orientation, and the energy levels of a standard BJT. If only the collector-emitter voltage ($V_{CE} < 0$) is applied and the base current is zero, almost no current flows at the output since the emitter-base diode is blocking. A negative input voltage ($V_{EB} < 0$) results in current flow at the input and electron are injected into the base and holes into the emitter. If the base is long, holes injected into the base (from the emitter) recombine with electrons inside the base before reaching the base electrode, thus, the base current has no influence on the collector current. However, if the base is shorter than the diffusion length of the minority carriers (here, holes in the n-base), they can diffuse into the p-doped collector side. The field inside the collector depletion zone is strong and removes all diffused holes towards the collector. A significant collector current is the result. More base current causes more minority carriers to diffuse through the base and be accelerated and amplified by the strong emitter-collector field, hence, the current signal from the base is amplified via the current of the collector.

The amplification of an ideal BJT can be calculated under the assumption of an ideal pn junction, as described in chapter 2.3.1 and proper boundary conditions [55]. To find the number of minority carriers reaching the collector, the distribution

---

[16]The npn-transistor works accordingly with swapped polarities.

[17]It is only used for low-frequency operation. The base-circuit is used for HF-amplification.

[18]Series and parallel resistors are used to limit base- and emitter current and define the operation point.
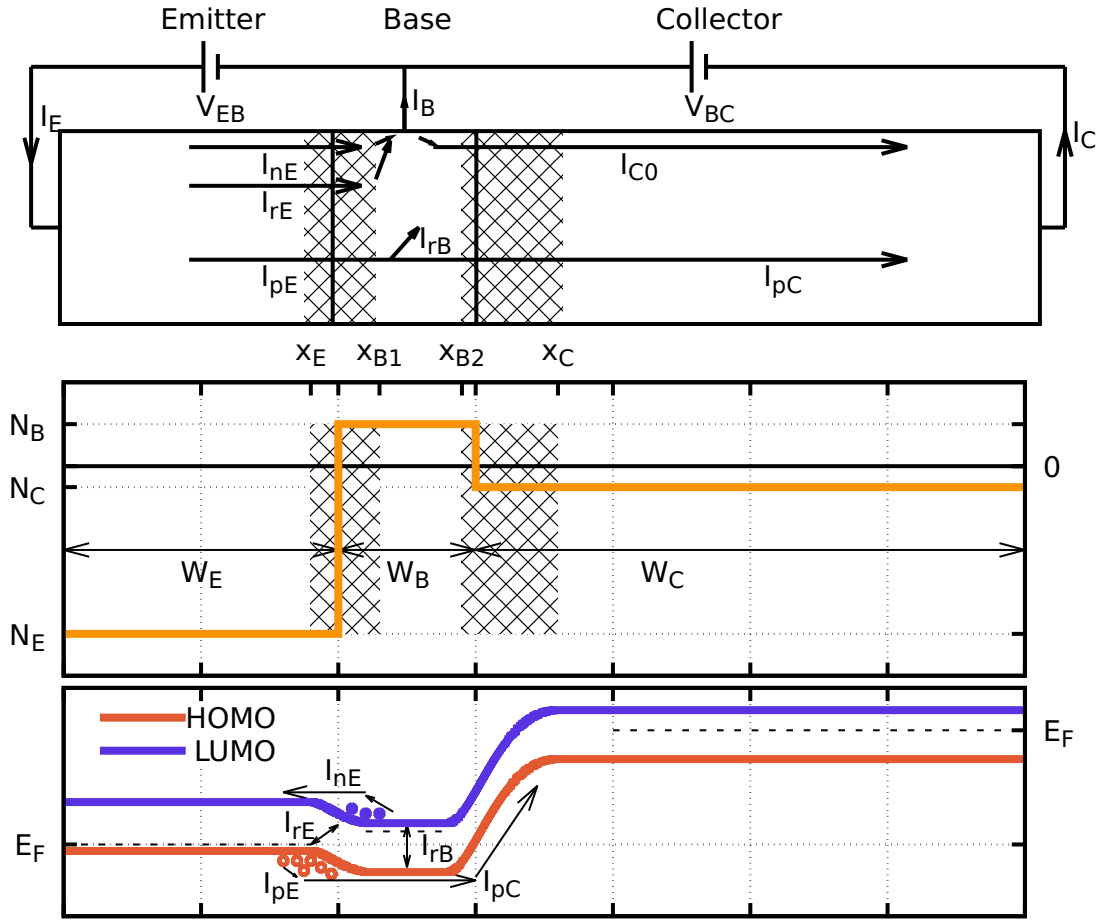
Figure 2.34: top: Schematic depiction of a pnp-type BJT. Shaded areas symbolize depletion zones between x_E to x_{B1} and x_{B2} to x_C.
Emitter-Collector voltage $V_{CE} = V_{EB} + V_{BC}$
middle: Doping profile of simplified box-profile. Base doping (N_B) is n-type, emitter and collector doping (N_E, N_C) are p-type.
bottom: Energy level diagram, assuming band-transport-like conduction with HOMO and LUMO levels. Fermi levels in the respective areas are indicated by dashed black lines.

of holes within the base (from the start of the base at 0 to the end of the base at W) can be calculated using the continuity equation under boundary conditions:

$$p_n(x) = p_{n0} + C_1 e^{\frac{x}{L_n}} + C_2 e^{-\frac{x}{L_n}}, \tag{2.86}$$

with C_i being constant, depending on the base-emitter and base-collector bias and the geometry.
The diffusion currents I_{pE} at the emitter edge ($x = 0$) and I_{pC} at the collector edge ($x = W$) can then be calculated:

$$I_{P(E,\,C)} = A_E q D_p \frac{dp_n}{dx} x \bigg|_{x=(0,\,W)}, \tag{2.87}$$

with A_E as the emitter-base junction cross-section and D_p the diffusion constant for holes. For $W \ll L_T$ (base thickness $\ll$ diffusion length), the ratio $\frac{I_{pC}}{I_{pE}}$, called the base transport factor α_T, is close to 1. That means, most of the minority carriers injected into the base reach the end of the base. In the limit of $\alpha_T = 1$ this can be written as:

$$I_{pE} \approx I_{pC} \approx \frac{A_E q D_p p_{n0}}{W} e^{\frac{qV_{BE}}{k_B T}} = \frac{A_E q D_p n_i^2}{W N_B} e^{\frac{qV_{BE}}{k_B T}}. \qquad (2.88)$$

Under normal operation (no saturation), the transport factor is given as:

$$\alpha_T = \frac{1}{cosh\left(\frac{W}{L_n}\right)} \approx 1 - \frac{W^2}{2L_P^2}. \qquad (2.89)$$

The base current is dominated by the electrons injected into the base towards the emitter. The regular Shockley equation can be assumed:

$$I_{nE} = \frac{A_E q D_{n,E} n_{p0,E}}{W_E} \left[e^{\left(\frac{qV_{BE}}{k_B T}\right)} - 1 \right]. \qquad (2.90)$$

Not all holes injected from the emitter into the base can be used for signal amplification. Additional – lost – current stems from recombination within the base I_{rE} and leakage current occurs through the reversed collector diode I_{C0}. The total current through each of the terminals can then be summarized to:

$$I_E = I_{pE} + I_{rE} + I_{nE} \qquad (2.91)$$
$$I_C = I_{pC} + I_{C0} \qquad (2.92)$$
$$I_B = I_{nE} + I_{rE} + (I_{pE} - I_{pC}) - I_{C0}. \qquad (2.93)$$

The transport factor of the transistor is defined by:

$$\alpha = \frac{I_C}{I_E}, \qquad (2.94)$$

describing the ratio of charge carriers injected into the emitter that reach the collector. Ideally, this value is close to 1, since then most of the emitter current is transmitted to the collector and only a small amount of base current is necessary. The common-emitter amplification is given by

$$\beta_0 = \frac{I_C}{I_B}. \qquad (2.95)$$

Using the Kirchoff law, this can be rewritten to:

$$I_C = \beta_0 I_B + I_{CE0}, \qquad (2.96)$$

where I_{CE0} is the open base leakage current at $I_B = 0$. An alternative version is:

$$\beta_0 = \frac{\alpha}{1 - \alpha}. \tag{2.97}$$

Thus, when α is close to 1, the current amplification is high. α can be split into several elements, the transport factor α_T, the emitter injection efficiency $\gamma = \frac{I_{pE}}{I_E}$, and the recombination factor δ_r, describing the losses due to recombination.

$$\alpha = \alpha_T \gamma \delta_r, \tag{2.98}$$

with α_T, γ, $\delta_r \leq 1$. All three factors reduce current amplification.

Considering $\alpha_T \approx 1$ and no recombination, β_0 can be estimated to:

$$\beta_0 = \frac{p_{n0} D_p W_E}{n_{p0,\,E} D_{n,\,E} L_p} coth \left(\frac{W}{L_p} \right) \approx \frac{p_{n0}}{n_{p0,\,E} W} \approx \frac{N_E}{N_B}. \tag{2.99}$$

Thus, several conditions are decisive for high current amplification:

- $\alpha_T \approx 1$: $W_B \ll L_p$, short base length and long diffusion

- $\delta_r \approx 1$: low recombination within the base

- $\gamma \approx 1$: $N_E \ll N_B$

- low leakage current from base to collector.

Ideal IV Characteristics   Graph 2.35 shows the IV characteristics of an idealized device in common-emitter configuration used to amplify current based signals. The output characteristic features a linear dependence of the collector current on the base current. For low emitter currents, the number of carriers injected into the collector might be small compared to the recombination currents inside the base and emitter. The result is a non-linearity and thus a variation in amplification. In contrast, for high base and collector currents, the density of minority carriers injected into the base is close to the majority carrier density. This effect is similar to doping, which effectively reduces the amplification, causing saturation at high base currents.

The saturation is visible in the output characteristics as a steep linear slope. Once sufficient emitter-collector voltage is applied (depending on the base current) the transistor reaches the active regime, where the output current is comparably constant with V_{CE}. The remaining linear slope is caused by the early effect. A change in V_{BC} – in reverse/blocking polarity –, increases the thickness of the depletion zone between base and collector. The increase in depletion layer thickness causes a decrease in thickness of the non-depleted parts of emitter and base. The emitter thickness has no significant effect, however, the decrease
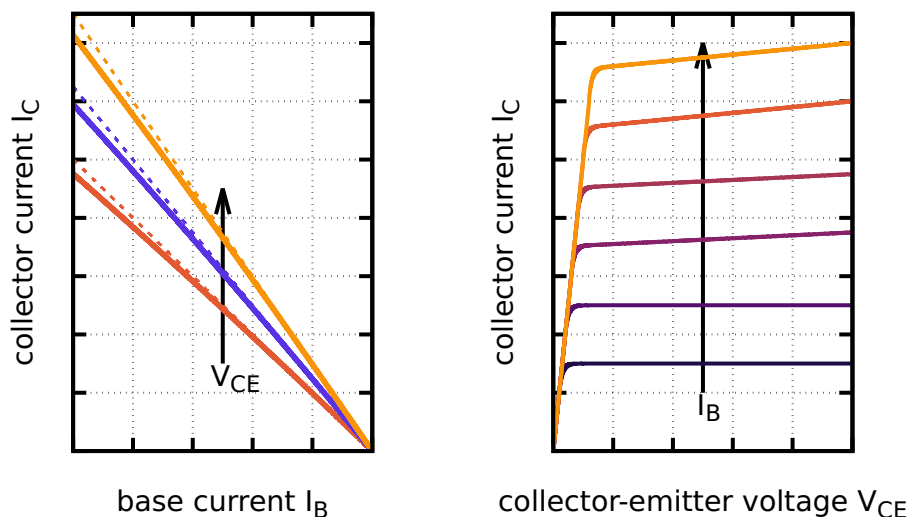
Figure 2.35: Idealized transistor curves in common-emitter configuration:
left: Transfer characteristics: Collector current depends linearly on base current. The slope increases with changing V_{CE}. For high base currents, deviations from linear behavior occur.
right: Output characteristics: In the saturation regime, collector current increases linearly with collector-emitter voltage. In the active regime, the current is close to constant. Remaining linear dependence stems from the early effect. For different base currents, higher collector-emitter voltages can be applied to reach higher collector currents in the active regime.

in base thickness is equivalent to an increase in α_T, causing an increase in total amplification.

Organic Bipolar Junction Transistors (OBJTs)   So far, there is no publication of a functioning OBJT. The only available document is a – by now abandoned – patent by Forrest et al. [176] from 2004, describing the general concept, while providing no useful information on material choice and manufacturing. The reasons for this absence are various, the most relevant can be explained easily analyzing the requirements of BJTs given in the previous chapter and comparing them to the properties of organic semiconductors.

One positive feature of organic semiconductors is their ease to process as thin-films. With this technology, it is easily possible to realize nm-sized layers and thus, a thin base, as needed for a BJT. However, the base width needs to be shorter than L_i, the diffusion length of minority carriers. As described in chapter 2.3.1, the diffusion length in organic semiconductors is extremely short – in the range of several nm. The base could be – theoretically – manufactured to be thinner than the diffusion length, however, a layer that thin would suffer significantly by tunneling related leakage current. Materials with less recombination and, hence, significantly larger diffusion length have to be used to allow for bipolar junction operation. One candidate is highly crystalline materials, like the rubrene used in this thesis..

The second criterium is related to doping. The difference between the emitter doping and the base doping should be high. However, as described in chapter 2.2.3, doping of organic semiconductors is more difficult than doping of inorganic semiconductors. Doping efficiency is in general lower and doping concentrations, therefore, much higher. Realizing a difference in doping of several orders of magnitude can be challenging.

Reduction of leakage current can be problematic too. Since the simple pn junction is not well suited for blocking of reverse currents [96], intrinsic layers have to be added to realize sufficiently low off-currents.

3 Experimental Methods

The following chapter describes the methods and procedures used to fabricate and analyze the layers, structures, and devices built [177]. The first section is about deposition and structuring methods, with a focus on thermal evaporation in vacuum. The second part of this chapter covers the experimental methods used to investigate devices as well as bulk and surface properties.

3.1 Sample Preparation

Although in theory quite simple, the manufacturing of an organic device is not just the consecutive deposition of its individual layers. The used substrate has to be made absolutely clean before the start of any deposition. This is especially important when dealing with surface-grown organic crystals, where each foreign particle or other defect on the surface creates a crystallization center. Thus, the substrate cleaning procedure used is shown in the first part. This is followed up by the material deposition techniques, namely thermal evaporation in vacuum, sputtering, and atomic layer deposition. At last, a description of structuring methods used is provided; shadow masking and photolithography.

3.1.1 Substrates and Substrate Cleaning

A clean substrate is important in two distinct ways. First, – true for all organic devices – the layers of semiconductor are comparably thin; between 10 nm to several 100 nm. Most dust particles are significantly larger and can cause short circuits between vertically spaced electrodes. Additionally, for some procedures and devices, the surface energy landscape and purity are essential. Field-Effect Transistors (FETs) and crystallization processes are extremely sensitive to interface quality. Use of a controlled clean room with reduced air-particle density is essential for successful crystallization.

Two types of substrate are used in this thesis: 25 mmx25 mm-sized plain float glass squares of 1.1 mm thickness and hand-cut silicon-wafer substrates of approximately the same area. The thickness of the wafer is 650 µm. They are strongly p-doped covered with either 2 nm to 5 nm of native SiO_2, 100 nm of wet-grown SiO_2, or 35 nm of Atomic Layer Deposition (ALD)-processed Al_2O_3. The wafers have been provided by Siegert wafers[1].

The standard cleaning procedure starts with a mechanical-chemical cleaning, consisting of ultrasonically-assisted baths in acetone, ethanol, isopropanol, and deionized water. The water-step can be skipped depending on further treatment. The substrates are flushed with the next solvent before each solvent change, such that no drying occurs on the surface. Devices that are not treated with Self Assembled Monolayers (SAMs) or Piranha-solution are blown dry with nitrogen and stored in dust-protective containers for further processing. To keep the

---

[1]Siegert wafer GmbH, Aachen, Germany

surface free of defects and optimize the chance for successful crystallization, speedy processing after the cleaning step is essential.

3.1.1.1 Surface Treatment

Considering the strong interaction area between the semiconductor and the substrate during the crystallization process, the significance of the energetic landscape of the substrate cannot be denied. Whether the surface of the substrate should be hydrophobic or hydrophilic for optimal rubrene crystallization is a matter of discussion. Conflicting information can be found in literature regarding the influence of the surface energy ([29] vs. [36]). At least some influence under certain conditions has been found, as discussed in chapter 4.1.1.4. One possibility to alter the surface energy of the system is via SAMs. An overview of the use of SAMs in organic electronics has been provided by Vericat et al. [178]. The substrate is either dipped into a liquid or kept in a vapor chamber to form a monolayer on the surface [28]. The materials used can create either a strongly hydrophilic, or hydrophobic surface or any state in between. To realize a hydrophobic surface, Hexamethyldisilazan (HMDS) is deposited by dipping the substrate into a diluted solution. For hydrophilic surfaces, the SAM n-Octadecylphosphonic acid (ODPA) is used. It is to be noted that the monolayer character of the deposition is decisive for later crystallization. Steps, clusters, or holes in the layer create condensation centers that would not exist without the SAM.

Alternatively, the surface can be treated chemically. A strong hydrophilic character can be achieved by exposing the substrate to heavily oxidizing agents. Oxygen plasma is known to result in hydrophilic surfaces by de-hydrogenation [179]. However, the effect is fleeting due to re-saturation of the surface. One positive side effect is the additional cleaning of the surface by oxidizing all possibly remaining organic residue. Another method of surface oxidization is chemical bathing. A common choice is so-called piranha-solution [28]. It consist of sulphuric acid (H_2SO_4) and hydrogen peroxide (H_2O_2). The solution is extremely caustic while simultaneously strongly oxidizing. The standard procedure (used in this thesis) contains bathing substrates directly after the solvent cleaning inside a $4:1^2$ ($H_2SO_4:H_2O_2$) ratio mixture of piranha. The process takes 15 min at 70 °C and is followed up with rinsing in deionized water and dry blowing with nitrogen. The hydrophilic nature of the surface is caused by hydroxylation and lasts for several hours. Especially the piranha treatment is well suited to generate clean surfaces. Ultimately, if the benefit for the crystallization stems from the hydrophilic nature or the cleanliness of the surface could not be decided.
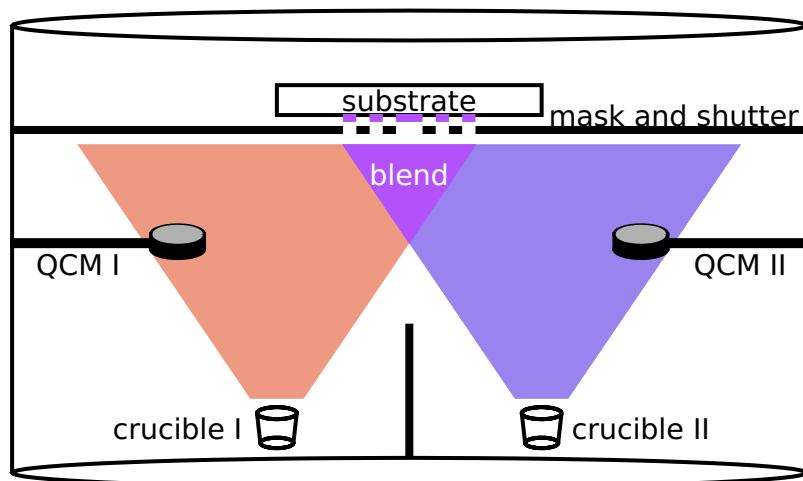
Figure 3.1: Schematic depiction of thermal evaporation in vacuum: Materials are heated electrically inside a vacuum chamber (base pressure $1 \cdot 10^{-8}$ bar). The deposited amount is measured using Quartz Crystal Microbalance (QCM) for each material separately. Shutters and shadow masks generate structuring.

3.1.2 Material Deposition

Most materials used are deposited via Physical Vapour Deposition (PVD). The material stays chemically unchanged during deposition, which separates it from Chemical Vapour Deposition (CVD), where the final product is formed in a chemical reaction during deposition. The method mainly used in the scope of this thesis is thermal evaporation in vacuum. It is a simple and robust but nevertheless versatile process used to deposit most of the organic semiconductors and metals. The basic procedure is depicted in figure 3.1. The pre-cleaned (usually via sublimation) material is placed in an aluminum-nitride crucible surrounded by tungsten wires. The wires are heated electrically and heat is transferred to the crucible. The whole process takes place in a base vacuum of $1 \cdot 10^{-8}$ mbar. Depending on the material, once either the sublimation or boiling point is reached, material is expelled as gas towards the sample. The thickness of the deposited layer is measured using QCM. The resonance frequency of a quartz crystal is permanently measured. If material is deposited onto the sample, the mass and thus the resonance frequency is shifted. From the density of the material and area of the crystal, the thickness of the deposited material can be calculated. To dope layers, co-evaporation is used, meaning two distinct crucibles are heated and the rate is measured using separate QCMs. The measurement itself is precise (1 Hz difference at a base frequency of 4 MHz to 6 MHz). Common devices detect deposition rates of $0.1\,\text{Å}\,\text{s}^{-1}$ or below. However, since the measurement head is not exactly at the position of the substrate, tooling of geometry is necessary. The correction between sample position and measurement position is called

---

[2]Note that mixing ratios below 1:1 may result in spontaneous combustion of the mixture.

tooling factor and changes with exact position and orientation of the samples, temperature gradient inside the crucible, the level of material inside the crucible, and many other parameters.

The density of the material influences the calculated layer thickness directly. As described in chapter 2.1.3.1, many materials do not show homogeneous growth behavior. The initial thin-film phases can deviate significantly from the following bulk structure. Densities found in literature or measured at a certain thickness or on a certain substrate do not necessarily translate to every setup. This is particularly problematic for re-crystallization processes. The thicknesses of layers in this thesis are always based on the amorphous bulk density of rubrene (see table 3.6). The change of density during the crystallization is therefore not accounted for. The difference between the individual crystal phases is also neglected. As a rule of thumb, layer thicknesses are precise to around 5 % to 10 %.

Doping is realized by simultaneously evaporating two materials at the same time, with a defined ratio of evaporation rates. The accuracy of doping heavily depends on the stability of the evaporation. Practically, the effective doping concentration changes throughout the layer. However, fluctuations within the Debye length do not matter [83]. For high doping concentrations, the accuracy of the doping concentration is thus governed by the accuracy of the evaporated layer thickness, similar to single layers. With Gaussian propagation of uncertainty, this results in an accuracy between 7 % to 14 %. To realize low doping concentrations, the deposition rate of the dopant must be extremely low. This increases the total inaccuracies through rounding and digitization errors to up to 28 %.

3.1.2.1 Sputtering

The evaporation temperature of some materials is too high to be deposited via thermal evaporation. One of these materials is SiO_2. Sputtering is used instead. An electric RF-field is set up inside a controlled Ar-based plasma. Ar-ions are accelerated towards a massive target of SiO_2 which breaks out individual molecules or small clusters of the target material. The energy of the Ar ions is increased with a perpendicular magnetic field. The resulting loose pieces of SiO_2 travel towards the substrate and are deposited as a layer. The thickness is measured via QCM. The layer quality and density of sputtered layers are in general lower than with other, slower methods.

3.1.2.2 Atomic Layer Deposition

The oxide layers created by sputtering are usually of comparably low density and highly porous. This is a result of the randomness of molecules and parts of molecules hitting the substrate. Layers of significantly higher quality can be generated by atomic layer deposition. This chemical vapor technique is based on the step-wise chemical reaction of precursor materials on the surface of the

substrate. Inside a vacuum chamber, the first precursor is brought into the reactor by opening a valve for a specific, short time. Molecules cover the surface of the substrate via adhesion. Remaining material is evacuated via vacuum pumps. After a programmed waiting time, the second precursor is brought into the reactor, causing all molecules of the first material that are bound to the surface of the substrate to react. This forms a layer of the final product on the surface. Remaining precursor is removed. These steps are repeated until the final layer thickness is reached. Material only forms directly on the surface of the substrate in a monolayer or sub-monolayer fashion.

3.1.2.3 Evaporation Tools

Two setups are used for the manufacturing of devices. Single 25 mmx25 mm-sized substrates are evaporated on in a cluster tool (called UFO) made by the company Bestec[3]. Distinct chambers for metal evaporation and organics materials are present. N-doping and p-doping take place in physically separated chamber, such that intermixing is avoided. Samples can be transferred from vacuum to a nitrogen atmosphere for further processing, without the break of clean atmosphere.

For screening of material properties, a larger tool (called Lesker) made by the company Lesker[4] is used. 6x6 of the same 25 mm samples can be processed at the same time or individually, depending on the stack. After processing, samples are transferred to nitrogen atmosphere as well. If necessary, a central area on each of the 36 single substrates can be encapsulated via glass-domes that are glued onto the substrate.

3.1.3 Shadow Masking

Many layers can be evaporated onto the entire surface of the substrate and structuring is not necessary. This is the case for many of the organic layers. However, all metal electrode layers need to be deposited selectively to allow a defined device area and avoid short circuits. For High Frequency (HF)-diodes, the organic layers are structured too, to avoid leakage current between input and output of the circuit and reduce stray capacitances.

Since both, thermal evaporation and sputtering, are targeted, beam deposition techniques, structuring can be achieved via a simple shadowing of the beam. This method is easy and fast and usually does not require exposing samples to atmosphere or any kind of lithographic chemicals. However, resolution and alignment are limited. Standard, sheet-metal based shadow masks that are positioned on top of the substrate allow for feature sizes down to 50 µm. Since the mask cannot lie evenly flat on the surface of the substrate, the finite

---

[3]Bestec GmbH, Berlin, Germany
[4]Kurt J. Lesker Company, Jefferson Hills (PA) USA

distance between sample and source causes evaporation into the shadowing area. Considering a distance between substrate and shadow mask of 0.5 mm at maximum and the distance between source and substrate of approximately 60 cm, the resulting maximum amount of over-evaporation on the edge of the substrate is 11 µm. The result is softened and widened structures, compared to the original mask.

If a higher resolution is needed, the mask design and material have to be changed. Stencil masks are structures that are photolithographically etched into silicon wafers[5]. The thickness of the wafer (650 µm) is reduced to around 50 µm in a window around the shadow structure. Without this step, evaporated material would not reach the other side of the mask for very small structures. The resolution of these masks can be as low as 1 µm, depending on the geometry. Due to their perfect flatness, stencil masks lay much closer to the surface than common metal shadow masks, reducing evaporation into shadowed areas. However, fine structures need intricate alignment that can only be realized with microscopy. Stencil masks that needed alignment (this excludes the bottom ground electrodes) are aligned in air using a microscope.

3.1.4 Photolithography

Photolithography is another – more complicated but ultimately more powerful and versatile – technique for structuring. In its core, it follows the same principle as shadow masking; which is making parts of the surface accessible to a process while shielding others. It can be seen as the formation of a shadow mask directly on the surface of the substrate instead of a temporary, distinct entity. A very detailed description of photolithography technology and related fields can be found in [28]. However, most books, publications, and descriptions, in general, are related to inorganic semiconductors, here, photolithography is the only viable option in achieving the nm-sized features used in modern integrated circuits. However, many chemicals and photoresist used in these processes do not harmonize with organic semiconductors. Thus, other material systems or method have to be used.

The basic principle is to deposit a thin layer of a photoactive polymer on the substrate, following a step to remove residual solvent. Next, targeted exposure takes place, to chemically transform the photoresist in certain spots while maintaining its initial structure in others. The following development step removes the resist at the desired areas. The result is an optically structured layer of photoresist. Photoresists can be either positive or negative. The former type becomes soluble in the developer liquid under the influence of light via the formation of carbonic acid. Thus, all areas exposed to light will be free of photoresist after development. The formation of carbonic acid releases N_2 while absorbing H_2O. This process can,

---

[5] The stencil masks used here are made by the Institute of semiconductor and microsystems TU Dresden(Dresden, Germany).
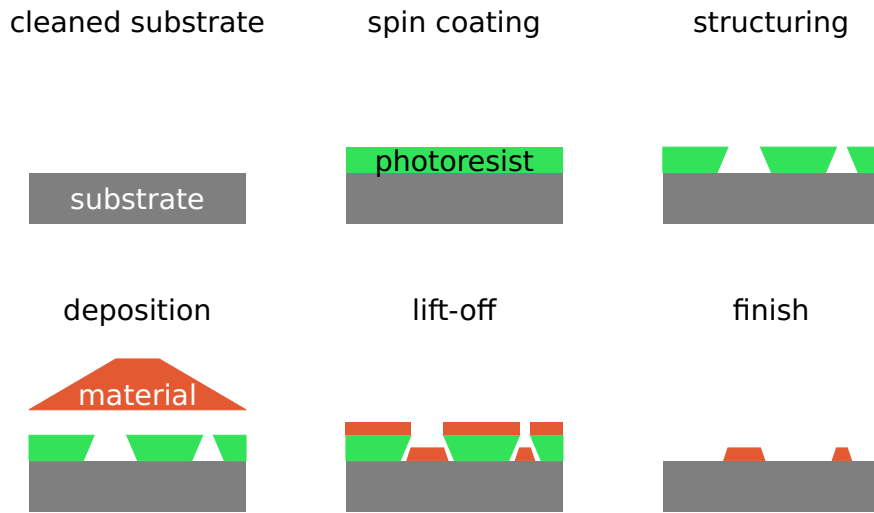
Figure 3.2: Schematic depiction of lift-off photolithography process.

hence, only take place in a water-containing atmosphere. Negative photoresists cross-link in the presence of light. Thus, areas exposed to light remain on the substrate after development, while unexposed parts are dissolved. Negative resist feature less heat-induced edge-rounding effects due to the cross-linking. However, they are also more difficult to remove, if necessary.

Photoresists can be deposited via a wide variety of methods, similar to solution-processed organic semiconductors. Common techniques are spin coating, spray-coating, and dip-coating. For this thesis, all resists are deposited via spin coating using a Sawatec SM-150[6]. The thickness of the film d depends on the concentration of the photoresist and the spin speed R ($d \propto \frac{1}{\sqrt{R}}$). The film thickness needed depends on the process and the degree of protection the resist has to offer. For galvanic-plating, layers up to 150 μm are used, while layers for precise photolithography on semiconductors are in the low μm-regime or below.

After the deposition, a heating step is usually used to remove excess solvent from the film, called softbake. The temperature and length of this step are important for the quality of the photolithographic mask. Especially the dark-etching – the removal of photoresist on non-desired areas – is sensitive to sub-optimal parameters. Negative resists commonly require a heating step after exposure to enable cross-linking. It is called the Post Exposure Bake (PEB). Heating of photoresists for this thesis is done with a Sawatec hotplate HP-150.

Most photoresist are sensitive to defined standard wavelength in the deep-blue or UV-regime (e.g. i-line (365 nm), g-line (435 nm), etc.). The smallest accessible feature-size also depends on the wavelength of the used light. Since sun-light (and some artificial light sources) contains these wavelength too, photolithography has to take place under exclusion of most sources of lighting. This is commonly

---

[6]Sawatec AG, Eschagger, Switzerland

done via filters on windows and lamps. For this work, a glovebox featuring filters is used to perform photolithography and other light sensitive procedures. Exposure of the film can take place either by steppers, mask aligners, or laser exposure. Steppers move over the surface exposing it with an image scaled-down via optics to a size significantly smaller than the substrate area. The quality of the mask can be lower than the final result, since the image is smaller than the mask itself. However, exposure takes significantly longer. A mask aligner aligns a premade mask with the substrate. Light is projected in parallel at a 1:1 ratio of mask to image. The quality of the mask is directly related to the quality of the final image. Exposure takes place on the entire surface at once. Precise exposure without the need for expensive premade masks can be achieved via laser exposure. A laser is scanning over the surface using a programmed geometry.

3.1.4.1 Etch Procedure

Photolithography can be used to etch specific areas on the surface of a substrate. In particular to etch off parts of a previously deposited thin layer to create structure. The general process is depicted in figure 3.3. The material that is to be structured is deposited onto the entire surface. Consecutively, the photoresist is deposited onto this layer, baked, exposed, and developed. Several parts of the surface are now exposed, allowing for the removal of material. As an example, Au can be etched with a mixture of KI and I_2 which does not damage organic semiconductors[7]. Organic semiconductors can be etched using oxygen plasma [180]. However, special fluorinated photoresists have to be used to not damage the underlying

---

[7]A small doping effect has been observed.
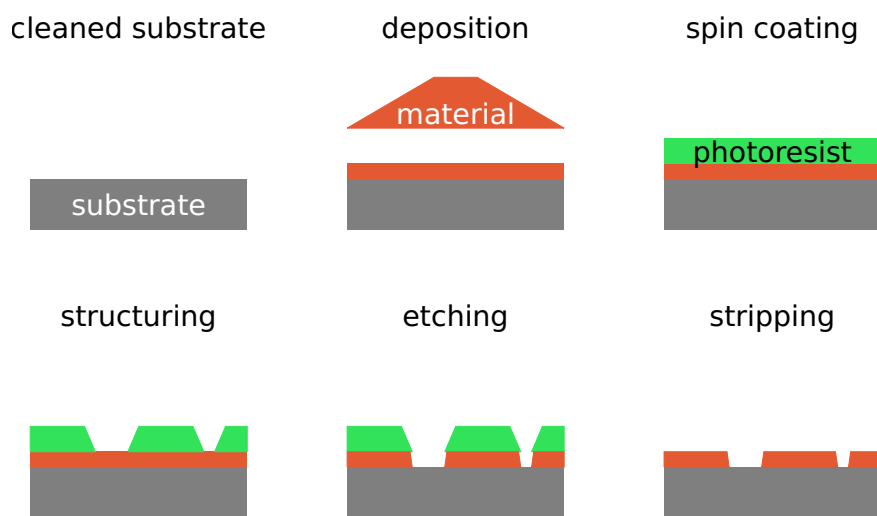
Figure 3.3: Schematic depiction of photolithography process for etching.

material. Note, that the oxygen plasma not only etches the semiconductor but the lithography mask itself too.

Since the shape of the resulting structure is defined by the part of the photoresist that is in direct contact with the bottom layer, positive photoresists lend themselves as etching-resists, due to their positive slope at the edge. A certain amount of material is removed underneath the photoresist, beginning from the edge, due to capillary effects. This is called under etching and the resulting removed material undercut. Proper adhesion between film and resist is necessary to avoid lifting of photoresist at the edges, which would lead to an increased undercut. Underetching can be increased by purposefully etching longer than necessary.

3.1.4.2 Lift-off Procedure

A photolithographic lift-off process is similar to shadow masked deposition in the sense that the mask – manufactured prior to deposition – represents a shadow mask directly at the surface. The simplified process is depicted in figure 3.2. The photoresist is deposited onto the substrate, baked, exposed, and developed. The resulting structured layer has photoresist absent in areas that are supposed to be covered with material. After the subsequent deposition of material, the entire substrate is covered initially. As the last step, the photoresist is dissolved, lifting the materials off of the areas that are still covered with photoresist and keeping it in areas that are directly at the substrate. This procedure results in a structured layer.

Since the purpose of the film is to be removed after the deposition, only a limited adhesion to the surface is desired. To utilize the shadowing effect, negative-type resists are commonly used for lift-off processes. They feature a positive slope at their edges caused by the increased scattering and absorption of upper laying parts of the film. The distinct undercut caused by this slope defines the distance between mask and surface. The undercut is usually below 1 μm. The resulting structure is practically a 1:1 representation of the mask. Positive resist, featuring a negative slope, do not have an a priori separation between the lift-off part and the structure part. Thus, borders tend to rip causing uneven edges.

The lift-off process is usable with practically any type of material, since it – in contrast to the etching process – does not rely on specific chemical reactions. However, certain processes make a lift-off more difficult. Heating during the deposition can cause an additional hardening of the resist layer and a subsequent reduction of solubility. Additionally, a thick and dense layer on top of the photoresist can reduce the effective solubility of the polymer by allowing access only through the edges. The result is a slow or incomplete lift-off.

Another phenomenon can occur with unidirectional deposition techniques (e.g. ALD) in combination with positive resists. The positive slope on the underside of the resist edge is not covered by beam deposition techniques but can be covered by unidirectional deposition techniques. Since no photoresist is underneath these

parts to cause a lift-off, material can remain at the edges of structures leading to additional shadowing and step phenomena with further processing ([58], [172]).

3.1.4.3 Double-Resist Procedure

When metals are to be structured on top of semiconductors (e.g. source and drain of an Organic Field-Effect Transistor (OFET)), the mask must be manufactured directly on the semiconductor. Almost all common photoresists are dissolved in organic solvents, many of them in Propylene Glycol Methyl Ether Acetate (PGMEA) (Propylenglycolmonomethyletheracetat). During the fabrication of a device, organic semiconductors would come into contact with PGMEA, dissolving or recrystallizing the layer. As an alternative, special highly fluorinated polymer photoresists in fluorinated solvents can be used that are inert towards organic semiconductors. One possible way of utilizing these materials is the double-resist lift-off process presented by Kleemann et al. [160]. It is depicted in figure 3.4. An additional inert sacrificial layer is deposited between the semiconductor and the standard photoresist. The bottom layer protects the organic material from damage by solvents or developers. After structuring of the photoresist, the pattern is transferred into the sacrificial layer via etching. The lithographic mask consists of two layers and can be used as a common lift-off mask. Lift-off takes place in the solvent of the fluorinated polymer.
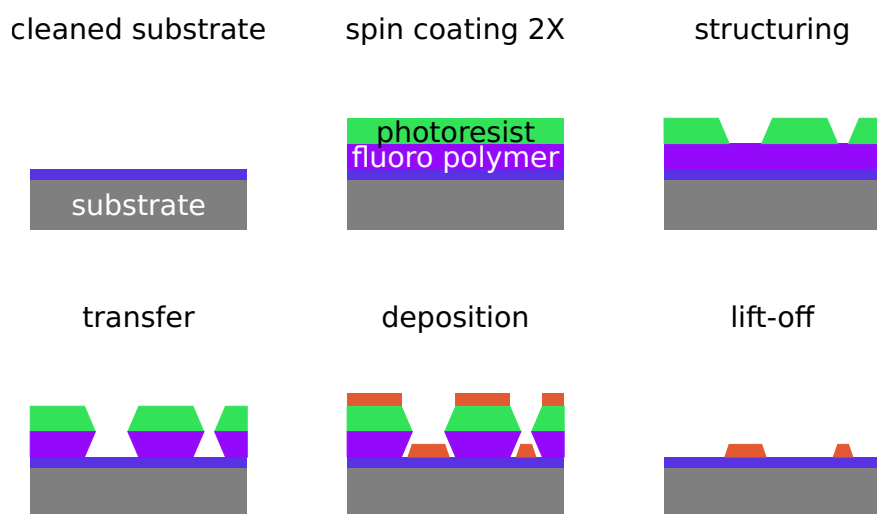
Figure 3.4: Schematic depiction of double-layer lift-off photolithography process used on organic semiconductors (blue).

3.1.4.4 Lithography Devices and Chemicals

Two different tools are used for exposure. First, a stepper-type maskless exposure tool SF-100 Extreme[8] which projects a black and white pattern using a mirror array. The image can be freely chosen within a grid of $1024\,\text{px} \times 768\,\text{px}$. The field of view is approximately $3.8\,\text{mm} \times 2.85\,\text{mm}$ with a theoretical resolution of $3.7\,\mu\text{m}\,\text{px}^{-1}$. The second tool is a SÜSS MJB4 mechanical mask aligner[9]. This mask aligner brings the substrate into contact with a premade glass-chromium mask. The substrate area is approximately $25.4\,\text{mm} \times 25.4\,\text{mm}$ with a theoretical minimal resolution of $0.6\,\mu\text{m}$.

Photolithography can be used for two distinct processes, lift-off, and etching. Both processes have different requirements for the adhesion of the film, thus, specialized photoresists exist as positive and negative versions. As positive resist, maP-1210 by micro-resist[10] is used (undiluted, 3000 rpm: $\approx 1\,\mu\text{m}$). Negative resists are provided by Microchemicals[11], nlof-2020 (1:1 (with PGMEA), 3000 rpm: $\approx 400\,\text{nm}$) as a lift-off oriented resist and AZ15nXT(115CPS) (1:1 (with PGMEA), 3000 rpm: $\approx 2\,\mu\text{m}$) for etching purposes. Highly fluorinated photoresists used for photolithography directly on top of semiconductors is provided by Orthogonal inc.[12]. Ortho310 is used as a sacrificial protection layer, while OSCOR5001 and OSCOR4000 are used as structuring resists (undiluted, 3000 rpm: $\approx 1\,\mu\text{m}$). Gold etchant in the form of a KI:I_2-solution, from the company Sigma-Aldrich[13] is used, diluted in a 1:10 ratio at an etching rate of approximately $1\,\text{nm}\,\text{s}^{-1}$.

3.2 Device Measurement

Measurements are necessary to evaluate the properties and applicability of materials, processes, and devices. The techniques used are described in this section. At first, electrical measurements are highlighted that evaluate the charge transport properties of individual layers and properties of finalized devices. A special emphasis is put on HF measurements of organic diodes in the form of rectification circuits and pulsed measurements. In the second half, fundamental analytical methods are described to analyze the structural properties of the crystalline layers. This includes Atomic Force Microscopy (AFM), polarization microscopy, and X-Ray Diffraction (XRD).

---

[8]Intelligent Micro Patterning LLC, St. Petersburg (FL) USA
[9]SÜSS MicroTec, Garching Germany
[10]micro resist technology GmbH, Berlin Germany
[11]MicroChemicals GmbH, Ulm Germany
[12]Orthogonal Inc. Rochester (NY) USA
[13]Sigma-Aldrich, St. Louis (MO) USA

3.2.1 Electrical Measurements

Electrical measurements are important to characterize the charge transport capabilities of materials. They are used for current-voltage (IV) measurements of intrinsic or doped vertical layers, full diode stacks, and three terminal devices like bipolar or field effect transistors. Room temperature measurements of two-terminal devices as well as field effect transistors are performed within a nitrogen atmosphere in a glovebox under ambient light conditions. Contact pads – previously coated with silver ink – are contacted using tungsten needles moved by micromanipulators. Several different source measure units (SMU) are used, depending on the requirements of the individual measurement:

- Keithley[14] 236 measure currents between 100 fA and 100 mA with an optimum accuracy of 450 fA or voltages between 100 µV to 110 V with an optimum accuracy of 650 µV.

- Keithley 2400 measure currents between 50 pA and 1 A at an optimum accuracy of 600 pA or voltages between 5 µV to 200 V with an optimum accuracy of 600 µV.

- Keithley 2600 measure currents between 2 pA and 10 A at an optimum accuracy of 100 pA or voltages between 5 µV to 40 V with an optimum accuracy of 250 µV.

The accuracy of measurement is changed depending on the current regime. Thus, larger currents have larger absolute measurement errors.

3.2.1.1 Capacitance measurements

For analysis of junctions in Schottky- and pn-diodes and at insulator interfaces, capacitance measurements are used. The current to voltage response of a sinusoidal voltage signal at a defined frequency ω is measured. Depending on the ohmic R, capacitive C, and inductive L components inside the circuit, a specific complex resistance Z can be calculated, featuring an absolute value Z_0 and a phase shift ϕ. If a model is assumed, values for the equivalent components can be deduced from these measurements. Neglecting any inductive components, two measured values – amplitude and phase shift – allow for two component values to be deduced analytically. Either a series or a parallel circuit between an ohmic resistor and a capacitor is possible. In reality, both circuits are present in form of parasitic parts. Since junction in reverse block current, a series resistance is usually the fitting choice for these measurements. The amplitude of the impedance of

---

[14]Keithley Instruments, Cleveland (OH) USA

the system is then:

$$Z_0 = \sqrt{R^2 + \left(\frac{1}{\omega C}\right)^2},$$ (3.1)

shifted by a phase

$$\phi = arccos\left(\frac{R}{\sqrt{R^2 + \left(\frac{1}{\omega C}\right)^2}}\right).$$ (3.2)

From that, the values for the capacitance and the ohmic series resistance can be calculated, while usually only the capacitive part is of interest. For an ideal capacitor, the resulting capacitance is constant with frequency. However, time-dependent processes caused by mobile ions in insulator layers or finite charge carrier generation processes can occur, effectively changing the capacitance once the signal is faster than the system can follow [148]. These effects can be observed in capacitance-frequency (Cf) measurements, thus varying the frequency of the input signal. To investigate the accumulation and depletion behavior, the junction can be biased, while the capacitance is measured. These measurements are called Capacitance-Voltage (CV) measurements. They are performed at a fixed, or stepped frequency.

Cf- and CV-measurements are performed using an Agilent 4284A LCR meter[15]. The frequency of the measurement can be set between 20 Hz and 1 MHz with a signal amplitude between 5 mV and 2 V and a DC-offset up to 40 V. Capacitances measured can range between 0.01 fF and 10 F at an accuracy of 0.05 %[16]. The standard signal amplitude used for all measurements is 20 mV. It needs to be high enough to allow for accurate measurement, but low enough to give an accurate value for the capacitance, since the capacitance is voltage-dependent. If the CV-measurement is given only at one frequency, a prior Capacitance-frequency (Cf)-measurement at 0 V Direct Current (DC) bias is used to determine a frequency at which the capacitance is stable. The LCR meter offers the possibility of a four-probe connection, thus, separate cables to measure voltage and current can be used. Since the impedance of the Device Under Test (DUT) test is significantly larger than the impedance of the setup (in investigated frequency range), all measurements are performed in a simpler, two-terminal configuration.

3.2.1.2 Cryostat

Some electronic effects and parameters are strongly temperature-dependent. This includes charge carrier mobility, carrier density, recombination, and diffusion. Temperature-dependent IV-measurements are done using a Cryo Janis ST-500

---

[15]Agilent Technologies, Santa Clara (CA) USA
[16]This only applies to the measurement itself. The error originating from neglecting leakage parallel currents can be significantly larger.

probe station[17]. It features four micromanipulators for probing of contact pads. Samples can be measured in a vacuum of $1 \cdot 10^{-5}$ mbar and can be electrically heated and cooled using liquid nitrogen down to $77\,K$ with temperature stability better than $50\,mK$.

All bipolar transistor devices are measured within the probe station due to its high magnifying camera necessary for contacting.

3.2.2 High Frequency (HF) Measurements

The geometry of electrodes, connecting cables, and the circuit as a whole is of no importance in DC-conditions, as long as the line series resistance is significantly lower than the DUT resistance. This changes for AC measurements, especially at high frequencies. For a series circuit of an ohmic resistor R and a capacitor C, the RC-time τ describes the time needed to charge the capacitor to $36.8\,\%(\frac{100}{e}\%)$ of its full charge:

$$\tau_C = \frac{1}{RC} \tag{3.3}$$

For faster charging, the current needs to be higher – thus R smaller – or the total amount of charge smaller – and thus C smaller. Similarly, for a series resistance of ohmic resistor and inductor L, an RL-time can be defined, describing the time needed to dissipate the initial magnetic field:

$$\tau_L = \frac{L}{R}. \tag{3.4}$$

Every circuit combination of different R, C, and L in series or in parallel has a defined resonance. To ensure that measured effects are properties of the device or circuit, the resonance of the contact and measurement system must be significantly higher in the frequency domain than the frequencies that are applied to the

---

[17]Janis Research LLC, Woburn (MA) USA
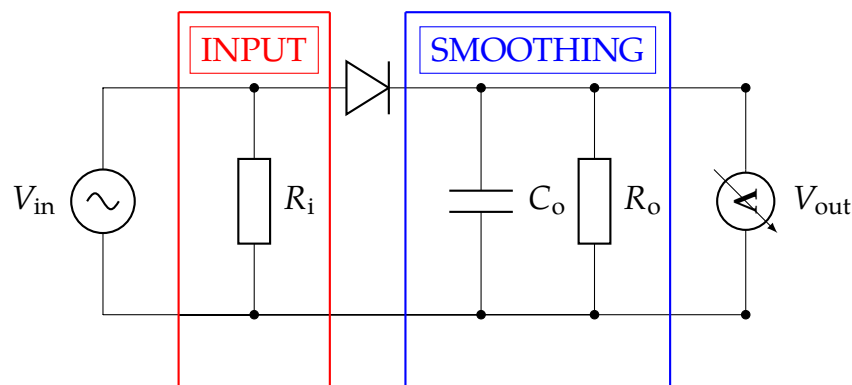
Figure 3.5: Equivalent circuit for a half-wave rectifier in simple layout: The input side is connected via $R_i = 50\,\Omega$ to ground to realize impedance matching. The output side features a smoothing capacitor of $C_o = 100\,nF$ and a varying load resistor R_o.

system. Thus, stray capacitances, ohmic line resistances, and ring inductances are to be avoided. At Ultra High Frequency (UHF), using sufficiently good electrodes, the capacitive and inductive components dominate. The resulting time constant in an LC-resonator is given by:

$$\tau_{\mathrm{LC}} = \frac{1}{\sqrt{LC}}. \tag{3.5}$$

To estimate the effect of geometric properties, a look at the most simple devices is helpful. Thus, for the ohmic resistor, plate capacitor, and single ring inductor the important parameters can be calculated respectively:

$$R = \rho \frac{l}{A}, \; l: \text{length of conductor}, A: \text{area of conductor} \tag{3.6}$$

$$C = \epsilon \frac{A}{r}, \; r: \text{distance between plates}, A: \text{area of plates} \tag{3.7}$$

$$L = \mu_0 \frac{d}{2}, \; d: \text{diameter of loop} \tag{3.8}$$

For the design of the circuit for the UHF rectifiers investigated in this thesis, several rules of thumb are useful:

- To minimize ohmic resistances on the HF side, electrodes and contacts are to be kept as large as possible, i.e. layer as thick and traces as wide as possible.

- To minimize stray capacitances, traces at signal and ground potential are to be distances as far as possible.

- To minimize series inductances, the loops on the input side (signal input – trace to diode – diode – trace to input resistor – input resistor) and output side have to be as small as possible.

These measures only affect the circuit and are independent of the HF capabilities of the individual components, i.e. the speed of the organic diode.

Two different designs are used, an older design HF1 used for first test-measurements – shown in table 3.7 of chapter 3.4 – which offers encapsulation of the organic diode and a new design HF2 without encapsulation but smaller total circuit size. Both circuit types are equipped with Surface Mount Device (SMD)-components directly glued to the surface of the substrate and connected with silver ink. The input side has to be terminated with $50\,\Omega$ from signal input to ground for impedance matching, while the output is equipped with a smoothing capacitor and a load resistor.

The resonance frequency of HF1 is at around $250\,\mathrm{MHz}$, while the second design HF2 can be measured up to several GHz. Note that because of equation 3.4, a decrease in either capacitance or inductance by a factor of a decreases the resonance frequency only by a factor of $\sqrt{a}$. Additionally to the decreased dimension, capacitors are added in parallel to the input resistors in HF2. It counteracts

the impact of the diode capacitance and raises the resonance frequency of the circuit. However, additional anomalies occur at lower frequencies. The size of the input capacitor is $0.4\,\text{pF}$ deduced from circuit simulations. To minimize thermal drift and account for finite electrode resistance, the input resistor is changed to two times $97\,\Omega$ in parallel, instead of one single $50\,\Omega$ resistor. The two input resistors are arranged to create a double loop at the input side oriented in opposite direction. The same arrangement is used for the capacitors at the output side. As a result, the impact of the single ring inductances on the input and output side is partly compensated and the resonance frequency is increased. The equivalent circuit of the simple circuit using the old layout is shown in figure 3.5, while the fully equipped improved layout is shown in figure 3.6.

The organic diodes measured here feature a distinct threshold turn-on voltage ($\approx 2\,\text{V}$). Thus, for low voltages, the forwards and reverse currents are almost identical and no rectification is visible. Common UHF signal generators do not operate at high voltage and power. The maximum amplitude that can be delivered by the available signal generators in the range of $100\,\text{MHz}$ to several GHz is $2.7\,\text{V}$. The organic diodes show little rectification for input signals that weak. Note that the voltage dropped over the diode V_{diode} is important and not only the applied signal input V_{in}. It can be calculated to be $V_{\text{diode}} = V_{\text{in}} - \overline{V_{\text{out}}}$. For UHF circuits, a constant DC voltage can be infused into the input side, to shift the operation point of the diode. The signal is inserted using a UHF Bias Tee. Since the output voltage of the rectifier is defined by the voltage drop over the load resistor and thus the current through the load resistor, a constant voltage at the input would cause an output voltage even without any input signal. A constant current supply is connected to the output side, to compensate for the constant DC current I_{DC} through the diode. Thus, voltages measured at the output originate
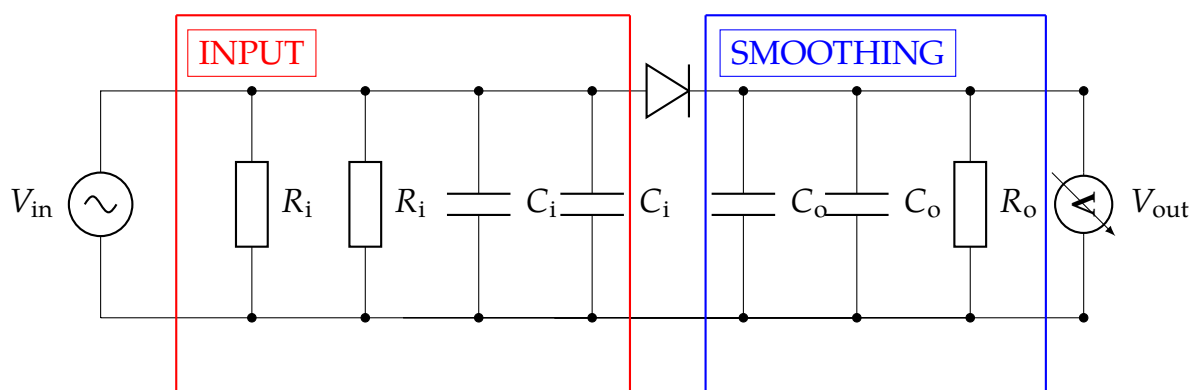
Figure 3.6: Equivalent circuit for a half-wave rectifier in optimized layout: The input side is connected via two times $R_{\text{i}} = 97\,\Omega$ to ground to realize impedance matching and maximize power input. In parallel to the input resistors are two $C_{\text{i}} = 0.4\,\text{pF}$ capacitors to compensate diode capacitance. The output side features two smoothing capacitors of $C_{\text{o}} = 100\,\text{nF}$ and a varying load resistor R_{o}.

from the rectification of the input signal alone and are not influenced by parasitic signals or reflection within the cables. The final DC pre-biased circuit is shown in figure 3.7.

The pulse generators used to supply the UHF input signals are a 81150A Pulse Function Generator featuring a maximum frequency of 250 MHz with a maximum amplitude of 10 V and a Keysight E8257D[18] featuring a maximum frequency of 67 GHz with a maximum power output of 18.7 dbm, corresponding to a maximum amplitude of 2.7 V. The system is tuned to have a variation below 1 % in amplitude at the input pin of the rectifier circuit. Simulations using ADS show that a worst-case scenario of resonance at the input would result in a shift of input voltage (at the diode) of 10 %. Traces at the output of rectifier circuits are measured using a Rohde& Schwarz RTM-2054 oscilloscope. This procedure is only viable for low-frequency measurements, since the output of the circuit is not shielded. the maximum bandwidth is 500 MHz. Voltages can be measured up to an accuracy of 25 mV. For UHF rectification a Rohde&Schwarz FSV 7 GHz signal analyzer[19] is used. The measurement error is below 2 %.
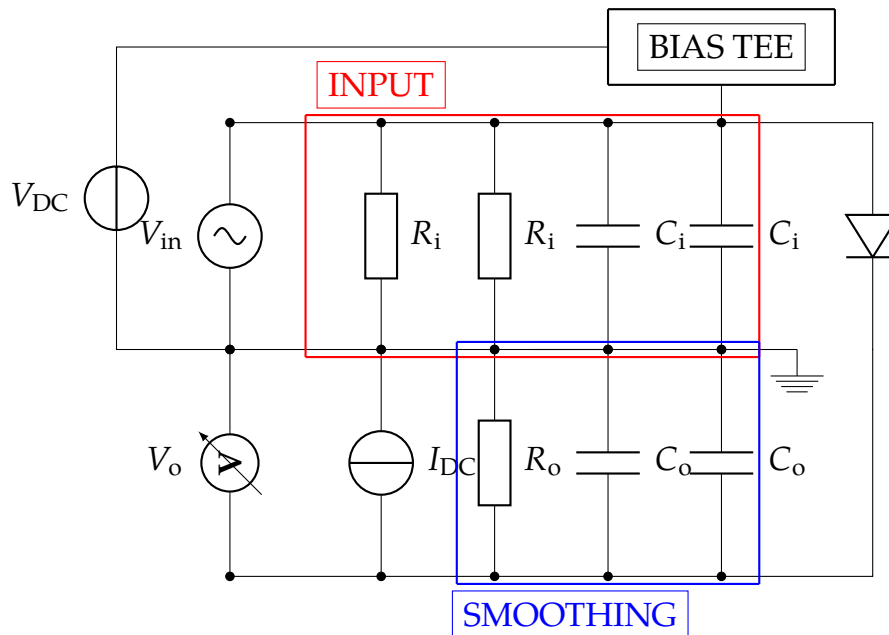
Figure 3.7: Equivalent circuit for a half-wave rectifier in optimized layout including DC pre-bias: The input side is connected via two times $R_i = 97\,\Omega$ to ground to realize impedance matching and maximize power input. In parallel to the input resistors are two $C_i = 0.4\,\text{pF}$ capacitors to compensate diode capacitance. The output side features two smoothing capacitors of $C_o = 100\,\text{nF}$ and a varying load resistor R_o. A constant DC voltage V_{DC} is applied at the input side to shift the operation point of the diode into a more favorable regime. A UHF Bias Tee is used to mix the DC bias into the UHF input signal. A constant power supply generates a current I_{DC} at the output to compensate for the DC current through the diode.

---

[18]Keysight Technologies, Santa Clara (CA) USA
[19]Rohde&Schwarz, München Germany

3.2.3 Pulsed Measurements

A current I flowing through a device with the resistance R, be it diode or transistor, always causes an increase in temperature by Joule heating $P = I^2 R$. Since the conductivity of semiconductors in particular is strongly temperature-dependent, this heating changes the conductivity, which in turn changes the heating. This cycle can lead to bi-stability or even destruction of devices by thermal runaway, as shown by Fischer et al. [181]. Even if the device is not directly damaged, measurements at medium to high power might change the measured currents from their intrinsic values. Since self-heating and heat-distribution effects take place in the order of ms [182], one solution to minimize the impact is the addition of relaxation times into the measurement routine. A gap of 0.5 s to 1 s between each step of a voltage sweep ensures the independence of each individual measurements. However, the measurement time of common Source Measure Units (SMUs) is also in the range of ms. Each individual measurement is thus influenced by itself.

To fully circumvent self-heating effects, pulsed measurements are necessary. The time in which the signal is applied and subsequently the measurement takes place is significantly shorter than any heating effects. A Keysight 8110A pulse pattern generator is used to generate voltage pulses in the ns to μs-regime. It can generate pulses up to 48 V, at a minimal pulse length of 9 ns. Since the impedance of all devices measured is significantly larger than any line resistances, the device was set to high output impedance, such that the use of an input resistor can avoided. The output of the DUT was connected via a defined, variable series resistance to ground, such that the current could be calculated via the voltage drop over the resistor. The voltage drop over the device and the resistor are monitored using a Rohde & Schwarz HMO3004 oscilloscope. The circuit of the pulse measurement setup is shown in figure 3.8.

Due to the comparably long connection lines and resulting stray capacitances, overshooting of the signal at the start of the pulse and subsequent oscillation
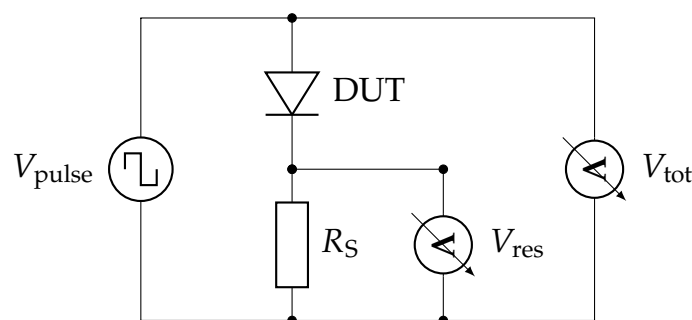
Figure 3.8: Equivalent circuit for pulsed measurements of two-terminal devices: The pulsed signal is applied to the DUT in series with a defined resistor R_S. Output voltages are measured using an oscilloscope. The voltage across the DUT is given by $V_{DUT} = V_{tot} - V_{res}$ and the current by $I_{DUT} = \frac{V_{res}}{R_S}$.

limits measurements to comparably long pulse lengths. Once a steady-state is reached, voltages can be measured to an accuracy of approximately 100 mV. The current values are deduced with an additional inaccuracy of 5 % originating from the series resistor.

3.2.4 Polarization Microscopy

To quickly assess phase, size, and quality of crystal films, methods like AFM, Scattering Electron Microscopy (SEM), or XRD are too slow. A fast analysis by simple microscopy, however, does not yield significant contrast between adjacent crystal grains. Details caused by topographical features are visible, however, orientation and phase variation are often not recognizable. Cross-polarization microscopy offers an easy path to evaluate crystal properties. It is based on the orientation and structural dependence of the birefringent behavior of light passing through the layer. Light – initially linearly polarized before the sample – is rotated. This rotation is slightly different for each crystal grain. Using a second polarizer (called analyzer) after the light exits the sample, specific optical length and therefore specific wavelength of light (when using white light) are filtered out. The individual areas appear to be colored in the complementary color of the wavelength removed. By tuning the rotatable polarizer – and optionally optical prisms – a color theme[20] can be selected that offer optimal contrast between adjacent grains. A detailed study on the imaging of thin crystalline films using polarization microscopy has been presented by Pan et al. [183].
As a microscope, a Nikon Eclipse LV100ND POL/DS[21] is used in combination with a DS-Fi2 digital camera featuring 5.24 Mpx at up to 400x magnification. Here, the polarizer at the light-output side is fixed and the initial polarization at the input can be varied instead.

3.2.5 X-Ray Diffraction (XRD)

To analyze the crystal structure and evaluate the degree of order, XRD is used. It is based on the constructive interference of monochromatic x-rays at the crystal lattice. X-rays are usually generated by a cathode ray tube and filtered using a monochromator to a wavelength λ. After aligning and focusing, they are diffracted at the target for angles Θ that fulfill the Bragg condition:

$$n\lambda = 2d sin\left(\Theta\right), \tag{3.9}$$

where d is the distance between two lattice planes. The general principle of Bragg diffraction is depicted in figure 3.9. In a powder sample, all orientations of the crystal towards the incoming x-ray are present, thus, by scanning over all angles

---

[20]The visible colors are an effect of the polarized filtering and do not represent the real "color" of the layers.

[21]Nikon, Minato Japan
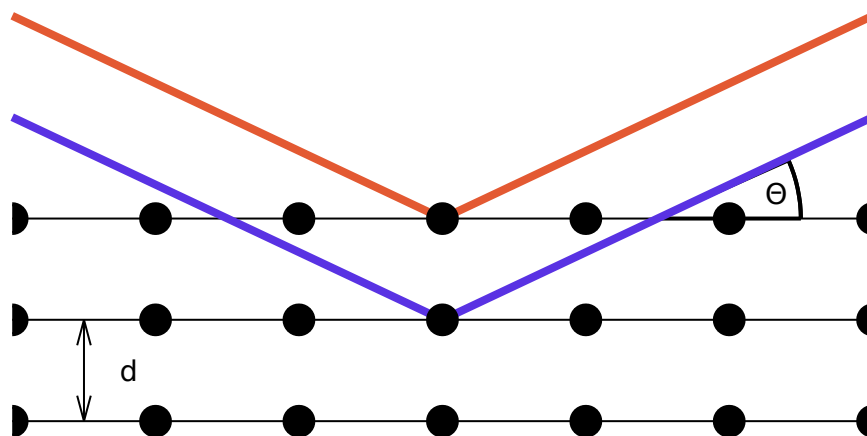
Figure 3.9: Schematic depiction of Bragg diffraction on crystal planes. Incoming x-rays are reflected at virtual crystal planes. Note that the actual reflexion is caused by the constructive interference of photons diffracted at the individual atoms. Only at sufficiently large distances does an incoming plane wave appear to be a reflected plane wave. Depending on the distance of the wavelength of the x-rays, the distance between crystal planes, and the incidence angle the components originating from different planes interfere constructively or destructively. Only the constructive parts are measurable.

2Θ, all possible constructive interfering rays can be detected. The same logic holds for an array of thin-film crystals, but limited to a 2D plane. A single-crystal has to be rotated to realize all possible orientation. From that, information about the crystal structure and lattice constants can be gained. Positions of peaks give information about internal lattice constants, while the width of the peaks represents the degree of order for this particular direction. Not all crystal planes cause diffraction signals. For example, in body or face-centered systems, signal from the intermediate crystal planes can interfere destructively and no signal is present in certain orientations. On the other side, in case of molecular crystals, additional signals can arise from the intramolecular bonds. Careful analysis is necessary to evaluate diffraction patterns.

A special problem regarding (organic) thin films compared to powder samples or bulk crystals, is the limited sample volume. In standard configuration, only a small number of atoms actually interfere with the x-ray, while most of the input signal passes through into the substrate. Additionally, the amount of the sample that contributes to diffraction changes, while scanning through Θ.

One possibility to solve these issues is illumination under small incident angles. The method is known under Grazing Incidence X-Ray Diffraction (GIXRD). A detailed description can be found in [184]. The geometry is shown in figure 3.10. Here, the illumination angle ω is small($< 5°$) compared to the standard configuration, so that the ray covers a significant volume of the thin film by moving in parallel to the surface of the sample. The width of the beam is increased from

d to $D = dsin(\omega)$. Since the incidence angle is fixed, the diffraction volume is fixed as well, resulting in an easier to analyze signal.

A Bruker D8 Discover[22] is used for x-ray diffraction. It features a copper target x-ray tube and a Lynxeye XE-T detector with an energy resolution of 380 eV that can be used as a 1D or 2D detector. Different collimators, slits, and other filters can be inserted into the optical path. The standard setup used in this thesis contains a 0.6 mm slit at the input and a Soller filter for parallelization at the detector side for quick measurements (measurement time: 12 h). For detailed analysis, a slit of 0.1 mm is used at the source side and a slit of 0.2 mm at the detector side (measurement time: 3 d). A metal beam guard was positioned several mm above the sample to reduce scattering in air. All thin films measured are deposited onto wafers of blank doped silicon. The substrates themselves are mounted on top of a 100 mm wafer, while the crystal orientation of the silicon was chosen to be at an odd angle with the optical path to avoid diffraction from the substrate. All data gathered is filtered to remove $K\alpha$-contributions and corrected by a fitted background.

---

[22]Bruker corporation, Billerica (MA) USA
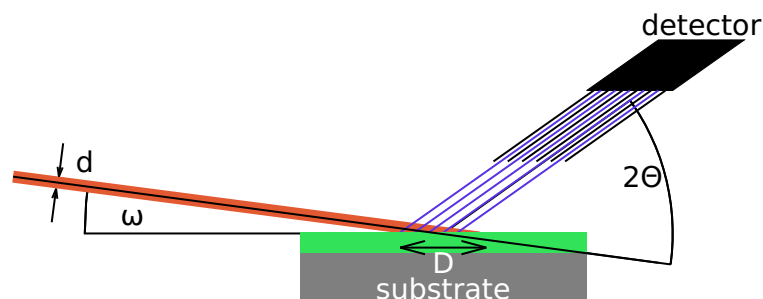
Figure 3.10: Schematic depiction of x-ray diffraction in GIXRD configuration: Illuminating the sample at a shallow angle ω, increases the effective depth of the beam from d to $D = dsin(\omega)$. Thus, less volume is needed. The detector measures the intensity of diffracted x-rays by scanning through 2Θ.

3.2.6 Atomic Force Microscopy (AFM)

A method to get highly accurate information about the surface of samples is atomic force microscopy. A fine tip attached to a cantilever is moved via piezoelectric motors over the substrate, as depicted in figure 3.11. The light from a laser is reflected by the cantilever and detected by a segmented photodiode. Even tiny deflection of the cantilever are geometrically magnified and create changing signals. In contact mode, the tip is in direct contact with the samples surface and follows it features. In AC-mode the tip usually does not touch the samples but is hovered in a defined distance oscillating. The forces between the tip and the tip (coulombic or Van der Waals) change the potential of the oscillating cantilever and introduce a change in amplitude and phase. From these data, information about the landscape of the surface can be obtained.

An AIST-NT Combiscope1000[23] is used for surface measurements, featuring a 0.05 % non-linearity in x, y, and, z direction as well as a 0.1 nm rooted mean surface roughness by the setup and a 1300 nm laser and diode pair with noise below 0.1 nm. The tip is a PPPNC-HR probe by nanosensors[24] made from aluminium coated highly doped silicon. The radius of the tip curvature is below 10 nm and the resonance frequency is at 330 MHz. Measurements are performed in non-contact AC mode with an amplitude of 50 nm and a scanning speed of $0.1 \, \text{s}^{-1}$. The height profile of an AFM measurement can be used to extract a medium roughness of the surface. Since information of the entire surface are condensed into a single number, special care has to be taken in regard of the chosen algorithm.

---

[23] AIST-NT, Novato (CA) USA
[24] nanosensors, Neuchâtel, Switzerland
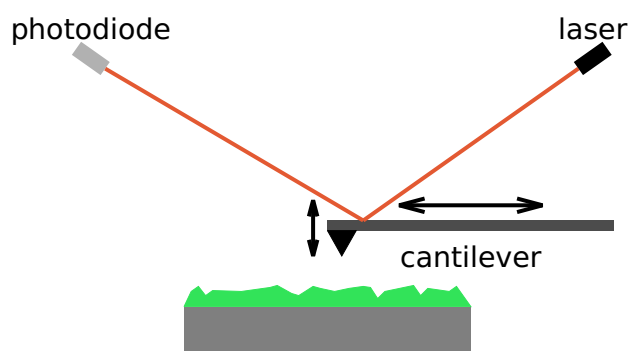
Figure 3.11: Schematic depiction of atomic force microscopy: The cantilever with nm-sized tip is moved over the surface of the substrate in constant vertical oscillation. Forces between tip and surface change amplitude and phase of the oscillation, measurable via the change in deflection of a reflected laser.

Two different parameters are calculated here to reduce the chance of outliers. The average deviation of n data points from the medium plane y_0 is given as:

$$R_{\mathrm{a}} = \frac{1}{n} \sum_{i=1}^{n} |y_0 - y_i| \tag{3.10}$$

and the Root Mean Square (RMS) as:

$$R_{\mathrm{q}} = \sqrt{\frac{1}{n} \sum_{i=1}^{n} (y_0 - y_i)^2}. \tag{3.11}$$

Since the distance to the mean is quadratically in R_{q}, many small peaks have a smaller effect than fewer large peaks. Thus, the larger the difference between R_{a} and R_{q}, the more strong variation is present on the surface.

3.3 Materials

The following tables give a summary of information about the materials used in this thesis. Literature values of HOMO and LUMO energies are given to assess energy alignment and feasibility of doping. Additionally, mobility values are summarized for rubrene in different structural configuration made with different methods. It serves as a comparison to mobility values shown in the results chapters 4.2.2.1 and 6. Crystallographic data of rubrene is used as a base for comparison with XRD-measurements in chapter 4.1.
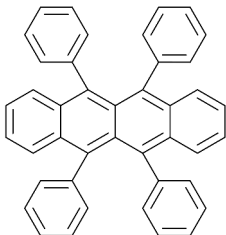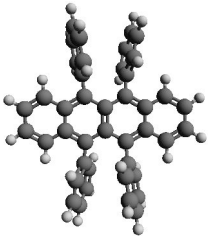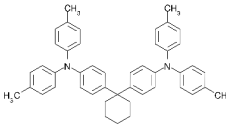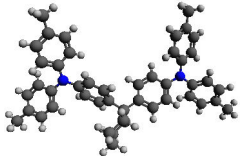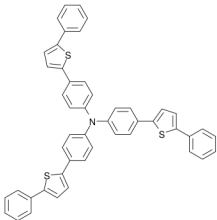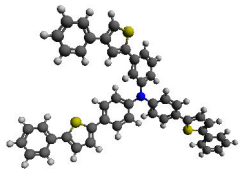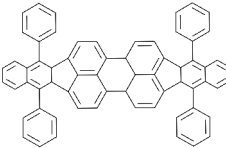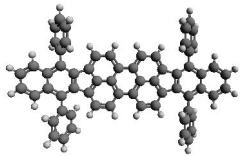
full name	abbreviation	structure	3D image	HOMO	LUMO
5,6,11,12-Tetra-phenyltetracene	rubrene			**5.4** ([185], [186], [187])	**3.2** ([185], [186]), **3.0** [187]
4,4-Cyclohexylidenebis [N,N-bis(4-methylphenyl) benzenamine]	TAPC			**5.5** ([188], [189], [190]), **5.4** [191]	**2.0** ([188], [189], [190]), **1.9** [191]
Tris(4-(5-phenylthiophen-2-yl)phenyl)amine	TPTPA			**5.57** [192], 5.4 [191]	**2.75** [192], 3.2 [191]
Tetraphenyl diben-zoperiflanthen	DBP			**5.4** [191]	**3.4** [191]

Table 3.1: List of used organic semiconductors.
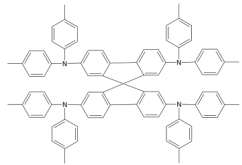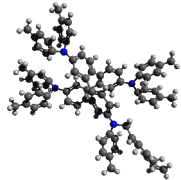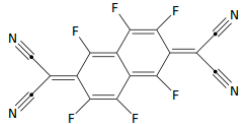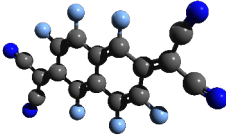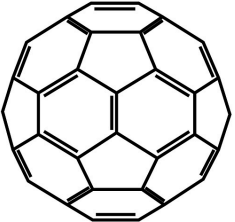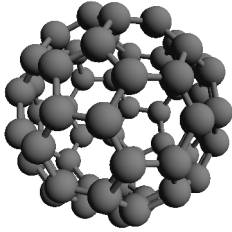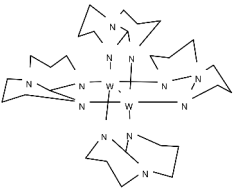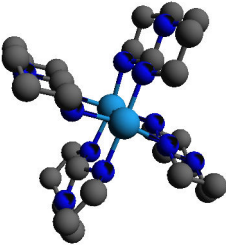
full name	abbreviation	structure	3D image	HOMO	LUMO
2,2,7,7-Tetra(N,N-di-p-tolyl)amino-9,9-spirobifluorene	Spiro–TTB			**5.25** [193], **4.9** [194]	-
1,3,4,5,7,8-hexafluoro-tetracyano naphthoquin-odimethane	F6TCNNQ			-	**5.37** [195]
$(C_{60}-Ih)[5,6]$-fullerene	C_{60}			**4.5** [196]	**6.1** [196], **6.2**
Tetrakis(hexahydro pyrimidinopyrim-idine) ditung-sten(II)	$W_2(hpp)_4$, tungsten paddlewheel			$E_I = $ **3.5** ([197], [198])	-

Table 3.2: List of used organic semiconductors.

full name	abbreviation	work function in eV [199]	specific resistivity in $\Omega\,m$[200]
gold	Au	5.1-5.47	$2.414 \cdot 10^{-8}$
silver	Ag	4.26-4.74	$1.587 \cdot 10^{-8}$
aluminium	Al	4.06-4.26	$2.65 \cdot 10^{-8}$

Table 3.3: List of used metals.

full name	abbreviation	dielectric constant	breakthrough field in $MV\,cm^{-1}$
silicon oxide	SiO_2	3.9 [201]	8-9 [202]
aluminium oxide	Al_2O_3	7 [203]	6-8 [203]
Cytop	-	2.1 [148]	0.5-1 [148]
5,6,11,12-Tetra-phenyltetracene	rubrene	2.6 [204]	-

Table 3.4: List of relevant dielectric properties.

published by	method	measurement	crystal phase	mobility in cm^2 V^{-1} s^{-1}
Soonjoo et al. [205]	thermal evaporation	field-effect (SiO$_2$)	amorphous	2.2·10^{-6}
Park et al. [35]	thermal evaporation	field-effect (SiO$_2$)	triclinic+amorphous	1.23·10^{-4}
Fusella et al. [36]	re-crystallization	field-effect (top-gate:N-parylene+Cytop)	orthorhombic (spherulites)	0.8-1.2
Fusella et al. [36]	re-crystallization	field-effect (top-gate:N-parylene+Cytop)	orthorhombic (platelets)	3-4
Pundsack et al. [64]	vapor transport	time of flight (c-axis)	orthorhombic single crystal	0.29-0.7
Jo et al. [49]	solution	field-effect (SiO$_2$)	orthorhombic (platelets)	0.07-0.52
Matsukawa et al. [44]	solution	field-effect (top-gate: parylene)	orthorhombic single crystal	0.75
Podzorov et al. [43]	vapor transport	field-effect (top-gate: N-parylene)	orthorhombic single crystal	8
Takeya et al. [41]	vapor transport	field-effect (vacuum gap)	orthorhombic single crystal	40

Table 3.5: Mobility values of rubrene.

published by	method	crystal phase	symmetry	a in Å	b in Å	c in Å	ρ in g cm^{-3}
da Silva et al. [73]	simulation	orthorhombic	-	14.43	7.18	-	-
Henn et al. [206]	vapor transport	orthorhombic (bulk)	Aea2 (Acam)	14.44	7.18	26.97	1.26
Tavazzi et al. [207]	vapor transport	orthorhombic (bulk)	D_{2h}^{18} (Cmce)	14.4	7.2	26.9	-
Jurchescu et al. [37]	vapor transport	orthorhombic (bulk)	Cmce	14.211 (100 K), 14.258 (150 K), 14.332 (200 K), 14.433 (293 K)	7.170 (100 K), 7.168 (150 K), 7.181 (200 K), 7.193 (293 K)	26.789 (100 K), 26.775 (150 K), 26.838 (200 K), 26.86 (293 K)	1.296 (100 K), 1.293 (150 K), 1.281 (200 K), 1.269 (293 K)
Verreet et al. [50]	re-crystallization	orthorhombic (film)	-	-	-	26.7	-
Fusella et al. [51]	re-crystallization	orthorhombic (film)	-	14.43	7.19	26.86	-
Jo et al. [49]	re-crystallization	orthorhombic (film)	-	14.14	6.86	25.91	-
Jo et al. [49]	re-crystallization	triclinic (film)	-	8.69	7.26	11.87	-
Huang et al. [45]	solution	triclinic	P1	8.5432 (173 K)	7.0196 (173 K)	11.948 (173 K)	1.294 (173 K)
Huang et al. [45]	solution	monoclinic	P2(1)/c	10.152 (173 K)	8.7397 (173 K)	15.635 (173 K)	1.279 (173 K)

Table 3.6: Crystallographic properties of rubrene.

3.4 Masks

The following tables show the mask-layout used for electrode design, their intended purpose, and defining geometric parameters:

Masks IV1 and IV2 are used for simple vertical conductivity measurements, capacitance measurements, and diode IV-measurements. While the layout IV1 offers a large number of devices with redundancy (each active area is present four times), the long electrodes proof to be sub-optimal in regard to series resistance. Additionally to the lower series resistance, the improved mask set IV2 offers the possibility of four-probe measurements.

Masks O1 and V1 can be used to build OFETs and VOFETs respectively. For the VOFET configuration, the second electrode that serves as the drain in the OFET configuration can be assigned as a second source. This mask design can be employed for shadow mask evaporation or photolithography.

Masks HF1 and HF2 are used for high-frequency measurements of half-wave rectifier circuits based upon a single organic diode. In both structures, the contact pads are designed to offer space for external circuitry in form of Surface Mount Device (SMD)-components. HF1 offers encapsulation of devices via a glued-on glass dome over the diode area (see figure 3.12). However, the resonance frequency of this geometry is at around 250 MHz, due to the long connections towards the diode. Devices built with HF2 can be measured up to the GHz-regime. Encapsulation was realized with a droplet of Cytop [208] on top of the diode area.

Masks B1 and B2 are used for the fabrication of three-terminal devices like bipolar transistors. B1 is a simpler design based on metal shadow masks. It can be aligned by eye inside a nitrogen atmosphere. The mask geometry B2 is realized via Si-stencil masks. The aspect ratio between the active area and the overlapping area of the base is significantly higher than for B1. However, consecutive masks have to be aligned under a microscope and thus in ambient atmosphere.
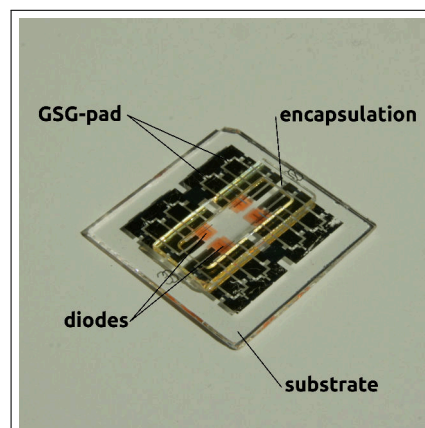
Figure 3.12: Photograph of the entire substrate of an Ultra High Frequency (UHF) rectifier circuit based on mask layout HF1, without external components.
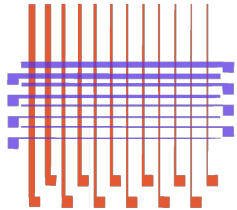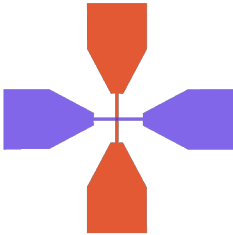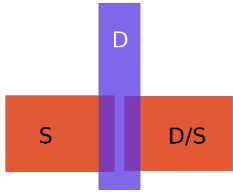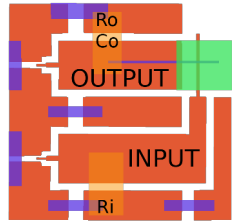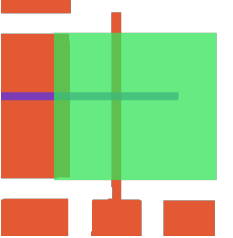
index	purpose	overview	active area	dimensions in μm
IV1	IV and diodes			50x50 to 500x500
IV2	IV and diodes			50x50 to 150x150
O1, V1	OFETs and VOFETs			W:1000, L:50-250
HF1	high frequency rectifiers			100x100 and 100x200

Table 3.7: List of used electrode geometries:
blue, red: top and bottom (source and drain) electrodes
green: structured semiconductor (if not shown, semiconductor is area-covering)
orange: external SMD-components.
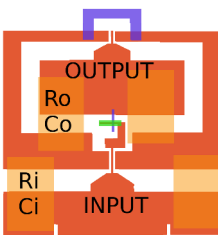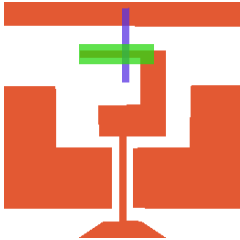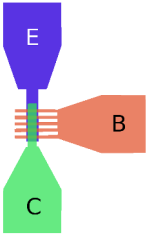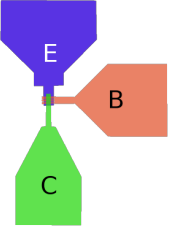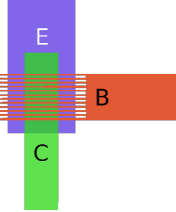
index	purpose	overview	active area	dimensions in µm
HF2	high frequency rectifiers			50x50
B1	bipolar transistors (metal)			E: 100-300, C: 50-200, B: 50-100
B2	bipolar transistors (Si-stencil)			E: 60-100, C: 40-80 , B: 5-20

Table 3.8: List of used electrode geometries:
blue, red: top and bottom (source and drain) electrodes
green: structured semiconductor (if not shown, semiconductor is area-covering)
orange: external SMD-components.

4 Growth and Characterization of Rubrene Crystals

This chapter describes the material system "crystalline rubrene thin-films" itself, while the following chapters focus on devices based on such layers. Doping of the crystalline layers is of major interest since it is the main difference to existing work from literature. The first section is focused on the crystallization process as such. Analysis of the external influences on the crystallization process – heating temperature, surface quality and energy, doping concentration, etc. – is presented, including structural measurements with Atomic Force Microscopy (AFM) and X-Ray Diffraction (XRD). This overview serves not only the purpose of classifying structural properties of different crystal polymorphs for later reference but also serves as a base for future developments with these and similar material systems.

The second section covers the electrical properties of crystalline rubrene layers. The focus is on electrical measurement of layers of different crystal structure and doping configuration.

4.1 Growth of Crystalline Rubrene Thin-Films

This section discusses the growth process of thin-films of rubrene crystals. To establish consistency and allow comparison with literature, the following naming scheme is used:

- A crystallite is a single grain of a crystalline thin-film that originates from a single condensation center until its growth stops at a neighboring crystallite or the edge of the substrate. It can be a single-crystal grain, a poly-crystal, a spherulite, or a dendritic network. It can itself consist of sub-grains of different crystal orientation, as long as they originate from the same condensation center. Some of the sub-types of crystallites are depicted in figure 4.1.

- A spherulite is a spherically grown crystallite.

- A platelet is a macroscopically single-crystalline crystallite. It can contain grain boundaries or fault lines but features a uniform periodicity and must originate from a single condensation center. A platelet can be broken and is then technically not a single-crystal. The name platelet is still used when the grain is sufficiently similar to other unbroken platelets and large enough to be utilized for devices.

Figure 4.1: Different types of crystallites: **(a):** dendritic spherulite with strong branching, **(b):** dendritic spherulite with low branching, **(c):** crystallite consisting of several sub-grains, **(d):** platelet type single crystal.
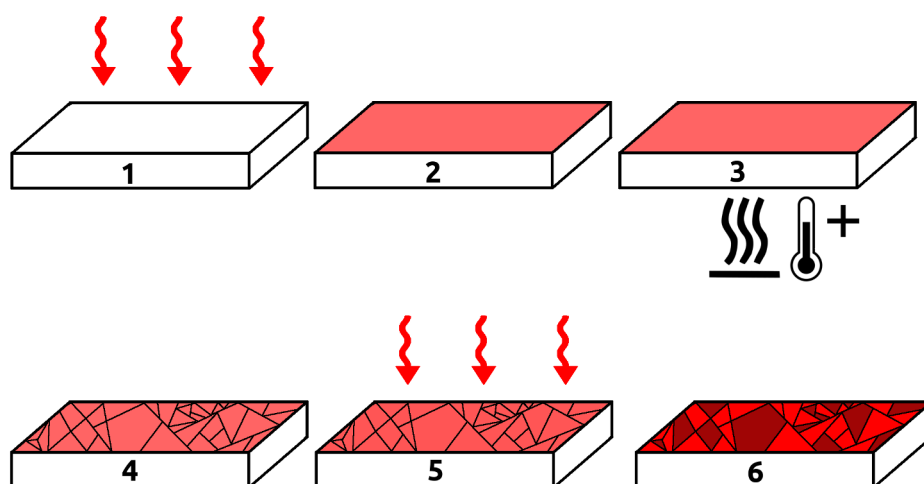
Figure 4.2: Procedure for growth of arrays of thin-film rubrene crystals: (1): cleaning and surface treatment of the substrate, (2): evaporation of an amorphous seed layer (thickness as a parameter, optional underlayer), (3): heating of substrate within nitrogen atmosphere (temperature and time as parameters), (4): results in an array of thin-film crystals (optional quality control under a microscope), (5): continuous evaporation increases thickness via epitaxy (rate and doping ratio as parameters), (6): thick crystalline layer.

- Macroscopic features relate to the shape and phase contrast of crystallites and grains within crystallites. Microscopic features relate to the fine structure of dendritic growth.

- An increase or decrease in crystal quality is related to the size of individual crystallites or grains and the density of defects.

The rubrene crystals investigated here are grown via thermal crystallization of previously amorphous thin-films on a substrate. State of the art and prior developments are described in section 2.1.3.5. The general procedure is depicted in figure 4.2 and is as follows: rubrene is evaporated onto a substrate to form an amorphous thin-film. The thickness of this so-called "seed" can range from 20 nm to 100 nm, it can be doped or left undoped depending on the polymorph. Prior to evaporation, the surface of the substrate can be treated, to generate a specific surface interaction energy. Adding a sublayer to the surface can aid in energetically decoupling the amorphous rubrene from its substrate. The sample is then heated on a hotplate inside a nitrogen glovebox, forming an array of crystallites. Speed of growth depends on the polymorph and temperature. Subsequent evaporation onto the formed seed increases the thickness of the crystallites, maintaining the initial crystallinity – epitaxy.

According to literature ([36], [49], [50]), only the triclinic and orthorhombic crystal phases are accessible using this method. Crystallization into the triclinic crystal phase starts at 125 °C – according to simulations [49] – while orthorhombic crystals appear above 170 °C. None of the triclinic polymorphs form "solid" single-crystals or oriented spherulites. They are characterized by clear dendritic growth. Although the sub-microscopic structural properties within the group

of "triclinic" crystals are similar, the superstructure, generated by the dendritic growth mode of these layers, can vary significantly. The shapes of crystallites can vary from seaweed-like, over heavily branched, to needles like growth, depending on the external parameters.

Orthorhombic crystals can be separated into two groups, orthorhombic platelets and orthorhombic spherulites. The first group consists of continuous single-crystal like crystallites with a large degree of uniformity and isotropy, while the spherulite type grows in long strings of dendrites and features a stronger anisotropy due to its non-uniform growth.

Many process parameters and structural properties vary substantially between the individual crystal phases. However, some properties and phenomena are universal or at least common:

- The density of crystallites depends on the density of condensation centers on the surface and thus on the degree of impurity. Edges of the substrates and structured electrodes can serve as additional condensation centers. Condensation centers can theoretically be caused by dynamic properties like local phonon resonance, however, these processes are not relevant for the systems investigated here due to the large density of impurities.

- Crystallization in ambient air or contact of the amorphous film to ambient air and subsequent heating inside nitrogen are not successful for any of the polymorphs investigated. It can be assumed that oxidation of rubrene molecules suppresses the possibility for crystallization in both cases ([187], [209]).

- The parameters of evaporation of the initial amorphous layer (i.e. the rate of evaporation) have no impact on the resulting crystals for any of the polymorphs.

- The temperature needed to generate a certain type of crystal or a certain behavior depends on the substrate and surface type. A lower temperature is appropriate for crystallization on Si substrates compared to glass. This can be attributed to the higher thermal conductivity and subsequent faster heating to the threshold temperature. Similarly, crystals grow faster on metals (e.g. Au) compared to the rest of the substrate.

- The heating temperature set at the hotplate is not identical to the temperature of the substrate itself. Parameters needed to generate a certain crystal type can vary depending on the specific hot plate and environment.

The following section describes a set of crystals generated by this method when heated between 110 °C to 180 °C. Higher temperatures usually show a decomposition of crystallites at the edges, presumably due to the evaporation of already formed structures. First, triclinic layers grown at different temperatures are discussed, followed by orthorhombic spherulites and platelets.

4.1.1 Triclinic Crystals

The triclinic polymorph of rubrene is significantly less investigated in literature than its orthorhombic counterpart. A higher degree of symmetry suggests a higher degree of order and consecutively better performance in electrical or other applications. It hence appears more promising to investigate the more ordered orthorhombic systems. Crystallites grown on surfaces using the heating method produce exclusively dendritic structures when crystallizing into the triclinic phase. Thus, additionally to the anisotropy resulting from the low symmetry of the unit cell, an even higher degree of anisotropy is introduced due to the high density of grain boundaries between neighboring branches of dendrites. These layers are presumably less suitable for lateral transport compared to the orthorhombic phase. This explains the focus on orthorhombic layers, since the interest in high order – high mobility – organic semiconductors originates from transistor research which requires good lateral conductivity. However, this does not necessarily correspond to vertical properties.

The individual strands of dendritic growth for all crystals encountered have a width of several µm. Within a single strand, the crystal can be assumed to be virtually single-crystalline in nature. Since the thickness of the seed layers is of nm-scale, the layers are well-ordered in the vertical direction. The vertical distance between individual layers of rubrene is lower in triclinic than in orthorhombic polymorphs [49]. Additionally, each of the layers of rubrene molecules is slightly tilted towards the next. Both these effects might result in a better overlap of molecular orbitals and thus a better charge transport in this direction.

Triclinic crystallites can be grown for a heating temperature between $120\,°C$ to $160\,°C$. Crystallites also appear when heating at $110\,°C$ or below. Their appearance differs significantly from triclinic dendrites found at higher temperatures and crystals presented in literature. Since structural measurements on these layers are difficult, due to the low degree of lateral order, a direct identification is not possible here. Crystals grown at $150\,°C$ to $160\,°C$ show both classic triclinic crystallites and orthorhombic platelets.

The macrostructure of the individual crystallites changes for each heating temperature. The following subsection presents the growth behavior at different temperatures and a statistical comparison of the growth dynamics.

4.1.1.1 Growth at 110 °C

Crystals grown from a 30 nm seed at SiO_2 are shown in figure 4.3a. Compared to crystallites presented in literature and obtained at higher temperatures, this polymorph features a flower-like shape. Internal grains are larger and microscopically less intermixed. However, different branches of one crystallite seem to overlap and obstruct each other's growth over larger distances, which indicates a weak twisting and strong anisotropy in microscopic growth. Figure 4.3b shows the

Figure 4.3: Rubrene crystallites grown at 110 °C (seed thickness: 30 nm): Crystals show a "flower-like" macroscopic shape, featuring distinct µm-sized areas of uniform phase (green vs. orange).
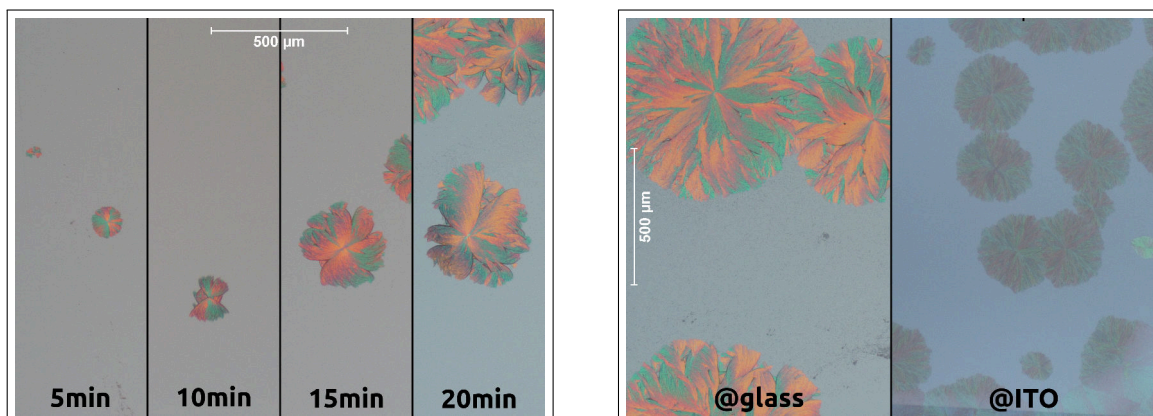
(a) Time-dependent growth on SiO_2 surface of Si substrates: Samples for measurements and micrographs are made from one single substrate that is split prior to crystallization. All timesteps have identical starting properties and are heated for a limited time.

(b) Comparison between crystals grown on pure glass and Indium Tin Oxide (ITO)-covered glass: While the crystals grown on glass show a unique "flower-like" shape, crystals grown on ITO resemble more the uniform polymorph appearing between 120 °C to 150 °C.

different growth behavior of this phase on two additional substrates. While the crystallites growing on glass appear identical to the films on SiO_2, the polymorph appearing on top of the ITO resembles the crystals grown at higher temperatures. It is the only polymorph that changes this strongly on different substrates. This behavior could be problematic if vertical devices are to be processed using this crystal phase.

To measure the speed of crystal growth, a layer of 30 nm is prepared on a SiO_2/Si-substrate which is split into four parts after evaporation. Each piece of the sample is crystallized for a different amount of time. It is worth noting that the images do not show the same crystal growing over time but different crystals grown for various amounts of time. Crystals do not show any further growth once they are subjected to ambient air which is necessary for microscopic imaging at each timestep. The resulting crystallites are shown in figure 4.3a, while the distribution of the size of these crystals is shown in figure 4.4. The size of the crystals is measured from five micrographs per timestep, each at an area of 3 mm × 2 mm. The resulting distributions show a steady increase of average crystal size around a Gaussian-looking distribution that features a skew towards smaller values. A perfect Gaussian distribution would suggest that all possible condensation centers result in the formation of a crystallite at the beginning of the process – virtually simultaneously. In contrast, a skewed distribution can be caused by a retarded crystallization process, where each possible condensation center has a distinct energy and a resulting chance to start condensation. This would lead to a skewed distribution, since crystallites that needed longer to start growing – but
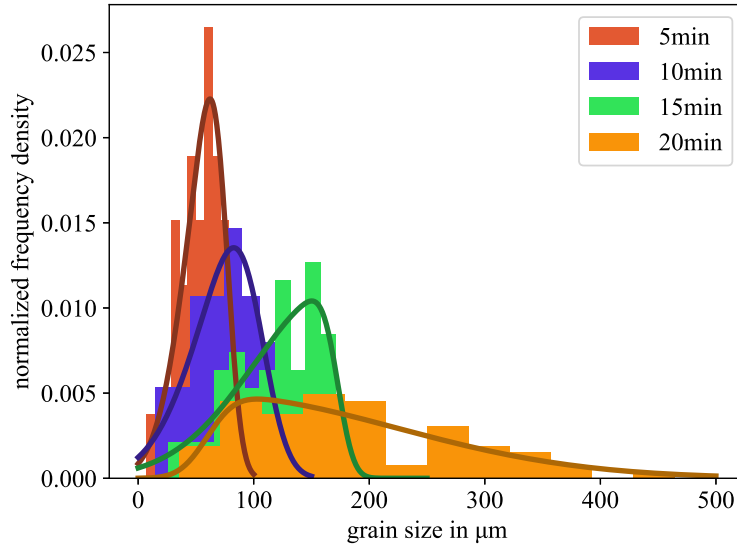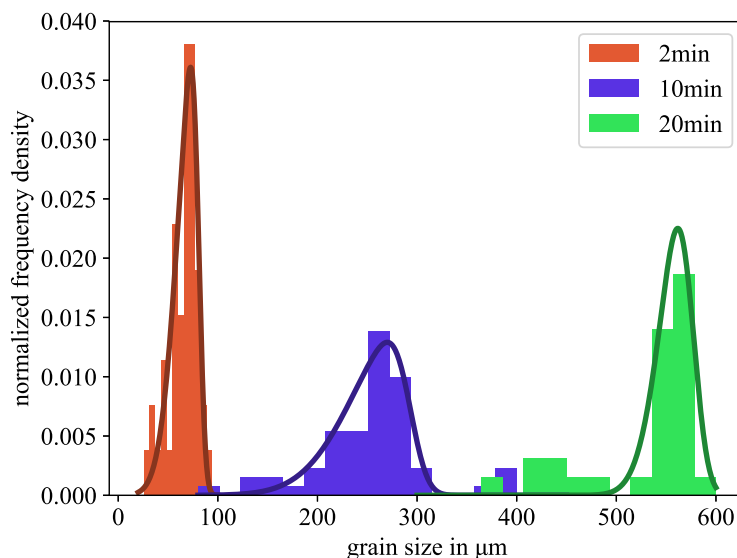
Figure 4.4: Distribution of the diameter of crystallites over time for the samples in figure 4.3a (bar graph). Five micrographs are taken at each timestep using the same magnification. The diameter of the crystals is measured for each visible crystallite. A fit of the distribution at each time is added (solid lines) based on the skew-normal distribution[*].

---

[*] The distribution at 20 min is skewed towards larger values due to the encapsulation of smaller crystallites into larger ones. It is excluded from further analysis.

grow with the same speed – are dragged behind the main peak of the distribution. Considering Boltzmann statistics, the probability of a condensation center with the energy E_a at temperature T to start a crystallite can be written as:

$$p \propto e^{\frac{E_a}{k_B T}}. \tag{4.1}$$

The resulting distribution of crystal size can be modeled via a skew-normal distribution:

$$f(x) = 2\Psi(x) \cdot \int_{-\infty}^{\alpha x} \Psi(t) dt \tag{4.2}$$

with

$$\Psi(x) = \frac{1}{\sqrt{2\pi\sigma^2}} e^{-\frac{(x-x_0)^2}{2\sigma^2}}, \tag{4.3}$$

as the standard normal distribution around a central value x_0 and a standard deviation σ. The parameter α describes the degree of skewness. In the scope of crystallization, a small α corresponds to a small variation in the start of the crystallization. Thus, the activation energy is low compared to the thermal energy and there is no large variation between individual starting points. In contrast, a large (negative[1]) α results in a heavily skewed distribution that can be caused by

---

[1] A positive α reverses the skewness of the distribution, indicating many crystals starting late. One plausible explanation for behavior like this could be a slow heat-up process.

high activation energy, or a strong variation in activation energy. The standard deviation σ of the distribution is then governed by the distribution of activation energy of the individual condensation centers and the measurement method itself.

Fitting of the skewed normal distribution yields good results for distributions of small crystals. However, once a significant amount of crystals merges and continuous growth on the connected sides of the crystallites is suppressed, measurement of the crystal diameter is difficult. Smaller crystals are trapped between larger crystals and their actual size cannot be deduced anymore. As a result, too many large crystallites dominate the distribution.

The center x_0 of the fit can be used to define an average diameter. The increase over time and corresponding fits can be seen in figure 4.21. Growth of these crystallites is clearly linear and is hence diffusion limited, as described by equation 2.5. Speed of growth at this temperature is the slowest among all measured crystals at $9.6\,\mu m\,min^{-1}$.

Crystals grown at 110 °C are not used for either electrical characterization nor devices. Further analysis might be interesting to evaluate if the differences in crystal structure correspond to any change in electrical properties.

4.1.1.2 Growth at 120 °C

Crystallites grown at 120 °C, shown in figure 4.5a, are the lowest temperature crystals that can be unequivocally identified as the triclinic crystal phase, as described in literature [19]. Sole crystals form almost perfect spheres. They contain large grains of uniform crystal phase, branching out from the center in rays. The inner-grain intermixing is larger than for crystals made at 110 °C but smaller than for hotter films. The microstructure – visible in figure 4.5b – is made up of finely interwoven dendrites. The individual strands are optically separable on microscope images. The rigid edges of the crystallites make it evident that the growth is not in itself spherulitic on a microscale, but the result of diffusive hindrance.

The time-dependent distribution of the crystal size was measured in accordance with the crystals made at 110 °C. The result is shown in figure 4.6. Speed of growth is $21.6\,\mu m\,s^{-1}$, showing skew-normal distributions for all measured timesteps.

Figure 4.5b shows the growth on different surfaces. In contrast to crystals grown at 110 °C, the crystal structure does not change. Optically, only a slight increase in branching on the Au layer is noticeable. There is no visible change of grain structure on the edge of the structured electrodes.

No electrical measurements are conducted with these layers, since they appear to be practically identical to devices made at 130 °C or 140 °C. Their slow speed of growth makes them unpractical for actual use.

Figure 4.5: Rubrene crystallites grown at 120 °C (seed thickness: 30 nm): Crystals show an almost perfectly spherulitic shape on macroscopic scales, featuring distinct μm-sized areas of uniform phase (green vs. orange).
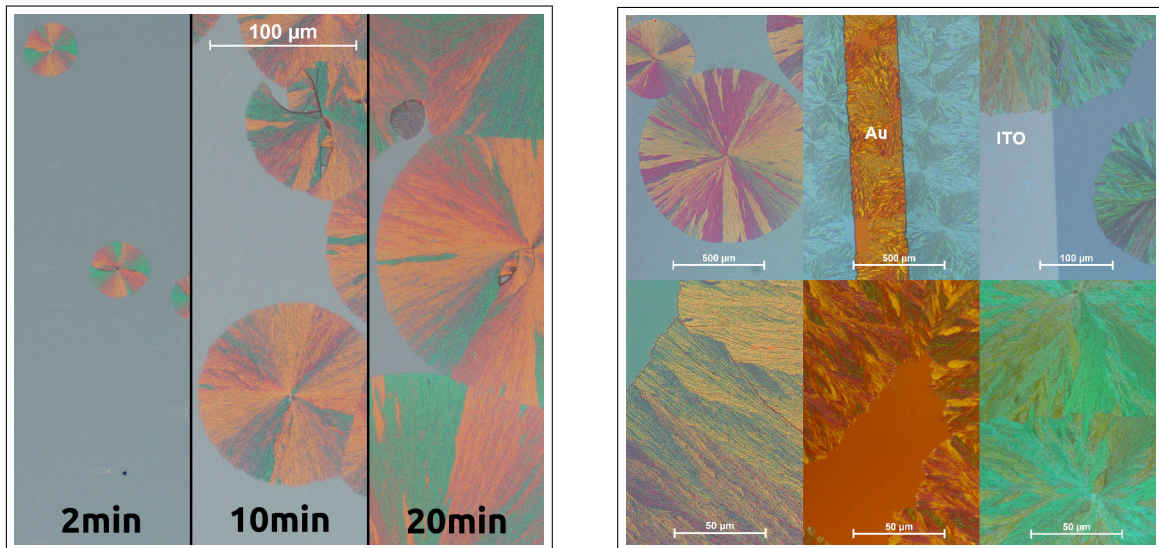
(a) Time-dependent growth on SiO$_2$ surface of Si substrates: Samples for measurements and micrographs are made from one single substrate that is split prior to crystallization. All timesteps have identical starting properties and are heated for a limited time.
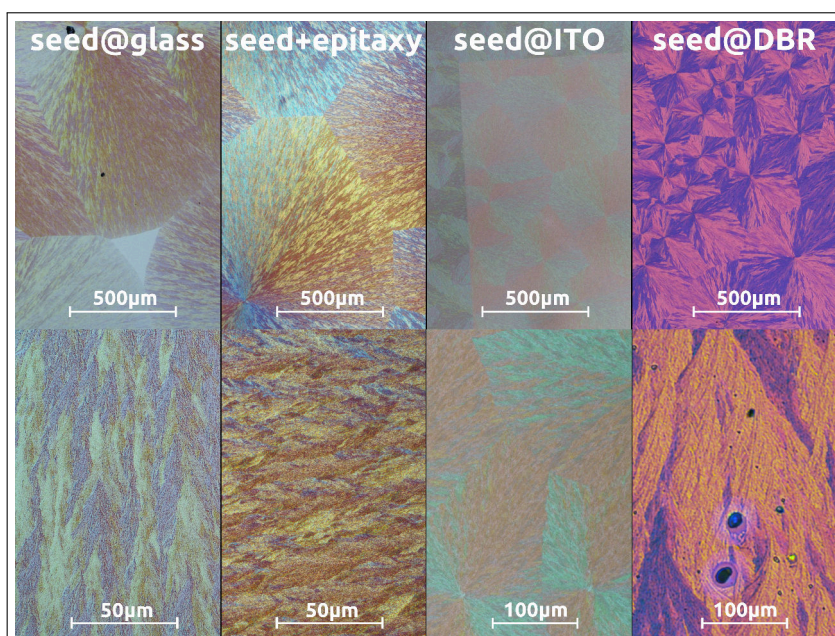

(b) Comparison between crystals grown on pure glass, structured Au on glass, and ITO-covered glass: The microstructure on both electrodes is almost identical. Compared to the films grown on glass, the branching is slightly increased. The macrostructure of the crystallites is undisturbed by the edges of electrodes.

Figure 4.6: Distribution of the diameter of crystallites over time for the samples in figure 4.5a (bar graph). Five micrographs are taken at each timestep using the same magnification. The diameter of the crystals is measured for each crystallite visible. A fit of the distribution at each time is added (solid lines) based on the skew-normal distribution.

4.1.1.3 Growth at 130 °C

Crystals grown at 130 °C are the crystal phase with the lowest temperature that is analyzed electrically in the next section and that is used in actual applications. Devices built on Si substrates or DBRs are made using these crystals, while devices on glass are heated at 140 °C, due to the higher yield of large crystallites on the respective surface. A typical example is shown in figure 4.7. On the macro scale, large round crystallites can be seen, although, compared to the lower temperature phase, a higher degree of distortion can be found, leading to slightly ellipsoid grains. There is less separation between adjacent internal grains. Microscopically, the crystal consists of finely interwoven dendrites. However, compared to the more slowly grown films, the individual strands are barely distinguishable. Growth of crystal diameter is linear and can be fitted well to skew-normal distributions, as is presented in figure 4.10. Speed of growth is once again faster compared to the colder crystallizations at $R = 69 \, \mu m \, s^{-1}$. A substrate that has been cleaned and treated with the standard procedure is fully covered with crystallites within $t = 15$ min to 20 min. Considering a uniform distribution, this value can be used to get a lower limit for the defect density,

$$ n_A^{min} = \left(\frac{t}{R} \right)^2 , \tag{4.4} $$

of $67 \, cm^{-2}$.

Figure 4.8 compares the growth on different substrates types and the effect of epitaxy. Films grown on SiO_2, glass, and ITO are virtually identical. There is no additional crystallization at the edge of structured electrodes. However, the end of the substrate often creates a source of condensation, leading to a band of small-grained crystallites near the corners. Crystals grown on DBRs appear similar to the other but feature increased densities of anomalies: lumps of material, ingrown disturbances, and voids without crystallization. It could be a result of the sub-par surface quality of DBRs and dirt particles. This problem is amplified since piranha treatment is not possible with these substrates [210].

Adding more material to the seed layer increases the initial contrast pattern. This is a strong indication that the crystallinity of the seed is transferred into the epitaxially grown parts. Since rubrene crystals feature total extinction under cross-polarized light [206], adding an amorphous film should decrease the contrast. Nevertheless, individual strands of dendrites are even less distinguishable with more material added. Changing the parameters of the evaporation (i.e. rate) of the initial seed layers has no observable impact on the final crystallization. However, a variation in the thickness of this initial film can change the result substantially. Figure 4.9a shows crystals grown at the same substrate type and parameters but different thicknesses. While crystallites with 30 nm and 40 nm appear to be similar, films grown from 20 nm of initial seed have a completely different dendrite structure, with a significantly decreased branching density
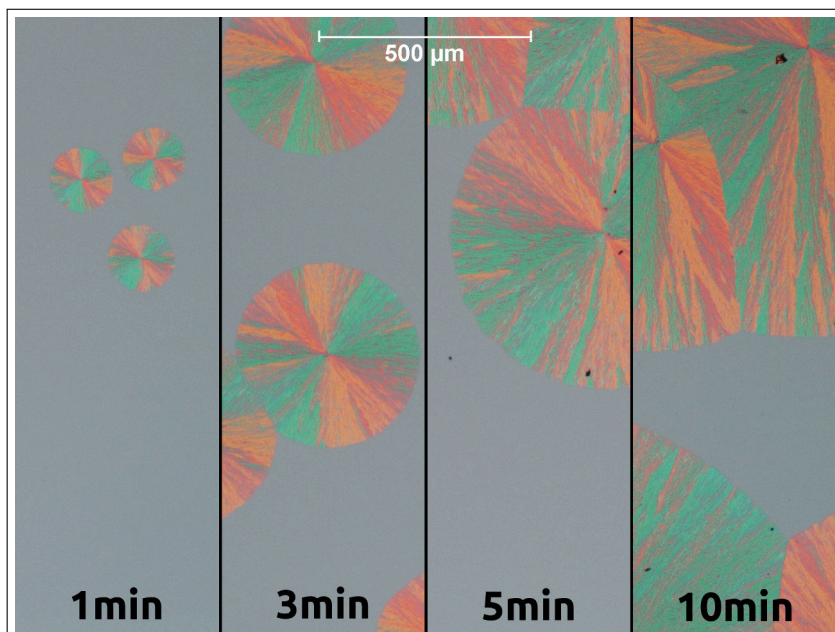
Figure 4.7: Time-dependent growth on SiO$_2$ surface of Si substrates at 130 °C (seed thickness: 30 nm): Samples for measurements and micrographs are made from one single substrate that is split prior to crystallization. All timesteps have identical starting properties and are heated for a limited time.
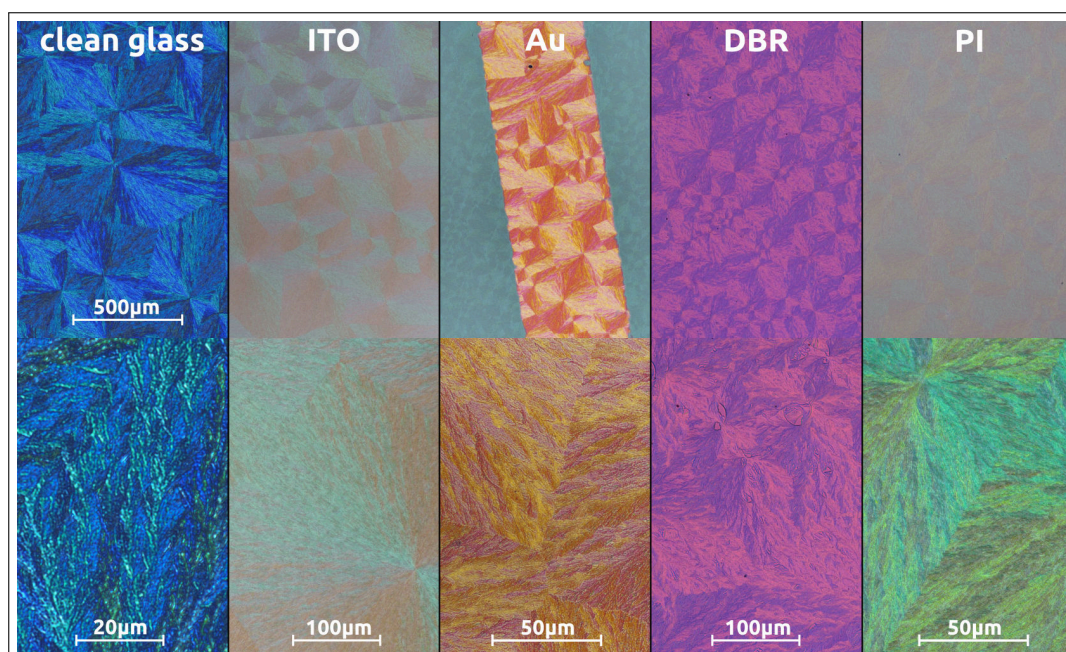

Figure 4.8: Comparison between crystals grown at 130 °C on pure glass (seed and epitaxy), ITO-covered glass, and Distributed Bragg Reflector (DBR) on glass (seed thickness: 30 nm).

Figure 4.9: Rubrene crystallites grown at 130 °C: Thickness and doping dependence.
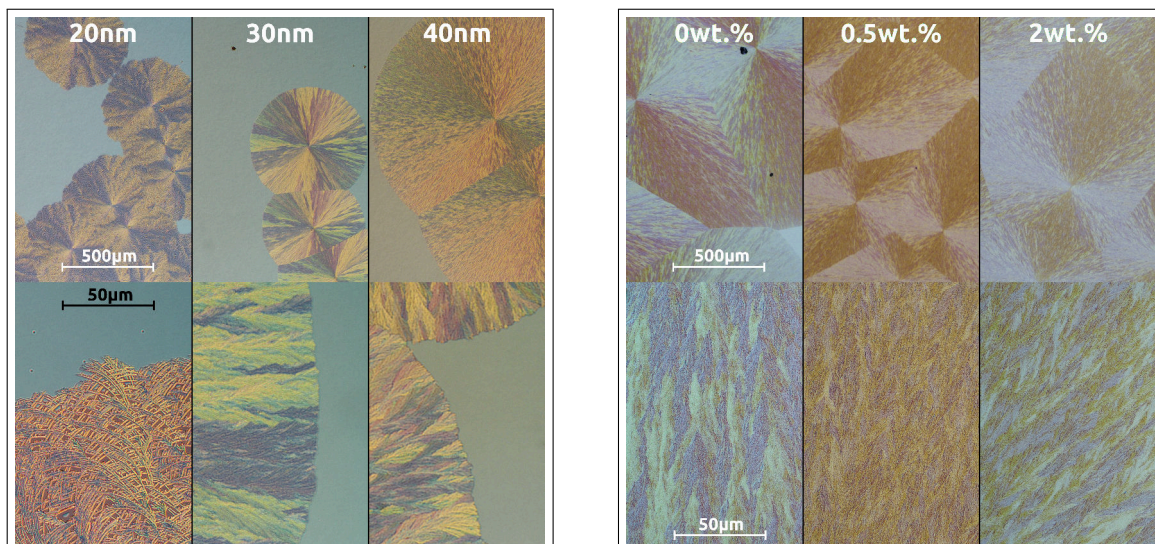
(a) Growth on SiO$_2$ surface of Si substrates with different thicknesses of the amorphous seed layer: A starting seed of 20 nm results in a completely different crystallization. 30 nm and 40 nm are similar to each other, with small differences in the branching of dendrites.

(b) Growth on SiO$_2$ surface of Si substrates with different doping concentration (F6TCNNQ) of the amorphous seed layer (seed thickness: 40 nm).

and subsequently large structures. Considering that dendritic growth is limited by diffusion, a reduction in available material at the growth front could lead to a significantly different balance in molecular transport. Up to a thickness of the seed of 100 nm, no significant change in crystallinity is noticeable. However, electrical measurements on doped layers (see section 4.2.3.6) show that a thinner seed layer is preferable.

As is presented in figure 4.9b, introducing doping into the seed layer does not change the morphology significantly. A decrease in internal grain size is observable between the doped and the undoped films. However, the effect is small and could be the result of random variation between individual samples. During the crystallization process, molecules have to be mobile to reach their appropriate position within the lattice. That the grain structure does not change with increasing doping is an indicator that the dopants are not integrated into the crystal structure but might be pushed towards the boundaries – presumably into the areas between the dendrites.
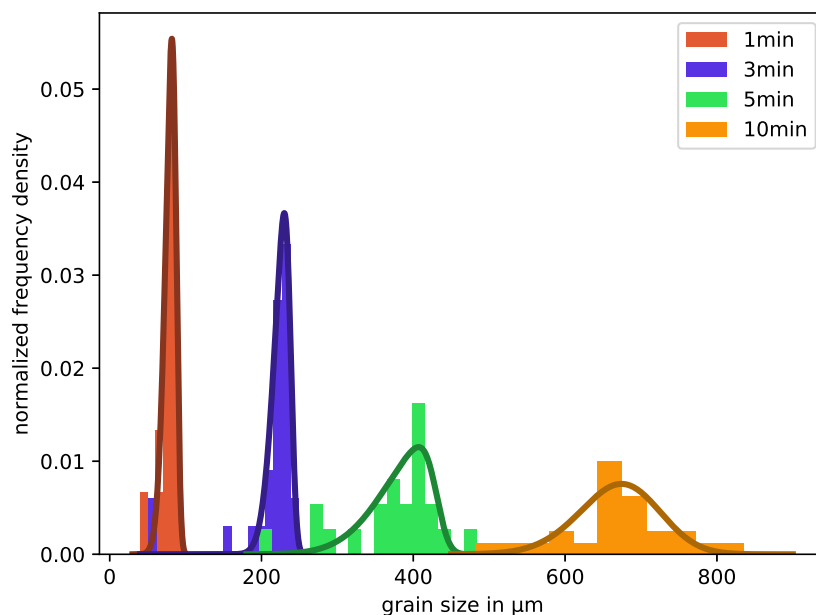
Figure 4.10: Distribution of the diameter of crystallites over time for the samples in figure 4.7 (bar graph). Five micrographs are taken at each timestep using the same magnification. The diameter of the crystals is measured for each visible crystallite. A fit of the distribution at each time is added (solid lines) based on the skew-normal distribution*.

---

* The distribution at 20 min is skewed towards larger values due to the encapsulation of smaller crystallites into larger ones. It is excluded from further analysis.

4.1.1.4 Growth at 140 °C

Crystals grown at 140 °C are very similar to crystallites made at 130 °C. However, a higher yield of large crystallites is obtained on glass substrates when using this temperature compared to Si substrates and DBRs. A typical example is shown in figure 4.11. The distribution of crystal size follows a skew-normal distribution too. Its evolution through time is shown in figure 4.15. The growth speed is significantly increased at 227 μm s^{-1}. A typical sample is properly covered with crystals within 5 min to 10 min, resulting in a minimum defect density of 35 cm^{-2}, using equation 4.4.

In figures 4.12 and 4.13, the growth on different types of substrates and differently treated substrates is compared. A special glass cleaning polymer did not show any improvement compared to the normal cleaning procedure (i.e. piranha cleaning). Crystals grown at DBRs show the same type and increase in defects as for the 130 °C samples. However, a shift from straight dendrites to a more seaweed-like configuration is visible on the DBR substrates.

The microstructure on Au, Ag, and ITO is similar to pure glass and Si-wafer samples. The size of crystallites grown directly on gold is increased compared to the parts that grow on glass alone. Additionally, the edge of the gold serves as
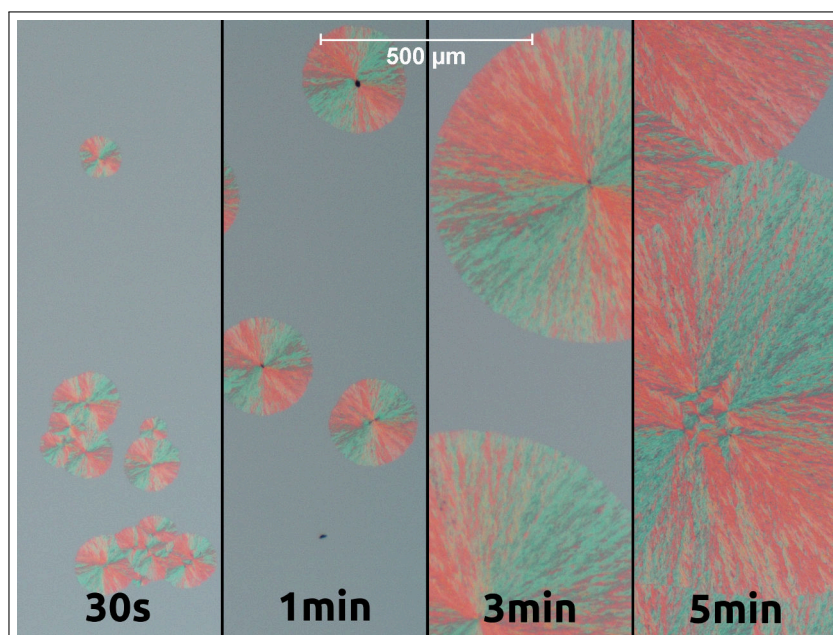
Figure 4.11: Time-dependent growth on SiO$_2$ surface of Si substrates grown at 140 °C: Samples for measurements and micrographs are made from one single substrate that is split prior to crystallization. All timesteps have identical starting properties and are heated for a limited time. (seed thickness: 30 nm).

Figure 4.12: Comparison between crystals grown at 140 °C on pure glass (cleaned with OptiClean*), structured Au on glass, ITO-covered glass, and DBR on glass. (seed thickness: 30 nm).

---

* Glass cleaning polymer by First Contact USA, Platteville.
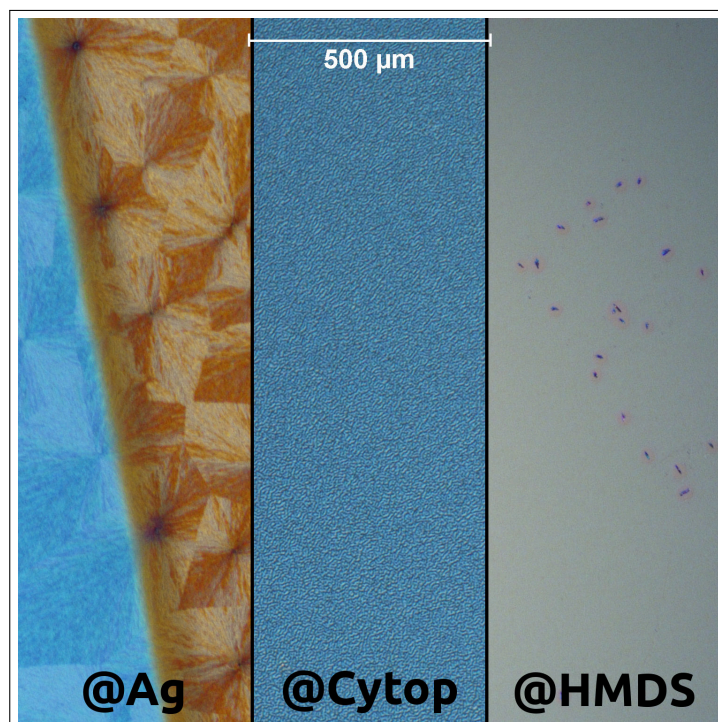
Figure 4.13: Growth at $140\,^{\circ}$C on SiO$_2$ surface of Si substrates with different surface treatment: Growth on Ag is identical to growth on Au or glass. Cytop reduces the yield of crystallization strongly. Most surfaces show granular features. No crystal can be grown on a Hexamethyldisilazan (HMDS)-treated surfaces.
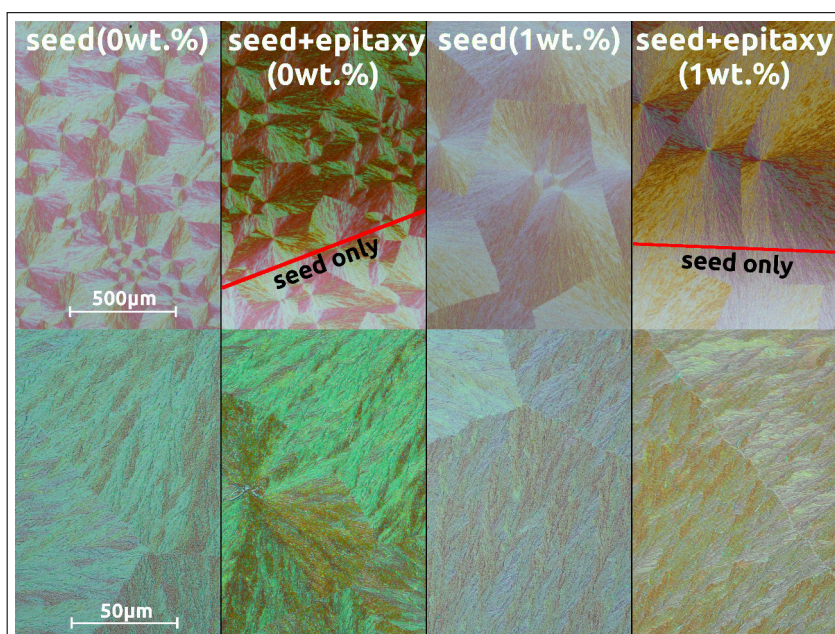
Figure 4.14: Growth at $140\,^{\circ}$C on SiO$_2$ surface of Si substrates with different doping concentration (F6TCNNQ) of the amorphous seed layers and the epitaxial layers (seed thickness: $40\,$nm).
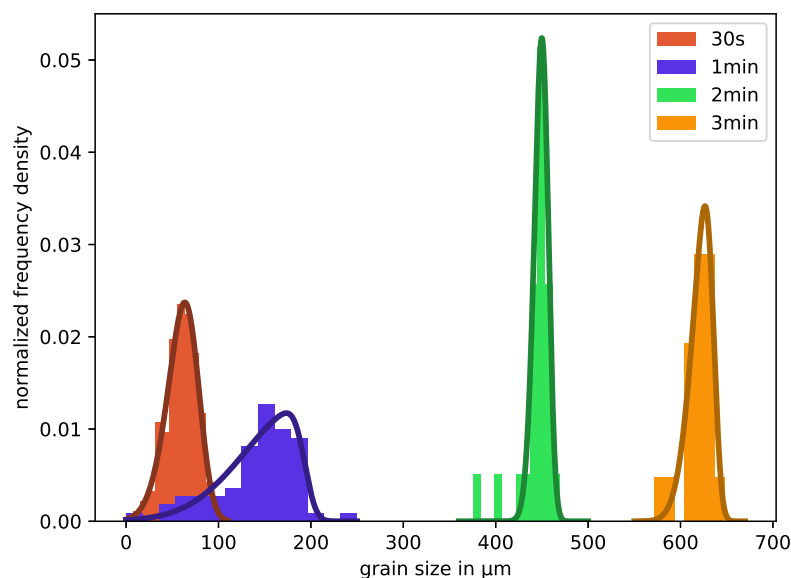
Figure 4.15: Distribution of the diameter of crystallites over time for the samples in figure 4.11 (bar graph). Five micrographs are taken at each timestep using the same magnification. The diameter of the crystals is measured for each visible crystallite. A fit of the distribution at each time is added (solid lines) based on the skew-normal distribution[*].

---

[*] The distribution at 20 min is skewed towards larger values due to the encapsulation of smaller crystallites into larger ones. It is excluded from further analysis.

condensation centers. It can be assumed that the gold surface itself has a lower density of defects that can trigger condensation, while the edge can now trigger crystallization due to the higher temperature.

Changing the surface energy to hydrophobic suppresses the growth of crystals. For HMDS treated substrates, de-wetting around the existing dirt particles can be observed. The remainder of the surface seems unchanged. Films grown on Cytop can sometimes crystallize into the typical triclinic crystal phase, albeit with a multitude of defects. However, in most cases, the result of heating is a heavily granulated surface of otherwise amorphous rubrene. Since treatment of the substrate with piranha solution or oxygen plasma improves the yield of crystallization, it can be assumed that – although not obligatory – providing a hydrophilic surface is beneficial. The effect is also noticeable on the top of the evaporated Au. This is surprising since the gold is added after the piranha treatment. The hydrophilic nature of the surface might be transferred towards the evaporated Au.

Similarly to the 130 °C films, moderate doping does not change the crystallization behavior significantly (see figure 4.14.) The contrast between individual grains is increased, while single strands are more difficult to distinguish when the thickness of crystals is increased via epitaxy. Both effects are visible for doped and undoped films.

Figure 4.16: AFM micrographs of uncrystallized amorphous rubrene at SiO_2 on a Si substrate (layer thickness: 40 nm).
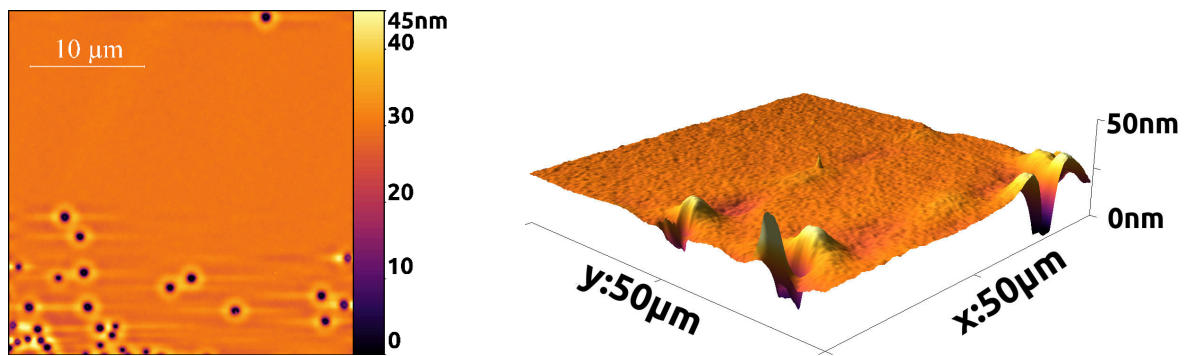
(a) Height profile of amorphous rubrene: Most of the surface is flat without any distinguishable features. Spherical holes appear randomly on the surface.

(b) 3D representation of the height profile in (a).
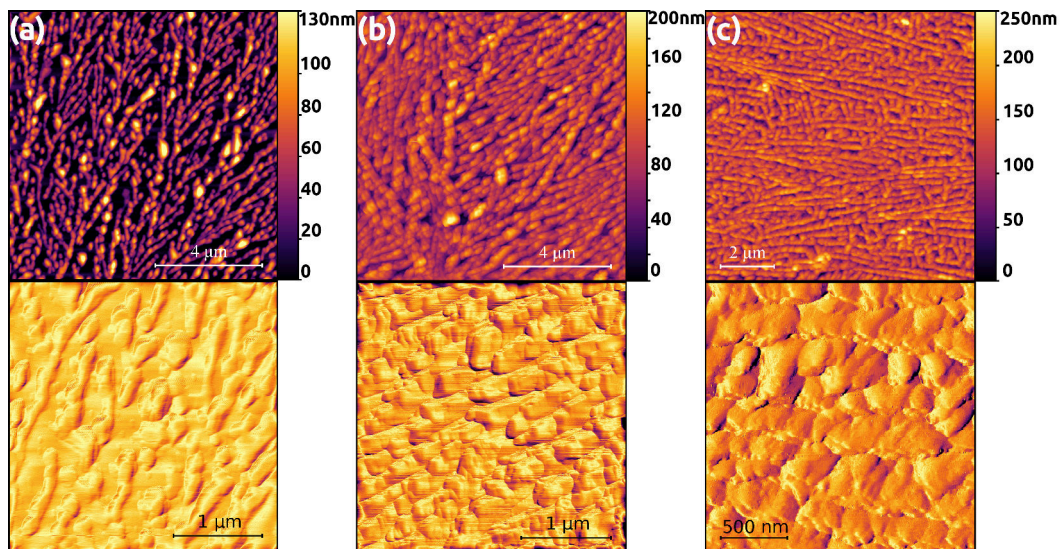
Figure 4.17: AFM micrographs of triclinic rubrene at SiO_2 on a Si substrate, crystallized at 140 °C (layer thickness: 40 nm): height profile (top), detailed shadowed profile (bottom)
(a): 40 nm seed layer only
(b): 40 nm seed layer + 40 nm undoped epitaxy
(c): entire device stack, 40 nm seed layer + 580 nm epitaxy (doped and undoped).

To analyze the exact shape of the dendrites, AFM measurements are used. As a baseline, figure 4.16a shows the surface profile of amorphous uncrystallized rubrene. The layer is smooth, at a roughness Root Mean Square (RMS) of 2.9 nm. Randomly spread over the surface, perfectly spherical holes can be found, empty of material and reaching down to the substrate. The origin is unclear, although the appearance makes a de-wetting process likely. These gigantic pinholes disappear during the crystallization process if the triclinic phase is grown. The holes remain intact (described in the next subsection) when orthorhombic spherulite crystals are grown. The lower temperature used for triclinic crystals might allow for more long-range material transport due to the slower growth speed. However,

Figure 4.18: Surface roughness extracted from AFM micrographs of triclinic crystals.
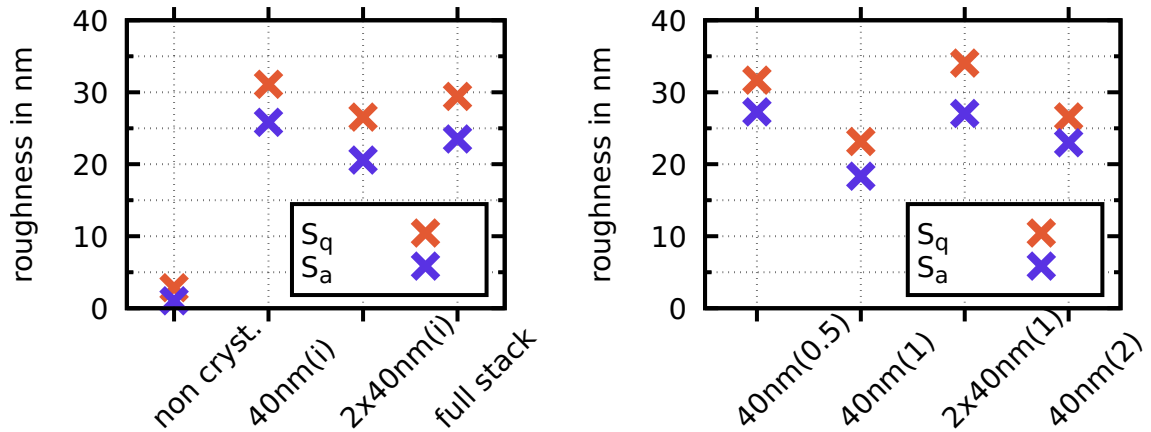
(a) Based on figure 4.17: Amorphous uncrystallized rubrene is significantly smoother than the triclinic dendritic crystals. Epitaxy reduces surface roughness only to a limited degree. The surface properties of a thick layer are defined by the properties of the seed.

(b) Based on figure 4.19 (doping concentration in brackets): Doping of the seed layer does not change the surface roughness of triclinic dendritic crystallites systematically.

molecular transport over several µm seems unlikely. Since the occurrence and distribution of these holes seems to be random, a detailed analysis seems difficult. In figure 4.17 AFM micrographs of the triclinic crystallites are shown. The seed is heavily dominated by a fine mesh of branched dendrites. They do not consist of solid lines but are formed by chains of droplets. Although it initially appears as if the entire film is concentrated within these droplets and the area between is only the naked substrate, a small degree of structure is visible between the dendrites. Nevertheless, the bulk of the material is visibly concentrated within the branches. When adding more material to the layer via epitaxy, both the dendrites and the areas between seem to grow at the same rate. The general shape of the dendrites seems to stay intact. Thus, no smoothing is visible, reflected in no change of surface roughness (see figure 4.18a).

However, examining the detailed structure, a shift from chains of individual droplets of material towards flake-like sheets of material is visible when transitioning from the seed to the epitaxially grown films. The seed effect that allows for the continuous growth of ordered, crystalline material is, therefore, not limited to the bulk strands of the dendritic part but is extended towards the intermediate area too. Especially in the measurement of the full stack device, a differentiation between originally dendritic areas and intermediate areas is not possible in the zoomed micrograph. Thus, it can be assumed that – although the large scale surface still resembles the initial chain structure and the surface roughness remains the same – the desired high degree of crystallinity is preserved across the entirety of the crystallite.
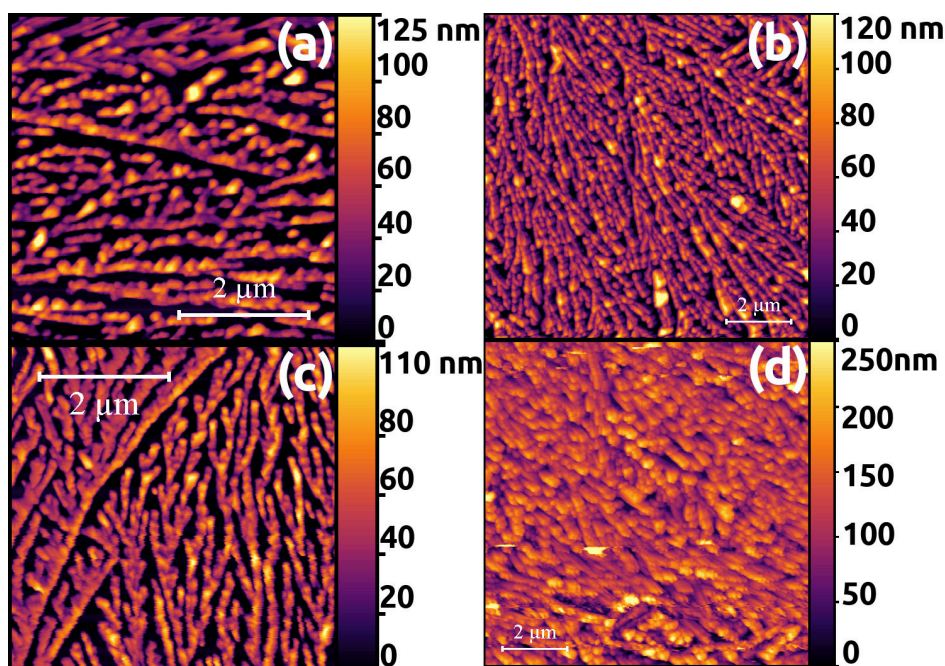
Figure 4.19: AFM micrographs of doped triclinic rubrene at SiO_2 on a Si substrate, crystallized at 140 °C (layer thickness: 40 nm):
(a): 40 nm with 0.5 wt.%, seed layer only
(b): 40 nm with 1 wt.%, seed layer only
(c): 40 nm with 1 wt.% seed layer + 40 nm 1 wt.% epitaxy
(d): 40 nm with 2 wt.%, seed layer only.

Figure 4.19 summarizes AFM images of doped triclinic layers. Doped layers appear and behave practically identical to undoped crystals. The seeds consist of the same droplet-like dendrites that are transformed into sheets via epitaxy. A significant change in surface roughness does not occur for moderate doping concentration (see figure 4.18b).

Since the global long-range vertical crystallinity of triclinic layers is low, XRD measurements yielded no detectable signal.

4.1.1.5 Growth at 150 °C

Substrates heated at 150 °C form crystallites that appear to be identical to crystals generated at 140 °C, although at an increased speed of growth. They are shown in figure 4.20. However, a detailed look at the microstructure of these films reveals the inclusion of small granular defects. Whether these defects have a negative effect on devices is not investigated. Additionally to the normal triclinic dendrites, orthorhombic single-crystals can appear randomly spread over the substrate, although rarely. Growth of this phase only occurs on the SiO_2 part or ITO-covered area but never on any of the metal electrodes. Significantly more of these crystals grow at higher temperatures. They are discussed in the following subsections. Since the increased speed of growth is negligible and no other benefit is apparent, no further measurements or devices are done using films grown at 150 °C temperature.
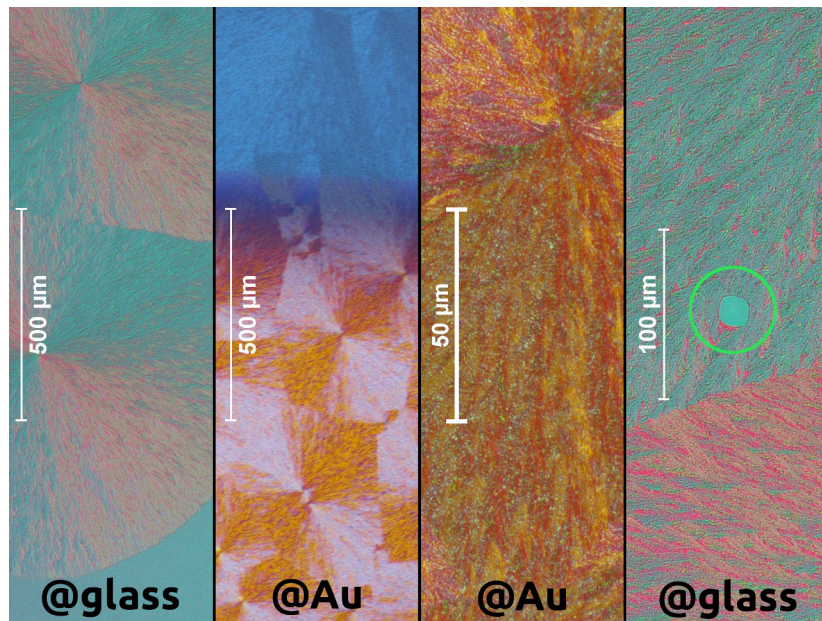
Figure 4.20: Rubrene crystallites grown at 150 °C (seed thickness: 30 nm) on pure glass and structured Au on glass: Crystallites appear identical to crystals grown at 140 °C, but present fine granular effects in their microstructure. 150 °C is the lowest temperature for which single-crystalline orthorhombic platelets can appear (right, green mark).
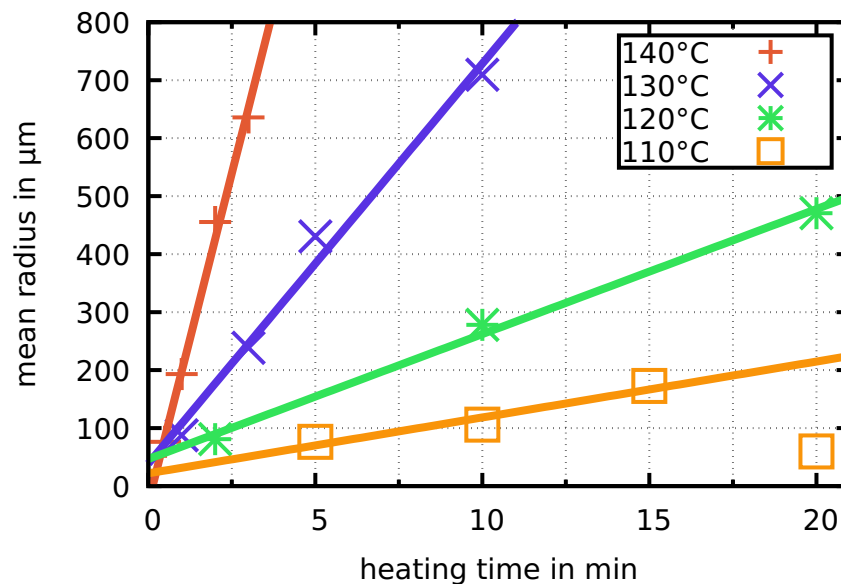
Figure 4.21: Time-dependence of medium diameter x_0: Distributions in figures are fitted to skew-normal distributions. The central peak growth linearly for all values that are taken into account.

4.1.2 Orthorhombic Spherulites

The second and in literature more prominent crystal phase of rubrene features an orthorhombic unit cell. Due to their additional rotational symmetries, these crystals have the potential for a higher degree of order within the solid itself. The record values for field-effect mobility found in literature, are based on this crystal phase, albeit with free-standing bulk single-crystals. However, thin-films of rubrene can be grown via the heating procedure too. They have been used in field-effect transistors [36] and organic solar cells [50].

Thin-film orthorhombic crystals appear in two different configurations: spherulites and platelets. The first type is discussed in this subsection, while the platelets are highlighted in the following subsection.

4.1.2.1 Broken vs. Solid Orthorhombic Spherulites

The crystal phase of orthorhombic spherulites is itself split into two different subcategories. One type of spherulite grows classic spherulites with almost no branching within its dendritic structure. Aside from the center of each crystallite – where usually a defect can be found – these crystals feature a high degree of radial symmetry, offering a supposedly higher degree of lateral conductivity compared to the random arrangement of triclinic layers. However, this only applies along the crystal growth direction. In perpendicular direction, the same arguments regarding grain boundaries apply that are discussed for the triclinic crystals.

The other type of spherulite features a similar microstructure, while the crystallites themselves are broken into smaller sub-crystallites. Although the crystallite as a whole originates from a single initial condensation center, the growth direction changes. The resulting crystal has a significantly lower degree of radial symmetry. Since the fragmentation into even smaller grains introduces additional grain boundaries, the lateral conductivity might be decreased. For most applications, the growth of the solid spherulitic polymorph is preferred.

As a general rule, at least 170 °C is required to generate any type of orthorhombic spherulite. Ray-like broken crystals usually appear at temperatures of around 180 °C and higher, although the exact set of parameters, that guarantee the occurrence of one or the other type of crystal, is difficult to determine. Even supposedly identical samples undergoing the identical process can yield different results. A yet unknown parameter must influence the crystallization.

Figure 4.23 presents a set of AFM micrographs at different degrees of magnification. The overview image (a) appears similar to the images made by polarization microscopy. The dendritic substructure is facing straight out from the center towards the rim of the crystallite. However, some of the surface features appear to be cracks in the crystalline structure void of any material. This is confirmed via the highly detailed measurements (b) and (c) since there is no visible structure within the crack. Due to the rugged nature of their edges, they seem to originate

Figure 4.22: Types of rubrene orthorhombic spherulite crystallites (seed thickness: 20 nm):
top: Films processed at 170 °C usually grow into solid spherulites with a semi-circular symmetry.
bottom: Films processed at more than 180 °C usually grow into ray-like broken spherulites.

from merging growth fronts competing for material. These cracks are filled up with epitaxy, as can be seen in the micrographs (e) and (f). Hence, these voids should not cause problems in the form of short circuits in vertical devices, as long as a thick enough layer is created using continuous evaporation. However, these voids can result in additional grain boundary-related scattering in vertical direction. This is especially interesting for bottom-gate transistor devices based on these layers, since the voids – and thus the defect – is directly positioned at the defining gate interface.

Even more detailed scans of the surface of the semiconductor (d) reveal plateau-like structures, separated by distinct steps. Figure 4.24a shows a cut through these plateaus averaging over a defined width. Since the plateaus are not perfect rectangles but laterally rounded structures, the resulting profile depends on the amount of lines used for the averaging. Only features that remain almost
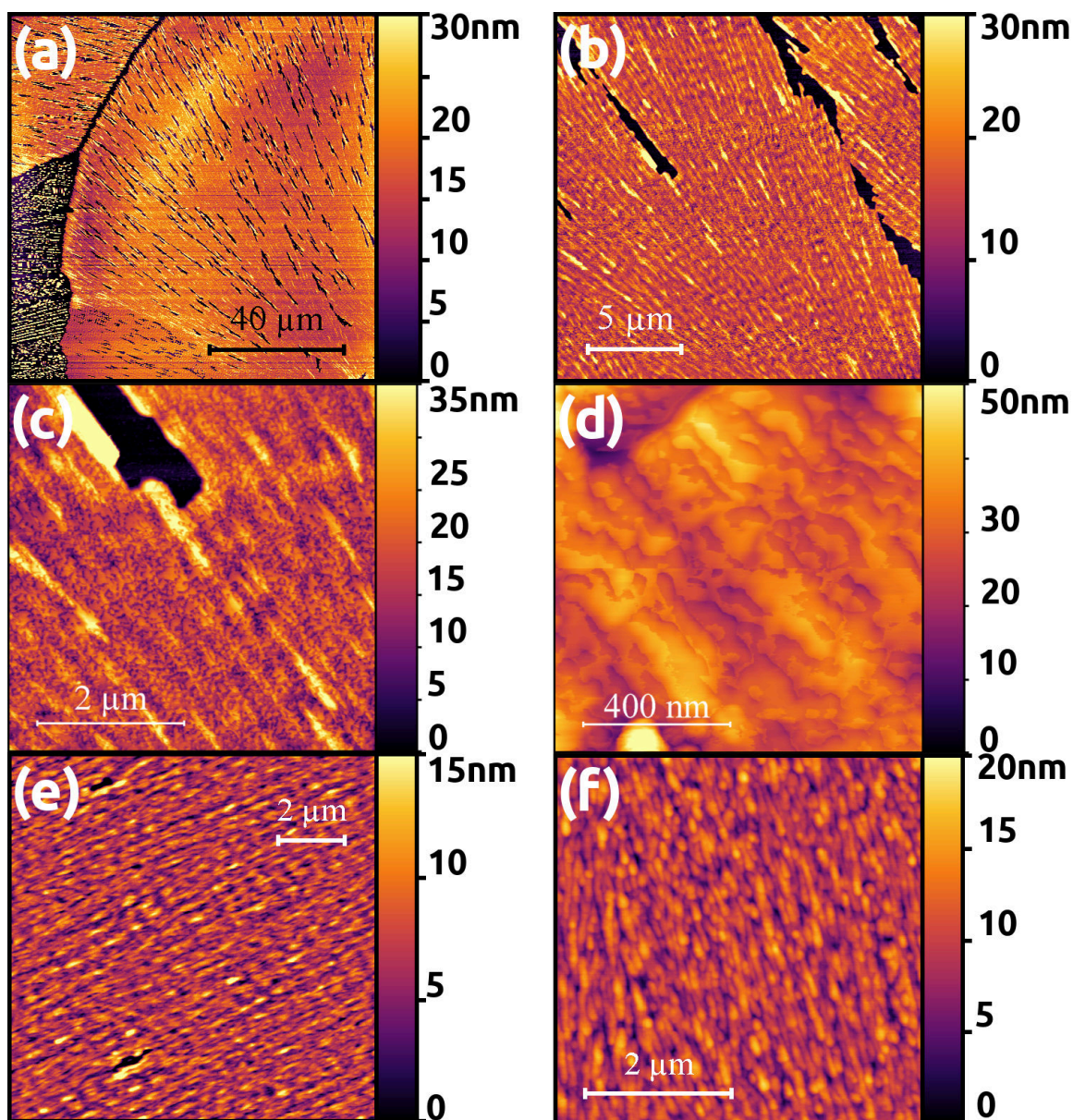
Figure 4.23: AFM micrographs of orthorhombic solid spherulites of rubrene at SiO_2 on a Si substrate, crystallized at 170 °C:
(a)-(d): 20 nm seed layer only in various degrees of magnification
(e)+(f): 20 nm seed layer + 80 nm undoped epitaxy in different degrees of magnification.

identical for different degrees of averaging are taken into account for analysis of the step height. Individual terraces are separates by (4.71 ± 0.22) nm. This does not directly correspond to any of the expected lattice parameters of thin-films rubrene crystals. Since molecules at the surface experience a different potential compared to the bulk, a slightly modified crystal lattice is feasible. A rotation of molecules on the surface is more likely than a change in the lattice constant itself. These plateaus could, however, be matched to simple double steps of the c-axis at 25.91 Å. The surface roughness (see figure 4.25a) of these crystallites is significantly lower than the triclinic crystals, since the surface features are defined by steps in the molecular lattice rather than dendritic features. The

Figure 4.24: Height profiles based on the AFM measurements of figure 4.23: A line is chosen through appropriate surface features, averaging the height values over a width of 60 px. Only features that do not change for different widths of the averaging are considered real surface features.
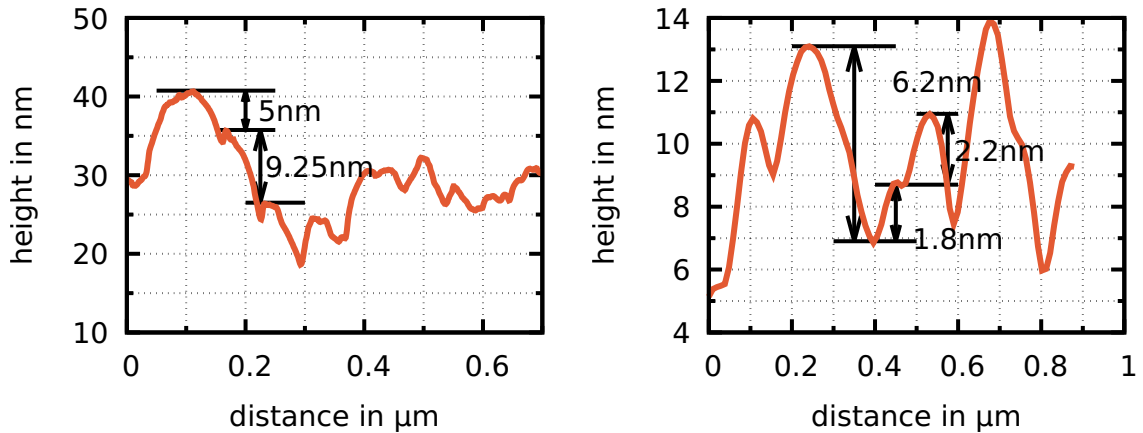
(a) Profile from micrograph (d): Distinct steps of multiples of 4.71 nm can be found on the surface. Smaller features (i.e. between 0.4 μm and 0.6 μm lateral) are considered artifacts caused by the averaging.

(b) Profile from micrograph (f): Distinct steps of multiples of 2 nm can be found on the surface.

average roughness is even smaller when only the real crystal surface – without the previously discusses voids – is taken into account. 37 % of the seeds surface roughness can be attributed to the voids. Similarly to the triclinic crystals, the macrostructure (lines from center to rim) is preserved during epitaxy, while the microstructure is altered. However, here the surface roughness is reduced to 39 % of the seed's initial value. Taking a closer look at the surface created by epitaxy reveals steps of (2.00 ± 0.12) nm (see figure 4.24b). This too does not correspond to any of the expected lattice dimensions of rubrene. However, it shows that at least a change in orientation of the molecular stacking takes place during the epitaxy process. One candidate for this change in stacking are oxidized forms of rubrene, as shown by Fumagalli et al. [211], using time-resolved AFM imaging of rubrene thin-films in ambient conditions.

Rubrene layers heated above 170 °C that form orthorhombic spherulites show a distinct feature that is not present for the triclinic crystals or the orthorhombic platelets: light-dependent recrystallization. Figure 4.26 shows the growth of these layers under ambient light conditions (LED ceiling lamps, no window blinds to block daylight) and samples that are grown inside a glovebox using a photolithography filter. If ambient light is present, initially formed spherulites recrystallize into a different polymorph that resembles the triclinic dendrites. Layers grown on metal are affected more than crystals on SiO_2. However, the effect is increased with heating time. Since the growth of spherulites is faster on the structured metal surfaces compared to the neighboring areas, the adverse

Figure 4.25: Surface roughness extracted from AFM micrographs of orthorhombic spherulitic crystallites.
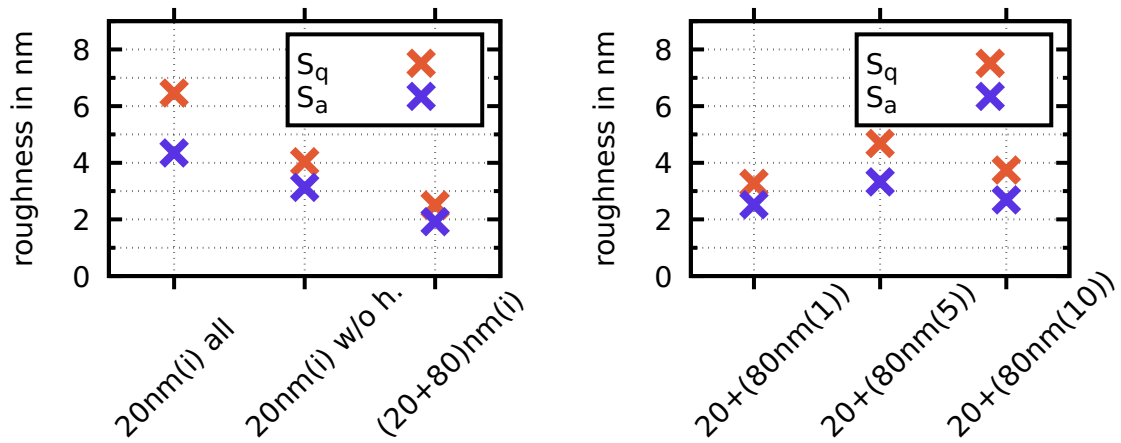
(a) Based on figure 4.23: Roughness of orthorhombic spherulites is significantly lower than any of the triclinic crystals. A significant degree of the surface roughness (all) stems from voids in the seed created at merging growth fronts. Epitaxy (20+80) decreases the surface roughness even below the value for the closed areas of the seed (w/o h.).

(b) Based on figure 4.27 (doping concentration in brackets): Doped layers grown via epitaxy show a slightly increased surface roughness compared to layers without doping.

recrystallization effect might just start earlier, creating the wrong assumption of only happening on metals. Usually, most of the surface of the electrode is covered in recrystallized material before the remainder of the substrate is covered with the desired crystals phase. Layers and devices featuring these structures show significantly reduced electrical performance in general and a heavy tendency to cause short circuits in vertical devices. Shielding the sample with a metal hood during the heating process decreases the occurrence of recrystallization. However, the process of positioning the substrate and removing it from the hot plate, requires a finite time, for which light can hit the substrate while it is hot. Growing crystals within a glovebox featuring a photolithographic filter yields films with a minimum amount of defects.
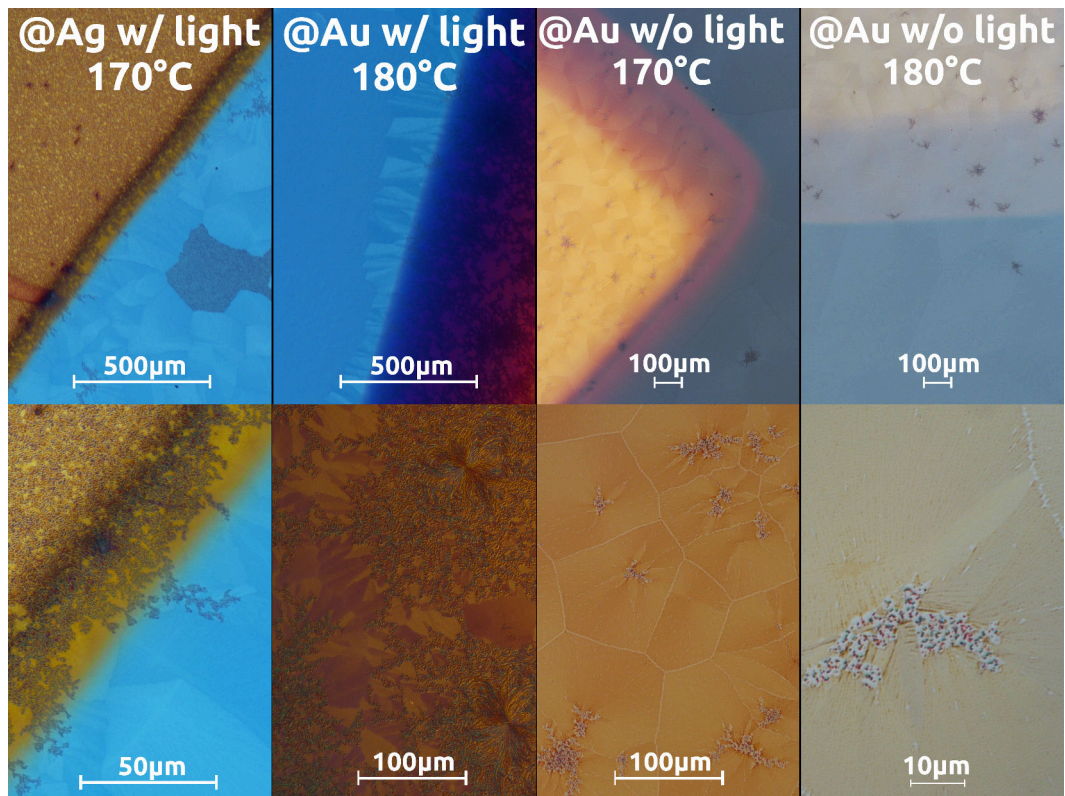
Figure 4.26: Influence of ambient light on the growth behavior of orthorhombic spherulitic crystallites (seed thickness: 20 nm): Devices w/ light are crystallized under ambient light conditions inside a nitrogen glovebox, device w/o light are crystallized in a nitrogen glovebox covered with photolithographic filter foil.

4.1.2.2 Doping of Spherulites

For use in a real vertical device (e.g. diodes or Bipolar Junction Transistors (BJTs)), doping of the crystals is necessary. The effects on the crystallization are discussed here, while the electrical properties of doped films are highlighted in the next section. Figure 4.27 shows a series of differently doped crystals. Doping of the seed is possible for low doping concentration (< 1 wt.%). The yield of crystallization and quality of the resulting seed is reduced. Doping of consecutive layers via epitaxy is possible to at least 10 wt.%. Similarly to the triclinic crystal phase, there is no visible change in crystallinity at any of the doping concentrations investigated. Even in AFM measurements (see figure 4.28), the surface structure remains virtually unchanged. The same straight line dendrites can be seen, as well as randomly distributed voids. Average surface roughness, shown in figure 4.25b, is slightly higher for the doped seeds compared to the thick undoped layers. Distinct steps or multiples can be found on the surface of doped layers too. Exemplary height profiles of doped films with 1 wt.% are shown in figure 4.29a and doped with 5 wt.% in figure 4.29b. The average distance is (4.5 ± 0.5) nm for 1 wt.% doping and (4.7 ± 0.3) nm for 5 wt.%. Thus, no significant change is noticeable compared to the (4.71 ± 0.22) nm of the undoped seeds.
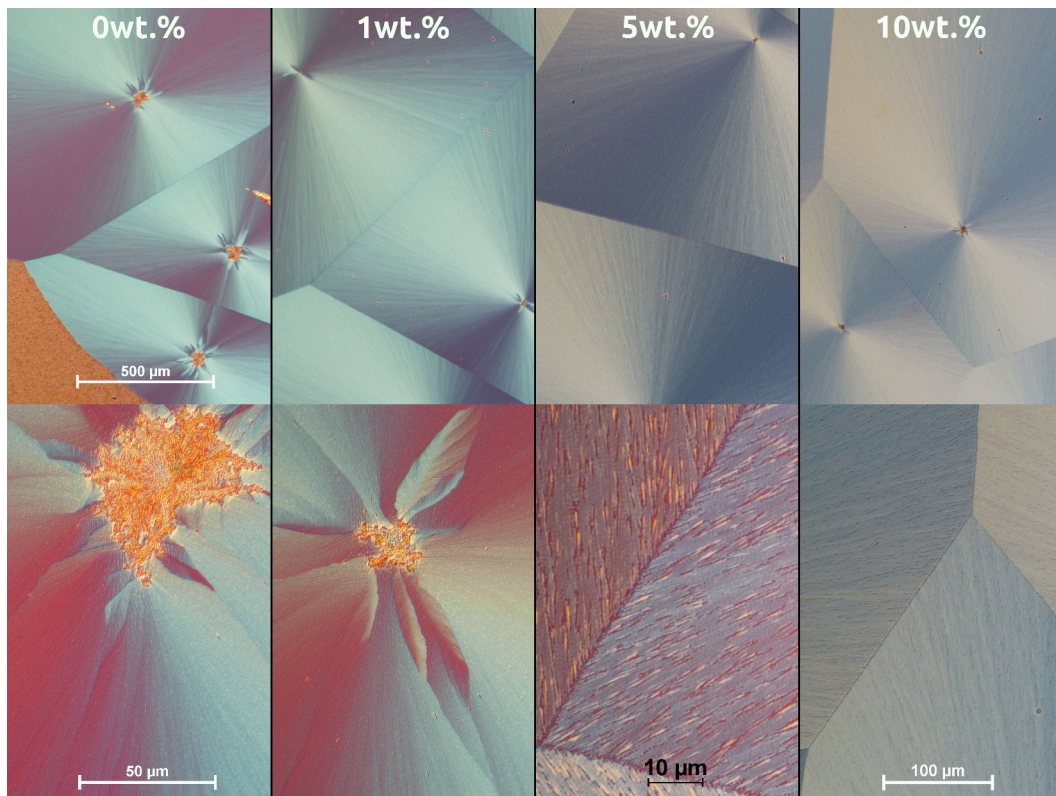
Figure 4.27: Doped films of rubrene orthorhombic spherulite crystallites: Undoped initial seed (20 nm) with added 80 nm of doped semiconductor.

No direct influence of the doping process on the morphology of the film is noticeable on the surface. To investigate the influence in the bulk of the crystals, XRD measurements are performed. The corresponding results are shown in figure 4.30a. At first glance, there is not much difference between the individual samples. Only the measurement on the single seed layer shows a significantly reduced intensity. The fact that the intensity of the XRD-signal is increased almost perfectly according to the increase scattering volume for the thicker grown layer is further proof of a real epitaxy, since the crystallinity of the seed is transferred into the added layers.

Two distinct peaks can be identified. One large peak is visible at an apparent lattice distance of 13.4 Å. This peak likely corresponds to the (002) lattice plane of the c-axis, resulting in a lattice constant of 26.8 Å. This result is in accordance with common literature values and the AFM measurements discussed earlier. It further proves that the c-axis is perpendicular to the surface of the substrate. A second, much weaker peak can be seen in high-resolution measurements, over long integration times only. Here, a slit of 0.1 mm at the detector side is used during a total measurement time of 3 d. The resulting peak is only properly distinguishable from the background in the thicker film grown via epitaxy. It corresponds to the (100) plane (a-axis) at 6.75 Å. A small area of the surface of the substrate must thus be oriented with the a-axis perpendicular to the substrate. If this effect is already present in the seed or is occurring during epitaxy cannot
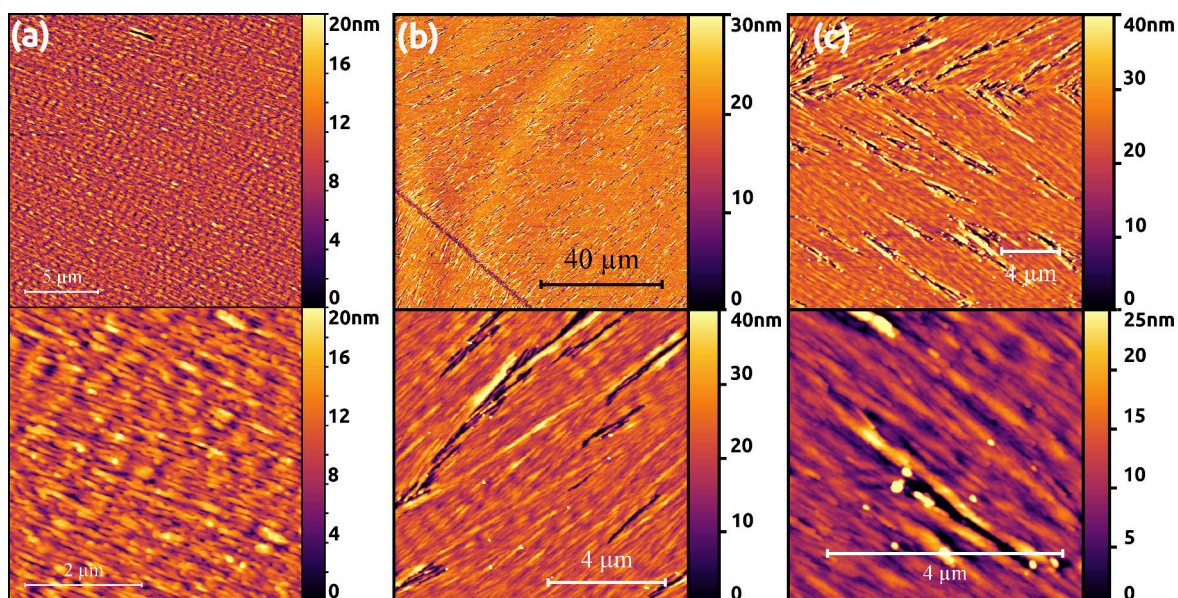
Figure 4.28: AFM micrographs of orthorhombic solid spherulites of rubrene at SiO_2 on a Si substrate, crystallized at 170 °C (top: overview, bottom: detailed):
(a): 1 wt.% doping concentration in 20 nm seed layer
(b): 5 wt.% doping concentration in 20 nm seed layer
(c): 10 wt.% doping concentration in 20 nm seed layer.

Figure 4.29: Height profiles based on AFM measurements of figure 4.28: A line is chosen through appropriate surface features, averaging the height values over a width of 60 px. Only features that do not change for different widths of the averaging are considered real surface features.
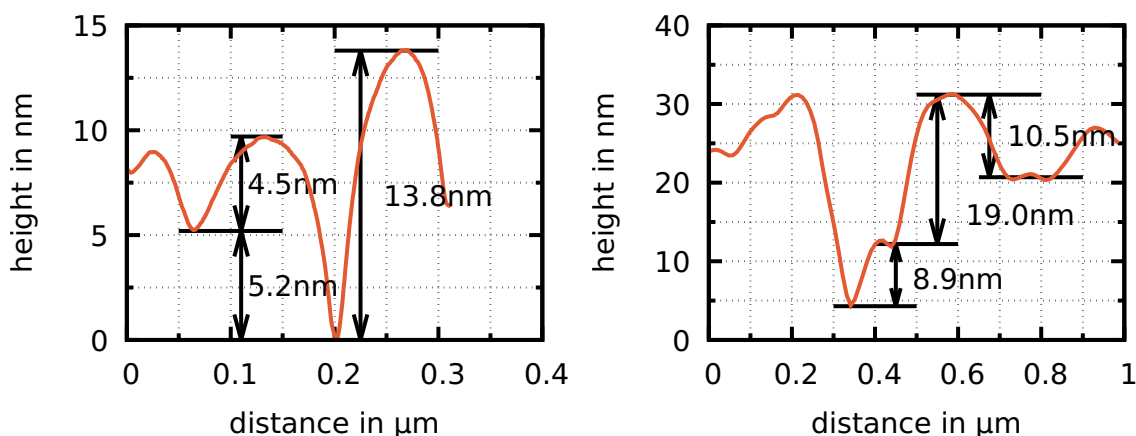
(a) Profile from micrograph (a): Distinct steps of multiples of 4.5 nm can be found on the surface.

(b) Profile from micrograph (b): Distinct steps of multiples of 4.7 nm can be found on the surface.

be decided, due to the weak signal. A similar effect has not been described in literature yet for these types of rubrene crystals. However, judging from the low intensity, less than 0.4 % of the total scattering volume are corresponding to this crystal orientation. It can hence be safely assumed that this rotation will not have any significant impact on electrical properties of these films. No discriminable

Figure 4.30: XRD measurements of orthorhombic spherulitic rubrene layers.
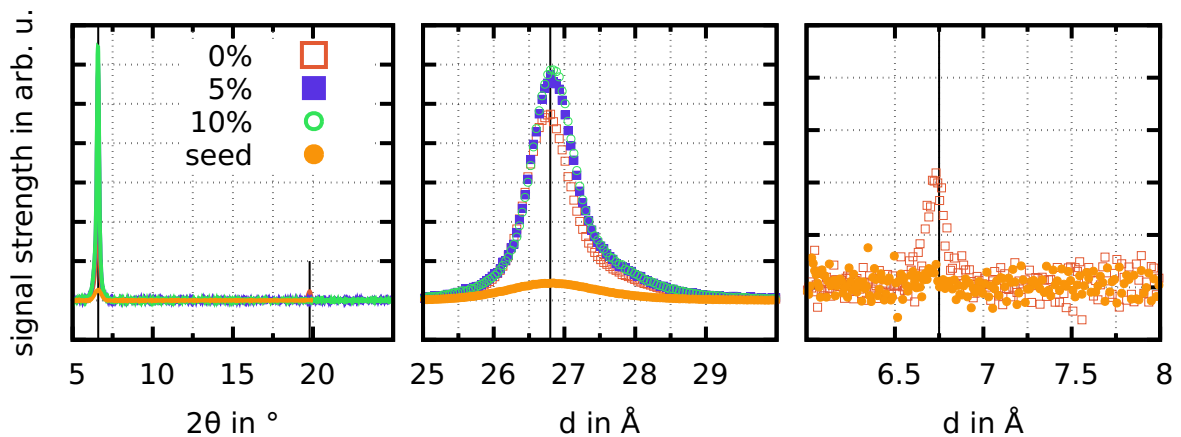
(a) Full range measurement in 2Θ-depiction. Peak positions are marked.

(b) Main peak at 26.8 Å, assuming second order diffraction.

(c) Auxiliary peak at 6.75 Å, assuming first order diffraction.

signal is visible in the area where the b-axis could be suspected based on common values from literature.

Figure 4.30b shows a focused graph of the main peak for devices with a different doping concentration in the epitaxially grown part. The position of the peak and the Full Width Half Maximum (FWHM) of 0.83 Å are identical for the seed, undoped thick, and doped thick layers. It can be concluded that the unit cell in c-direction and the degree of crystallinity do not change significantly during epitaxy, neither for the undoped films nor the doped layers. The unit cell of orthorhombic rubrene is base centered. It is, therefore, possible to fit individual molecules of dopant between the rubrene molecules at the positions of a body-centered or face-centered lattice. However, only one of the three crystal directions can be analyzed with the XRD setup that is used here. An x-ray measurement with a higher accuracy and off-axis capability would be necessary to distinguish the exact position of dopants and decide if the unit cell as a whole is changed.

4.1.2.3 Surface Properties of Spherulites

All orthorhombic crystals are significantly more sensitive to the quality and properties of the substrate compared to triclinic crystals. Defect-free growth on metal electrodes can only be achieved under certain lighting conditions as shown previously. On certain materials (e.g. Cytop and AlOx), growth of these crystals is completely impossible. This is particularly problematic, since these two materials are well-suited as gate dielectrics in organic field-effect transistors, due to their tendency to form trap-free interfaces. For growth on glass and SiO_2, treatment of the surface using piranha solution increased yield and quality of the crystallization, for triclinic and orthorhombic polymorphs alike. However, Cytop

and AlOx are not stable within piranha. A different method to optimize surface energy is the use of Self Assembled Monolayers (SAMs) or coating with inorganic materials. HMDS is commonly used to create highly hydrophobic surfaces. No crystals of any kind grow on any substrate coated with HMDS. Figure 4.31 shows the result for HMDS on an AlOx-coated Si-wafer. Instead of crystals, a granular structure appears, showing de-wetting effects around every visible surface defect. ODPA is a SAM used to create hydrophilic surfaces. The results here are less clear. AlOx substrates still do not show any successful crystallization (see figure 4.31). However, SiO$_2$-covered wafers allow for growth. Treatment of the surface with piranha remains the best option for optimal crystal growth.

Another special effect for these polymorphs is related to the circular defects found on the amorphous thin-films shown in figure 4.16a of the previous subsection. While for the triclinic crystals these holes are overgrown during the heating and crystal formation, they often remain during the growth of orthorhombic spherulites. The effect is shown in figure 4.32. Epitaxy onto these holes does not fill them effectively. Unfilled effects usually lead to short circuits or at least a significant increase in leakage currents for vertical devices. Only a sufficiently thick layer fills them eventually. However, treatment of the surface with piranha prior to the crystallization, enables an effective filling of the holes via the subsequent evaporation during epitaxy. The hydrophilic nature of the piranha treated substrate might support a wetting of the surface within the holes,
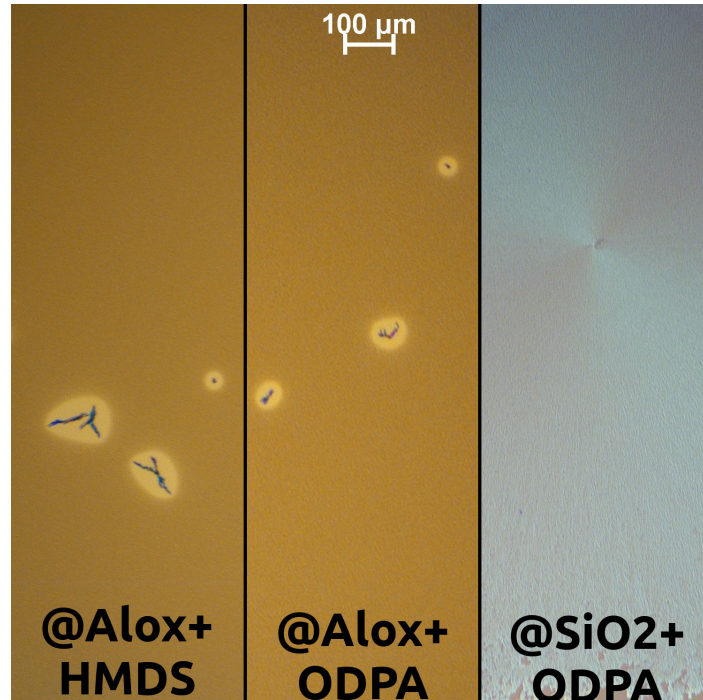
Figure 4.31: Growth of orthorhombic spherulites on different SAMs: HMDS is a SAM used to create a hydrophobic surface, while n-Octadecylphosphonic acid (ODPA) creates a hydrophilic surface: Regardless of surface treatment, growth of these polymorphs is not successful on AlOx-covered substrates. ODPA can be used as a substitute for Piranha treatment, with a decrease in crystal quality.

although it is unclear why these defects emerge at all. It is worth noting that the material grown within the pinholes does not feature the same crystal phase as the surrounding material. It is difficult to decide which exact polymorph is present within the holes due to their small size. Films and devices built on seeds with filled holes and devices built on seeds without any holes have the same properties within the normal variation.
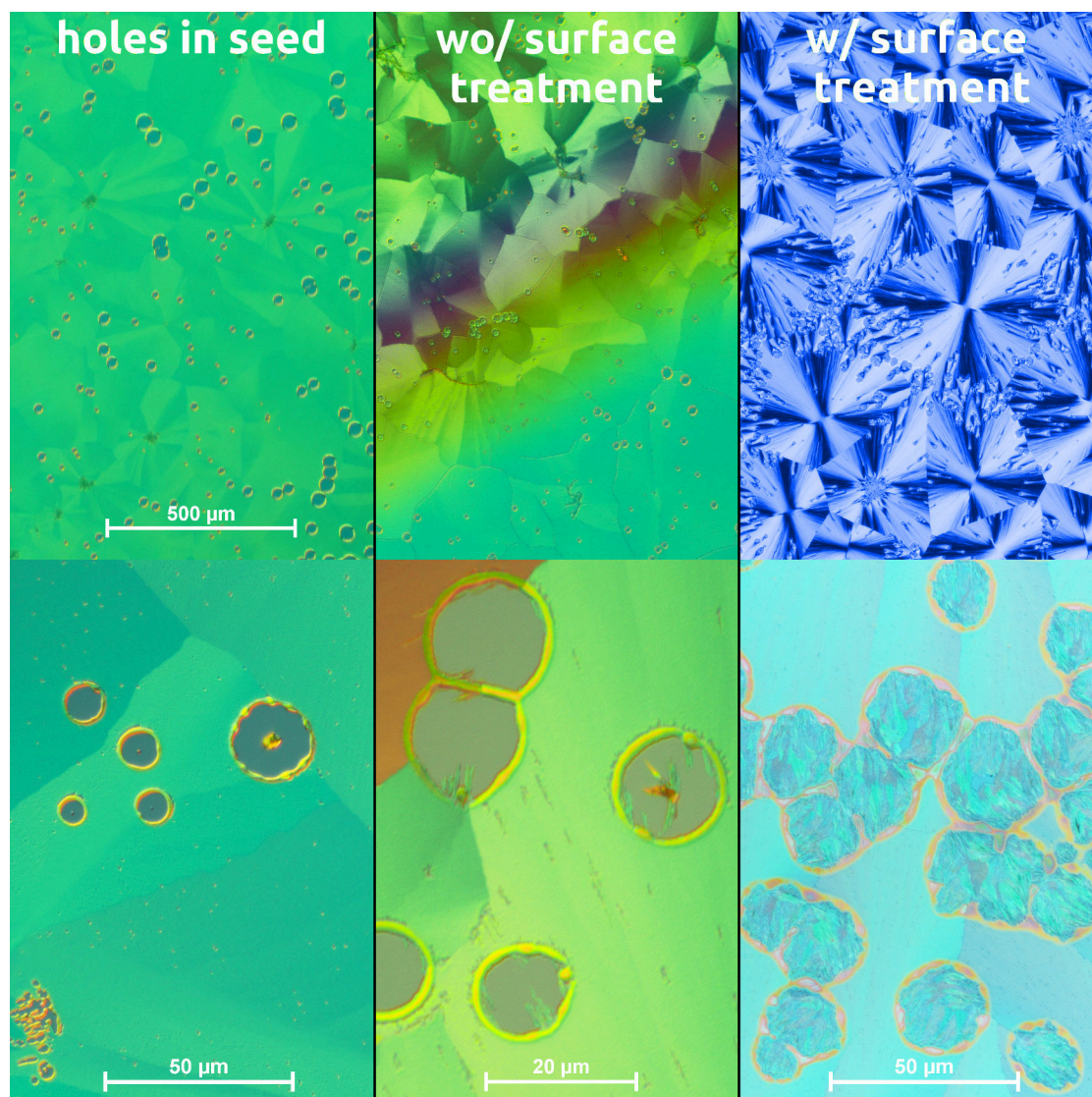
Figure 4.32: The μm-sized pinholes (shown in figure 4.16a) present in amorphous films of rubrene remain after crystallization into orthorhombic spherulites:
left: Spherical holes reach down to the substrate in the crystallized seed.
center: For an untreated substrate, holes are not filled after epitaxial growth of 40 nm.
right: If the substrate is treated with piranha prior to crystallization, holes are filled during further evaporation.

4.1.3 Orthorhombic Platelets

Orthorhombic platelets are by far the most studied form of thin-film rubrene crystals. They can be considered as quasi-single-crystals, since, although usually

growing as an array of crystal grains, the size of each of those grains is significantly larger than most organic electronic devices. Thus, from the perspective of the device, every single platelet represents its own single-crystal. This enables the extremely high charge carrier mobilities measured in rubrene single-crystals, without the disadvantages associated with free-floating vacuum gap devices. Unfortunately, orthorhombic platelets is also the crystal phase that is the most difficult to grow reproducibly and is the most sensitive to the properties of the substrate.

4.1.3.1 Orthorhombic Platelets With and Without an Underlayer

The occurrence of orthorhombic single-crystals on the surface is heavily tied to the interaction strength of the amorphous rubrene with the substrate. A strategy shown in literature [36] is to introduce an underlayer underneath the amorphous rubrene to decouple the interaction with the substrate. The key parameter here
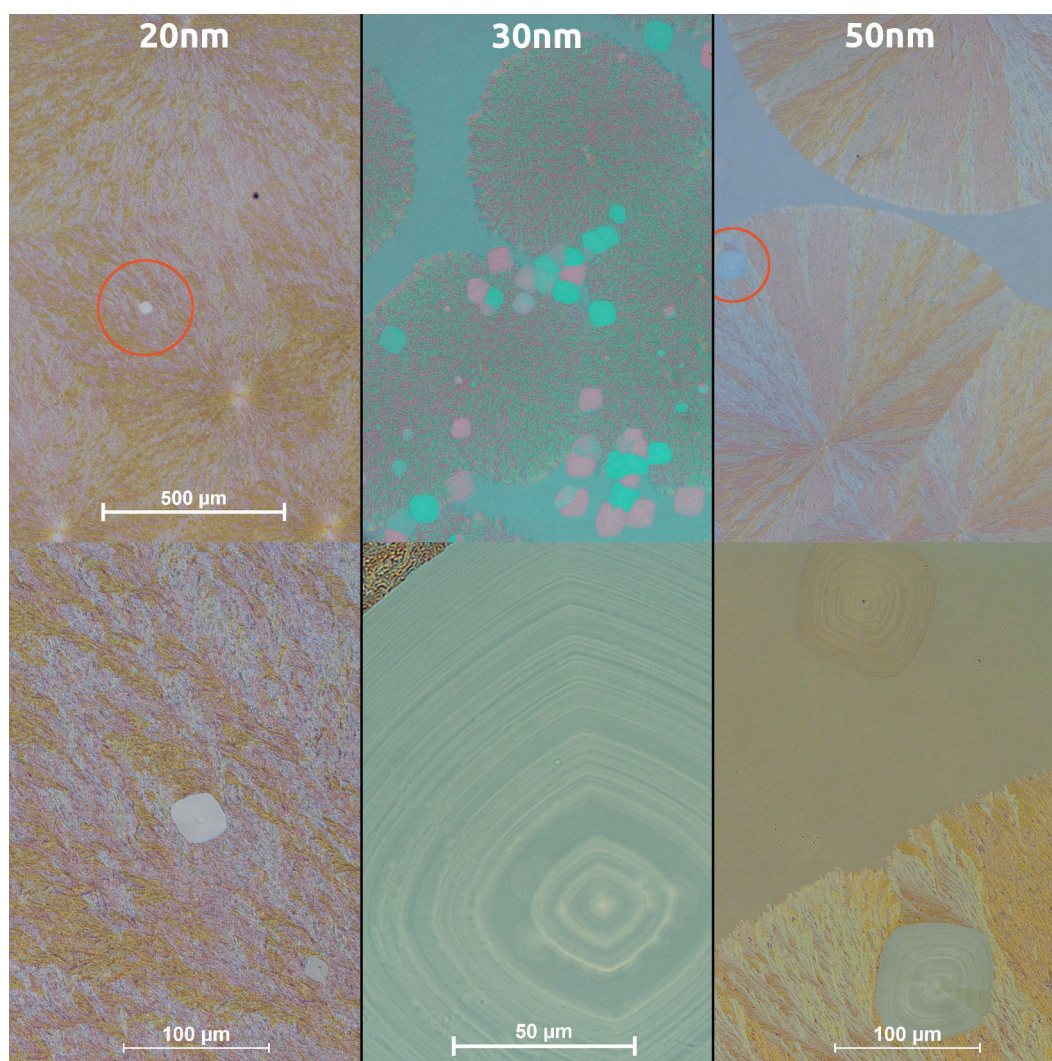
Figure 4.33: Rubrene orthorhombic platelets grown from amorphous layers of different thickness without an underlayer at SiO_2 on a Si substrate (heating temperature 160 °C).

is the glass transition temperature T_G: if the crystallization temperature is high enough, rubrene can freely float on the liquified underlayer and crystallizes into the energetically best polymorph. However, if T_G is too low, too much noise created by thermal movement suppresses effective formation of crystals. Thus, a glass transition temperature between 90 °C to 100 °C is ideal for platelet formation [36]. However, this underlayer is not strictly required. Given the right parameters, orthorhombic platelets can grow on SiO_2 substrates, glass, and ITO-covered glass, without any use of an underlayer. However, under these conditions, the total number of individual crystals is small and films virtually never fill the entire sample. The position, grouping, and orientation of the existing crystals are completely random. Figure 4.33 presents a set of orthorhombic platelets grown
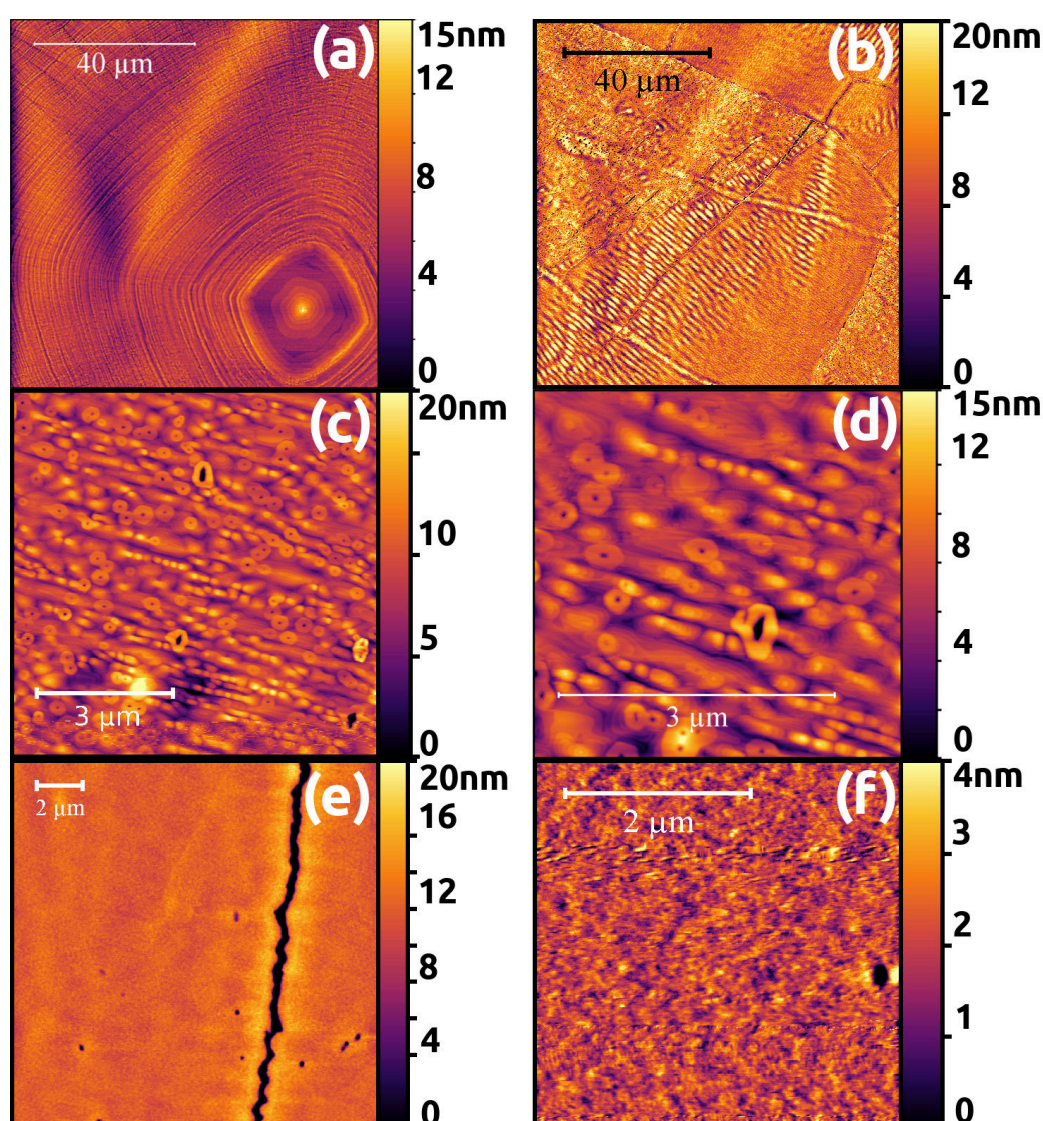
Figure 4.34: AFM micrographs of undoped orthorhombic platelets grown at SiO_2 on a Si substrate:
(a): 30 nm, seed only (no underlayer)
(b)-(d): 20 nm seed + 80 nm epitaxy (5 nm TAPC underlayer)
(e)+(f): 20 nm seed + 40 nm Al + 80 nm epitaxy (5 nm TAPC underlayer).

without an underlayer. Single-crystals can appear alone, in separated groups, or clustered together. They can be surrounded by uncrystallized amorphous material or by a different polymorph, commonly some variation of the triclinic dendrites. Despite numerous efforts and systematic studies, no pattern could be established which parameters influence the occurrence, density, size, and quality of the platelets themselves and their surrounding material. However, theoretically single isolated crystals can still be used for applications. In particular simple versions of thin-film transistors can be built onto the single-crystal, since the position defining electrodes can be deposited after the film is already grown. However, the benefit of a more flexible and efficient preparation compared to the bulk single crystals is lost. Furthermore, it does not seem viable to use these crystals in vertical devices that require the preparation of an electrode underneath the seed.

The general appearance between individual crystals is similar, presenting a central region with ring-like features of partly uniform coloring. The width of each inner ring varies between 1 μm to 10 μm. The outer structure is made up of rings of significantly smaller width, decreasing further with distance to the center. The inner and outer rings follow a rounded-square shaped symmetry. The width of these sub-region ranges from 0.2 μm to 4 μm.

AFM measurements of the crystal surface, shown in figure 4.34a, reveal a structure that resembles wave patterns on water. The surface features almost perfectly flat plateaus separated by defined steps in the central region and oscillating outer rings. The height difference of these plateaus (see figure 4.36a) is (8.9 ± 1.7) Å, while the width of each ring is increasing with distance from the center. The outer parts do not feature any distinct plateaus but rings of rapidly changing height. The outer rings height is changed not by a fixed amount but by multiples of (9.5 ± 1.3) Å. They consist of one to three molecules. Based on comparisons with literature, these steps can be associated with the b-axis. The rings distance is significantly smaller than for the inner structure but features a pattern. Larger peaks appear every (0.97 ± 0.24) μm, overlain by smaller peaks every (0.46 ± 0.14) μm.

To realize area-covering platelet arrays, an underlayer has to be used. A series of crystals grown on TPTPA[2] as an underlayer is shown in figure 4.35. A complete filling of the entire substrate is very unlikely, even if an underlayer is used. However, the coverage can be elevated to a usable degree.

Similar to the spherulites, one type of platelet is spherically symmetric and solid, while a second type is ray-like broken. To reduce unnecessary internal grain boundaries, the goal is to generate the unbroken crystal phase. However, as long as one device (e.g. a field-effect transistors channel) is within one single sub-grain, results should be equivalent. Thicknesses of the underlayer below 5 nm usually do not result in successful crystallization. It can be assumed that a closed layer of the TPTPA is not realized yet. A thickness of 10 nm and more of the sublayer

---

[2]TPTPA is the original underlayer material introduced by Fusella et al.
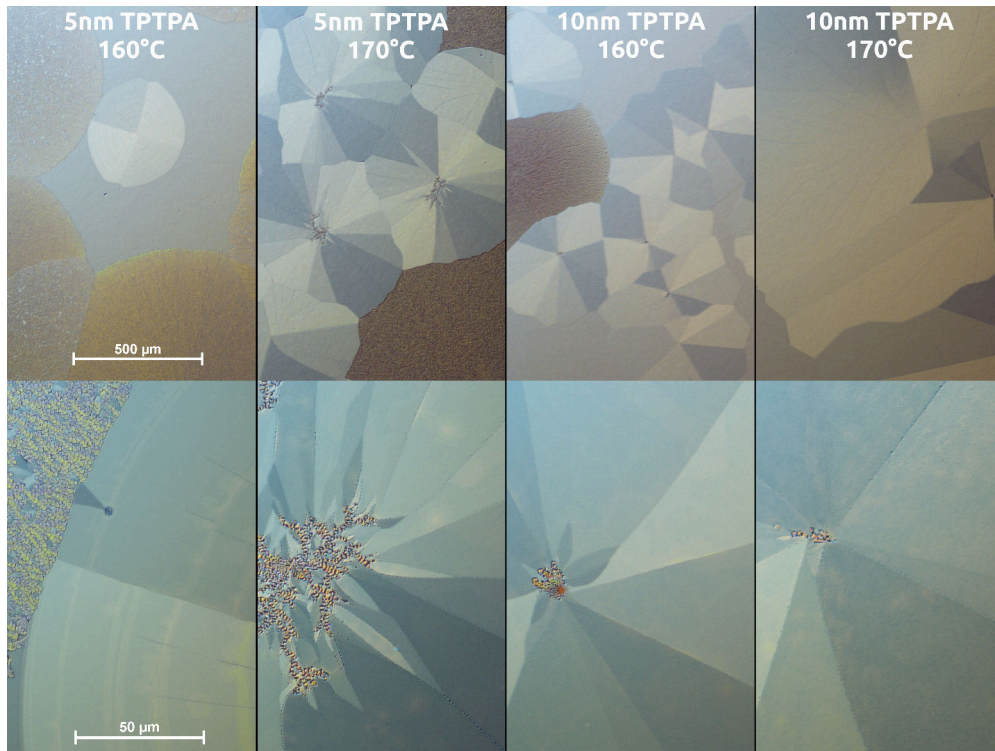
Figure 4.35: Rubrene orthorhombic platelets grown from amorphous layers at SiO_2 on a Si substrate (heating temperature 160 °C, seed thickness: 20 nm) at different temperatures and thickness of the underlayer TPTPA.

increases the chance of broken crystals. The same is valid for temperatures above 160 °C during crystallization.

The only requirement on the material of the underlayer is its glass transition temperature. TAPC has a T_G in the appropriate region but features a comparably wide bandgap. The interface between semiconductor and insulator is decisive for the performance of Field-Effect Transistors (FETs) in bottom-gate configuration made from these films. The channel formation should take place within the rubrene and not within the underlayer, to achieve high transconductance. A wider bandgap is thus beneficial. Using TAPC instead of TPTPA yields similar results regarding the crystallization process, while offering a significantly lower bandgap.

Figures 4.34b-d show the surface of platelets grown on 5 nm of TAPC. The center of each grain has a similar appearance as crystals grown without the underlayer, featuring squared rings. However, the bulk of the crystal is dominated by areas covered with stress lines and cracks. Use of the underlayer seems to facilitate the orthorhombic crystal phase, while simultaneously causing stress in the lattice. A detailed measurement on the surface of epitaxially grown layers presents plateaus of distinct distance of (1.38 ± 0.29) nm (see figure 4.36b). Visible are line defects and screw dislocations, both described in literature for these types of crystals. However, pinholes that are associated with fast evaporation during the epitaxy are not present.

Figure 4.36: Height profiles based on AFM measurements in figure 4.34: A line is chosen through appropriate surface features, averaging the height values over a width of 30 px. Only features that do not change for different widths of the averaging are considered real surface features.
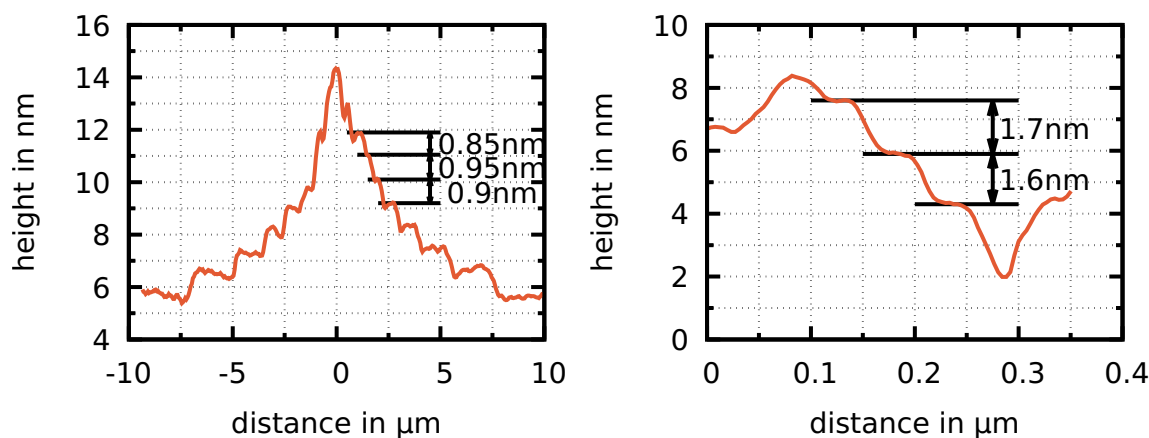
(a) Surface profile of subfigure (a) of the center region of an orthorhombic platelet grown without an underlayer.

(b) Surface profile of subfigure (d) of the bulk region of an orthorhombic platelet grown with 5 nm TAPC as underlayer.

Films grown without an underlayer show a low roughness, comparable to the spherulitic films. Crystals created using the underlayer have significantly higher average surface roughness, originating from stress-related features and cracks (see figure 4.40). XRD measurements (see figure 4.37) reveal two peaks, one at a similar position as the spherulites and a second peak at approximately 27.5 Å. The second peak could be identified with the c-axis distance in first order (001). The large deviation to the value of the second order reflex could be explained with the large width and weak signal of this peak. Alternatively, diffraction caused by the two molecular configurations of rubrene (straight and twisted tetracene core [53]) could reveal signals that would vanish via interference, if only one of the two phases is present. This might also explain the slight shift between the first and second order signals. However, this does not explain how a first order peak can be observed in these crystals when they are missing from the spherulitic films. The large peak at the lower lattice distance is a double structure, with a main peak at 13.45 nm, corresponding to the (002) reflex, and a side peak at 14.6 nm. The side peak corresponds almost perfectly with values for the b-axis found in literature, while the main peak fits the data found for spherulitic crystals and the step height found via AFM with a c-axis distance of 26.9 Å. Layers grown with epitaxy show an increase in signal strength for the main peak, while the signal strength for the side peak remains constant. The position of the main peak shifts slightly to 13.4 Å (26.8 Å). Epitaxy increases the thickness while maintaining the original crystal structure of the seed only for the c-axis component of the crystals. Some of the devices that are based upon these layers (i.e. Organic Bipolar Junction Transistors (OBJTs)) feature a metal layer in the middle of the organic stack. It is,

Figure 4.37: XRD measurements of orthorhombic platelet rubrene layers (black lines indicate peak positions).
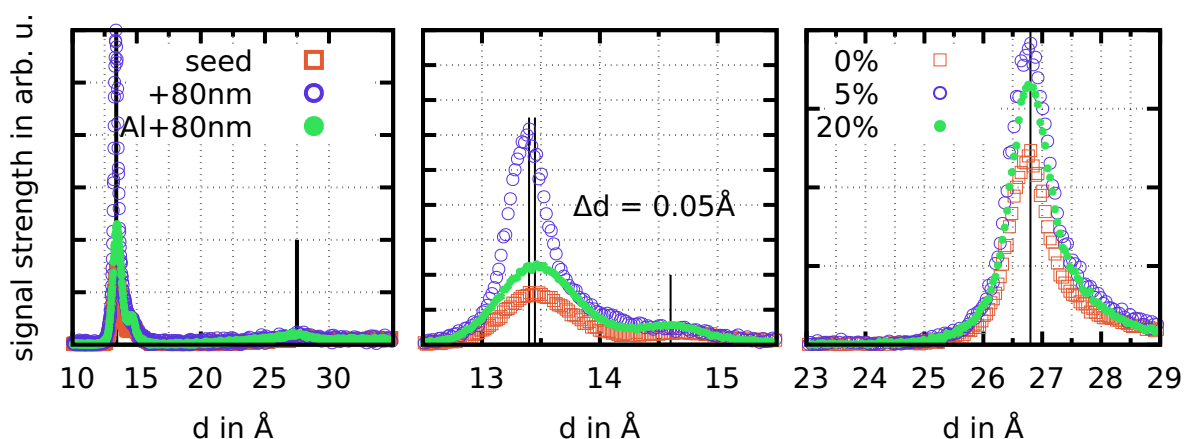
(a) Overview measurement of seed layers and layers grown by epitaxy, assuming first order diffraction.

(b) Detailed depiction of the double peak of the seed and epitaxially grown layers, assuming first order diffraction.

(c) Detailed depiction of the main peak of differently doped layers, assuming second order diffraction.

therefore, of interest, to assess the influence of an intermediate metal layer on the subsequent film growth. Figure 4.39 (right) shows a microscopy micrograph of a crystal seed that is covered with 20 nm Al prior to epitaxy. The contrast of individual grains is severely reduced. In the AFM images in figure 4.34e-f the surface of these crystals is shown. Instead of the terraces visible in the undisturbed layers, a significantly finer surface structure is visible. A similar result can be seen in the XRD data. An increase in thickness after the Al increases the signal strength only slightly. Continuation of the crystal structure is not likely under these circumstances. However, the film is not completely amorphous either, since it shows a distinct structure. An increased level of conductivity can still be assumed compared to amorphous films.

4.1.3.2 Doping of Orthorhombic Platelets

Orthorhombic platelets can be doped too, similar to the spherulitic crystals. However, directly doping the seed is difficult and usually results in a failed crystallization or bad quality crystals. Figure 4.38 shows a comparison between samples at different doping concentrations of the epitaxially grown layers. No change is visible for samples till medium doping concentrations of 5 wt.%. Originating from the cracks and stress-related structures seen previously on the intrinsic layers, bundles of recrystallized material appear at 10 wt.% doping concentration for some of the crystals. However, the general structure of the crystallite is still intact. For even higher doping concentrations, these features disappear, while the phase contrast between adjacent grains is decreased. Data

gained from XRD measurements (figure 4.37c), however, show a contradicting result. Peak height and position are identical for all doping concentrations, within the normal variation of the measurement setup. In summary, despite the XRD result, it appears unlikely that proper epitaxy is still possible at these extreme doping concentrations.

The AFM measurements shown in figure 4.39 support this assessment. Films with 5 wt.% of dopant still feature distinct steps. The plateau-like structure with line and screw defects is replaced by a more snake-like pattern. For the heavily doped samples, no proper crystalline structure is noticeable. The average roughness of the film (shown in figure 4.40) is decreased with doping. This smoothening indicates a decrease in order, towards a more amorphous surface.

In conclusion: orthorhombic platelets can be doped via the same technique of co-evaporation during epitaxy as the triclinic films and the orthorhombic spherulites. However, the impact of this doping on the crystal structure seems to be more noticeable. Since this crystal phase represents a real single-crystal-like order over significantly larger distances than the other two crystal phases, less leeway is possible to account for the space required by the doping molecules and the consecutive disturbance that is introduced. This hints at the dopants being concentrated between the individual strands of the dendritic structure of the other two crystal phases, otherwise, they would suffer from the same effects. However, it is difficult to determine using the data at hand, how exactly the dopant molecules are arranged within the film and how they move during the growth process.
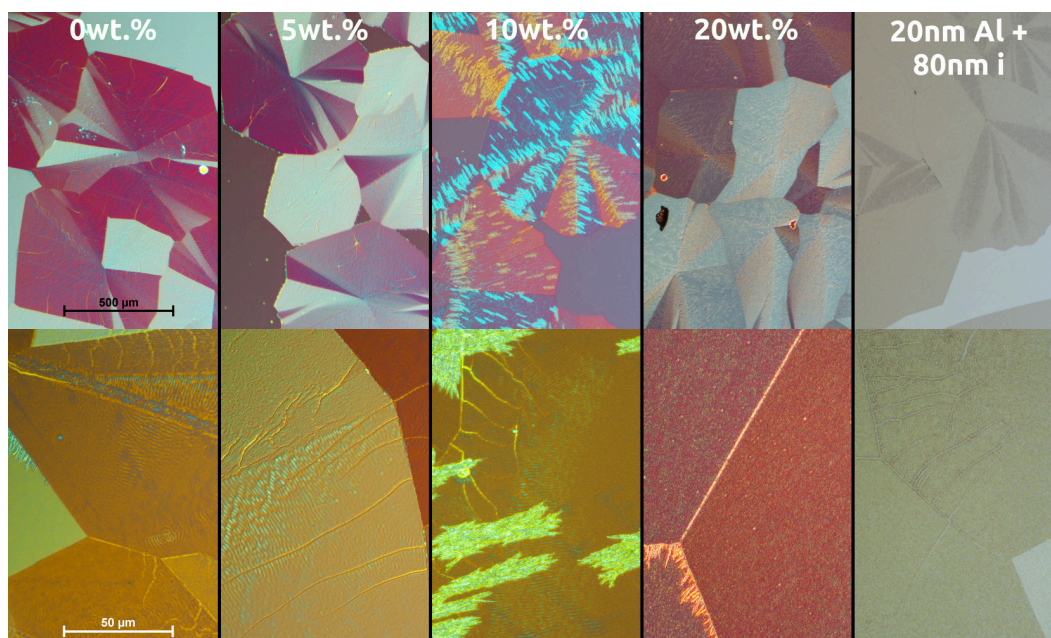
Figure 4.38: Rubrene orthorhombic platelets grown from at SiO_2 on a Si substrate (heating temperature 160 °C, seed thickness 20 nm, 5 nm TAPC underlayer) at different doping concentrations of the epitaxial part.
right: 20 nm of Al are added prior to epitaxy.
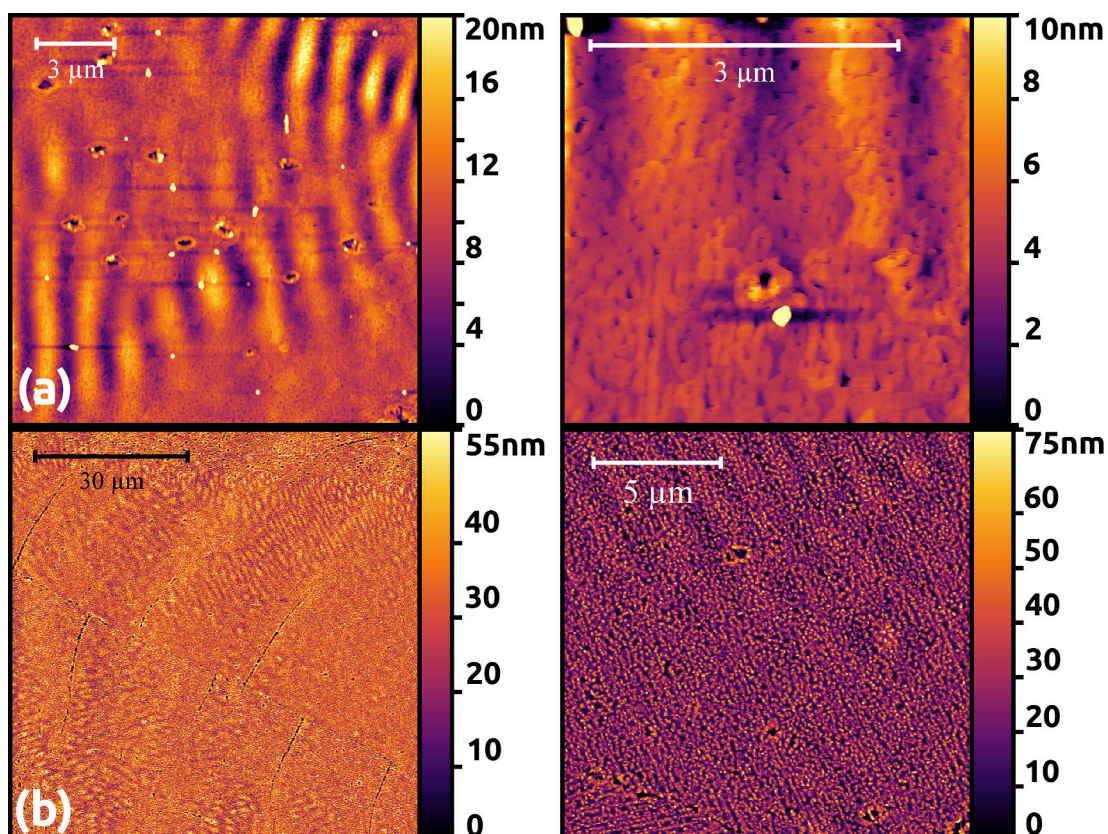
Figure 4.39: AFM micrographs of undoped orthorhombic platelets grown at SiO$_2$ on a Si substrate: **(a):** 20 nm seed + 80 nm epitaxy 5 wt.% (5 nm TAPC underlayer) **(b):** 20 nm seed + 80 nm epitaxy 20 wt.% (5 nm TAPC underlayer).
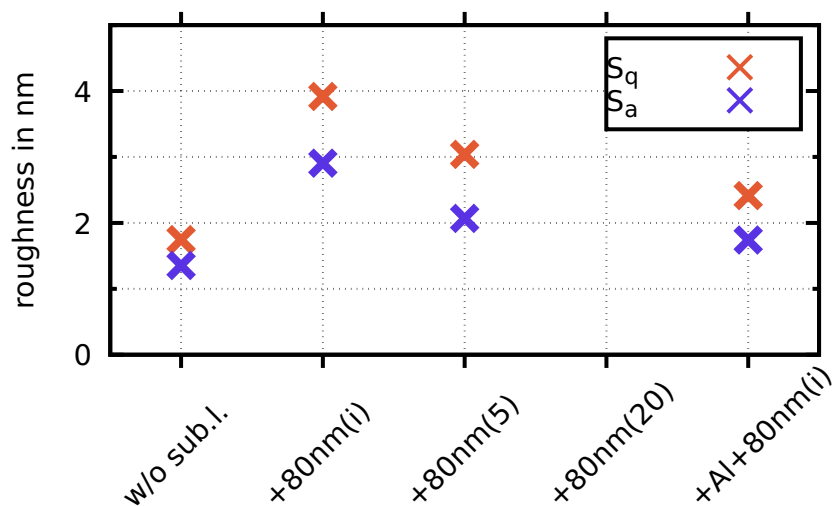
Figure 4.40: Surface roughness measured via AFM micrographs in figures 4.34 and 4.39: Roughness of orthorhombic platelets is comparable to the other orthorhombic crystal phase. Material added via epitaxy increases the surface roughness, while the introduction of dopant results in a decrease.

4.1.4 Other Crystal Phases

The previous chapters might suggest that the process of surface crystallization is stable and well-understood. This is only true to a limited extent. Although for a

majority of crystallization processes on most of the substrates, recipes are found to realize the best possible result (large crystal with few defects), even supposedly identical treatment can sometimes lead to vastly different results or no crystals at all. All of this should be considered in addition to the randomness inert to poly-crystalline growth processes.

Figure 4.41 contains a set of commonly encountered failed crystallizations. It serves as a source of reference for future work with this material system. The films shown here are distinct from the crystals from earlier sections because most of them cannot be reproduced at all, but only appear randomly. This collection and the corresponding naming is not found in literature, since failed or unwanted crystals are commonly not discussed.
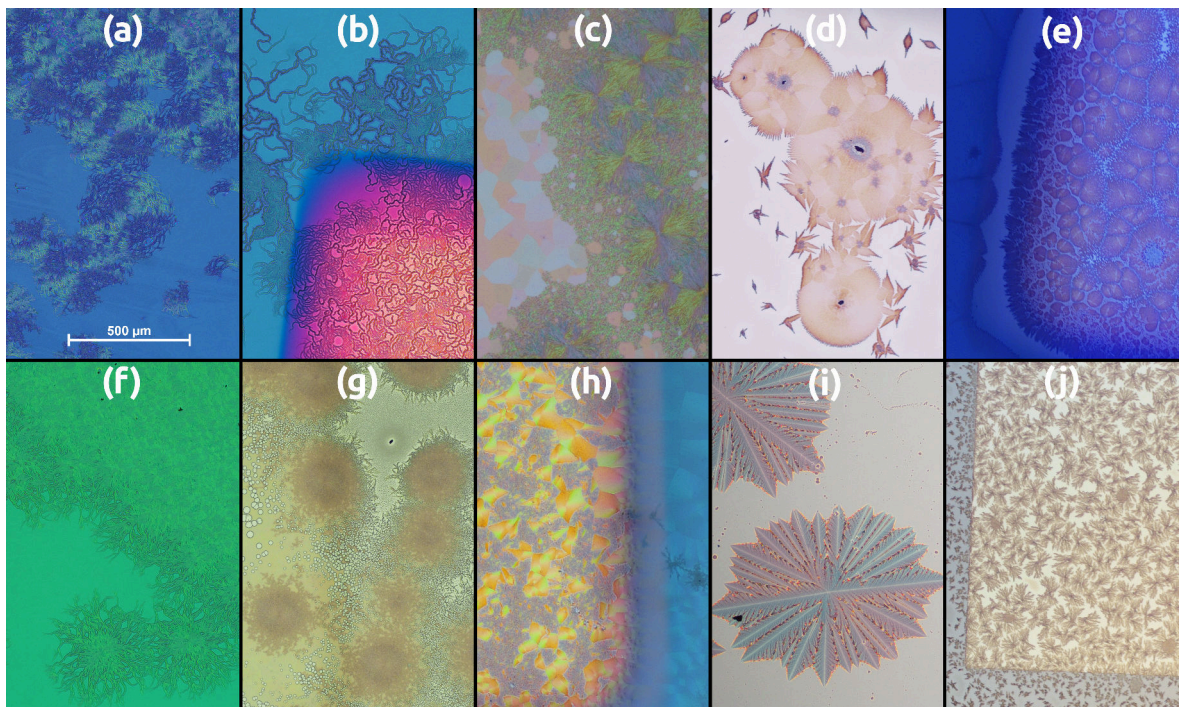
Figure 4.41: (a): Pasta-phase, assumingly triclinic polymorph with increased curving, (b): random vein-like structures, (c): mixed polymorphs (triclinic within platelets), (d): clustering and discontinued growth of orthorhombic spherulites, (e): disintegration of previously closed crystal surface, (f): seaweed-phase (similar to (b), end result can appear identical to normal triclinic phase), (g): extreme de-wetting of the surface, (h): heavily granulated surfaces (appears between platelet crystals), (i): Christmas-tree phase (appears when growing orthorhombic platelets on contaminated underlayer), (j): bushel-phase, extreme branching in dendritic growth.

4.1.5 Summary

Three different crystal phases – triclinic, orthorhombic spherulites, and orthorhombic platelets – can be grown reproducibly, in doped and undoped form. Crystallization is carried out by rapid heating of a previously amorphous thin-films. The ideal substrates are SiO_2-covered Si wafers or glass. Crystallization requires an oxygen-free environment at least till the crystallization step is finished.

Table 4.1: Summary of parameters extracted from structural measurements. (d: step-height on surface extracted via AFM, a,b, and c: diffraction peak positions extracted via XRD).

crystal structure	d in Å	a in Å	b in Å	c in Å
orthorhombic spherulite seed	47.1±2.2	-	-	26.8
orthorhombic spherulite epitaxy	20.0±1.2	6.75	-	26.8
orthorhombic spherulite epitaxy (1 wt.%)	45±5	-	-	26.8
orthorhombic spherulite epitaxy (5 wt.%)	47±3	-	-	26.8
orthorhombic platelets seed	8.9±1.7	-	-	-
orthorhombic platelets seed(TAPC)	13.8±2.9	-	14.6	27.5/26.9

Table 4.2: Summary of properties of thin-film rubrene crystals.

triclinic	orthorhombic spherulites	orthorhombic platelets
• heavily branched dendritic growth	• weakly branched or un-branched dendritic growth	• quasi-single-crystalline faceted growth
• most stable growth process • hydrophillic surface of sub-strate beneficial	• average reproducibility • sensitive to light during growth	• random and low yield when grown directly on substrate • increased yield and coverage when used with sublayer
• doping of the seed possible for concentrations <2 wt.%	• doping of the seed possible for concentrations <2 wt.%	• doping of the seed possible for concentrations <0.5 wt.% • yield further decreased
• ideal growth parameters: 130 °C to 140 °C for 10 min to 15 min	• ideal growth parameters: 170 °C for 60 s	• ideal growth parameters: 160 °C for 60 s to 90 s

4.2 Electrical Properties of Crystalline Rubrene Thin-Films

This sub-chapter presents the electrical properties of the undoped and doped thin-films of crystalline rubrene discussed in the previous section 4.1. The analysis contains Current-Voltage (IV) measurements of intrinsic layers including Space Charge Limited Current (SCLC) analysis of triclinic and orthorhombic platelet films, as well as measurements on doped films. The effect of p- and n-doping on the films is investigated with IV measurements of Metal-Semiconductor-Metal (MSM) devices and capacitance measurements of Shockley diodes. The section closes with a summary of additional effects, like air-, load-, and light-sensitivity.

4.2.1 Analysis of Current-Voltage (IV) Characteristics

A simple way to evaluate electrical properties of a material is via the IV characteristic of MSM devices. The material is sandwiched between two structured metal electrodes, whose overlap defines an active area A while the thickness of the stack determines the length of charge transport L. All devices investigated here are thin-film vertical stacks. This arrangement defines the resistance R as:

$$R = \rho \frac{L}{A}, \tag{4.5}$$

Figure 4.42: IV analysis of MSM devices made from triclinic rubrene: Seeds are grown at $140\,°C$ for $10\,min$ on a glass substrate with structured Au electrodes. Additional rubrene is added via thermal evaporation to reach the indicated total thickness.
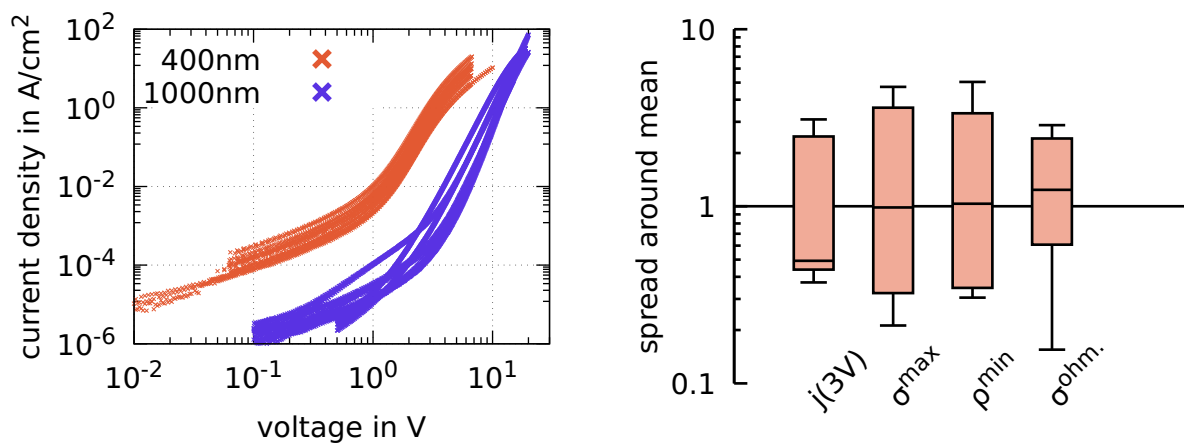
(a) Two sets of devices with different total thickness. Identically made devices with varying active areas are plotted in the same color as a set.

(b) Variation of parameters extracted from eight samples of the 400 nm-set of (a) around the geometric mean value: current density at 3 V, maximum conductivity, minimum specific resistance, and ohmic (low-voltage) conductivity. Detailed definitions are given in the running text.

with ρ as a material-specific property. However, several effects make measuring of R – and thus ρ – difficult. A simple IV measurement neglects the impact of contact resistance, which can only be overcome by elaborate measurements at different thicknesses. Proper four-probe measurements are difficult to realize in vertical arrangements. In addition, the specific resistance ρ is rarely constant. It can change depending on the applied voltage, temperature, total thickness of the material, or lighting conditions. The result of a vertical IV measurement of organic materials is usually a highly non-linear curve with several distinct regimes, each dominated by different effects. Quantification and analysis of these effects are broadly discussed in literature ([101], [103], [104], [105], [106], [182], [212], [213], [214], and [215]) and – except for a few special cases – no real standard is established for the extraction of parameters. However, to compare and discuss the properties of layers and the effects of doping and other changes to the films, definition of parameters is essential for quantitative analysis. A simple comparison of IV curves is not satisfactory. It is, however, highly unlikely that one parameter alone can combine all relevant aspects at once. The capability to easily inject charge carriers into one material does not necessarily correspond with its conduction behavior at high electric fields and vice versa. One additional problem arises from the stochastic nature of the growth process of the films investigated here. Especially dendritic growth is by definition random. The exact distribution of the crystal phase, orientation and stacking can change the local properties significantly. Figure 4.42a shows the current density at different applied voltages of Au-rubrene-Au samples with a total thickness[3] of 400 nm and 1000 nm of triclinic rubrene. The general shape of the IV characteristic is similar for most devices, however, the current density between stack-wise identical devices can vary by more than an order of magnitude at the same voltage. Parameters for comparison have to reflect these variations. The set of devices with 400 nm features at least three distinct regimes: a linear regime at low voltages limited by injection, a middle regime with a high power-law dependency dominated by trap-release or recombination and an onset into SCLC-behavior at high fields. The thicker film shows in principle similar properties; shifted along the voltage and current axis. Some parameters should reflect this and highlight the differences between samples, since the thicker samples are evidently less conductive than the thinner devices. On the other hand, the dynamic properties (e.g. maximum slope) can be identical, which should be represented too.

To gain values for a specific quantity that can be used for further calculations, averaging over the extracted parameters is necessary. However, a simple arithmetic mean is unsuitable for correlated data that spread over more than one order of magnitude. Thus, unless otherwise stated, the averages given are geometric averages that are less susceptible to outliers. The average of a parameter x_i over

---

[3]The total thickness corresponds to the semiconductor part only. It includes the seed layers but not the metal electrodes.

N values is thus

$$\bar{x} = \sqrt[N]{\prod_{n=1}^{N} x_i}. \tag{4.6}$$

Figure 4.42b shows plots of the distributions of five parameters chosen for comparison. The values are normalized by the average of each set. The resulting boxplots are hence gathered around the value "1". This depiction allows for judgments about the quality of each parameter and how well it represents the variation intrinsic to the data. Not all parameters are used for every experiment and the list is not exhaustive. As a group, they fulfill the above-mentioned criteria and allow a discussion of device properties, changes, and trends.

- **current density** j: Comparing the current density at a fixed voltage is the most direct representation of changes in the IV characteristics. It is the best representation of the variation between individual samples of the same type. However, the voltage chosen for the comparison has a significant impact on the result and only devices that are somewhat similar can be fairly compared with this parameter. At a fixed voltage, one sample can be limited by injection, while a second one is already highly conductive (e.g. undoped vs. doped layers). It can still be useful to highlight strong changes resulting from doping.

- **conductivity** σ^{max}: The conductivity, here, is defined as the first derivative of the IV curve. It is normalized by the active area and thickness of the device. Since none of the IV curves measured show perfect ohmic behavior, the slope is changing throughout the measurement. The chosen parameter is the maximum conductivity found in a single sweep. This eliminates the problem of choosing a specific voltage as a point of comparison. If a certain conductivity is reached at a low voltage – due to good injection – or high voltage – caused by a barrier – does not change the value. However, the result is influenced by the voltage range chosen for each measurement since higher fields usually result in higher conductivities. The maximum voltage is chosen so that the device is not damaged while reaching the maximum current possible. σ^{max} is a property reflecting the *dynamic* properties of the film around a set point of operation. Its variation is similar but slightly larger than the variation shown by the current density.

- **specific resistivity** ρ^{min}: The specific resistance is defined according to equation 4.5 and calculated via $R = \frac{U}{I}$. Analogous to the conductivity, here the lowest value during one measurement is chosen to avoid defining a specific voltage. It is not just the inverse value of the conductivity discussed before, since here the absolute values for I and U are used and not the slope at each point. If a device "turns on" late due to an injection barrier influences the result significantly. Thus, ρ is a *static* parameter describing the position

of the point of operation of a device. The variation is similar to the variation found for the conductivity.

In this chapter, *dynamic* properties are derived from differential dependencies, while *static* properties are derived from absolute values. This is equivalent to small signal and large signal parameters used in device parametrization for circuits.

- **ohmic conductivity** $\sigma^{ohm.}$**:** σ^{max} and ρ^{min} describe the *best* values within each measurement which are usually found at high voltages. The ohmic conductivity $\sigma^{ohm.}$ is defined analogously to the maximum conductivity, however, the slope is fitted via the lowest 10 % of all data points. In the low-voltage region, the IV characteristic usually shows a distinct ohmic behavior. The slope describes the effectiveness of injection. When the measured current at low voltages is below the accuracy of the measurement tool, the slope of the IV curve is not corresponding to the properties of the film. This parameter cannot be used.

Most of the measurements in this section are presented with a graph showing the IV characteristic of the individual samples as an array of curves. This serves to highlight the spread within the individual measurement. These graphs are accompanied by boxplots of the extracted parameters that are relevant for the specific measurement. Boxplots are color-coded to match the curves in the IV-graphs. The middle line within each box corresponds to the median value, the upper and lower end of the box indicate the next 25 % values. Whiskers are drawn towards the most distant value that lies within 1.5 times the interquartile range. The average values of each set are added as black circles.

The variation found in the measurements of rubrene thin-films stems from the intrinsic variation in crystal properties. No consistent trend with active area, electrode edge length, or length of the electrode is found. A weak connection exists between higher current densities and smaller active areas. If this is the result of edge-effects or series resistance due to long electrodes is difficult to decide, especially since the effect is not visible in all devices.

4.2.2 Electrical Properties of Intrinsic Rubrene Thin-Films

Figure 4.43 shows sets of IV curves of MSM devices with three of the crystal phases discussed in the previous section 4.1: triclinic dendritic crystals grown at 140 °C for 10 min with an initial seed thickness of 40 nm, orthorhombic spherulites grown at 170 °C for 60 s with an initial seed thickness of 20 nm, and orthorhombic platelets grown at 160 °C for 90 s with an initial seed thickness of 30 nm on an underlayer of 5 nm TAPC. The conduction behavior varies significantly between the individual crystal phases. Triclinic devices feature significantly larger conductivities in most voltage regimes. The current density at 6 V is up to five orders of magnitude greater than for the platelets. This result is surprising,
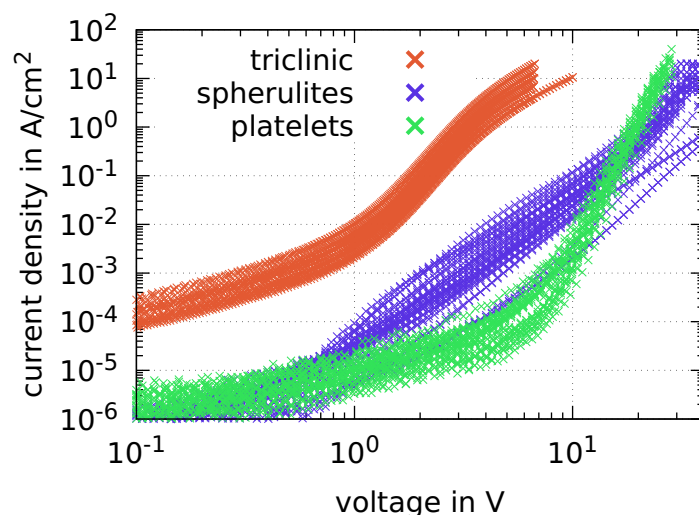
Figure 4.43: Current density over voltage of MSM devices with a total thickness of 400 nm rubrene: Triclinic seeds are grown at 140 °C for 10 min, orthorhombic spherulites at 170 °C for 60 s inside a light-filtered glovebox, and orthorhombic platelets at 160 °C for 90 s with a 5 nm underlayer of TAPC.

since the triclinic crystals feature a supposedly lower degree of order. The two orthorhombic crystal phases show a similar order of conductivity at high voltages but differ significantly in the ohmic low-voltage regime. The platelet type is heavily limited by injection resistance and shows an ohmic behavior until 6 V. This can be explained by the sublayer of TAPC which creates a large barrier for charge carriers to enter the stack. Once the injection barrier is overcome, the current rises steeply. At high voltages, current through the platelet layers is higher than through the spherulites.

Figure 4.44a shows the distribution of maximum conductivity measured in the curves of all three crystal phases. The difference between the crystal phases is significantly smaller than the IV characteristic might indicate. The average peak conductivity for the orthorhombic crystals is smaller by a factor of 3.2 compared to the triclinic layers. The differential – dynamic – properties of the crystal are not that different. Between the two orthorhombic polymorphs, the platelets show the on average higher conductivity with a smaller variation. Considering the structural measurements from sections 4.1.2.2 and 4.1.3, it seems unlikely that the difference in conductivity between these two phases is caused by a fundamentally different morphology. It seems more likely that the defects (see section 4.1.2) present in the center of spherulitic crystals[4] are responsible for the slight decrease. Since some crystals are free from this effect, it would explain why the best performing orthorhombic spherulites are similar to platelet-based devices. A similar trend can be seen in figure 4.44b, presenting the minimum specific resistance – a Direct Current (DC) static property. The value for the spherulites is roughly twice that of the triclinic film, while the two orthorhombic

---

[4]Defects can be reduced by crystallization in darkness but not avoided completely.

polymorphs are similar. The variation of the spherulites is larger than the triclinic layers and the platelets again. The most prominent difference between the two orthorhombic phases is the late onset of the platelet layers. Figure 4.44c shows the ohmic resistance at low voltage. The conductivity is 1.7 times lower for the spherulites than for the triclinic films and another 3.7 times smaller for the platelets. The orthorhombic films, in general, seem to feature a less efficient injection compared to triclinic films. The bad injection coupled with the late onset of the platelets is likely caused by the TAPC underlayer. While the Highest Occupied Molecular Orbital (HOMO) of TAPC is only 100 meV below that of rubrene and thus only 200 meV below the work function of Au, the mobility of TAPC and thus the conductivity is comparably low. The exact orientation of the rubrene molecules towards the TAPC compared to growth directly on the metal can have a significant impact on injection, too.

From these first measurements, it is already evident that the triclinic phase seems to be superior in regard to vertical transport compared to the orthorhombic phases. Additionally, the injection into platelets suffers from the impact of the underlayer that is necessary for their growth. To realize efficient devices, doping will be essential.

Figure 4.44: Parameters extracted from figure 4.43 for eight samples per crystal phase for triclinic crystals (T), orthorhombic spherulites (S), and orthorhombic platelets (P) (Middle lines mark median value, dots are the geometric average).

(a) Maximum conductivity.

(b) Minimum specific resistance.

(c) Conductivity of the low-voltage ohmic regime.
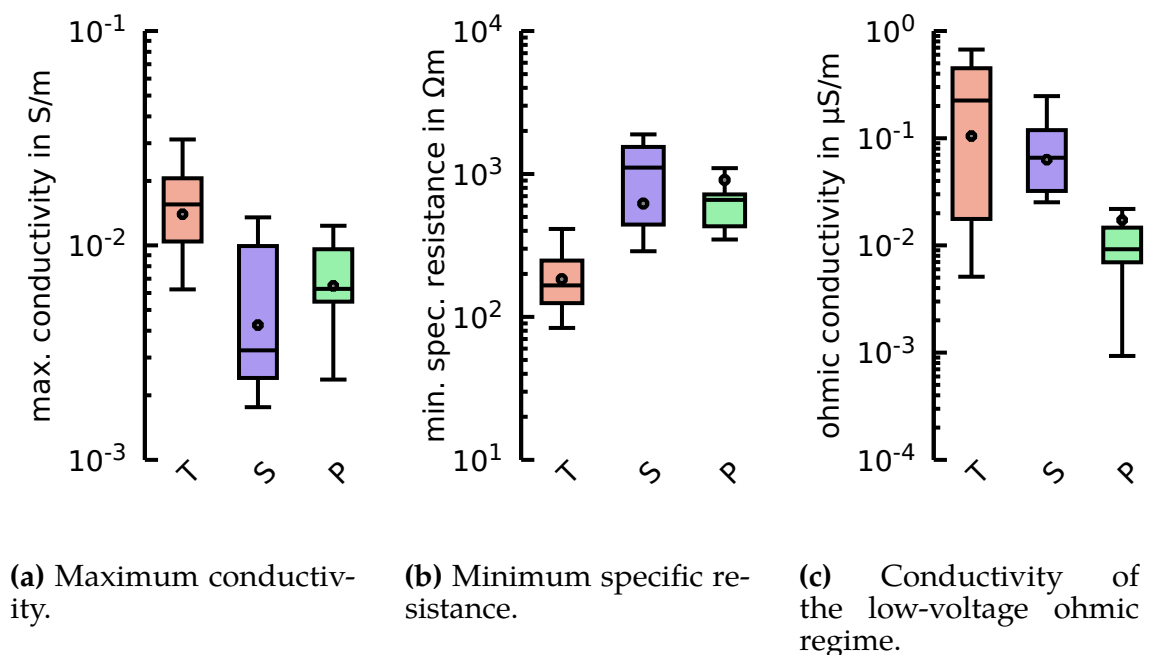
4.2.2.1 Mobility Analysis of Undoped Films: Triclinic Dendrites and Orthorhombic Platelets

To quantitatively analyze the conductive properties of crystalline rubrene films, an SCLC analysis is useful to deduce the vertical mobility of the majority charge carriers within the system. It is known from literature that rubrene shows intrinsic hole-dominant conduction in undoped films [205]. Unintentional doping of charge carriers is unavoidable, especially in organic semiconductors since the materials used cannot be purified to the same degree as inorganic materials yet. Due to the tendency to oxidize, electrons are easily trapped and cannot participate in transport. In rubrene, a strong disparity in charge carrier mobility between holes and electrons can be found. All records for carrier mobility in this material system are based on hole conduction. Even under ideal circumstances – trap free band transport – hole conduction is dominating due to a higher charge carrier mobility. Bisri et al. [216] propose an estimation based on the bandwidth of a

Figure 4.45: IV measurement of MSM devices with different thicknesses aimed towards SCLC analysis: The intrinsic layers are sandwiched between 40 nm of rubrene doped with 5 wt.%(11.1 mol%) F6TCNNQ to ensure barrier-free injection. The injection layers do not include the seed. Devices are measured with stops of 0.5 s between each step to reduce the impact of sample self-heating.
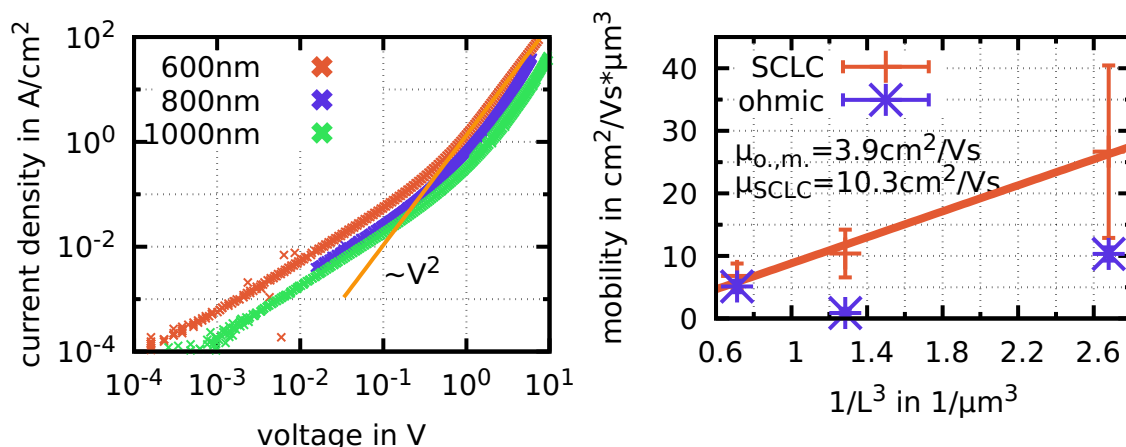
(a) Example IV curves for each thickness of the intrinsic layer. A fit at high voltage is added for the 400 nm device, featuring a V^2-dependence.

(b) Charge carrier mobility per inverse device thickness calculated via equation 2.51 for the SCLC-regime and 2.49 for the ohmic regime: The SCLC measurements follow the $\frac{1}{L^3}$-dependence. The resulting mobility is given by the fitted line (red). Results from the ohmic equation do not show the required $\frac{1}{L^3}$-dependence. Fitting the mobility is not possible. The result given is the average of the individual measurements. Error bars originate from the variation of devices with different active areas within the same sample.

supposed band-like transport. The mobility is then inversely proportional to the effective mass which in turn is proportional to the bandwidth:

$$\frac{\mu_{\text{el}}}{\mu_h} \propto \frac{m_{\text{h}}}{m_{\text{el}}} = \frac{\Delta E_{\text{LUMO}}}{\Delta E_{\text{LUMO}}} = \frac{159\,\text{meV}}{341\,\text{meV}} = 0.47. \tag{4.7}$$

The values for the bandwidth are based on Ultraviolet Photon Spectroscopy (UPS) data from da Silva et al. [73]. Experiments based on flash-photolysis by Saeki et al. [217], showed a ratio of 0.43. It can be concluded that any intrinsic mobilities extracted are holes mobilities[5].

The samples optimized for good hole injection accordingly. Devices with 600 nm, 800 nm, and 1000 nm of intrinsic rubrene are sandwiched between 30 nm of injection layers, doped with 5 wt.% F6TCNNQ and Au electrodes. The seeds of all devices are made from 30 nm undoped rubrene heated at 140 °C for 10 min. The effectiveness of the p-doping using F6TCNNQ is discussed in subsection 4.2.3.1. Devices show a thermal activation at high current densities caused by self-heating. Self-heating describes a self-propelling loop in which current through a device causes heat, which in turn increases conductivity and thus current. It is thoroughly discussed by Fischer et al. [181]. If left unlimited, this spiral leads to the destruction of the sample. To minimize this effect, breaks of 0.5 s are introduced between each measurement point. Using the Mott-Gurney-law (equation 2.51), the mobility can be extracted from the V^2-dependence of the IV characteristic. Only devices that show an unambiguous regime with a slope between 1.85 and 2.15 are used for further calculations. An example for each thickness of the intrinsic layer can be seen in figure 4.45a. To further increase the accuracy, the final mobility is extracted from the slope of the thickness dependence of these measurements shown in figure 4.45b. The variation at each total thickness originates from the variation between individual samples of different active area. This variation out-weights the deviation of the fit. A linear dependence in the graph over $\frac{1}{L^3}$ is visible; the slope gives the vertical hole mobility to:

$$\mu_{\text{h, tric.}}^{\text{SCLC}} = (10.3 \pm 4.9)\,\text{cm}^2\,\text{V}^{-1}\,\text{s}^{-1}. \tag{4.8}$$

The variation of this value is based on the variation of the individual measurement points within a 1σ-interval and not the accuracy of the fit. These triclinic thin-films represent the highest vertical mobility in organic semiconductors, surpassing the previous record by Skrypnychuk et al. [218] measured in aligned P3HT using a complicated chain alignment method and measured via SCLC[6]. Wetzelaer et al. [106] introduced a second method to estimate the vertical mobility based on

---

[5]The injection of charge carriers influences the dominant conduction type additionally. Depending on the order of magnitude of the mismatch between hole and electron mobilities, values for electron mobilities could be measured when appropriate interface design is used.

[6]Only the central regions of the used micropattern is used to define the active area instead of the area of the full "device".
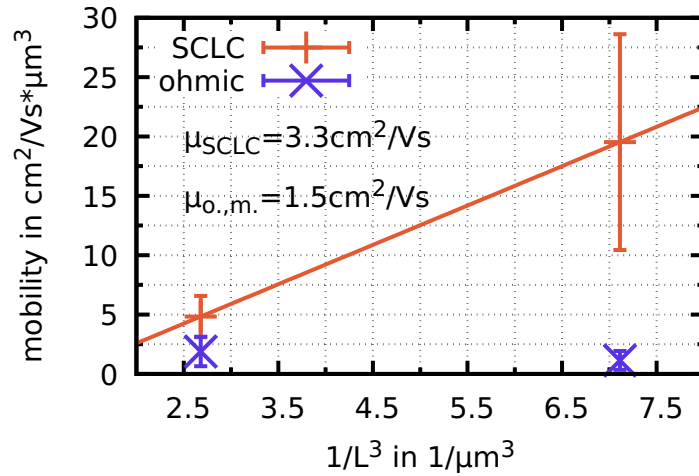
Figure 4.46: Charge carrier mobility per inverse device thickness extracted from MSM devices with two different thicknesses calculated via equation 2.51 for the SCLC-regime and 2.49 for the ohmic regime. The intrinsic layers are sandwiched between 40 nm of rubrene doped with 5 wt.% F6TCNNQ to ensure injection. The 30 nm seed is grown on 5 nm of TAPC at 160 °C for 90 seconds into the orthorhombic platelet polymorph. Devices are measured with stops of 0.5 s between each step to reduce the impact of self-heating. SCLC mobility is calculated assuming a $\frac{1}{L^3}$-dependence. The resulting mobility is given by the fitted line (red). The ohmic mobilities extracted via equation 2.49 do not follow the expected behavior. The resulting mobility given is the average of the individual measurements.
Error bars originate from the variation of devices with different active areas within the same sample.

the diffusion at the electrode. Equation 2.49 can be used, utilizing a fit of the low-voltage ohmic regime. Theoretically, the same $\frac{1}{L^3}$-dependence should arise. This is not the case in this set of measurements. This is not surprising, since the original equation is based on a quasi-insulating layer. Although the validity of the value is questionable, the average of the mobilities calculated from the individual data points can still serve as a check for the order of magnitude of the real mobility. The vertical hole mobility in triclinic layers extracted via this method is thus:

$$mu_{h,\,tric.}^{ohmic} = (3.9 \pm 3.3)\,cm^2\,V^{-1}\,s^{-1}. \tag{4.9}$$

A lower value, however, is to be expected, since charge carrier mobility commonly increases with field and carrier density.

The same type of device is used to determine the vertical mobility of the orthorhombic platelet polymorph. Seeds of 30 nm are grown on 5 nm TAPC underlayer. The effectiveness of the doping to overcome the injection problems for this crystal type is discussed in chapter 4.2.3.4. Devices with 400 nm and 600 nm of intrinsic semiconductor, sandwiched between 30 nm of rubrene doped with 5 wt.% F6TCNNQ, are measured and evaluated the same way as described the triclinic films. The result is shown in figure 4.46. Only two different intrinsic thicknesses are measured for this crystal phase. However, the variation within

each (thickness) data point is larger than the variation between the two samples. An average mobility can be calculated using all measurements individually. It follows for the vertical hole mobility of orthorhombic platelets:

$$\mu_{\text{h, orth.p.}}^{\text{SCLC}} = (3.3 \pm 2.5)\,\text{cm}^2\,\text{V}^{-1}\,\text{s}^{-1}. \tag{4.10}$$

Similarly to the triclinic polymorph, evaluation of the data using equation 2.49 does not yield a satisfying result. The average of all individual measurements gives a vertical mobility of

$$mu_{\text{h}}^{\text{ohmic}} = (1.5 \pm 1.0)\,\text{cm}^2\,\text{V}^{-1}\,\text{s}^{-1}. \tag{4.11}$$

Since the basic paradigm of the derivation of this equation is not fulfilled, the value can at best be used as a failsafe for the order of magnitude of the SCLC measurement. It is worth noting that the values gained by this method are by a factor of around 2.5 smaller than the values extracted via SCLC measurements for both crystal phases independently.

The vertical mobility of the platelets corresponds well with the $3.5\,\text{cm}^2\,\text{V}^{-1}\,\text{s}^{-1}$ found for the c-axis of furnace-grown orthorhombic single-crystals [204]. At first, it might be surprising that thin-film crystals feature the same mobility as single-crystals grown without the influence of a substrate. However, the thin-films are the most ordered along the z-direction. According to Lee et al. [219], this corresponds to the c-axis for all types of rubrene crystal thin-films. It can thus be assumed that the epitaxial growth along the z-direction creates indeed a quasi-single-crystal.

In loose crystals, the mobility along the c-axis is significantly smaller ($0.7\,\text{cm}^2\,\text{V}^{-1}\,\text{s}^{-1}$ [64]) compare to the record b-direction $40\,\text{cm}^2\,\text{V}^{-1}\,\text{s}^{-1}$ [41]. This effect is commonly explained with the larger distance between neighboring molecules along this direction and better orientation of molecular orbitals. Lateral mobilities of orthorhombic thin-films along the b-axis show mobilities of up to $4\,\text{cm}^2\,\text{V}^{-1}\,\text{s}^{-1}$ [36] in field-effect measurements.

While furnace-grown single-crystals feature a strong anisotropy in charge carrier mobility between the lateral a/b-directions and the vertical c-direction, the mobility in thin-film crystals is almost identical in all directions. This effect is partly caused by the methods to measure these charge carrier mobilities. The values for the lateral transport are generated from FET measurements that rely on surface properties. These are negatively affected when crystals are grown on a substrate. In contrast, vertical mobilities extracted from SCLC-devices are bulk-measurements, which in turn are much closer to the properties of the bulk crystal.

The vertical mobility of the triclinic phase is by a factor of 3.1 higher than that of the orthorhombic platelets. This result was expected from the simpler IV measurements of the previous subsection. The maximum conductivity in the

measured films is also 3.2 times larger for the triclinic phase than for the orthorhombic polymorphs. Rang et al. [220] describe an increase of mobility with external static pressure. They argue with a reduced intermolecular distance and a resulting more favorable orbital overlap. Similarly, the closer packing along the c-axis of the triclinic crystal phase and the slight tilt of neighboring molecules might result in a better orbital orientation. The c-axis distance of the triclinic phase is c=11.87 Å [19] in comparison to c=25.91 Å for the orthorhombic platelets. Simulations of the energetic landscape of these films are necessary to investigate the exact mechanisms causing these phenomena.

The vertical mobility measured in triclinic rubrene is not only impressive in the scope of rubrene single-crystals, it represents the highest value for the vertical charge carrier mobility in organic semiconductors to date, above the current record of $3.2\,cm^2\,V^{-1}\,s^{-1}$, measured in aligned P3HT by Skrypnychuk et al. [218].

4.2.2.2 Dependence on Evaporation Rate

The high vertical mobilities featured in these rubrene layers are the result of the high structural order. The bulk of the thin-films is created via epitaxy of thermally evaporated material and thus not by direct crystallization. To realize the necessary arrangements of a single molecule into the crystal structure, a certain amount of time is needed. A fast crystallization can have negative effects on crystal quality, as is the case for Si [221]. Nevertheless, in some systems non-equilibrium processes can create well-ordered structures too [222], although mostly on a local scale. The speed of growth for these rubrene layers is determined by the rate of evaporation during the thermal deposition of the bulk film. A decrease in crystal quality is likely at higher rates, since molecules have less time to arrange themselves into the crystal matrix. Figure 4.47a shows IV measurements of MSM devices based on undoped triclinic rubrene built on 30 nm seeds grown at 140 °C for 10 min on glass substrates. Electrodes are made from Au. Note, that the evaporation speed of the initial seed does not influence the crystallization or the final quality of the film. The bulk layers are evaporated at $0.5\,Å\,s^{-1}$, $1\,Å\,s^{-1}$, and $6\,Å\,s^{-1}$. The general behavior of the curve arrays for the three rates of evaporation is comparable. The major difference is significantly stronger thermal activation at high currents for the fast grown devices. Current densities at each voltage seem to be simply shifted towards higher values for the films that are grown faster. Figure 4.47b presents extracted parameters from these IV characteristics. Thus, the average current density at 6 V is decreased by a factor of 1.6 when doubling the evaporation rate from $0.5\,Å\,s^{-1}$ to $1\,Å\,s^{-1}$ and by another factor of 0.8 when increasing to $6\,Å\,s^{-1}$. The values taken at 6 V are outside the range of self-heating for these layers and thus comparable. The opposite trend can be seen when investigating the maximum conductivity. However, the higher conductivity found in the faster-grown samples stems from the pronounced self-heating at higher current densities. It is therefore not a sign of a more efficient conduction

Figure 4.47: MSM devices with a total thickness of 400 nm triclinic rubrene: Seeds are grown at 140 °C for 10 min on a glass substrate. Additional rubrene is added via thermal evaporation to reach the indicated total thickness at various rates of evaporation.
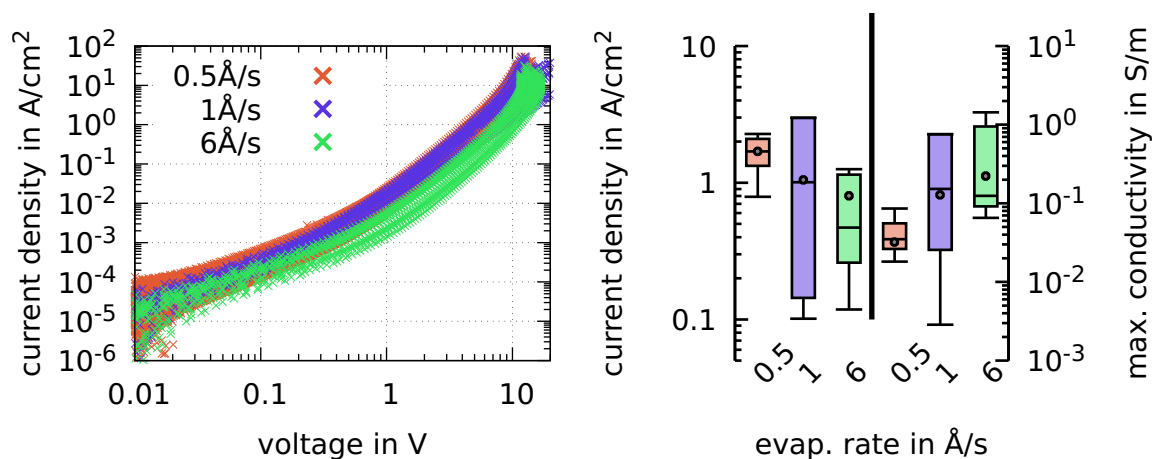
(a) Current density over voltage of at least five different devices per set.

(b) Current densities at 6 V external bias (left) and maximum conductivity (right) for five samples for each of the speeds of evaporation. (Middle lines mark median value, dots are the geometric average).

mechanism. The occurrence of thermal activation is not necessarily a sign against band transport, since only the conductivity and not necessarily the mobility needs to be positively activated for self-heating to occur. That the faster-grown devices feature a stronger thermal activation is, in fact, an argument that speaks towards band transport, since a decrease in order of a hopping-limited system would not necessarily result in a stronger temperature-dependence. In summary: the lower the evaporation speed, the better crystal quality and thus electrical performance. This has to be weighed against the time and effort necessary for sample preparation. As a point of reference, forming a single 400 nm film at $1\,\text{Å}\,\text{s}^{-1}$ requires 67 min, at $0.5\,\text{Å}\,\text{s}^{-1}$ 2.2 h, and at $0.1\,\text{Å}\,\text{s}^{-1}$ 11 h.

4.2.3 Electrical Properties of Doped Rubrene Thin-Films

The next subsection covers doping of crystalline films of rubrene in different polymorphs. The first part discusses the p-doping of all three crystal phases using different small molecule dopants, while the second part presents the n-doping using $W_2(hpp)_4$ in triclinic layers only.

4.2.3.1 p-Doping of Triclinic Films

Doping of organic small molecules is an established procedure. Mostly, co-evaporation is used: matrix and dopant are evaporated at the same time with a controlled ratio resulting in an ideally homogeneous mixture of both materials. The same technique is used here to dope the thin-film organic crystals presented

Figure 4.48: Current density over voltage of MSM devices featuring different concentrations of p-dopant with a total thickness of 400 nm triclinic crystal. Seeds are grown from 30 nm undoped rubrene at 140 °C for 10 min. Electrodes are made of Au.
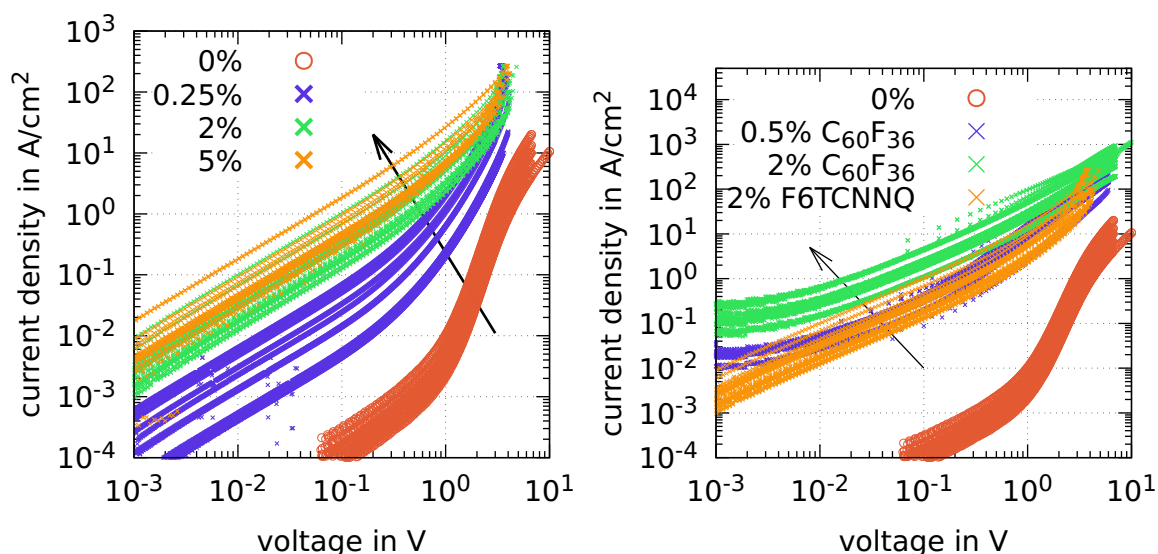
(a) Doping with F6TCNNQ: The direction of the trend following the doping concentration is indicated with an arrow.

(b) Doping with F6TCNNQ and $C_{60}F_{36}$: The direction of the trend following the doping concentration is indicated with an arrow.

in the previous section. It would not be possible to dope classic organic single-crystals grown in a vacuum furnace using this method. It is a distinct advantage to generate highly crystalline – and thus high mobility – films while still maintaining full control of doping concentration, type of doping, and sequence of doped layers. At first, p-doping is analyzed. Since conduction is carried by hole-transport in the undoped films, due to higher hole mobility, introduction of additional free holes should increase the conductivity of the system significantly.

 Within a simple stack, two parts could technically be subjected to doping: the seed and the bulk. Bulk doping of all three crystalline polymorphs is discussed first. Figure 4.48a shows sets of IV measurements on MSM devices with films doped with the common p-dopant F6TCNNQ with different doping concentrations. All films are grown on glass substrates, with structured Au electrodes and 30 nm thick undoped triclinic seed layers grown at 140 °C for 10 min. Doping concentrations are set as wt.%, based on the assumption of constant average density. All samples have a total thickness of 400 nm. Already for a moderate doping concentration of 0.25 wt.% (0.6 mol%), the current is increased significantly by up to two orders of magnitude, depending on the voltage. Further increase in doping concentration leads to even higher currents, however, the increase is smaller than for the initial doping. This shows the expected decrease in doping efficiency with higher doping concentration. The strongest effect on the IV curves is visible in the low-voltage regime, indicating a significant improvement of injection.

Figure 4.49: Parameters extracted from figure 4.48a for eight samples per doping concentration. Crystals are in the triclinic phase and doped with F6TCNNQ. (Middle lines mark median value, dots are the geometric average).
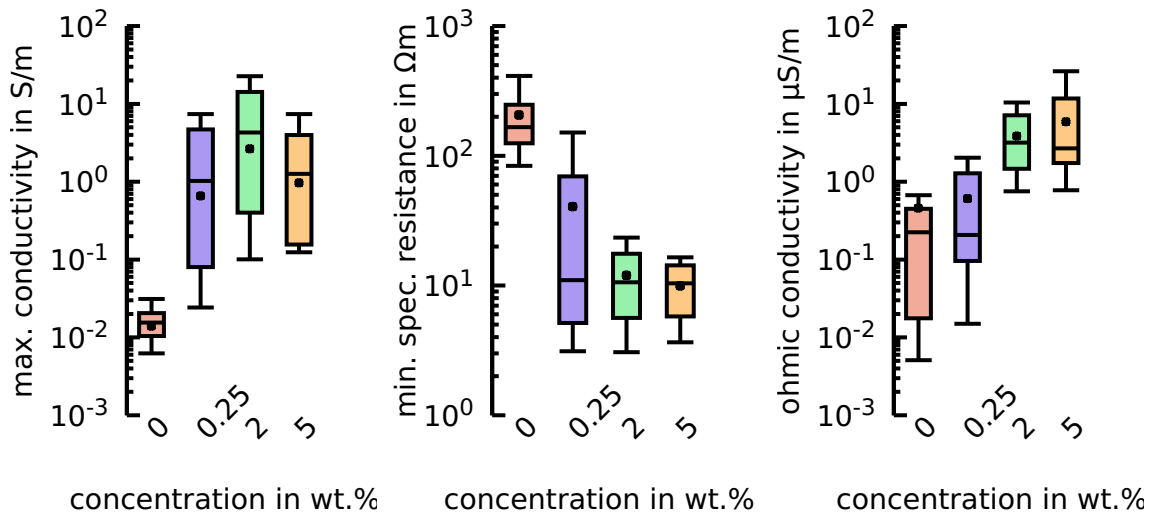
(a) Maximum conductivity.

(b) Minimum specific resistance.

(c) Conductivity in the low-voltage regime.

Figure 4.49a shows the distribution of the maximum conductivity extracted from the F6TCNNQ doping series of figure 4.48a. In accordance with the shape of the IV curves, there is a strong increase in conductivity from the undoped to the lightly doped devices. The average value grows by a factor of 50. Raising the doping to 2 wt.% (4.6 mol%), increases the maximum conductivity by an additional factor of 4. The conductivity, however, is decreased again to a third, when the doping concentration is increased even further. A decrease in dynamic conductivity could indicate a decrease in the mobility of the film. It could be caused by the decreased order in the film, resulting from a large degree of defects. However, the spread of values is comparably large and overlaps significantly between the differently doped films. Especially the values extracted for 2 wt.% seem to be influenced by self-heating effects and are less trustworthy than the other data points. In summary, the dynamic properties of the doped layers do not seem to be affected strongly by an increase in doping concentration. Figure 4.49b shows the minimum static resistance of each set. Here, the impact of the doping is more gradual. The resistance drops by a factor of 4.5 once doping is introduced and by an additional factor of 4 when the concentration is increased from 0.25 wt.% to 2 wt.%. Raising the doping concentration to 5 wt.% does not decrease the static resistance further significantly. However, an increase in doping concentration shows a clear trend towards lower static resistance. Finally, 4.49c presents the conductivity in the low-voltage regime, indicative of the injection properties. Surprisingly, the initial low doping only has a small impact on the average ohmic conductivity. Nevertheless, the variation is decreased and the distribution is shifted towards higher values as a whole. Higher doping

Figure 4.50: Parameters extracted from figure 4.48b for eight samples per doping concentration. Crystals are in the triclinic phase, doped with $C_{60}F_{36}$ and F6TCNNQ (marked F).
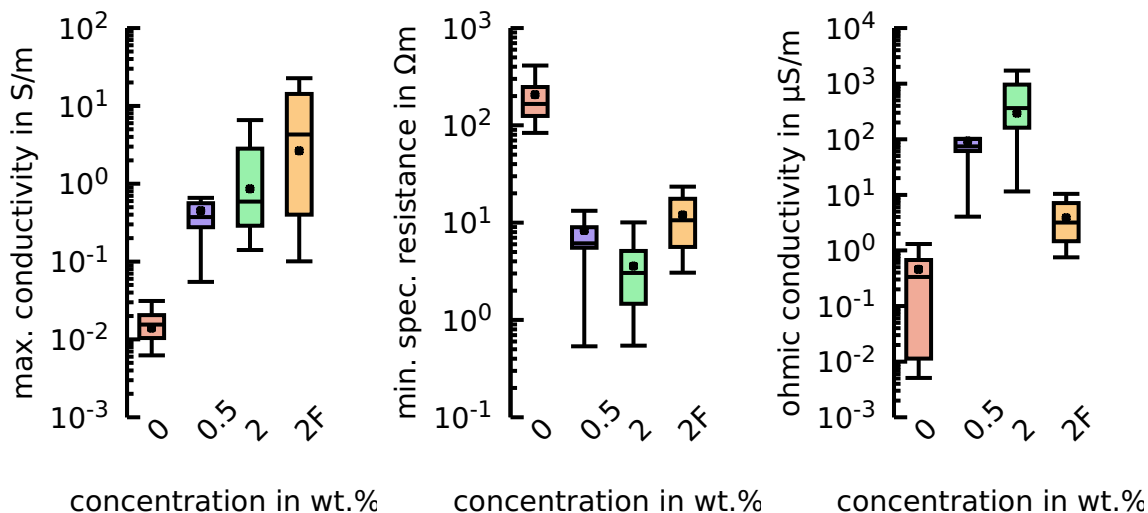
(a) Maximum conductivity. **(b)** Minimum specific resistance. **(c)** Conductivity in the low-voltage regime.

concentration increases the low-voltage conductivity as intended. At 5 wt.%, the injection is improved on average by over one order of magnitude compared to the undoped devices.

As a comparison, a similar set of samples is made based on $C_{60}F_{36}$ as p-dopant. Procedures and manufacturing are identical to the devices built with F6TCNNQ. Resulting IV curves can be seen in figure 4.48b. Evidently, $C_{60}F_{36}$ is suited as a p-dopant for rubrene crystals as well. The current density of the measured samples is increased in every voltage regime. The doping efficiency seems to be higher than for F6TCNNQ, since 0.5 wt.% of $C_{60}F_{36}$ has a similar impact as 2 wt.% of F6TCNNQ. An even higher concentration of $C_{60}F_{36}$ results in an even higher current density. The extracted maximum conductivity is presented in figure 4.50a. The initial change from doped to undoped films is less pronounced than for F6TCNNQ: the conductivity rises by a factor of 32. An increase in doping concentration increases the conductivity further. Regarding this parameter, the F6TCNNQ seems to be superior. The impact of the doping at low doping concentration is stronger for the $C_{60}F_{36}$ compared to the F6TCNNQ – indicating a higher doping efficiency at lower concentrations. A better judgment of the IV characteristics is given by the specific resistance shown in figure 4.50b. The minimum specific resistance drops by a factor of 27 for the initial doping and by a factor of 1.5 with the doping increased to 2 wt.%. This is a stronger effect than for the F6TCNNQ samples. An even stronger differentiation to the F6TCNNQ can be seen in the injection-related regime shown in figure 4.50c. Even the moderate doping at 0.5 wt.% increases the ohmic conductivity by a factor of 2000, much more than even the high doping concentration of the F6TCNNQ samples. In

regard to injection doping, $C_{60}F_{36}$ seems to be the by far superior dopant. The differences in bulk doping are noticeable but not that significant.

Two factors are relevant for an efficient charge transfer from host to guest molecule. The energy level must fit and the molecules must be in sufficient proximity and orientation to each other. Since the Lowest Unoccupied Molecular Orbital (LUMO)-values of both dopants are close (F6TCNNQ: 5.37 eV vs. $C_{60}F_{36}$: 5.38 eV), the energy levels are less likely to be significant here. However, the shape of both molecules is significantly different. $C_{60}F_{36}$ is the more compact and isotropic molecule. It is less dependent on an ideal orientation towards the rubrene molecules to interact. Especially in crystal structures, the position and orientation of the matrix material are fixed due to the ordered structure. There is less leeway to accommodate a sub-optimal dopant orientation. This is especially important directly at the substrate, since the interaction with the surface might cause the rubrene host molecules to be even less movable.

In summary, $C_{60}F_{36}$ appears to be the superior dopant for this type of polymorph, especially in regard to injection doping. However, due to simple supply reasons, all further measurements and devices are based on F6TCNNQ.

4.2.3.2 Doping Efficiency of F6TCNNQ in Triclinic Films

The conductivity describes the amount of current flow at a given voltage. According to equation 2.13, it is governed by the density of free charge carriers and their mobility. The mobility for undoped layers can be extracted using various methods. SCLC measurements from section 4.2.2.1 found a vertical mobility of $(10.3 \pm 4.9)\,\mathrm{cm^2\,V^{-1}\,s^{-1}}$ for intrinsic films of triclinic rubrene. Assuming the mobility is independent of electric field and carrier density, a rough estimate can be given for the minimum free carrier density based on the maximum conductivity measured for undoped films of $14\,\mathrm{mS\,m^{-1}}$:

$$N_0^{\mathrm{min}} = 8.5 \cdot 10^{13}\,\mathrm{cm^{-3}}. \tag{4.12}$$

The density extracted via equation 2.52, based on the crossover between ohmic bulk conduction and the SCLC gives a similar order of magnitude for the background doping concentration:

$$N_0 = 3 \cdot 10^{14}\,\mathrm{cm^{-3}}. \tag{4.13}$$

Doped films are more difficult to analyze using SCLC measurements, the $\propto V^2$-regime is usually hidden. The doped films discussed in this section show a change of slope indicating the start of an SCLC-regime. However, due to thermal activation, measurements are not possible. One possibility to measure the carrier density is based on Capacitance-Voltage (CV) measurements. The width of the depletion layer of a Schottky diode is bound to the density of ionized dopants. By measuring the capacitance in dependence of the external bias, the carrier density
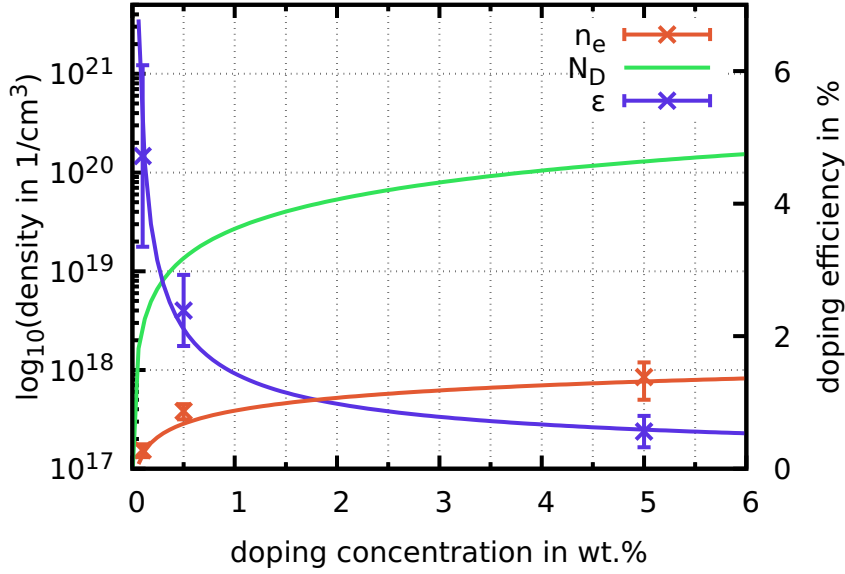
Figure 4.51: Results of Mott-Schottky analysis of Schottky diodes with differently doped p-layers:

red: Extracted average free hole density. The error bars are based on the variation of samples built with different active areas and thicknesses of the doped layer.

green: Density of dopant molecules, based on a molecular density of the rubrene matrix of $1.36 \cdot 10^{21}$ cm^{-3}.

blue: Resulting doping efficiency $\epsilon = \frac{n_e}{N_D}$. Error bars are based on the variation of n_e and the accuracy of the doping dictated by the evaporation procedure. The solid line is a fit using a $\frac{1}{\sqrt{c}}$-dependence of the concentration.

can be calculated from the Mott-Schottky-plot using equation 2.38, under the assumption that these additional charge carriers are free.

Schottky diodes with 0.1 wt.% (0.24 mol%), 0.5 wt.%, and 5 wt.% of F6TCNNQ are prepared. The stack contains the seed on a hole injecting electrode (Au), the p-doped film, an intrinsic layer, and an Al-Schottky contact. The p-doped side has a thickness (including the seed) of 200 nm, 250 nm, or 300 nm, the intrinsic films are 50 nm, 100 nm, or 200 nm thick. The thickness of the doped layer should not have any influence on the capacitance, while the thickness of the intrinsic layer is represented by an offset in the Mott-Schottky-plot. The slope is independent of both properties. The individual devices function as a failsafe; their variation serves as a measure for the uncertainty of the measurement.

The extracted carrier density p_h is presented in figure 4.51. It increases from $(1.54 \pm 0.23) \cdot 10^{17}$ cm^{-3} at 0.1 wt.% doping to $(8.47 \pm 0.24) \cdot 10^{17}$ cm^{-3} at 5 wt.%. The dopant concentration can be calculated from the weight-doping concentration c_m via the molar doping concentration c_{mol} using the molar density of the rubrene matrix $N_{Rub}=1.36 \cdot 10^{21}$ cm^{-3} (based on the thin-film density) and the ratio between the molar masses of matrix and the dopant $\beta = \frac{M_{Rub}}{M_{F6}} = 2.375$ to:

$$N_A(c_m) = c_{mol} * N_{rub} = \frac{\beta c_m}{c_m (\beta - 1) + 1} N_{rub}. \tag{4.14}$$

The efficiency of the doping process – which percentage of the doping molecules are ionized and assumingly create free charge carriers – can then be calculated to:

$$\epsilon = \frac{N_A^+}{N_A} = \frac{p_h}{N_A}. \tag{4.15}$$

The efficiency decreases from $(4.7 \pm 1.4)\%$ at 0.1 wt.% doping concentration to $(0.56 \pm 0.23)\%$ at 5 wt.%. A fit is added following a $\frac{1}{\sqrt{c_m}}$-dependence. There is no physical reason for this connection but it serves as a feasible parametrization within the investigated regime. It can in return be used to extrapolate the expected carrier density for any given doping concentration that is not measured. A low doping efficiency [223] and a decrease in doping efficiency are common in organic semiconductors [87]. The low doping efficiency even for the moderate concentrations and the strong decrease might be a cause of the crystalline nature of these films. As previously discussed, orientation of the dopant molecule by chance, such that effective charge transport to a rubrene molecule is possible, is already unlikely in a rigid crystal structure. The problem might increase in severity with increasing dopant density. An increase in dopants does not only create a decrease in free un-ionized matrix molecules but also decreases the space within the grid to host dopant molecules. Tietze et al. [85] found that based on the width of the Density of States (DOS) alone, doping efficiency in crystalline systems is reduced compared to an equivalent amorphous system.

The IV experiments with $C_{60}F_{36}$ suggest a higher doping concentration and better geometric adaptation than the F6TCNNQ. Further analysis of the doping properties with this and other dopant molecules could improve the performance of devices based on these layers even more. Kiefer et al. [224] show that as long as the energy of the guest molecule is lower than the least bound electron of the host, further ionization is possible. Given a fitting dopant, doping efficiencies of over 100 % are feasible. This might offset the reduced efficiency, potentially caused by steric hindrance. Measurements at significantly lower doping concentration – as is common for fundamental studies – and different dopant molecules might shine light on the doping process itself and the associated mechanisms.

4.2.3.3 Impact of Seed Doping in Triclinic Films

Till now, all devices shown had an undoped seed layer. This setup can be justified with data from measurements of doped and undoped films shown in figure 4.52a. Two sets of devices based on triclinic layers grown on 30 nm seeds are compared. The seeds are prepared at 140 °C on glass substrates and Au electrodes. Since doping with $C_{60}F_{36}$ has a significantly stronger impact on the injection behavior, this dopant is used for evaluation of seed doping. The bulk of the device is doped with 2 wt.% for both devices. One set is built on undoped seeds, while the other set has a seed doped with 2 wt.% $C_{60}F_{36}$. The behavior of the two sets

Figure 4.52: IV analysis of MSM devices with doped and undoped seeds and a total thickness of 400 nm triclinic crystals. Seeds are grown from 30 nm rubrene at 140 °C for 10 min. Electrodes are made of Au. The bulk of all layers is doped with 2 wt.% $C_{60}F_{36}$. Half of the samples feature a seed doped with 2 wt.% $C_{60}F_{36}$, the other half has undoped seeds.
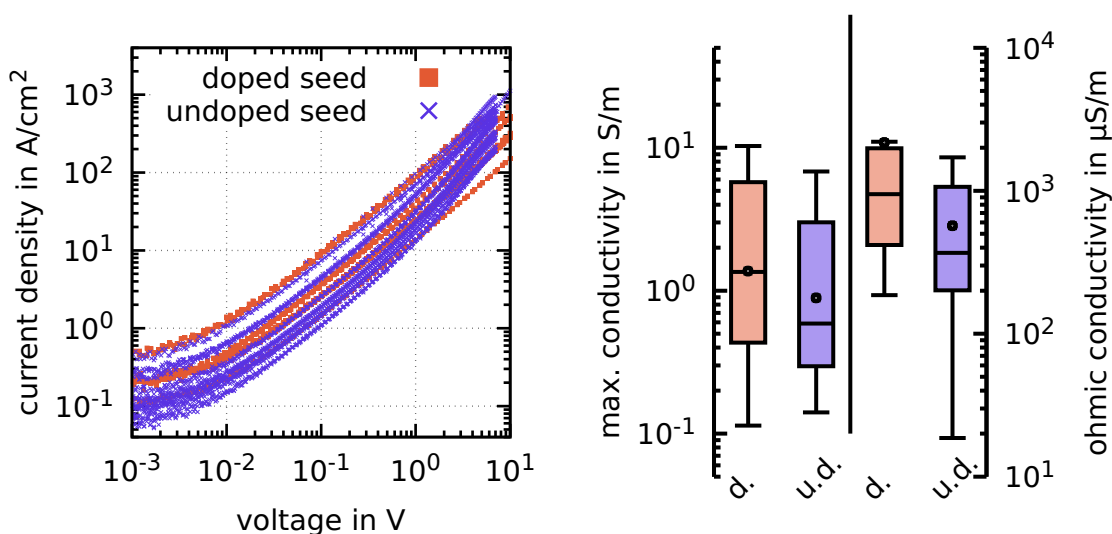
(a) Current density over voltage of sets with different active areas.

(b) Maximum conductivity (left) and ohmic conductivity in the low-voltage regime (right) extracted of devices with doped (d.) and undoped (u.d.) seeds and doped bulk layers with eleven values per type.

is almost identical. A slight variation at low and high voltages can be seen for some of the curves. The middle part, however, is close to congruent. Parameters extracted from this data, shown in figure 4.52b, support this assessment. The maximum conductivity of both films is similar. The average of the devices with a doped seed is slightly larger, however, the bulk of both sets overlaps significantly. Differences are more likely to be the result of process variation. The difference in low-voltage ohmic conductivity is more relevant. The majority of the devices in both sets are quite similar too, showing a slightly better result for the seed-doped set. The average ohmic conductance of the undoped films is influenced by a set of underperforming devices. It might be interesting to study if the use of seed doping reduces the occurrence of these outliers. Nevertheless, the impact of seed doping seems to be minor and not worth the reduced yield for crystallization.

4.2.3.4 p-Doping of Orthorhombic Crystals

Despite showing lower vertical mobility than the triclinic films, the orthorhombic polymorphs can be valuable systems in devices or applications that require a large vertical and lateral mobility and conductivity at the same time (e.g. various transistor designs). It is worth investigating the properties of doping in these material systems too. The analysis is shortened and only tackles the direct

conductive properties in the form of IV measurements. Aside from the bad injection caused by the additional layer of TAPC, orthorhombic platelets behave similarly to the orthorhombic spherulites. This is not surprising, since the crystal structure in z-direction of both polymorphs is almost identical (see sections 4.1.2.2 and 4.1.3.2). The main distinction is in the lateral ordering. Similar behavior of both crystal phases can be assumed for the doping experiments too. Results of the orthorhombic spherulites are presented first:

A set of devices with 20 nm seeds on glass substrates with structured Au electrodes is prepared. The undoped seeds are heated at 170 °C for 60 s in a light-filtering glovebox to reduce the formation of defects as much as possible. The bulk layers of the samples are doped with varying concentrations of F6TCNNQ. The resulting set of IV curves is shown in figure 4.53 (left). This graph shows as an illustration or the spread of the individual sets. A representation of the detailed shape for one exemplary sample per doping concentration is shown in figure 4.53 (right). The general behavior is similar to that shown by the triclinic samples, featuring a strong jump in current density once doping is introduced, followed by a steady but slower increase at higher doping concentrations. The strongest relative increase is noticeable in the low-voltage ohmic regime.

Extracted parameters are summarized in figures 4.54a to 4.54c. The initial doping increases the maximum conductivity significantly by a factor of 29. Further doping causes only a small increase in conductivity. The 10 wt.% (20.1 mol%)-doped device has a conductivity 3.5-times higher than the lowest doped sample.
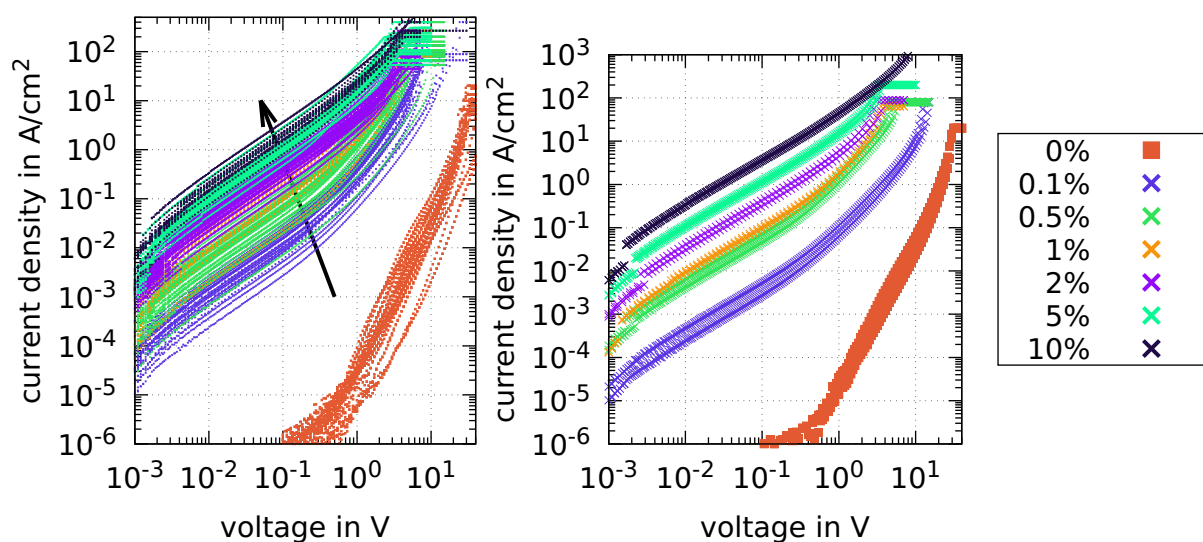
Figure 4.53: Current density over voltage of MSM devices featuring different concentrations of doping with F6TCNNQ in orthorhombic spherulite crystals. The total thickness of all devices is 400 nm. The undoped seeds are grown from 20 nm at 170 °C for 60 s in a light-blocking glovebox. Electrodes are made of Au. The direction of the trend following the doping concentration is indicated with an arrow. **left:** all devices, **right:** one exemplary device per doping concentration.

Figure 4.54: Parameters extracted from figure 4.53 for ten samples per doping concentration. Crystals are in the orthorhombic spherulite phase. The dopant is F6TCNNQ.

(a) Maximum conductivity.

(b) Minimum specific resistance.

(c) Conductivity in the low-voltage regime.
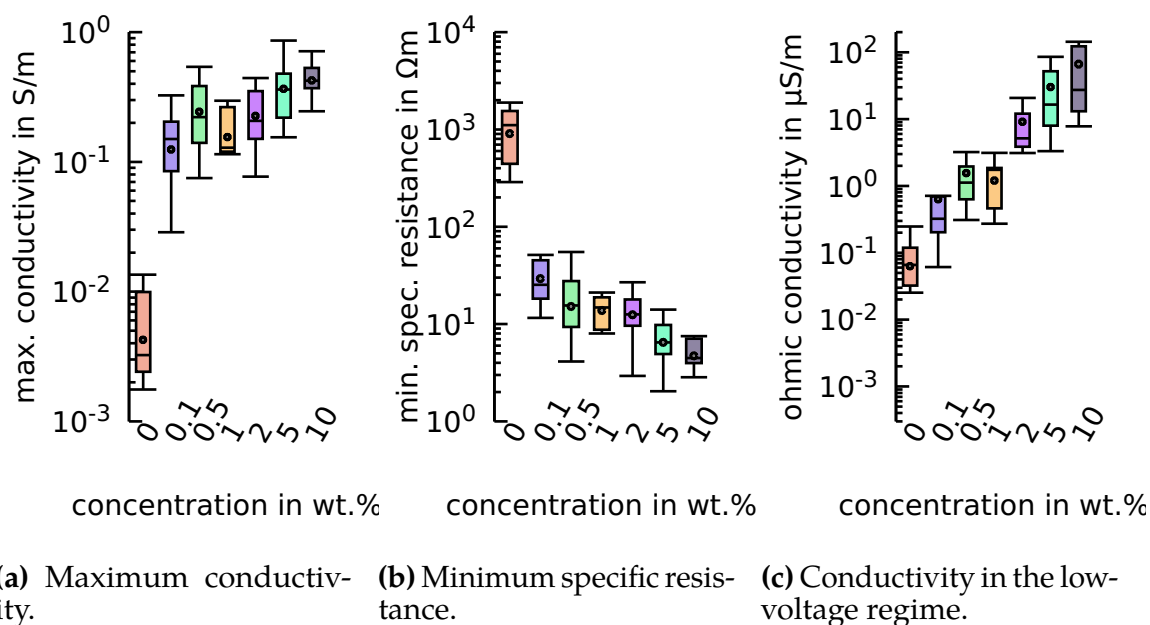
Comparison of the specific static resistance in figure 4.54b, shows a slightly stronger effect. Resistance drops too, once doping is introduced – by a factor of 31. Further increase in doping concentration reduces the resistance by an additional factor of 6.2 (from 0.1 wt.% to 10 wt.%). The strongest effect of the doping can be seen in the low-voltage resistance of the films. The initial average injection conductance increases by over three orders of magnitude; further doping adds two more order of magnitude. The injection conductivity of the undoped films is comparably low, significantly lower than the values measured in triclinic films, even when taking the higher vertical mobility into account. It is imaginable that the different orientation of the molecules towards the metal electrodes creates different dipole moments at the surface, resulting in inferior injection properties. Further analysis of the growth and injection properties of the different crystal polymorphs might be of value. Since the injection resistance is higher to begin with, it is not surprising that doping has such a significant impact on the low-voltage conductivity. However, it also shows that injection doping is essential for any type of device to function effectively.

Based on the measurements of intrinsic conduction properties, vertical conduction through orthorhombic spherulites and platelets is similar. However, the injection into the platelets is severely disturbed by the TAPC underlayer that is required for efficient crystallization. A small set of samples is prepared with 400 nm of total rubrene thickness on glass substrates and Au electrodes. Seeds are grown on a 5 nm film of TAPC, from a 30 nm layer at 160 °C for 90 s. The seed layers are undoped. The resulting IV characteristics are shown in figure 4.55. Apparent is the strong injection resistance, causing a large onset voltage for the undoped
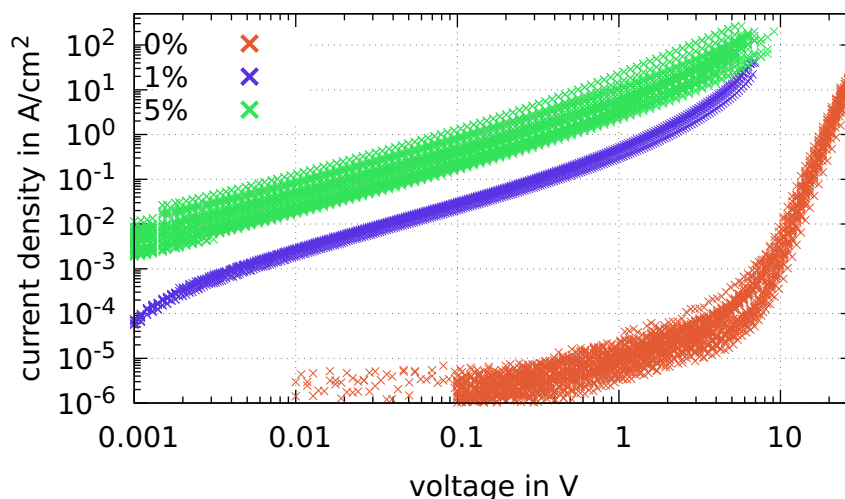
Figure 4.55: Current density over voltage of MSM devices featuring different concentrations of doping with F6TCNNQ in orthorhombic platelet crystals. The total thickness of all devices is 400 nm. The undoped seeds are grown from 30 nm at 160 °C for 90 s on a sublayer of 5 nm TAPC. Electrodes are made of Au.

devices. This effect is overcome via doping. The IV curves of the doped samples appear to be virtually identical in shape when compared to the spherulite samples. A quantitative analysis (figures 4.56a to 4.56c) reveals that the negative effect of the underlayer can be suppressed. The maximum conductivity of the platelet films increases by a factor of 40, when doping of 5 wt.% is introduced, while the conductivity rises by a factor of 109 for the spherulites. However, the initial intrinsic value for the platelets is slightly larger, a smaller increase is to be expected. The average maximum conductivity with 5 wt.% of the platelets is 71 % of the conductivity shown by the spherulites at the same concentration. The specific resistance and the low-voltage conductivity change accordingly and are similar to the performance shown from spherulite devices at similar doping concentrations. Aside from injection, both crystal phases show similar behavior with doping and similar performance at higher doping concentrations.

Figure 4.56: Parameters extracted from figure 4.55 for ten samples per doping concentration. Crystals are in the orthorhombic platelet phase. The dopant is F6TCNNQ.
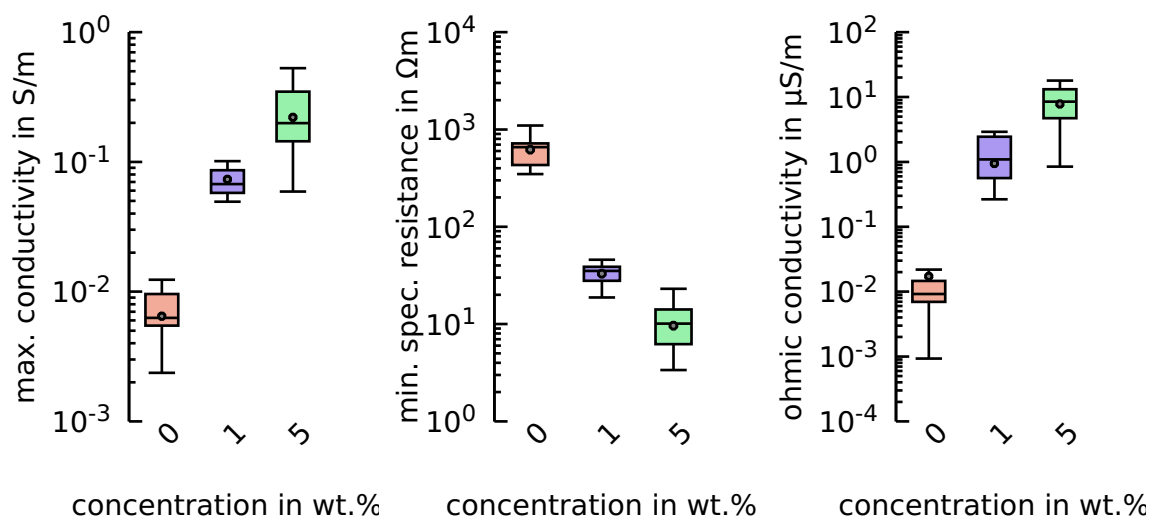
(a) Maximum conductivity.

(b) Minimum specific resistance.

(c) Conductivity in the low-voltage regime.

4.2.3.5 n-Doping of Triclinic Films

Effective p-doping can be realized with all three crystal phases. For the sake of simplicity, n-doping is investigated based on the triclinic crystal phase alone. The results can be extrapolated towards the other crystal phases according to their behavior with p-doping. Since the electron mobility in rubrene is significantly lower [216], p-doping should be used in real devices whenever possible, to utilize the higher charge carrier mobility. In the scope of this thesis, the specifics of n-doping process are not as important as the specifics of p-doping, since these layers will only make up a small fraction of the devices investigated here.

Finding suitable electron dopants for organic semiconductors is significantly more difficult than finding p-dopants [225]. Here, $W_2(hpp)_4$ is used as an n-dopant, a well known and effective doping molecule [197]. However, processing of this material is more complicated than all other materials used in this thesis due to its incompatibility with ambient air. This fact, combined with a limited supply of $W_2(hpp)_4$, results in the use of large amounts of dopants exclusively for essential experiments. Finding a suitable replacement for $W_2(hpp)_4$ as n-dopant – preferably an air-stable molecule – would simplify manufacturing of ambipolar devices based on crystalline rubrene significantly.

Equivalently to the IV experiments of the p-doped films, devices with varying degrees of n-doping are prepared. Triclinic seeds are made from 40 nm undoped rubrene, heated at 140 °C for 10 min on glass substrates with Au electrodes. The n-doping is added to the epitaxially grown films. IV curves measured from these devices are shown in figure 4.57. The strong variation visible in the intrinsic and p-doped films is also present in the n-doped devices. It is further indication
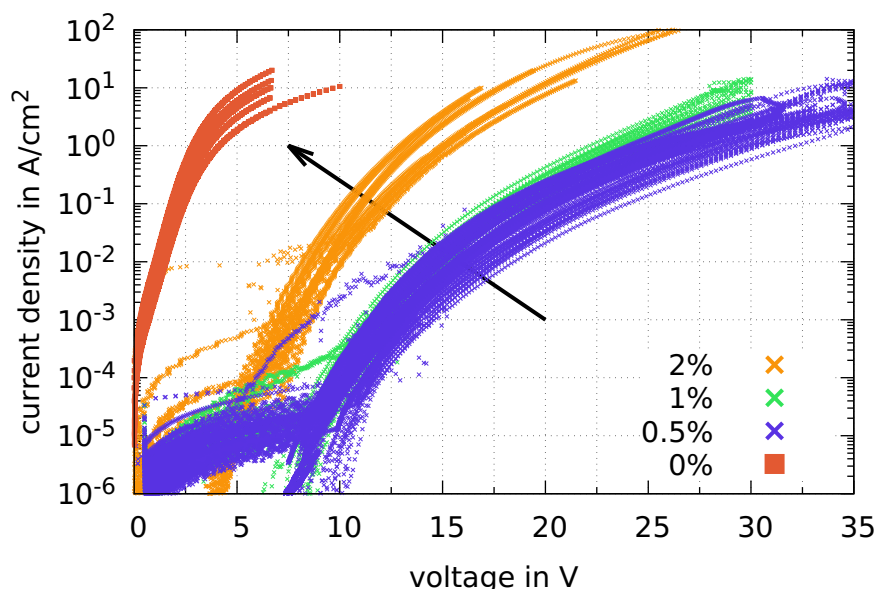
Figure 4.57: Current density over voltage of MSM devices featuring different doping concentrations with a total thickness of 400 nm triclinic crystals, based on 30 nm undoped seeds grown at 140 °C for 10 min. Electrodes are made of Au. Doping with $W_2(hpp)_4$ is introduced for the bulk layers only. The direction of the trend following the doping concentration is indicated with an arrow.

that the strong variation is caused by the randomness of the crystallization and subsequent randomness of the structure rather than the fluctuation introduced by the doping itself. Doping is commonly introduced to increase the conductivity of the film via the increase of free carrier density. The contrary is happening in these doped films initially. The current is significantly reduced compared to even the supposedly intrinsic devices. For most of the devices, a current could not be measured that exceeds the limitations of the setup below an onset voltage of 5 V to 7 V. A related effect is a stark difference in the IV-behavior at low-voltages depending on the sweep direction (low to high voltages vs. high to low voltages). It is a result of the current-defined measurement[7]. The extended shoulder with an almost constant current visible below 5 V is only present for the initial upwards sweep. When the order of measurement is reversed, the current follows the general trend of the curve. This process is reproducible. However, if immediately after reaching the lowest set current, a new upwards sweep begins, the measurement remains on the second – straight – branch. Since self-heating can be excluded in the low current regime, a possible explanation is charging effects. Because the semiconductor is unstructured and the conductivity (especially at low fields) is low, a significant amount of charge can be stored on the surface. The initial part of the IV curve is then dominated by charging currents. Once the surface is sufficiently charged, the real characteristic of the film is measurable. This explanation is supported by figure 4.59c. One single device is measured at

---

[7]The setup is programmed to realize a series of defined currents and measures the voltages necessary.

Figure 4.58: Parameters extracted from figure 4.57 for eight samples per doping concentration. Crystals are in the triclinic phase and doped with $W_2(hpp)_4$.
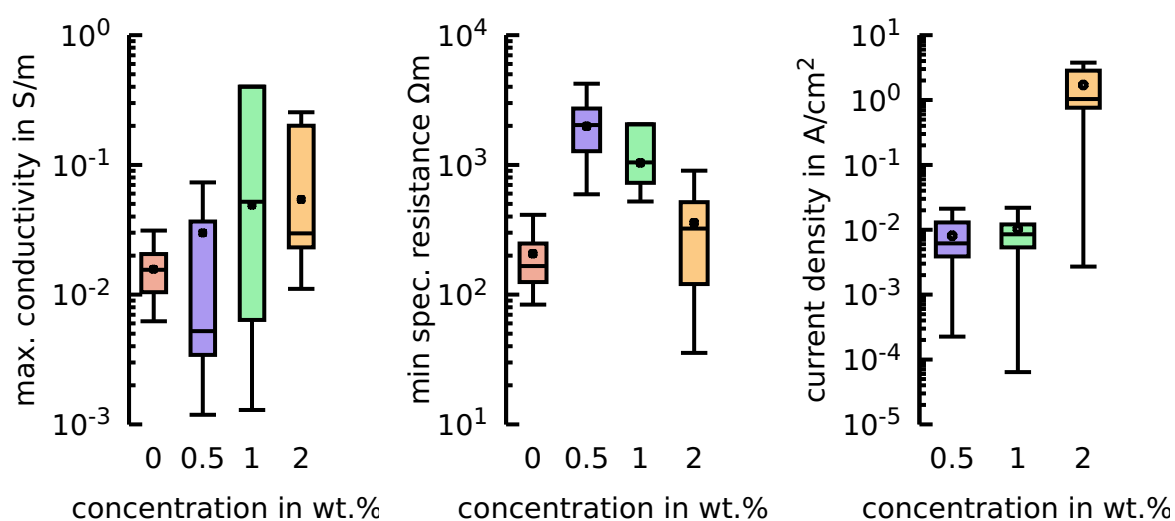
(a) Maximum conductivity.

(b) Minimum specific resistance.

(c) Current density at 15 V.

different speeds of measurement, i.e. the time for which the signal is averaged at each data point. The effect is decreased when measuring with longer integration time, since this allows the surface capacitance to be charged sooner. However, the maximum current at the highest voltage is decreasing as well. This indicates a heavily trap limited transport.

This large onset voltage can at least partly be explained by injection-related problems. To allow for a better comparison to the intrinsic measurements, Au electrodes are used. However, injection of electrons is hindered by this material combination. Generating a high carrier density – as is intended by doping – should reduce the impact of the surface barrier. The influence of the electrode can, therefore, not be too strong in this experiment. The main reason for the decreased conductivity of these films is the low electron mobility in rubrene. Even in furnace-grown single-crystals, along the most ideal crystal axis, electron mobility is smaller than hole mobility. Comparing the highest measured value for holes ($18\,cm^2\,V^{-1}\,s^{-1}$ to $40\,cm^2\,V^{-1}\,s^{-1}$ [41]) with those of electrons ($0.3\,cm^2\,V^{-1}\,s^{-1}$ [216]) shows a difference of at least two orders of magnitude. Since the mobility of these doped films might be even lower than the values from literature, due to the additional scattering introduced by the dopant molecules, the effect might be even stronger.

Parameters are extracted from the devices, similarly to the p-doped experiments. Since the low-voltage regime is dominated by charging effects, figure 4.58c shows the variation of the current density of the three doping concentrations at 20 V instead of the injection conductivity. The majority of the devices within each set are comparably similar, while each set shows a small group of outliers towards

even smaller values.The n-doped samples seem to show a stronger tendency towards faulty devices. Evidently, devices doped with 2 wt.% show significantly more current (two orders of magnitude) than the lower doped devices. It proves that electrons are indeed being created within the film. The samples doped with 0.5 wt.% and 1 wt.% (2.3 mol%) do not show significant differences to each other. To conserve material, the evaporation rates set for the $W_2(hpp)_4$ are chosen low in general. The doping concentrations are thus less accurate and might be closer to each other than intended.

Although the current of the doped films is in general smaller than the intrinsic devices and the variation found within the sets is large, the average maximum conductivity for the doped films is higher than the undoped samples and further increases with higher doping concentration (see figure 4.58a). The static specific resistance reflects the effect seen in the current better. The initial doping increases the resistance by a factor of 10. Further doping decreases the resistance close to the initial value of the intrinsic film. These effects can be explained as follows: Currents in intrinsic films are carried by high mobility hole transport. Doping a low density of donators into the system, increases the density of free electrons while decreasing the hole density compared to the intrinsic semiconductor. As a result, the conductivity decreases, since the average mobility over all carriers that take place in conduction sinks. A higher doping concentration creates a higher density of free electrons. Once the density of electrons is high enough to overcompensate the lower mobility, the conduction improves. The explanation is consistent with the available data. For a definitive analysis, Hall effect measurements are needed, to determine the carrier type and capacitance measurements to investigate the carrier density.

4.2.3.6 Impact of Seed Thickness in Doped Seeds

The impact of the seed doping is comparably small, as is shown in subsection 4.2.3.3. Thus, to increase the reproducibility of the crystallization process, most devices are made from undoped seeds. If doping of the subsequent layer is necessary – which means the seed is supposed to be remotely doped – it is important to reduce the thickness of the seed as much as possible to guarantee diffusion of charge carriers. Since the conductivity of the n-doped films is lower than the p-doped films, all devices that require both types of doping should be set up to contain the smallest amount of n-type material possible. Thus, n-doped films in devices should be thin. If a device is built such that the n-doped film is at the bottom, directly on top of the seed, only a small amount of n-doped material is present to transfer charges to the undoped film. In that case, it can be beneficial to dope the seed directly, even if this increases the risk of crystallization to fail. It might also reduce the complexity of device manufacturing if the entire n-doped film is made from on thicker n-doped seed, instead of a thin seed with n-doped material added. As an example: crystallizing 50 nm of n-doped rubrene
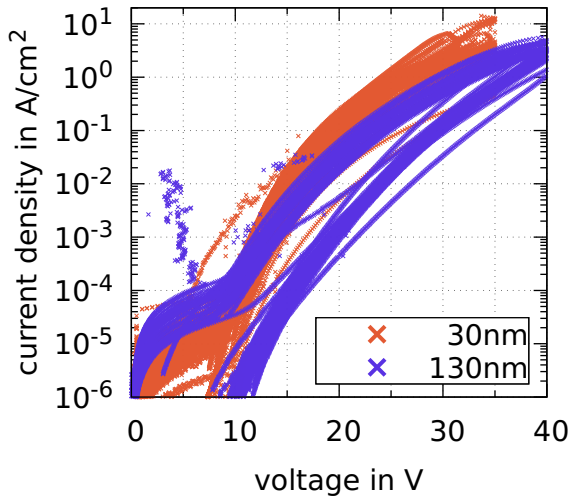
(a) IV characteristics of devices with different thickness of the initial seed (30 nm vs. 130 nm).
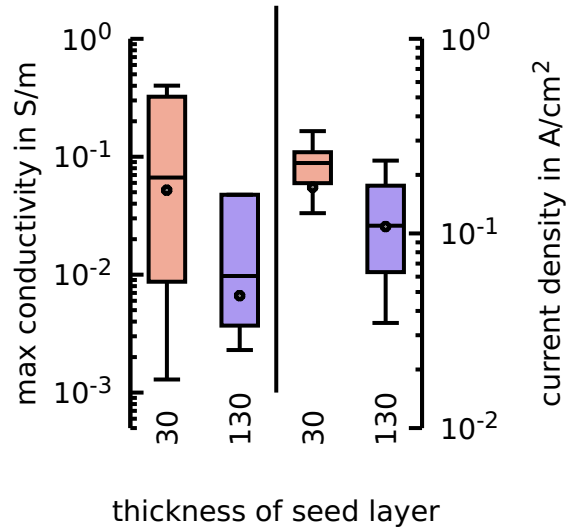
(b) Parameters extracted from measurement in figure 4.59a: **left:** maximum conductivity, **right:** current density at 25 V

Figure 4.59: MSM devices with 400 nm of total thickness: Seeds are grown at 140 °C for 10 min. The bulk is doped at 1 wt.%.
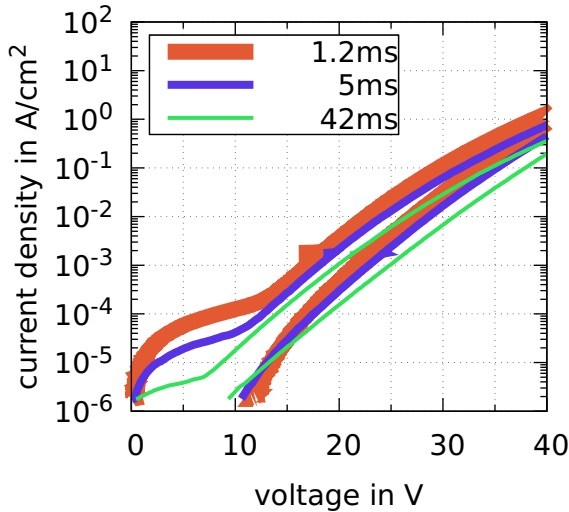
(c) IV measurement at different integration times: The seed is made from 30 nm undoped rubrene.

instead of crystallizing 20 nm of undoped material and then adding 30 nm of doped material is less complex in total.

To investigate this idea, two sets of devices are prepared: one with a thin, doped seed (30 nm, 1 wt.%) and one with a thick doped seed (130 nm, 1 wt.%). The thickness of both films is then increased by the usual epitaxy to 400 nm in total, with the same doping concentration. The thickness of the film has to be increased to avoid short circuits. The results of the measurements of these devices can be seen in figure 4.59a. In general, the behavior of both sets is similar, while most of the devices made with the thicker seed show a lower current at the same voltage. This is reflected in the variation of current density at 25 V shown in figure 4.59b, where the thicker doped devices have on average only half of the current density of the standard configuration. A similar result can be seen, comparing the maximum conductivity.

Two explanations are feasible: The presence of dopants in thick seeds prior to crystallization hinders proper crystal growth to a stronger degree than for thin seeds, reducing the mobility for a significant portion of the film. Alternatively, doping could be less effective when introduced in the seed, resulting in a smaller effective carrier concentration in a significant part of the film. In summary, it is not advisable to increase the thickness of the seed more than necessary for crystallization. Crystal formation might not be influenced, however, the electrical performance decreases in the case of thick doped seeds.

4.2.4 Temperature-Dependence of Undoped and Doped Rubrene Thin-Films

All data in this section so far are collected at room temperature. It is possible to extract valuable information about physical properties from the temperature-dependence of certain properties. The thermal activation of the carrier density of a doped system can give access to the energetic distance between the states involved. Thermal activation of charge carrier mobility is an indicator for or against band transport. Extracting information from IV curves at room temperature alone is difficult – as is described at the beginning of this section – since the material parameters themselves cannot be accessed directly. Trying to extract the temperature behavior of one specific parameter from the change of the IV characteristics, adds one additional level of complexity. Physical processes like the activation of charge carriers in doped and undoped semiconductors with temperature can be modeled via the Arrhenius equation

$$k \propto e^{\frac{E_A}{k_B T}}, \tag{4.16}$$

with k as the likelihood of the process and E_A as the activation energy. Presented in an Arrhenius plot ($ln\left[f\left(\frac{1}{T}\right)\right]$), these processes present a linear dependence, from which the activation energy can be deduced. The activation energy for

the charge transport in typical organic semiconductors is between 200 meV to 600 meV [226].

None of the measurements shown in this chapter features a clear Arrhenius dependence over the entire temperature range. This is not surprising, since different processes can counteract each other (e.g. charge carrier density decreases, while mobility increases with decreasing temperature). Different regimes can be indicative of different processes. Most graphs are nonetheless provided including an Arrhenius fit or an appropriate other mathematical description. It should not be mistaken as a claim that a certain process involves a specific energetic dependence. It serves as a parametrization of the behavior and gives a sense of the degree of change.

weight-based concentration in wt.%	mole-based concentration in mol% (F6TCNNQ)	mole-based concentration in mol% ($C_{60}F_{36}$)	mole-based concentration in mol% ($W_2(hpp)_4$)
0.1	0.24	0.26	0.17
0.25	0.59	0.66	0.43
0.5	1.2	1.3	0.86
1	2.3	2.6	1.7
2	4.6	5.1	3.4
5	11.1	12.2	8.4
10	20.9	22.7	16.1
20	37.3	39.8	30.2

Table 4.3: Reference for different definitions of doping concentration for a selected set of values.

4.2.4.1 Temperature-Dependence of Undoped Rubrene Thin-Films

In doped films, one of the primary influences on the temperature-dependence is the activation of charge transfer from the dopant molecules to the host. Measuring intrinsic – undoped – films gives access to the activation of charge carrier mobility and – theoretically – intrinsic carrier generation, although in an intertwined way. However, since most organic semiconductors are slightly doped due to impurities, the influence of activation of this impurity doping might overshadow the other effects. It is nevertheless an important starting point for discussion.

MSM devices based on undoped triclinic rubrene (glass substrate and Au electrodes) are characterized with IV measurements at different temperatures. Seeds are grown from 30 nm at 140 °C for 10 min. The total thickness is increased via epitaxy to 400 nm for the first and 1000 nm for the second sample. IV curves for the 400 nm device are shown in figure 4.60a. The current density is virtually independent of temperature over the entire temperature range measured. It
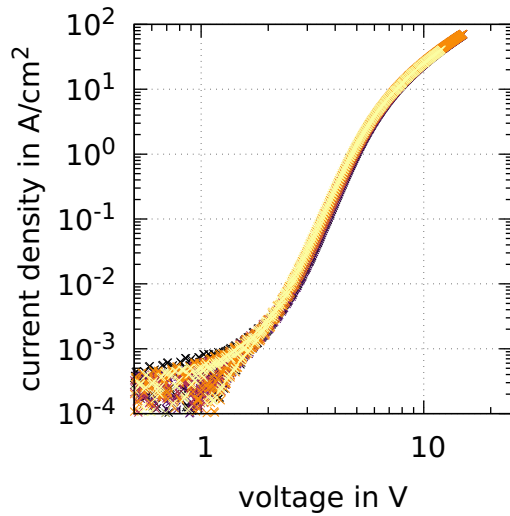
(a) Temperature-dependence of the current density of an MSM device with a total thickness of <u>400 nm</u> of undoped rubrene. The temperature is changed from 300 K to 120 K (bright to dark colors).
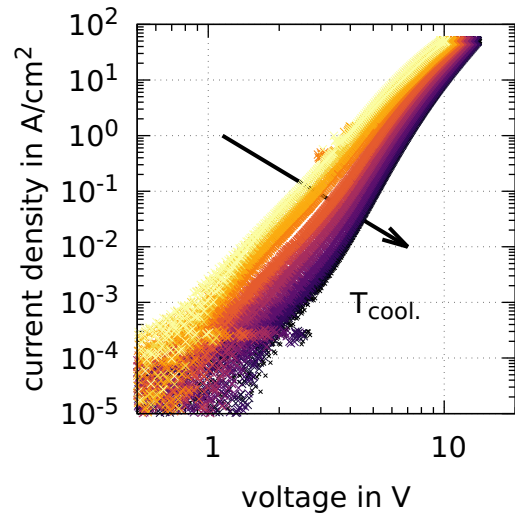
(b) Temperature-dependence of the current density of an MSM device with a total thickness of <u>1000 nm</u> of undoped rubrene. The temperature is changed from 300 K to 80 K (bright to dark colors).
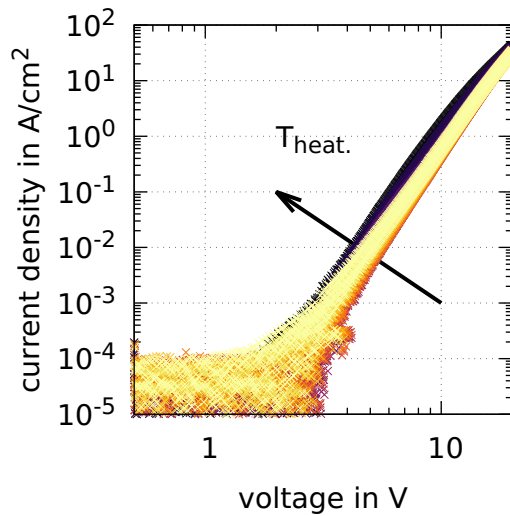
Figure 4.60: Temperature-dependence of the current density of undoped MSM devices. Arrows indicate the direction of temperature change. Arrows indicate direction of the change within each set of curves.
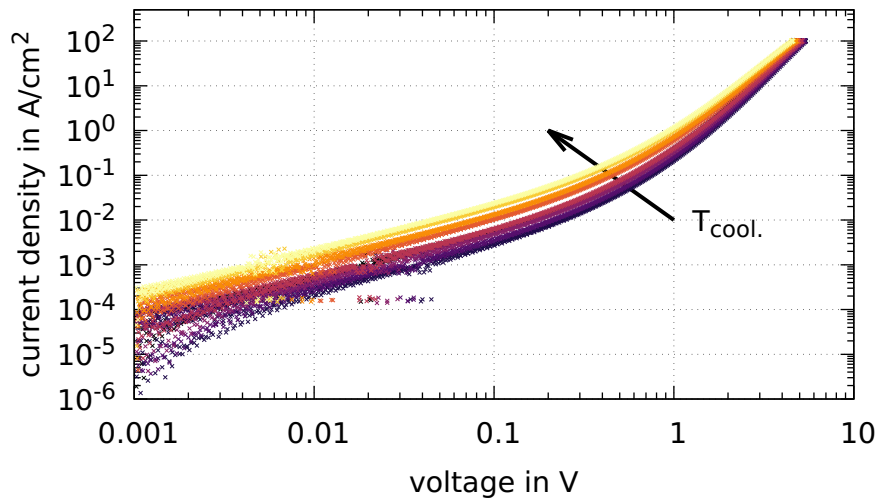

(c) Temperature-dependence of the current density of an MSM device with a total thickness of <u>1000 nm</u> of undoped rubrene. The temperature is changed from 77 K to 340 K (bright to dark colors).

Figure 4.61: Parameters extracted from data in figure 4.60b and 4.60c.
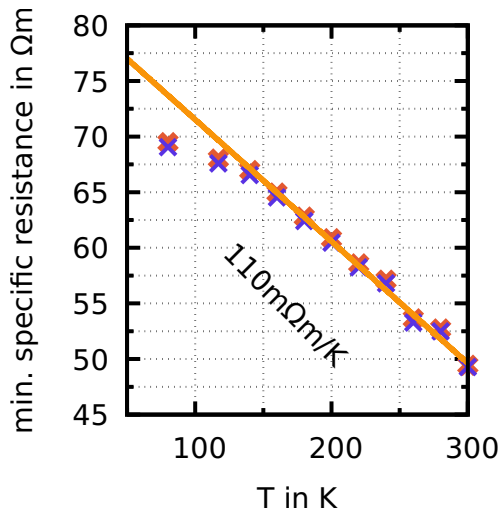
(a) Minimum specific resistance (figure 4.60b, T from high to low): **blue (dark), thin:** voltage low to high, **red (bright), fat:** voltage high to low, **orange:** linear fit for values above 120 K serving as parametrization.
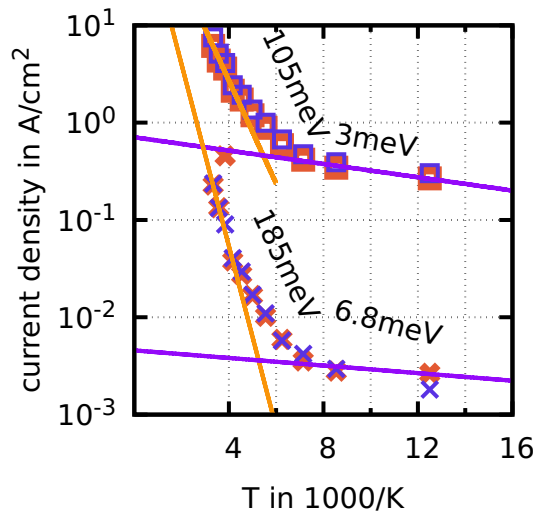
(b) Current density at 3 V(crosses) and 6 V(boxes) (figure 4.60b, T from high to low): **blue (dark), thin:** voltage low to high, **red (bright), fat:** voltage high to low, **orange:** Arrhenius fit for high-temperature regime, **violet:** Arrhenius fit for the low-temperature regime.
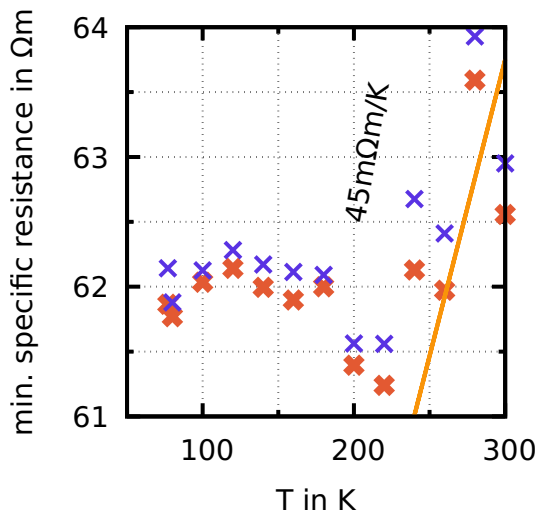
(c) Minimum specific resistance (figure 4.60c, T from low to high): **blue (dark), thin:** voltage low to high, **red (bright), fat:** voltage high to low, **orange:** linear fit for values above 260 K serving as parametrization.
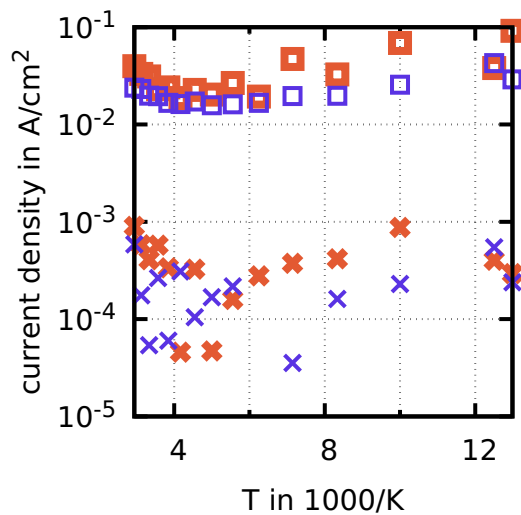
(d) Current density at 3 V(crosses) and 6 V(boxes) (figure 4.60b, T from high to low): **blue (dark), thin:** voltage low to high, **red (bright), fat:** voltage high to low.

is unlikely that all parameters influencing the conduction are independent of temperature. The most probable explanation is that counteracting effects cancel each other out in the observed temperature regime. Since it is physically infeasible to assume that carrier density increases with decreasing temperature, the conclusion has to be an increasing mobility. That would be a strong hint for band-like transport in the c-direction of these crystals. A similar conclusion in regard to the temperature-dependence of the charge transport in the c-axis is drawn by Blülle et al. [227].

This behavior changes for the thicker device. The behavior during cooling (see figure 4.60b) and subsequent re-heating (see figure 4.60c) is not identical. Cooling the sample leads to a steady decrease in current density. The decrease is moderate in comparison to common organic semiconductors [110]. Increasing the temperature[8] after initial heating does not recover the lost conductivity but results in an almost temperature-independent behavior. Only the medium-voltage regime shows any significant change. To quantify the change, the same parametrization is applied that is used for the doped devices. Figures 4.61a and 4.61b summarize the behavior of the cooling part. Neither the maximum conductivity nor the minimum resistance showed any strong change within the temperature range. An Arrhenius fit was not applicable. A linear fit can be applied for the specific resistance over a large part of the temperature regime. Thus, resistance increases by $110\,\text{m}\Omega\,\text{K}^{-1}$ when the film is cooled. Scaling this to a specific temperature (here, 300 K is chosen), defines the linear temperature coefficient as:

$$\rho\left(T\right) = \rho_0\left(1 + \alpha(T - T_0)\right), \tag{4.17}$$

with $\rho_0 = \rho(300\,\text{K})$, the resistance at the temperature reference point. For this measurement follows: $\alpha = -2.2 \cdot 10^{-3}\,\text{K}^{-1}$. The magnitude is comparable with common metals like silver ($3.8 \cdot 10^{-3}\,\text{K}^{-1}$ [200]) or gold ($3.4 \cdot 10^{-3}\,\text{K}^{-1}$). Inorganic semiconductors show a stronger temperature response: Si: $-75 \cdot 10^{-3}\,\text{K}^{-1}$, Ge: $-48 \cdot 10^{-3}\,\text{K}^{-1}$.

The current density shows a stronger dependence on the temperature. However, the behavior changes for different temperature regimes and is not identical for different external biases. Two distinct regimes can be defined in the Arrhenius plot. They can be described by an activation energy of 185 meV at 3 V and 105 meV at 6 V in the high-temperature regime and 6.8 meV at 3 V and 3 meV at 6 V in the low-temperature regime. Taking the crossing position of the two Arrhenius fits as a reference, the transition appears at 180 K. A change in behavior is not uncommon in organic semiconductors. Ullah et al. [228] measured the field-effect mobility of C_{60}-based devices and their temperature-dependence. They describe a shift in activation energy from 300 meV at 4 V gate bias visible

---

[8]The up and down-sweep are not the same samples but neighboring devices on the same substrate, due to a short circuit of the initial device mid-measurement. While the absolute values show a slight offset, the general behavior matches that of the other measured samples. These two devices are chosen because their temperature sets are complete.

at high temperatures, to an activation energy of 50 meV at low temperatures. The change appears at 170 K. An explanation is not given. Pundsack et al. [64] measured the c-axis mobility in furnace-grown orthorhombic rubrene crystals. Here, the mobility increases from 300 K to 180 K and decreases for further cooling. Activation energies are not provided. If the points at which the trend changes are similar due to a fundamental property of the material or out of coincidence is difficult to evaluate with the data at hand. To give a further point of reference, measurements by Minari et al. [229] on pentacene transistors show activation energies between 75 meV to 100 meV for poly-crystalline films and 57 meV to 60 meV for single-grain devices. Thus, the data measured for the activation energy of rubrene thin-films is in a similar range as other organic crystalline systems. How much of the temperature-dependence can be attributed to a change in mobility and how much is activation of charge carriers can only be evaluated with temperature-dependent mobility measurements.

Most publications do not discuss if the temperature behavior is reversible. In the case of the measured thick crystals, this is not the case. Figure 4.61c shows the minimum specific resistance heating the device back up from 77 K to 340 K. Initially, the resistance is constant. It starts rising at approximately 220 K at a rate of 45 mΩ K^{-1}, corresponding to α =0.7 · 10^{-3} K^{-1}. It thus shows the opposite behavior of the initial cooling experiment. The current density – in figure 4.61d – does not match the first experiment either. Initially, the current decreases with temperature untill around 200 K, after which it increases. The general change is small. A fit is not reasonable. A non-reversible temperature-dependence is difficult to explain with fundamental electronic phenomena. A different interpretation might be a phase transition within the crystals structure. Jurchescu et al. [37] report such an effect in orthorhombic rubrene single-crystals. The mobility drops suddenly at 150 K, which cannot be reversed. They argue that the mechanical stress within the crystal resulting from thermal shrinking and expansion during cooling and heating causes cracking and thus additional grain boundaries. The presence of local stress in orthorhombic thin-films is confirmed by Verreet et al. [50]. This theory might also explain why the temperature-dependence of the thin (400 nm) device is negligible, while the thicker device (1000 nm) shows the discussed effects. A minimum thickness might be required to create enough internal stress to cause local cracks. These effects are interesting from a fundamental standpoint alone. Structural measurements of cooled and heated samples might give further insight into these phenomena.

4.2.4.2 Temperature-Dependence of p-Doped Rubrene Thin-Films

Now that a baseline is established for undoped films, doped devices are focused. Since intrinsic devices feature a negligible temperature-dependence when the film is thin (400 nm), any changes in temperature-dependence can be attributed to the doping. This change can stem from either the activation energy of the carrier
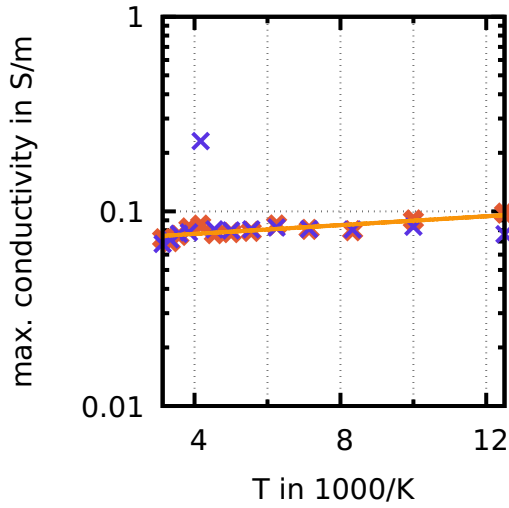
Figure 4.62: Temperature-dependence of the current density of an MSM device with a total thickness of 400 nm of 0.1 wt.%-doped rubrene in the triclinic crystal phase. The temperature is changed from high to low: 300 K to 120 K (bright to dark colors).

generation or a change in mobility due to a change in morphology. In figure 4.62, the IV characteristics of a MSM device doped with 0.1 wt.% are shown. The seed is made from 30 nm undoped rubrene, heated at 140 °C for 10 min to reach the triclinic phase on a glass substrate with Au electrodes. In contrast to the undoped device from figure 4.60a, a clear temperature-dependence is noticeable. However, the effect is smaller than in the thick undoped films (figure 4.60b) and reversible. The observed temperature-dependence can thus be attributed to the doping. Extracted parameters are described in figures 4.63a to 4.63c. Similar to the thick, undoped film, the resistance is increasing when cooled. The rate is lower at $16 \, \mathrm{m\Omega \, K^{-1}}$, equivalent to $\alpha = -1.45 \cdot 10^{-3} \, \mathrm{K^{-1}}$. The maximum conductivity of this device does not change significantly with temperature. A different way to describe this shift is via the voltage necessary to reach maximum conductivity. The data are shown in figure 4.63c. An equivalent parametrization can then be given as $4.6 \, \mathrm{mV \, K^{-1}}$ of additional driving voltage needed.

An Arrhenius plot of the current density shows a linear regime at temperatures above 160 K. Activation energies of 39 meV at 6 V and 43 meV at 3 V can be extracted. At even lower temperatures, the decrease in current density levels off and reverses partially. Since the effect is reversible and extracted activation energies at different voltages are close, it seems likely that the temperature-dependence is caused by the activation of the dopant. Presumably, a counteracting effect regarding the mobility takes over at low temperatures.

To separate the charge carrier density from the mobility, a separate temperature-dependent CV-analysis is shown in figure 4.64. The experiment is analogous to the measurements of doping efficiency in chapter 4.2.3.2. A linear fit of the Arrhenius plot gives an activation energy of 74 meV for a device doped with 5 wt.%. It corresponds well with the difference in energy between the corresponding

energetic states of rubrene and F6TCNNQ of approximately 100 meV. This temperature-dependence is stronger than the overall dependence of the IV data in figure 4.63b. This is indicative of an increase in mobility with decreasing temperature; a sign for band transport. However, the doping concentrations of the device used for the IV measurement and the Schottky diode used in the CV-analysis are not the same in these experiments. A different dependence on the individual properties depending on the doping concentration is feasible. Nevertheless, Pundsack et al. [64] found hints for band-like transport in c-axis direction in orthorhombic single-crystals. Considering the high vertical mobility found in these layers, band-like transport seems likely.
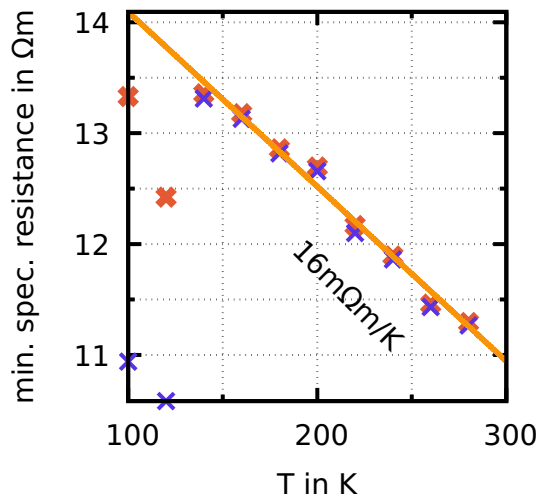
(a) Temperature-dependence of the minimum specific resistance, **orange:** linear fit in the high-temperature regime for parametrization.
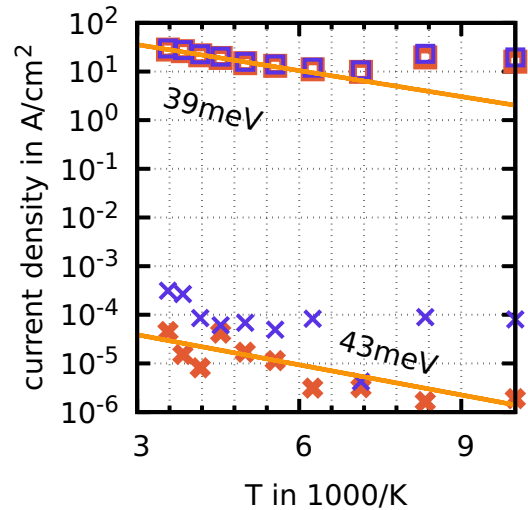
(b) Temperature-dependence of the current density at 3 V(crosses) and 6 V(boxes), **orange:** Arrhenius fit in the high-temperature regime.

Figure 4.63: Parameters of temperature-dependence of MSM devices with a total thickness of 400 nm of 0.1 wt.%-doped triclinic rubrene: Data are extracted from figure 4.62. **red (bright), fat:** voltage sweep from low to high, **blue (dark), thin:** voltage sweep from high to low.
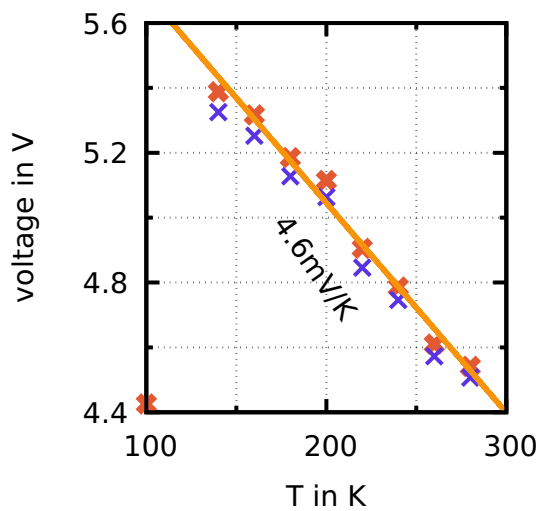
(c) Temperature-dependence of the voltage at which maximum conductivity occurs $V(\sigma^{max})$, **orange:** linear fit for parametrization.
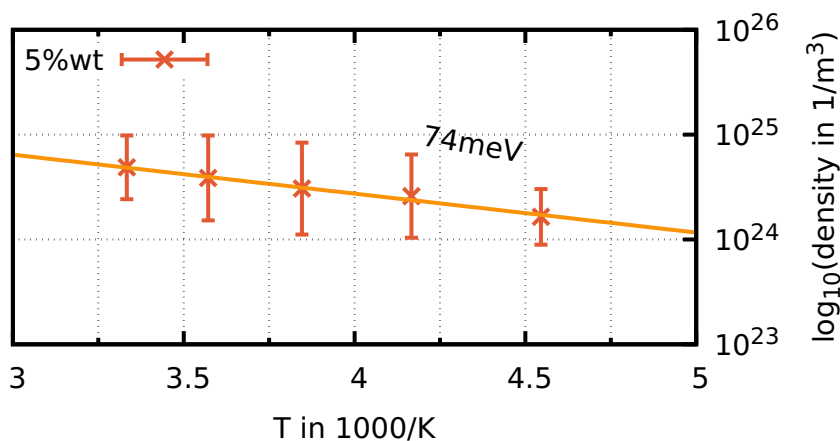
Figure 4.64: Free carrier density extracted from the Mott-Schottky plot of the CV measurement of Schottky diodes with 250 nm of p-doped layer and 50 nm intrinsic at different temperatures. The resulting Arrhenius fit is added as a line.

4.2.4.3 Temperature-Dependence of n-Doped Rubrene Thin-Films

To complete the temperature analysis, n-doped samples are investigated using the same procedure. Since hole mobility is significantly greater than electron mobility, the intrinsic films are hole dominated. The n-doped films show the properties of electron transport; a direct comparison between the intrinsic films and the n-doped films – as it was helpful for the p-doped experiments – is not possible. An MSM device is prepared with 400 nm of rubrene – to avoid cooling induced cracking – doped with 1 wt.% $W_2(hpp)_4$. The seed is made from 30 nm undoped rubrene, heated at 140 °C for 10 min on a glass substrate with Au electrodes. The corresponding IV curves are presented in figures 4.65a and 4.65b. Especially films with a low n-doping show distinct charging effects at low voltages during the initial part of the measurement. For clarity, the sweep from low to high voltages (figure 4.65a) and the sweep from high to low voltages (figure 4.65b) are shown in separate figures to make distinguishing individual curves easier. However, the general behavior of the down-up and up-down voltage sweeps is almost identical. The resulting temperature-dependence is similar to the p-doped devices. The shape of the IV curve stays intact but is shifted along the voltage axis towards higher values. The kink and subsequent plateau that is present in the upwards slopes of figure 4.65a does not shift with temperature. It is further indication that this effect is not related to the device itself but caused by surface charging. This type of kink is not present in the backward sweeps at high temperatures but appears – to a significantly lesser extent – when the device is cooled. The origin and cause of this change are unclear.

Figure 4.66a shows the change of maximum conductivity with temperature. As can be seen in the IV curves, the maximum slope – conductivity – does not change with temperature. It is not feasible to fit any dependence on these data. However, similar to the p-doped films, the minimum specific resistance decreases with temperature (see figure 4.66b). This shows that while the dynamic

Figure 4.65: Temperature-dependence of the current density of an MSM device with a total thickness of 400 nm of 1 wt.% $W_2(hpp)_4$ doped rubrene. The temperature is changed from high to low: 300 K to 80 K (bright to dark colors).
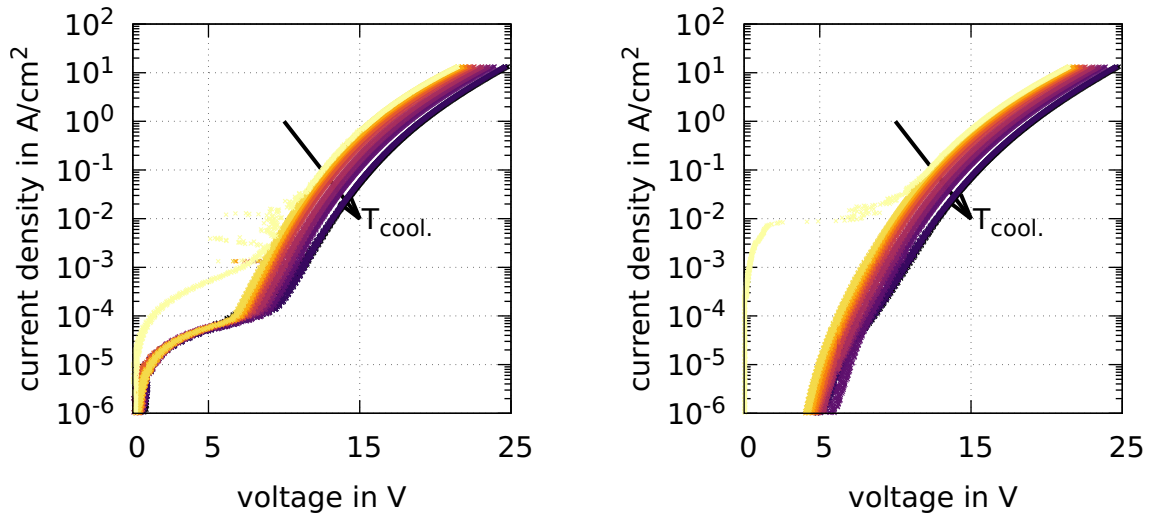
(a) Upwards slope = low to high voltages.

(b) Downwards slope = high to low voltages.

properties (differential conductivity) stay constant, the static properties – absolute resistance – can change. Here, the specific resistance changes by $220\,m\Omega\,m\,K^{-1}$. This is the strongest absolute change from all films, twice as large as the intrinsic film. However, the relative change is smaller than the p-doped device and the thick intrinsic film with $\alpha = -0.81 \cdot 10^{-3}\,K^{-1}$, due to the larger initial resistance. Arrhenius plots of the data, shown in figure 4.66c, present a complicated picture. At 20 V bias, linearization can be applied for high temperatures, featuring an activation energy of 29 meV. The low-temperature region of this measurement does not show a proper linear region. Current densities measured at 15 V show two distinct regimes: a high-temperature activation, showing a decrease in current with cooling with an activation energy of 112 meV and a low-temperature region where the current is increasing again when cooled. The corresponding activation energy is 5.4 meV. Interpretation of this behavior is even more difficult than for the p-doped films, since neither values for carrier densities nor electron mobility for the relevant scenarios are available. Nevertheless, the total temperature-dependence of the n-doped films is – similar to the p-doped devices – moderate. Neither the doping nor charge carrier mobility shows a strong activation with temperature in the investigated regime.

(a) Temperature-dependence of the maximum conductivity, **orange:** linear fit in the high-temperature regime.
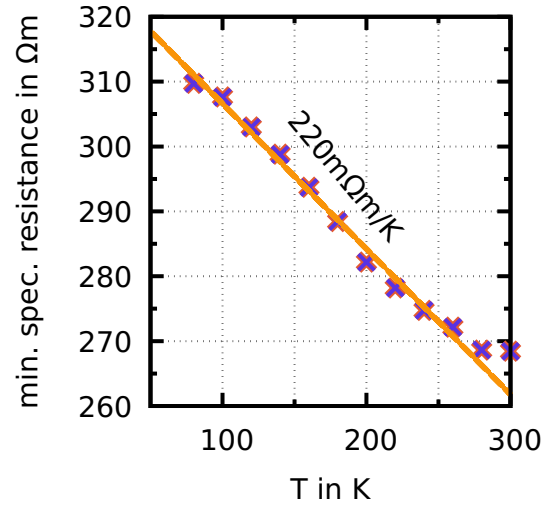
(b) Temperature-dependence of the minimum specific resistance, **orange:** linear fit in the medium temperature regime.

Figure 4.66: Temperature-dependence MSM devices with a total thickness of 400 nm rubrene doped with 1 wt.% $W_2(hpp)_4$: Data are extracted from figure 4.65a and 4.65b. **red (bright), fat:** voltage sweep from low to high, **blue (dark), thin:** voltage sweep from high to low.
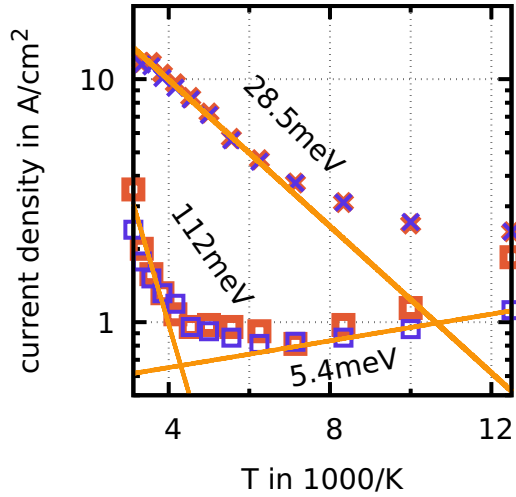
(c) Temperature-dependence of the current density at 15 V(boxes) and 20 V(crosses), **orange:** Arrhenius fits.

type	d_{total}	T-change	E_A at V	$\frac{\partial \rho}{\partial T}$	$\alpha(300\,\text{K})$
unit	nm	-	meV(volt)	$\text{m}\Omega\,\text{m}\,\text{K}^{-1}$	K^{-1}
intrinsic	1000	high to low	185(3), 105(6)	−110	$-2.2 \cdot 10^{-3}$
intrinsic	1000	low to high	-	45	$0.7 \cdot 10^{-3}$
p-type	400	high to low	43(3), 39(6)	−16	$-1.45 \cdot 10^{-3}$
n-type	400	high to low	112(15), 28.5(20)	−220	$-0.8 \cdot 10^{-3}$

Table 4.4: Summary of parameters extracted from temperature-dependent measurements.

4.2.5 Light-, Load-, and Air-Dependence of Rubrene Thin-Films

This last subsection summarizes measurements that do not fit into previous sections but highlight special effects that are relevant for further developments or might open up future applications. The first effect regard the light sensitivity of thin-films of rubrene. The IV characteristic of an MSM device with a total thickness of 400 nm of undoped triclinic rubrene is shown in figure 4.67a. During one measurement, the measurement chamber is covered with a lid, such that no light can reach the device. In a second measurement, the same device is illuminated with a halogen lamp that is connected to the setup. The sample is measured in vacuum and the light from the lamp is transferred using an optical waveguide. Heating of the sample can be excluded. The two resulting IV curves behave similarly. However, the illuminated device shows an increased

Figure 4.67: Current density over voltage of MSM devices with 400 nm undoped rubrene at different lighting conditions: Devices are built on glass with 30 nm of structured Au as electrodes.
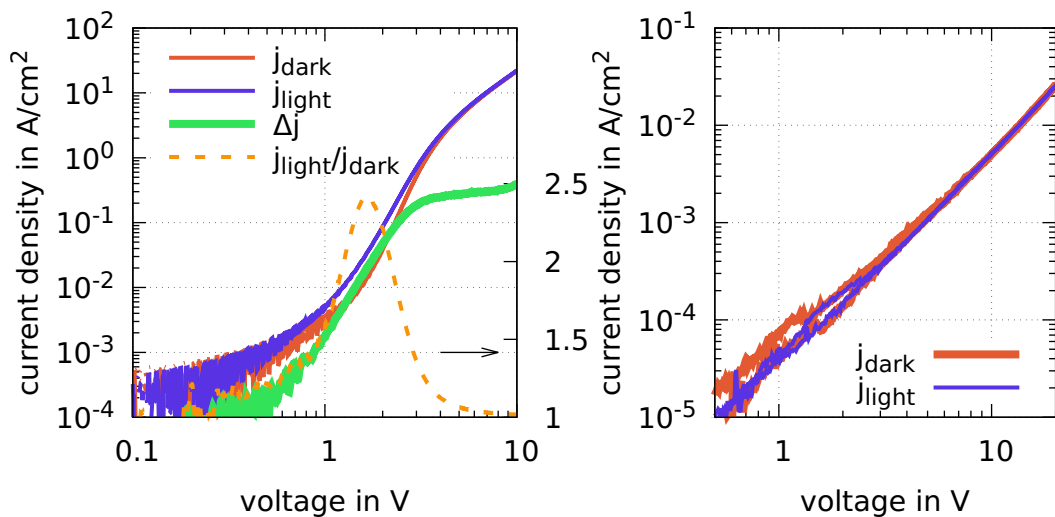
(a) Crystalline triclinic layers: The seed is made from 30 nm of undoped rubrene heated at 140 °C.

(b) Light sensitivity of uncrystallized amorphous rubrene.

current throughout most of the measured voltage range. For further analysis, the difference between the two curves is calculated. Due to the strong variation at low voltages, a Savitzky-Golay algorithm is used to smoothen the curves prior to calculation. The extra current originating from the illumination (green in figure 4.67a) grows with voltage. However, the increase levels off strongly at around 2 V to 3 V. The orange curve shows the ratio between the current density of the illuminated device and the dark device. It describes how much more current flows when light is present. The maximum of this relative current appears at 1.63 V. The illuminated samples feature current 2.4 times larger than the dark device.

Light absorption by rubrene has been shown already in literature. Solar cells based on orthorhombic rubrene films shown by Verreet et al. [50] are among the first vertical devices utilizing this material system. However, triclinic devices have not been presented yet. It is also noteworthy that amorphous films of the same thickness and device structure do not show any additional current through illumination (see figure 4.67b). The absorption must thus be a property of the crystal and not the individual molecules. It must be taken into account that the device shown here is not optimized to function as a light detector. Significant improvement could be achieved utilizing the effects at semiconductor (pn-)junctions and replacing the Au electrodes with transparent ITO. Triclinic thin-films of rubrene might be a suitable material system for use in organic photodiodes. There are, however, indications regarding singlet fission, suggesting the use of the monoclinic polymorph [230].

4.2.5.1 Load-Dependence of Rubrene Thin-Films

As shown in the previous sections, thin-films of crystalline rubrene are capable of sustaining high current densities and thus large power densities. Nevertheless, a high current through a resistive load always results in resistive losses in the form of heat. It is, therefore, relevant to investigate how reproducible individual measurements are, if damage to films or devices is common, and to which extent it influences the measurement.

Figure 4.68a shows the IV curves measured for a 400 nm sample made from a triclinic seed of 30 nm grown at 140 °C for 10 min. The entire voltage sweep is repeated 50 times. Each measurement takes 32 s. The entire set is, thus, measured within 27 min. The individual curves experience a shift along the voltage axis with each new measurement. However, fits of the maximum conductivity show no change. The dynamic properties of the device stay the same. The change in the behavior of the device is reflected in the specific resistance, shown in figure 4.68b. A linear dependence is visible and a rate of the increase in resistance can be determined to $0.34\,\Omega\,m$ per complete measurement. This process and the corresponding parameter cannot be universal, since the measurements for the temperature-dependence do not show any significant change with temperature.
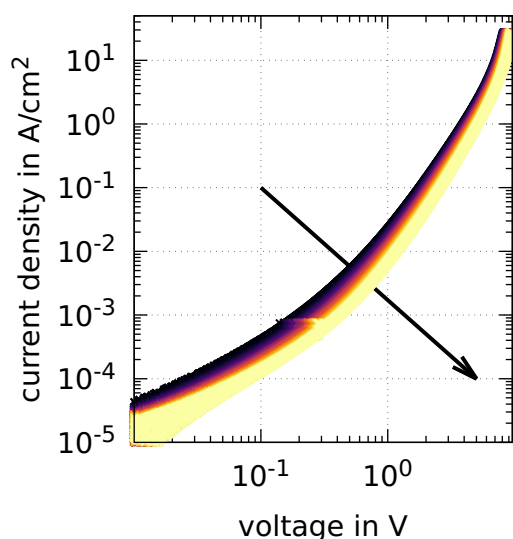
(a) Repeated IV measurement of a MSM device: The same voltage sweep is repeated 50 times (dark to bright = first to last).
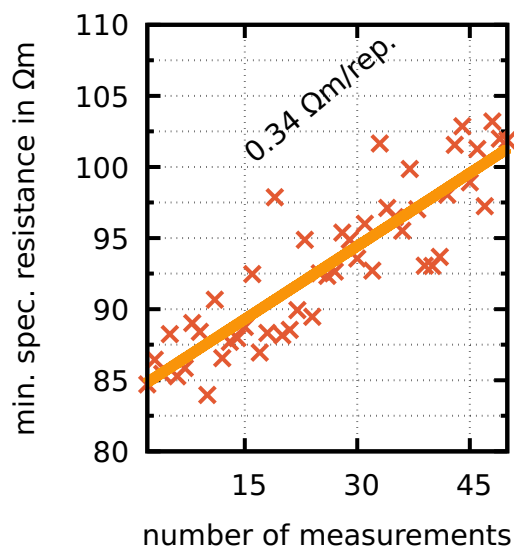
(b) Minimum specific resistance extracted from figure 4.68a: Resistance increases linearly with each additional sweep.

Figure 4.68: Load resistance of doped and undoped films of triclinic rubrene: Total thickness of all devices is 400 nm. Seeds are grown from 30 nm at 130 °C for 15 min.
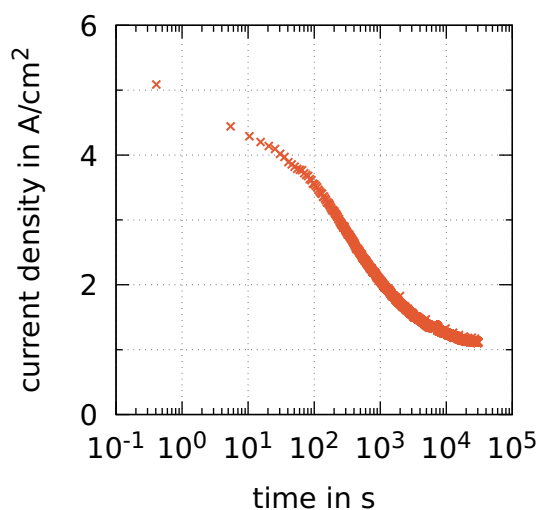
(c) Current density at 30 V of 400 nm of rubrene doped with 0.5 wt.% $W_2(hpp)_4$: data points are 5 s apart.

During these measurements, the samples are stressed even stronger (higher peak voltage and current density) but do not show any change. The stress measurement can nevertheless serve as a self-check for the temperature-dependent measurement with the 1000 nm thick samples. There, a rate of $0.11\,\Omega\,\mathrm{m\,K^{-1}}$ is found. With steps of 20 K between individual sweeps, this results in a change of $2.2\,\Omega\,\mathrm{m}$ between measurements. It can be assumed that the measured dependence is mostly caused by the reduction in temperature. However, some part could be caused by degradation due to repeated measurement.

Similar results can be found for doped devices. Figure 4.68 shows the change in current density of a sample consisting of 400 nm of triclinic rubrene doped with 0.5 wt.% $W_2(hpp)_4$ at 30 V. The current through the device sinks during the entire measurement. After 8 h, the current density is only 20 % of its initial value.

4.2.5.2 Air-Stability of Rubrene Thin-Films

Devices based on organic semiconductors are usually not suitable to be used or stored in ambient air. Water and oxygen are both typical sources for device degradation due to the formation of traps and chemical decomposition [231]. This subsection presents the changes in properties of doped rubrene thin-films based on electrical measurements. It is not a full analysis but gives hints towards the compatibility of this material system with ambient atmosphere.

Figure 4.69a shows the IV curves of a p-doped triclinic film. The total thickness of the film doped with 2 wt.% F6TCNNQ is 400 nm. It is grown on a 30 nm seed at a glass substrate with Au electrodes that is heated at 140 °C for 10 min. The device is measured in vacuum[9], immediately after being exposed to air, and 20 min after being exposed to air. Even in the linear plot, no significant change between the three measurements is visible. It can be concluded that p-doped films of triclinic rubrene do not show significant degradation in ambient atmosphere on a short timescale.

---

[9]Flooding experiments in nitrogen are less precise, since a quick replacement of the initial gas is more difficult to realize.

Figure 4.69: Current density over voltage of MSM device with 400 nm of doped triclinic rubrene in dependence of air exposure.
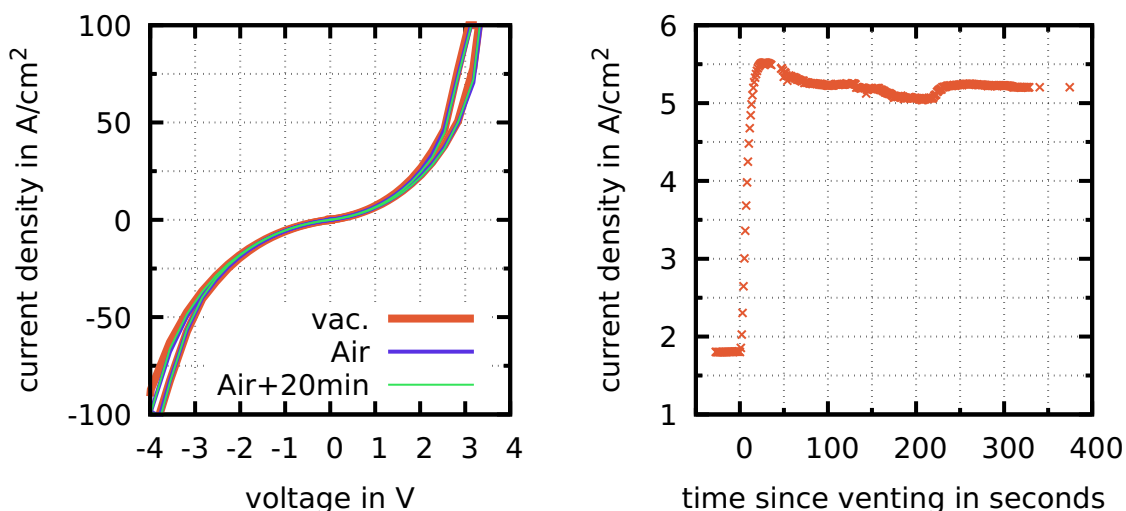
(a) Layer is doped with 2 wt.% F6TCNNQ: Comparison between device measured in vacuum, immediately after flooding with ambient air, and 20 min after the flooding of the chamber.

(b) Device is doped with 0.1 wt.% F6TCNNQ: The device is initially in a vacuum. The measurement chamber is flooded with ambient air at $t = 0$ s.

Different behavior can be seen when the measurement is done during the flooding of the chamber. In figure 4.69b, a similar device is shown with a doping concentration of 0.1 wt.%. The current density is measured every 1 s at an external bias of 2 V. Prior to flooding, the current is stable. Once gas is let into the chamber, the current density rises within 25 s by a factor of 3. After an initial small decrease, the current density remains stable. This phenomenon could have two different reasons. First, the increase in current might be caused by doping via oxygen. Many organic semiconductors have been found to be p-dopable in ambient air [232]. The molecular doping of the first experiment is significantly higher than that of the second one. It is conceivable that 2 wt.% is sufficient to suppress any additional p-doping of the material. The increase by a factor of 3 is below the effect of an increase in doping from 0.1 wt.% to 2 wt.%.

The second explanation is based on the measurement method itself. The device in the second experiment is initially kept in a vacuum, since a flooding experiment in nitrogen is less precise due to the problematic mixing of the two gases. Sudden flooding can change parameters of the film that are not necessarily related to the type of the surrounding gas. Rang et al. [220] found a dependence of the carrier mobility in rubrene on the hydrostatic pressure surrounding the film.

Regardless of the exact phenomenon at play, the change introduced by the flooding is comparably small. No significant change in conduction can be expected for the p-doped thin-films of triclinic rubrene crystals.

That neither of the doped films shows a strong immediate change in behavior due to ambient air is convenient for processing of these films. Nevertheless, considering the tendency for oxidization of rubrene as a molecule [233] and as a crystal [234] that is surprising. Experiments by Raimondo et al. [235] showed evidence for an epitaxial layer of rubrene oxide on the surface of thin-film crystals which actively suppress further oxidation. Thus, a degradation of the bulk of the semiconductor seems to be effectively slowed. It is worth mentioning, however, that devices made in the scope of this thesis which are stored for an extended amount of time in ambient air, show significant reduction in performance.

4.2.6 Summary

All three crystal structures analyzed in the first half of this chapter are conductive in vertical directions. The variation in conductivity is large within sets of theoretically identical devices, due to the random nature of the crystallization. The vertical conductivity of the triclinic crystal phase is the largest among these three polymorphs due to a large charge carrier mobility of $10.3\,\mathrm{cm^2\,V^{-1}\,s^{-1}}$. This is the highest value for vertical charge carrier mobilities in organic semiconductors reported in literature to date. The vertical mobility of the orthorhombic platelets type is slightly lower at $3.3\,\mathrm{cm^2\,V^{-1}\,s^{-1}}$.

All crystals can be p-doped using F6TCNNQ. The doping efficiency is in general low (<5 %), even for modest doping concentrations and decreases further for

higher doping ratios. Doping universally increases the conductivity of all crystal phases. Both, absolute currents and effectiveness of hole injection are improved. The triclinic films are shown to be n-dopable with $W_2(hpp)_4$, although the doping efficiency seems to be even lower than for the p-system. The conductivity of the n-doped films initially decreases, due to the lower electron mobility in the system. Large injection barriers are present in the n-doped devices. Doping of the seed is possible for the triclinic and spherulitic crystal phase. If sufficient doped material is added on top of an undoped seed, the doping of the seed is not necessary, though.

The temperature-dependence of these films is low in general. The strongest change is measured for the doped films, indicating a freeze-out of the doping. For short amounts of time, the effect of air on the films is small. However, longer exposure tends to reduce device quality.

4.3 Chapter Summary

The last section of this chapter contains a total summary of the most important parameters of the three important crystal phases in a tabularized form. It is meant as a quick reference for parameters. Less fleshed-out topics like temperature and air-sensitivity and the details of each experiment can be found in the main text.
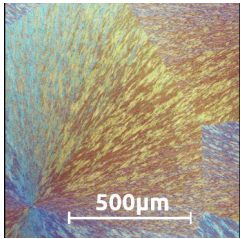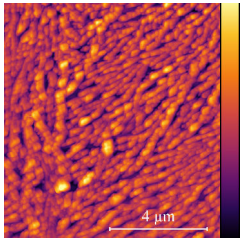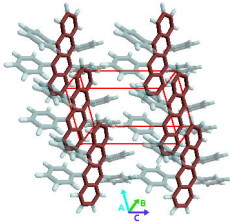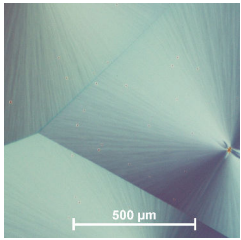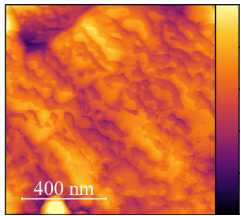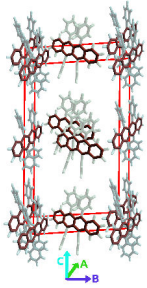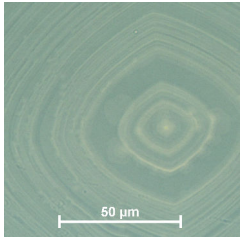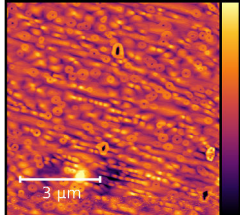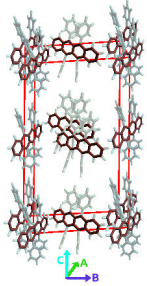
type	polarized micrograf	structure (identification)	AFM micrograf	roughness	structure	vertical axis
triclinic		• dendritic branching • radially changing birefringence		20 nm to 40 nm (defined by seed thickness)		b-axis (no XRD signal)
orthorhombic spherulite		• straight dendrites • radially changing birefringence		2 nm to 6 nm (plateaus of 2 nm to 5 nm)		mainly: c-axis (26.8 Å), side peak a-axis (6.75 Å)
orthorhombic platelets		• single crystals • grain-wise uniform birefringence		1 nm to 4 nm (plateaus of 1 nm to 2 nm)		mainly: c-axis (26.9 Å), side peak b-axis (14.6 Å)

Table 4.5: Summary of physical properties of rubrene films I

type	growth temperature	mobility vertical, lateral	tested dopants	highest successfully tested doping concentration	doping efficiency
triclinic	120 °C to 150 °C	$(10.3 \pm 4.9)\,cm^2\,V^{-1}\,s^{-1}$, $1.5 \cdot 10^{-2}\,cm^2\,V^{-1}\,s^{-1}$	• F6TCNNQ • $C_{60}F_{36}$ • $W_2(hpp)_4$	• 2 wt.% in seed • 10 wt.% in bulk	• 4.7 % to 0.56 % for doping of 0.1 wt.% to 5 wt.% F6TCNNQ • lower for $W_2(hpp)_4$
orthorhombic spherulite	170 °C to 180 °C	vertical not measured $3 \cdot 10^{-1}\,cm^2\,V^{-1}\,s^{-1}$	• F6TCNNQ • $W_2(hpp)_4$	• 2 wt.% in seed • 20 wt.% in bulk	• p-efficiency higher than n-efficiency
orthorhombic platelets	160 °C to 170 °C	$(3.3 \pm 2.5)\,cm^2\,V^{-1}\,s^{-1}$, $7 \cdot 10^{-2}\,cm^2\,V^{-1}\,s^{-1}$	• F6TCNNQ • $W_2(hpp)_4$	• 0.5 wt.% in seed • 10 wt.% in bulk	• p-efficiency higher than n-efficiency

Table 4.6: Summary of physical properties of rubrene films II

5 Diodes Based on Crystalline Rubrene Thin-Films

This chapter discusses the first real electronic devices based on the rubrene thin-film crystals shown in section 4.1. The properties derived from the intrinsic and doped films presented in section 4.2 are the base for the following discussion. This investigation of organic diodes serves a double role. First, these diodes represent the precursor to the bipolar junction transistors that are subject to chapter 7. Secondly, they are interesting in themselves, to extract material properties or function as an electronic device. Similarly to the doping analysis, possible parameters that can be extracted from the data are discussed first. This is followed by an investigation of Schottky diodes, as the simplest possible configuration and at last pin diodes as the most complex structure. The chapter closes with a discussion of technological applications in the form of Organic Light Emitting Diodes (OLEDs) and Ultra High Frequency (UHF) rectifier circuits based on these diodes.

5.1 Parametrization of Electrical Properties of Organic Diodes

In section 4.2.1, the lack of proper parameters for the assessment and comparison of organic semiconductor materials (i.e. Metal-Semiconductor-Metal (MSM) devices) is discussed. In principle, the same problem prevails for organic semiconductor diodes. Several parameters (e.g. on/off-ratio, threshold voltage) derive themselves from the intended purpose of the device and are widely used. However, the exact way of extraction is not always obvious. Due to noise and intermediate outliers in the measurement, parameters are extracted from data that is filtered via a Savitzky-Golay algorithm, using a fifth-order power-law over a window of eleven data points. The data shown in Current-Voltage (IV) curves is unfiltered. Figure 5.1b shows a model IV curve of the pin design. It is useful to separate the IV curve into forward (depletion layer is flooded with charge carriers = high current) and reverse (depletion layer thickness increases = low current) direction. The forward direction is split into three parts again. Regime I is the low-voltage regime dominated by leakage currents. Regime II is the Shockley regime ideally dominated by diffusion through the depletion layer. Regime III is the conduction regime. It is reached once the current is limited by neither injection nor the diode itself but trap-release or Space Charge Limited Current (SCLC).

- **current density** j, **conductivity** $\sigma^{\mathbf{max}}$, and **specific resistivity** $\rho^{\mathbf{min}}$ are defined analogously to section 4.2.1. The properties of these parameters, their benefits, and their flaws are in principle identical.

- **threshold voltage** $V_{\mathbf{Th}}$**:** In general, a threshold voltage describes a voltage above which the behavior of the IV characteristic of a device changes significantly and reproducibly[1]. At first, this value is thus a purely technical property that describes the onset of rectification (split of forward and reverse

---

[1]This excludes the point at which a device is destroyed by thermal-load or high electric field.

Figure 5.1: Definition of parameters for extraction from IV curves of diodes.
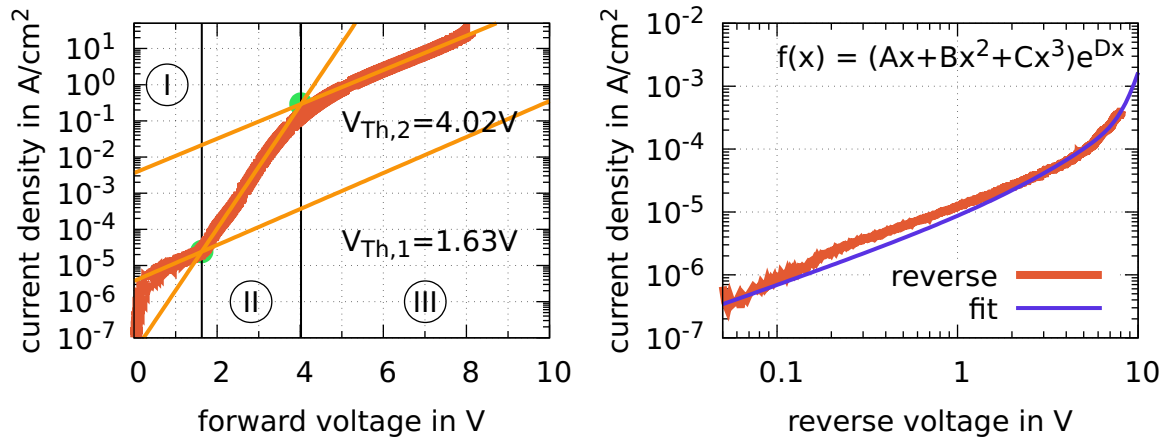
(a) Define regime I (leakage), II (Shockley), and III (conduction) with exponential fits for each regime: intercepts between lines define threshold voltages $V_{Th,1}$ and $V_{Th,2}$, intercept of the linear fits with the x-axis defines saturation current $j0$.

(b) Reverse current can be modeled via $f(x)$ for most diodes, as long as measurement is not limited by the accuracy of the measurement tool and breakdown of the diode does not occur.

direction) in these diodes. Whether a physical meaning can be derived from this value is not necessarily decisive as long as it can be used as a useful tool for comparison between different designs. Here, two distinct threshold voltages are defined. The first marks the transition from regime I to regime II while the second gives the onset of regime III. The values are generated as the crossing points of linear fits onto the lin-log depiction of the forward current.

- **exponential fits and saturation current j_0:** The linear fits used to extract threshold voltages are in their core representations of the form $j = j_0 e^{\frac{V}{\beta}}$. The parameter j_0 can be used as a rough measure of magnitude, while β represents the degree of voltage dependence. Regime I is dominated by ohmic leakage currents and features a mostly linear or low power-law dependence, particularly well visible in log-log depictions. An exponential function is not well-suited to describe the overall shape of the curve. The fit is more useful to extract the previously discussed threshold voltage. Regime III is dominated by trap-release or SCLC currents. Series resistance can be limiting at high currents as well. Ideally, this regime should be parameterized via various power-laws [98]. Although theoretically usable as a measure of magnitude, j_0 extracted from these regimes are only used sparingly in the following discussion.
  The most interesting part is regime II which is ideally dominated by diffusion current through the depletion zone of the diode. It is suited the most to extract properties of the junction. An ideal diode follows the Shockley

Figure 5.2: Influence of changing leakage current and physical threshold voltage on the technical threshold voltage defined in figure 5.1a: Shockley current is modeled via $j_{\text{Sh.}}(V) = j_0 \left(e^{\left(V - V_{\text{Th}}^{\text{ph.}} \right)} - 1 \right)$, while leakage current is modeled via $j_{\text{le.}}(V) = aV^2$.
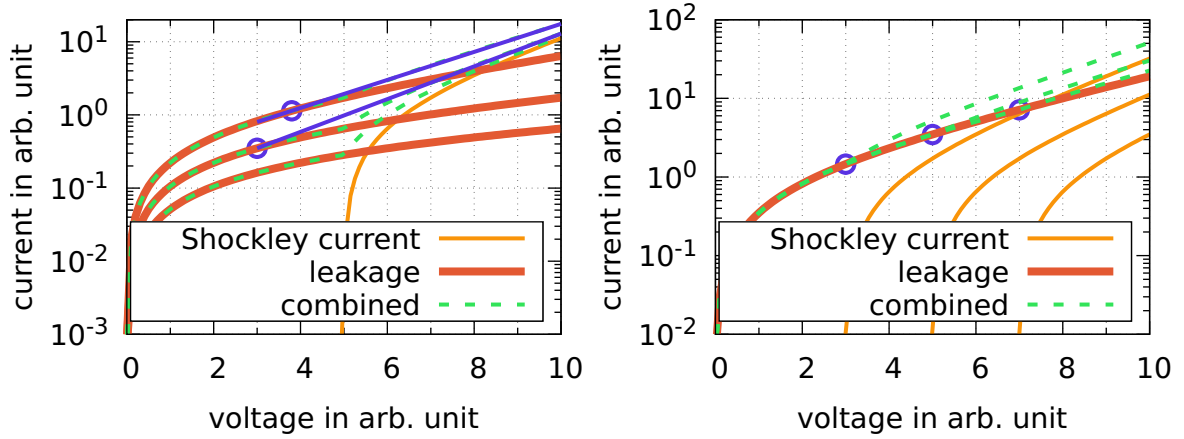
(a) Impact of a shift in leakage current on the extracted threshold voltage: Although the onset of the Shockley regime (II) is identical for all three cases, the resulting threshold voltage shifts and is thus not representative of the physical threshold voltage. For certain ratios between leakage current and Shockley regime current, a threshold voltage cannot be extracted at all.

(b) Impact of a shift of the onset of the Shockley regime, represented by a shift in the physical threshold voltage $V_{\text{Th}}^{\text{ph.}}$, with constant leakage current: The technical threshold voltages follows the physical threshold voltage accordingly.

equation 2.46. It is problematic that the supposed Shockley regime is only visible at comparably large voltages ($\gtrsim 2\,\text{V}$ in forward direction). The ideal Shockley equation is only valid for voltages smaller than the built-in potential, since the depletion layer is completely flooded at that voltage and current is no longer purely diffusion-based. It is likely that other processes such as injection limitation, trap-release, and recombination are influencing the regime II, since these types of effects are visible in the regimes I and III as well. Two explanations are possible here. First, the Shockley equation does not describe the entire device but only the junction itself. A more precise description takes the existence of series resistances into account. This approach effectively splits the voltages between the individual components (resistor vs. ideal diode) and thus shifts the onset of the Shockley regime to higher external biases. When the series resistance itself shows a non-linear voltage dependence (SCLC, second diode in series, etc.), the resulting voltage shift can be complicated and difficult to analyze, depending on the exact distribution of voltage drop within the series. In strongly granular materials[2], charge carriers can lump up at the interfaces

---

[2]A material is granular, when it consists mainly of highly ordered crystalline material, interrupted

between the individual grains, effectively creating two distinct regions for SCLC [67]. The crystals are assumed to be well-ordered in vertical direction, however, sufficient structural measurements are not available. Furthermore, the Shockley equation can be expanded with an ideality factor, taking recombination and similar effects into account. In the following analysis, the ideality factor is commonly close to two. Some devices show a large ideality. These diodes are not used for comparison.

Once the voltage is significantly larger than the thermal voltage (»25 mV), which for these diodes is always given in regime II due to the usually large leakage currents, the Shockley equation can be reduced to a simple exponential dependence. It is then possible to define a threshold voltage for this exponential increase that is governed by the defining energetic gap [236] (e.g. the equivalent bandgap) as

$$j(V) = j_0 e^{\left(\frac{eV}{nk_{\mathrm{B}}T} - \frac{E_{\mathrm{A}}}{nk_{\mathrm{B}}T} \right)} = j_0 e^{\left(\frac{e\left(V - V_{Th}^{ph.}\right)}{nk_{\mathrm{B}}T} \right)}. \tag{5.1}$$

Information about the activation energy of the system can then be extracted from the threshold voltage. However, the threshold voltage $V_{Th}^{ph.}$ is difficult to extract from simple IV data. Only from temperature-dependent measurements, the absolute values can be calculated [236]. The threshold voltages $V_{Th1,2}$ defined earlier are only technical parameters (device properties) and do not directly correspond with the physical property (energetic properties of the material system). However, under certain circumstances, $V_{Th,1}$ behaves equivalently to the physical threshold voltage as described in equation 5.1. From the change of this quantity, it is then possible to deduce the change of the physical threshold voltage, if other parameters are sufficiently similar between devices (i.e. the ideality factor). Figures 5.2a and 5.2b show model IV curves for the change of regime I to regime II. The leakage current is modeled with quadratic equations aV^2 with varying factors a, appropriate for the voltage-regime closer to the threshold. At low voltages, a linear extrapolation is usually more fitting, however, the explicit shape of the leakage current is not relevant for the following discussion. The diode current is given by the simplified Shockley equation 5.1 with varying threshold voltages. The resulting diode current is the sum of both components. In figure 5.2a the physical threshold voltage of the diode component is kept constant, while the magnitude of the leakage current is changed. Despite the threshold voltage of the diode part being identical for all three devices, the technical threshold voltage extracted with the previously described method changes. It is worth noting that the strong change in the position

---

rarely by hard grain boundaries. The majority of the transport is effective, while a "pile-up" of charge carriers can occur at the internal interfaces.
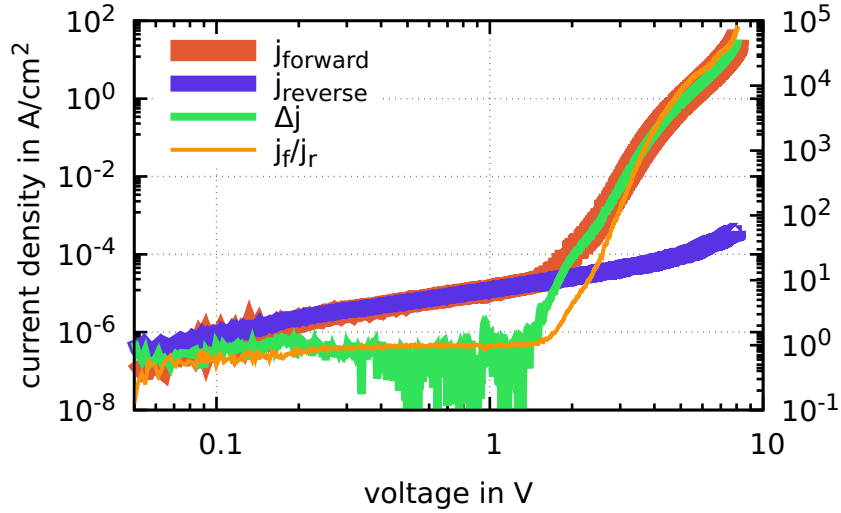
Figure 5.3: Definition for the extraction of the on/off-ratio: Current in reverse and forward direction is extrapolated point-wise by a quadratic algorithm. The on/off-ratio is defined as the highest ratio between forward and reverse current at the same absolute voltage.
left axis: forward current, reverse current, and $\Delta j = j_\mathrm{f} - j_\mathrm{r}$,
right axis: on/off-ratio = $\frac{j_\mathrm{f}}{j_\mathrm{r}}$.

of the threshold voltage that can be seen here is caused by the extreme change in leakage current between the individual devices set in this analysis. Nevertheless, although the effect might be significantly weaker in real devices, the technical threshold voltage shows a "fake" shift when the leakage current is not constant between devices. In contrast, figure 5.2b presents devices with constant leakage currents and varying diode current. Here, the crossing points change according to the change in threshold voltage. If the low-voltage leakage current is comparable, a shift in technical threshold voltage can be taken as an indication for a shift in the physical threshold voltage and thus a shift in activation energy E_A.

Alternatively, this bandgap is included in the saturation current density j_0 too in the form of:

$$ j_0 \propto e^{\frac{E_\mathrm{A}}{k_\mathrm{B}T}}. \tag{5.2} $$

- **on/off-ratio:** The on/off-ratio is a technical property of a diode aimed at rectification. It is defined as

$$ on/off(V) = \frac{j_\mathrm{forward}(V)}{j_\mathrm{reverse}(V)}. \tag{5.3} $$

Since the current increases exponentially in forward direction and the leakage current in reverse is governed by power-laws, the on/off-ratio is voltage-dependent and usually increases with voltage. Figure 5.3 shows the forward and reverse current of an exemplary pin diode and the corresponding on/off-ratio at each voltage. Since the forward and reverse currents are virtually

identical below the threshold voltage, the on/off-ratio is approximately one. The maximum on/off-ratio is usually found at the maximum applied voltage. Thus, similar to the maximum conductivity, the value extracted depends on the measurement routine. The value is nonetheless useful, since IV curves are measured close to the point of destruction of each device. The corresponding on/off-ratio represents the maximum capability that could be expected in a real application during continuous (non-pulsed) operation. IV characteristics are measured with different settings for forward and reverse sweeps. The maximum voltages that can be applied before thermal breakdown of the device are different in both directions. Since the points measured during one sweep are separated via a logarithmic scaling, identical points for forward and reverse direction are thus not common. To fill the gaps between points, quadratic extrapolation is used. Due to the high density of measurement points, the derivation is small.

Similar to the previous analysis, not all parameters can be extracted from every IV measurement and not every parameter is valuable in every context. The following section presents data mostly in the form of sets of full IV curves, followed by a selection of parameters that are relevant for the discussion. If data are shown in lin-log representation, forward direction is displayed on the positive voltage side. For figures in log-log representation, the upper branch depicts the forward direction.

The diode devices presented in this chapter are produced at two different vacuum evaporation tools. One (called UFO) is based on single 25 mm × 25 mm substrates, utilizing mask IV2. The operation of this tool is highly flexible and allows for a large degree of freedom when designing the stack of a diode. Due to the mask layout, 25 single diodes with varying active areas are produced per substrate. Since the individual layers alone already show a significant variation in their conduction properties, these devices are used to assess the statistical variation of the diodes devices. The second evaporation tool (Lesker) produces sets of 6 × 6 substrates of size 25 mm × 25 mm. It is ideal to generate a series of varying layer thicknesses with high reproducibility. The mask used here is design HF1. However, only 4 individual devices are made per layer stack. This number is too low to allow for a proper statistical analysis, especially considering that a certain amount of devices shows defects and cannot be measured at all. Thus, the influence of variation in certain parts of the diode (layer thickness, doping concentration, etc.) is presented using data based on single devices made via the Lesker evaporation tool, while the variation of individual properties is assessed from larger sets of devices created at the UFO tool. Since the materials and general procedure are the same for both setups, it might be valuable to study the different behavior of devices made at both tools.

5.2 Schottky Diodes Based on Triclinic Rubrene Crystals

The decisive property of a diode is its rectifying behavior: conductivity in forward direction is larger than in reverse direction. The simplest possible diode configuration is the Schottky diode. It is based on the Schottky contact formed between a semiconductor and a metal electrode with fitting energy levels. The specifics are discussed in section 2.3.1. Schottky diodes are used for high-frequency applications in electronic circuits due to their generally low depletion capacitance. Since the depletion width in organic semiconductors are short, organic Schottky diodes contain an additional layer of intrinsic semiconductor material to reduce leakage currents. For the Schottky diodes, only the triclinic phase is used as a model material. The seed crystals of all devices are grown from 30 nm to 40 nm undoped rubrene at 130 °C for 15 min.

In contrast to pin diodes, Schottky diodes are unipolar devices. Since the charge carrier mobility of holes is significantly larger than the mobility of electrons [216], hole-based Schottky diodes are investigated only. As a p-dopant, F6TCNNQ is used exclusively. The devices investigated here are built using the Lesker evaporation tool. Thus, statistical analysis is not available for these experiments. Two different stack configurations are used. The first (shown in figure 5.4a) is equivalent to the MSM devices investigated earlier and originates from a set of devices in which Schottky diodes and pin diodes are built side by side. It is used for Schottky diodes with a 5 wt.% doping of F6TCNNQ. The seed itself is initially undoped but is doped remotely by the p-doped layer, as described in section 4.2.3.3. The remotely doped seed is considered to be part of the p-doped

Figure 5.4: Standard stack order for Schottky diodes based on crystalline rubrene.
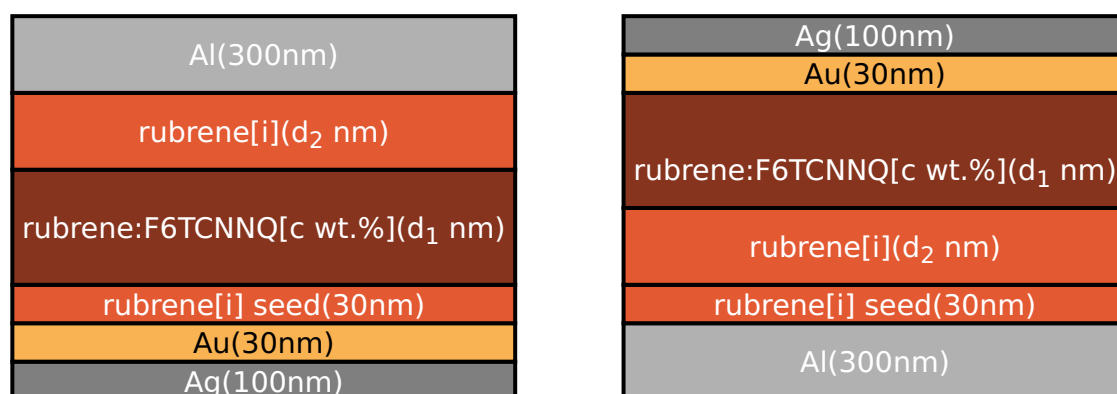
(a) Standard configuration for Schottky diodes: Since the stack starts with the p-layer, remote doping of the seed is required to realize efficient hole injection. This configuration is compatible with pin diodes in the same manufacturing run.

(b) Upside down configuration used for Schottky diodes built with the Lesker tool: Since the intrinsic layer is on the bottom, no reliance on remote doping is necessary to allow for good injection. Comparability with other measurements might be limited.

film, thus, the total thickness of the p-side contains the thickness of the seed. The thickness of the intrinsic layer is well-defined in this configuration as the thickness of the intrinsic film added via epitaxy. The second set of devices uses a reverse stack order (shown in figure 5.4b), aimed directly at Schottky diodes. It is used for devices with 0.1 wt.%, 0.5 wt.%, and 10 wt.% of doping with F6TCNNQ. The undoped seed is now part of the intrinsic layer of the film. Remote doping of the seed at the p-side, to allow for optimal hole injection, is thus not necessary. The thickness of the intrinsic layer discussed here is thus the thickness of the seed combined with the added intrinsic material. Considering the rough surface of this crystal phase (discussed in 4.1.1.4), the total thickness of the intrinsic film is less well-defined as the first configuration. Additionally, the defining (Schottky) interface between the Al and the intrinsic layer is not identical for both device types due to the reversed order of deposition.

Both configurations result in well-functioning Schottky diodes, with in principle similar behavior. However, a direct comparison between the two configurations is sometimes not possible. The comparison between the two sets of devices is limited to where deviation seems acceptable. Data are marked accordingly.

5.2.1 Area-Dependence and Burn-in Phenomena

All Schottky diodes are prepared with the Lesker evaporation system, thus, proper statistical data are not available for the following analysis. Per substrate, only four devices are made, two with an active area of $100\,\mu m \times 100\,\mu m$ and two at $200\,\mu m \times 200\,\mu m$. To evaluate the influence of certain parameters of the diode (i.e. doping concentrations and layer thicknesses), it is especially important to investigate external influences first. A weak dependence on the electrode size can be seen in the IV experiments of section 4.2.3, however, the variation between identical samples is larger than between differently sized samples in single layers. This is most likely a result of the random crystallization process. The variation in forward direction between technically identical diodes is smaller than for individual layers. The details are discussed in section 4.2.1 during the statistical analysis of the pin devices. The variation introduced by the crystallization seems to be reduced due to the junction. Thus, the influence of the electrode size might not be irrelevant here. Figure 5.5 shows two Schottky exemplary diodes with identical stack (p-layer: 200 nm[5 wt.%], i-layer: 200 nm p-bottom configuration) from the same substrate. The device with the larger active area shows a larger current density. This behavior is consistent with most other devices investigated, which can be explained in two different ways. The assumed active area might not be identical to the real active area. However, the deviation from the intended electrode size is measured via microscopy and is similar for both electrodes. Due to the size of the carrier-substrate (6×6 individual substrates), the deviation is not identical between different samples. However, the total variation is small.
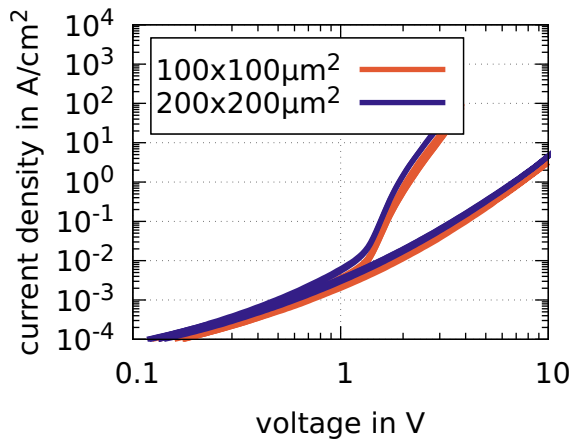
Figure 5.5: Influence of the active area on the current density for Schottky diodes based on rubrene: Large active areas show a higher current density, hinting at additional lateral leakage currents.
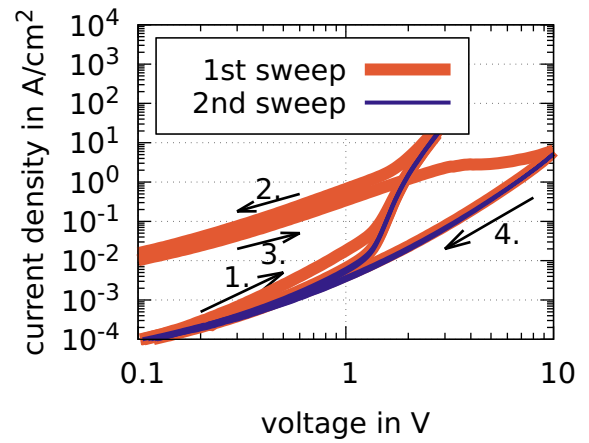
Figure 5.6: Instability and burn-in behavior: Most devices show an initial instability or tendency to follow branches in the IV characteristic of higher conductivity. After one full sweep, the IV curve resets itself to its final form. (arrows give the temporal order for the 1st sweep).

Alternatively, the change in current density can stem from additional current being transported around the active area. As a conclusion, for direct comparison between samples when no statistical evaluation is possible, only devices featuring the same active area are used.

A phenomenon that is present in all types of triclinic rubrene-based diodes, but much more common in the Schottky diodes is a distinct burn-in. It manifests itself in different ways, of which all have in common that the first IV sweep of a diode has in at least some parts a significantly increased current. However, once sufficient voltage is applied to the device or a sufficiently high current flows, the diode is set to a stable state. Consecutive voltage sweeps are stable and reproducible. Figure 5.6 shows one example for which the current does not return to the initial branch after reaching the highest current in forward direction. It remains on this higher current branch initially even in reverse bias. It can be assumed that additional parallel leakage paths are created during the first sweep that remain during reverse operation. Once the diode is swept to its maximum in reverse direction, the final low-current branch is set. Since the surface and consecutively the structure of the layer stack shows a high roughness (see section 4.1.1.4), pinholes are likely. A burn-in is necessary to destroy any initial pinholes via thermal damage to reveal the bulk properties of the device. If a device shows this or a similar type of behavior to a significant degree, a burn-in is performed prior to the proper measurement.

5.2.2 Influence of Doping on Schottky Diodes Based on Triclinic Rubrene

The Schottky diodes discussed here feature only two active parts (p-layer and i-layer) and hence in total three possible parameters to vary (thickness and doping concentration). The variation of these parameters can change the characteristic of the devices, however, it can also serve as a tool to extract the physical properties of the material system. At first, the doping concentration is varied. Devices with four different doping concentrations are presented in figures 5.7a and 5.7b. The p-doped film has a total thickness of 300 nm. The intrinsic layer thickness is in total 100 nm. The overall stack of all these devices is thus identical, aside from a slight variation resulting from the doping.

All four devices show rectification behavior, however, the order of magnitude of the current is changed significantly when doping is varied. For an ideal organic Schottky diode, the doping concentration of the p-doped side should have minor influence on the device parameters. This is not the case here. Devices built with 0.1 wt.% and 0.5 wt.% doping are similar to each other. The same is true for devices built with 5 wt.% and 10 wt.% of doping. However, it has to be noted that the device with 5 wt.% is built with a different geometry than the others.

Parameters extracted from these data are shown in figures 5.8. The absolute specific resistance is significantly reduced, once higher doping is introduced. This means, significantly less dc-bias voltage is needed to bring the diode into its point of operation which in turn simplifies the circuit design. The higher current for stronger doping implies a series resistance in the lightly doped devices. This is supported by the shape of the IV curves. While the highly doped devices show

Figure 5.7: Influence of the p-doping concentration on the IV characteristics of Schottky diodes based on triclinic rubrene (thickness of p-layer: 300 nm, thickness of intrinsic layer: 100 nm), key is valid for both figures (*: device is built according to stack in figure 5.4a).

(a) lin-log representation.

(b) log-log representation.
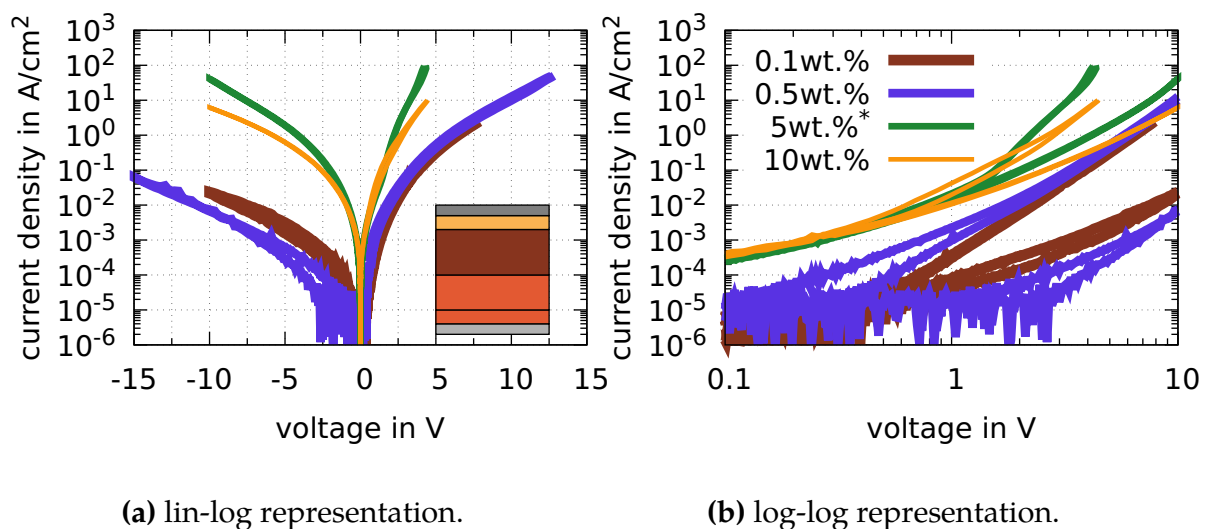
Figure 5.8: Parameters extracted from data shown in figure 5.7 (data points at 5 wt.% are based on devices built according to stack in figure 5.4a).
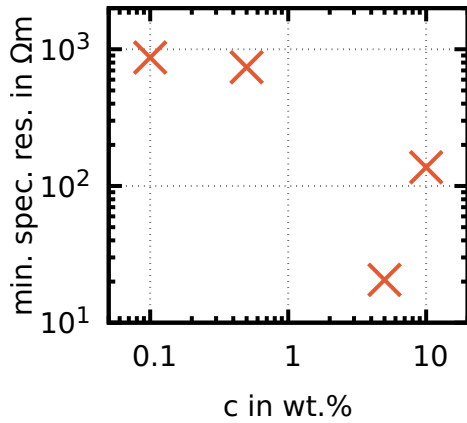
(a) minimal specific resistance, assuming a constant field.
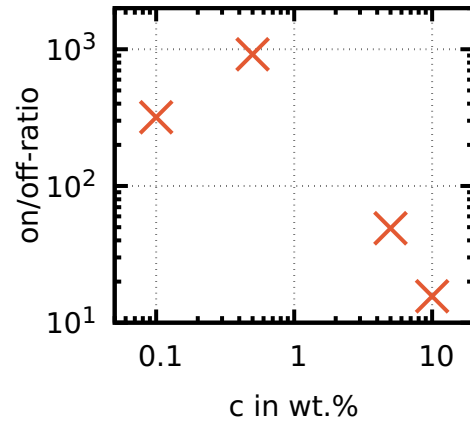
(b) Maximum on/off-ratio.
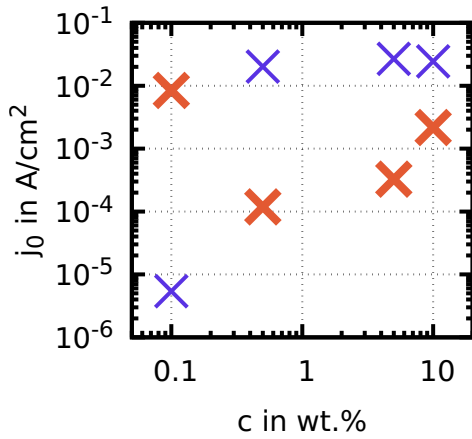
(c) Saturation current for exponential fit in the Shockley regime II (red, (bright), fat), and regime III (blue (dark), thin).
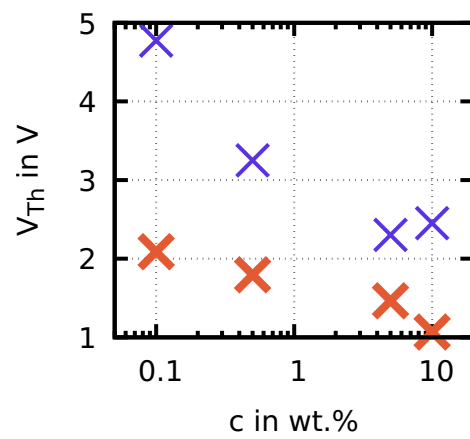
(d) Threshold voltages: $V_{\text{Th},1}$ (red (bright), fat), $V_{\text{Th},2}$ (blue (dark), thin).

distinct regimes, indicating an SCLC or trap-release type charge transport for higher voltages, the lightly doped devices show a more linear high-current regime. This might be caused by the comparably thick doped film, since the conductivity is lower based on the lower doping. However, this should facilitate SCLC-like transport. Alternatively, an injection barrier at the Au interface can cause an additional series resistance that might be reduced by the stronger doping.

On the other hand, the on/off-ratio of the lightly doped devices is higher by up to two orders of magnitude. The increase in current in forward direction is overcompensated by an even stronger increase in reverse bias for the strongly doped devices. The total thickness of the stack is identical for all devices and it is unlikely that the doped film is the limiting part of the vertical transport. Inferential, the bulk of the reverse and forward leakage current must originate

from an area effect. Current is collected from the area surrounding the active part of overlapping electrodes, since the organic material is not structured. Especially the part of the electrode leading toward the active area. A higher doping concentration can thus facilitate a more efficient lateral transport while keeping the vertical conductivity comparable.

Figure 5.8d shows the threshold voltage of these diodes. A steady decrease is visible with increasing doping concentration for both threshold voltages. However, since the leakage current is changing, this is only true for the technical threshold voltage. No further information about the intrinsic physical threshold voltage defined by the bandgap can thus be extracted from this set of devices. Analyzing the saturation currents extracted via the exponential fits can only give rough information about the order of magnitude of the current in certain regimes. The saturation current of regime III is almost identical for the three devices with the higher doping. It indicates that in this regime all devices are limited by the same process. In regime II, j_0 increases with doping concentration (except for the lowest doping concentration). The theory of an ideal pn junction, however, would predict a decrease in saturation current.

In summary, the properties of Schottky diodes based on triclinic rubrene depend strongly on the doping concentration. If high on/off-ratios are required (e.g. power-efficient applications), doping concentration should be low. If a diode for rectification is to be built aimed at high power or high frequency, doping concentration can be chosen high to reduce series resistance and threshold voltage. The decrease in on/off-ratio is not decisive for these applications.

5.2.3 Variation of Film Thickness in Schottky Diodes Based on Triclinic Rubrene

Aside from the doping concentration of the p-doped layer, the other two parameters that can be changed are the respective thicknesses of the intrinsic layer and the p-layer. In an ideal device, the thickness of the p-doped film should not have a relevant influence on the device, since the conductivity of this film is significantly higher than the conductivity of the intrinsic film or even the depleted parts of the structure. As shown in figure 5.9, the current density of devices with 100 nm intrinsic layer and 200 nm or 300 nm of 5 wt.%-doped p-layer have indeed a virtually identical current in forward direction, once the Shockley regime II is reached. However, leakage current in regime I and the reverse current are slightly increased for the thicker device. This is further proof that a significant part of low-voltage and reverse leakage current originates from lateral area effects. Vertical leakage current through the active area would decrease with increasing layer thickness. In contrast, lateral leakage current increases, since the lateral conductance is proportional to the lateral cross-section of current flow. This is further supported by data shown in figure 5.10. Here, the devices feature a constant concentration of F6TCNNQ and a constant thickness of the p-doped film.

Only the nominal thickness of the intrinsic layer is changed. In accordance with laterally dominant leakage current, the low-voltage current is close to identical between the individual devices. Nevertheless, the reverse leakage at high voltage decreases for thicker intrinsic layers. A shift from laterally dominated leakage to – at least partly – vertically carried leakage occurs here, for which the intrinsic layer is the limiting part.

Surprisingly, the maximum conductivity, shown in figure 5.11b, increases with higher intrinsic film thickness. It seems counterintuitive that a thicker film shows better vertical charge transport. This is true for all tested doping concentrations. The maximum conductivity is slightly increased for intrinsic films below 50 nm. This can be attributed to pinholes through the device, especially, since a majority of this intrinsic film is made up of the seed crystal itself. The maximum conductivity is higher for devices with 5 wt.% doping than for 0.5 wt.%. It decreases again when the doping concentration is further increased to 10 wt.%. Whether this is just the result of the different order of deposition for the 5 wt.%-doped device or another physical effect is difficult to decide with the data at hand. Consequently, since the reverse current decreases and the forward current increases with increasing intrinsic layer thickness, the resulting on/off-ratio increases significantly, as shown in figure 5.11a. For the stronger doped devices, the change is less pronounced, however, within the thicknesses measured here, a thicker film of intrinsic is improving most of the relevant properties of these diodes.

To understand the increased conductivity for thicker intrinsic films, an investigation of the threshold voltage is necessary. The leakage current between these devices is the same when only the intrinsic film thickness is varied. Hence, the shift in technical threshold voltage is equivalent to the change in physical threshold voltage, as discussed earlier. The threshold voltage is decreasing with
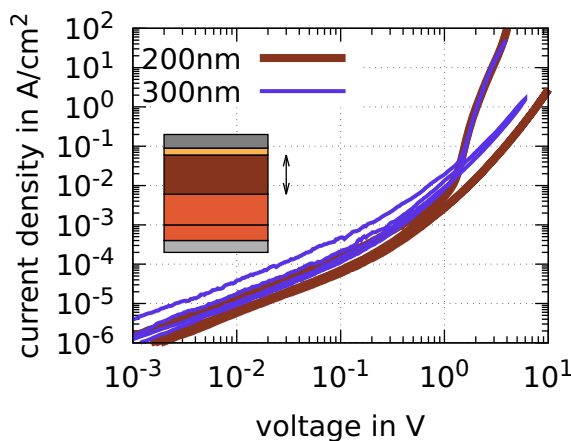
Figure 5.9: Influence of the variation of p-layer thickness on the IV characteristic of a pin diode based on triclinic rubrene (p-doping concentration: 5 wt.%, intrinsic layer thickness: 100 nm).
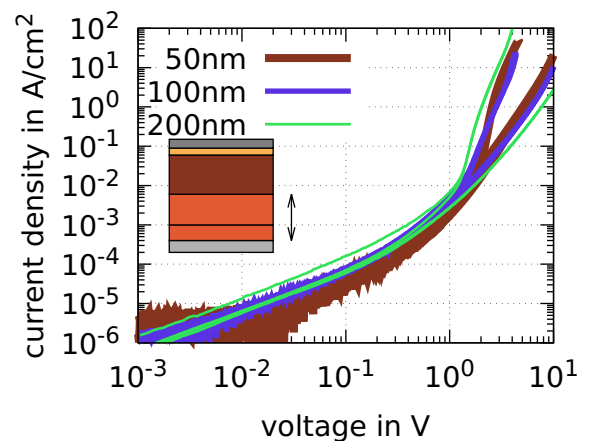
Figure 5.10: Influence of the variation of intrinsic layer thickness on the IV characteristic of a pin diode based on triclinic rubrene (p-doping concentration: 5 wt.%, p-layer thickness: 200 nm).

Figure 5.11: Parameters extracted from data shown in figure 5.10 (*: device is built according to stack in figure 5.4a).
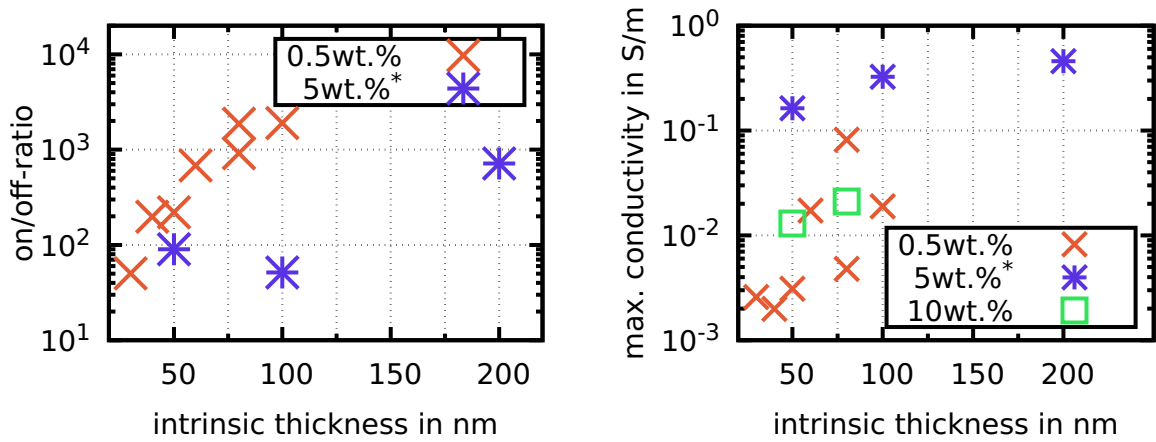
(a) Dependence of the on/off-ratio on the intrinsic layer thickness for different doping concentrations of the p-doped layer.

(b) Dependence of the maximum conductivity on the intrinsic layer thickness for different doping concentrations of the p-doped layer.

Figure 5.12: Threshold voltage $V_{\mathrm{Th},1}$ extracted from data shown in figure 5.10 (*: device is built according to stack in figure 5.4a).
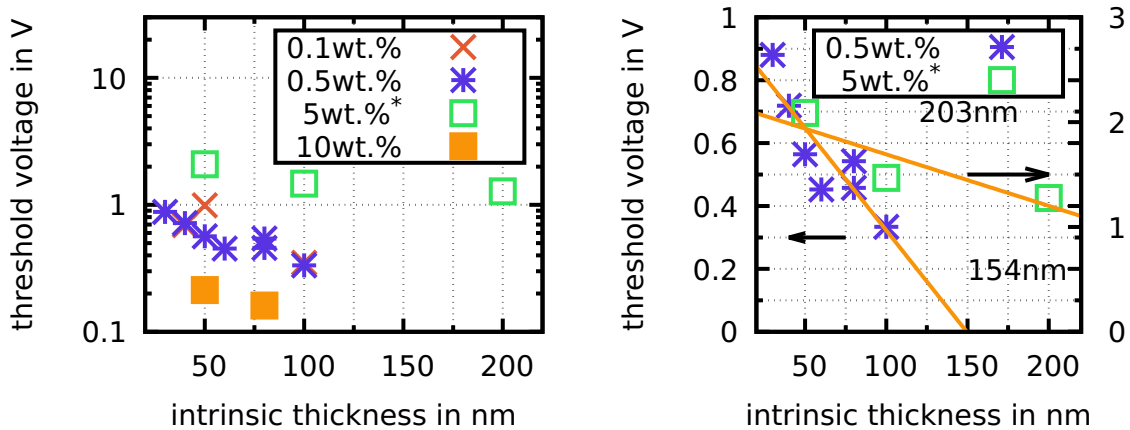
(a) Dependence of threshold voltage of all measured devices: $V_{\mathrm{Th},1}$ decreases with intrinsic film thickness for all doping concentrations.

(b) Detailed depiction for devices with 0.5 wt.% and 5 wt.% doping concentration of the p-doped film, including linear fits.

increasing intrinsic layer thickness. Thus, the increase in conductivity is not an increase in the intrinsic property of the stack to conduct current, but an earlier onset of regime II. This might be caused by the diffusion of holes through the intrinsic film towards the Al electrode. The hole density in the intrinsic directly at the interface between intrinsic and p-doped layer is high, since carriers diffuse into the intrinsic film. The density of charge carriers decreases with distance to the interface, depending on the diffusion length L_p. In the limit of an infinitely long intrinsic layer, the carrier density at the Al electrode is the intrinsic hole density of intrinsic rubrene p_{i0}. The resulting energetic distance that defines the properties of the diodes is given by the metal work function W_A and the intrinsic Fermi level of rubrene $E^i_{F^i}$. However, for a finite distance x, the density $p_i(x)$ of holes in the undoped intrinsic layer is given as:

$$p_i(x) = p_{i0} + p_{p0}e^{-\frac{x}{L_p}}, \tag{5.4}$$

with p_{p0} as the equilibrium hole density in the p-doped region and L_p as the diffusion length for holes in intrinsic rubrene. If the thickness of the intrinsic d_2 is smaller than the diffusion length L_p, the density of holes at the metal electrode is increased, compared to the equilibrium condition. The resulting Fermi energy is shifted according to [55]:

$$\Delta E_F \propto \Delta \ln(p). \tag{5.5}$$

Since the threshold voltage V_{Th} of the diode is defined by the energetic difference between the two materials ($\Delta (E_F - W_A)$, with W_A as the metal work function), it follows:

$$\Delta V_{Th} \propto \Delta \left(\frac{E_A}{e}\right) \propto \Delta (E_F - W_A) \propto \Delta ln(p) \propto \Delta \left(\ln \left[e^{-\frac{d_2}{L_p}}\right]\right) \propto -\Delta \left(\frac{d_2}{L_p}\right). \tag{5.6}$$

A decrease in intrinsic layer thickness should thus cause a linear decrease in threshold voltage. Fitting the slope of this decrease can give the diffusion length of holes in the intrinsic film. Applying this procedure to the data obtained from devices with 0.5 wt.% and 5 wt.%, gives diffusion lengths of 154 nm and 203 nm, respectively. The measurement at higher doping concentrations seems to level of at higher values for the intrinsic thickness. That fits well to the derived theory, since once the intrinsic layer is thicker than the diffusion length, the effect vanishes. The first value of 154 nm seems, thus, more trustworthy.

The extracted diffusion lengths are smaller than expected based on the previously measured high charge carrier mobility of $10.3\,\mathrm{cm^2\,V^{-1}\,s^{-1}}$. Values for the charge carrier lifetime are not available in literature and Capacitance-Voltage (CV) measurements performed on these pin diodes did not yield any useful result due to the limited measurement range given by the used equipment. The diffusion and lifetime of excitons in rubrene, however, is broadly investigated, yielding values in the range of seconds [237]. Unfortunately, processes regarding exciton

recombination are not directly comparable to single charge carriers. Typical values for the carrier lifetime in organic semiconductors are in the range of ns to ms ([238], [239], and [240]). Garcia-Belmonte et al. [241] present CV measurements of P3HT revealing electron lifetimes of 0.1 ms to 0.3 ms. Estimating via equation 2.27 based the charge carrier mobility measured previously and a carrier lifetime of 0.1 ms would result in a large diffusion length of 52 μm. However, the measured diffusion length of 154 nm suggests a carrier lifetime of only 0.9 ns. An efficient relaxation path must be present to result in such a short charge carrier lifetime. An estimation of the precision of this result seems therefore not reasonable. Especially the exact relationship between the technical threshold voltage and the corresponding physical threshold voltage is not completely clear. Furthermore, the equivalence of physical threshold voltage and the built-in potential is based on idealized assumptions. These results should thus be seen as an indication for the order of magnitude for the diffusion length.

5.2.4 Temperature-Dependence of Schottky Diodes Based on Triclinic Rubrene

Temperature-dependent measurements of diodes can be useful in two distinct ways. First, physical parameters can be extracted that change with temperature. In section 4.2.4.2, temperature-dependent CV measurements are shown to extract the activation energy of the doping process. Secondly, devices that are integrated into circuits can experience a significant increase in temperature through Joule heating. Although not directly comparable, the temperature dependence while cooling can give hints regarding the behavior for heated devices too. However, effects regarding the self-destruction of devices via positive heat-driven feedback loops behave often differently [242]. The effect is usually local, since the high conductivity of the "hottest" spot on the surface acts as a shunt for the current. Power dissipation is thus channeled there. Nevertheless, information about the "global" temperature dependence can still be valuable to assess the tendency of a system towards these destructive effects.

Figure 5.13 shows a set of IV curves of Schottky diodes measured at different temperatures. For technical reasons[3], these devices could not be cooled as far as the single rubrene films. Similar to the previous measurements on the doped and undoped films in section 4.2.4, the temperature dependence is extremely small. Schottky diodes with weak doping (figure 5.13a: 0.1 wt.%) are virtually unchanged when cooled. Devices with a high doping concentration (figure 5.13d: 10 wt.%) show a slight decrease in leakage current at low voltages and a small shift of regime II, corresponding to the Shockley regime. This is expected

---

[3]Devices built at the Lesker tool are encapsulated via a glass dome glued to the glass substrate. Since the dome contains a nitrogen atmosphere at 1 bar pressure and the temperature-dependent measurements take place in a vacuum, cooling was limited to above 200 K to not cause detachment of the encapsulation due to the glue getting brittle.

Figure 5.13: Temperature dependence of Schottky diodes with different doping concentration and intrinsic layer thickness. Temperature is changed from 280 K to 220 K (dark to bright).
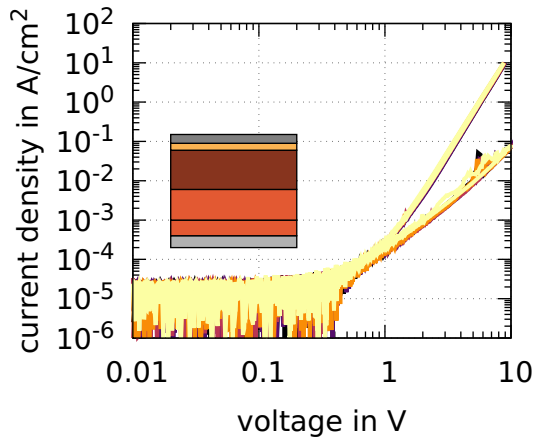
(a) p-layer: 250 nm [0.1 wt.%],
i-layer: 100 nm.
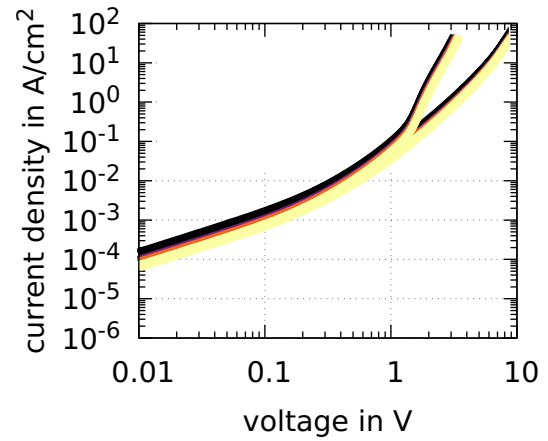
(b) p-layer: 300 nm [5 wt.%],
i-layer: 200 nm.
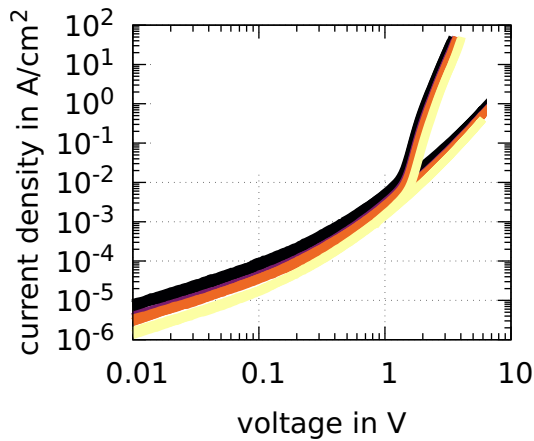
(c) p-layer: 200 nm [5 wt.%],
i-layer: 100 nm.
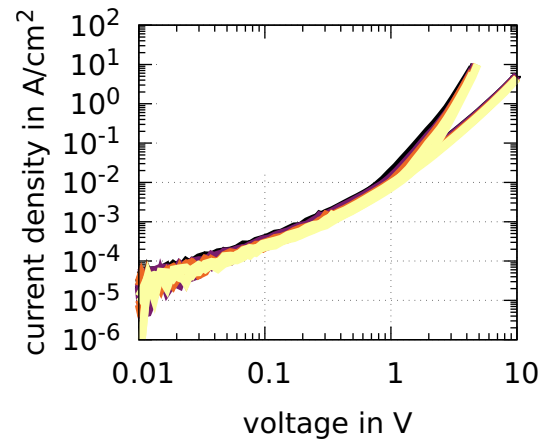
(d) p-layer: 250 nm [10 wt.%],
i-layer: 30 nm.

considering the temperature dependence of the saturation current $j_0 \propto T^3 e^{-\frac{B}{T}}$ [67]. Devices doped with 5 wt.% and the bottom-up geometry feature the strongest temperature-related effects. Current decreases with decreasing temperature, although the overall effect is mild and only relevant in the leakage regime. The change in leakage current can be attributed to the de-activation of dopants, since lateral currents through the doped films have been identified to be the main contributor to leakage paths. The change in regime II appears similar to the stronger doped device and fits a decrease in saturation current.

In summary, the temperature dependence of these devices is relatively small [236]. Although extrapolation from cooling data is not ideal, it seems unlikely that these devices show a strong thermal activation in operation, aside from localized effects.

5.3 pin Diodes Based on Triclinic Rubrene Crystals

After discussing p-type Schottky diodes, the next logical step is to add the additional n-doped layer and investigate pin and pn diodes. The p-dopant here is once again F6TCNNQ while $W_2(hpp)_4$ is used as the n-dopant. The investigation of these devices serves two distinct purposes. First, the diodes are a precursor to the Bipolar Junction Transistor (BJT) investigated in chapter 7. It is essential to understand the influence of each of the parameters of each component. Specific requirements have to be matched – low reverse current, low threshold voltage, thin thickness of the n-doped layer = base of the BJT – to allow for transistor amplification. Second, the diodes can be used as a stand-alone device. OLEDs and diodes aimed at UHF rectification are presented as a possible application in the next sections.

This section presents the influence of the layer thicknesses and doping concentration of the individual components on the properties of the diodes. Several parameters are extracted from the data based on the description in section 4.2.1. As discussed earlier, the conductivity of the n-doped layer is significantly lower than that of the p-doped and intrinsic films, due to the lower electron mobility. As far as possible, the thickness of the n-doped films is kept low. Compared to the Schottky diodes, two additional parameters can be varied; the thickness of the n-doped film and its doping concentration. This gives a total of five parameters. A second question arises regarding the mode of comparison when investigating changes in layer thickness: is the total thickness of the device to be kept constant (e.g. 200 nm:100 nm vs. 100 nm:200 nm) to assure a comparable average electric field in both devices or should all parameters be kept constant while only one is changed (e.g. 200 nm:100 nm vs. 200 nm:150 nm vs. 200 nm:200 nm) to guarantee that any changes shown by the samples can be attributed to one parameter alone? Both approaches are used in the following subsections. First, devices manufactured at the UFO evaporation tool are discussed featuring a fixed total thickness of

Figure 5.14: Stack design for pin diodes based on crystalline rubrene: Seed is undoped.

| Al(300nm) |
| rubrene:$W_2(hpp)_4$[c_3 wt.%](d_3 nm) |
| rubrene[i](d_2 nm) |
| rubrene:F6TCNNQ[c_1 wt.%](d_1 nm) |
| rubrene[i] seed(30nm) |
| Au(30nm) |
| Ag(100nm) |
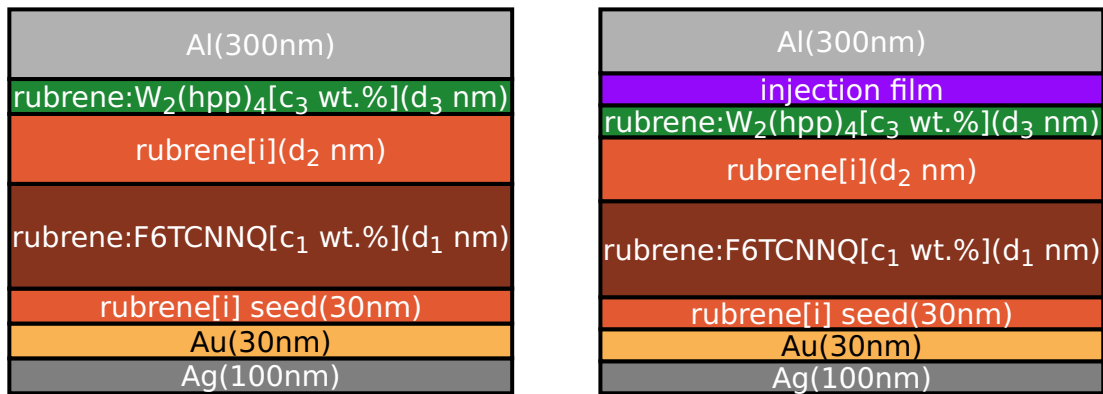
(a) Standard pin diode stack.

(b) pin diode stack for electron injection experiments.

400 nm. Single-substrate manufacturing allows for absolute freedom during the construction of the device. However, due to the increased effort in manufacturing, the degree of variation in parameters is limited. Nevertheless, usually a large number of identical devices can be manufactured at once, thus, a statistical assessment can be made based on these data. The second type of device is manufactured using the Lesker evaporation tool. The variation in combination of layers is limited, however, it is easier to generate a large degree of similar devices with only one parameter varied in steps. Similarly to the Schottky diodes of section 5.2, these devices are compared on a single device basis, since not enough data are available for statistical analysis.

pin diodes from both evaporation tools are based on the stack design shown in figure 5.14a. Unless stated otherwise, all devices are based on the triclinic crystal phase of rubrene, grown from 30 nm undoped rubrene at 140 °C for 10 min on glass substrates.

5.3.1 Statistical Analysis of the Influence of the Variation of Layer Thickness

This section discusses the influence of variation in thickness of the p-,n-, and intrinsic layer on the IV characteristics of pin diodes based on triclinic rubrene. The doping concentrations are fixed at 0.5 wt.% for p-doping and 1 wt.% for n-doping. Devices are designed such that the total thickness of the semiconductor material is fixed at 400 nm, thus, always two thicknesses are changed, while a third is varied.

5.3.1.1 Thickness of the p-, n-, and Intrinsic Layer

For the first set of devices, the p-layer thickness and the intrinsic layer thickness are coupled. Sets of devices based on triclinic crystals made with the standard procedure and a fixed n-layer thickness of 100 nm are shown in figure 5.15a. Based on the previous results observed for the Schottky diodes, a thicker doped film should increase reverse leakage, while a change in intrinsic thickness should only influence the reverse current at high voltages. That is not the case here. The reverse current in the low-voltage regime is initially larger for the device with the thinner doped film. Only at higher reverse bias, the device with the thicker film shows a larger current. Apparently, a different effect is limiting the reverse current for these devices. It cannot be explained by the different electrode geometry between the UFO-made pin devices and the Lesker-made Schottky devices, since pin diodes built in the Lesker shows the same phenomenon. Current that flows laterally through the p-doped film might not be able to pass as easily through the barrier of the pn-junction compared to the Schottky barrier. Other effects – like vertical leakage through the active area – might thus play the dominant role. The forward regime at medium voltages is similar for both devices. This is also reflected in the threshold voltages $V_{\mathrm{Th},1}$ extracted, shown in figure 5.16c, according to which the Shockley regime II starts at approximately the same voltage for both configurations. These threshold voltages do not correlate with the physical threshold, since the leakage current is not the same. The higher saturation current for the devices with the thicker intrinsic layer, shown in figure 5.16d, suggests a

Figure 5.15: Variation of layer thickness for diodes based on triclinic rubrene: Seed is grown from 40 nm undoped rubrene at 140 °C for 10 min on a glass substrate. Bottom electrode is made from Au, top electrode is made from Al. Stack according to figure 5.14a.
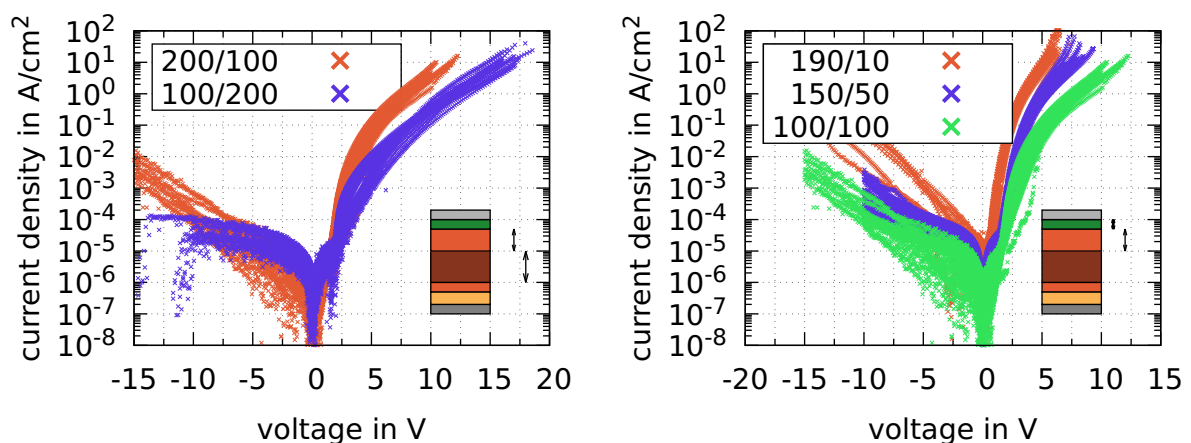
(a) Variation of layer thickness, key: p-thickness/i-thickness in nm. p-doping is 0.5 wt.% and n-doping 1 wt.% for all devices. The thickness of the n-layer is 100 nm.

(b) Variation of layer thickness, key: i-thickness/n-thickness in nm. p-doping is 0.5 wt.% and n-doping 1 wt.% for all devices. The thickness of the p-layer is 200 nm.

Figure 5.16: Distribution of parameters extracted from curves in figure 5.15a of pin diodes with varying thicknesses of the p- and intrinsic layers. p-doping is 0.5 wt.% and n-doping 1 wt.% for all devices. The thickness of the n-layer is 100 nm.
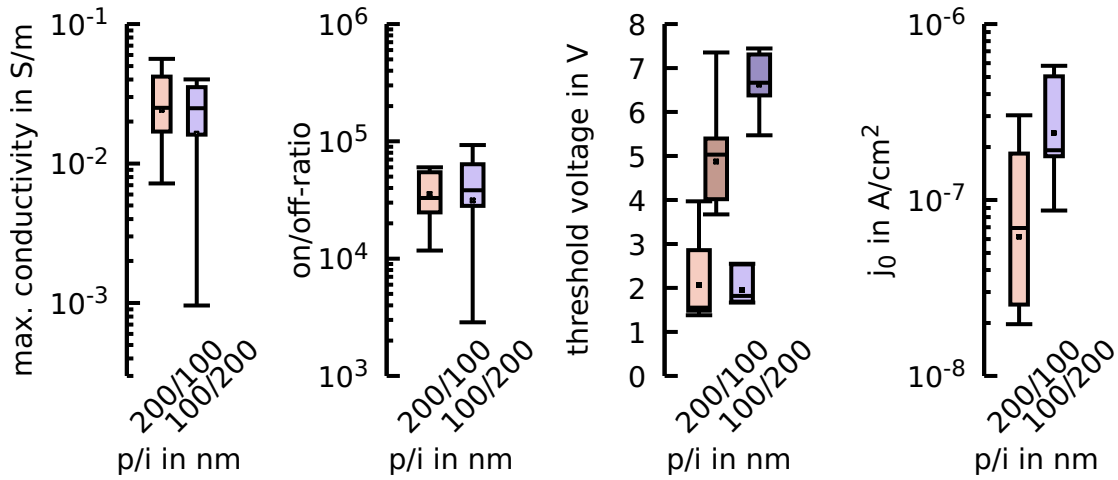
(a) Maximum conductivity.

(b) on/off-ratio.

(c) Threshold voltage: **bottom:** $V_{Th,1}$, **top:** $V_{Th,2}$.

(d) Saturation current j_0 in the Shockley regime II.

smaller energetic gap [236]. However, estimating via the saturation current is not precise since the ideality factor for both devices could be vastly different, caused by a different recombination behavior.

The forward current at high voltages is by around one order of magnitude smaller for devices with a thicker intrinsic layer. The maximum conductivity in this regime is, however, only slightly reduced (see figure 5.16a). The dynamic properties at high fields are thus comparable for both devices. The difference can be explained by a later onset of the conductive regime III, indicated by an increased threshold voltage $V_{Th,2}$ (see 5.16c). The distribution of on/off-ratios, presented in figure 5.16b, is almost identical for both devices types. However, this is a coincidence caused by the uncommon shape of the reverse current of these two sets. The on/off-ratio is nonetheless similar for both devices in each voltage regime.

The second set of devices is made in a similar fashion. Now, the p-doped film is fixed at 200 nm and intrinsic and n-doped layers are varied accordingly. The corresponding IV curves are shown in figure 5.15b. In reverse direction, a clear trend is observable with thinner n-doped layers resulting in higher leakage currents. The increase in thickness of the intrinsic layer cannot compensate for the blocking ability of the n-doped film. If this effect is due to a better blocking via the junction or due to the lower charge carrier (electron) mobility in the n-doped film is difficult to decide based on the reverse current alone. It is worth noting that the reverse leakage current even for the device with only 10 nm of n-doped film is significantly lower than in the Schottky diodes shown in section 5.2, when similar p-doping is used.

Figure 5.17: Distribution of parameters extracted from curves in figure 5.15b of pin diodes with varying thicknesses of the intrinsic and n-layers. p-doping is 0.5 wt.% and n-doping 1 wt.% for all devices. The thickness of the p-layer is 200 nm.
A: 190 nm intrinsic / 10 nm n-layer, **B:** 150 nm intrinsic / 50 nm n-layer, **C:** 100 nm intrinsic / 100 nm n-layer.
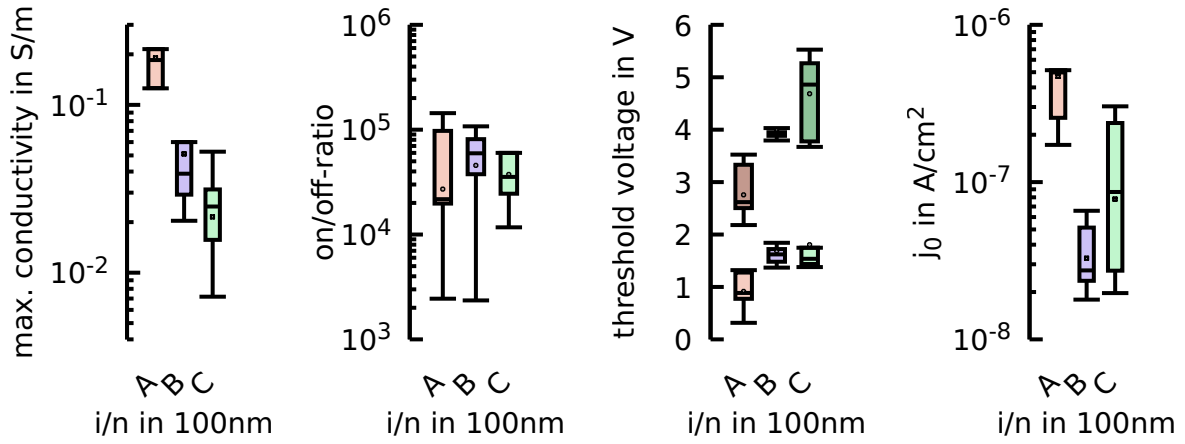
(a) Maximum conductivity. **(b)** on/off-ratio. **(c)** Threshold voltage: **bottom:** $V_{Th,1}$, **top:** $V_{Th,2}$. **(d)** Saturation current j_0 in the Shockley regime II.

The forward direction shows a similar picture with lower n-layer thickness resulting in higher currents. However, there is a qualitative difference between the transition from the 100/100 sample to the 150/50 device, compared to the pair 150/50 to 190/10. For the first set, only the low-voltage regime and the high-voltage regime are changed, while the onset and slope of the Shockley regime II are quasi-identical. It is unlikely that the thicker n-layer contributes to a lateral leakage current, which is further indication that leakage current in forward and reverse in these pin diodes is dominated vertically. The change in the high-voltage regime can be explained by the lower conductivity of the n-doped film. Once the depletion zone is flooded, the layers function as a series of resistors, with the n-layer as the part with the lowest conductivity. Both regimes behave equivalently for the devices with an n-doped layer of 10 nm. Evidently, these devices also feature the highest maximum conductivities, shown in figure 5.17a. Since the forward currents and the reverse current increase and decrease almost in the same ratio, the resulting on/off-ratios of these three sets are comparable (see figure 5.17b). However, devices with a thin n-layer show a slightly lower on/off-ratios with a larger spread, while devices with a thick 100 nm n-layer show the least degree of variation. The most significant distinction between the three sets is in the Shockley regime. While the two devices with the thicker n-layer show an almost identical onset and shape of regime II, indicated by the practically identical threshold voltage $V_{Th,1}$ shown in figure 5.17c, devices with only 10 nm n-layer show an earlier onset of the Shockley regime at an increased slope. The corresponding threshold voltage (figure 5.17c) is lower and the saturation current

(figure 5.17d) is larger (the same care regarding the interpretation of saturation currents applies as discussed earlier). It appears as if the energetic gap for this junction is closer to the Schottky diode than to the other pin diodes. This suggests undisturbed diffusion of holes through the n-doped film, over at least 10 nm. This is especially remarkable, since the weight-doping concentration of the hole doping in the p-layer is larger than the n-doping in the n-layer. Direct measurements are not available for the efficiency of the n-doping process, however, the previous results suggest that the n-doping efficiency must be even smaller than the doping efficiency measured for the p-type system.

5.3.1.2 pn Diodes Based on Triclinic Rubrene

The classic inorganic diode is of pn-design and thus only contains a p-doped part in direct contact with an n-doped part. The intrinsic layer used in organic diode is added to reduce leakage currents caused by the thin depletion layer width common in organic junctions. In figure 5.18, two sets of equivalent devices are shown: pin devices featuring 200 nm of p-layer and 100 nm of intrinsic film and pn devices with 300 nm p-layer and no intrinsic film. Both sets feature a 100 nm layer of n-doped material and are based on standard triclinic crystals.

The reverse current in the pn devices is increased by up to three orders of magnitude, proving the usefulness in regard to leakage suppression of the intrinsic film for this device type. Nevertheless, these pn diodes show acceptable rectification behavior with on/off-ratios (see figure 5.19b) larger than many of the previously discussed Schottky diodes but still lower by almost three orders of magnitude compared to full pin devices. As a comparison, the width of the depletion layer of a p-Schottky diode without any intrinsic material can be estimated to 12 nm using equation 2.36 and the charge carrier density of $4 \cdot 10^{24} \, \mathrm{m}^{-3}$ measured in chapter 4.2.3.2 for a doping concentration of 0.5 wt.%.
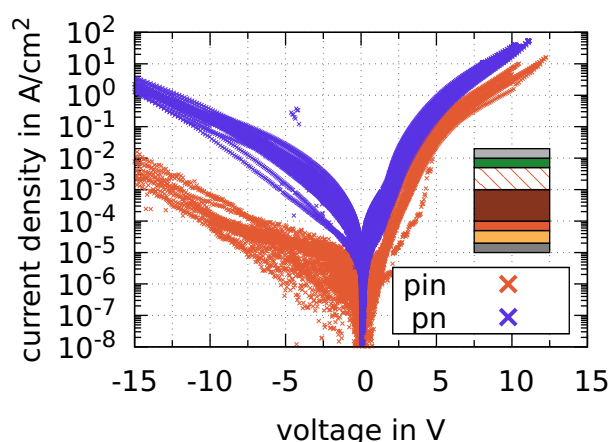
Figure 5.18: Comparison between pin diodes and pn diodes with similar stack design: p-doping is 0.5 wt.% and n-doping 1 wt.% for all devices.
pin device: 200 nm/100 nm/100 nm
pn device: 300 nm/100 nm.

Figure 5.19: Distribution of parameters extracted from curves in figure 5.18: Comparison between pin diode and pn diode with similar stack design: p-doping is 0.5 wt.% and n-doping 1 wt.% for all devices.
pin device: 200 nm/100 nm/100 nm
pn device: 300 nm/100 nm.
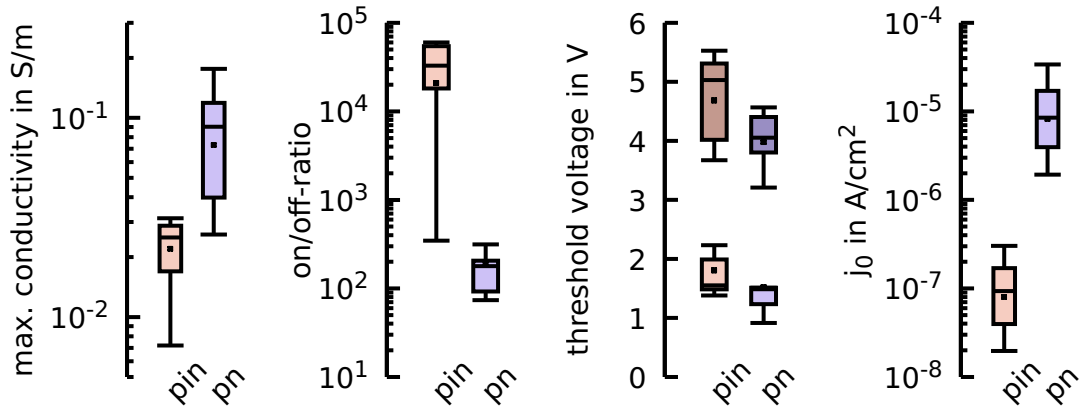
(a) Maximum conductivity. **(b)** on/off-ratio. **(c)** Threshold voltage: **bottom:** $V_{Th,1}$, **top:** $V_{Th,2}$. **(d)** Saturation current j_0 in the Shockley regime II.

All prior experiments suggest the doping efficiency for the n-layers to be even lower than the doping efficiency of the p-system. The corresponding thickness of the depletion zone has thus at least twice – but most likely more – the value of the Schottky device. A total width of the depleted film of more than 24 nm is already comparable to the layer thicknesses for the intrinsic films added in the pin devices. Rectification – although not efficient – can be expected. The current in forward direction is higher in all voltage regimes for the pn devices, resulting in a higher maximum conductivity (see figure 5.19a). Both types of threshold voltage are reduced by a similar amount (see figure 5.19b), probably equivalent to the linear voltage drop over the intrinsic film thickness. $V_{Th,1}$ in the pn diodes is, however, larger than $V_{Th,1}$ for the pin device discussed previously with only 10 nm of n-layer. It can be assumed that the relevant energetic gap here is between the two doped states of rubrene (proper pn junction) and not towards the Al electrode (Schottky junction). The saturation current is significantly higher for the pn devices (see figure 5.19d), however, the recombination and diffusion behavior is not comparable between these two device types.

5.3.2 Systematic Investigation of the Variation of Doping Concentration and Layer Thickness

The following section discusses devices manufactured at the Lesker evaporation tool. The comparison is thus based on single devices instead of entire sets. In contrast to the earlier section, only one parameter is varied at the time which results in different total thicknesses between the devices. First, parameters

(thickness and doping concentration) of the p-doped part are discussed, followed by the intrinsic part, and at last the n-layer. All devices are based on the same triclinic seed crystals made with the standard procedure of heating an undoped film of 30 nm for 10 min at a temperature of 140 °C.

Unfortunately, devices made from the UFO and Lesker behave differently in some aspects, even when their stacks are supposedly identical. Leakage currents in Lesker devices are significantly higher for an unknown reason. The resulting on/off-ratios are reduced by several orders of magnitude. The discussion of these devices is nevertheless valuable. However, a direct comparison between devices made at different tools is not feasible.

5.3.2.1 Influence of the p-doped Layer

The p-layer is the first part that is investigated. The following pin devices have an intrinsic layer of 100 nm and an n-layer thickness of 20 nm doped at 5 wt.%. Figure 5.20a shows two devices with different thicknesses of the p-doped layer, both doped at 5 wt.%. The behavior is identical to the UFO-made device of section 5.3.1. In contrast to the Schottky diodes of section 5.2, the leakage current decreases with increasing thickness of the p-doped film. Here, the current in forward direction is virtually identical, once the Shockley regime is reached for both devices. Although it is exactly the behavior expected from an ideal diode with constant intrinsic film thickness, this high degree of overlap is surprising, considering the large variability seen in the single-crystalline layers in chapter 4.2.1. These two curves also highlight the phenomenon discussed at the beginning of this chapter 5.2.1, for which the apparent threshold voltage shifts with leakage current.

Figure 5.20: Variation of the properties of the p-doped film in pin diodes with 100 nm intrinsic and 20 nm n-doped film doped with 5 wt.%.
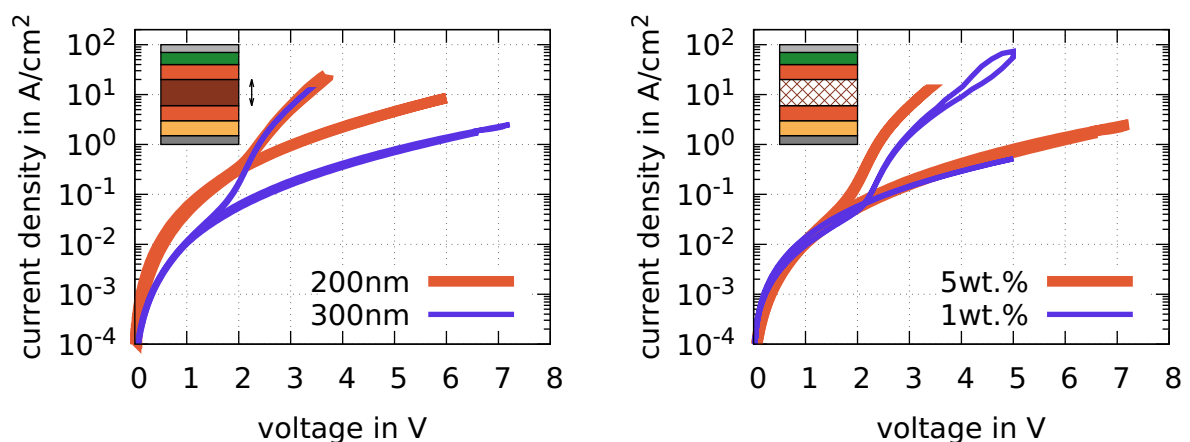
(a) Variation of the p-doped film thickness doped with 5 wt.%.

(b) Variation of doping concentration of the p-doped film of 200 nm total thickness.

Figure 5.21: Variation of the intrinsic film thickness in pin diodes with varying p- and n-doped films.
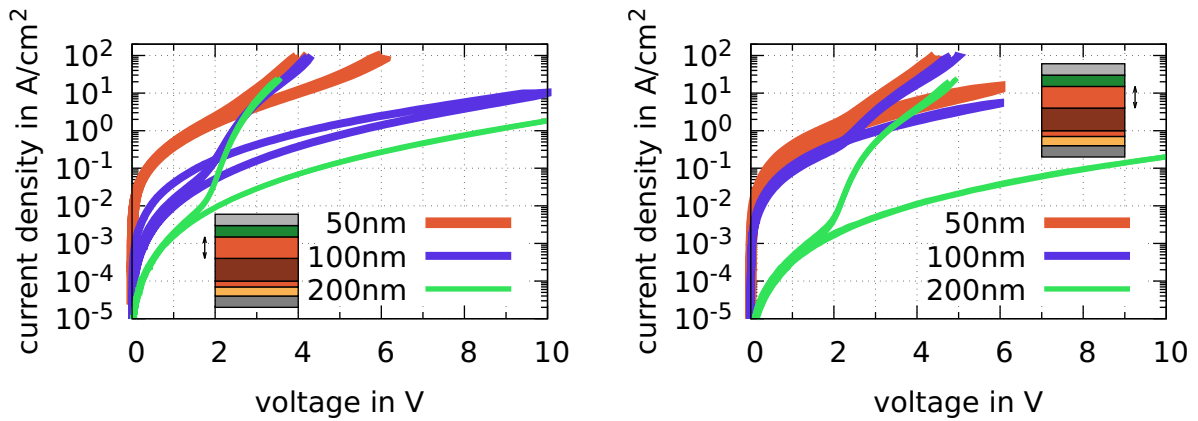
(a) Variation of the intrinsic film thickness in pin diodes with 300 nm p-doped layer doped with 5 wt.% and 20 nm n-doped film doped with 2 wt.%.

(b) Variation of the intrinsic film thickness in pin diodes with 300 nm p-doped layer doped with 5 wt.% and 20 nm n-doped film doped with 5 wt.%.

For the devices shown in figure 5.20b, the thickness of the p-film is kept constant at 200 nm, while the doping concentration is changed. Here, the leakage currents in both directions are close to identical for both devices. This means that the conductivity of the p-doped film cannot be the limiting factor for the leakage current. However, an increase in p-doped film thickness does indeed decrease the – supposedly vertical – leakage current as discussed before. This would indicate a smoothening or pinhole filling mechanism that increases in effectiveness with thicker films. However, a decrease of surface roughness cannot be observed with thicker layers, as shown in chapter 4.1.1.4. Therefore, only the filling of extremely small pinholes remains as an explanation for the change in IV behavior.

The general shape of the Shockley regime II is identical for both devices, aside from the loop at the tip of the blue curve caused by this device being measured at higher voltages. The onset of the Shockley regime is shifted towards a lower voltage for the higher-doped device. Semiconductor theory would predict a shift towards larger voltages, since the shift in doping concentration in the p-doped film results in a shift in the Fermi level and thus an increase in the energetic gap between the p- and the n-doped side. Since the n-layer thickness is only 20 nm, diffusion through this film could be relevant here, as discussed earlier. An increase in the hole doping concentration might result in more holes diffusing through the n-doped part and recombine at the metal interface instead of the pn-junction. The result is a mixture of both recombination method described by an effective energy gap $\overline{E_g} = \gamma E_A + (1 - \gamma)E_B$, with γ describing the degree of mixture between the two possible energetic gaps E_A and E_B, resulting in a shift in threshold voltage. A direct comparison to threshold voltages of previous measurements is not possible due to the increased leakage currents in the Lesker devices.

5.3.2.2 Influence of the Intrinsic Layer

As the second parameter, the thickness of the intrinsic layer is varied. For each of the sets in figure 5.21, the intrinsic layer thickness is varied from 50 nm to 200 nm while the other parameters are kept constant. The p-layer (thickness: 300 nm, doping concentration (5 wt.%) and the thickness of the n-doped film (20 nm) is identical for both sets. Both sets show that leakage currents and forward currents decrease with increasing intrinsic layer thickness. The degree of this change is influenced by the other layers. This is in accordance with earlier results with the UFO samples.

In figure 5.21a, the n-doping concentration is set to 2 wt.%. The shape of the IV curves of devices with 100 nm and 200 nm appear almost identical, aside from a shifted leakage current. The Shockley regime of these two devices is almost matching. In contrast, figure 5.21b presents the same type of devices with an n-doping concentration of 5 wt.%. Here, additionally to the shift in leakage current, a constant shift of the onset of the Shockley regime towards higher voltages can be seen with increasing intrinsic layer thickness. An increase in the threshold voltage is to be expected with increasing intrinsic layer thickness. However, if the intrinsic thickness and more importantly the n-layer thickness is too short to allow for recombination within the diode, recombination takes place at the metal interface, as discussed earlier. This seems to be the case for the devices shown in figure 5.21a. The increased n-doping concentration of the samples in figure 5.21b generates sufficient recombination within the diode itself, resulting in the expected stronger dependence on the intrinsic film.

5.3.2.3 Influence of the n-doped Layer

The last part that is investigated is the n-layer. The p-layer is kept constant at 200 nm doped with 5 wt.%, similar to the previous measurements. Two sets are compared for which the n-layer is varied; three devices with an intrinsic layer thickness of 200 nm shown in figure 5.22a and two devices with an intrinsic thickness of 100 nm 5.22b. Holes have to diffuse through the intrinsic layer first. Thus, 200 nm of intrinsic thickness should decrease the amount of diffusion through the n-doped film significantly, compared to the 100 nm of the second set. The reverse current in figure 5.22a is similar for all three devices. Neither the n-doping concentration nor the n-layer thickness have a limiting effect on the leakage current. This is not surprising, since the maximum n-layer thickness is 50 nm and thus approximately as large as the average surface roughness. The comparison between 2 wt.% and 5 wt.% reveals the expected slight shift in threshold voltage and an increase in saturation current (slope). However, comparing the two devices with the same 2 wt.% n-doping concentration shows a decrease in saturation current with n-layer thickness. A significant amount of holes must thus still be able to diffuse through the n-layer, despite the thick intrinsic film.

That the thicker 2 wt.%-doped device and the thinner 5 wt.%-doped device show almost identical high-voltage characteristics seems coincidental. It is nevertheless noteworthy that 2 wt.%·50 nm results in the same total amount of charges per area as 5 wt.%·20 nm and thus – considering all processes involved are perfectly linear – the same recombination cross-section.

The devices in figure 5.22b feature only 100 nm of intrinsic layer. A larger amount of holes is thus able to effectively reach the n-doped film via diffusion. Consequentially, the threshold voltage is significantly shifted when the n-doping concentration is increased from 2 wt.% to 5 wt.%, stronger than could be expected from the shift in Fermi level alone. It can thus be assumed that a significant amount of holes can diffuse through the 20 nm of n-layer doped with 2 wt.%. An analysis with finer steps in n-layer thickness and doping concentration is necessary to evaluate up to which values this effect can still be observed.

Figure 5.22: Variation of the n-doped film thickness and doping concentration in pin diodes with constant p-thickness (200 nm) and p-doping concentration of 5 wt.%.
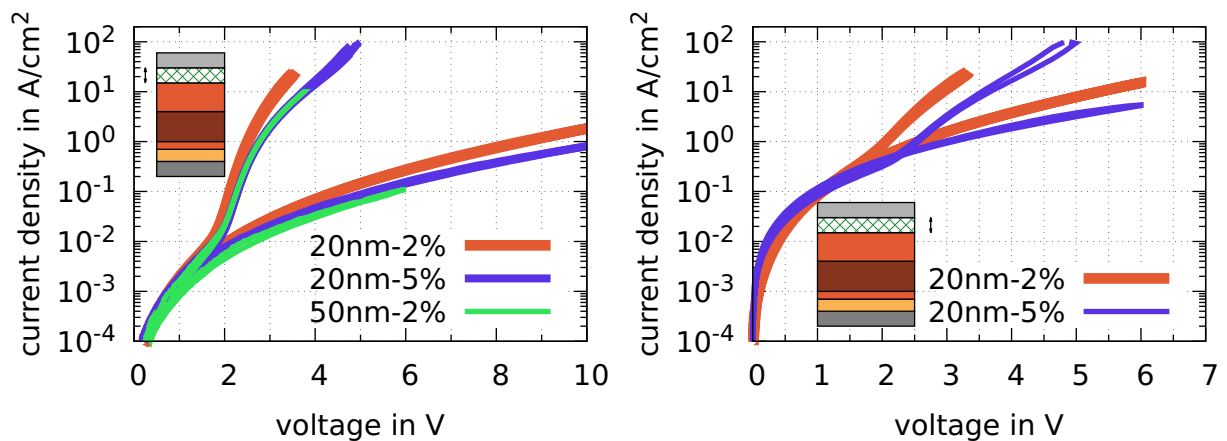
(a) Variation of n-doping concentration and n-layer thickness in pin diodes with an intrinsic layer thickness of 200 nm.

(b) Variation of n-doping concentration in pin diodes with an intrinsic layer thickness of 100 nm and n-thickness of 20 nm.

5.3.3 Injection Doping in pin Diodes Based on Rubrene Crystals

One issue regarding the application of these diodes is the comparably large threshold voltage, namely the technological threshold voltage for which rectification can be observed. In rectifier applications in general and in laboratory measurements in particular, the signal amplitude at UHF is usually limited. As an example: Considering a signal with an amplitude of 3 V that has to be rectified with a diode turning on at 2 V forward bias, only a minority of a cycle is used for rectification, while the majority contributes to forward and reverse leakage. Even when a higher amplitude is available, the Alternate Current (AC)-power dissipated in the device increases quadratically with amplitude voltage. It is thus beneficial to reduce the onset voltage as much as possible. Since the technical threshold voltage is given as the intercept of the forward leakage and the Shockley regime current, both can be tuned. In the previous two sections, methods are shown on how to manipulate the leakage current by modifying doping concentrations and layer thicknesses. Here, experiments are described that are aimed at improvement of the onset of the Shockley regime by reducing the series resistance of the diode via injection doping. Based on the conductivity measurements in chapter 4.2.3.5, a high injection barrier for electrons for the n-doped films seems likely, which might be overcome via injection doping. Initially, three different injection dopants (bulk $W_2(hpp)_4$, Cs, and LiF) common in OLED technology are introduced into the stack, according to figure 5.14b. The resulting curves can be seen in figure 5.23a. These devices are based on a 250 nm p-layer doped with 1 wt.%, an intrinsic film

Figure 5.23: Influence of an additional electron injection layer underneath the Al top electrode on the IV characteristic of pin diodes with constant p-thickness of 250 nm, intrinsic thickness of 100 nm, n-layer thickness of 20 nm, and n-doping concentration of 2 wt.% (stack according to figure 5.14b).
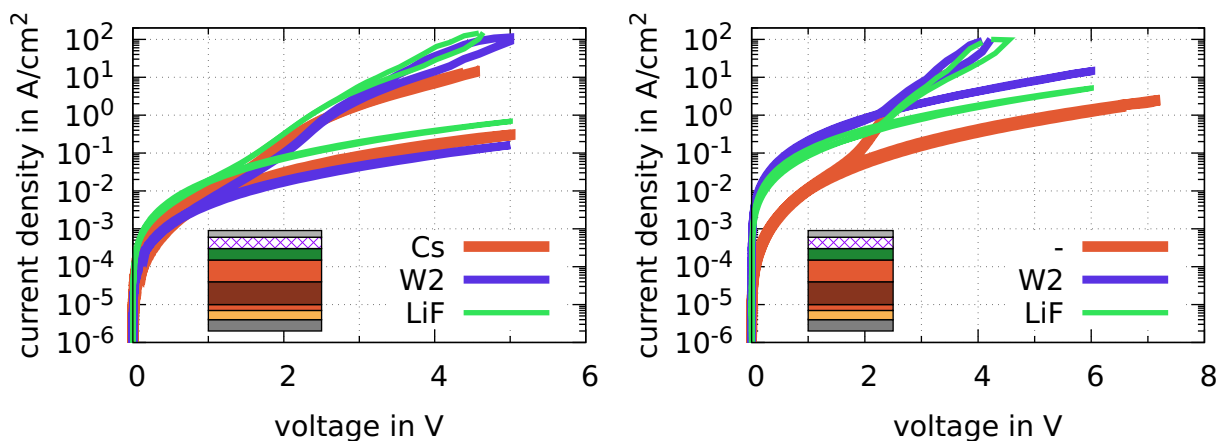
(a) Comparison between Cs (constant power settings used for BPhen doping for 60 s, no thickness measurable), $W_2(hpp)_4$ (0.7 nm), and LiF (0.7 nm) as injection film, concentration of the p-doping: 1 wt.%.

(b) Comparison between $W_2(hpp)_4$ (0.7 nm), and LiF (0.7 nm) as injection film and a device without injection assistance, concentration of the p-doping: 5 wt.%.

Figure 5.24: Influence of an additional electron injection layer underneath the Al top electrode made from 30 nm C_{60} doped with 2 wt.% $W_2(hpp)_4$ on the IV characteristic of pin diodes based on crystalline rubrene (stack according to figure 5.14b).
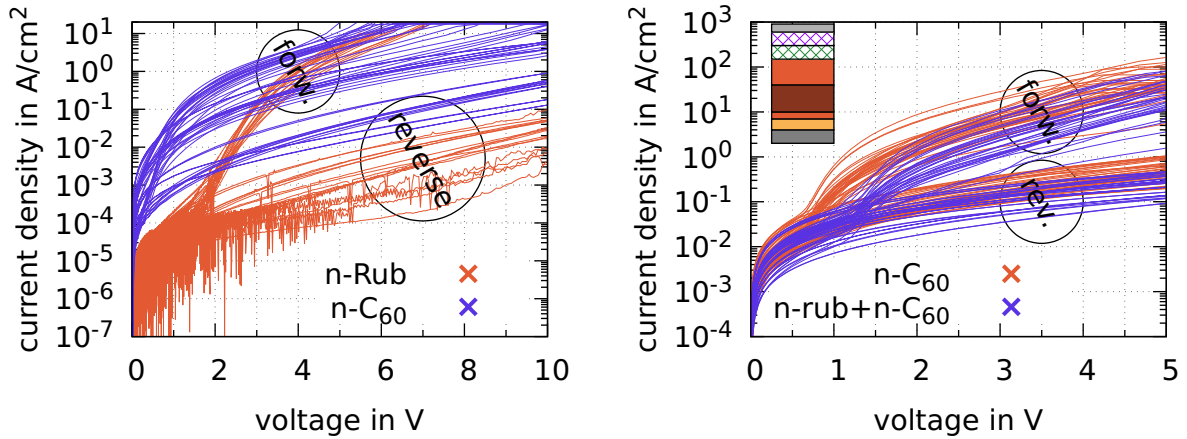
(a) pin diode based on triclinic rubrene: Seed is grown from 30 nm undoped rubrene at 130 °C for 15 min. The p-layer thickness is in total 300 nm, the intrinsic layer thickness is 80 nm.
n-rub: p-doping concentration: 0.5 wt.%, n-layer: 20 nm rubrene doped with 1 wt.%
n-C_{60}: p-doping concentration: 5 wt.%, n-layer: 30 nm C_{60} doped with 2 wt.%.

(b) pin diode based on rubrene in the orthorhombic platelet phase: Seed is grown from 40 nm undoped rubrene on 5 nm TAPC at 160 °C for 2 min. The p-layer thickness is in total 300 nm, doped at 5 wt.%, the intrinsic layer thickness is 100 nm.
n-C_{60}: n-layer: 30 nm C_{60} doped with 2 wt.%
n-rub+n-C_{60}: n-layer:20 nm rubrene doped with 1 wt.% + 30 nm C_{60} doped with 2 wt.%.

thickness of 100 nm, and a 20 nm of n-layer doped with 2 wt.%. The devices are all similar to each other (the strongest effect is visible for LiF), only shifted slightly along the current axis. An improvement of the threshold voltage is not visible for any of the devices. The on/off-ratio of the Cs-doped diode is decreased compared to the others. Similar behavior can be seen in figure 5.23b. Here, the p-layer is doped with 5 wt.%, while all other stack parameters are identical. Instead of the device with Cs doping, one diode is left without any additional injection doping. This results in the best switch-on behavior and the highest on/off-ratios from all tested devices in this series. Since the Shockley- and conduction current-regimes are overlapping for the devices in figure 5.23b, the only difference appears to be a shift in leakage current. This type of injection doping has the opposite effect that was intended and worsens the switch-on behavior of pin diodes based on rubrene crystals.

A second attempt at improving the injection of electrons is based on n-doped C_{60}, which is known to feature efficient electron injection and conduction [243]. These devices are fabricated at the UFO evaporation tool. For the first experiment, the n-doped film of rubrene is replaced entirely by a layer of C_{60} doped with 2 wt.% $W_2(hpp)_4$. In figure 5.24a, two sets of devices are shown based on triclinic crystals made with the standard seed procedure. Unfortunately, exactly fitting counterparts for the comparison are not available and the p-doping concentration

of the n-C_{60} device is significantly larger than that for the device with the n-doped rubrene. However, the effects seen here are significantly stronger than for other experiments with similar changes in doping concentrations shown in previous sections. It can thus be assumed that the effect can be attributed mainly to the C_{60} layer.

Once again, the leakage current is significantly increased once doping is introduced. However, for these devices, the forward current is higher as well and the threshold voltage is indeed shifted towards lower values. The variation between individual devices is significantly increased compared to the devices with only rubrene. Replacing the n-doped rubrene layer with C_{60} seems to be a viable strategy to generate devices with a lower threshold voltage. Nevertheless, a pre-selection of "well-suited" devices is advised and only applications that do not require a high on/off-ratio are applicable. Regarding the on/off-ratio, these diodes are among the worst-performing, especially considering that UFO-made devices usually feature a higher on/off-ratio.

The orthorhombic platelet polymorph is less suited as a purely vertical device, due to its lower vertical charge carrier mobility. However, for devices that require good conduction in lateral and vertical direction they might be more suitable. Some of the BJT devices discussed in chapter 2.3.4 are based on this crystal phase. Since the balance of voltages is a relevant factor in these devices, modifying the threshold voltage is relevant too. In figure 5.24b, two sets of diodes are shown, based on the orthorhombic platelet polymorph. Seeds are grown on 5 nm TAPC from 40 nm of undoped rubrene heated at 160 °C for 2 min. The majority of the stack is identical, with a p-layer of 300 nm doped with 5 wt.% and an intrinsic film of 100 nm. One of the devices consists of only a single n-layer made of 30 nm of C_{60} doped with 1 wt.% $W_2(hpp)_4$, while the second one is a combined layer made of 20 nm rubrene doped with 2 wt.% and the same layer of n-doped C_{60}. Here too, the leakage and forward current are significantly increased. However, the shift in threshold voltage is less pronounced in these devices. This might be a sign of a different type of leakage current or a different type of injection problem. The inferior injection properties of this crystal phase are already visible in the doping experiments of chapter 4.2.3.5.

A layer of n-doped C_{60} can improve the injection and consequently reduce the threshold voltage of pin diodes based on crystalline rubrene. However, leakage currents are increased significantly. Other injection layers based on bulk $W_2(hpp)_4$, Cs, or LiF do not show the desired behavior.

5.3.4 Pulsed Current-Voltage (IV) Measurements of pin Diodes Based on Triclinic Rubrene Crystals

The intrinsic and doped films measured in chapters 4.2.2.1 and 4.2.3 show an impressive conductivity due to the high vertical charge carrier mobility. Thin-films of undoped triclinic rubrene can be safely driven at currents in the $100\,\mathrm{A\,cm^{-2}}$-

regime, while strongly doped devices can even reach $1000\,\mathrm{A\,cm^{-2}}$ for a short time. The diodes based on these films are similarly resilient. However, current densities beyond the low $100\,\mathrm{A\,cm^{-2}}$-regime usually result in the thermal destruction of the devices. Some applications do not rely on current flow over an extended time. Short bursts of digital signals could be processed within a fraction of a second, reducing power loss within the device to a minimum. A potential application in electrically-driven organic lasers could be realized via a pulsed operation too. Figure 5.25 presents the results of initial pulsed IV experiments to gauge the limits of the devices. The diodes are connected in series with a $120\,\Omega$ ohmic resistor and voltage pulses are applied to the circuit. The voltage drop over the resistor V_R and over both components V_{in} is probed using an oscilloscope. The voltage drop over the diode is then given as $V_D = V_{in} - V_R$ and the corresponding current as $I_D = \frac{V_R}{R}$. Since the setup is not optimized for high-frequency/short-pulsed operation (e.g. long cables are necessary to connect the setup and proper coaxial shielding is not available around the diode and the resistor), strong oscillations are visible in the resulting measurements (see figure 5.25a). The length of the pulse (here 300 ns) is chosen so that the onset of the plateau is visible without exposing the device to unnecessarily long pulses. Other experiments show, however, that even pulse lengths of up to $400\,\mu s$ do not damage the devices.

Figure 5.25b shows the resulting IV curves, including the corresponding conventional measurements. Two devices are compared, both have a p-layer with a thickness of 200 nm, doped at 5 wt.% and an intrinsic layer thickness of 100 nm. The concentration of the n-doping is identical for both at 5 wt.%. The thickness

Figure 5.25: Exemplary pulsed measurement of pin diodes based on triclinic rubrene.
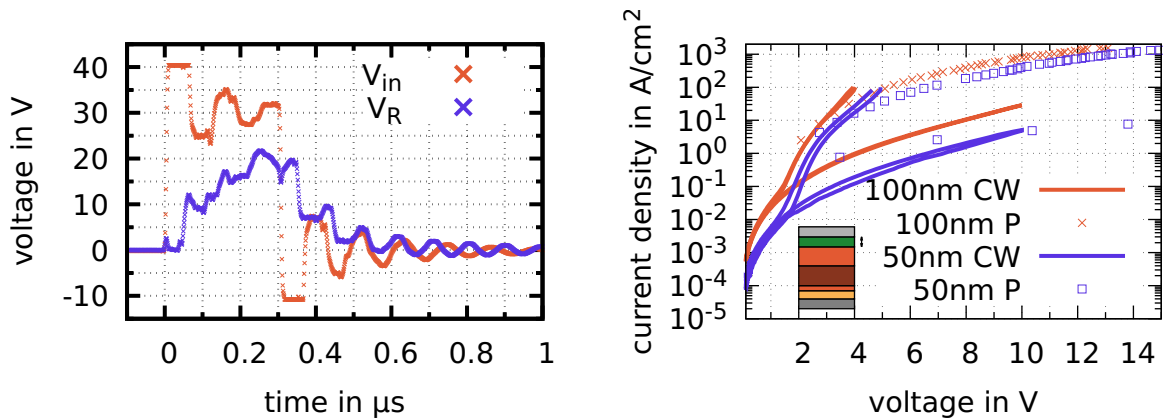
(a) Oscilloscope traces of input pulse and voltage drop over the series resistor $(120\,\Omega)$: The voltage drop over the diode is then given as $V_D = V_{in} - V_R$, the corresponding current as $I_D = \frac{V_R}{R}$. Pulse length (here 300 ns) is chosen so that the onset of the plateau is visible. The trace is the average of 256 single pulses, repeated at 111 Hz.

(b) Constant power sweep and pulsed measurement of pin diodes based on triclinic rubrene with 200 nm p-layer doped with 5 wt.% and 100 nm intrinsic layer, the thickness of the n-layer (doped at 5 wt.%) is indicated in the key.
CW: constant power sweep, **P:** pulsed data explained in figure 5.25a.

for the n-layers is 50 nm and 100 nm, respectively. Except for the sudden change in slope at high currents visible in the CW-data, the data points from the pulsed measurements seem to naturally follow the curve. If that upwards kink is a sign of self-heating is difficult to tell. The pulsed measurement is only accurate at high currents when the voltage drop over the series resistor is larger than the voltage drop over the stray capacitance within the measurement system. Nevertheless, these measurements show that currents of at least $2 \, \text{kA} \, \text{cm}^{-2}$ can be driven by these diodes in pulsed mode. It is worth noting that the diode is not destroyed at the highest voltage applied during this experiment. The maximum magnitude of the pulse generator is reached and a smaller series resistor was not available at the time. Significantly higher current densities might be reached.

5.3.5 Temperature-Dependent Current-Voltage (IV) Measurements of pin Diodes Based on Triclinic Rubrene Crystals

In this subsection, the temperature dependence of the IV characteristics of diodes based on triclinic rubrene crystals is discussed. Two devices are chosen exemplarily for the general behavior: one pin and one pn diode, both manufactured at the UFO evaporation tool. The IV characteristics of these two devices are combined in figure 5.3.5. The change in IV behavior is reproducible and reversible for both diodes. Cracking of the crystal – as discussed in chapter 4.2.4.1 – can be excluded. Since the temperature dependence of the single intrinsic and doped layers is small, no strong effect is expected from the diodes either.

Figure 5.27a shows the temperature dependence of a diode grown on a standard triclinic seed, a p-layer of 200 nm total thickness, doped at 0.5 wt.%, an intrinsic film thickness of 150 nm, and an n-layer thickness of 50 nm, doped at 1 wt.%. The current density is decreasing with temperature throughout the entire voltage regime. Surprisingly, the effect seems stronger in regime I, regime III, and the reverse leakage than in the Shockley regime. The change in threshold voltage over temperature for this device is shown in figure 5.27a. $V_{\text{Th},1}$ that corresponds to the physical threshold voltage decreases with temperature, in accordance with theory. The rate of change is $1.8 \, \text{mV} \, \text{K}^{-1}$. The onset of the conduction regime III shows an even stronger temperature dependence at $6.2 \, \text{mV} \, \text{K}^{-1}$. The temperature dependence of the exponential fits of the Shockley regime can be used to extract the relevant energetic distance E_{A} in this system, by calculating the crossing voltage for fits at different temperatures. The method is described in [236]. The resulting energy is $(1.5 \pm 1.3) \, \text{eV}$. This result seems plausible, however, the variation is large – which can be attributed to a significant degree to the "by-hand" selection of the fit parameters. The maximum conductivity of this diode does not change with temperature. The current density at 3 V, shown in figure 5.27b, allows for a fit of activation energy of 63 meV for the high-temperature regime. Which exact process is limiting in each regime is – similar to the single-layer measurements – difficult to decide.

Figure 5.26: Temperature-dependent IV measurements of pin and pn diodes based on triclinic rubrene.
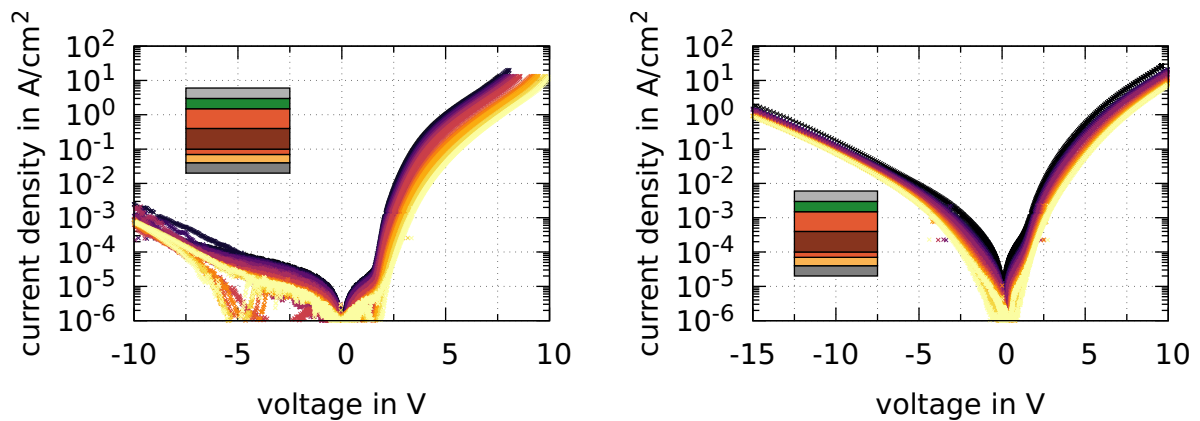
(a) pin diode with 200 nm p-layer doped with 0.5 wt.%, 150 nm intrinsic layer, and 50 nm n-layer doped with 1 wt.%, temperature decreased from 300 K to 80 K (dark to bright).

(b) pn diode with 300 nm p-layer doped with 0.5 wt.% and 100 nm n-layer doped with 1 wt.%, temperature decreased from 300 K to 80 K (dark to bright).

Figure 5.26b shows the temperature dependence of one of the previously discussed pn diodes. The p-layer is 300 nm, doped at 0.5 wt.% and the n-layer is 100 nm, doped at 1 wt.%. The behavior is slightly different compared to the pin diode, since the change in current is the same in each voltage regime. Subsequently, neither of the two threshold voltages show any significant change with temperature (see figure 5.27c). The entirety of the IV curve is shifted towards lower currents when the device is cooled. The corresponding activation energy for the high-temperature regime can be estimated to 37 meV.

Figure 5.27: Extracted parameters from pin and pn diodes shown in figures 5.26.
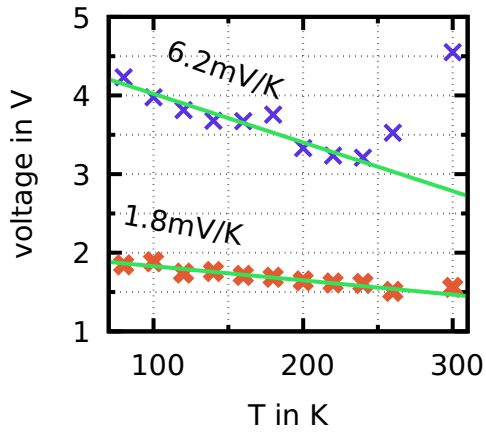
(a) Temperature dependence of threshold voltages from IV characteristics shown in figure 5.26a: **red (bright), fat:** $V_{Th,1}$, **blue (dark), thin:** $V_{Th,2}$, **green:** linear fit of low temperature regime.
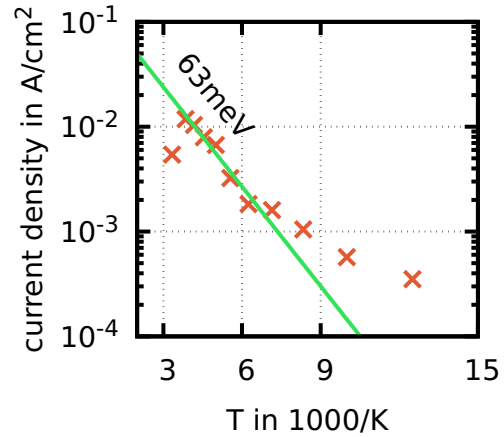
(b) Temperature dependence of current density at 3 V from IV characteristics shown in figure 5.26a: **green:** exponential fit of high-temperature regime.
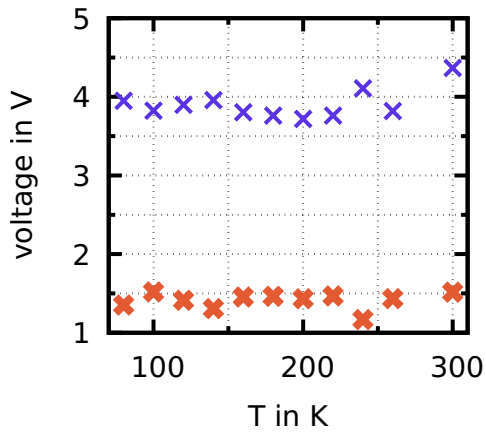
(c) Temperature dependence of threshold voltages from IV characteristics shown in figure 5.26b: **red (bright), fat:** $V_{Th,1}$, **blue (dark), thin:** $V_{Th,2}$.
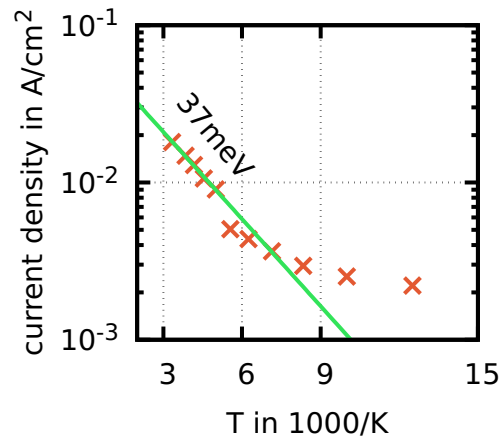
(d) Temperature dependence of current density at 3 V from IV characteristics shown in figure 5.26b: **green:** exponential fit of high-temperature regime.

5.4 Application for Organic Diodes Based on Crystalline Rubrene

5.4.1 Organic Light Emitting Diodes (OLEDs) Based on Crystalline Rubrene

The two most successful applications for organic semiconductors that are both used in commercial products are Organic Solar Cells (OSCs) and OLEDs. Since OSCs are already investigated by Verreet et al. [50] – although based on the orthorhombic platelet polymorph – OLEDs will be the focus here. A majority of an OLED is made up of transport layers that can greatly benefit from a high mobility material like crystalline rubrene. The question to be answered is if the optical properties of the material system can be tuned to allow for efficient light emission.

The final goal for these devices is to be used in electrically pumped organic lasers. Although research regarding the optical properties shows much progress ([245], [246], [247]), the pumping intensities needed to allow lasing operation with common designs have not been reached yet. This is, in part, due to the low conductivity of typical OLED materials. Most of the work relating the use of rubrene crystals for organic lasers is summarized in a PhD-thesis by Stefan Meister [210]. Here, a summary of pre-tests is given. A significant part of this work was created in the scope of a Bachelor thesis by Tobias Antrack [244].

The stack of the diodes investigated here is shown in figure 5.28. Rubrene by itself can technically be used as an emitter material [93], and indeed, the pin diodes presented in section 5.3 show faint light emission at high current densities.
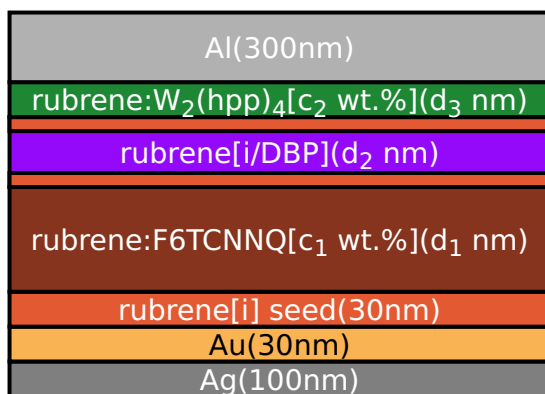
Figure 5.28: Standard stack for OLEDs based on crystalline rubrene: The emitter material is mixed into the intrinsic film. A layer of pure intrinsic material can be added underneath, on top of, or on both sides of the emitter film.
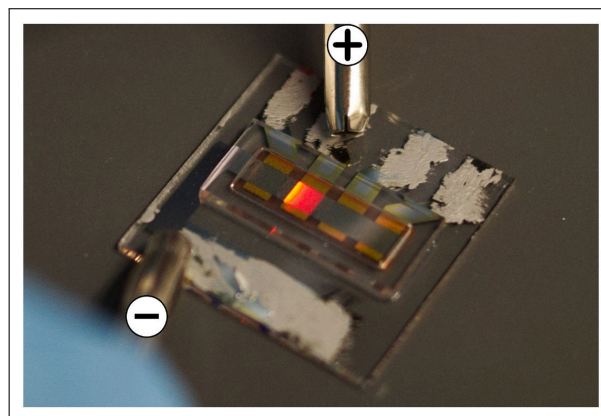
Figure 5.29: Light emission of triclinic rubrene-based OLED with DBP as emitter (figure from Tobias Antrack [244]).
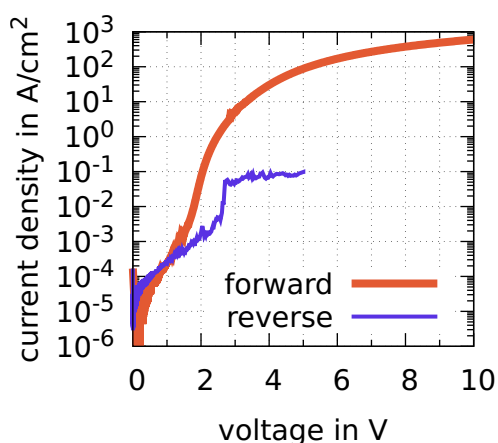
Figure 5.30: IV characteristic of an OLED based on triclinic rubrene crystals: p-layer: 300 nm, doped with 0.5 wt.% F6TCNNQ; n-layer: 50 nm, doped with 1 wt.% $W_2(hpp)_4$; intrinsic layer: 150 nm, doped with 2 wt.% DBP.
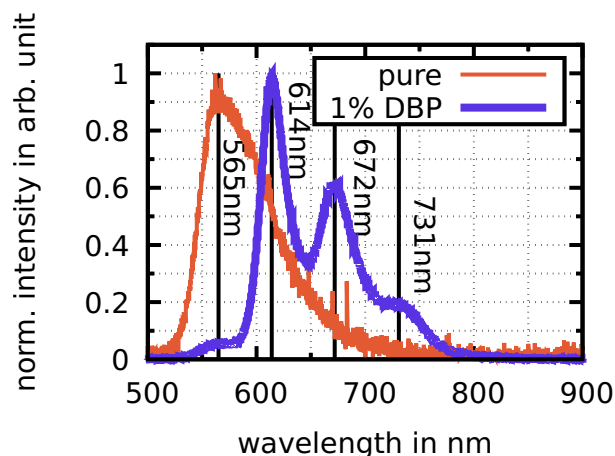
Figure 5.31: Emission spectra of pin diode based on triclinic rubrene and pin diode based on rubrene mixed with the emitter DBP.

The spectrum of this emission is shown in figure 5.31 and corresponds well with spectra of singe-crystalline rubrene emission found in literature [248], which depends in itself on the crystal axis along the light emission. It is distinct from emission of amorphous rubrene [249]. The spectrum for the measured films shows one single peak at 565 nm with a Full Width Half Maximum (FWHM) of 78 nm. It is surprising that the supposedly crystalline emission spectrum of orthorhombic crystals matches so well with these triclinic thin-films. Nevertheless, the efficiency of light emission for the purely rubrene-based devices is unusably low. An External Quantum Efficiency (EQE) below 0.05 % is measured. A low EQE is expected considering the long diffusion length and comparably low rates of recombination discussed in earlier sections. To realize efficient light emission, an emitter material must be used. The energy levels and the emission and absorption spectra of matrix and emitter must match for excitons to be transferred. An experiment based on the emitter material DCM[4] showed no change in the emission spectrum compared to the pure rubrene layer. Choi et al. [94], present OLEDs based on an active layer consisting of rubrene mixed with DBP. To date, DBP seems to be the only emitter material compatible with rubrene mentioned in literature.

A first test device (made at the UFO evaporation tool) is based on triclinic rubrene grown on a 40 nm seed heated at 140 °C for 10 min. The p-layer is 300 nm in total, doped with 0.5 wt.% F6TCNNQ. The n-layer is 50 nm doped with 1 wt.% $W_2(hpp)_4$. The intrinsic film is mixed with 2 wt.% DBP through the entire film of 150 nm. Later, experiments showed that not the entirety of the intrinsic film

---

[4]The energy levels of both materials fit. However, the emission and absorption spectra do not overlap sufficiently, which is necessary for the typical Förster Resonant Energy Transfer (FRET).
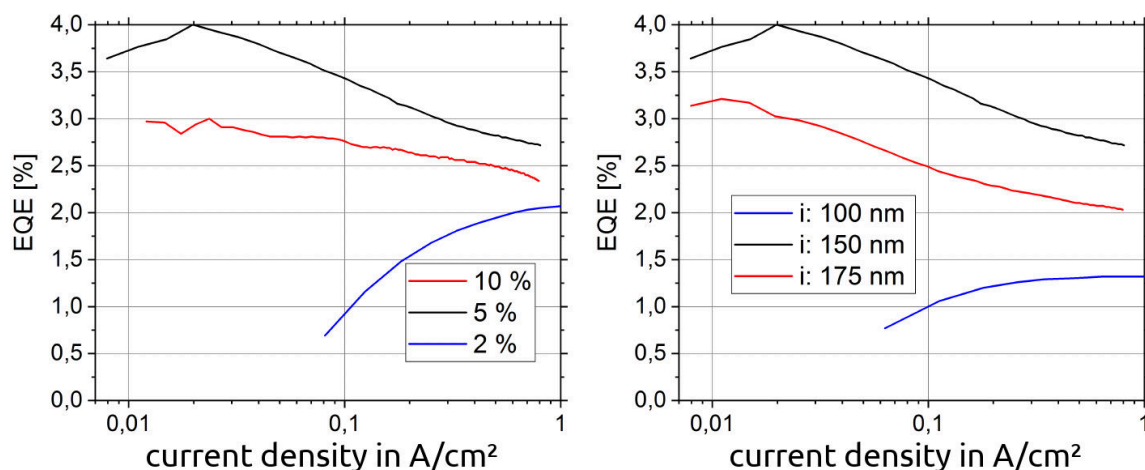
Figure 5.32: EQE measured for OLED devices based on triclinic rubrene with changing emitter doping concentration and a fixed intrinsic layer thickness of 150 nm (**left**) and changing thickness of the intrinsic layer with a fixed emitter concentration of 5 wt.% (**right**): p-layer: 200 nm, doped at 5 wt.%, n-layer: 100 nm, doped at 5 wt.%, thickness of the emitter layer: 20 nm, figure from [244].

must be doped with emitter material. The transfer of excitons to the emitter and subsequent emission is highly efficient. The IV curve of a diode from this initial test can be seen in figure 5.30. Surprisingly, this specific set of devices showed an extremely high conductivity and resilience. Current densities up to $1\,\mathrm{kA\,cm^{-2}}$ can be reached, even in normal – non-pulsed – sweeps. However, reverse current is unstable in these devices and shows many breakdowns. Thus, most of these diodes do not show any kind of reproducible rectification. Nevertheless, the light emission of these OLEDs is strong and changed to a dark red. The corresponding spectrum is shown in figure 5.31. Additional to the original rubrene peak at 565 nm, three significantly stronger peaks can be seen at 614 nm, 672 nm, and 731 nm. Experiments by Tobias Antrack showed that the relative intensity of these peaks depends on the stack composition. If this is the result of standing waves within the structure or different recombination processes could not be ultimately decided. In the same scope, a limited variety of parameters and evaluation of efficiencies of the resulting devices are performed. The maximum EQE of 4 % was measured for devices with a p-layer of 200 nm, doped at 5 wt.%, an n-layer of 100 nm, doped at 5 wt.%, and a total intrinsic layer thickness of 150 nm. The emission layer of 20 nm is doped with 5 wt.% DBP. A decrease in emitter concentration (2 wt.%) had a strong negative effect on the efficiency of the device. An increase to 10 wt.% caused a decrease in EQE too, but to a much smaller extent. A similar effect can be seen with thinner and thicker intrinsic films. The effect of the position of the emission layer is minor.

The performance achieved is comparably high, especially considering a non-optimized device without any kind of blocking layers. Further investigations into the viability of high-intensity OLEDs might be interesting.

5.4.2 Ultra High Frequency (UHF) Rectifiers Based on Crystalline Rubrene

A second application that is directly utilizing the high charge carrier densities of crystalline rubrene thin-films is signal diodes. Diodes, even when not light-emitting or absorbing, can fulfill a large array of functions in electronic circuits. One of which is the filtering of signals which in the simplest case is a rectifier circuit. The theoretical background of AC-signal rectification is given in chapter 2.3.2.2. This section is split into two parts. The first presents measurement on half-wave rectifier circuits at UHF, while the second section discusses numerical simulations of this rectification process, based on static IV measurements.

5.4.2.1 Measurements of Ultra High Frequency (UHF) Rectifiers

Two sets of rectifier circuits are discussed: The first is based on Schottky and pin diodes made at the Lesker evaporation tool. The circuit is based on the circuit diagram in figure 3.5 with the corresponding mask design HF1. The second set of devices is optimized towards UHF rectification and built at the UFO evaporation tool. It is made according to the circuit diagram in figure 3.6 and uses the mask layout HF2. A microscope micrograph of one of the devices from the second set is shown in figure 5.33c, marking the input and output side, as well as the positions of external circuitry. The manufacturing and design of the circuit are discussed in chapter 3.2.2. The first set is measured using an Agilent 81150A as the signal source, which allowed for a maximum frequency of only 240 MHz at a high amplitude of up to 10 V. The output is measured using a Rohde& Schwarz RTM-2054 oscilloscope. For the sake of simplicity, initial tests are done using the built-in capacitor (100 pF) and ground-resistor (1 MΩ) of the oscilloscope probe. This procedure is justified, since a low load resistance is realistic for a signal filtering application at UHF. The output of this circuit is likely to be fed into a Field-Effect Transistor (FET) circuit which features a high input impedance. The low smoothing capacitance is only relevant at low frequencies when more charge escapes the capacitor during one cycle than is loaded. The effect can be seen in the waveform shown in figure 5.34a, where only a low frequency of 10 kHz is used. A significant – non-harmonic – wobble is present at the output. However, once the frequency is raised to higher values (see figure 5.34b, at 1 MHz), only a small sinusoidal AC-signal on top of the Direct Current (DC)-output remains, as is to be expected. The frequency regime that is relevant in this scope can be covered without problems.

In first order, the maximum frequency at which a rectifier diode can operate can be estimated by its *RC*-time, as given by equation 3.3. In inorganic electronics, usually Schottky diodes are used for UHF applications, since the capacitance of these devices is smaller than comparable pn diodes. Based on the data from previous chapters, Schottky diodes based on triclinic rubrene should be even
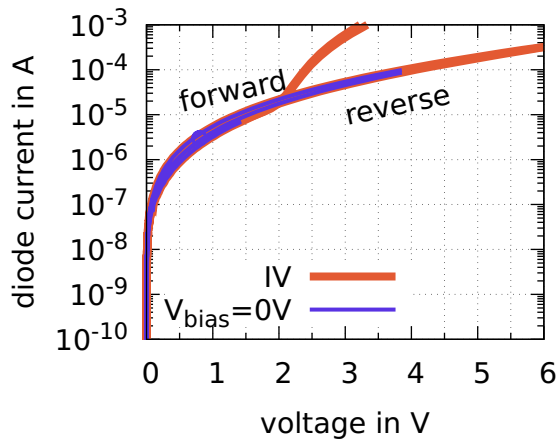
(a) pin diode with original stack and electrode design (no injection assistance, made at Lesker tool).
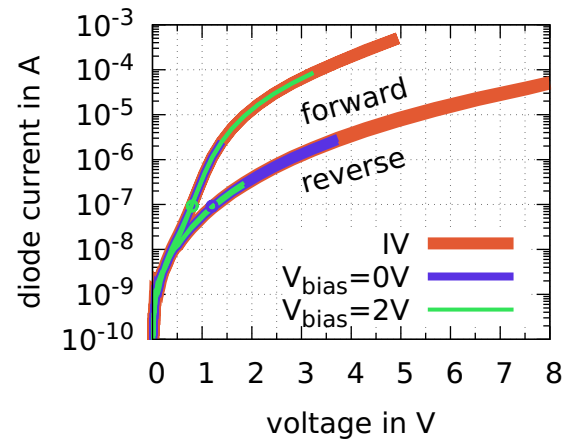
(b) Device with improved stack design (n-C_{60} injection, made at UFO tool).
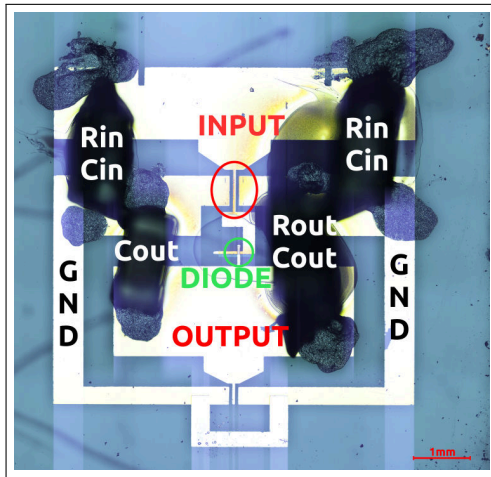
(c) Overview image of UHF rectifier circuit, based on mask design HF2.

Figure 5.33: red: IV characteristics of diodes measured prior to UHF measurement: **blue:** section of IVs for V_{ac}=2.7 V, V_{out}=0.8 V, and V_{dc}=0 V: "on-state" is not reached for old design
green: section of IVs for V_{ac}=2.7 V, V_{out}=0.8 V, and V_{dc}=2 V, circles mark the central point (V_{out}) of the oscillation.

more superior over their pin diode counterparts due to the higher conductivity, especially at low voltages. The frequency-dependent rectification performance of circuits based on Schottky and pin diodes are shown in figures 5.35. Both are based on triclinic seeds grown from 40 nm undoped rubrene. The Schottky diode (shown in figure 5.35a) features a p-layer of 200 nm doped at 5 wt.% and an intrinsic film of 100 nm. The circuit shows a maximum DC-voltage of 4 V, at an input of 9 V. However, the voltage drops off noticeably, starting at 0.5 MHz. The corresponding 3 dB-cutoff frequency is at 5.7 MHz (f_0=7 GHz).

The pin diode is made with a p-layer of 200 nm doped at 5 wt.%, an intrinsic film of 200 nm, and an n-layer of 20 nm doped at 5 wt.%. The rectification performance is shown in figure 5.35b, using the same conditions as the Schottky diode. The DC-output voltage is in maximum at 2.5 V with an input amplitude of 6 V and – similar to the Schottky diode – at 4 V with an input amplitude of 9 V. In contrast to the Schottky diode, the drop-off in performance starts here at a higher

Figure 5.34: Input and output signal of a half-wave rectifier made with the first set of diodes: input amplitude: 6 V, no pre-bias, load resistor: 1 MΩ, load capacitor: 100 pF, **orange:** average DC output voltage.
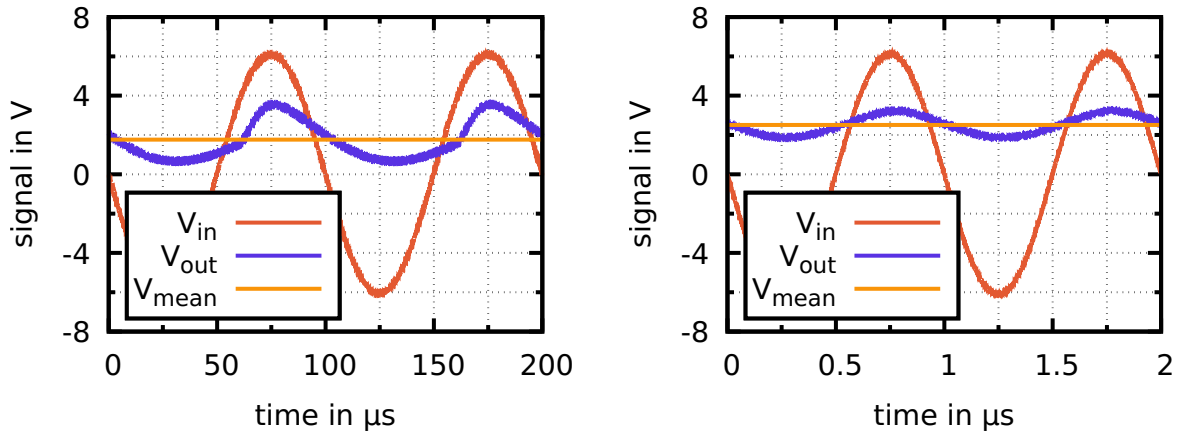
(a) Measurement at f =10 kHz: The distortions are a result of the small output capacitor.

(b) Measurement at f =1 MHz: Distortions are changed into normal output ripple at higher frequencies.

frequency (2 MHz) and is significantly milder. Within the measurement range of this experimental setup, the cutoff frequency could not be reached and f_{3db} could not be estimated reasonably. However, from the data it is clear that pin diodes based on crystalline rubrene show significantly better UHF properties than comparable Schottky diodes.

To still estimate a limit and test the current driving capabilities, the same experiment is repeated with a load resistor of 33 kΩ. The resulting measurement is shown in figure 5.35c. The maximum output voltage is at 0.9 V with an input amplitude of 6 V, which translates into an average load current of 27 µA. The drop in frequency starts approximately at the same point as the previous devices, however, the slope of the decrease is significantly higher when a larger load is used. The cutoff frequency can be estimated to 18.1 MHz. The pin diode is thus even under extremely adverse circumstances faster than its Schottky diode counterpart. The cause of this difference is likely in the reverse recovery time. It is the time required to remove excess charge carriers from the depletion zone after full-forward operation. It is usually associated with the recombination of charge carriers. If the input signal is slow enough, charges are recombined before reverse voltage is applied and normal rectification takes place. However, if the period of the input signal is in the same order of magnitude as the reverse recovery time, a significant amount of charge carriers is left in the depletion zone. The reverse conductivity is thus the same as the forward conductivity for a certain amount of time. The technical parameter of the reverse recovery time as it is described in datasheets of commercial diodes is based on a strictly defined procedure[5]. In

---

[5]A defined positive bias is switched via a step-function to a defined reverse bias. The reverse recovery time is defined as the time that passes – since the switching event – till the initial high
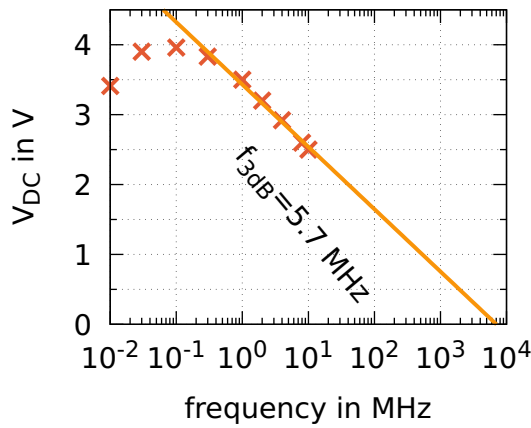
(a) Schottky diode based on a p-layer of 200 nm doped at 5 wt.% and an intrinsic film of 100 nm (load resistor: 1 MΩ, load capacitor: 100 pF, amplitude: 9 V).
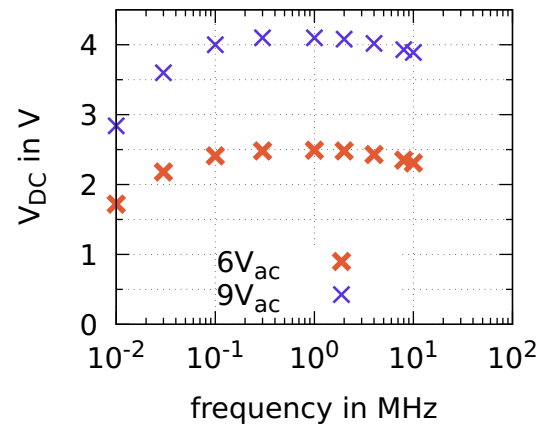
(b) pin diode based on a p-layer of 200 nm doped at 5 wt.%, an intrinsic film of 200 nm, and an n-layer of 20 nm doped at 5 wt.% (load resistor: 1 MΩ, load capacitor: 100 pF).
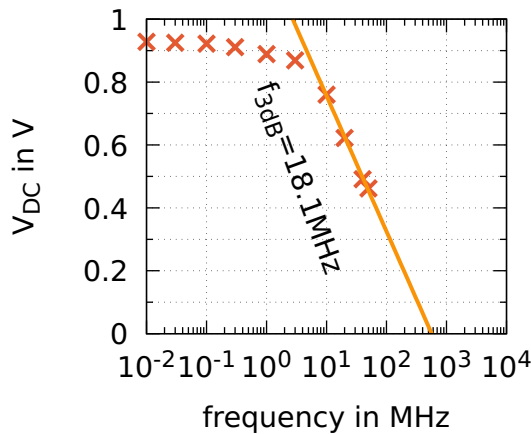
(c) pin diode based on a p-layer of 200 nm doped at 5 wt.%, an intrinsic film of 200 nm, and an n-layer of 20 nm doped at 5 wt.% (load resistor: 33 kΩ, load capacitor: 100 pF, amplitude: 6 V).

Figure 5.35: Output voltage over frequency of input signal for different types of diodes and circuits. All diodes are based on triclinic rubrene crystals with a 40 nm undoped seed grown at 130 °C for 15 min on glass substrates. The decrease of voltage at high frequencies can be attributed to the operation of the diode. The lower output at low voltages is caused by the small output capacitor.

itself, it does not contain any assumption regarding the process that governs the time dependence. The last subsection of this chapter takes a closer look at this phenomenon using simulations of charge balance in these rectification processes. The second set of experiments is run using pin diodes that are more optimized towards rectification. The problem of the high threshold voltage is reduced by introducing an n-doped layer of C_{60} between the n-layer of rubrene and the Al electrode. The thickness of the n-layer is reduced to increase overall conductivity. Most importantly, the electrode setup is changed to mask design HF2. Due to the more compact geometry and the introduction of compensation capacitors at

---

reverse current is decreased to 25 % of its maximum value.
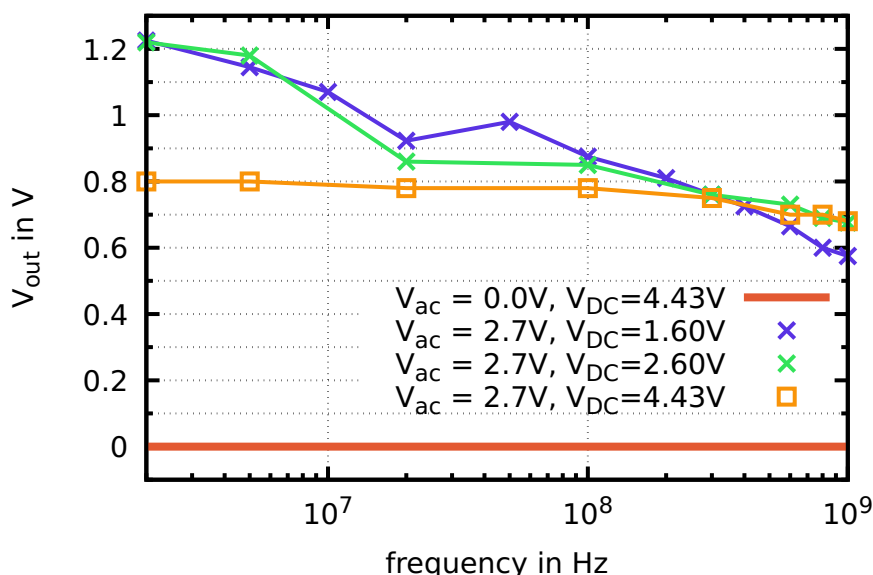
Figure 5.36: Output voltage over frequency of input signal for pin diode aimed at rectification, based on triclinic rubrene crystals with a 40 nm undoped seed grown at 130 °C for 15 min on a glass substrate. The total p-layer thickness is 300 nm doped at 5 wt.%, intrinsic layer thickness is 100 nm, and the n-layer thickness is 20 nm doped at 0.5 wt.%. An additional layer of 20 nm, 1 wt.%-doped C_{60} is introduced on top of the n-rubrene. The diode is DC-biased to compensate for threshold voltage.

the input, resonance-free measurement is possible beyond 1 GHz. Unfortunately, the available signal generator for the GHz-range (Keysight E8257D) can only supply an AC-amplitude of 2.7 V. Regardless of technical limitations, a lower input amplitude is beneficial from a stability point, since the power dissipated in the device can be estimated to

$$P = 2\pi^2 R_d (C_d V_d f)^2. \tag{5.7}$$

The power increases strongly at higher voltages. A decrease in signal amplitude can counteract this effect and protect the diode from overheating. However, despite the improvement by the n-doped C_{60}, driving the circuit at an amplitude of 2.7 V proves to be non-satisfactory. A DC-bias is introduced (via an SHFBT65B Bias Tee) to the circuit to set the diode at a more favorable point of operation. This procedure is illustrated in figures 7.11a and 7.11b. The first graph shows the static DC IV curves of a corresponding diode from the first set of rectification tests, the second graph shows a diode from the second set in red. The diode of a rectifier circuit driven by an amplitude of 2.7 V and an output voltage of 0.8 V is biased between 1.9 V in forward direction and −3.5 V in reverse. The corresponding area is marked in blue in both graphs. The higher the – positive – output voltage, the less time is spent in forwards direction. At this biasing condition, the device from the first set is not reaching its on-state at all, while the device from the second series is reaching its on-state but is "switched-off" for the majority of each period. Only an increase in signal amplitude can extend the

on-time. Alternatively, introducing a DC-bias of 2 V, changes the effective voltage range to 3.9 V to −1.5 V, increasing the time in the high-conductivity regime. the parts of the IV curve that are active with a 2 V bias are marked in green in figure 7.11b.

Figure 5.36 shows the frequency-dependent output of a rectifier based on the improved setup. Because the output signal is measured using a signal analyzer (Rohde&Schwarz FSV 7 GHz), no waveforms are available. The output of the circuit is made up of a 10 MΩ resistor and a 5.4 nF capacitor. The capacitor is split into two single devices with 2.7 nF each, oriented in opposite directions. This arrangement reduces the influence of stray inductances. On the input side, two pairs of resistors (94 Ω) and capacitors (0.5 pF) are placed in opposite orientation to ensure impedance matching with the signal source. Compensation of stray capacitances within the cables and the remaining measurement setup is performed prior to any measurement to ensure the input voltage at the circuit is identical for all frequencies. The current generated by the DC-biasing is compensated at the output via a current source. A measurement with DC-biasing but without any AC-signal yields thus no output voltage (see red line in figure 5.36). As expected, the frequency behavior is different depending on the external biasing. When the diode is biased with 1.6 V and 2.6 V the results are similar. The highest output measured is at 1.2 V, with a slow but steady decrease with frequency. Considering 1.2 V as the plateau, the cutoff frequency can be estimated to 30 MHz. Increasing the bias to 4.43 V changes the behavior significantly. The maximum output voltage is decreased to 0.8 V, which is a result of the shift in the point of operation. At this high bias, the diode is operating mostly in the "on-state", even in reverse biasing condition. Rectification is thus caused by the strong non-linearity of the IV curve. The current for the positive half of each cycle is high, since the diode is operating in the high-conductivity fork of its IV curve, while the current in reverse direction is low, since the diode is operating on the low-current side. A linear device would not feature any rectification at all, but the exponential increase in conductivity of these diodes causes more current to flow in the positive half than in reverse. However, the decrease in output voltage with frequency is now even weaker than before. At 1 GHz, the loss in signal strength is only 1.4 dB and thus significantly better than the currently fastest organic rectifier diode by Kang et al. [131]. The decrease in output voltage over frequency is only indicated slightly in this measurement, an estimation of the cutoff frequency is thus extremely difficult. It can be assumed to be between 2 GHz to 30 GHz. Measurement beyond 1 GHz is not possible due to the destruction of the diode. Heat-induced damage seems likely considering the large current through the device at this frequency (400 A cm^{-2}rms, additionally to the DC-current of 0.2 A cm^{-2}). However, the temperature-dependent measurements of section 5.3.5 suggest only a low temperature-dependence. A different cause for the destruction of the device could be found in exposure to ambient air. Due

to the miniaturization of the circuit, common encapsulation methods are not possible. The diode is thus only covered by a drop of the polymer Cytop. This offers acceptable protection from water, but virtually no protection from oxygen. A heat-induced increased rate of oxidization can thus also be the cause of the destruction of the diode. It can be assumed that even higher frequencies could be reached, once proper encapsulation is implemented.

One further way to estimate the capabilities of these films is via the transit time through the vertical stack. Utilizing equation 2.57 and the charge carrier mobility of $10.3\,\mathrm{cm^2\,V^{-1}\,s^{-1}}$ measured in chapter 4.2.2.1, a total layer thickness of 400 nm, and a maximum potential difference over the diode of 3 V, charge carrier can effectively transit the stack up to a frequency of 19.3 GHz. This result is only a rough estimation, not considering other effects like field- and density-dependent mobilities or non-homogeneous field distribution. Alternatively, the RC-time of the device measured can be calculated via

$$f_{RC} = \frac{1}{2\pi RC}. \tag{5.8}$$

With a differential resistance of $r_{\mathrm{diff}} = 2.7\,\mathrm{k\Omega}$ at the point of operation and a junction capacitance of $25\,\mathrm{nF\,cm^{-2}}$, f_{RC} can be estimated to 3.7 GHz.

5.4.2.2 Simulation of Ultra High Frequency (UHF) Rectifiers

This section presents numerical simulations of the half-wave circuits discussed in the previous section. The simulation is based on the static IV characteristics of real devices and applies this to a dynamic balance of charges. The forward current during forward bias (as seen by the diode) must supply enough charges Q_{forward} to compensate for reverse current during reverse bias Q_{reverse} and current through the load Q_{load}. The current in forward direction is larger than in reverse. The output capacitor is thus charged more positively than discharged and a finite positive charge remains on the capacitor each cycle. This defines the output voltage V_{out}. Since the output now has a finite DC-voltage, the voltage as "seen" by the diode changes. The absolute positive voltage and the time it is applied to the diode is decreased. Subsequently, the absolute negative voltage and the time it is applied to the diode is increased. This process continues, until

$$Q_{\mathrm{forward}} = Q_{\mathrm{reverse}} + Q_{\mathrm{load}}, \tag{5.9}$$

for each full cycle. The following simulation is based on this steady-state condition. The current used for the calculation is based on static measurements of diodes but includes the influence of a finite reverse recovery time. Other electronic processes, like a carrier activation time, or capacitive influences are neglected. A flow chart of the simulation is given in figure 5.37. A series of sinusoidal signals is generated with the frequency f and the amplitude V_{ac}. They are offset by N_{N}

- define $V(t) = V_{ac}sin(2\pi f t)$
- shift $V(t, V_{out}) = V(t) - V_{out}$
- $0 < V_{out} < V_{ac}$
- N_N number of V_{out}
- t spaced at Δt

- $V > 0$ (blue)
- forward current
- $V_{out} \uparrow = t_{for.} \downarrow$

- $V < 0$ (red)
- reverse current
- $V_{out} \uparrow = t_{rev.} \uparrow$

- input: real IV curve
- separate forward and reverse

- define $\gamma_i(t) = e^{\left(\frac{t-t_i}{\tau}\right)^n}$ for each time t_i
- $I(t) = \max\limits_{i(t_i \leq t)} \left(\frac{I(t_i)}{U(t_i)}\gamma_i(t)\right) U(t)$

- $Q(V_{out}) = \int_0^T I(t)dt + \frac{V_{out}}{R} * T$
- $V_{out} = V_{out}(\min |Q|)$

- repeat for each f
- **parameter:**
  - delay time τ
  - delay coefficient n
  - amplitude V_{ac}
  - bias V_{dc}
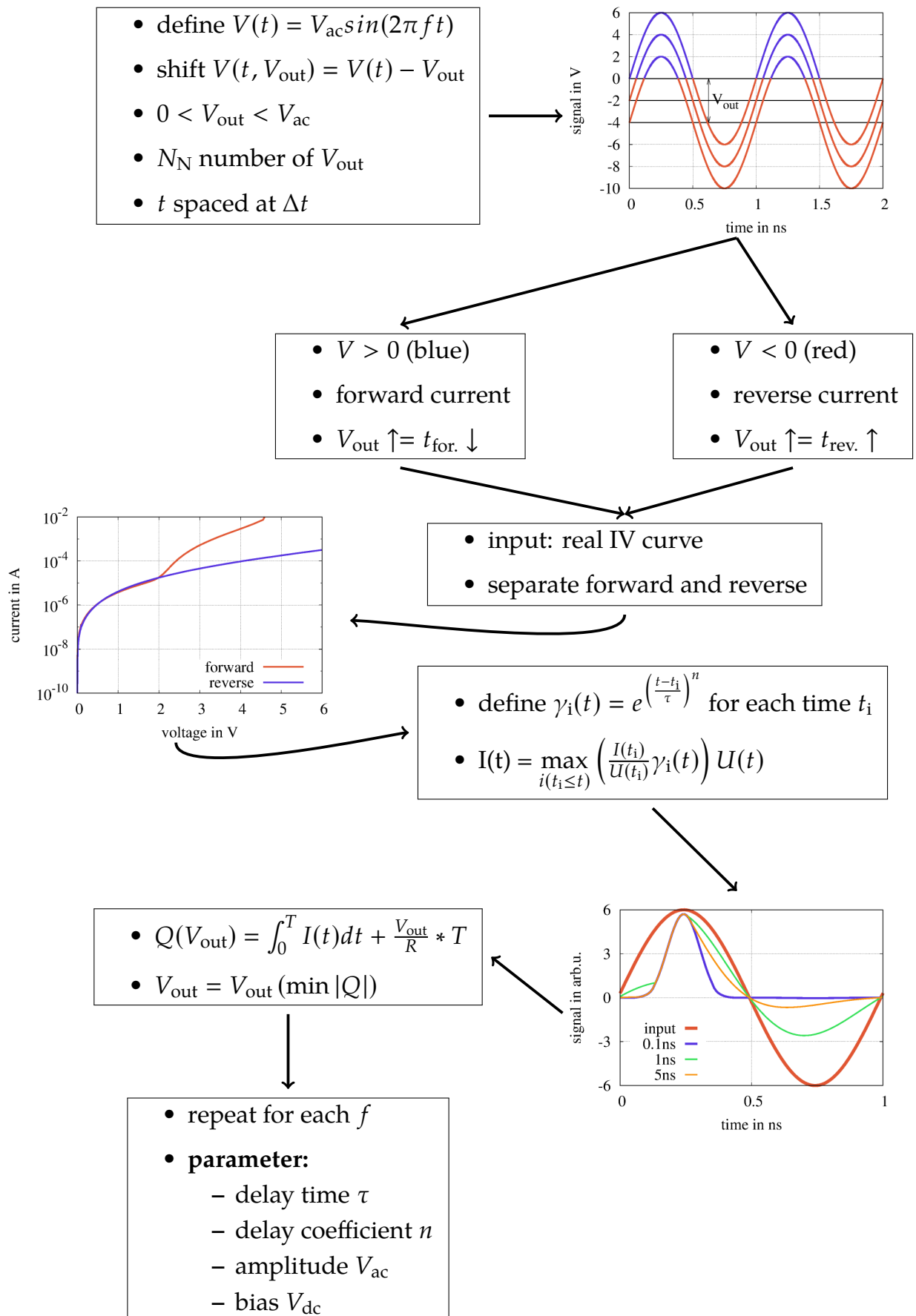
Figure 5.37: Simulation flowchart.

Figure 5.38: Output voltage of half-wave rectifier for different biasing conditions gained from simulations: τ=1 ns, n=1.
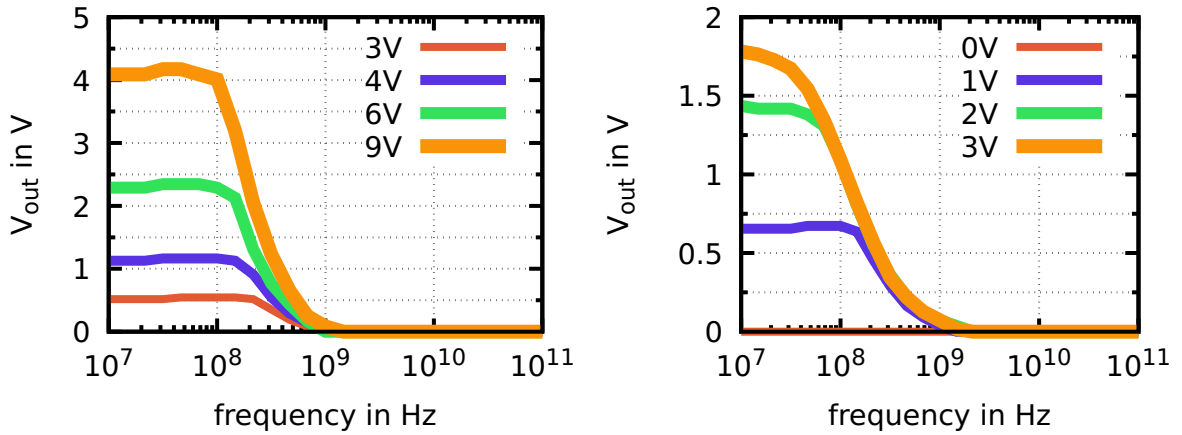
(a) Output voltage at different AC-amplitude: V_{dc}=0 V.

(b) Output voltage at different DC-biasing: V_{ac}=2 V.

different threshold voltages. The forward and reverse current through the diode are calculated based on the measured IV curve, including a reverse recovery time as follows. The conductivity $\sigma(t_i) = \frac{I(t_i)}{V(t_i)}$ is defined for each time step of the simulation based on I and V of the static measurement. This conductivity remains active for the following timesteps. A delay factor is defined as

$$\gamma = \gamma_i(t) = e^{\left(\frac{t-t_i}{\tau}\right)^n}, \tag{5.10}$$

with τ as the reverse recovery time and n as the relaxation exponent. It describes how much the conductivity σ_i of the timestep t_i still influences the conductance at the time t. Similar to free charge carriers in real devices, a certain amount of time is needed till charge carriers are relaxed. The current at each time t is calculated from the highest conductivity $\sigma_i \gamma_i(t)$ that is active at that time t. If the input voltage is above 0 V, the corresponding charge is added to $Q_{forward}$. If the input voltage is below 0 V, the corresponding charge is added to $Q_{reverse}$. This is equivalent to a time integral of the current over one full period. This procedure is repeated for all of the possible output voltages. If V_{out} is to low, $Q_{forward}$ is larger than $Q_{reverse}$ and vice versa if it is too large. Thus, the resulting output voltage must generate the minimum of $|Q_{forward} - Q_{reverse} - \frac{V_{out}}{R}T|$, with T as the time of one full period. This procedure is repeated for each of the frequencies. Since a large variety of parameters is measured with the first set of devices, the simulation uses the IV of one of the diodes from the first set. The corresponding curve is shown on the left half of figure 5.33. The results of the simulation are summarized in figures 5.38 and 5.39. To evaluate if the simulation shows the correct rectification behavior, two different AC-amplitudes are set, without any DC-bias and with a constant τ of 1 ns (see figure 5.38a). It should correspond

Figure 5.39: Output voltage of half-wave rectifier for different time constants and exponents of the charge carrier relaxation process gained from simulations: V_{ac}=6 V, V_{dc}=0 V.
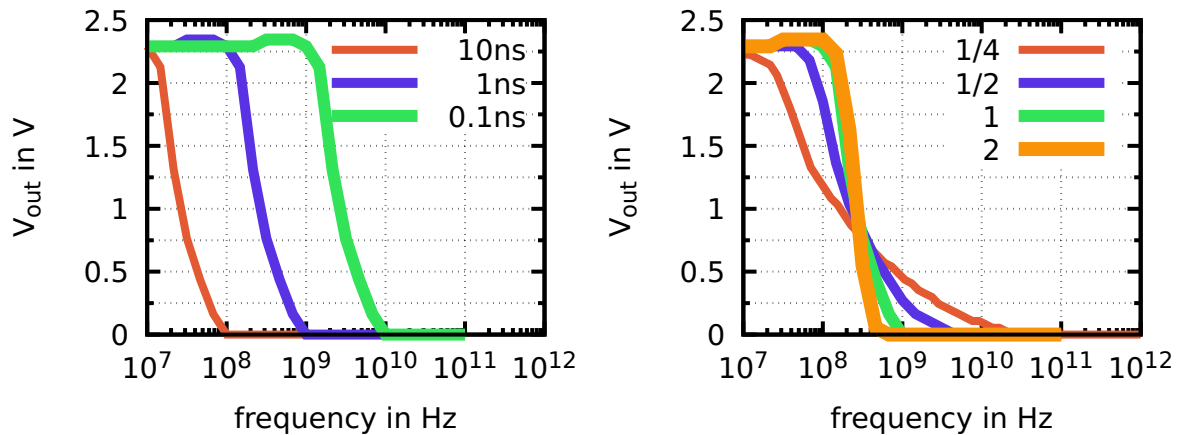
(a) Output voltage frequency for different relaxation times τ of carrier recombination: $n = 1$.

(b) Output voltage frequency for different exponents n of carrier recombination function: $\tau = 1$ ns.

to the measurement shown in figure 5.35b. Indeed, the maximum voltages predicted by the simulation correspond well with the measurement results at 6 V and 9 V amplitude. In figure 5.38b, the amplitude is fixed at 2 V. In measurement, no output voltage is measurable, since the maximum voltage that is applied is below the threshold of the diode. The same result can be seen for the simulation. However, once a DC-bias is introduced, an output voltage can be seen. It is worth noting that the output voltage cannot exceed the input amplitude, regardless of the DC-bias. The simulation reproduces the output voltages predicted by the diode and the correct dependence on amplitude and bias.

The onset of the decrease in output voltage can be modeled via the relaxation time τ, as can be seen in figure 5.39a. Here, the amplitude is fixed at 6 V at 0 V DC-bias. Not surprisingly, the behavior of the circuit is identical for all relaxation times, just shifted along the frequency axis. However, even though the position of the initial decrease in output voltage can be set in the simulation to match the measurement, the decrease that can be measured in real devices is significantly milder than predicted by the simulation. The slope of the decrease is not dependent on the time parameter τ itself. It only describes at which frequency the drop-off starts. For all simulations the relaxation exponent n is set to 1 till now, since recombination would suggest a simple exponential decay. However, by tweaking n, the slope of the loss in output signal can be tweaked, as is presented in figure 5.39b. There does not seem to be any physical meaning that can be extracted from this parameter and even for small relaxation exponents, the overall shape of the decrease seen in measurements cannot be modeled correctly. The relevant process governing the reduction in reverse blocking at high frequencies cannot be the recombination of charge carriers. Considering the successful operation

of an Organic Bipolar Junction Transistor (OBJT) as shown in the last chapter 7, effective recombination would have been surprising. Modeling the relaxation of reverse current via a linear $1 - \frac{\Delta t}{\tau}$ or quadratic dependence $1 - \left(\frac{\Delta t}{\tau}\right)^2$ – as would be fitting for diffusion-limited system – does not yield the appropriate result either. The same applies to an inverse dependence $\frac{1}{\tau - \Delta t}$. The real defining process could not be identified. An alternative explanation for the behavior might be found in the operation in forward direction. A forward capacitance is present in the AC operation of these diodes, due to the charges that have to be moved in and out of the depleted film. A different forward capacitance based on the differently sized depletion layers in pin and Schottky diodes could create a transient behavior as seen here. However, measurements and analysis of transient properties in forward direction are difficult. Regardless of the exact nature of the dominant process, the defining time constant is in the order of magnitude of 50 ns. The extremely slow decrease of the output voltage is atypical when compared to classical diode theory and other publications. A comparison with values of other devices seems thus not feasible.

5.5 Summary

Three different types of organic semiconductors diodes are shown, Schottky diodes, pn, diodes, and pin diodes. Devices can be built from all of the previously investigated crystal polymorphs of rubrene, although the majority of the available data is based on the triclinic crystals. Schottky diodes show the highest conductivities and lowest threshold voltages. However, they also feature the worst rectification. Variation in the thickness of the intrinsic film in Schottky diodes allows for an estimation of the hole diffusion length in triclinic crystals of 154 nm.

The electrical performance of the pin diodes can be adjusted by varying the thicknesses of the individual layers and the respective doping concentrations. In general, thinner layers and higher doping concentration increase the overall current. However, both forward and leakage currents are affected. A special effect can be observed regarding the n-doped films. Several experiments indicate a total depletion of the n-layers. The efficiency of n-doping with $W_2(hpp)_4$ must be extremely low.

Two exemplary applications for these diodes are presented. OLEDs made from triclinic rubrene feature acceptable EQE. If these films can be used for high-power lighting applications has to be analyzed further. One promising field of application is electrically pumped organic lasers. The high speed of these diodes is investigated with half-wave rectifier circuits. The range of operation of these devices is beyond the GHz-range, faster than any other organic circuit shown to date.

parameter	p Schottky diode	pin diode
p doping concentration	• decreased on/off and V_{Th} • increased conductivity	• decreased V_{Th} • no influence on leakage
p layer thickness	• no significant impact	• no influence on V_{Th} • reduced leakage current
i layer thickness	• increased on/off and conductivity • decreased V_{Th}	• decreased leakage current • change of V_{Th} depends on other layers
n doping concentration	-	• increased V_{Th} • strong influence on reverse blocking
n layer thickness	-	• increased V_{Th} • strong influence on reverse blocking
injection doping	• p-side sufficiently doped by bulk	• p-side sufficiently doped by bulk • n-side can be improved with n-doped C_{60} • n-side doping unsuccessful with Cs, LiF, and $W_2(hpp)_4$

Table 5.1: Summary rubrene-based diodes I (gives result of increasing or introducing each parameter)

parameter	p Schottky diode	pin diode
highest reached current density	• $500\,\mathrm{A\,cm^{-2}}$ (DC sweep)	• $500\,\mathrm{A\,cm^{-2}}$ (DC sweep) • $2\,\mathrm{kA\,cm^{-2}}$ (pulsed sweep)
highest f_{3dB} rectification frequency reached	• $5.7\,\mathrm{MHz}$	• $>2\,\mathrm{GHz}$
temperature dependence of current density	• not measurable	• $\approx 37\,\mathrm{meV}$ to $63\,\mathrm{meV}$
highest reached EQE in OLED	-	• $4\,\%$ (emitter: DBP)

Table 5.2: Summary rubrene-based diodes II

6 Organic Field-Effect Transistors (OFETs) Based on Crystalline Rubrene Thin-Films

This chapter presents studies of OFET devices based on the thin-films of crystalline rubrene discussed in chapter 4. In the previous chapter, the properties of vertical charge transport are focused, while the next chapter discusses experiments on Organic Bipolar Junction Transistors (OBJTs) that are predominantly vertical devices as well. Nevertheless, the high charge carrier mobilities found in these films can be used in lateral or unidirectional devices too. A typical application for high mobility materials is field-effect transistors. Additionally to their use as switching and amplification devices, OFETs can be used to measure properties of the films (e.g. field-effect mobility) or investigate fundamental processes at the surface and interface of the semiconductor. It has to be taken into account that the parameters extracted are not intrinsic properties of the semiconductor but properties of the entire device system. Special care has to be taken when interpreting these data.

Here, a preliminary study is shown, discussing the viability of each crystal phase for use in OFETs, including an investigation of lateral charge carrier mobilities that are not accessible via the methods and devices of previous chapters. At last, VOFET devices based on these thin-film crystals are presented, highlighting the possible application in devices utilizing both lateral and vertical transport. Note that none of the devices shown here are optimized and the study and analysis of these devices are only a first step.
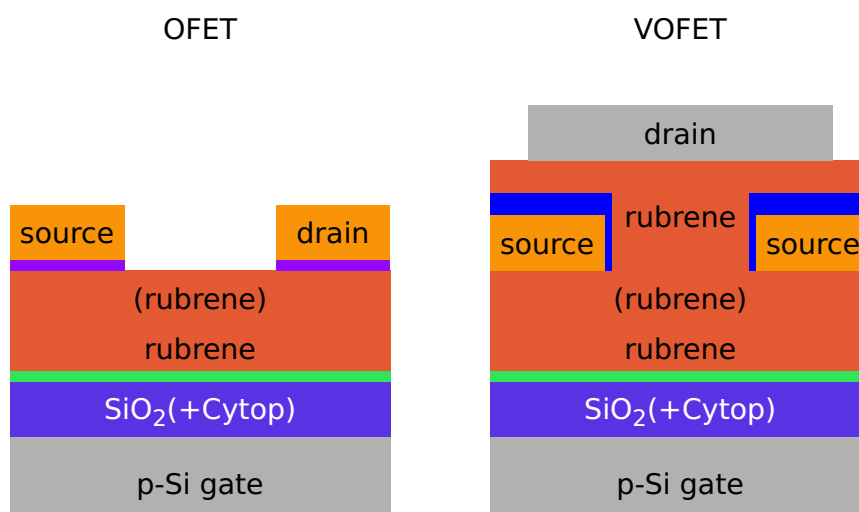
Figure 6.1: Stack composition for rubrene-based Organic Field-Effect Transistors (OFETs) (left) and Vertical Organic Field-Effect Transistor (VOFET) (right): The gate insulator consists of 100 nm of SiO_2 with an optional layer of 50 nm of Cytop. Seeds for each of the crystal phases are grown according to their standard procedures. For orthorhombic platelets, a sublayer of 5 nm TAPC is used (green). An additional layer of rubrene can be added on top of the seed. Injection doping (violet) can be added for OFET devices underneath source and drain (Au). Source insulator in VOFET devices consists of photoresist polymers.

6.1 Organic Field-Effect Transistors (OFETs) Based on Triclinic Rubrene Thin-Films

First, the triclinic crystal phase is investigated for the use in OFET devices. It is by far the most stable and reproducible of the three crystal phases investigated in chapter 4 and shows the highest vertical charge carrier mobility. However, the lateral structure of these films is dendritic with a strong tendency for branching. Along each of the individual branches, the crystal structure is quasi single-crystalline. However, hard grain boundaries are present between neighboring branches. This might result in a significantly reduced effective charge carrier mobility in lateral direction, since the resulting charge transport would be limited by hopping over the borders between branches.

Initially, purely lateral OFETs are investigated in a bottom-gate/top-contact configuration. Devices are built on doped Si-substrates that serve as the global gate electrode of the transistor. Source and drain electrodes are made from Au and are structured via shadow masking on top of the semiconductor. Channel width is 1000 µm, while channel length is varied from 50 µm to 200 µm. Devices that are based on the seed alone do not show any gate control over the drain current and almost no current in general. The Atomic Force Microscopy (AFM)

Figure 6.2: Current-Voltage (IV) characteristics of a bottom-gate/top-contact OFET based on triclinic rubrene thin-films: channel width W =1000 µm, channel length L =50 µm, dielectric: 100 nm SiO_2 + 50 nm Cytop (deposited by spin-coating), the seed is grown from 40 nm of undoped rubrene at 130 °C for 15 min, additional 20 nm are added via epitaxy.
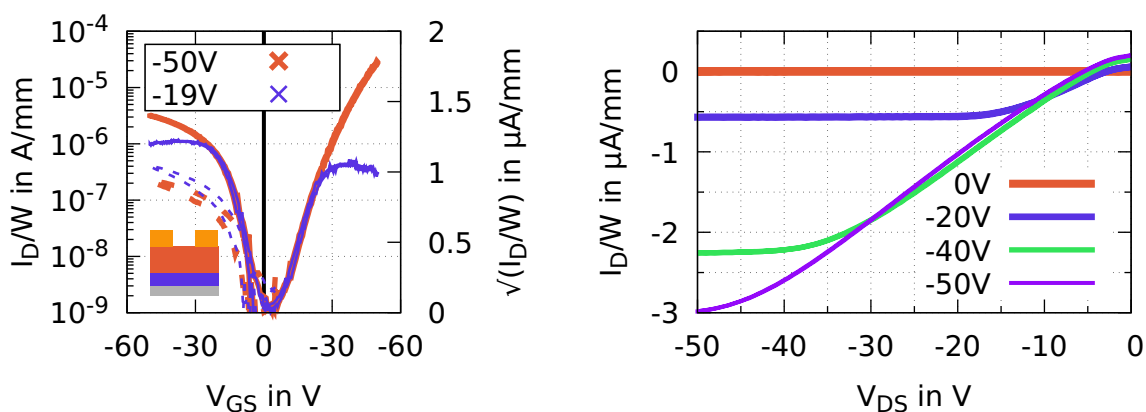
(a) Transfer characteristic: drain current normalized to the width of the channel over gate-source voltage at different drain-source voltages (key)
left: logarithmic plot
right: square root of absolute current over absolute voltage
dotted: corresponding gate current.

(b) Output characteristic: drain current normalized to the width of the channel over drain-source voltage at different gate-source voltages (key).
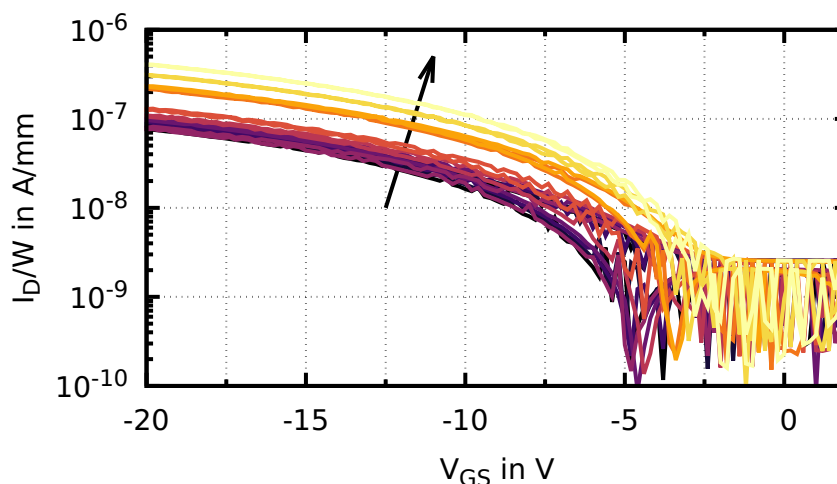
Figure 6.3: Transfer characteristics of bottom-gate/top-contact OFETs based on triclinic rubrene thin-film built on different gate dielectrics: channel width W =1000 μm, channel length L =50 μm
dielectrics: SiO_2: 100 nm, Al_2O_3: 35 nm, Cytop: 50 nm (deposited by spin-coating), the seed is grown from 40 nm of undoped rubrene at 130 °C for 15 min, additional 20 nm are added via epitaxy
x-axis: effective gate-source field strength
y-axis: drain current per channel width and drain-source voltage.
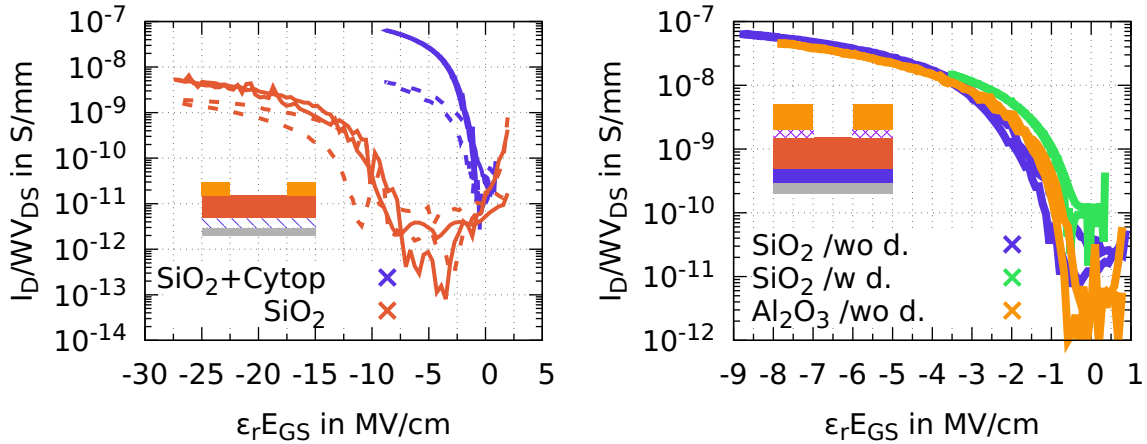
(a) Comparison between OFET with SiO_2 as gate dielectric and OFET with a SiO_2/Cytop dual layer gate dielectric, **dotted:** gate current.

(b) Comparison between OFETs with different gate dielectrics (SiO_2 and Al_2O_3, both combined with Cytop) with (/w d.) and without (/wo d.) a 1 nm layer of F6TCNNQ as contact doping underneath the source and drain electrodes.

measurements (see chapter 4.1.1.4) show that little rubrene is present between the individual strands of the dendrites. These intermediate areas might be too thin to allow for lateral charge transport. Once an additional layer of 20 nm rubrene is added after the initial crystallization, Field-Effect Transistor (FET) operation is observed. The areas between the branches seem to be filled up sufficiently with the extra layer, as can also be seen via AFM.

The IV characteristics of an exemplary device are shown in figure 6.2. The gate dielectric in this device consists of 100 nm SiO_2 and 50 nm Cytop. The SiO_2 is grown via wet-oxidization by the manufacturer of the Si wafer. Cytop is added on top of the SiO_2 via spin-coating at 4000 rpm of a Cytop solution diluted to 2 wt.%. The device shows normal OFET operation with low hysteresis in all transfer and output curves. By fitting a linear function to the square root of the drain current over the gate-source voltage of the saturation regime, the effective charge carrier mobility of this device can be calculated via equation 2.70. The average effective mobility μ_{eff} over a set of 20 devices with varying channel length and three different source-drain voltages is $(0.012 \pm 0.007)\,cm^2\,V^{-1}\,s^{-1}$.
This charge carrier mobility is – as expected – significantly smaller than the value found for the vertical direction of these crystals. Via the position of the intersect

of this linear fit with the voltage axis, a threshold voltage can be defined. It is a technological parameter that describes when the device is *effectively* switched on. For these transistors, the threshold voltage is (-7.8 ± 2.9) V. It is an acceptable result considering the low capacitance of the gate. Judging by the low mobility and the comparably long channels, no limitation by injection barriers is likely. That assessment is affirmed in the output characteristic. However, the slight shift in the linear regime of the output characteristic indicates a significant gate-leakage current. That is not a property of the semiconductor but rather of the used dielectric. The other devices investigated in this chapter do not suffer from such large leakage currents through the gate.

The device shown in figure 6.2 features a gate insulator consisting of two separate layers. One layer of SiO_2, to block current and keep leakage low and one layer of Cytop in direct contact with the semiconductor, to improve interface quality. Cytop is known to create low-defect interfaces with organic semiconductors and is well suited for OFET applications ([148], [250]). Figure 6.3a shows a comparison between two geometrically identical devices (W=1000 µm, L=50 µm, semiconductor=40 nm+20 nm, electrodes structured via shadow masking), with one being built on the previously mentioned two-layer dielectric, while the other is fabricated directly onto SiO_2. To compare both devices despite the different geometry and biasing, instead of the drain current, the drain conductivity is depicted as $\frac{I_D}{V_{DS}}$ on the y-axis. Similarly, instead of the gate-source voltage the effective gate field given as $E_{eff} = \epsilon_{eff} \frac{V_{GS}}{d_{dielectric}}$ is used for the x-axis. Here, $d_{dielectric}$ is the total thickness of the gate dielectric and ϵ_{eff} is the effective dielectric constant, calculated via the relative permittivities of the two individual layers (series connection of two capacitors). The current through the device with only SiO_2 as its dielectric is significantly smaller, although much stronger effective fields are applied to the gate. The turn-on behavior appears similar, however, the single-layer device turns on at a significantly larger voltage. Figure 6.4b shows the statistical distribution of the threshold voltage of these OFET devices, proving a threshold voltage twice as high for the device without the Cytop. The corresponding charge carrier mobility of the two sets of devices is shown in figure 6.4a and the surface traps extracted from the subthreshold swing via equation 2.79 in figure 6.4c. Evidently, the interface between the SiO_2 and the rubrene is significantly worse compared to the interface between Cytop and the rubrene. Large threshold voltages are associated with deep traps at the interface. These deep traps have to be filled up via the gate field prior to the creation of the conductive channel. The trap density calculated from the subthreshold swing is associated with shallow traps. It seems that the SiO_2 surface creates a large density of deep traps at the interface, resulting in a large threshold voltage and a decrease in effective mobility. An increase by one order of magnitude in effective mobility via the introduction of Cytop is for example shown by Diemer et al. [251] too. It is likely that filled deep traps function as scatterers for holes, effectively
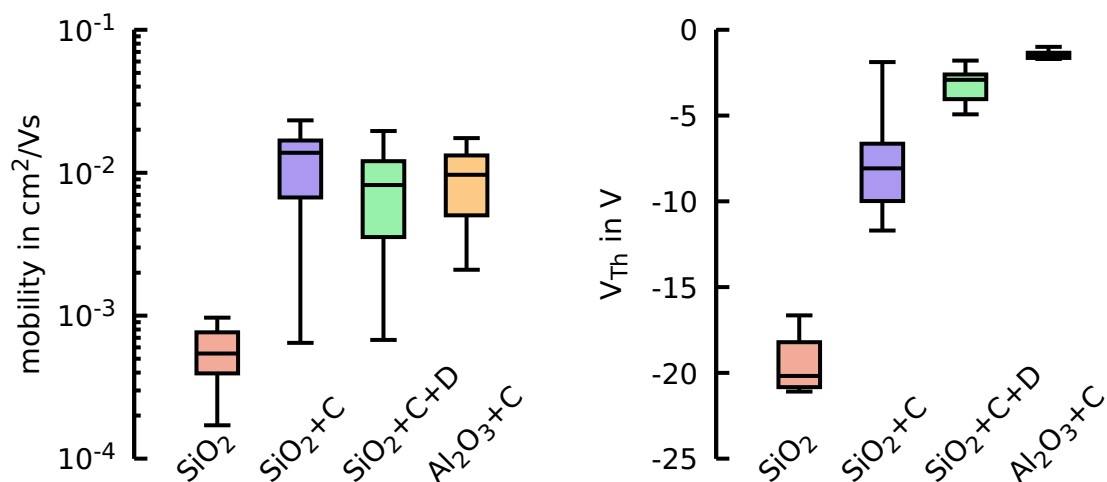
(a) Field-effect charge carrier mobility extracted from the saturation regime, according to equation 2.70.

(b) Threshold voltage as crossing point with voltage axis of linear fit of square root of drain current.
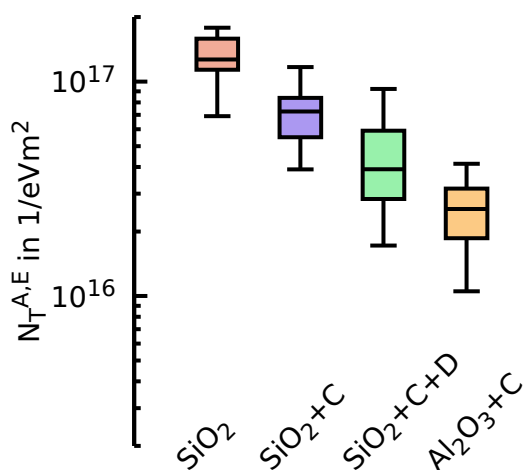
Figure 6.4: Parameters extracted from figure 6.3 highlighting the effects of variation of the gate dielectric:
SiO_2: (SiO_2 only)
SiO_2+C: combined SiO_2 + Cytop
SiO_2+C+D: combined SiO_2+Cytop with contact doping
Al_2O_3: combined Al_2O_3+Cytop.

(c) Trap density calculated from subthreshold swing according to equation 2.79.

reducing the lateral hole mobility. Shallow traps, represented by the exponential switch-on behavior, are only increased slightly compared to the device with the Cytop interface. In summary, devices for which the relevant interface is defined by Cytop show significantly better performance.

Figure 6.3b compares different devices that are all built with an additional thin-film of Cytop on top of the oxide dielectric at the gate. The comparison between the devices featuring a SiO_2- and Al_2O_3-based gate does not show any significant difference when correcting for the resulting effective fields. That is not surprising, since the decisive interface is between the semiconductor and the Cytop, which is identical for both transistors. The third device is built with the

Figure 6.5: Transfer characteristic of bottom-gate/top-contact OFET based on triclinic rubrene thin-films at different temperatures: The seed is grown from 50 nm undoped rubrene heated at 130 °C for 15 min. 50 nm rubrene are added via epitaxy after crystallization. gate dielectric: 100 nm SiO_2 + 50 nm Cytop (deposited via spin-coating), $V_{GS} = -20$ V
Temperature is varied from 300 K to 100 K (bright to dark). Arrow indicates direction of increasing temperature.

same SiO_2+Cytop double layer dielectric, however, a thin layer of 1 nm F6TCNNQ (p-dopant) is evaporated underneath the source and drain electrodes. This way, injection into the semiconductor should be improved. The current is increased slightly for the switched-on transistor, despite the operation of these transistors being clearly limited by the channel and not by injection. However, the off-current of these devices is increased too. Although the addition of dopant reduces the on/off-ratio in these particular devices, it shows that injection doping can work in rubrene-based OFETs. The same concept can be used for the other crystal phases and device with shorter channels when injection-related resistances are more relevant.

Figure 6.4 summarizes the device parameters of these three devices. The effective charge carrier mobility is virtually identical between the three setups, proving that this property is mainly defined by the material system and the interface between semiconductor and gate dielectric. It appears as if the undoped device with the SiO_2-based gate insulator shows a significantly larger threshold voltage. This is an artifact stemming from the extraction method. The higher the source-drain voltage during the transfer measurement (limited to -20 V for one device due to the measurement setup), the larger the apparent threshold voltage. Correcting for this difference shows that the relative threshold of these three devices and thus the density of deep traps is similar.

Finally, the temperature-dependence of the device with the gate insulator made with SiO_2+Cytop and 1 nm injection doping is studied. The corresponding set of transfer curves is shown in figure 6.5, measured at a constant drain-source
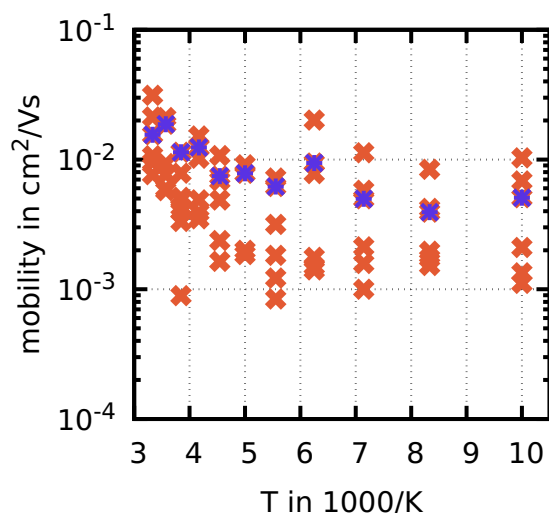
(a) Field-effect charge carrier mobility extracted from the saturation regime, according to equation 2.70.
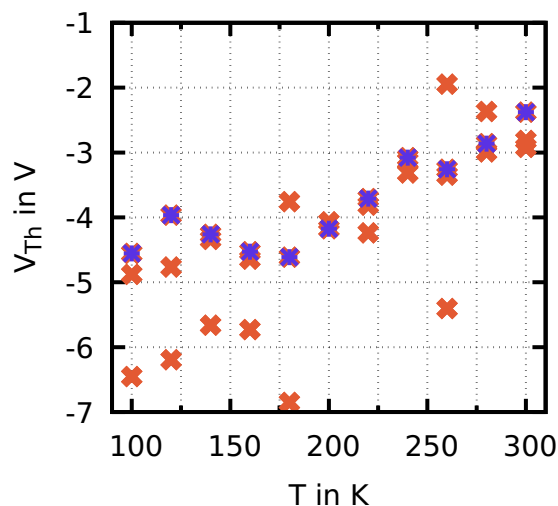
(b) Threshold voltage as crossing point with voltage axis of linear fit of square root of drain current.
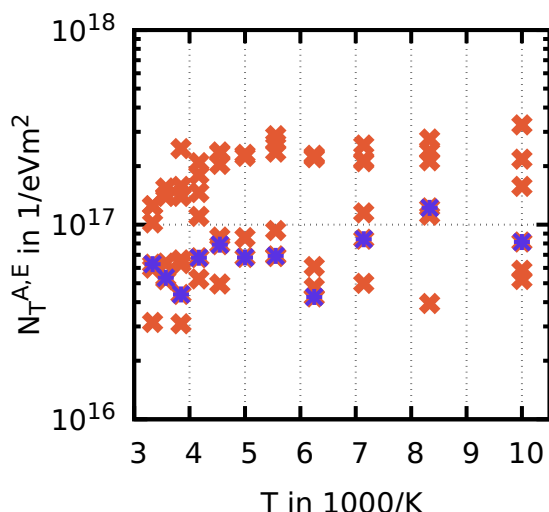
Figure 6.6: Parameters extracted from data shown in figure 6.5: **red (bright), fat:** Parameters extracted from different devices with the same channel geometry at different source-drain voltages, up and down sweep. **blue (dark), thin:** Parameters from up sweep at $V_{DS} = -20$ V.

(c) Trap density calculated from subthreshold swing according to equation 2.79.

voltage of -20 V. Evidently, the current is decreasing with decreasing temperature. However, the change is comparably mild; Abbas et al. [252] show a change of three orders of magnitude in the current of OFETs in the same temperature regime using sexithiophene as the semiconductor.

The general shape of the IV curve does not seem to be changed much. A distinct shift in threshold voltage can be observed, though. Figure 6.6 summarizes parameters extracted from these curves, illustrating the doubling of the threshold voltage within the temperature regime. In contrast, the charge carrier mobility only decreases moderately while cooling. The decrease is equivalent to an activation energy of 17 meV. This value is close to the 19 meV measured by Terao

et al. [253] in tetracene single-crystal OFETs in the high-temperature regime. A strong increase in threshold voltage is reported for these devices too. They suggest a freeze out of deep traps at the interface, causing an increase in threshold voltage and a decrease in mobility. That is in good accordance with earlier measurements that show a significant increase threshold voltage for the less ideal SiO_2 interface. Furthermore, the low temperature-dependence measured for the conductivity of vertical devices (see chapter 4.2.4), indicates a low temperature-dependence of the material system itself. Surprisingly, trap densities extracted via the subthreshold swing feature only a minor dependence on the temperature, as can be seen in figure 6.6c. The effects causing the individual types of defects seem to have significantly different energy scales and thus supposedly different origins (morphological defects vs. impurities).

6.2 Organic Field-Effect Transistors (OFETs) Based on Orthorhombic Spherulite Rubrene Thin-Films

For the next set of devices, the spherulitic orthorhombic crystal phase is used. This crystal structure is technically also dendritic and might suffer from the same problem as the triclinic crystals regarding lateral transport. However, a significantly lower tendency for branching is found in these crystallites. It is thus much more likely that the channel of a transistor is aligned with the individual strands, resulting in an uninterrupted crystal from source to drain. Even a sub-optimal orientation of the crystal might allow for transport between source and drain, be it with an increased effective channel length. As a result, a significantly increased degree of variation can be expected from these transistors.

Figure 6.7 shows the IV characteristic of an OFET built similarly as described in the previous section. The gate dielectric is made up of 100 nm SiO_2 only. Growth of this crystal phase on top of a highly hydrophobic material like Cytop is not successful. Channel geometry is defined by shadow masking, resulting in a channel width of 1000 μm and a channel length of 50 μm. The crystal seed is grown from 20 nm of undoped rubrene heated at 170 °C for 60 s. An additional layer of 40 nm undoped rubrene is added prior to the deposition of the Au electrodes for source and drain.

The performance of this device is only slightly better than the transistors made from triclinic crystals shown in figure 6.2, based on the triclinic crystal phase. However, it is worth noting that the first transistor is made on a buffer layer of Cytop which – as shown in the previous section – significantly improves the performance of the device by reduction of trap states at the interface. The average charge carrier mobility extracted from these spherulite-based devices is thus not much higher than for the triclinic devices at $(0.028 \pm 0.020)\,cm^2\,V^{-1}\,s^{-1}$. The variation in mobility is indicative of the orientational dependence of this crystal phase. A matching of crystal direction to performance is not possible here, since

Figure 6.7: IV characteristics of a bottom-gate/top-contact OFET based on orthorhombic spherulitic rubrene thin-film: channel width W =1000 μm, channel length L =50 μm, dielectric: 100 nm SiO_2, seed is grown from 20 nm of undoped rubrene at 170 °C for 90 s, additional 40 nm are added via epitaxy.

(a) Transfer characteristic: Drain current normalized to the width of the channel over gate-source voltage at different drain-source voltages (key)
left: logarithmic plot
right: plot of square root of absolute current over absolute voltage
dotted: corresponding gate current.

(b) Output characteristic: Drain current normalized to the width of the channel over drain-source voltage at different gate-source voltages (key).

the width of the channel is larger than a typical crystallite. It seems plausible that the effective charge carrier mobility can be increased by a similar amount as for the triclinic crystal phase, once a better interface can be created between semiconductor and dielectric. Since growth of these spherulitic crystals on Cytop is not viable, only the reverse structure with a top-gate configuration is possible. The output characteristic of this device shows proper saturation and no s-kink that would indicate a strong injection resistance. However, the decreasing slope in the $\sqrt{I_D} - V_{GS}$ curve and the sub-quadratic increase in maximum saturation current suggest a non-constant field-effect mobility.

Figure 6.8 presents the transfer curves of four devices of the same type but slightly different configurations. Two sets of devices are made using shadow masking. One set consists of the 20 nm seed layer only (20 S), while the second set features an additional layer of 40 nm of rubrene to fill any potential gaps in the film (20+40 S). Although the orthorhombic spherulite films are significantly denser than the triclinic crystals, they are still dendrites. That means that a decreased amount of material is present between each branch, limiting the interbranch transport. Transistors based on triclinic rubrene do not show any measurable drain current
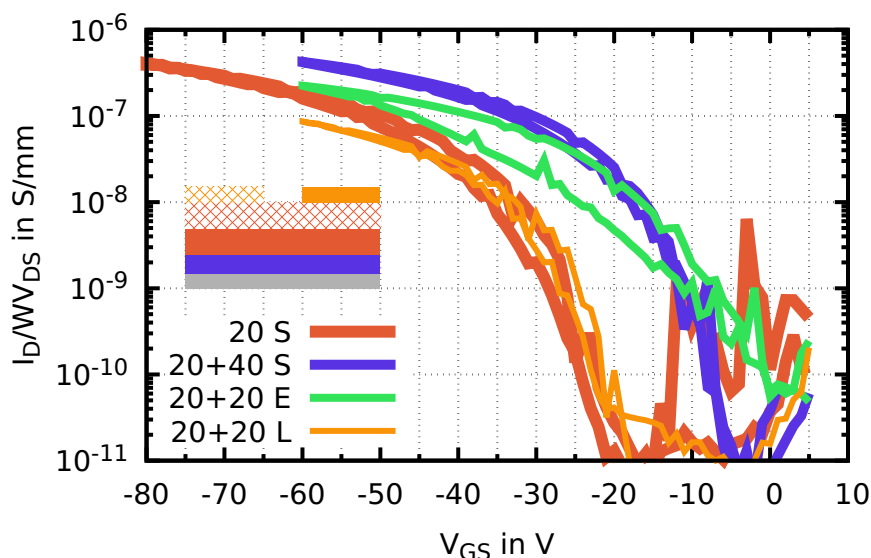
Figure 6.8: Transfer characteristics of bottom-gate/top-contact OFETs based on orthorhombic spherulite rubrene thin-film, built with different techniques to structure source and drain electrodes: channel width W =1000 µm, channel length L =50 µm, gate dielectric: SiO_2 (100 nm)
Seed is grown from 20 nm of undoped rubrene at 170 °C for 90 s
key: thickness of the seed + added layer via epitaxy, S: shadow mask structuring, E: etched electrodes, L: electrodes via lift-off
x-axis: effective gate-source field strength
y-axis: drain current per channel width and drain-source voltage.

when only the seed is used. Functioning spherulitic devices can be built on the seed alone. However, threshold voltage is increased by on average 10 V, while mobility decreases slightly, as can be seen in figure 6.9. As a result, these devices show overall reduced performance. Thus, either the amount of material between individual branches is larger in the spherulitic crystals or the increased conductivity along the strands, combined with the more straight growth can counteract the effectively longer channel at least partly. Nevertheless, the addition of material on top of the seed seems to be universally beneficial.

The other two devices in figure 6.8 are based on this two-film semiconductor layer as well. However, instead of shadow masking, etching (20+40 E) and lift-off (20+40 L) of the Au electrode via photolithography are used. The device with etched electrodes is similar to the two-layer device with shadow masking. The maximum current is slightly decreased, as a result of a slightly decreased charge carrier mobility. However, the negative threshold voltage seen in the shadow masked device is reduced for the etched transistors. Partly even a positive threshold voltage is noticeable, indicating weak doping of the semiconductor. In contrast, devices built via the lift-off process show a significantly decreased performance, mostly originating from a large threshold voltage, while the effective mobility is similar to the other devices. It is unlikely that the increase in threshold voltage is the result of the lithographic process itself, since the photochemistry for the
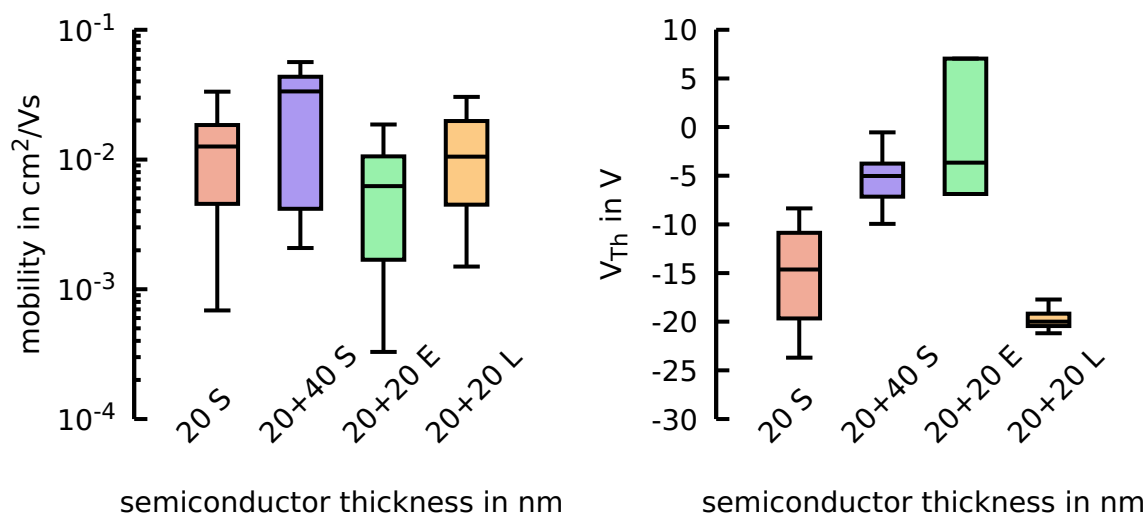
(a) Field-effect charge carrier mobility extracted from the saturation regime, according to equation 2.70.

(b) Threshold voltage as crossing point with voltage axis of linear fit of square root of drain current.
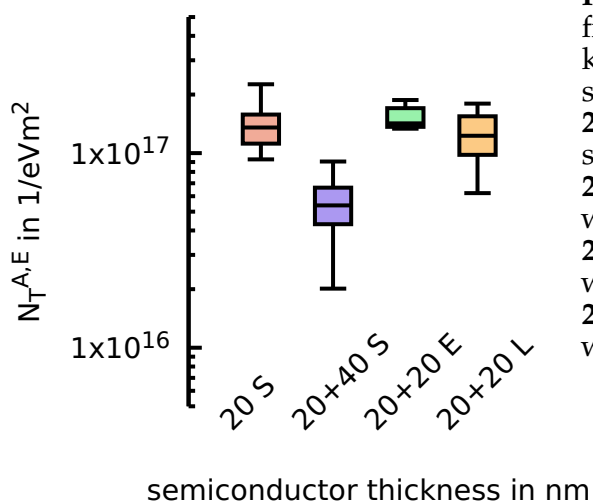
(c) Trap density calculated from sub-threshold swing according to equation 2.79.

Figure 6.9: Parameters extracted from figure 6.3,
key: thickness of the semiconductor and structuring method:
20 S: 20 nm seed only, structured with shadow masking
20+40 S: +40 nm epitaxy, structured with shadow masking
20+40 E: +40 nm epitaxy, structured with etching photolithography
20+40 L: +40 nm epitaxy, structured with lift-off photolithography.

lift-off is assumed to be milder than the etching process [160]. However, the lift-off itself takes several hours, for which the device is exposed to ambient air. The reduced performance might be the result of simple oxygen degradation. At last, a set of VOFETs is produced to assess the potential of this crystal phase for use in devices that require vertical and lateral transport. The devices are based on the stack design shown in figure 2.3.3.3 and produced via the methods explained in 3.1.4. The mask system V1 used here is a comparably simple and rough electrode design based on rectangles. Similar to the previously described OFETs, the gate is defined by the Si wafer as a global gate, with a layer of 100 nm SiO_2 as the gate insulator. Both electrodes are formed using a Au etching process with nlof2020

Figure 6.10: IV characteristics of a bottom-gate/top-contact VOFET based on orthorhombic spherulitic rubrene thin-film: channel width W =1000 µm, gate dielectric: 100 nm SiO_2, source insulator: 400 nm nlof2020, seed is grown from 20 nm of undoped rubrene at 170 °C for 90 s, additional 40 nm are added via epitaxy prior to the deposition of the source electrode. No semiconductor is added between source and drain.
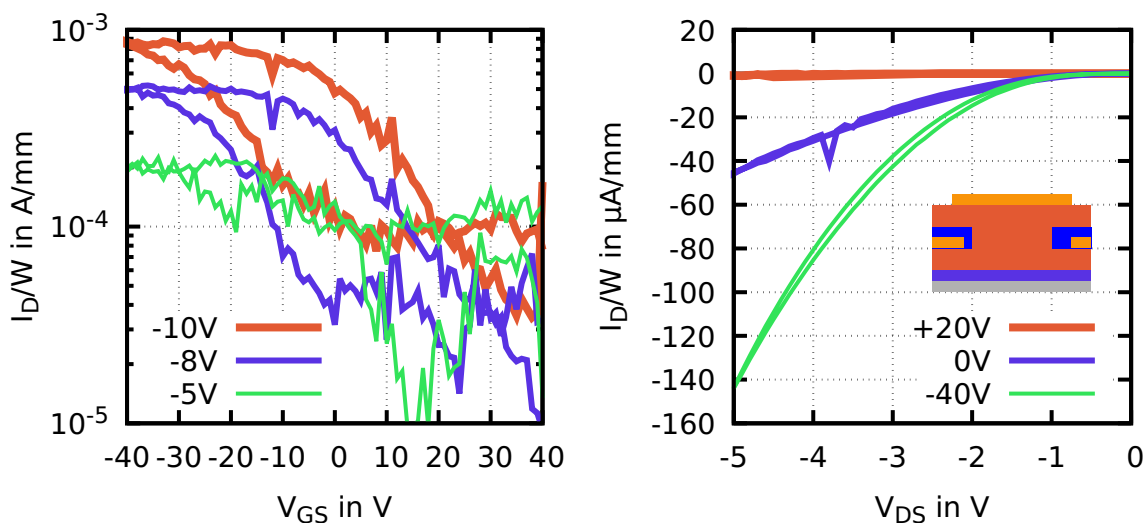
(a) Transfer characteristic: Drain current normalized to the width of the channel over gate-source voltage at different drain-source voltages (key).
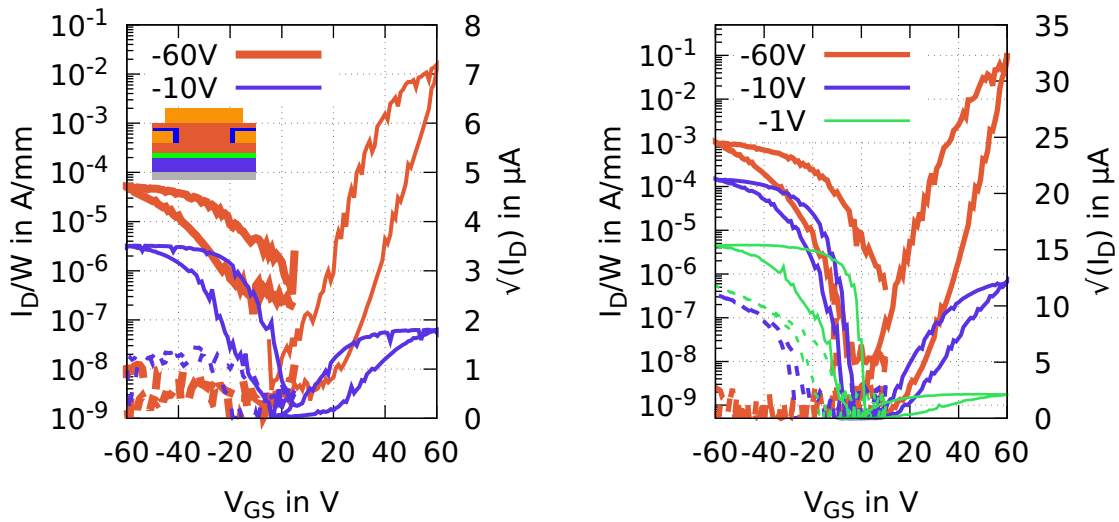Gate current is in the range of $1 \cdot 10^{-9}\,\mathrm{A\,mm^{-1}}$ to $1 \cdot 10^{-8}\,\mathrm{A\,mm^{-1}}$.

(b) Output characteristic: Drain current normalized to the width of the channel over drain-source voltage at different gate-source voltages (key).

as photoresist. This photoresist (200 nm) remains on top of the electrodes after structuring. The channel has a width of 1000 µm. The semiconductor is grown identically to the OFETs, as a 20 nm + 20 nm double layer.

The resulting IV characteristics are presented in figures 6.10. Two aspects are prominent compared to the OFET devices: off-currents are significantly increased, in particular for higher drain-source voltages. Furthermore, a strong hysteresis is visible in the transfer characteristic. High off-currents are typical for short channel devices when either the semiconductor is lightly doped or the source-drain insulator is of poor quality. Both aspects might be at play in these devices. A light doping effect can already be seen in the etched OFET devices. It seems plausible that this effect is even more pronounced when two consecutive lithographic procedures are used. The output curve of the transistor is typical for a short channel device. A positive source-gate voltage is needed to fully turn the device off and only a badly defined saturation can be seen. This might be partially mitigated by the use of a better quality source-drain insulator. The observed strong hysteresis is only visible in the transfer curve but not in the output characteristic. This behavior is usually associated with surface charging effects, caused by the global gate configuration of these FETs.

Regardless of the initially problematic properties, the current normalized to the source-drain voltage driven by these VOFETs is almost two orders of magnitude larger than in comparable OFETs. This illustrates the potential that these films offer for vertical transistor structures. Significantly better devices could be made utilizing a tailored structuring technique, optimized geometry, and most importantly, a trap-reduced interface between semiconductor and dielectric. The absolute current that can be driven by these devices is already now comparable to state of the art vertical transistors based on other materials.

6.3 Organic Field-Effect Transistors (OFETs) Based on Orthorhombic Platelet Rubrene Thin-Films

Rubrene crystallized in the orthorhombic platelet phase used in OFET devices has already been presented in literature by Fusella et al. [36]. However, investigating the properties of these films in lateral direction can give valuable insight for other devices (e.g. lateral transport in the base of OBJTs). Furthermore, vertical transistor designs like the VOFET or the Organic Permeable Base Transistor (OPBT) have not been realized using highly crystalline or even single-crystal semiconductors yet.

The devices shown in figure 6.11 are OFETs built on doped Si as the gate, with a layer of 100 nm of SiO_2 as the gate dielectric. Hence, the same problem regarding the heavily trap dominated interface applies as discussed for the spherulitic crystals. Since the platelet crystals only grow reproducibly, when an underlayer of appropriate glass transition temperature is used, the interface configuration is even more complicated here. In literature, OFETs are shown by Fusella et al. [36] built on a 5 nm layer of TPTPA underneath the rubrene, with a bandgap of only 1.2 eV. It is hence likely that a significant part of the field-effect channel might form within this underlayer. As a suitable replacement, TAPC is used in these transistors, featuring a similar T_g, combined with a significantly larger bandgap of 3.5 eV. The initial seed is grown from 40 nm of undoped rubrene. Additionally, 20 nm are evaporated onto the seed. This crystal phase is not dendritic. If the second film of semiconductor is necessary is thus unclear. However, a negative effect is unlikely. Source and drain electrodes are structured via the Au etching process, using AZ15nXT as photoresist.

The transistor shows normal field-effect operation, similar to the results discussed for the spherulitic crystals. The resulting average charge carrier mobility is $(0.07 \pm 0.05)\,cm^2\,V^{-1}\,s$, with low threshold voltages of $(-1.7 \pm 2.2)\,V$. As expected from the higher lateral symmetry, the performance is slightly better than for comparable spherulitic devices, since the underlying crystal structure is identical. However, the charge carrier mobility measured in these transistors is still significantly lower than the results shown in literature. Apparently, the interface

Figure 6.11: IV characteristics of a bottom-gate/top-contact OFET based on orthorhombic platelet rubrene thin-film: channel width W =1000 µm, channel length L =50 µm, gate dielectric: SiO_2 (100 nm)
The seed is grown from 20 nm of undoped rubrene at 160 °C for 2 min on top of a 5 nm layer of TAPC.
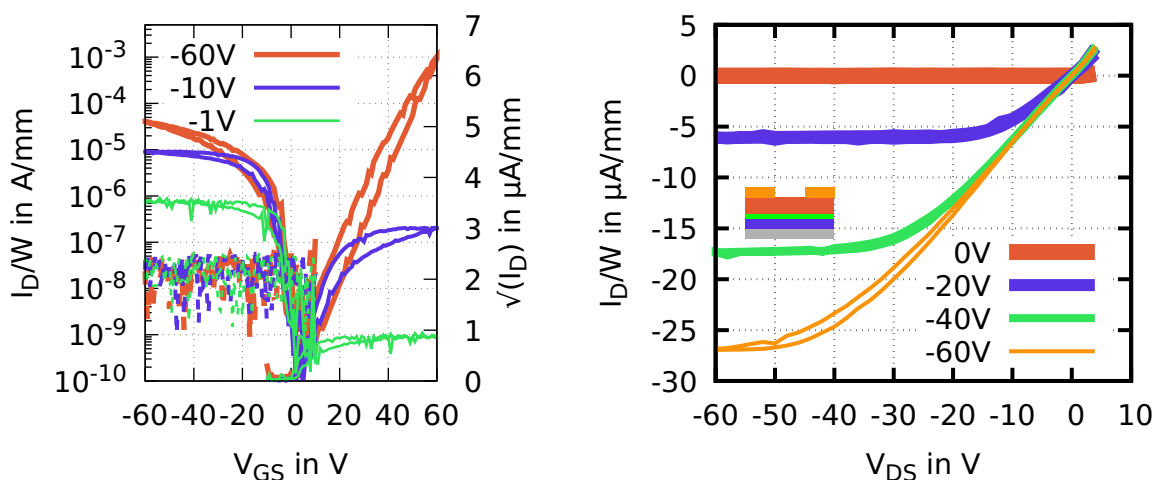
(a) Transfer characteristic: Drain current normalized to the width of the channel over gate-source voltage at different drain-source voltages (key)
left: logarithmic plot
right: plot of square root of absolute current over absolute voltage
dotted: corresponding gate current.

(b) Output characteristic: Drain current normalized to the width of the channel over drain-source voltage at different gate-source voltages (key).

between the underlayer and the semiconductor is of similarly bad quality as the interface between rubrene and SiO_2. However, since this crystal phase requires the underlayer, a change of dielectric to better-suited materials (e.g. Cytop), is not feasible in a bottom-gate configuration. Thus, a top-gate device is necessary to get closer to the intrinsic properties of this material setup. At last, two sets of VOFET devices are studied based on this crystal phase. The gate configuration and the processing of the rubrene films are identical to the OFET devices. One set of devices is built using the same underlayer TAPC while the other set uses TPTPA as the underlayer. The source electrodes are formed via Au etching using AZ15nXT as photoresist. The source-drain is hence made from 400 nm AZ15nXT, which allows for a significantly higher maximum source-drain voltage compared to nlof2020-based devices. The drain electrode is formed using the double-photoresist lift-off procedure. The transfer characteristics of both sets of devices are shown in figure 6.12. Similar to the VOFETs based on the spherulitic crystal phase, a strong hysteresis is introduced into the system. That might either be caused by the lithographic processes or by the short channel character of these devices in conjecture with the global gate configuration. The devices using the TPTPA are significantly worse than the comparable spherulitic transistor and

Figure 6.12: IV characteristics of a bottom-gate/top-contact VOFETs based on orthorhombic platelet rubrene thin-film: channel width W =1000 µm, gate dielectric: 100 nm SiO$_2$, source insulator: 500 nm AZ15nXT, the seed is grown from 40 nm of undoped rubrene at 160 °C for 2 min. Additionally, 40 nm are added via epitaxy prior to the deposition of the source electrode. No semiconductor is added between source and drain.

(a) Transfer characteristic: Drain current normalized to the width of the channel over gate-source voltage at different drain-source voltages (key) for devices with a 5 nm layer of TPTPA as underlayer.
left: logarithmic plot
right: plot of square root of absolute current over absolute voltage
dotted: corresponding gate current.

(b) Transfer characteristic: Drain current normalized to the width of the channel over gate-source voltage at different drain-source voltages (key) for devices with a 5 nm layer of TAPC as underlayer.
left: logarithmic plot
right: plot of square root of absolute current over absolute voltage
dotted: corresponding gate current.

its counterpart using the TAPC. Based on these devices, using TAPC as the underlayer is greatly improving the overall performance of all types of OFETs, when this crystal structure is used. Since the lateral charge carrier mobility of the orthorhombic platelets is not yet at the high performance-level desired, due to the lack of proper gate interface, the overall performance of the corresponding VOFETs is not yet impressive. Maximum current, on/off-ratio, and transconductance are similar to other devices based on pentacene, TIPS – pentacene, or DNTT. However, if the problems regarding the gate can be overcome, this material system can be used to set new performance standards for organic transistors, based on the high, almost isotropic charge carrier mobility.

6.4 Summary

Since this chapter is only a preliminary analysis showing off the possibility in regards to the use of these films in the scope of OFETs, the set of results is not complete and many questions and possible tests are still left open. Regardless,

the standard FET designs are realized with all three crystal phases. The lateral field-effect mobilities extracted from the IV analysis of these devices prove the previously expected lower carrier mobility for the triclinic crystal phase. Thus, as a rule of thumb for future development: orthorhombic crystals should be used for devices relying on lateral transport.

Orthorhombic spherulite-based devices show a larger spread of properties than the other two crystal phases. This can be fully explained by the orientation of the crystal grain towards the channel. This problem is less relevant for the platelet-based transistors. However, the reliance on a sublayer makes the interface design significantly more challenging. As a result, the apparent mobility is higher for the spherulitic devices. In contrast, the absolute performance of orthorhombic platelet-based VOFETs is better than their spherulitic counterparts, highlighting the importance of overall increased molecular order. In general, the current densities reached here, especially considering the large device area and the small degree of optimization, are promising sign for future developments with these and other high-mobility organic semiconductors.

parameter	triclinic	orthorhombic spherulites	orthorhombic platelets
devices	• bottom-gate, top-contact OFET	• bottom-gate, top-contact OFET • bottom-gate VOFET	• bottom-gate, top-contact OFET • bottom-gate VOFET
note	• Cytop interface necessary for measurement due to low mobility • adding layer to fill gaps in seed is beneficial	• bottom-gate on Cytop is not possible • strongest directional dependence	• bottom-gate on Cytop is not possible • sublayer needed for proper crystallization: complicated interface

Table 6.1: Summary rubrene-based FETs I

parameter	triclinic	orthorhombic spherulites	orthorhombic platelets
photolithography	• etching and lift-off process functional • quality of epitaxially grown layer followed by lithography is reduced	• etching functional, lift-off not tested • epitaxy not tested	• etching functional, lift-off not tested • epitaxy not tested
lateral FET mobility in cm^2 V^{-1} s^{-1}	• $1.5 \cdot 10^{-2}$	• $3 \cdot 10^{-1}$	• $7 \cdot 10^{-2}$
highest reached current density in µA mm^{-1}	• 4 in OFETs	• 40 in OFETs, • 140 in VOFETs	• 26 in OFETs • 1000 in VOFETs

Table 6.2: Summary rubrene-based FETs II

7 Organic Bipolar Junction Transistors (OBJTs) Based on Crystalline Rubrene Thin-Films

This chapter presents experiments on Organic Bipolar Junction Transistors (OBJTs) based on the crystalline rubrene films discussed in chapter 4. Basics of Bipolar Junction Transistor (BJT) operation are described in chapter 2.3.4. The study of these transistors is strongly related to the diodes shown previously in chapter 5. It is advised to read both parts, since information and equations are referenced directly. For the sake of simplicity, devices that are aimed at BJT operation are named in the following as such, even for those devices that do not show amplification.

The following chapter is structured differently to the previous chapters. Instead of analyzing groups of devices and investigating the influence of specific parameters, individual devices are shown and discussed here. Compared to the already complex structures and devices shown in earlier chapters, the transistors presented here have an even greater complexity. The combination of crystallization process, small-scale (non-lithographic) structuring, and complex doping profiles, results in an extremely low yield for the manufacturing of these transistors. Fewer than 5 % of all devices measured show behavior that can be analyzed. Furthermore, OBJTs have not been realized and shown in literature until now. There is hence no recipe or given model structure on how to fabricate such a device. Considering the increased set of parameters (crystal structure, doping concentration, and thickness of at least five different layers, three distinct masks/electrodes, etc.), a systematic analysis would, of course, be beneficial but is simply not realizable within the limited time scale.

Thus, only model devices are shown, including the relevant measurements and discussions. The chapter is split into three different parts. The first section shows an analysis of an OBJT device based on the triclinic crystal phase of rubrene. Transmission through the base is present, but no amplification. This section contains the description of the stack, the electrode geometry, the measurement procedure, and mode of analysis that are valid for the consecutive discussion too. The second section presents an OBJT based on spherulitic orthorhombic crystals showing actual current amplification. The last section summarizes experiments related to optimizing certain aspects of the devices utilizing pinip type devices.

7.1 Organic Bipolar Junction Transistors (OBJTs) Based on Triclinic Rubrene Thin-Films

The knowledge from the experiments on pin diodes shown in chapter 5 and the material system itself in chapter 4.2 is the basis for the design of the OBJT. Devices based on organic semiconductors often behave differently from the theoretical models derived for inorganic counterparts. The basic concepts that govern the fundamental processes are nonetheless identical, although the final properties might deviate from the ideal case. Two of the requirements that must be fulfilled according to BJT theory to allow for bipolar operation are:

- The emitter doping concentration must be larger than the base doping concentration.
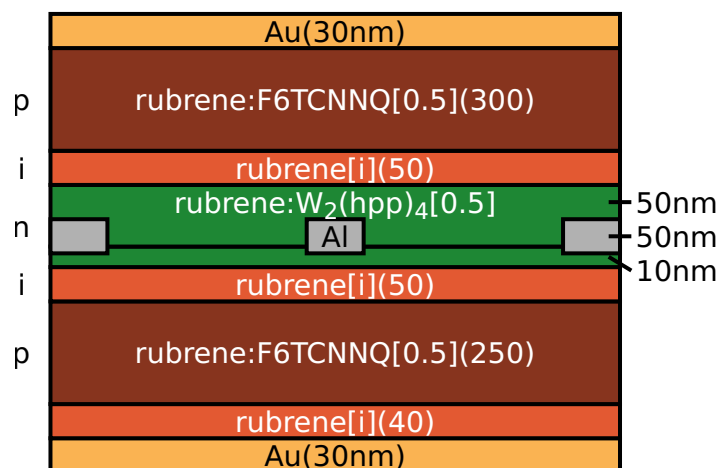
Figure 7.1: Stack of an OBJT based on triclinic rubrene crystals: Device is based on the pinip-design to function as a pnp-transistor. The n-layer on both sides of the base electrode is doped identically. The film below the base has a thickness of 10 nm, the film above the base has a thickness of 50 nm. The electrode geometry is based on mask design B1. key: matrix:dopant[doping concentration](thickness).

- The width of the base must be shorter than the diffusion length of minority charge carriers in the base.

The doping efficiency of p-doping via F6TCNNQ is low in this material system, as shown in chapter 4.2.3.2. The real density of free charge carriers is thus significantly lower than the concentration of dopant. In the following discussion, the phrase *doping concentration* is equivalent to the effective doping concentration, taking a reduced probability for dopant ionization and filling of traps into account. Based on the behavior shown by pin diodes when the n-doping concentration is changed, it can be assumed that the doping efficiency of $W_2(hpp)_4$ is even lower than the values measured for p-doped films. It is hence logical to choose an n-doped base, since that makes it easier to realize the first criterion of lower base than emitter doping. The charge carrier mobility of holes in rubrene is significantly larger than that of electrons [216]. A diffusion length of holes in intrinsic materials has been estimated in chapter 5.2.3 to be at least 150 nm. Some of the experiments with rubrene-based pin diodes indicate a diffusion length in the n-doped film of several tens of nm. Information about the diffusion length of electrons is not available and diffusion of majority carriers is not directly transferable. Nevertheless, the information at hand also suggests choosing an n-doped base to fulfill the second criterion.

Thus, the design for the OBJT is based on a pinip structure, featuring two stacked and inverted pin diodes with a common electron injecting electrode in the middle. The stack of an initial device is shown in figure 7.1. Here, the triclinic phase of rubrene is used to benefit from the large vertical mobilities for holes and to assure efficient diffusion through the base. The seed is made using the standard procedure of crystallizing 30 nm of undoped rubrene at 130 °C for 15 min. Emitter
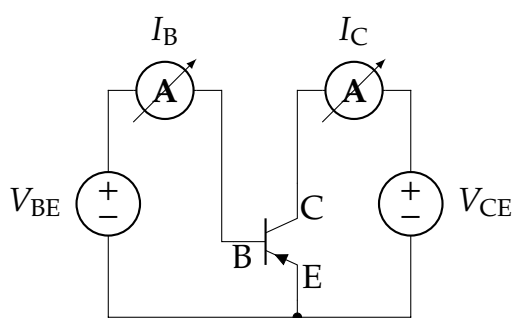
Figure 7.2: Equivalent circuit for measurement of BJT characteristics in common-emitter configuration: collector-emitter voltage (V_{CE}) is varied in discrete steps between individual sweeps. The current I_C is measured as the current through the collector pin. A power supply at the base provides a defined current I_B through the base pin. The voltage V_{BE} required to generate this current is measured.

and collector are both p-doped with 0.5 wt.%[1]. Both p-doped films have a total thickness of approximately 300 nm. The base is made up of an Al electrode, embedded in an n-doped film on both sides of the stack. The n-layer thickness on the collector side of the base is thicker to allow more efficient blocking of current in reverse direction of the base-collector diode. The total thickness of the base that holes have to diffuse through is 60 nm. The doping concentration of the n-doped film is 0.5 wt.%. The films of p-doped and n-doped rubrene are separated by 50 nm of intrinsic material on both sides of the base.

   Prior to any characterization of the transistor capabilities of the device, the individual parts are checked via IV measurements. For this, only two of the three-terminals of each device are connected and the third electrode is left floating. Thus, the functionality of each of the diodes in forward and reverse direction can be assessed, as well as the properties of the pinip structure. These two-terminal measurements can then be used to correct for known leakage paths within the fully set-up bipolar transistor, measured in three-terminal configuration (e.g. correct the collector current of the full transistor by the base-collector leakage current for a particular biasing). Figure 7.3a shows the IV curves of both diodes and the pinip structure. The behavior of these diodes is similar to what can be seen from single devices investigated in chapter 5.3. The forward and – to a lesser degree – the reverse current for the base-collector diode is reduced compared to the emitter-base diode. This can be attributed to the thicker n-doped film on this side of the structure. The direct current through the pinip structure – when biasing the emitter and collector only – is comparably large. In part, that is a result of the unfortunate electrode configuration. Further details are discussed later. Regardless of any geometric consideration, the barrier present in the junction is weak. It might be caused via a similar effect as described earlier for the pin diodes. A closer analysis of the blocking behavior of the pinip structure follows in section 7.4.

Because the conductivity of the pinip structure is larger than that of the base-emitter diode, only a low collector-emitter voltage V_{CE} can be applied, before reaching an already high current density. This is particularly problematic, since

---

[1]Doping concentrations are kept low for initial experiments, because experiments regarding doping efficiency and stability were not available at that time.

Figure 7.3: Current-Voltage (IV) measurements of single diodes and pinip structures within the OBJT.
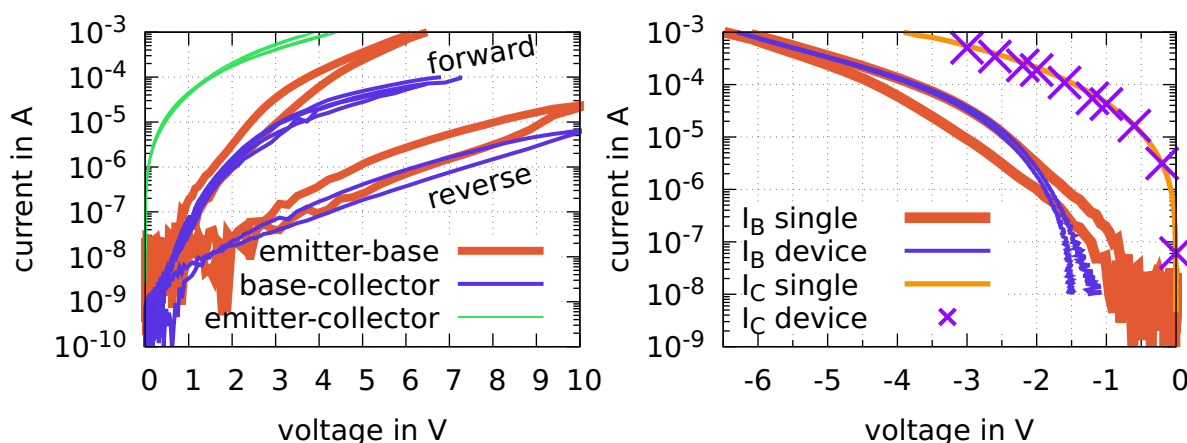
(a) Only two of the three terminals are connected at any given time, while the third is left floating. Emitter-base and base-collector diodes function as usable rectifiers, comparable to devices shown in chapter 5.3. The emitter-collector pinip structure is fully symmetric but shows high currents at low voltages.

(b) Comparison between two-terminal measurements of figure 7.3a (labeled single) and three-terminal measurements (labeled device) for which the third electrode is pulled to ground: I_B is the current through the base electrode when biasing the emitter-base diode in forward direction. I_C is the current through the collector electrode when biasing the emitter-collector pinip structure.

the emitter-collector current is already highly conductive at voltages comparable to the (technological) threshold voltage of the emitter-base diode – and thus at the point at which forward current surpasses leakage current. Contrary to the normal operation of a bipolar transistor, the voltage that can be applied at the output has to be chosen smaller than the voltage that is necessary at the input.

The next step to assess the functionality of the device is to measure the bipolar transistor as a three-terminal device. The transistor is connected to two separate power supplies according to the circuit diagram in figure 7.2 in a *common-emitter circuit*. The power supply at the input side – connected between base and emitter – is set to generate a defined current I_B and measures the voltage V_{BE} required to generate this current. On the output side, a step-wise constant voltage V_{CE} is applied between collector and emitter and the resulting current I_C is measured. As a verification of the device, the same measurements of the single components are performed in the three-terminal configuration, keeping the third pin at ground level. The resulting IV curves compared to the earlier measurements are shown in figure 7.3b. Both curves cannot be fully identical, since the potential landscape between the three electrodes of the two measurement methods is not the same. As an example, in the two-terminal configuration, sweeping a voltage from $0\,\text{V}$ to $-3\,\text{V}$ at the emitter-base diode creates a current between the emitter and base directly and some lateral leakage currents indirectly. If

Figure 7.4: Transfer characteristics of an OBJT based on triclinic rubrene: The change ΔI_C in collector current I_C with increasing absolute base current I_B, compared to the initial value $I_{C0}(I_B = 0)$. ΔI_C^* is the change in collector current corrected by the base-to-collector leakage current $I_{C\text{-}B}(V_{BC})$. ($V_{CE} = -3\,V$ for all measurements).
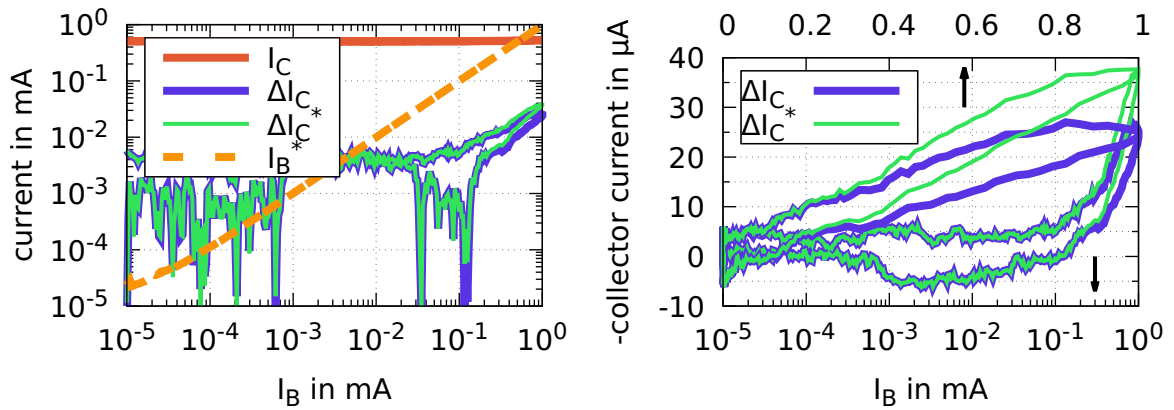
(a) log-log depiction of the transfer characteristic showing the full collector current I_C and the change in collector current ΔI_C. I_B^* is the current through the base corrected by the current from base to collector $I_{C\text{-}B}(V_{BC})$.

(b) lin-log (bottom) and lin-lin (top) depiction of the transfer characteristic showing the change in collector current ΔI_C.

additionally the collector is set to $0\,V$, the sweep of the base from $0\,V$ to $-3\,V$ corresponds to a sweep of $0\,V$ to $3\,V$ of the base-collector diode. This results in an additional current from base to collector that is measured at the base. The same reasoning applies to the measurements of the emitter-collector structure. Comparing the measurements in both configurations allows for a verification of current paths. If the corresponding curves do not overlap sufficiently – especially at higher voltages – it can be assumed that a different current path than intended is dominating this measurement. Since the relevant currents are low and the leakage currents comparably high in most of the devices measured here, this assessment is performed prior to any further analysis to ensure that a change in output current is caused by base control and not by a shift of leakage currents. Now that the proper function of all three subcomponents is established, the transistor can be measured as an amplifying device according to the circuit diagram in figure 7.2. The common-emitter configuration is used to amplify an incoming current-based signal I_B into a larger signal I_C with a constant driving voltage V_{CE}. The corresponding amplification is called the Direct Current (DC) current gain $\beta_A = \frac{I_C}{I_B}$. The transfer curve of such a transistor shows the emitter (output) current I_C with changing base (input) current I_B. The transfer curve of a device biased at $V_{CE} = -3\,V$ is shown in figures 7.4 in logarithmic and linear depiction. The absolute value of I_C is virtually unchanged when varying the base current. Only at the highest I_B, a slight increase in absolute collector current is

noticeable. From that, it is instantaneously clear that the static absolute current amplification β_A is close to zero. This is not surprising, considering the large – leakage – current flowing from emitter to collector even without any base involvement. Nevertheless, the collector current is not as constant as might initially appear. If instead of the absolute current I_C, the change of collector current

$$\Delta I_C(I_B) = I_C(I_B) - I_C(I_B = 0) = I_C(I_B) - I_{C0} \qquad (7.1)$$

is used, a relative amplification can be defined as

$$\beta = \frac{\Delta I_C}{I_B}, \qquad (7.2)$$

which describes how much current is added/removed from the collector current per base current. This parameter is the closest equivalent to a static DC amplification, if the large leakage current is ignored. A device that shows a relative amplification but no absolute amplification cannot be used for DC power amplification without further circuitry. However, Alternate Current (AC) signal amplification is not disturbed by a constant offset current at the output, which can be compensated. This configuration results in low efficiency of the entire setup, however. To prove the existence of a collector current that is controlled by a base current in the sense of a bipolar transistor and thus diffusion of minority carriers through the base, a constant offset of the collector current is not problematic either.

The change in collector current with base current is also shown in figures 7.4. For low and medium I_B, the output shows a lot of noise, fluctuating around zero. However, beginning at approximately $10\,\mu A$ of base current, the absolute change in collector current increases. The negative collector current grows – even more negative. This change is a clear indication for control of the collector current via the base current and thus controllable transmission through the device. The change of collector current is however still smaller than the base input current. Even when using the more favorable definition of the relative amplification in equation 7.4, amplification is far below one.

To understand the operation of the transistor, identify leakage paths, and subsequently find possible ways of improvement, a closer look at the geometry of the device and resulting current paths is necessary. A simplified cross-section of the structure is shown in figure 7.5, including all vertical current paths. It is worth noting that additionally, lateral currents can create leakage currents too. The experiments with rubrene-based diodes of chapter 5 show that these currents can have a dominating impact on the IV characteristics. They are implicitly included in the following reasoning, although they cannot be mapped on to a 2D-depiction of the device. The following derivation and analysis are based on Kirchhoff's circuit laws: The sum of all current in one node and the sum of voltages in one closed circuit loop must vanish.
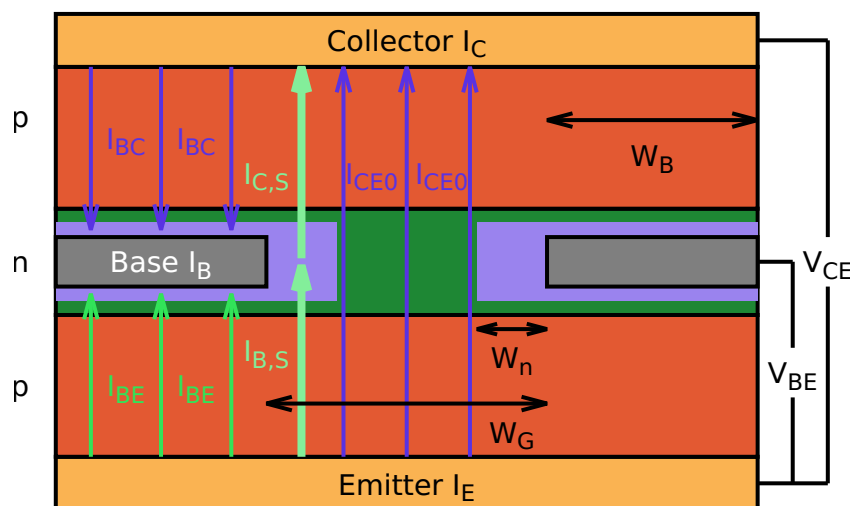
Figure 7.5: Definition of current paths through a geometrically idealized pnp BJT: The area of the n-layer that carries the base potential and can thus control the current from emitter to collector is indicated in violet around the base electrode. A direct overlap between the base and collector/emitter creates voltage-dependent leakage currents that do not contribute to BJT operation. The area of the emitter-collector overlap that is not covered with the base field creates a constant leakage.

Current into the emitter can be split into two categories, leakage currents and signal currents. Leakage into the collector I_C^L has two different origins, current from the emitter and current from the base. The current directly from the emitter to the collector is defined by the voltage difference – here V_{CE} – and the overlap area of these two electrodes. The overlap is in an ideal case given by the gap distance W_G between two adjacent electrodes of the pad. Aside from the desired control via the base current, this part of collector leakage does not change in normal operation, since neither the area nor the voltage change. It is thus defined as $I_{CE0} = I_{CE}(I_B = 0)$.

The second origin for collector leakage currents is the overlap with the base, defining the direct base-collector diode. The size is defined by the width of the base electrode W_B[2]. In normal operation, the collector is at a higher negative bias than the base. The diode is operating in reverse mode and the absolute value of the resulting leakage current I_{BC} is low. The current – as "seen" by the collector is negative. While measuring the transfer curve of such a transistor, the voltage between collector and base is the highest at zero base input current, since the base potential is (theoretically) equal to the emitter and thus zero. The effective voltage difference between base and collector is then $V_{BC} = V_{CE}$. When increasing the base current, the base potential is increased and thus the voltage between base and collector decreased. The direct leakage current from base to emitter is thus decreasing when base current is increased. Hence, even when the direct

---

[2]The area is given via $W_B \cdot W_E$. However, the width of the emitter electrode is also defining the controllable output current. An increase or decrease does not change the signal to noise ratio.

current from emitter to the collector is increased via bipolar control over the base, the increase in current via this control mechanism must be stronger than the decrease in leakage current from base to collector. Otherwise, the effect cannot be measured as an increase in collector current. As a measure to evaluate the emitter current that is changed by the bipolar effect alone, a corrected quantity can be defined as

$$\Delta I_C^* = I_C(I_B) - I_{C0} + I_{C\text{-}B}(I_B), \tag{7.3}$$

with a corresponding amplification

$$\beta^* = \frac{\Delta I_C^*}{I_B}, \tag{7.4}$$

The currents values for $I_{C\text{-}B}$ are the corresponding two-terminal currents measured for the single diode at the appropriate V_{BC}. These new, corrected quantities have no value from a circuit point of view. They do not represent the signal processing properties of the device but only of a part of the device while ignoring other parts. It is nevertheless useful to assess the real strength of the control of the base over the collector current.

Leakage currents into the base are relevant too. As already discussed, one source of leakage current into the base is the collector. The direction of this current as "seen" by the base is inverted and the current is thus positive. However, the measurement performed here is set up as a current-defined measurement at the base. A certain negative current I_B is enforced by applying a sufficiently large voltage V_{BE} at the emitter-base diode. For the three currents into the metal electrode of the base follows $I_B + I_{B\text{-}E} + I_{C\text{-}B} = 0$. Hence, even to generate $I_B=0$, a finite negative voltage has to be applied to the base, such that the emitter-base diode can compensate the current from the base-collector diode. The diodes on both sides of the base show similar leakage currents. Since a large voltage is applied to the base-collector (leakage) diode, the emitter-base diode has to be biased enough to be switched on to surpass the reverse current of the other diode at lower voltages. A similar correction can be done as for the collector current. For a defined current I_B, the larger current

$$I_B^* = I_{B\text{-}E} = I_B + I_{BC} \tag{7.5}$$

has to flow through the base-emitter diode. $I_{B\text{-}E}$ causes the control of the collector current. Thus, a larger current is influencing the collector current than indicated by I_B. This correction is not relevant from a circuit point of view as well. However, in contrast to the correction of the collector current, this represents a stricter criterion. The influence of the base has to be stronger to still realize current

amplification. The appropriate amplification is then defined as

$$\beta^+ = \frac{\Delta I_C}{I_B^*}.$$

(7.6)

It describes the increase in collector current per current from the emitter to the base and is thus a stricter criterion for amplification.

Even though the emitter-base current is intended to be defined by the input current, not the entirety of this current contributes to transistor operation. The current from emitter to the base can be split into the part that goes directly from emitter to the base electrode I_{BE} and the second part that goes from emitter into the area of the base that is influenced by the base field $I_{B,S}$. Only the second part has any control over the collector current $I_{C,S}$ and defines the signal. The area around the base electrode that can contribute to this current control is indicated in figure 7.5 in violet (brighter shaded). The effective reach of this influence protruding from the base electrode is defined as W_n. Ideally, it takes up the entire gap area, such that $2W_n = W_G$, to reach full control. The remaining current I_{BE} is not leakage current in the sense discussed earlier, since the emitter-base diode is operated in forward direction and methods to block this current might inadvertently reduce the effectiveness of the entire device. It can be seen as an additional, parallel diode connected between the base and emitter, increasing the base current without participating in the control of the collector current. Treating the devices discussed here as a circuit instead of a monolithic device, can offer a deeper understanding of the exact phenomena. A first simple model is presented in a following section 7.3.

Now that all beneficial and leakage currents are identified, an analysis of the electrode structure and the resulting active areas is useful to assess the severity of each problem. The electrodes of this device are based on mask setup B1 and are aligned via macroscopic alignment in nitrogen. Emitter and collector are made up of overlapping rectangles, while the base is a comb consisting of a set of rectangles. The alignment of the individual masks is done by hand. Lateral and rotational misalignment can easily create some of the electrodes to not overlap, overlap only partly, or overlap more than necessary. The resulting active areas – especially between emitter and collector – are thus badly defined and not constant between devices. The minimum spacing between adjacent pads of the base and the minimum width of each base pad is 50 µm. The resulting geometry is shown in figures 7.6 for a hypothetical n(3)-fingered base electrode. Figure 7.6a marks the areas for each of the leakage paths described earlier. I_{CE0} increases with emitter-collector overlap, marked in violet. Since masks are aligned by hand, large tolerances have to be chosen along the long axis of both electrodes, exceeding 300 µm. Via an optimized mask design and especially by automatized alignment, the area of uncontrollable emitter-collector leakage could be minimized significantly. However, the leakage current through the pinip

Figure 7.6: Definition of active and leakage areas based on an ideal overlap of all three electrodes. n=number of fingers of base electrode.
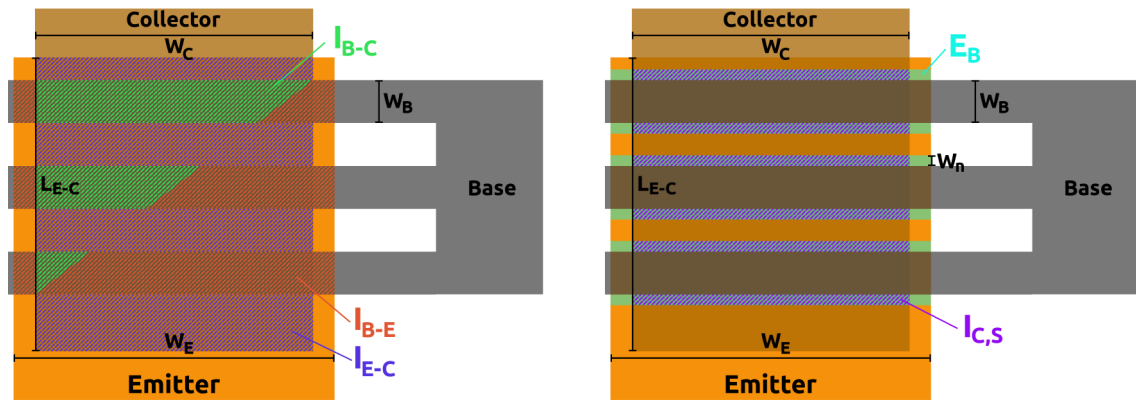
(a) Definition of area contributing to leakage currents:
emitter-base: given by nW_B x $W_E \rightarrow I_{B\text{-}E}$
emitter-collector: given by W_C x $(L_{E\text{-}C} - nW_B) \rightarrow I_{CE0}$
base-collector: given by nW_B x $W_C \rightarrow I_{C\text{-}B}$.

(b) Definition of area contributing to controllable current:
base reach: given by W_E x $2W_n \rightarrow$ suppress I_{C0}
amplification: given by W_C x $2nW_n \rightarrow I_{C,S}$.

structure is higher by several orders of magnitude compared to the corresponding diodes. Although a disadvantageous ratio of active and leakage areas is likely given, it cannot be the defining problem here. A different approach regarding the pinip stack structure must be taken to reduce I_{CE0}. The blocking capability of the pinip structure must be improved.

The base-collector overlap is responsible for I_{BE} which is a pure leakage current. It is defined by the width of the base electrode and the width of the collector. Reducing the collector width is not helpful, since that reduces the output current too. A reduction in the width of the base electrode, however, is beneficial. Thus, not only the direct leakage between base and emitter is reduced, but the "false" current created by the unnecessary parts of the emitter-base diode too. Alternatively, the electrode directly on top of the base can be blocked with a material of low conductivity, since the directly overlapping base-collector diode serves no purpose.

Figure 7.6b shows the areas of the device that actively participate in transistor operation. Two slightly different parts are relevant. For both, the reach of the base field into the n-doped area W_n is decisive. It is marked in green. The area that defines the controllable current is defined via the collector width $2W_n \cdot W_C$. The area influenced by the base field that overlaps with the emitter is slightly larger than the part that overlaps with the collector. These parts cannot amplify current, however, the base can still participate in improving blocking between emitter and collector. Thus, decisive for the operation of the transistor is the reach of the base field into the gap area between adjacent base electrodes. For these devices follows with a distance between adjacent base pads of 50 μm, the resulting optimal reach

of the base field is at least 25 μm. This has to be seen in relation to less than 1 μm vertical distance. A large lateral mobility is hence beneficial, in addition to the large vertical mobility required for vertical diffusion through the base.

7.2 Organic Bipolar Junction Transistors (OBJTs) Based on Orthorhombic Spherulitic Rubrene Thin-Films

This section describes the design and measurement of an improved device based on the orthorhombic spherulite crystal phase of rubrene. The corresponding stack is shown in figure 7.7. The following improvements are implemented:

- Mask design B2 is used, featuring a smaller feature size of 5 μm.
  - The overlap area between emitter and base per finger of the base is reduced, effectively decreasing the influence of the emitter-base diode that does not participate in transistor operation.
  - The gap between adjacent base fingers is reduced, decreasing the reach of the base potential necessary to create control over the emitter current.

- The spherulitic orthorhombic crystal phase is used instead of triclinic crystals.
  - The lower vertical charge carrier mobility of this crystal phase makes diffusion of holes through the n-doped base more difficult.
  - The higher lateral mobility of this crystal phase increases the reach of the base field laterally into the base area.

- Semiconductor material is added through the mask of the base electrode, to manipulate the properties of the diodes on both sides without interfering significantly with the emitter-collector pinip structure.
  - An injection layer is added to the emitter-base side of the base to facilitate electron injection.
  - More n-doped rubrene and intrinsic rubrene are added to the collector side to reduce base-collector leakage currents.

Aside from the material added through the base electrode, the stack is almost symmetric. The seed is grown from 20 nm of undoped rubrene at 170 °C for 60 s in a light-blocking nitrogen glovebox. The p-side on both sides of the pinip structure is doped with 5 wt.% F6TCNNQ and has a thickness of 300 nm. The intrinsic film is identical on both sides of the base with a thickness of 100 nm. The base itself is made up of 20 nm rubrene doped with 1 wt.% $W_2(hpp)_4$. A layer of 20 nm C_{60} doped with 1 wt.% $W_2(hpp)_4$ is added underneath the base electrode to improve electron injection into the base. An additional layer of 20 nm n-doped rubrene and 80 nm intrinsic rubrene is added on top of the base mask to reduce leakage via the base-collector diode.
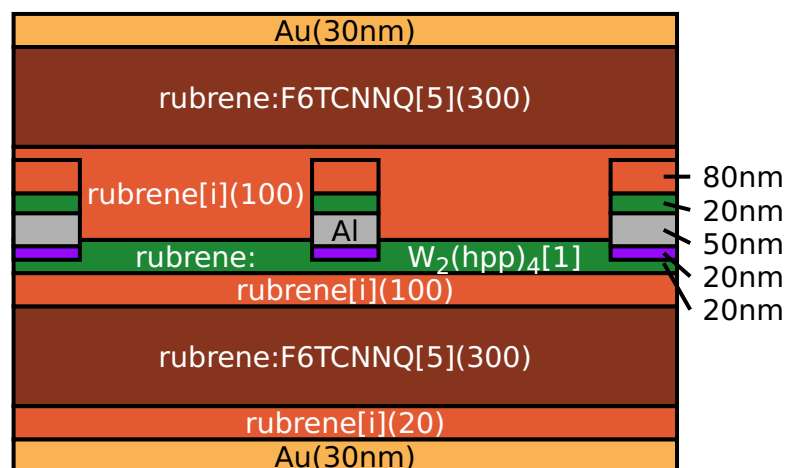
Figure 7.7: Stack of an OBJT made from spherulitic orthorhombic rubrene crystals (seed grown from 20 nm undoped rubrene at 170 °C for 90 s): Device is based on the pinip-design to function as a pnp-transistor. The n-layer for the vertical pinip stack is evaporated only below the base electrode (20 nm). A film of n-doped rubrene is placed above the base electrode (20 nm). The doping concentration for both films is identical. The Al base electrode (grey) has a thickness of 50 nm. A film of C_{60} (20 nm), doped with 1 wt.% $W_2(hpp)_4$ is present below the base electrode as an injection layer (violet). A thick film of 80 nm intrinsic rubrene is placed above the n-doped film on the collector side to reduce base-collector leakage currents. key: matrix:dopant[doping concentration](thickness).

Figure 7.8 shows the IV characteristics of the individual parts of the diode. A comparison between these and three-terminal measurements is performed as described earlier in section 7.1. No significant discrepancies are noticeable. The emitter-base diode and the base-collector diode function as usable diodes, showing forward current and reverse blocking. Reverse currents of both diodes are virtually identical, despite the increased thickness of the base-collector diode, indicating that reverse leakage is carried by lateral currents in these devices. Forward current for the emitter-base diode is higher, as expected. However, the improvement regarding the threshold voltage that can be seen in single pin diodes, as described in chapter 5.3.3, is not visible here. This might be caused by air exposure. The intricate masks used for this device cannot be effectively aligned inside a nitrogen glovebox without a high magnifying microscope. During the manufacturing, devices are exposed to ambient air for each of the mask alignments. The n-doping of the C_{60} might be deactivated ([254], [255]) and the improvement vanishes.

Despite the improved mask geometry and the resulting higher ratio of active to inactive areas, the leakage current from emitter to collector remains large. However, the collector current is only at low voltages significantly higher than the currents through the diodes. It is thus possible to apply higher emitter-collector voltages without damaging the pinip structure. Nevertheless, the blocking behavior of the emitter-collector double junction is not satisfactory. A possible solution for this problem is discussed in section 7.4. Figures 7.9 show the transfer characteristics
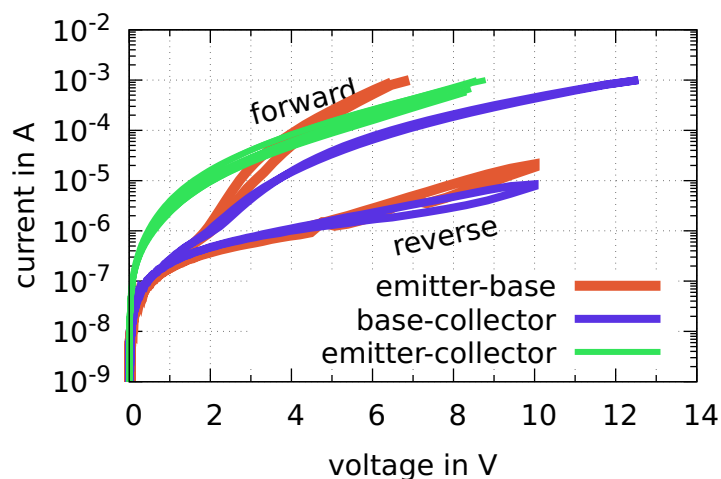
Figure 7.8: Two-terminal measurements of the individual components of an OBJT based on the stack design shown in figure 7.7. The third electrode is left floating. Emitter-base and base-collector diode function as usable diodes. Emitter-collector pinip structure is symmetrical and has a reduced current compared to the device shown in figure 7.3a. The emitter-collector current at low voltages remains higher than the diode current.

of this transistor measured in common-emitter configuration. Figure 7.9a shows only measurements at $V_{CE} = -8$ V. As expected from the high current through the emitter-collector junction, the collector current in the transistor structure is high and almost constant throughout the transfer sweep. Only at high base currents above $100\,\mu$A, an increase in current is noticeable in the logarithmic depiction. The procedure described in section 7.1 is used to analyze the change of emitter ΔI_C current only. In this device, the output signal presents as a smooth function of base current with significantly decreased noise. The previously discussed correction of the emitter current, compensating for the emitter-base leakage does not change the curve in a significant way. It is worth noting that the absolute value of the leakage current from base to collector is not small. Contrary, at low base currents, the leakage current is larger than the change in collector current. However, the change in collector current is significantly larger than the change in leakage at all times. This is the decisive property for amplification, while the absolute currents are of course relevant for the final application.

The current added to the emitter ΔI_C increases throughout the entire sweep, showing three distinct regimes. The slope of ΔI_C is the strongest below $1 \cdot 10^{-10}$ A. It is difficult to decide if this strong increase is related to the "switch-on" behavior of the transistor. As explained earlier, even at zero external base current I_B, the emitter-base diode is "switched on" and the corresponding direct current is not zero. The regime for which the emitter-base diode is not in forward operation is not measurable in this configuration. For medium base currents, the slope saturates. It increases again – although not as strong as before – for currents above 0.1 mA. The individual plateaus of the collector current could be related to the regimes seen in the IV curves of the pin diodes. Each regime is indicative of a different type of conduction and thus a different distribution of charge carrier
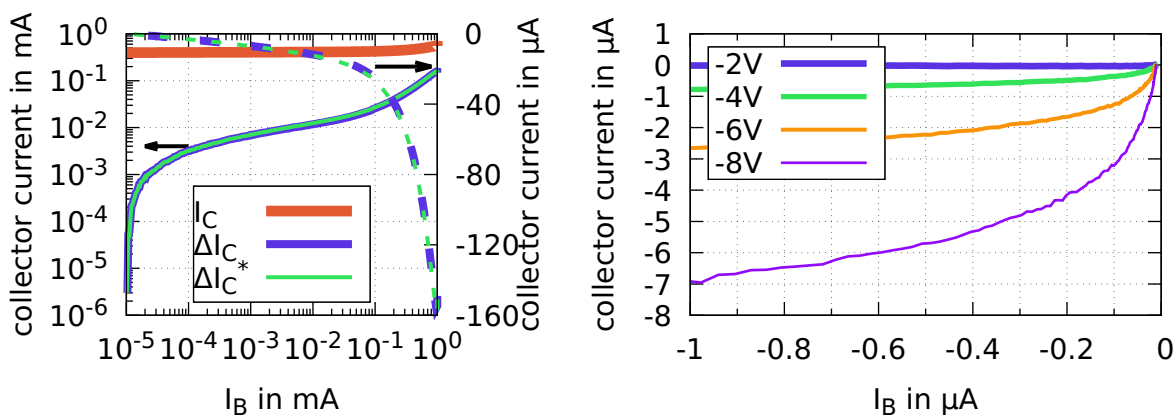
(a) log-log depiction of the transfer characteristic, showing the collector current I_C and the change in collector current ΔI_C and the change in collector current corrected by the current from base to collector ΔI_C^*. (V_{CE} = −8 V).

(b) Transfer characteristic in the regime from 0 µA to −1 µA at different emitter-collector voltages V_{CE}.
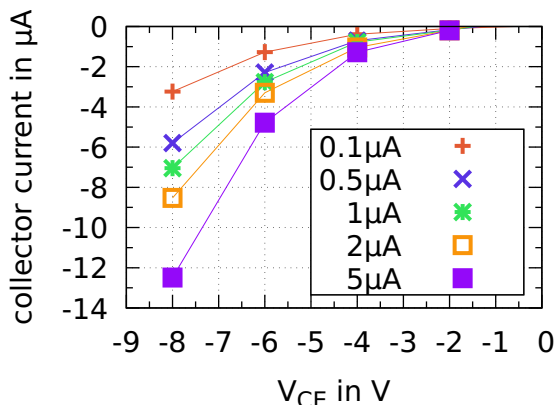
Figure 7.9: IV characteristic of an OBJT based on the stack shown in figure 7.7.

(c) Output characteristic at fixed base currents in the regime in which amplification can be observed.

density and field within the structure. A well-founded and detailed description cannot be given based on the data at hand.

Figure 7.9b shows the transfer curves for the same device at various emitter-collector voltages in the medium-current regime from 0 µA to −1 µA. In accordance with the theoretical expectations for the BJT, the current increases with increasing base current for all measured emitter-collector voltages. An increase in V_{CE} also increases the collector current, as is expected. However, the linear dependence between base current and collector current that would be expected for low base currents is not observed. A linear connection between the collector current and emitter-collector voltage is not shown either. That could be a sign of saturation of the transistor effect. However, considering the complicated structure
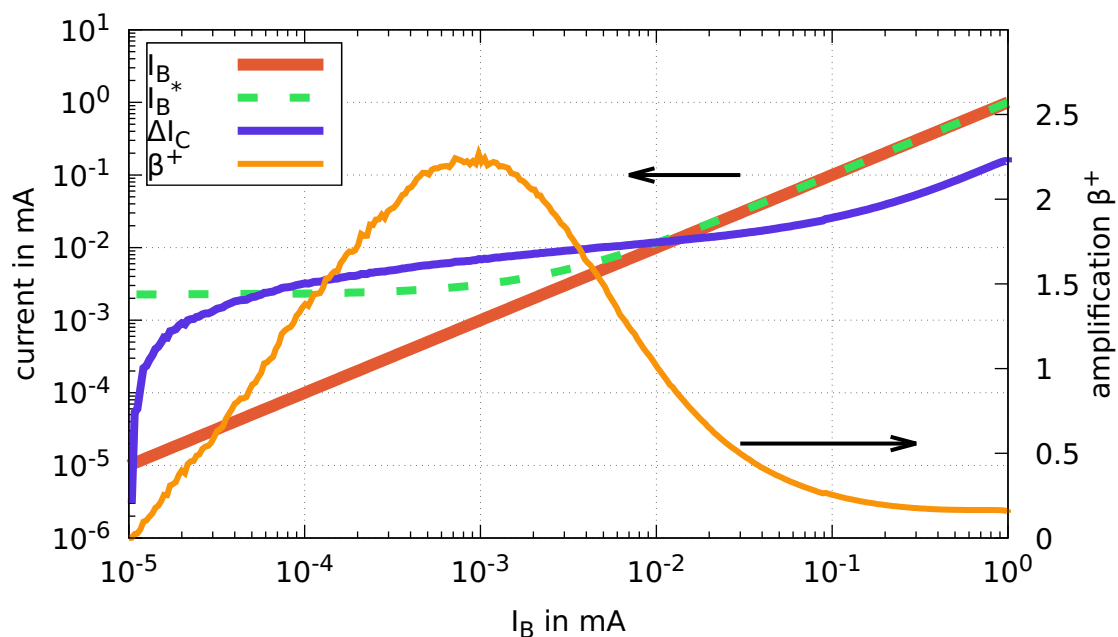
Figure 7.10: Detailed view of the transfer characteristic shown in figure 7.9a:
I_B: input current through base electrode
I_B^*: current from the emitter to the base (I_B corrected by $I_{C\text{-}B}$)
ΔI_C: change in output current through collector electrode compared to $I_{C0} = I_C(I_B = 0)$
β^+: amplification based on the strict definition $\beta^+ = \frac{\Delta I_C}{I_B^*}$
all measurements at $V_{CE} = -8\,\text{V}$.

of the device and the strong non-ideality of most of the individual components, behavior diverging strongly from the theoretical description is to be expected.

To answer the question if this device is operating *as a transistor*, the output signal – the collector current I_C – has to be compared to the input signal I_B. Different definitions of the amplification can be chosen, depending on which process is highlighted. The first choice here is to discuss the change in emitter current ΔI_C, instead of the full emitter current I_C, as explained earlier. The initial offset can be described as a parallel ohmic resistor. Correcting for this parallel resistance does not reduce the validity of the analysis of the transistor operation as is shown in the following section via circuit simulations.

One major goal is to prove the direct control of the collector-emitter current by the base-emitter current. In an idealized device that corresponds to the control of the collector current via the base current. That would in itself prove effective diffusion of minority carriers through the base. By variation of the base thickness, a minority carrier diffusion length could be calculated. In an ideal BJT, some of the previously discussed current paths do not occur. The base-collector leakage and the emitter-collector leakage are zero, since at least one junction is biased in reverse direction. Additionally, emitter-base currents that do not participate in the bipolar effect do not exist – aside from recombination currents. To prove the
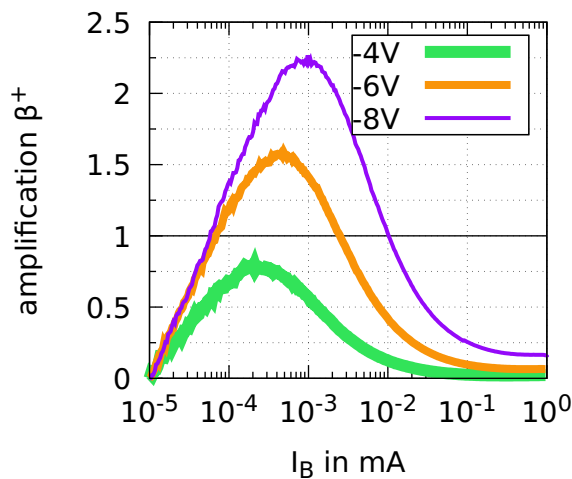
(a) Strict definition $\beta^+ = \frac{\Delta I_C}{I_B^*}$.
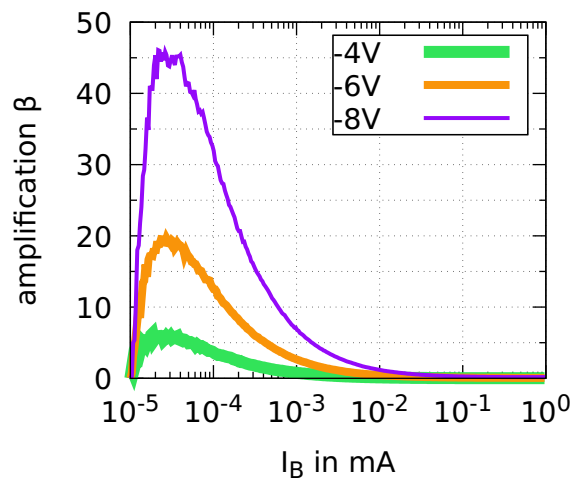
(b) Technological definition $\beta = \frac{\Delta I_C}{I_B}$.
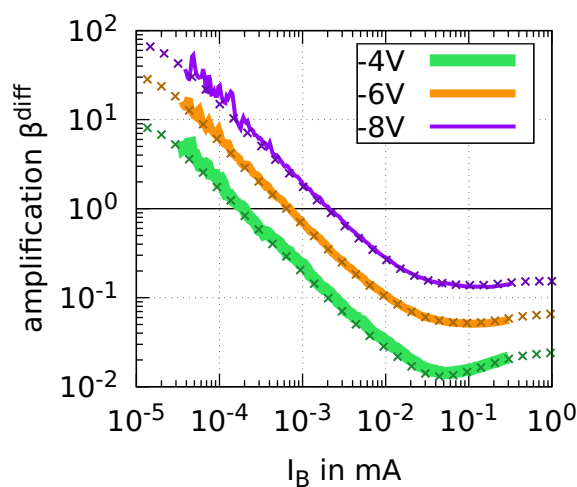
(c) Differential definition
solid: $\beta^{\text{diff}} = \frac{\frac{\partial I_C}{\partial V_{\text{BE}}}}{\frac{\partial I_B}{\partial V_{\text{BE}}}}$,
dots: $\beta^{\text{diff}} = \frac{\partial I_C}{\partial I_B}$.

Figure 7.11: Amplification β over base current I_B for different V_{CE} extracted from the IV curves of figure 7.9. The definition for each of the amplification is given underneath the graphs. The ΔI_C used is corrected by the constant offset at zero base current but not by the base-collector leakage. The barrier for amplification of $\beta = 1$ is marked in graphs (a) and (c).

existence of amplification in these devices with certainty, the strictest possible definition for amplification β^+ is chosen, as described in equation 7.6. Here, the change of current into the collector $|\Delta I_C|$ without any (beneficial) correction of the base-collector leakage is compared to the current from emitter to the base, defined as $|I_B^*| = |I_B| + |I_{C\text{-}B}|$. This is the current that is supposed to facilitate the current control. However, not all of this current is fed through the input of the transistor. Figure 7.10 shows the input current I_B compared to this corrected emitter-base current I_B^*. The latter is always larger. Demanding β^+ to be larger than one as a threshold for amplification is thus a stricter requirement to overcome.

The change in collector current and the resulting amplification from equation 7.6 are added in figure 7.10. β^+ is above one between $-60\,\mathrm{nA}$ and $-10\,\mathrm{\mu A}$ of base current. The maximum of 2.24 in amplification is found at a base current of $-6.4\,\mathrm{\mu A}$. Amplification is low in the low base current regime, since the added collector current has to catch up with the offset in base current created via the base-collector leakage. After reaching its maximum, amplification decreases again due to the base diode increasing in current faster than the output of the transistor. This can easily be explained by the large parallel diode at the input side. Circuit simulations regarding this behavior are shown in the following section 7.3.

The same analysis is repeated for the measurements at lower emitter-collector voltages. The resulting β^+ are shown in figure 7.11a. The general behavior is similar for all three V_{CE}. For lower voltages, however, the absolute amplification decreases and the peak of the curve shifts to lower base currents. Amplification above one is not reached anymore for an emitter-collector voltage of $-2\,\mathrm{V}$.

An alternative – less strict – definition for the signal amplification is based on equation 7.4, using $\beta = \frac{\Delta I_C}{I_B}$,. Here, the change in collector current is compared to the base current I_B, without the correction of the base-collector current. This is the amplification that is relevant in an amplifier circuit, given that the offset in collector current is compensated. The resulting amplification, shown in figure 7.11b, is significantly larger, since the corresponding control currents I_B are smaller. The values initially increase with base current, and show a peak of 48 at a base current of $-26\,\mathrm{nA}$ for an emitter-collector voltage of $-8\,\mathrm{V}$. Similarly to the other definition, the amplification decreases for higher base currents due to the parallel current of the input emitter-base diode. For high currents, β^+ and β are identical, since I_B^* approaches I_B and the impact of the emitter-collector diode becomes negligible.

At last, the differential amplification can be analyzed. It describes the capability of the transistor to amplify a dynamic voltage signal at the input. It is defined either as

$$\beta^{\mathrm{diff}_1} = \frac{\frac{\partial I_C}{\partial V_{BE}}}{\frac{\partial I_B}{\partial V_{BE}}} \tag{7.7}$$

or

$$\beta^{\text{diff}_2} = \frac{\partial I_C}{\partial I_B},$$ (7.8)

where the first equation is based on the full set of S-parameters used in a full device characterization. The second equation is a simplified version that results in the same behavior for most cases.

None of the corrections discussed earlier are necessary in both cases. Even the large offset in the emitter current, created by the emitter-collector leakage I_{CE0} is removed automatically, since it does not change with emitter-base voltage. The corresponding values are presented in figure 7.11c. Measurements at low base currents suffer from strong noise and fluctuation of the corresponding voltages. The measurement of the emitter-base voltage needed to realize a specific base current is less precise than the measurement of the base current itself. The voltages have to be smoothed using a Savitzky-Golay algorithm, with a linear extrapolation over 20 data points, prior to differentiation if equation 7.7 is used. The differential conductivities gained from these curves are smooth and follow the overall trend of the remaining curve. However, the smoothing algorithm changes once the edge of the data range is reached. These areas are poorly defined and are thus cut from the corresponding data in figure 7.11c. The amplification is decreasing with increasing base current but is larger than one for currents up to $-2\,\mu\text{A}$. No maximum is present within the measured range. Not surprisingly, both definitions of the differential amplification give close to identical results.

In summary, amplification of base current is found in these OBJT devices, regardless of the strictness of definition. Operation as a BJT seems likely, including diffusion of minority holes through the base. The true performance of these transistors is covered by the many sources of leakage current within the system.
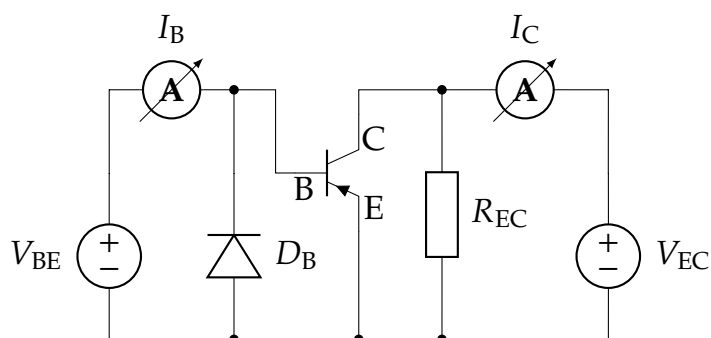
Figure 7.12: Equivalent circuit of the investigated OBJT, including a diode D_B in parallel to the emitter-base diode and an ohmic resistor R_{EC} in parallel to the emitter-base output. Measurement procedure is equivalent to circuit in figure 7.2.

7.3 Circuit Simulation of Bipolar Junction Transistors (BJTs) in Common-Emitter Configuration Including Leakage Components

In the previous sections, two sets of BJT devices are discussed. One device shows amplification and one device does not. Significant leakage currents are present in these devices between each of the three electrodes. Additionally, the emitter-base diode is split into two parts, one part that adds to the controllable collector current and one part that does not. This section presents a simple Spice simulation based on off-the-shelf components to illustrate the effect of these types of additional elements within the pseudo-circuit. The advantage of a model circuit is that certain parasitic components can be switched on or off and the corresponding impact on the overall circuit can be observed. It serves simultaneously as a description of the problem and a posteriori justification for the claims and definitions of the previous sections.

The simulation tool used is the open-source software *LTSpice*. The corresponding models are standard SPICE models provided by the manufacturer of the individual components. The equivalent circuit that is used is shown in figure 7.12. It is worth noting that the circuit as it is shown here is not suitable for operation. Connecting external voltages of this magnitude directly to the transistor and diode without any series resistance would certainly destroy the device. This analysis serves exclusively as a demonstration of the effect certain components have on the measurement of an OBJT as is described in the previous sections. The BJT used here is a 2N3906, pnp-transistor by NXP with a base current amplification of 100 and a maximum emitter-base voltage of –5 V. The diode D_B that represents the parallel diode between emitter and base is a 1N4148 by OnSemi, a standard Si diode. The resistor used is a generic ideal component, set to 1 kΩ. Figure 7.13a shows the single component IV curves of the chosen parallel diode D_B and of the emitter-base input diode of the BJT without any influence of the rest of the circuit. As can be seen, both devices are chosen such that the parallel diode has a significantly higher conductivity than the emitter-base diode at all times. Figure 7.13b presents the properties of the single BJT. This includes the emitter current of the single transistor I_C^T, the current of the base of the transistor I_B^T, and the corresponding amplification of the transistor β^T, over the voltage applied to the base V_{BE}. The current of the collector starts at $1 \cdot 10^{-12}$ A and then increases as soon as the emitter-base diode switches on. The corresponding amplification of the transistor is at 100, as expected from the datasheet of the component. It is now clear that the BJT in itself has a high amplification over a large range of input current.

The next step is to investigate the behavior of the full "circuit". The resulting current is shown in figure 7.14. The terminology used for the OBJT of the previous section is valid. The current entering the circuit on the input side into the base

Figure 7.13: *LTSpice* simulations based on the circuit shown in figure 7.12: The diode D_B is based on the Spice model of a 1N4148 by OnSemi. The BJT is based on a 2N3906 by NXP. R_{EC} is an ideal ohmic resistor with $1\,k\Omega$.
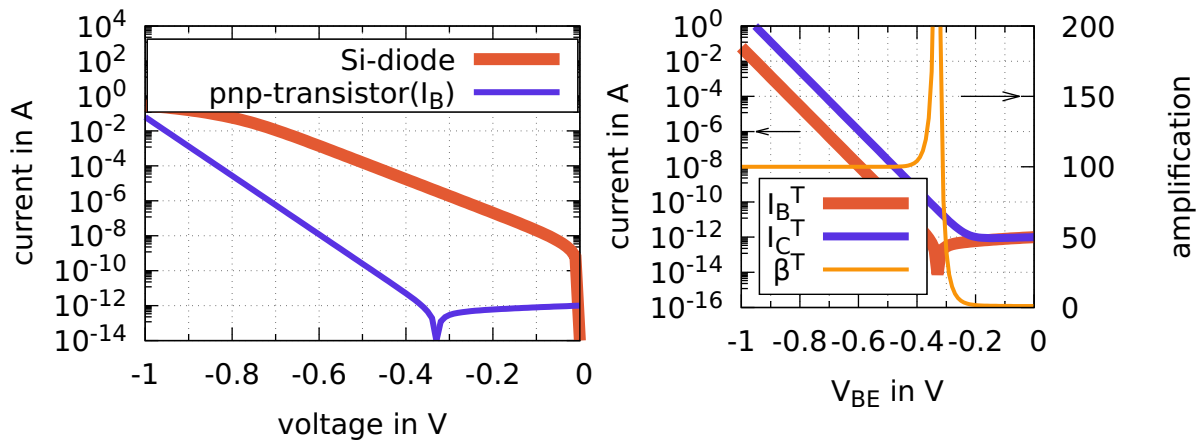
(a) Single device IV characteristic of the diode and the emitter-base diode of the transistor in comparison.

(b) Current through the base of the transistor compared to current through the emitter of the transistor and resulting amplification factor β. This is the equivalent result to a circuit without the input diode and output resistor.

of the transistor and the parallel diode is called I_B. Current through the emitter pin is labeled as I_C without the resistor R_{CE} and I_{C2} including the resistor at the output. Figure 7.14 shows the transfer curve at $V_{CE} = -3\,V$. The output current I_C is identical to the collector current of the BJT. The input current, however, is now significantly higher than the current going into the base of the transistor. The output current is thus mostly below the input current, similar to what can be seen in the previous measurements of the OBJTs. Since the output current is amplified by the transistor operation, it gets larger than the input current at around $10\,mA$. The output current drops below the input current for base currents above $1\,A$, due to the saturation of the transistor. The resulting "amplification of the transistor" has a similar shape than measurements of the OBJT, with a peak amplification of below two.

Introducing an ohmic resistor R_{EC} to the output, ads a constant component to the emitter current I_{C2}. If this constant current $R_{EC} \cdot V_{CE}$ is subtracted, the result is identical to the pure transistor collector current.

Two conclusions can be drawn from this simulation: First, the high offset in the collector current can be explained by a parallel current path. Correcting for this extra current does not devalue the analysis of the transistor operation. Secondly, it is better to see the OBJTs discussed earlier as a circuit including a diode in parallel to the input. The low amplifications shown by the device can be easily explained by this phenomenon. The real amplification of only the active part of the device might be significantly higher. Theoretically, the influence of this
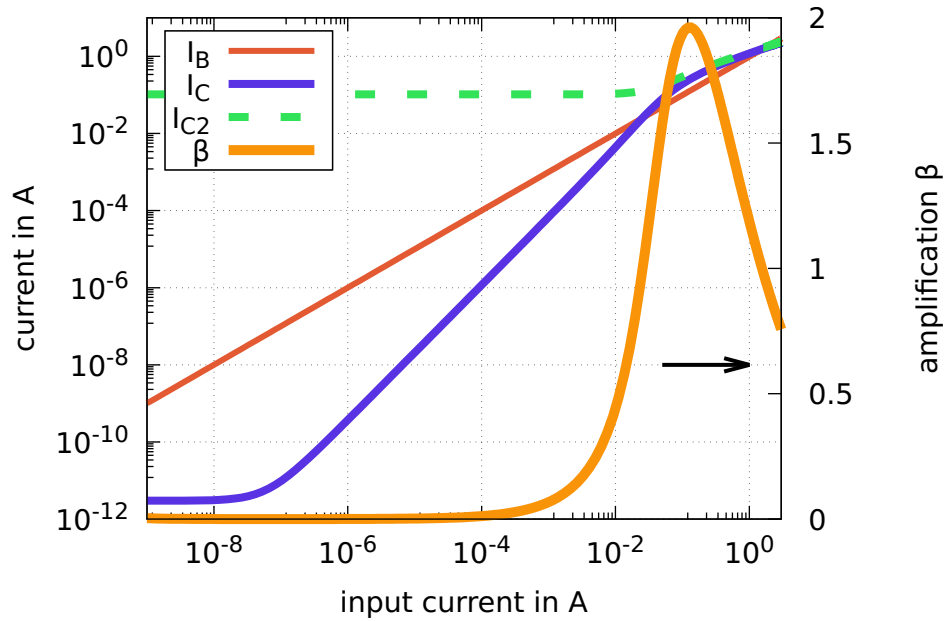
Figure 7.14: Input and output current of an *LTSpice* simulations based on the circuit shown in figure 7.12. The IV characteristic of the individual devices is shown in figures 7.13:

I_B is the input current, split between the diode D_B and the emitter-base diode. It is dominated by the diode current I_D.

I_C is the output current through the circuit at $R_{EC} = \infty$, identical to the emitter current of the transistor.

I_{C2} is the output current through the circuit at $R_{EC}=1\,\mathrm{k\Omega}$, equivalent to a large parallel leakage current between emitter and collector.

β is the resulting amplification based on $\beta = \frac{I_B}{\Delta I_{C2}}$.

parasitic diode can be extracted from the data, such that the pure performance of the bipolar transistor is visible. This is, however, only possible if the exact geometry of the device (i.e. the base reach) is known.

7.4 Further Improvements of Organic Bipolar Junction Transistors (OBJTs)

The last section of this chapter discusses a few possible methods to improve these OBJTs. Based on the previous measurements and the circuit simulations, two main problems can be identified. The offset in collector current caused by leakage through the collector-emitter pinip structure and the parallel diode connected to the input side. These issues are already partly addressed via the improvement of the electrode design. Decreasing the ratio between the width of the individual base pads and the active area can reduce the impact of the parasitic diode. Additionally, reducing the width of the gap between neighboring base electrodes increases the ratio of controllable to uncontrollable emitter-collector overlap. Nevertheless, the leakage current through the emitter remains high, regardless of the mask geometry.

Figure 7.15: IV characteristics of pinip devices with varying thicknesses of the intrinsic and n-doped layers. n-doping concentration is 1 wt.%, p-doping concentration is 2 wt.% for all devices. p-layer thickness is 250 nm on both sides. Key is given as (intrinsic film thickness/n-layer thickness/intrinsic film thickness in nm).
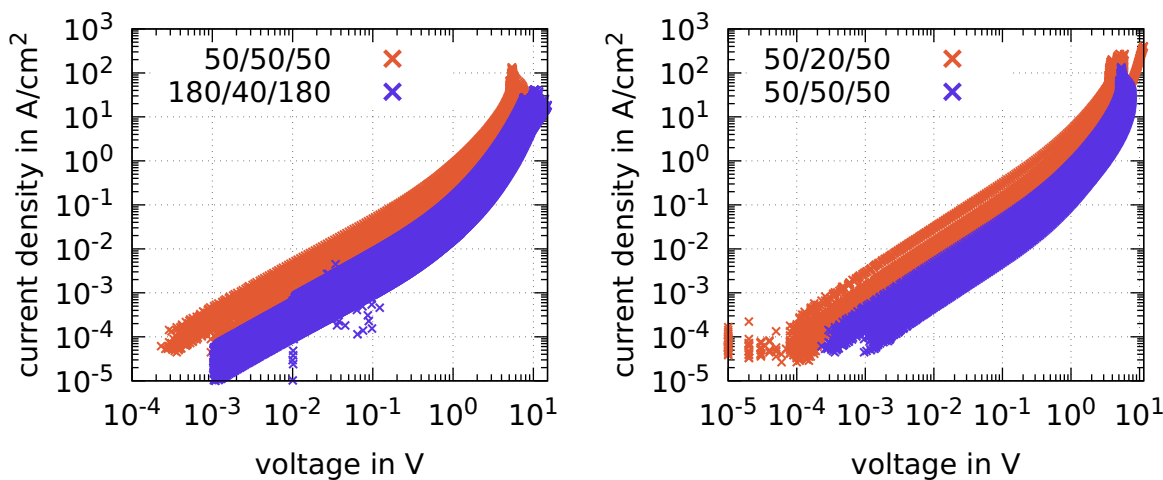
(a) Variation in i-layer thickness: The increase of intrinsic layer thickness on both sides of the double junction shows a decrease in overall current.

(b) Variation in n-layer thickness: Increasing the n-layer thickness has a stronger effect than increasing the intrinsic film thickness.

Thus, the double junction within the pinip structure itself must be investigated and improved. A set of devices is produced at the UFO evaporation tool, varying the thickness and doping concentration of the n-type and intrinsic layers to analyze the blocking behavior. The triclinic crystal phase is used for these experiments as a model material. The seeds are grown from 40 nm of undoped rubrene at 130 °C for 15 min. For the electrodes, mask design IV2 is used, identically to the pin diodes. The thickness of the p-doped film is kept constant, since its only purpose is the transport of holes to and from the individual junctions. Figures 7.15 show sets of pinip devices with varying thicknesses. The p-doped films are identical for all devices, with a total thickness of 250 nm, doped at 2 wt.% on both sides of the structure. The electrode material is Au. The concentration of $W_2(hpp)_4$ is identical in all devices at 1 wt.%. In figure 7.15a, IV curves are shown of devices with a comparable n-layer thickness and vastly different thicknesses of the intrinsic layer. The – along the voltage axis – fully symmetric IV curves are shifted towards lower current densities for the devices with thicker intrinsic films. However, considering an increase in intrinsic film thickness by a factor of almost 4, the improvement in blocking capability is small. Several 100th of nm of intrinsic layer would be required to reduce vertical leakage to an acceptable degree. The exact distribution of fields and charge carriers within the OBJT devices is not clear yet, however, it seems unlikely that a moderate increase in intrinsic layer thickness would hurt the bipolar effect. Such a strong increase in intrinsic layer thickness might be problematic nonetheless.
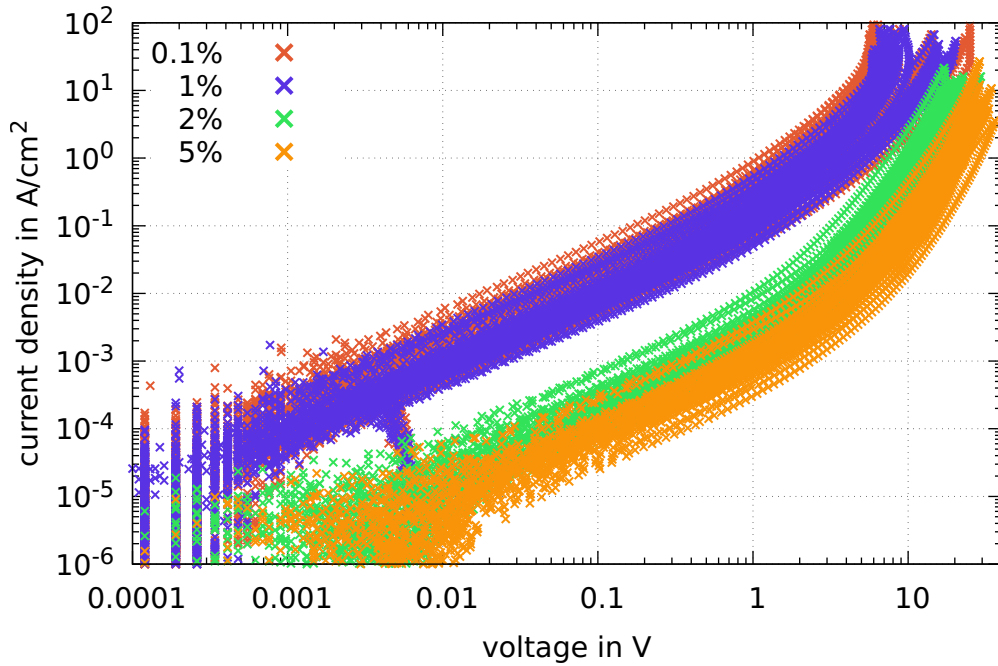
Figure 7.16: IV characteristics of pinip devices with varying doping concentrations of the n-doped film. p-doping concentration is 2 wt.% for all devices. p-layer thickness is 250 nm and intrinsic layer thickness is 50 nm on both sides. The n-layer is 50 nm for all devices: Increasing the n-doping concentration has by far the strongest effect on the blocking behavior of the double junction.

Figure 7.15b shows the reversed experiment. Here, the thickness of the intrinsic films is fixed to 50 nm, while the thickness of the n-doped film is varied. The effect is similarly strong than in the first experiments, reducing the current density by approximately one order of magnitude when the n-layer thickness is increased by 150 %. Reducing the collector leakage by an increase in thickness of the n-doped film seems to be more effective than by an increase in intrinsic layer thickness. However, a thin base is one of the requirements for bipolar current control. A trade-off must be found between optimal blocking and diffusion through the base.

At last, figure 7.16 shows the impact of the doping concentration of the n-doped layer. For these devices, both intrinsic films and the n-doped layer have a thickness of 50 nm. The doping concentration of the n-doped film is varied from 0.1 wt.% to 5 wt.%. The difference in current density between the devices with 0.1 wt.% and 1 wt.% doping is negligible. This might be caused by the low accuracy of doping for low doping concentrations. Hence, the actual doping concentration of these two sets might be closer than intended. However, an increase of doping concentration to 2 wt.% and then further to 5 wt.%, has a significant impact on the current through the pinip structure. The current density decreases strongly, by up to two orders of magnitude. This behavior is unexpected, since an increase in doping should result in a decreased thickness of the depleted film, which in turn should lead to increased leakage via tunneling. One possible explanation

for this counterintuitive behavior can be found in earlier experiments with pin diodes in chapter 5.3.2.3. Experiments with the n-layer (thickness and doping concentration) suggest that the total amount of electrons within the n-layer is too low to create an equilibrium of charge carriers in the pn-junction. The n-doped film is then fully depleted of electrons and might contain a remaining amount of diffused holes. A barrier is still present, although significantly weaker than suggested by theory. An increase in the thickness of the n-doped film or in doping concentration of the n-doped film would increase the total amount of electrons. The strength of the blocking is then increased until enough electrons are present to realize an equilibrium. Since the density of the holes in the p-doped film is known, this procedure might be used to calculate electron densities and subsequently doping efficiencies of n-doped films, without creating thick and expensive Schottky diodes for Capacitance-Voltage (CV) measurements.

For the use in OBJTs, however, the n-doping concentration must not be too high, since the ratio between p- and n-doping is essential for the efficiency of emitter injection. A trade-off must be found to realize effective blocking while keeping the bipolar effect. Additionally, a lower n-doping concentration in the base might create a film of higher ordering and hence a longer hole diffusion length. It might be more beneficial to reduce the doping concentration of the p-layer close to the pn-interface instead of increasing the n-doping concentration.

The leakage current between base and collector is less problematic, since it is generally lower than the controllable collector current. Nevertheless, it can be valuable to reduce this leakage path since it adds an offset to the base current and thus introduces nonlinearities to the system. A reduction can be achieved easily by the introduction of blocking layers on top of the base electrode. Material can be deposited through the same mask that is used to create the base electrode itself. An initial experiment using sputtered SiO_2 showed good suppression of base-collector leakage current at high fields. However, depending on the geometry of the evaporation system, this blocking layer can protrude further into the base than the base electrode itself. In that case, valuable channel area is covered. Furthermore, some of the leakage paths are laterally dominated. Structuring of the organic semiconductor might improve the performance and simplify the analysis significantly.

Finally, it has been shown that the direct overlap of base and emitter creates a diode at the input that does not directly participate in transistor operation. Ideally, the width of the individual fingers of the base electrode can be reduced even further. Alternatively, a structuring method might be used that allows for an alternating arrangement of the three electrodes. That way, the amount of overlap can be reduced as much as possible. Both of these approaches can be theoretically tackled using photolithography. Structuring of Au electrodes on rubrene crystals is possible, as is described in chapter 6.2. However, only the topmost electrode is structured via photolithography in these devices. Initial experiments for the

triclinic crystals show that consecutive epitaxy on films that have been structured photolithographically is significantly hampered. The contrast in polarization microscopy of the crystalline structure is reduced, indicating a reduction in crystal quality. It might be caused by parts of the photoresist remaining in the valleys of the rough surface of these films. If the same is true for the orthorhombic crystal phases has not been investigated yet.

7.5 Summary

The devices shown and discussed in this chapter are not yet usable as an electronic component in any type of circuit. Considering that they represent the first device of their kind at all, however, many promising results are visible. First, the devices can in their current state be used to investigate and analyze the behavior of minority charge carriers in organic semiconductors. Variations of base thickness, doping concentration, temperature, external illumination, and many more parameters can enable new insights into the fundamental properties of diffusion-driven transport.

As an outlook, the following table gives an overview about the most promising and relevant issues regarding the future development of these devices, including possible solutions for obstacles.

issue	current state	problem to solve	solution
bipolar transistor current control	• current amplification clearly shown for orthorhombic crystal system • maximum current amplification large	• only differential (AC) current amplification, due to large DC leakage • amplification not constant • system represents "circuit" and not "single device" • measured via DC measurements only (sweeps)	• reduction of DC leakage through optimization of doping profile and electrode geometry • reduction of currents through BE-leakage diode via improved geometry • additional measurements with AC signals
minority diffusion length	• signal amplification is measurable • → minority carrier must diffuse through base • → diffusion length longer than base layer thickness	• diffusion length cannot be calculated from single datapoint • yield of device fabrication is bad	• manufacturing of devices with varying base thickness and doping concentration • increasing yield by improved stack design and geometry

Table 7.1: Summary bipolar transistors I

issue	current state	problem to solve	solution
electrode geometry			
	• all electrodes created via shadow-masking using Si-based stencil masks	• manufacturing of stencil mask expensive (geometry fixed and masks fragile)	• photolithography offers smaller features with easier and more precise alignment
	• manual alignment necessary under microscope	• manual alignment requires large overlap margins and causes damage to underlying layers	• → compatibility of epitaxy and photolithography?
	• emitter and collector are rectangles, base is finger structure	• contact to ambient air is necessary for alignment	• improved stencil mask design and manual alignment within nitrogen atmosphere
		• minimal feature length limited	

Table 7.2: Summary bipolar transistors II

8 Conclusion and Outlook

The foremost vision of this work is the realization of the Organic Bipolar Junction Transistor (OBJT), a transistor design that is common in inorganic electronics but has not been realized yet with organic semiconductors. Putting all technological questions aside, the major task is to find a material system that features long diffusion lengths while simultaneously being dopable with electrons and holes. The structure of a semiconductor is often closely related to the diffusion length of charge carriers. Most organic semiconductors are strongly amorphous and feature extremely short diffusion lengths, which makes it necessary to find an ordered organic semiconductor system. Here, rubrene is chosen as the base material. Via a special rapid heating technique, thin-films of amorphous rubrene can be crystallized on a substrate. Consecutive deposition of rubrene grows the crystal film in an epitaxial way.

The majority of the work done in the scope of this thesis is related to the growth of these thin-films of rubrene crystals. Crystallization in general, and crystallization of Van der Waals crystals in particular, has a certain degree of randomness. A variety of different global and local configurations of the crystal structure are possible, resulting in different polymorphs and microscopic configurations. In the end, three crystal phases – triclinic dendrites, orthorhombic spherulites, and orthorhombic platelets – are optimized to allow for a reasonably reproducible manufacturing. All three types of crystals show high conductivities vertically as a result of high vertical charge carrier mobilities ($10.3\,\mathrm{cm^2\,V^{-1}\,s^{-1}}$ for the triclinic phase and $3.3\,\mathrm{cm^2\,V^{-1}\,s^{-1}}$ for the orthorhombic phase). A high charge carrier mobility is a prerequisite for a long diffusion length. All three types of crystals can be p-doped, increasing the conductivity in a controllable way, albeit with a low doping efficiency. The triclinic crystal phase is analyzed in regard to n-doping as a model material. However, the other crystals are used in devices in n-doped form successfully, indicating that these polymorphs can be n-doped too. The shift in conductivity in Current-Voltage (IV) experiments of bulk films and diodes clearly hints at the creation of free electrons. Unfortunately, the efficiency of the n-doping process is even lower than the p-doping process. Measurements show that the efficiency of the doping can be improved by a different type of dopant ($C_{60}F_{36}$ dopes more efficiently than F6TCNNQ). A broader investigation of doping efficiency in crystalline system can be beneficial for the manufacturing and efficiency of all devices based on these rubrene films and comparable systems. Furthermore, investigation of the other crystal phases that are only investigated in a superficial way can be promising. Especially crystals grown below 120 °C, and thus below the first theoretical phase transition temperature, feature a distinct macrostructure compared to the other crystal phases.

First preliminary analyses are done regarding the structure of these films, helping to understand differences in charge transport between the polymorphs and optimizing related devices. However, the question regarding the position of the dopant within the crystal structure is not answered yet. In the Atomic Force

Microscopy (AFM), X-Ray Diffraction (XRD), and polarized microscopy measurements available, no strong effect on the structure is noticeable when doping these films. An extended analysis using off-axis XRD and Energy Dispersive X-ray spectroscopy (EDX) measurements is necessary to solve this and related questions. Glancing Incident Wide-Angle X-Ray Spectroscopy (GIWAXS) measurements for all relevant crystal phases are planned in the future to at least evaluate any change in the unit cell of the system.

Following the structural and electrical analysis of the intrinsic and doped films made from the three polymorphs, an analysis of Schottky, pn, and pin diodes is shown. The influence of stack composition, layer thickness, and doping concentration of the individual layers is analyzed. The resulting diodes can handle large current densities (hundreds of $A\,cm^{-2}$ in constant power and >2 $kA\,cm^{-2}$ pulsed), show on-off/ratios of up to $1 \cdot 10^5$, and feature low temperature-dependence. One problem is the high threshold voltages required to switch on the diode in forward direction. Some improvement was found using injection doping. Strong leakage currents are usually present in these devices. Some experiments indicate significant lateral currents contributing to this leakage. Studying the effect of structuring of the semiconductor would reduce leakage currents, subsequently increase on/off-ratios, decrease the threshold voltage, and improve overall performance. Further, the impressive load-resistance shown in the initial pulsed measurement can be investigated further by changing the measurement setups to lower series resistances.

The main purpose of analyzing the pin diodes is to assess sensible parametrization for the OBJT. Nevertheless, these diodes can be useful by themselves. Two applications are discussed, Organic Light Emitting Diodes (OLEDs) and rectifiers circuits. The high tolerance for current makes these films ideal for high-power lighting devices. A preliminary analysis showed External Quantum Efficiencys (EQEs) of around 5 % (although not at the highest current density), which is close to devices with similarly simple configurations. Significant improvement might be possible, via the introduction of blocking layers and more viable transparent electrodes. Further research on these films is carried out with the final goal of using these OLEDs in electrically pumped organic lasers utilizing the comparably large efficiencies combined with the high current densities possible. An more detailed analysis of the growth of these films on different types of mirrors is needed, as well as an deeper investigation of the optical and emission properties of the films.

The second investigated application is diodes for half-wave rectifier circuits. These circuits can be used as signal filters for Ultra High Frequency (UHF) applications and represent an ideal test-bed for an analysis of the switching speed. The best devices measured here showed rectification in the GHz-regime, faster than any other organic devices shown in literature till now, highlighting the potential of this material system for fast organic devices in general. The speed at which these

diodes can operate can be further improved in many different ways, since the optimization in the experiments here is more focused on the circuit than the diode. Implementation of encapsulation, structuring of the semiconductor, improvement of the doping procedure, and optimization of the stack configuration are a few possibilities. Additionally, more complicated circuits are planned with these diodes, like mixers and signal filters. Si-based diodes cannot operate at these high frequencies and more "exotic" and expensive inorganic semiconductors are used. Hence, the diodes analyzed here, represent a real technological alternative for cost effective UHF circuits.

Based on the analysis of pin diodes, functioning bipolar transistors are realized. Devices in an OBJT configuration are built that show control of the collector current via the base current. The differential amplification of the current shown by these devices is larger than one, proving signal amplification. It can thus be assumed that minority carriers (holes) can effectively diffuse through the n-doped base. However, although it is a success to demonstrate the principle of a Bipolar Junction Transistor (BJT) with organic semiconductors, in the current state, these devices cannot be used in most types of circuits reasonably, due to a dominating degree of leakage.

This implementation of the OBJT has implications for fundamental semiconductor physics and technology. Since the operation of any type of BJT is linked to charge carrier diffusion, a variation of base thickness offers an approach to directly measure the charge carrier diffusion length in organic semiconductors. Till now, studies in literature always rely on models to extract this parameter in different systems. Therefore, the result is only as solid as the model. One of the next logical steps is, thus, to study the amplification behavior of these devices with increasing base width and base doping.

From a technological perspective, BJTs have specific applications for which they are preferable to Field-Effect Transistors (FETs). Properties like linearity, noise, input impedance, and operation frequency are usually arguments for bipolar devices. In this sense, the implementation of the OBJT can help push the development of organic electronics as a whole and open up new circuit designs and applications. However, the initial success should not blind from the many tasks at hand necessary to make these devices applicable. Two main challenges can be identified: leakage current and parasitic current. The collector current at zero base input of all tested devices is too large, in particular, this current is significantly larger than any of the signal currents. As discussed, this problem can be attributed to a large degree to the pinip structure itself. Several measurements indicate that an increase in n-doping concentration or a decrease in p-doping concentration might reduce the leakage significantly. If the concept of a double homo-junction transistor is abandoned, replacing the collector side with a different material might be a valid strategy. Instead of relying on the depletion barrier defined by the relative doping of the rubrene, using another organic semiconductor with a

fitting energy level can create a significantly better barrier. A second problem is the parasitic diode that is connected in parallel to the base-emitter input. It is caused by the direct overlap between the base electrode and the emitter electrode and results in a significant share of the base current to "not participate" in signal amplification. Ideally, this overlap is reduced to zero. This can be realized with optimized geometries for the electrodes. However, a large degree of precision is necessary to allow for a minimal overlap only, which is almost impossible to realize with a shadow mask system. The next logical step is, therefore, to adopt photolithography for the structuring of these devices. Structuring of metal on top of these crystalline rubrene films is already shown for Vertical Organic Field-Effect Transistors (VOFETs). The added difficulty for the OBJTs is to maintain the epitaxial character of layer deposition after the structuring of the base electrode. As prior experiments show, epitaxy after lithography is problematic for the triclinic films, however, it might be possible for spherulitic and platelet type crystals due to their smoother surface. An alternative method to reduce the parasitic current can be realized using the available geometry. A film of low conductivity could be deposited through the base mask, prior to the deposition of the base metal. The direct path between base and emitter is thus blocked. However, realizing the lateral connection of the base electrode to the base can be a challenging problem. An analysis of the geometry surrounding the base electrode and the resulting stack configuration and field distribution is necessary. Transmission Electron Microscopy (TEM) measurements of the edge regions could offern insight into the exact problems at hand.

The final class of devices that is investigated are Organic Field-Effect Transistors (OFETs). Performance of lateral devices (especially for transistors based on the triclinic crystals) is only average. The main reason for the sub-par performance is the bad interface between the rubrene crystals and the SiO_2 that is used as gate insulator. However, VOFET devices based on the orthorhombic crystal phases already show impressive performance, comparable to state of the art vertical transistors of the same design but standard materials. It seems promising to optimize manufacturing and design of VOFETs, to accommodate for specific requirements of the interface. Especially a top-gate configuration seems promising since the defining interface can be towards low-defect materials like Cytop while simultaneously the growth can take place on SiO_2. VOFETs and OFETs built from these crystals can set new standards for organic transistors utilizing the high mobility of these films, combined with the possibility of contact doping.

Two final conclusions can be drawn. First, the material setup of crystalline rubrene in almost all of its polymorphs is promising in itself. It can be used in a large array of different devices types that can benefit from the high electrical performance. Despite rubrene being one of the most investigated organic semiconductors, especially for these thin-film crystals, many questions are still open and need further analysis. This is true for structural analysis and doping-related studies.

Furthermore, a generalization of the crystallization and doping process would be beneficial to find other material systems with similar or better properties. Secondly, the OBJT has been realized. It is yet not a useful device from a circuit point of view. Nevertheless, the road map to optimize and improve it towards a functioning transistor is clear and the possible performance promising.

322

Acknowledgments

I have been told once that during the course of a phd project, a student finds around 300 ways of how to NOT do something and maybe one way how to actually do it. During the course of my own PHD project, I found this to be very true. It was closer to 300 ways of doing something else, though. This is one of the main reasons for the quite exorbitant length of this thesis.

All these different topic of course meant that many different people were involved in preparations, measurements, and discussion. Science rarely works alone. I am thus grateful for the opportunities I have at the research labs of the IAPP and for all of my colleagues and friends.

First and foremost I want to thank my supervisor Prof. Karl Leo who is head of the IAPP to grant me the opportunity to work on this topic. I particularly appreciated that I could freely investigate the parts that I found the most interesting and promising by my own discretion. It might have contributed to the vastness of the results gathered. Furthermore I want to thank to Prof. Björn Lüssem, my second referee, who also used to be my first group leader when I started in the IAPP during my Bachelors thesis.

The biggest help of all during my work on this thesis was of course my current group leader Hans Kleemann. Visiting him in his office to discuss new results and challenge ideas and assumptions was always a pleasure. More for me than for him, maybe. I am also thankful and sorry that he had to bear the brunt side of having to proofread this overboarding thesis, especially since he usually was the first to receive each new piece of text in its most raw state with most of the Titivillus' work still present.

Science is only possible if "stuff works". That is why I very much appreciate the work of our technical and administrative stuff, in particular Sven Kunze and Andreas Büst (masters of fixing), Anette Zeika (master of sublimation), and Annette Polte, Carla Schmidt, and Fanny Uhlig (masters of heavy paperwork).

Several people worked directly with me on this topic. At first there is of course Bahman Kheradmand Boroujeni, who conducted the UHF measurements of the rectifier circuits and proved to be a diligent and precise engineer. Then, Stefan Meister and Shu-Jen Wang, who use the OLED version of the rubrene-based diodes for their organic laser experiments. I am happy to see that my work has some uses outside of my own scope.

During my time as a phd student I had the pleasure to assist several students towards their own degrees, namely Jörn Vahland, Tobias Antrack, Max Böttcher, and Markus Müller. Especially Markus showed an enthusiasm and eagerness to work and research that I have not seen in any other student before and ever since. I am also especially pleased that Jörn will continue my work on organic bipolar transistors. He will surely be successful, as long as he remembers that from time to time the material IS the problem.

Most of my time working on my thesis I spent my office with David Kneppe, Stefan Meister, and Jörn Vahland. The time we spent playing cards, watching

movies, or going to ice hockey and all-you-can-eat buffets was always a welcomed distractions from the usual daily work in the lab.

There are of course a whole bunch of people that supported me on a non-scientific level. First and foremost my parents and family. Without their support I would not have had the opportunity and means to finish or even start this work in the first place. I am also thankful to my girlfriend Seongae for supporting me and excuse the extraordinary amount of time I spent on working and finishing this thesis.

There are also my good friends Richard and Alex; who else would could you have a discussion at 1am about the human rights of robots or hypothetical dystopian societies? Although not directly involved in the development of this thesis but certainly in preparation of it, I have to mention my former tutor during my master thesis Alrun Günther as well as my high-school physics teacher Beatrix Weiser. In the end I can only say "Thank you!" to all these people and all others I might have carelessly forgotten to mention.

Bibliography

[1] H. Nikolic. "Would Bohr be born if Bohm were born before Born?" In: *American Journal of Physics* 76.2 (2008), pp. 143–146. DOI: 10.1119/1.2805241.

[2] T. Mainman. "Stimulated Optical Radiation in Ruby". In: *Nature* 187 (1960), pp. 493–494. DOI: 10.1038/187493a0.

[3] J. Bardeen and W. H. Brattain. "The Transistor, A Semiconductor Triode". In: *Proceedings of the IEEE* 86.1 (Jan. 1998), pp. 29–30. ISSN: 0018-9219. DOI: 10.1109/JPROC.1998.658753.

[4] J. E. Lilienfeld. CA272437A. P. University. expired. July 1927.

[5] W. Shockley, M. Sparks, and G. K. Teal. "$p - n$ Junction Transistors". In: *Phys. Rev.* 83 (1 July 1951), pp. 151–162. DOI: 10.1103/PhysRev.83.151.

[6] D. Kahng. "A historical perspective on the development of MOS transistors and related devices". In: *IEEE Transactions on Electron Devices* 23.7 (July 1976), pp. 655–657. ISSN: 1557-9646. DOI: 10.1109/T-ED.1976.18468.

[7] C. W. Tang and S. A. Van Slyke. "Organic electroluminescent diodes". In: *Applied Physics Letters* 51.12 (1987), pp. 913–915. DOI: 10.1063/1.98799.

[8] C. W. Tang. "Two-layer organic photovoltaic cell". In: *Applied Physics Letters* 48.2 (1986), pp. 183–185. DOI: 10.1063/1.96937.

[9] A. Hepp, H. Heil, W. Weise, M. Ahles, R. Schmechel, and H. von Seggern. "Light-Emitting Field-Effect Transistor Based on a Tetracene Thin Film". In: *Phys. Rev. Lett.* 91 (15 Aug. 2003), p. 157406. DOI: 10.1103/PhysRevLett.91.157406.

[10] H. S. White, G. P. Kittlesen, and M. S. Wrighton. "Chemical derivatization of an array of three gold microelectrodes with polypyrrole: fabrication of a molecule-based transistor". In: *Journal of the American Chemical Society* 106.18 (1984), pp. 5375–5377. DOI: 10.1021/ja00330a070.

[11] B. Siegmund, A. Mischok, J. Benduhn, O. Zeika, S. Ullbrich, F. Nehm, M. Böhm, D. Spoltore, H. Fröb, C. Körner, K. Leo, and K. Vandewal. "Hole-phonon coupling effect on the band dispersion of organic molecular semiconductors". In: *Nature Communications* 8.1 (2017). DOI: 10.1038/ncomms15421.

[12] S. Hunklinger. *Festkörperphysik*. München, Germany: Oldenbourg Verlag, 2007. ISBN: 978-3-486-57562-0.

[13] N. W. Ashcroft and N. Mermin. *Solid State Physics*. United States of America: Thomson Learning, 2003. ISBN: 0-03-083993-9.

[14] H. Hart, L. Crain, and D. Hart. *Organische Chemie*. Weinheim, Germany: Wiley-VCH Verlag, 2002. ISBN: 3-527-30379-0.

[15] J. N. Israelachvili. *Intermolecular and Surface Forces*. Academic Press, 2011. ISBN: 9780123919335.

[16] P. J. Skabara, J.-B. Arlin, and Y. H. Geerts. "Close Encounters of the 3D Kind – Exploiting High Dimensionality in Molecular Semiconductors". In: *Advanced Materials* 25.13 (2013), pp. 1948–1954. DOI: `10.1002/adma.201200862`.

[17] C. Wang, H. Dong, L. Jiang, and W. Hu. "Organic semiconductor crystals". In: *Chem. Soc. Rev.* 47 (2 2018), pp. 422–500. DOI: `10.1039/C7CS00490G`.

[18] G. R. Desiraju. "Cryptic crystallography". In: *Nature Materials* 1 (2002), pp. 1476–4660. DOI: `10.1038/nmat726`.

[19] T. R. Fielitz and R. J. Holmes. "Crystal Morphology and Growth in Annealed Rubrene Thin Films". In: *Crystal Growth & Design* 16.8 (2016), pp. 4720–4726. DOI: `10.1021/acs.cgd.6b00783`.

[20] M. Schwoerer and H. C. Wolf. *Organic Molecular Solids*. Weinheim, Germany: Wiley-VCH Verlag, 2007. ISBN: 978-3-527-40540-4.

[21] G. H. Gilmer and P. Bennema. "Simulation of Crystal Growth with Surface Diffusion". In: *Journal of Applied Physics* 43.4 (1972), pp. 1347–1360. DOI: `10.1063/1.1661325`.

[22] S. Liu, W. M. Wang, A. L. Briseno, S. C. B. Mannsfeld, and Z. Bao. "Controlled Deposition of Crystalline Organic Semiconductors for Field-Effect-Transistor Applications". In: *Advanced Materials* 21.12 (2009), pp. 1217–1232. DOI: `10.1002/adma.200802202`.

[23] Y. Li, H. Sun, Y. Shi, and K. Tsukagoshi. "Patterning technology for solution-processed organic crystal field-effect transistors". In: *Science and Technology of Advanced Materials* 15.2 (2014), p. 024203. DOI: `10.1088/1468-6996/15/2/024203`.

[24] Y. Diao, L. Shaw, Z. Bao, and S. C. B. Mannsfeld. "Morphology control strategies for solution-processed organic semiconductor thin films". In: *Energy Environ. Sci.* 7 (7 2014), pp. 2145–2159. DOI: `10.1039/C4EE00688G`.

[25] W. Demtröder. *Experimatalphysik 1: Mechanik und Wärme*. 4th ed. Berlin, Germany: Springer Verlag, 2005. ISBN: 3-540-26034-X.

[26] V. Lughi. "Surface Energy and Chemical Potential at Nanoscale". In: *Encyclopedia of Nanotechnology*. Ed. by B. Bhushan. Dordrecht: Springer Netherlands, 2012, pp. 2565–2573. ISBN: 978-90-481-9751-4. DOI: `10.1007/978-90-481-9751-4_276`.

[27] N. Koch. "Electronic Structure of Interfaces with Conjugated Organic Materials". In: *Physics of Organic Semiconductors*. Ed. by W. Brütting and C. Adachi. 2nd ed. Weinheim, Germany: Wiley-VCH Verlag, 2012. ISBN: 3527410538.

[28] C. Koch and T. J. Rinke. *Photolithography. Basics of Microstructuring*. Friedrichshafen, Germany: MicroChemicals, 2017. ISBN: 3981878213.

[29] S. Sinha, C.-H. Wang, A. K. M. Maidul Islam, Y.-W. Yang, and M. Mukherjee. "Growth and morphology of rubrene thin films on hydrophilic and hydrophobic substrates". In: *AIP Conference Proceedings* 1512.1 (2013), pp. 746–747. DOI: `10.1063/1.4791253`.

[30] "Zone Refining". In: *Van Nostrand's Scientific Encyclopedia*. John Wiley and Sons, Inc., 2006. ISBN: 9780471743989. DOI: `10.1002/0471743984.vse8557`.

[31] L. Yu, M. R. Niazi, G. O. Ngongang Ndjawa, R. Li, A. R. Kirmani, R. Munir, A. H. Balawi, F. Laquai, and A. Amassian. "Programmable and coherent crystallization of semiconductors". In: *Science Advances* 3.3 (2017). DOI: `10.1126/sciadv.1602462`.

[32] L. Gránásy, T. Pusztai, G. Tegze, J. A. Warren, and J. F. Douglas. "Growth and form of spherulites". In: *Phys. Rev. E* 72 (1 July 2005), p. 011605. DOI: `10.1103/PhysRevE.72.011605`.

[33] R. Kobayashi. "Modeling and numerical simulations of dendritic crystal growth". In: *Physica D: Nonlinear Phenomena* 63.3 (1993), pp. 410–423. ISSN: 0167-2789. DOI: `https://doi.org/10.1016/0167-2789(93)90120-P`.

[34] A. Fang and M. Haataja. "Simulation study of twisted crystal growth in organic thin films". In: *Phys. Rev. E* 92 (4 Oct. 2015), p. 042404. DOI: `10.1103/PhysRevE.92.042404`.

[35] S.-W. Park, J. M. Hwang, J.-M. Choi, D. K. Hwang, M. S. Oh, J. H. Kim, and S. Im. "Rubrene thin-film transistors with crystalline and amorphous channels". In: *Applied Physics Letters* 90.15 (2007), p. 153512. DOI: `10.1063/1.2723656`.

[36] M. A. Fusella, S. Yang, K. Abbasi, H. H. Choi, Z. Yao, V. Podzorov, A. Avishai, and B. P. Rand. "Use of an Underlayer for Large Area Crystallization of Rubrene Thin Films". In: *Chemistry of Materials* 29.16 (2017), pp. 6666–6673. DOI: `10.1021/acs.chemmater.7b01143`.

[37] O. D. Jurchescu, A. Meetsma, and T. T. M. Palstra. "Low-temperature structure of rubrene single crystals grown by vapor transport". In: *Acta Crystallographica Section B* 62.2 (Apr. 2006), pp. 330–334. DOI: `10.1107/S0108768106003053`.

[38] V. Podzorov, E. Menard, A. Borissov, V. Kiryukhin, J. A. Rogers, and M. E. Gershenson. "Intrinsic Charge Transport on the Surface of Organic Semiconductors". In: *Phys. Rev. Lett.* 93 (8 Aug. 2004), p. 086602. DOI: `10.1103/PhysRevLett.93.086602`.

[39] T. Hasegawa and J. Takeya. "Organic field-effect transistors using single crystals". In: *Science and Technology of Advanced Materials* 10.2 (2009), p. 024314. DOI: `10.1088/1468-6996/10/2/024314`.

[40] V. C. Sundar, J. Zaumseil, V. Podzorov, E. Menard, R. L. Willett, T. Someya, M. E. Gershenson, and J. A. Rogers. "Elastomeric Transistor Stamps: Reversible Probing of Charge Transport in Organic Crystals". In: *Science* 303.5664 (2004), pp. 1644–1646. ISSN: 0036-8075. DOI: `10.1126/science.1094196`.

[41] J. Takeya, M. Yamagishi, Y. Tominari, R. Hirahara, Y. Nakazawa, T. Nishikawa, T. Kawase, T. Shimoda, and S. Ogawa. "Very high-mobility organic single-crystal transistors with in-crystal conduction channels". In: *Applied Physics Letters* 90.10 (2007), p. 102120. DOI: `10.1063/1.2711393`.

[42] V. Podzorov, V. M. Pudalov, and M. E. Gershenson. "Field-effect transistors on rubrene single crystals with parylene gate insulator". In: *Applied Physics Letters* 82.11 (2003), pp. 1739–1741. DOI: `10.1063/1.1560869`.

[43] V. Podzorov, S. E. Sysoev, E. Loginova, V. M. Pudalov, and M. E. Gershenson. "Single-crystal organic field effect transistors with the hole mobility 8 cm2/Vs". In: *Applied Physics Letters* 83.17 (2003), pp. 3504–3506. DOI: `10.1063/1.1622799`.

[44] T. Matsukawa, Y. Takahashi, T. Tokiyama, K. Sasai, Y. Murai, N. Hirota, Y. Tominari, N. Mino, M. Yoshimura, M. Abe, J. Takeya, Y. Kitaoka, Y. Mori, S. Morita, and T. Sasaki. "Solution Growth of Rubrene Single Crystals Using Various Organic Solvents". In: *Japanese Journal of Applied Physics* 47.12 (Dec. 2008), pp. 8950–8954. DOI: `10.1143/jjap.47.8950`.

[45] L. Huang, Q. Liao, Q. Shi, H. Fu, J. Ma, and J. Yao. "Rubrene microcrystals from solution routes: their crystallography, morphology and optical properties". In: *J. Mater. Chem.* 20 (1 2010), pp. 159–166. DOI: `10.1039/B914334C`.

[46] N. Stingelin-Stutzmann, E. Smits, H. Wondergem, C. Tanase, P. Blom, P. Smith, and D. de Leeuw. "Organic thin-film electronics from vitreous solution-processed rubrene hypereutectics". In: *Nature Materials* 4 (2005), pp. 601–606. DOI: `10.1038/nmat1426`.

[47] H. M. Lee, J. J. Kim, J. H. Choi, and S. O. Cho. "In Situ Patterning of High-Quality Crystalline Rubrene Thin Films for High-Resolution Patterned Organic Field-Effect Transistors". In: *ACS Nano* 5.10 (2011). PMID: 21923165, pp. 8352–8356. DOI: `10.1021/nn203068q`.

[48] J. J. Kim, H. M. Lee, J. W. Park, and S. O. Cho. "Patterning of rubrene thin-film transistors based on electron irradiation of a polystyrene dielectric layer". In: *J. Mater. Chem. C* 3 (11 2015), pp. 2650–2655. DOI: `10.1039/C4TC02731K`.

[49] P. S. Jo, D. T. Duong, J. Park, R. Sinclair, and A. Salleo. "Control of Rubrene Polymorphs via Polymer Binders: Applications in Organic Field-Effect Transistors". In: *Chemistry of Materials* 27.11 (2015), pp. 3979–3987. DOI: `10.1021/acs.chemmater.5b00884`.

[50] B. Verreet, P. Heremans, A. Stesmans, and B. P. Rand. "Microcrystalline Organic Thin-Film Solar Cells". In: *Advanced Materials* 25.38 (2013), pp. 5504–5507. DOI: 10.1002/adma.201301643.

[51] M. A. Fusella, F. Schreiber, K. Abbasi, J. J. Kim, A. L. Briseno, and B. P. Rand. "Homoepitaxy of Crystalline Rubrene Thin Films". In: *Nano Letters* 17.5 (2017). PMID: 28394623, pp. 3040–3046. DOI: 10.1021/acs.nanolett.7b00380.

[52] O. V. Mikhnenko, P. W. M. Blom, and T.-Q. Nguyen. "Exciton diffusion in organic semiconductors". In: *Energy Environ. Sci.* 8 (7 2015), pp. 1867–1888. DOI: 10.1039/C5EE00925A.

[53] C. Sutton, M. S. Marshall, C. D. Sherrill, C. Risko, and J.-L. Brédas. "Rubrene: The Interplay between Intramolecular and Intermolecular Interactions Determines the Planarization of Its Tetracene Core in the Solid State". In: *Journal of the American Chemical Society* 137.27 (2015). PMID: 26075966, pp. 8775–8782. DOI: 10.1021/jacs.5b04066.

[54] B. Sapoval and C. Hermann. *Physics of Semiconductors*. New York, USA: Springer Verlag, 1995. ISBN: 978-0-387-94024-3.

[55] S. Sze and K. Ng. *Physics of Semiconductor Devices*. Hoboken, New Jersey, United States: John Wiley and Sons, 2007. ISBN: 978-0-471-14323-9.

[56] W. Brütting and C. Adachi, eds. *Physics of organic semiconductors*. 2nd ed. Weinheim, Germany: Wiley-VCH Verlag, 2012. ISBN: 3527410538.

[57] W. Demtröder. *Experimatalphysik 3: Atome, Moleküle und Festkörper*. 3rd ed. Berlin, Germany: Springer Verlag, 2005. ISBN: 3-540-21473-9.

[58] M. Sawatzki. "Vertical Organic Light Emitting Transistors". MSc thesis. Dresden, Germany: Technische Universität Dresden, 2015.

[59] H. Sirringhaus, T. Sakanoue, and J.-F. Chang. "Charge-transport physics of high-mobility molecular semiconductors". In: *physica status solidi (b)* 249.9 (2012), pp. 1655–1676. DOI: 10.1002/pssb.201248143.

[60] G. Schweicher, Y. Olivier, V. Lemaur, and Y. H. Geerts. "What Currently Limits Charge Carrier Mobility in Crystals of Molecular Semiconductors?" In: *Israel Journal of Chemistry* 54.5-6 (2014), pp. 595–620. DOI: 10.1002/ijch.201400047.

[61] J. E. Anthony, A. Facchetti, M. Heeney, S. R. Marder, and X. Zhan. "n-Type Organic Semiconductors in Organic Electronics". In: *Advanced Materials* 22.34 (2010), pp. 3876–3892. DOI: 10.1002/adma.200903628.

[62] A. A. Günther, J. Widmer, D. Kasemann, and K. Leo. "Hole mobility in thermally evaporated pentacene: Morphological and directional dependence". In: *Applied Physics Letters* 106.23 (2015), p. 233301. DOI: 10.1063/1.4922422.

[63] M. Klues and G. Witte. "Crystalline packing in pentacene-like organic semiconductors". In: *CrystEngComm* 20 (1 2018), pp. 63–74. DOI: 10.1039/C7CE01700F.

[64] T. J. Pundsack, N. O. Haugen, L. R. Johnstone, C. Daniel Frisbie, and R. L. Lidberg. "Temperature dependent c-axis hole mobilities in rubrene single crystals determined by time-of-flight". In: *Applied Physics Letters* 106.11 (2015), p. 113301. DOI: 10.1063/1.4914975.

[65] K. Seeger. *Halbleiterphysik - Eine Einführung*. 1st ed. Braunschweig, Wiesbaden, Germany: Vieweg, 1992. ISBN: 3-528-06506-0.

[66] A. Troisi. "Charge transport in high mobility molecular semiconductors: classical models and new theories". In: *Chem. Soc. Rev.* 40 (5 2011), pp. 2347–2358. DOI: 10.1039/C0CS00198H.

[67] P. Stallinga. *Electrical Characterization of organic electronic materials and devices*. Cornwal, Great Britain: John Wiley and Sohns Ltd, 2009. ISBN: 978-0-470-75009-4.

[68] T. Minari, T. Nemoto, and S. Isoda. "Temperature and electric-field dependence of the mobility of a single-grain pentacene field-effect transistor". In: *Journal of Applied Physics* 99.3 (2006), p. 034506. DOI: 10.1063/1.2169872.

[69] Z. Q. Ren, L. E. McNeil, S. Liu, and C. Kloc. "Molecular motion and mobility in an organic single crystal: Raman study and model". In: *Phys. Rev. B* 80 (24 Dec. 2009), p. 245211. DOI: 10.1103/PhysRevB.80.245211.

[70] S. Illig, A. S. Eggeman, A. Troisi, L. Jiang, C. Warwick, M. Nikolka, G. Schweicher, S. G. Yeates, Y. Henri Geerts, J. E. Anthony, and H. Sirringhaus. "Reducing dynamic disorder in small-molecule organic semiconductors by suppressing large-amplitude thermal motions". In: *Nature Communications* 7 (10736 Feb. 2016). DOI: 10.1038/ncomms10736.

[71] F. Bussolotti, J. Yang, T. Yamaguchi, K. Yonezawa, K. AU - Sato, M. Matsunami, K. Tanaka, Y. Nakayama, H. Ishii, N. Ueno, and S. Kera. "Hole-phonon coupling effect on the band dispersion of organic molecular semiconductors". In: *Nature Communications* 8.173 (2017). DOI: 0.1038/s41467-017-00241-z.

[72] A. S. Eggeman, S. Illig, A. Troisi, H. Sirringhaus, and P. A. Midgley. "Measurement of molecular motion in organic semiconductors by thermal diffuse electron scattering". In: *Nature Materials* 12 (2013), pp. 1045–1049. DOI: 10.1038/nmat3710.

[73] D. A. da Silva Filho, E.-G. Kim, and J.-L. Brédas. "Transport Properties in the Rubrene Crystal: Electronic Coupling and Vibrational Reorganization Energy". In: *Advanced Materials* 17.8 (2005), pp. 1072–1076. DOI: 10.1002/adma.200401866.

[74] M. A. Reyes-Martinez, A. J. Crosby, and A. L. Briseno. "Rubrene crystal field-effect mobility modulation via conducting channel wrinkling". In: *Nature Communications* 6 (6948 May 2015). DOI: `10.1038/ncomms7948`.

[75] T. Kubo, R. Häusermann, J. Tsurumi, J. Soeda, Y. Okada, Y. Yamashita, N. Akamatsu, A. Shishido, C. Mitsui, T. Okamoto, S. Yanagisawa, H. Matsui, and J. Takeya. "Suppressing molecular vibrations in organic semiconductors by inducing strain". In: *Nature Communications* 7 (Apr. 2016). DOI: `10.1038/ncomms11156`.

[76] M. Matta, M. J. Pereira, S. M. Gali, D. Thuau, Y. Olivier, A. Briseno, I. Dufour, C. Ayela, G. Wantz, and L. Muccioli. "Unusual electromechanical response in rubrene single crystals". In: *Mater. Horiz.* 5 (1 2018), pp. 41–50. DOI: `10.1039/C7MH00489C`.

[77] Y. Mei, P. J. Diemer, M. R. Niazi, R. K. Hallani, K. Jarolimek, C. S. Day, C. Risko, J. E. Anthony, A. Amassian, and O. D. Jurchescu. "Crossover from band-like to thermally activated charge transport in organic transistors due to strain-induced traps". In: *Proceedings of the National Academy of Sciences* 114.33 (2017), E6739–E6748. ISSN: 0027-8424. DOI: `10.1073/pnas.1705164114`.

[78] G.-J. Wetzelaer and P. Blom. "Diffusion-driven currents in organic semiconductor diodes". In: *Npg Asia Materials* 6.e110 (2014). DOI: `10.1038/am.2014.41`.

[79] K. Harada, A. G. Werner, M. Pfeiffer, C. J. Bloom, C. M. Elliott, and K. Leo. "Organic Homojunction Diodes with a High Built-in Potential: Interpretation of the Current-Voltage Characteristics by a Generalized Einstein Relation". In: *Phys. Rev. Lett.* 94 (3 Jan. 2005), p. 036601. DOI: `10.1103/PhysRevLett.94.036601`.

[80] O. V. Mikhnenko, F. Cordella, A. B. Sieval, J. C. Hummelen, P. W. M. Blom, and M. A. Loi. "Temperature Dependence of Exciton Diffusion in Conjugated Polymers". In: *The Journal of Physical Chemistry B* 112.37 (2008). PMID: 18729397, pp. 11601–11604. DOI: `10.1021/jp8042363`.

[81] C. Jacoboni, C. Canali, G. Ottaviani, and A. A. Quaranta. "A review of some charge transport properties of silicon". In: *Solid-State Electronics* 20.2 (1977), pp. 77–89. ISSN: 0038-1101. DOI: `https://doi.org/10.1016/0038-1101(77)90054-5`.

[82] H. Najafov, B. Lee, Q. Zhou, L. C. Feldman, and V. Podzorov. "Observation of long-range exciton diffusion in highly ordered organic semiconductors". In: *Nature Materials* 9 (938 2010). DOI: `10.1038/nmat2872`.

[83] B. Lüssem, M. Riede, and K. Leo. "Doping of Organic Semiconductors". In: *Physics of Organic Semiconductors*. Ed. by W. Brütting and C. Adachi. 2nd ed. Weinheim, Germany: Wiley-VCH Verlag, 2012. ISBN: 3527410538.

[84] I. E. Jacobs and A. J. Moulé. "Controlling Molecular Doping in Organic Semiconductors". In: *Advanced Materials* 29.42 (2017), p. 1703063. DOI: 10.1002/adma.201703063.

[85] M. L. Tietze, J. Benduhn, P. Pahner, B. Nell, M. Schwarze, H. Kleemann, M. Krammer, K. Zojer, K. Vandewal, and K. Leo. "Elementary steps in electrical doping of organic semiconductors". In: *Nature Communications* 9.1182 (2018). DOI: 10.1038/s41467-018-03302-z.

[86] Y. Xu, H. Sun, A. Liu, H.-H. Zhu, W. Li, Y.-F. Lin, and Y.-Y. Noh. "Doping: A Key Enabler for Organic Transistors". In: *Advanced Materials* 30.46 (2018), p. 1801830. DOI: 10.1002/adma.201801830.

[87] C. Gaul, S. Hutsch, M. Schwarze, K. S. Schellhammer, F. Bussolotti, S. Kera, G. Cuniberti, K. Leo, and F. Ortmann. "Insight into doping efficiency of organic semiconductors from the analysis of the density of states in n-doped C60 and ZnPc". In: *Nature Communications* 17.444 (2018). DOI: 10.1038/s41563-018-0030-8.

[88] G. Parthasarathy, C. Shen, A. Kahn, and S. R. Forrest. "Lithium doping of semiconducting organic charge transport materials". In: *Journal of Applied Physics* 89.9 (2001), pp. 4986–4992. DOI: 10.1063/1.1359161.

[89] P. Reiser, F. S. Benneckendorf, M.-M. Barf, L. Müller, R. Bäuerle, S. Hillebrandt, S. Beck, R. Lovrincic, E. Mankel, J. Freudenberg, D. Jänsch, W. Kowalsky, A. Pucci, W. Jaegermann, U. H. F. Bunz, and K. Müllen. "n-Type Doping of Organic Semiconductors: Immobilization via Covalent Anchoring". In: *Chemistry of Materials* 31.11 (2019), pp. 4213–4221. DOI: 10.1021/acs.chemmater.9b01150.

[90] R. Fujimoto, Y. Yamashita, S. Kumagai, J. Tsurumi, A. Hinderhofer, K. Broch, F. Schreiber, S. Watanabe, and J. Takeya. "Molecular doping in organic semiconductors: fully solution-processed, vacuum-free doping with metal–organic complexes in an orthogonal solvent". In: *J. Mater. Chem. C* 5 (46 2017), pp. 12023–12030. DOI: 10.1039/C7TC03905K.

[91] J. J. Kim, S. Bachevillier, D. L. G. Arellano, B. P. Cherniawski, E. K. Burnett, N. Stingelin, C. Ayela, Ö. Usluer, S. C. B. Mannsfeld, G. Wantz, and A. L. Briseno. "Correlating Crystal Thickness, Surface Morphology, and Charge Transport in Pristine and Doped Rubrene Single Crystals". In: *ACS Applied Materials and Interfaces* 10.31 (Aug. 2018). DOI: 10.1021/acsami.8b04451.

[92] C. Ohashi, S. Izawa, Y. Shinmura, M. Kikuchi, S. Watase, M. Izaki, H. Naito, and M. Hiramoto. "Hall Effect in Bulk-Doped Organic Single Crystals". In: *Advanced Materials* 29.23 (2017), p. 1605619. DOI: 10.1002/adma.201605619.

[93] Z. Zhi-lin, J. Xue-yin, X. Shao-hong, T. Nagatomo, and O. Omoto. "The effect of rubrene as a dopant on the efficiency and stability of organic thin film electroluminescent devices". In: *Journal of Physics D: Applied Physics* 31.1 (Jan. 1998), pp. 32–35. DOI: 10.1088/0022-3727/31/1/005.

[94] M. S. Choi and H.-N. Lee. "Hall Effect in Bulk-Doped Organic Single Crystals". In: *International Journal of Photoenergy* 2014.361861 (2013). DOI: `10.1155/2014/361861`.

[95] N. B. Kotadiya, H. Lu, A. Mondal, Y. Ie, D. Andrienko, P. W. M. Blom, and G.-J. A. H. Wetzelaer. "Universal strategy for Ohmic hole injection into organic semiconductors with high ionization energies". In: *Nature Materials* 17.329 (2018). DOI: `10.1038/s41563-018-0022-8`.

[96] H. Kleemann, B. Lüssem, and K. Leo. "Controlled formation of charge depletion zones by molecular doping in organic pin-diodes and its description by the Mott-Schottky relation". In: *Journal of Applied Physics* 111.12 (2012), p. 123722. DOI: `10.1063/1.4730771`.

[97] H. Kleemann, R. Gutierrez, F. Lindner, S. Avdoshenko, P. D. Manrique, B. Lüssem, G. Cuniberti, and K. Leo. "Organic Zener Diodes: Tunneling across the Gap in Organic Semiconductor Materials". In: *Nano Letters* 10.12 (2010). PMID: 21033756, pp. 4929–4934. DOI: `10.1021/nl102916n`.

[98] J. Fischer, W. Tress, H. Kleemann, J. Widmer, K. Leo, and M. Riede. "Exploiting diffusion currents at Ohmic contacts for trap characterization in organic semiconductors". In: *Organic Electronics* 15.10 (2014), pp. 2428–2432. ISSN: 1566-1199. DOI: `https://doi.org/10.1016/j.orgel.2014.06.029`.

[99] P. Pahner, H. Kleemann, L. Burtone, M. L. Tietze, J. Fischer, K. Leo, and B. Lüssem. "Pentacene Schottky diodes studied by impedance spectroscopy: Doping properties and trap response". In: *Phys. Rev. B* 88 (19 Nov. 2013), p. 195205. DOI: `10.1103/PhysRevB.88.195205`.

[100] V. I. Arkhipov, H. von Seggern, and E. V. Emelianova. "Charge injection versus space-charge-limited current in organic light-emitting diodes". In: *Applied Physics Letters* 83.24 (2003), pp. 5074–5076. DOI: `10.1063/1.1633967`.

[101] A. Ioannidis, E. Forsythe, Y. Gao, M. W. Wu, and E. M. Conwell. "Current–voltage characteristic of organic light emitting diodes". In: *Applied Physics Letters* 72.23 (1998), pp. 3038–3040. DOI: `10.1063/1.121533`.

[102] P. López Varo, J. Jiménez Tejada, J. López Villanueva, and M. Deen. "Effect of doping in the current voltage characteristics of organic diodes". In: *2015 10th Spanish Conference on Electron Devices (CDE)*. 2015, pp. 1–4. DOI: `10.1109/CDE.2015.7087510`.

[103] P. L. Varo, J. J. Tejada, J. L. Villanueva, J. Carceller, and M. Deen. "Modeling the transition from ohmic to space charge limited current in organic semiconductors". In: *Organic Electronics* 13.9 (2012), pp. 1700–1709. ISSN: 1566-1199. DOI: `https://doi.org/10.1016/j.orgel.2012.05.025`.

[104] S. C. Jain, W. Geens, A. Mehra, V. Kumar, T. Aernouts, J. Poortmans, R. Mertens, and M. Willander. "Injection- and space charge limited-currents in doped conducting organic materials". In: *Journal of Applied Physics* 89.7 (2001), pp. 3804–3810. DOI: 10.1063/1.1352677.

[105] C. Hyun Kim, O. Yaghmazadeh, Y. Bonnassieux, and G. Horowitz. "Modeling the low-voltage regime of organic diodes: Origin of the ideality factor". In: *Journal of Applied Physics* 110.9 (2011), p. 093722. DOI: 10.1063/1.3660221.

[106] G. A. H. Wetzelaer and P. W. M. Blom. "Ohmic current in organic metal-insulator-metal diodes revisited". In: *Phys. Rev. B* 89 (24 June 2014), p. 241201. DOI: 10.1103/PhysRevB.89.241201.

[107] C. Sah, R. N. Noyce, and W. Shockley. "Carrier Generation and Recombination in P-N Junctions and P-N Junction Characteristics". In: *Proceedings of the IRE* 45.9 (Sept. 1957), pp. 1228–1243. DOI: 10.1109/JRPROC.1957.278528.

[108] N. Mott and R. Gurney. *Electronic processes in ionic crystals*. Oxford, United Kingdom: Oxford Clarenodn press, 1948.

[109] R. Agrawal, P. Kumar, S. Ghosh, and A. K. Mahapatro. "Thickness dependence of space charge limited current and injection limited current in organic molecular semiconductors". In: *Applied Physics Letters* 93.7 (2008), p. 073311. DOI: 10.1063/1.2974084.

[110] G. A. H. Wetzelaer. "Analytical description of the current-voltage relationship in organic-semiconductor diodes". In: *AIP Advances* 8.3 (2018), p. 035320. DOI: 10.1063/1.5021989.

[111] J. Widmer, J. Fischer, W. Tress, K. Leo, and M. Riede. "Electric potential mapping by thickness variation: A new method for model-free mobility determination in organic semiconductor thin films". In: *Organic Electronics* 14.12 (2013), pp. 3460–3471. ISSN: 1566-1199. DOI: https://doi.org/10.1016/j.orgel.2013.09.021.

[112] O. A. Abdulrazzaq, V. Saini, S. Bourdo, E. Dervishi, and A. S. Biris. "Organic Solar Cells: A Review of Materials, Limitations, and Possibilities for Improvement". In: *Particulate Science and Technology* 31.5 (2013), pp. 427–442. DOI: 10.1080/02726351.2013.769470.

[113] A. Khalil, Z. Ahmed, F. Touati, and M. Masmoudi. "Review on organic solar cells". In: *2016 13th International Multi-Conference on Systems, Signals Devices (SSD)*. Mar. 2016, pp. 342–353. DOI: 10.1109/SSD.2016.7473760.

[114] L. Lu, T. Zheng, Q. Wu, A. M. Schneider, D. Zhao, and L. Yu. "Recent Advances in Bulk Heterojunction Polymer Solar Cells". In: *Chemical Reviews* 115.23 (2015). PMID: 26252903, pp. 12666–12731. DOI: 10.1021/acs.chemrev.5b00098.

[115] W. Brütting, J. Frischeisen, T. D. Schmidt, B. J. Scholz, and C. Mayr. "Device efficiency of organic light-emitting diodes: Progress by improved light outcoupling". In: *physica status solidi (a)* 210.1 (2013), pp. 44–65. DOI: `10.1002/pssa.201228320`.

[116] A. Salehi, X. Fu, D.-H. Shin, and F. So. "Recent Advances in OLED Optical Design". In: *Advanced Functional Materials* 29.15 (2019), p. 1808803. DOI: `10.1002/adfm.201808803`.

[117] S. Reineke, M. Thomschke, B. Lüssem, and K. Leo. "White organic light-emitting diodes: Status and perspective". In: *Rev. Mod. Phys.* 85 (3 July 2013), pp. 1245–1293. DOI: `10.1103/RevModPhys.85.1245`.

[118] H.-W. Chen, J.-H. Lee, B.-Y. Lin, S. Chen, and S.-T. Wu. "Liquid crystal display and organic light-emitting diode display: present status and future perspectives". In: *Light: Science & Applications* 7.17168 (2018). DOI: `10.1038/lsa.2017.168`.

[119] M. Elsobky, Y. Mahsereci, Z. Yu, H. Richter, J. N. Burghartz, J. Keck, H. Klauk, and U. Zschieschang. "Ultra-thin smart electronic skin based on hybrid system-in-foil concept combining three flexible electronics technologies". In: *Electronics Letters* 54.6 (2018), pp. 338–340. ISSN: 0013-5194. DOI: `10.1049/el.2017.4682`.

[120] T. Sekitani and T. Someya. "Human-friendly organic integrated circuits". In: *Materials Today* 14.9 (2011), pp. 398–407. ISSN: 1369-7021. DOI: `https://doi.org/10.1016/S1369-7021(11)70184-5`.

[121] M. Elsobky, M. Elattar, G. Alavi, F. Letzkus, H. Richter, U. Zschieschang, M. Strecker, H. Klauk, and J. N. Burghartz. "A digital library for a flexible low-voltage organic thin-film transistor technology". In: *Organic Electronics* 50 (2017), pp. 491–498. ISSN: 1566-1199. DOI: `https://doi.org/10.1016/j.orgel.2017.08.028`.

[122] W. Xiong, Y. Guo, U. Zschieschang, H. Klauk, and B. Murmann. "A 3-V, 6-Bit C-2C Digital-to-Analog Converter Using Complementary Organic Thin-Film Transistors on Glass". In: *IEEE Journal of Solid-State Circuits* 45.7 (July 2010), pp. 1380–1388. ISSN: 0018-9200. DOI: `10.1109/JSSC.2010.2048083`.

[123] B. Kheradmand-Boroujeni, M. P. Klinger, A. Fischer, H. Kleemann, K. Leo, and F. Ellinger. "A Pulse-Biasing Small-Signal Measurement Technique Enabling 40MHz Operation of Vertical Organic Transistors". In: *Scientific Reports* 8.7643 (2018). DOI: `10.1038/s41598-018-26008-0`.

[124] H. Kleemann, S. Schumann, U. Jörges, F. Ellinger, K. Leo, and B. Lüssem. "Organic pin-diodes approaching ultra-high-frequencies". In: *Organic Electronics* 13.6 (2012), pp. 1114–1120. ISSN: 1566-1199. DOI: `https://doi.org/10.1016/j.orgel.2012.03.011`.

[125] N. Sani, M. Robertsson, P. Cooper, X. Wang, M. Svensson, P. Andersson Ersman, P. Norberg, M. Nilsson, D. Nilsson, X. Liu, H. Hesselbom, L. Akesso, M. Fahlman, X. Crispin, I. Engquist, M. Berggren, and G. Gustafsson. "All-printed diode operating at 1.6 GHz". In: *Proceedings of the National Academy of Sciences* 111.33 (2014), pp. 11943–11948. ISSN: 0027-8424. DOI: `10.1073/pnas.1401676111`.

[126] K. Jung and S. Lee. "A systematic review of RFID applications and diffusion: key areas and public policy issues". In: *Journal of Open Innovation: Technology, Market, and Complexity* 1.1 (Sept. 2015), p. 9. ISSN: 2199-8531. DOI: `10.1186/s40852-015-0010-z`.

[127] J. Lou, G. Andrechak, M. Riben, and W. Yong. "A review of radio frequency identification technology for the anatomic pathology or biorepository laboratory: Much promise, some progress, and more work needed". In: *Journal of Pathology Informatics* 2.1 (2011), p. 34. DOI: `10.4103/2153-3539.83738`.

[128] H. Kleemann. "Organic Electronic Devices - Fundamentals, Applications, and Novel Concepts". PhD thesis. Institut for Applied Photophysics, 2012.

[129] S. Steudel, K. Myny, V. Arkhipov, C. Deibel, S. De Vusser, J. Genoe, and P. Heremans. "50 MHz rectifier based on an organic diode". In: *Nature Materials* 4 (2005), pp. 1476–4660. DOI: `10.1038/nmat1434`.

[130] C. Kang, H. Shin, and C. Lee. "High-frequency organic rectifiers through interface engineering". In: *MRS Communications* 7.4 (2017), pp. 755–769. DOI: `10.1557/mrc.2017.100`.

[131] C.-m. Kang, J. Wade, S. Yun, J. Lim, H. Cho, J. Roh, H. Lee, S. Nam, D. D. C. Bradley, J.-S. Kim, and C. Lee. "1 GHz Pentacene Diode Rectifiers Enabled by Controlled Film Deposition on SAM-Treated Au Anodes". In: *Advanced Electronic Materials* 2.2 (2016), p. 1500282. DOI: `10.1002/aelm.201500282`.

[132] T. M. Kraft, P. R. Berger, and D. Lupo. "Printed and organic diodes: devices, circuits and applications". In: *Flexible and Printed Electronics* 2.3 (Sept. 2017), p. 033001. DOI: `10.1088/2058-8585/aa8ac3`.

[133] J. Zhang, H. Wang, J. Wilson, X. Ma, J. Jin, and A. Song. "Room Temperature Processed Ultrahigh-Frequency Indium-Gallium–Zinc-Oxide Schottky Diode". In: *IEEE Electron Device Letters* 37.4 (Apr. 2016), pp. 389–392. ISSN: 0741-3106. DOI: `10.1109/LED.2016.2535904`.

[134] S. G. Higgins, T. Agostinelli, S. Markham, R. Whiteman, and H. Sirringhaus. "Organic Diode Rectifiers Based on a High-Performance Conjugated Polymer for a Near-Field Energy-Harvesting Circuit". In: *Advanced Materials* 29.46 (2017), p. 1703782. DOI: `10.1002/adma.201703782`.

[135] H. Gleskova and S. Wagner. "Electron mobility in amorphous silicon thin-film transistors under compressive strain". In: *Applied Physics Letters* 79.20 (2001), pp. 3347–3349. DOI: 10.1063/1.1418254.

[136] D. Joshi and R. Srivastava. "Mobility and carrier concentration in polycrystalline silicon". In: *Solar Cells* 12.3 (1984), pp. 337–344. ISSN: 0379-6787. DOI: https://doi.org/10.1016/0379-6787(84)90112-1.

[137] S. J. Konezny, M. N. Bussac, and L. Zuppiroli. "Hopping and trapping mechanisms in organic field-effect transistors". In: *Phys. Rev. B* 81 (4 Jan. 2010), p. 045313. DOI: 10.1103/PhysRevB.81.045313.

[138] H. Klauk. "Organic thin-film transistors". In: *Chem. Soc. Rev.* 39 (7 2010), pp. 2643–2666. DOI: 10.1039/B909902F.

[139] H. Sirringhaus. "25th Anniversary Article: Organic Field-Effect Transistors: The Path Beyond Amorphous Silicon". In: *Advanced Materials* 26.9 (2014), pp. 1319–1335. DOI: 10.1002/adma.201304346.

[140] W. Tang, Y. Huang, L. Han, R. Liu, Y. Su, X. Guo, and F. Yan. "Recent progress in printable organic field effect transistors". In: *J. Mater. Chem. C* 7 (4 2019), pp. 790–808. DOI: 10.1039/C8TC05485A.

[141] B. Lüssem, M. L. Tietze, H. Kleemann, C. Hoßbach, J. W. Bartha, A. Zakhidov, and K. Leo. "Doped organic transistors operating in the inversion and depletion regime". In: *Nature Communications* 4.2775 (2013). DOI: 10.1038/ncomms3775.

[142] A. A. Günther, C. Hossbach, M. Sawatzki, D. Kasemann, J. W. Bartha, and K. Leo. "Controlling threshold voltage and leakage currents in vertical organic field-effect transistors by inversion mode operation". In: *Applied Physics Letters* 107.23 (2015), p. 233302. DOI: 10.1063/1.4937439.

[143] G. Horowitz, R. Hajlaoui, H. Bouchriha, R. Bourguiga, and M. Hajlaoui. "The Concept of "Threshold Voltage" in Organic Field-Effect Transistors". In: *Advanced Materials* 10.12 (1998), pp. 923–927. DOI: 10.1002/(SICI)1521-4095(199808)10:12<923::AID-ADMA923>3.0.CO;2-W.

[144] J. F. Martínez Hardigree and H. E. Katz. "Through Thick and Thin: Tuning the Threshold Voltage in Organic Field-Effect Transistors". In: *Accounts of Chemical Research* 47.4 (2014). PMID: 24684566, pp. 1369–1377. DOI: 10.1021/ar5000049.

[145] F. Ante, D. Kälblein, T. Zaki, U. Zschieschang, K. Takimiya, M. Ikeda, T. Sekitani, T. Someya, J. N. Burghartz, K. Kern, and H. Klauk. "Contact Resistance and Megahertz Operation of Aggressively Scaled Organic Transistors". In: *Small* 8.1 (2012), pp. 73–79. DOI: 10.1002/smll.201101677.

[146] M. Halik, H. Klauk, U. Zschieschang, G. Schmid, C. Dehm, M. Schütz, S. Maisch, F. Effenberger, M. Brunnbauer, and F. Stellacci. "Low-voltage organic transistors with an amorphous molecular gate dielectric". In: *Nature* 431.7011 (2004). DOI: `10.1038/nature02987`.

[147] R. P. Ortiz, A. Facchetti, and T. J. Marks. "High-k Organic, Inorganic, and Hybrid Dielectrics for Low-Voltage Organic Field-Effect Transistors". In: *Chemical Reviews* 110.1 (2010). PMID: 19852443, pp. 205–239. DOI: `10.1021/cr9001275`.

[148] F. M. Sawatzki. "Charakterisierung von Polymeren zur Eignung als Gate-Dielektrikum in organischen Feldeffekttransistoren". BSc thesis. Dresden, Germany: Technische Universität Dresden, 2013.

[149] Y. Wang, X. Huang, T. Li, L. Li, X. Guo, and P. Jiang. "Polymer-Based Gate Dielectrics for Organic Field-Effect Transistors". In: *Chemistry of Materials* 31.7 (2019), pp. 2212–2240. DOI: `10.1021/acs.chemmater.8b03904`.

[150] H. H. Choi, Y. I. Rodionov, A. F. Paterson, J. Panidi, D. Saranin, N. Kharlamov, S. I. Didenko, T. D. Anthopoulos, K. Cho, and V. Podzorov. "Accurate Extraction of Charge Carrier Mobility in 4-Probe Field-Effect Transistors". In: *Advanced Functional Materials* 28.26 (2018), p. 1707105. DOI: `10.1002/adfm.201707105`.

[151] F. Yang, L. Sun, J. Han, B. Li, X. Yu, X. Zhang, X. Ren, and W. Hu. "Low-Voltage Organic Single-Crystal Field-Effect Transistor with Steep Subthreshold Slope". In: *ACS Applied Materials & Interfaces* 10.31 (2018). PMID: 29508994, pp. 25871–25877. DOI: `10.1021/acsami.7b16658`.

[152] B. Blülle, R. Häusermann, and B. Batlogg. "Approaching the Trap-Free Limit in Organic Single-Crystal Field-Effect Transistors". In: *Phys. Rev. Applied* 1 (3 Apr. 2014), p. 034006. DOI: `10.1103/PhysRevApplied.1.034006`.

[153] H. Klauk. "Will We See Gigahertz Organic Transistors?" In: *Advanced Electronic Materials* 4.10 (2018), p. 1700474. DOI: `10.1002/aelm.201700474`.

[154] K. Zojer, E. Zojer, A. F. Fernandez, and M. Gruber. "Impact of the Capacitance of the Dielectric on the Contact Resistance of Organic Thin-Film Transistors". In: *Phys. Rev. Applied* 4 (4 Oct. 2015), p. 044002. DOI: `10.1103/PhysRevApplied.4.044002`.

[155] C. Liu, Y. Xu, and Y.-Y. Noh. "Contact engineering in organic field-effect transistors". In: *Materials Today* 18.2 (2015), pp. 79–96. ISSN: 1369-7021. DOI: `https://doi.org/10.1016/j.mattod.2014.08.037`.

[156] J.-L. Hou, D. Kasemann, J. Widmer, A. A. Günther, B. Lüssem, and K. Leo. "Reduced contact resistance in top-contact organic field-effect transistors by interface contact doping". In: *Applied Physics Letters* 108.10 (2016), p. 103303. DOI: `10.1063/1.4943646`.

[157] Y. Xu, R. Gwoziecki, I. Chartier, R. Coppard, F. Balestra, and G. Ghibaudo. "Modified transmission-line method for contact resistance extraction in organic field-effect transistors". In: *Applied Physics Letters* 97.6 (2010), p. 063302. DOI: 10.1063/1.3479476.

[158] K.-D. Jung, B.-J. Kim, Y. C. Kim, B.-G. Park, H. Ehin, and J. D. Lee. "A novel gated transmission line method for organic thin film transistors". In: *2007 International Semiconductor Device Research Symposium*. Dec. 2007, pp. 1–2. DOI: 10.1109/ISDRS.2007.4422501.

[159] S. Locci, M. Morana, E. Orgiu, A. Bonfiglio, and P. Lugli. "Modeling of Short-Channel Effects in Organic Thin-Film Transistors". In: *IEEE Transactions on Electron Devices* 55.10 (Oct. 2008), pp. 2561–2567. ISSN: 0018-9383. DOI: 10.1109/TED.2008.2003022.

[160] H. Kleemann, A. Zakhidov, M. Anderson, T. Menke, K. Leo, and B. Lüssem. "Direct structuring of C60 thin film transistors by photo-lithography under ambient conditions". In: *Organic Electronics* 13.3 (2012), pp. 506–513. ISSN: 1566-1199. DOI: https://doi.org/10.1016/j.orgel.2011.12.009.

[161] L. Ma and Y. Yang. "Unique architecture and concept for high-performance organic transistors". In: *Applied Physics Letters* 85.21 (2004), pp. 5084–5086. DOI: 10.1063/1.1821629.

[162] A. J. Ben-Sasson and N. Tessler. "Patterned electrode vertical field effect transistor: Theory and experiment". In: *Journal of Applied Physics* 110.4 (2011), p. 044501. DOI: 10.1063/1.3622291.

[163] N. Stutzmann, R. H. Friend, and H. Sirringhaus. "Self-Aligned, Vertical-Channel, Polymer Field-Effect Transistors". In: *Science* 299.5614 (2003), pp. 1881–1884. ISSN: 0036-8075. DOI: 10.1126/science.1081279.

[164] K. Kudo, T. Takano, H. Yamauchi, M. Iizuka, and M. Nakamura. "High-Speed Operation of Step-Edge Vertical-Channel Organic Transistors with Pentacene and 6,13-Bis(triisopropyl-silylethynyl) Pentacene". In: *Japanese Journal of Applied Physics* 49.4 (Apr. 2010), 04DK03. DOI: 10.1143/jjap.49.04dk03.

[165] M. Uno, K. Nakayama, J. Soeda, Y. Hirose, K. Miwa, T. Uemura, A. Nakao, K. Takimiya, and J. Takeya. "High-Speed Flexible Organic Field-Effect Transistors with a 3D Structure". In: *Advanced Materials* 23.27 (2011), pp. 3047–3051. DOI: 10.1002/adma.201101179.

[166] R. Parashkov, E. Becker, S. Hartmann, G. Ginev, D. Schneider, H. Krautwald, T. Dobbertin, D. Metzdorf, F. Brunetti, C. Schildknecht, A. Kammoun, M. Brandes, T. Riedl, H.-H. Johannes, and W. Kowalsky. "Vertical channel all-organic thin-film transistors". In: *Applied Physics Letters* 82.25 (2003), pp. 4579–4580. DOI: 10.1063/1.1584786.

[167] K. Nakamura, T. Hata, A. Yoshizawa, K. Obata, H. Endo, and K. Kudo. "Metal-insulator-semiconductor-type organic light-emitting transistor on plastic substrate". In: *Applied Physics Letters* 89.10 (2006), p. 103525. DOI: `10.1063/1.2347152`.

[168] H. Kleemann, A. A. Günther, K. Leo, and B. Lüssem. "High-Performance Vertical Organic Transistors". In: *Small* 9.21 (2013), pp. 3670–3677. DOI: `10.1002/smll.201202321`.

[169] A. A. Günther, M. Sawatzki, P. Formánek, D. Kasemann, and K. Leo. "Contact Doping for Vertical Organic Field-Effect Transistors". In: *Advanced Functional Materials* 26.5 (2016), pp. 768–775. DOI: `10.1002/adfm.201504377`.

[170] F. M. Sawatzki, D. H. Doan, H. Kleemann, M. Liero, A. Glitzky, T. Koprucki, and K. Leo. "Balance of Horizontal and Vertical Charge Transport in Organic Field-Effect Transistors". In: *Phys. Rev. Applied* 10 (3 Sept. 2018), p. 034069. DOI: `10.1103/PhysRevApplied.10.034069`.

[171] G. Lee, I.-H. Lee, H.-L. Park, S.-H. Lee, J. Han, C. Lee, C.-M. Keum, and S.-D. Lee. "Vertical organic light-emitting transistor showing a high current on/off ratio through dielectric encapsulation for the effective charge pathway". In: *Journal of Applied Physics* 121.2 (2017), p. 024502. DOI: `10.1063/1.4974008`.

[172] F. M. Sawatzki, A. A. Hauke, D. H. Doan, P. Formanek, D. Kasemann, T. Koprucki, and K. Leo. "On Razors Edge: Influence of the Source Insulator Edge on the Charge Transport of Vertical Organic Field Effect Transistors". In: *MRS Advances* 2.23 (2017), pp. 1249–1257. DOI: `10.1557/adv.2017.29`.

[173] S. Fujimoto, K. Nakayama, and M. Yokoyama. "Fabrication of a vertical-type organic transistor with a planar metal base". In: *Applied Physics Letters* 87.13 (2005), p. 133503. DOI: `10.1063/1.2061866`.

[174] A. Fischer, R. Scholz, K. Leo, and B. Lüssem. "An all C60 vertical transistor for high frequency and high current density applications". In: *Applied Physics Letters* 101.21 (2012), p. 213303. DOI: `10.1063/1.4767391`.

[175] M. P. Klinger, A. Fischer, F. Kaschura, R. Scholz, B. Lüssem, B. Kheradmand-Boroujeni, F. Ellinger, D. Kasemann, and K. Leo. "Advanced Organic Permeable-Base Transistor with Superior Performance". In: *Advanced Materials* 27.47 (2015), pp. 7734–7739. DOI: `10.1002/adma.201502788`.

[176] S. Forrest. US 2005/0275056A1. P. University. abandoned. Dec. 2005.

[177] A. L. Blackler, R. Gomez, V. Popovic, and M. H. Thompson. "Life Is Too Short to RTFM: How Users Relate to Documentation and Excess Features in Consumer Products". In: *Interacting with Computers* 28.1 (July 2014), pp. 27–46. ISSN: 0953-5438. DOI: `10.1093/iwc/iwu023`.

[178] C. Vericat, M. E. Vela, G. Corthey, E. Pensa, E. Cortés, M. H. Fonticelli, F. Ibañez, G. E. Benitez, P. Carro, and R. C. Salvarezza. "Self-assembled monolayers of thiolates on metals: a review article on sulfur-metal chemistry and surface structures". In: *RSC Adv.* 4 (53 2014), pp. 27730–27754. DOI: 10.1039/C4RA04659E.

[179] E. V. Shun'ko and V. S. Belkin. "Cleaning properties of atomic oxygen excited to metastable state 2s22p4(S10)". In: *Journal of Applied Physics* 102.8 (2007), p. 083304. DOI: 10.1063/1.2794857.

[180] M. Höppner, D. Kneppe, H. Kleemann, and K. Leo. "Precise patterning of organic semiconductors by reactive ion etching". In: *Organic Electronics* (2019). ISSN: 1566-1199. DOI: https://doi.org/10.1016/j.orgel.2019.07.015.

[181] A. Fischer, P. Pahner, B. Lüssem, K. Leo, R. Scholz, T. Koprucki, J. Fuhrmann, K. Gärtner, and A. Glitzky. "Self-heating effects in organic semiconductor crossbar structures with small active area". In: *Organic Electronics* 13.11 (2012), pp. 2461–2468. ISSN: 1566-1199. DOI: https://doi.org/10.1016/j.orgel.2012.06.046.

[182] A. Fischer, P. Pahner, B. Lüssem, K. Leo, R. Scholz, T. Koprucki, K. Gärtner, and A. Glitzky. "Self-Heating, Bistability, and Thermal Switching in Organic Semiconductors". In: *Phys. Rev. Lett.* 110 (12 Mar. 2013), p. 126601. DOI: 10.1103/PhysRevLett.110.126601.

[183] Z. Pan, N. Rawat, I. Cour, L. Manning, R. L. Headrick, and M. Furis. "Polarization-resolved spectroscopy imaging of grain boundaries and optical excitations in crystalline organic thin films". In: *Nature Communications* 6.8201 (2015). DOI: 10.1038/ncomms9201.

[184] M. Birkholz. *Thin Film Analysis by X-Ray Scattering. Techniques for Structural Characterization*. Weinheim, Germany: Wiley-VCH, 2005. ISBN: 3527310525.

[185] *Osilla company*. https://www.ossila.com/products/rubrene. Accessed: 2019-09-30.

[186] *Sigma Aaldrich company*. https://www.sigmaaldrich.com/catalog/product/aldrich/551112?lang=de&region=DE. Accessed: 2019-09-30.

[187] F. Anger, T. Breuer, A. Ruff, M. Klues, A. Gerlach, R. Scholz, S. Ludwigs, G. Witte, and F. Schreiber. "Enhanced Stability of Rubrene against Oxidation by Partial and Complete Fluorination". In: *The Journal of Physical Chemistry C* 120.10 (2016), pp. 5515–5522. DOI: 10.1021/acs.jpcc.5b12293.

[188] *Osilla company*. https://www.ossila.com/products/tapc. Accessed: 2019-09-30.

[189] *Sigma Aaldrich company*. https://www.sigmaaldrich.com/catalog/product/aldrich/757284?lang=en&region=US. Accessed: 2019-09-30.

[190] X. Wang, L. Liu, S. Zhu, and L. Li. "Preparation of organic fluorescent nanocomposites and their application in DNA detection". In: *Colloids and Surfaces A: Physicochemical and Engineering Aspects* 520 (2017), pp. 72–77. ISSN: 0927-7757. DOI: https://doi.org/10.1016/j.colsurfa.2017.01.072.

[191] Y. Zheng, C. Wang, F. Yang, J. Zhang, J. Chen, X. Li, and J. Zhang. "Comparative investigation of molecular orientation and charge collection in highly efficient mixed heterojunctions based on three planar-shaped donors and C70". In: *Journal of Physics D: Applied Physics* 49.46 (Oct. 2016), p. 465106. DOI: 10.1088/0022-3727/49/46/465106.

[192] H. Kageyama, H. Ohishi, M. Tanaka, Y. Ohmori, and Y. Shirota. "High-Performance Organic Photovoltaic Devices Using a New Amorphous Molecular Material with High Hole Drift Mobility, Tris[4-(5-phenylthiophen-2-yl)phenyl]amine". In: *Advanced Functional Materials* 19.24 (2009), pp. 3948–3955. DOI: 10.1002/adfm.200901259.

[193] R. A. Belisle, P. Jain, R. Prasanna, T. Leijtens, and M. D. McGehee. "Minimal Effect of the Hole-Transport Material Ionization Potential on the Open-Circuit Voltage of Perovskite Solar Cells". In: *ACS Energy Letters* 1.3 (2016), pp. 556–560. DOI: 10.1021/acsenergylett.6b00270.

[194] T. Reichert and T. P. I. Saragi. "Ultrasmall magnetic field-effect and sign reversal in transistors based on donor/acceptor systems". In: *Beilstein Journal of Nanotechnology* 8 (2017), pp. 1104–1114. ISSN: 2190-4286. DOI: 10.3762/bjnano.8.112.

[195] Y. Karpov, T. Erdmann, M. Stamm, U. Lappan, O. Guskova, M. Malanin, I. Raguzin, T. Beryozkina, V. Bakulev, F. Günther, S. Gemming, G. Seifert, M. Hambsch, S. Mannsfeld, B. Voit, and A. Kiriy. "Molecular Doping of a High Mobility Diketopyrrolo-pyrrole–Dithienylthieno[3,2-b]thiophene Donor–Acceptor Copolymer with F6TCNNQ". In: *Macromolecules* 50.3 (2017), pp. 914–926. DOI: 10.1021/acs.macromol.6b02452.

[196] *Sigma Aaldrich company*. https://www.sigmaaldrich.com/catalog/product/aldrich/379646?lang=de&region=DE. Accessed: 2019-09-30.

[197] F. A. Cotton, N. E. Gruhn, J. Gu, P. Huang, D. L. Lichtenberger, C. A. Murillo, L. O. Van Dorn, and C. C. Wilkinson. "Closed-Shell Molecules That Ionize More Readily Than Cesium". In: *Science* 298.5600 (2002), pp. 1971–1974. ISSN: 0036-8075. DOI: 10.1126/science.1078721.

[198] M. L. Tietze. "Molecular Doping Processes inOrganic Semiconductors investigatedby Photoelectron Spectroscopy". PhD thesis. Institut for Applied Photophysics, 2014.

[199] P. Bhattacharya, R. Fornari, and H. Kamimura. *Comprehensive Semiconductor Science and Technology*. Elsevier Science, 2011. ISBN: 9780444531438.

[200] CRC press. *CRC Handbook of Chemistry and Physics*. Taylor & Francis Ltd, 2018. ISBN: 1138561630.

[201] J. Robertson. "High dielectric constant oxides". In: *European Physics Journal Applied Physics* 28.3 (2004), pp. 265–291. DOI: `10.1051/epjap:2004206`.

[202] C. Osburn and D. Ormond. "Dielectric Breakdown in Silicon Dioxide Films on Silicon". In: *Journal of Electrochemical Society* 119.5 (1972), pp. 591–597. DOI: `10.1149/1.2404268`.

[203] M. Groner, J. Elam, F. Fabreguette, and S. George. "Electrical characterization of thin Al2O3 films grown by atomic layer deposition on silicon and various metal substrates". In: *Thin Solid Films* 413.1 (2002), pp. 186–197. ISSN: 0040-6090. DOI: `10.1016/S0040-6090(02)00438-8`.

[204] D. Braga, N. Battaglini, A. Yassar, G. Horowitz, M. Campione, A. Sassella, and A. Borghesi. "Bulk electrical properties of rubrene single crystals: Measurements and analysis". In: *Phys. Rev. B* 77 (11 Mar. 2008), p. 115205. DOI: `10.1103/PhysRevB.77.115205`.

[205] S. Seo, B.-N. Park, and P. G. Evans. "Ambipolar rubrene thin film transistors". In: *Applied Physics Letters* 88.23 (2006), p. 232114. DOI: `10.1063/1.2210294`.

[206] D. E. Henn, W. G. Williams, and D. J. Gibbons. "Crystallographic data for an orthorhombic form of rubrene". In: *Journal of Applied Crystallography* 4.3 (June 1971), p. 256. DOI: `10.1107/S0021889871006812`.

[207] S. Tavazzi, L. Silvestri, M. Campione, A. Borghesi, A. Papagni, P. Spearman, A. Yassar, A. Camposeo, and D. Pisignano. "Generalized ellipsometry and dielectric tensor of rubrene single crystals". In: *Journal of Applied Physics* 102.2 (2007), p. 023107. DOI: `10.1063/1.2759188`.

[208] J. M. Kim, J. Oh, K.-M. Jung, K. Park, J.-H. Jeon, and Y.-S. Kim. "Ultrathin flexible thin film transistors with CYTOP encapsulation by debonding process". In: *Semiconductor Science and Technology* 34.7 (June 2019), p. 075015. DOI: `10.1088/1361-6641/ab2201`.

[209] D. D. T. Mastrogiovanni, J. Mayer, A. S. Wan, A. Vishnyakov, A. V. Neimark, V. Podzorov, L. C. Feldman, and E. Garfunkel. "Oxygen Incorporation in Rubrene Single Crystals". In: *Scientific Reports* 4.4753 (2014). DOI: `10.1038/nmat1426`.

[210] S. Meister. "Towards an Electrically Pumped Organic Solid State Laser". PhD thesis. Institut for Applied Physics, 2019.

[211] E. Fumagalli, L. Raimondo, L. Silvestri, M. Moret, A. Sassella, and M. Campione. "Oxidation Dynamics of Epitaxial Rubrene Ultrathin Films". In: *Chemistry of Materials* 23.13 (2011), pp. 3246–3253. DOI: `10.1021/cm201230j`.

[212] J. C. Scott. "Metal–organic interface and charge injection in organic electronic devices". In: *Journal of Vacuum Science & Technology A* 21.3 (2003), pp. 521–531. DOI: 10.1116/1.1559919.

[213] L. Zhang, L. Wang, W. Wu, and M. Chan. "Modeling Current–Voltage Characteristics of Bilayer Organic Light-Emitting Diodes". In: *IEEE Transactions on Electron Devices* 66.1 (Jan. 2019), pp. 139–145. ISSN: 1557-9646. DOI: 10.1109/TED.2018.2843681.

[214] S.-K. Kim, D.-H. Chung, J.-W. Hong, T.-G. Chung, H.-S. Lee, J.-W. Park, T.-W. Kim, M.-J. Song, and W.-S. Choi. "Current-Voltage Characteristics of Organic Light-Emitting Diodes Depending on the Application of Forward-Reverse Bias Voltage". In: *Molecular Crystals and Liquid Crystals* 377.1 (2002), pp. 133–136. DOI: 10.1080/713738546.

[215] P. Kumar, S. Jain, V. Kumar, A. Misra, S. Chand, and M. Kamalasanan. "Current–voltage characteristics of an organic diode: Revisited". In: *Synthetic Metals* 157.22 (2007), pp. 905–909. ISSN: 0379-6779. DOI: https://doi.org/10.1016/j.synthmet.2007.08.021.

[216] S. Z. Bisri, T. Takenobu, T. Takahashi, and Y. Iwasa. "Electron transport in rubrene single-crystal transistors". In: *Applied Physics Letters* 96.18 (2010), p. 183304. DOI: 10.1063/1.3419899.

[217] A. Saeki, S. Seki, T. Takenobu, Y. Iwasa, and S. Tagawa. "Mobility and Dynamics of Charge Carriers in Rubrene Single Crystals Studied by Flash-Photolysis Microwave Conductivity and Optical Spectroscopy". In: *Advanced Materials* 20.5 (2008), pp. 920–923. DOI: 10.1002/adma.200702463.

[218] V. Skrypnychuk, G.-J. A. H. Wetzelaer, P. I. Gordiichuk, S. C. B. Mannsfeld, A. Herrmann, M. F. Toney, and D. R. Barbero. "Ultrahigh Mobility in an Organic Semiconductor by Vertical Chain Alignment". In: *Advanced Materials* 28.12 (2016), pp. 2359–2366. DOI: 10.1002/adma.201503422.

[219] H. M. Lee, H. Moon, H.-S. Kim, Y. N. Kim, S.-M. Choi, S. Yoo, and S. O. Cho. "Abrupt heating-induced high-quality crystalline rubrene thin films for organic thin-film transistors". In: *Organic Electronics* 12.8 (2011), pp. 1446–1453. ISSN: 1566-1199. DOI: https://doi.org/10.1016/j.orgel.2011.05.015.

[220] Z. Rang, M. I. Nathan, P. P. Ruden, V. Podzorov, M. E. Gershenson, C. R. Newman, and C. D. Frisbie. "Hydrostatic pressure dependence of charge carrier transport in single-crystal rubrene devices". In: *Applied Physics Letters* 86.12 (2005), p. 123501. DOI: 10.1063/1.1875761.

[221] S. Kasap and P. Capper. *Springer Handbook of Electronic and Photonic Materials. Single-Crystal Silicon: Growth and Properties*. Springer, Cham, 2017. ISBN: 9783319489315.

[222] K. Haase, C. Teixeira da Rocha, C. Hauenstein, Y. Zheng, M. Hambsch, and S. C. B. Mannsfeld. "High-Mobility, Solution-Processed Organic Field-Effect Transistors from C8-BTBT:Polystyrene Blends". In: *Advanced Electronic Materials* 4.8 (2018), p. 1800076. DOI: 10.1002/aelm.201800076.

[223] M. Lehnhardt, S. Hamwi, M. Hoping, J. Reinker, T. Riedl, and W. Kowalsky. "Charge carrier densities in chemically doped organic semiconductors verified by two independent techniques". In: *Applied Physics Letters* 96.19 (2010), p. 193301. DOI: 10.1063/1.3427416.

[224] D. Kiefer, R. Kroon, A. I. Hofmann, H. Sun, X. Liu, A. Giovannitti, D. Stegerer, A. Cano, J. Hynynen, L. Yu, Y. Zhang, D. Nai, T. F. Harrelson, M. Sommer, A. J. Moulé, M. Kemerink, S. R. Marder, I. McCulloch, M. Fahlman, S. Fabiano, and C. Müller. "Double doping of conjugated polymers with monomer molecular dopants". In: *Nature Materials* 18 (2019), pp. 1476–4660. DOI: 10.1038/s41563-018-0263-6.

[225] J.-M. Kim, S.-J. Yoo, C.-K. Moon, B. Sim, J.-H. Lee, H. Lim, J. W. Kim, and J.-J. Kim. "N-Type Molecular Doping in Organic Semiconductors: Formation and Dissociation Efficiencies of a Charge Transfer Complex". In: *The Journal of Physical Chemistry C* 120.17 (2016), pp. 9475–9481. DOI: 10.1021/acs.jpcc.6b01175.

[226] S. Züfle, S. Altazin, A. Hofmann, L. Jäger, M. T. Neukom, W. Brütting, and B. Ruhstaller. "Determination of charge transport activation energy and injection barrier in organic semiconductor devices". In: *Journal of Applied Physics* 122.11 (2017), p. 115502. DOI: 10.1063/1.4992041.

[227] B. Blülle, A. Troisi, R. Häusermann, and B. Batlogg. "Charge transport perpendicular to the high mobility plane in organic crystals: Bandlike temperature dependence maintained despite hundredfold anisotropy". In: *Phys. Rev. B* 93 (3 Jan. 2016), p. 035205. DOI: 10.1103/PhysRevB.93.035205.

[228] M. Ullah, T. B. Singh, H. Sitter, and N. S. Sariciftci. "Meyer–Neldel rule in fullerene field-effect transistors". In: *Applied Physics A* 97.3 (Sept. 2009), p. 521. ISSN: 1432-0630. DOI: 10.1007/s00339-009-5397-6.

[229] T. Minari, T. Nemoto, and S. Isoda. "Fabrication and characterization of single-grain organic field-effect transistor of pentacene". In: *Journal of Applied Physics* 96.1 (2004), pp. 769–772. DOI: 10.1063/1.1760237.

[230] X. Wang, T. Garcia, S. Monaco, B. Schatschneider, and N. Marom. "Effect of crystal packing on the excitonic properties of rubrene polymorphs". In: *CrystEngComm* 18 (38 2016), pp. 7353–7362. DOI: 10.1039/C6CE00873A.

[231] S. Scholz, D. Kondakov, B. Lüssem, and K. Leo. "Degradation Mechanisms and Reactions in Organic Light-Emitting Devices". In: *Chemical Reviews* 115.16 (2015). PMID: 26230864, pp. 8449–8503. DOI: 10.1021/cr400704v.

[232] C.-K. Lu and H.-F. Meng. "Hole doping by molecular oxygen in organic semiconductors: Band-structure calculations". In: *Phys. Rev. B* 75 (23 June 2007), p. 235206. DOI: `10.1103/PhysRevB.75.235206`.

[233] J. T. Ly, S. A. Lopez, J. B. Lin, J. J. Kim, H. Lee, E. K. Burnett, L. Zhang, A. Aspuru-Guzik, K. N. Houk, and A. L. Briseno. "Oxidation of rubrene, and implications for device stability". In: *J. Mater. Chem. C* 6 (14 2018), pp. 3757–3761. DOI: `10.1039/C7TC05775J`.

[234] S. Sinha, C.-H. Wang, M. Mukherjee, T. Mukherjee, and Y.-W. Yang. "Oxidation of Rubrene Thin Films: An Electronic Structure Study". In: *Langmuir* 30.51 (2014). PMID: 25383646, pp. 15433–15441. DOI: `10.1021/la503357t`.

[235] L. Raimondo, S. Trabattoni, M. Moret, N. Masciocchi, M. Masino, and A. Sassella. "Oxidation of Crystalline Rubrene Films: Evidence of an Epitaxial Native Oxide Layer". In: *Advanced Materials Interfaces* 4.23 (2017), p. 1700670. DOI: `10.1002/admi.201700670`.

[236] A. Fischer, M. Pfalz, K. Vandewal, S. Lenk, M. Liero, A. Glitzky, and S. Reineke. "Full Electrothermal OLED Model Including Nonlinear Self-heating Effects". In: *Phys. Rev. Applied* 10 (1 July 2018), p. 014023. DOI: `10.1103/PhysRevApplied.10.014023`.

[237] P. Irkhin, H. Najafov, and V. Podzorov. "Steady-state photoconductivity and multi-particle interactions in high-mobility organic semiconductors". In: *Scientific Reports* 5.15323 (2015). DOI: `10.1038/srep15323`.

[238] V. I. Arkhipov, V. A. Kolesnikov, and A. I. Rudenko. In: *Journal of Physics D: Applied Physics* 17.6 (June 1984), pp. 1241–1254. DOI: `10.1088/0022-3727/17/6/021`.

[239] C. Vijila, S. P. Singh, E. Williams, P. Sonar, A. Pivrikas, B. Philippa, R. White, E. Naveen Kumar, S. Gomathy Sandhya, S. Gorelik, J. Hobley, A. Furube, H. Matsuzaki, and R. Katoh. "Relation between charge carrier mobility and lifetime in organic photovoltaics". In: *Journal of Applied Physics* 114.18 (2013), p. 184503. DOI: `10.1063/1.4829456`.

[240] D. Taguchi, T. Shino, X. Chen, L. Zhang, J. Li, M. Weis, T. Manaka, and M. Iwamoto. "Analyzing carrier lifetime of double-layer organic solar cells by using optical electric-field-induced second-harmonic generation measurement". In: *Applied Physics Letters* 98.13 (2011), p. 133507. DOI: `10.1063/1.3574002`.

[241] G. Garcia-Belmonte, A. Munar, E. M. Barea, J. Bisquert, I. Ugarte, and R. Pacios. "Charge carrier mobility and lifetime of organic bulk hetero-junctions analyzed by impedance spectroscopy". In: *Organic Electronics* 9.5 (2008), pp. 847–851. ISSN: 1566-1199. DOI: `https://doi.org/10.1016/j.orgel.2008.06.007`.

[242] A. Fischer, T. Koprucki, K. Gärtner, M. L. Tietze, J. Brückner, B. Lüssem, K. Leo, A. Glitzky, and R. Scholz. "Feel the Heat: Nonlinear Electrothermal Feedback in Organic LEDs". In: *Advanced Functional Materials* 24.22 (2014), pp. 3367–3374. DOI: 10.1002/adfm.201303066.

[243] Y. H. Kim, S. Schubert, R. Timmreck, L. Müller-Meskamp, and K. Leo. "Collecting the Electrons on n-Doped Fullerene C60 Transparent Conductors for All-Vacuum-Deposited Small-Molecule Organic Solar Cells". In: *Advanced Energy Materials* 3.12 (2013), pp. 1551–1556. DOI: 10.1002/aenm.201300658.

[244] F. T. Antrack. "Organische lichtemittierende Dioden auf Basis hochkristalliner Rubrenschichten". BSc thesis. Dresden, Germany: Technische Universität Dresden, 2018.

[245] S. Meister, R. Brückner, M. Sudzius, H. Fröb, and K. Leo. "Optically pumped lasing of an electrically active hybrid OLED-microcavity". In: *Applied Physics Letters* 112.11 (2018), p. 113301. DOI: 10.1063/1.5016244.

[246] S. Meister, R. Brückner, M. Sudzius, H. Fröb, and K. Leo. "Intracavity metal contacts for organic microlasers". In: *Journal of Materials Research* 34.4 (2019), pp. 571–578. DOI: 10.1557/jmr.2018.457.

[247] A. S. D. Sandanayaka, T. Matsushima, F. Bencheikh, S. Terakawa, W. J. Potscavage, C. Qin, T. Fujihara, K. Goushi, J.-C. Ribierre, and C. Adachi. "Indication of current-injection lasing from an organic semiconductor". In: *Applied Physics Express* 12.6 (May 2019), p. 061010. DOI: 10.7567/1882-0786/ab1b90.

[248] D. H. Park, S. G. Jo, Y. K. Hong, C. Cui, H. Lee, D. J. Ahn, J. Kim, and J. Joo. "Highly bright and sharp light emission of a single nanoparticle of crystalline rubrene". In: *J. Mater. Chem.* 21 (22 2011), pp. 8002–8007. DOI: 10.1039/C1JM10530B.

[249] L. Ma, K. Zhang, C. Kloc, H. Sun, C. Soci, M. E. Michel-Beyerle, and G. G. Gurzadyan. "Fluorescence from rubrene single crystals: Interplay of singlet fission and energy trapping". In: *Phys. Rev. B* 87 (20 May 2013), p. 201203. DOI: 10.1103/PhysRevB.87.201203.

[250] W. L. Kalb, T. Mathis, S. Haas, A. F. Stassen, and B. Batlogg. "Organic small molecule field-effect transistors with Cytop gate dielectric: Eliminating gate bias stress effects". In: *Applied Physics Letters* 90.9 (2007), p. 092104. DOI: 10.1063/1.2709894.

[251] P. J. Diemer, Z. A. Lamport, Y. Mei, J. W. Ward, K. P. Goetz, W. Li, M. M. Payne, M. Guthold, J. E. Anthony, and O. D. Jurchescu. "Quantitative analysis of the density of trap states at the semiconductor-dielectric interface in organic field-effect transistors". In: *Applied Physics Letters* 107.10 (2015), p. 103303. DOI: 10.1063/1.4930310.

[252] M. Abbas, A. Pivrikas, E. Arici, N. Tekin, M. Ullah, H. Sitter, and N. S. Sariciftci. "Temperature dependent charge transport in organic field-effect transistors with the variation of both carrier concentration and electric field". In: *Journal of Physics D: Applied Physics* 46.49 (Nov. 2013), p. 495105. DOI: 10.1088/0022-3727/46/49/495105.

[253] S. Terao, T. Hirai, N. Morita, H. Maeda, K. Kojima, and M. Tachibana. "Temperature-dependent carrier mobility and threshold voltage of field-effect transistors with tetracene single crystals". In: *Journal of Applied Physics* 108.12 (2010), p. 124511. DOI: 10.1063/1.3499631.

[254] M. L. Tietze, B. D. Rose, M. Schwarze, A. Fischer, S. Runge, J. Blochwitz-Nimoth, B. Lüssem, K. Leo, and J.-L. Brédas. "Passivation of Molecular n-Doping: Exploring the Limits of Air Stability". In: *Advanced Functional Materials* 26.21 (2016), pp. 3730–3737. DOI: 10.1002/adfm.201505092.

[255] T. Menke, P. Wei, D. Ray, H. Kleemann, B. D. Naab, Z. Bao, K. Leo, and M. Riede. "A comparison of two air-stable molecular n-dopants for C60". In: *Organic Electronics* 13.12 (2012), pp. 3319–3325. ISSN: 1566-1199. DOI: https://doi.org/10.1016/j.orgel.2012.09.024.

Acronyms

AC Alternate Current. 72, 243, 253, 257, 258, 261–263, 292

AFM Atomic Force Microscopy. 104, 112, 115, 126, 140–143, 145, 147–152, 157, 158, 160–163, 165, 268, 269, 315, 354, 355, 360

ALD Atomic Layer Deposition. 94

ARUPS Angle Resolved Photo Electron Spectroscopy. 47

BJT Bipolar Junction Transistor. 13–15, 17, 48, 51, 54, 86–88, 91, 150, 232, 245, 287, 289, 293, 300, 301, 304–306, 317, 353

C8-BTBT 2,7 – Dioctyl[1]benzothieno[3,2 – b][1]benzothiophene. 47

Cf Capacitance-frequency. 106

CV Capacitance-Voltage. 106, 182, 200, 201, 203, 229, 230, 310

CVD Chemical Vapour Deposition. 96

DBR Distributed Bragg Reflector. 134, 135, 137, 138

DC Direct Current. 71, 72, 106, 109, 110, 171, 253–255, 257–259, 261, 262, 291, 292, 354

DOS Density of States. 184

DUT Device Under Test. 106, 107, 111

EDX Energy Dispersive X-ray spectroscopy. 316

EQE External Quantum Efficiency. 251, 252, 263, 265, 316

ETL Electron Transport Layer. 64

FET Field-Effect Transistor. 13, 14, 17, 27, 54, 72, 74, 77–79, 86, 87, 94, 159, 176, 253, 269, 278, 281, 284, 317, 353

FRET Förster Resonant Energy Transfer. 251

FTS fluoroalkyltrichrolosilane. 53

FWHM Full Width Half Maximum. 153, 251

GIWAXS Glancing Incident Wide-Angle X-Ray Spectroscopy. 316

GIXRD Grazing Incidence X-Ray Diffraction. 113, 114

HF High Frequency. 54, 65, 68, 71, 98, 104, 108

HMDS Hexamethyldisilazan. 95, 139, 140, 154

HOMO Highest Occupied Molecular Orbital. 64, 172

HTL Hole Transport Layer. 64

ITO Indium Tin Oxide. 130, 132, 134, 135, 137, 138, 143, 157, 207

IV Current-Voltage. 58–62, 68, 77, 79, 90, 167–171, 173, 174, 176, 177, 179–181, 184–190, 193–195, 200, 201, 203, 206–209, 215, 216, 218, 220, 222–224, 227, 230, 233, 235, 240, 241, 243, 244, 246–249, 251–254, 257–259, 261, 268, 269, 273–275, 278, 280, 281, 289, 290, 292, 298, 300, 302, 305–309, 315, 353, 356

LCAO Linear Combination of Atomic Orbitals. 18

LUMO Lowest Unoccupied Molecular Orbital. 64, 182

MIS Metal-Insulator-Semiconductor. 74, 353

MOSFET Metal-Oxide-Semiconductor Field-Effect Transistor. 13, 72

MSM Metal-Semiconductor-Metal. 167, 170, 171, 173, 175, 177–179, 185, 186, 188, 190, 193, 195, 196, 200, 202–206, 208, 209, 215, 221

OBJT Organic Bipolar Junction Transistor. 7, 14, 15, 87, 91, 160, 263, 267, 279, 287, 288, 290, 291, 298–300, 304–308, 310, 315–319

ODPA n-Octadecylphosphonic acid. 95, 154

OFET Organic Field-Effect Transistor. 7, 14, 15, 45, 73, 77, 84, 85, 87, 103, 267–269, 271–281, 283, 284, 318

OLED Organic Light Emitting Diode. 14, 15, 53, 63, 64, 215, 232, 243, 250–252, 263, 265, 316, 321, 357

OPBT Organic Permeable Base Transistor. 85, 279

OSC Organic Solar Cell. 250

PEB Post Exposure Bake. 100

PGMEA Propylene Glycol Methyl Ether Acetate. 103

POEM Electric Potential Mapping by Thickness Variation. 63

PVD Physical Vapour Deposition. 96

QCM Quartz Crystal Microbalance. 96, 97

RFID Radio Frequency Identification. 65

RMS Root Mean Square. 116, 141

List of Figures

List of Tables

Statement of authorship

I herewith declare that I have produced this paper without the prohibited assistance of third parties and without making use of aids other than those specified; notions taken over directly or indirectly from other sources have been identified as such. This paper has not previously been presented in identical or similar form to any other German or foreign examination board.

Dresden, 2020/04/18

Franz Michael Sawatzki